GEOLOGICAL SURVEY OF CANADA
OPEN FILE 8358

Targeted Geoscience Initiative:
2017 report of activities, volume 1

N. Rogers (ed.)

2018

Canada

GEOLOGICAL SURVEY OF CANADA
OPEN FILE 8358

Targeted Geoscience Initiative:
2017 report of activities, volume 1

N. Rogers (ed.)

2018

Permanent link: https://doi.org/10.4095/306391

This publication is available for free download through GEOSCAN (http://geoscan.nrcan.gc.ca/).

Targeted Geoscience Initiative:
2017 report of activities, volume 1

Edited and compiled by
Neil Rogers

Uranium-rich ore systems project: Subproject 1 – Uranium fluid pathways

Gold project: Subproject 1 – System controls on gold through time and space (source to trap)

Gold project: Subproject 2 – Tectonic influences on gold deposits (tectonic drivers and conduits)

Ni-Cr-PGE ore systems project: Subproject 1 – System scale and deposit scale controls on Ni-Cu-PGE mineralization in cratonic areas and their margins

Volcanic- and sedimentary-hosted base metal mineralization project: Subproject 1 – Seafloor ore deposition through space and time

Volcanic- and sedimentary-hosted base metal mineralization project: Subproject 2 – Base metal sources and mineralizing processes

Foreword – Targeted Geoscience Initiative: 2017 report of activities

N. Rogers

Geological Survey of Canada, 601 Booth Street, Ottawa, Ontario, K1A 0E8

The Targeted Geoscience Initiative (TGI) is a Government of Canada led geoscience research program that is directed towards providing next generation knowledge and methods to facilitate more effective targeting of buried mineral deposits. The program aims to enhance the effectiveness of exploration for Canada's major mineral systems by resolving foundational geoscience problems that constrain the geological processes responsible for the liberation metals from their source region, transportation of these ore metals and control their eventual deposition. In the course of this research TGI will mentor and assist in the training of students who will become the next generation of highly qualified personnel available to the mineral exploration industry.

TGI uses a thematic, 'ore system' approach, whereby an ore system is defined as a mineralized system across a range of scales that culminates in a group of related deposits sharing common genetic and geologic characteristics. At the large scale, an ore system is defined by the geodynamic and tectonic settings that result in ore deposition. Ore deposits within an ore system can differ in style, position in the crust and timing, but share common causative ore-forming processes and controlling parameters. For the TGI program, four aspects of the ore system concept are more specifically addressed, namely: what terrane, region or geological/tectonic setting to look in; where to look in a specific terrane, region or geological/tectonic setting; how to vector towards mineralized rocks; and detection methods.

The thematic, ore systems approach to research program design enables TGI to conduct its research on the best-suited areas, districts and deposits from across Canada to support, develop and test next generational geoscience knowledge. TGI supports projects on gold, Ni-Cr-PGE, porphyry-style mineralization, uranium and volcanic- and sedimentary-hosted base metal mineralization ore systems, with each project divided into subprojects focused on resolving specific knowledge gaps by integrating data and studies from multiple sites across Canada. Herein, we present interim results and interpretations from a selection of the research activities currently being conducted under the auspices of TGI.

Wireline logging and distributed acoustic sensing VSP to characterize host rocks and alteration of porphyry deposits: Preliminary results from the New Afton mine

G. Bellefleur[1], E.M. Schetselaar[1], D. Wade[2] and D. White[1]

[1]*Geological Survey of Canada, 601 Booth St., Ottawa, Ontario, K1A 0E8*
[2]*New Afton Mine, 4050 West Trans Canada HWY, Kamloops, British Columbia, V1S 2A3*

Abstract

Wireline logs and vertical seismic profile (VSP) data were acquired in two boreholes intersecting the Cu-Au New Afton porphyry deposit located near Kamloops, British Columbia. The wireline logs and VSP data are components of an integrated geophysical imaging and 3D geological modelling study that aims to improve knowledge of the role of magmatic hydrothermal processes and structural controls in concentrating metals in porphyry deposits. Log data provide physical rock properties for the propylitic, phyllic, and potassic alteration zones. Both propylitic and phyllic zones are characterized by a broad distribution of density and P-wave velocities whereas the feldspar-dominant potassic alteration zone has generally high velocities. The VSP survey was conducted with a distributed acoustic sensing (DAS) system that utilized fibre-optic cables cemented in two boreholes at the New Afton mine. Fibre-optic cables comprised standard and Constellation™ fibres in both straight and helically-wound configurations for comparison purposes. Seismic sources consisted of fifty shot points each loaded with one kilogram of pentolite explosive placed in a 20 m deep shot hole. VSP data from both types of fibre show clear down going waves and reflections although signal-to-noise ratio is significantly higher on the Constellation™ fibre-optic cable. A preliminary analysis of VSP data from one shot point shows reflections possibly associated with the potassic zone and the picrite unit located just below the bottom of the borehole.

Introduction

The Geological Survey of Canada's Targeted Geoscience Initiative is developing an integrated geophysical imaging and 3D geological modelling research study of the New Afton porphyry deposit located in the Canadian Cordillera of south-central British Columbia. This alkaline copper-gold porphyry deposit previously supported an open pit operation and is currently being mined at deeper levels through underground workings, providing geological constraints extending beyond 1.5 km in depth. The study intends to combine new vertical seismic profile (VSP) and 3D magneto-telluric (MT) surveys, along with multi-parameter deep drillhole geophysical logs, and 3D modelling to elucidate the magmatic hydrothermal processes and structural controls responsible for concentrating metals in porphyry deposits. Here, we present acoustic and elastic rock properties from wireline logs and show preliminary results from a VSP survey acquired with a distributed acoustic sensing (DAS) system deployed in two boreholes that intersect the main mineralized zone. The two boreholes are intersecting the porphyry alteration halo with a gradual but not necessarily homogeneous increase of alteration intensity towards the mineralized zone. The wireline logs and DAS data also provide information on lithology and fault zones.

Geology

This summary of the local mine geology is based on drill core logging, 3D geological modelling and surface mapping recently conducted by New Gold (Lipske and Wade, 2014; Bergen et al., 2015). Figure 1 summarizes this description of the geology by showing a plan view of the main lithologies and alteration zones. The copper-gold New Afton porphyry deposit is dominantly hosted by fragmental and crystalline volcanic rocks (BXF) of the Late Triassic Nicola Formation and to a lesser extent by the 204 Ma Cherry Creek monzonite of the Iron Mask batholith. The latter is interpreted to be the heat source that caused alteration and mineralization in this alkalic porphyry (Lipske and Wade, 2014). A subvertical southwest-plunging zone of primary hypogene mineralization, largely coincident with the potassic alteration zone, contains disseminated chalcopyrite and bornite (Lipske and Wade, 2014). This hypogene ore zone is controlled structurally by two subvertical northeast striking fault zones, known as the footwall and hanging wall faults. The hanging wall fault, juxtaposes BXF with a subvertical body of serpentinized picrite (Lipske and Wade, 2014). This tectonic contact is within the incompetent serpentinized picrite defined by a high strain zone of ductile deformation rich in magnetite and locally confines a zone of calcic alteration composed of magnetite, epidote, ac-
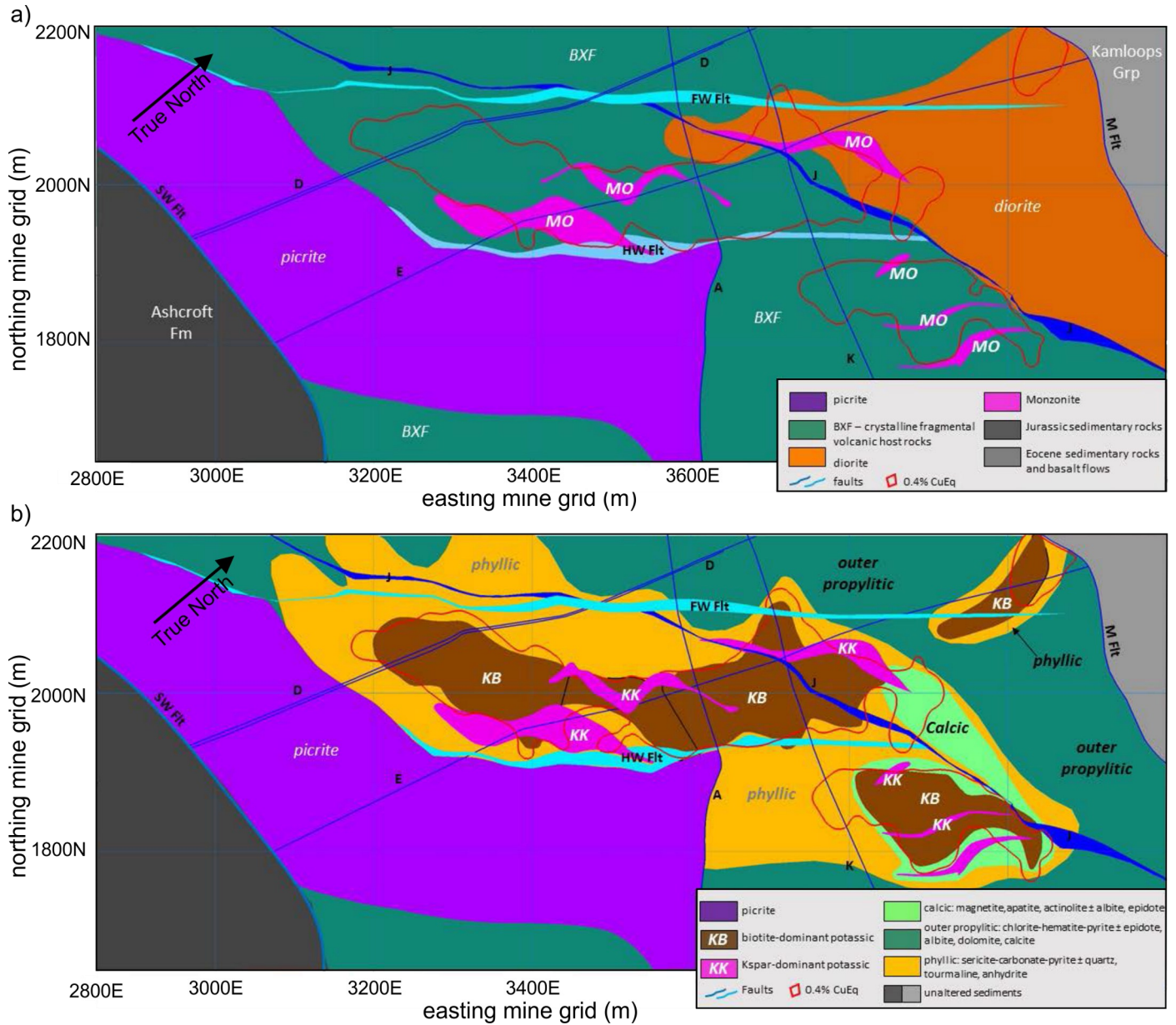
Figure 1. a) Plan view of the main lithological units and b) main alteration zones at New Afton. The main hypogene mineralized zone is outlined in red with no colour fill and is associated with the biotite-dominant and feldspar-dominant potassic alteration zone. Units are in mine grid coordinates (from Lipske and Wade, 2014).

tinolite and apatite (Lipske and Wade, 2014). The primary hypogene ore zone is cut by numerous moderately to steeply dipping fault zones that control secondary hypogene mineralization of tetrahedrite and tennantite. Supergene mineralization of native copper and chalcocite in hematite-rich oxidation zones is more abundant at higher structural levels in the vicinity of the open pit but native copper extends to 700 m below surface beneath the pit along older, long-lived structures (Lipske and Wade, 2014; Bergen et al., 2015).

Wireline logging

Wireline logs were acquired in June and July 2017 in two boreholes (EA16-171 and EA17-197) collared underground approximately 650 m below the surface. The two boreholes start from the same drill bay but have different dip and azimuth. Borehole EA1-197 has a length of 701 m whereas EA16-171 is 870 m long. Both boreholes intersect numerous faults that tend to cave in open drill holes, a factor that significantly complicated acquisition of the wireline logs Both boreholes. A

drill rig was used to ream out and maintain boreholes open for the entire duration of the logging program. Logging was conducted in short open-hole sections starting from the bottom of the borehole while drill rods covered unstable areas above the interval being measured. Drill rods were then lifted to uncover the next interval of stable open hole for logging. Probes were not deployed over larger fault zones or caved sections. Logging measurements included calliper, density, natural and spectral gamma-ray spectrometry, magnetic susceptibility, resistivity, induced polarization, induction conductivity, and full-waveform sonic logs. All wireline logs will be calibrated with petrophysical measurements on drill core samples (ongoing). Density measurements were conducted through drill rods and subsequently calibrated with values measured over a short section of stable open hole. This approach minimized the risk of having the radioactive source used for density measurements stuck in a borehole.

Figure 2 presents some logs for borehole EA17-197 plotted together with the main fault zones, alteration, and lithological units from drill core geological logging conducted by New Gold. In general, density and velocity values vary significantly especially in the upper part of the borehole. Some of this variability is due to faults and caved zones indicated by large values on the calliper log. The large values on the calliper log correlate with low density and to some extent with lower velocity values on P- and S-wave velocity logs. Some variations occur over depth intervals corresponding to one lithology and one type of alteration (for example near 400 m). The cause of those variations still need to be investigated. The lower part of EA17-197 shows fewer faults or caved zones. Latite dikes near 560 m are characterized by lower P- and S-wave velocities. Below 560 m, the sonic logs show higher P- and S-wave velocities with less variability than for rocks above. This deepest interval comprises the potassic alteration zone (KK and KB on Figure 2).

Figure 3 shows P-wave velocities and densities for the various alteration types intersected in the borehole. Also shown on this figure are ellipses from principal component analysis representing the mean and scaled eigenvectors of the covariance matrix of the distribution of each alteration type. The major
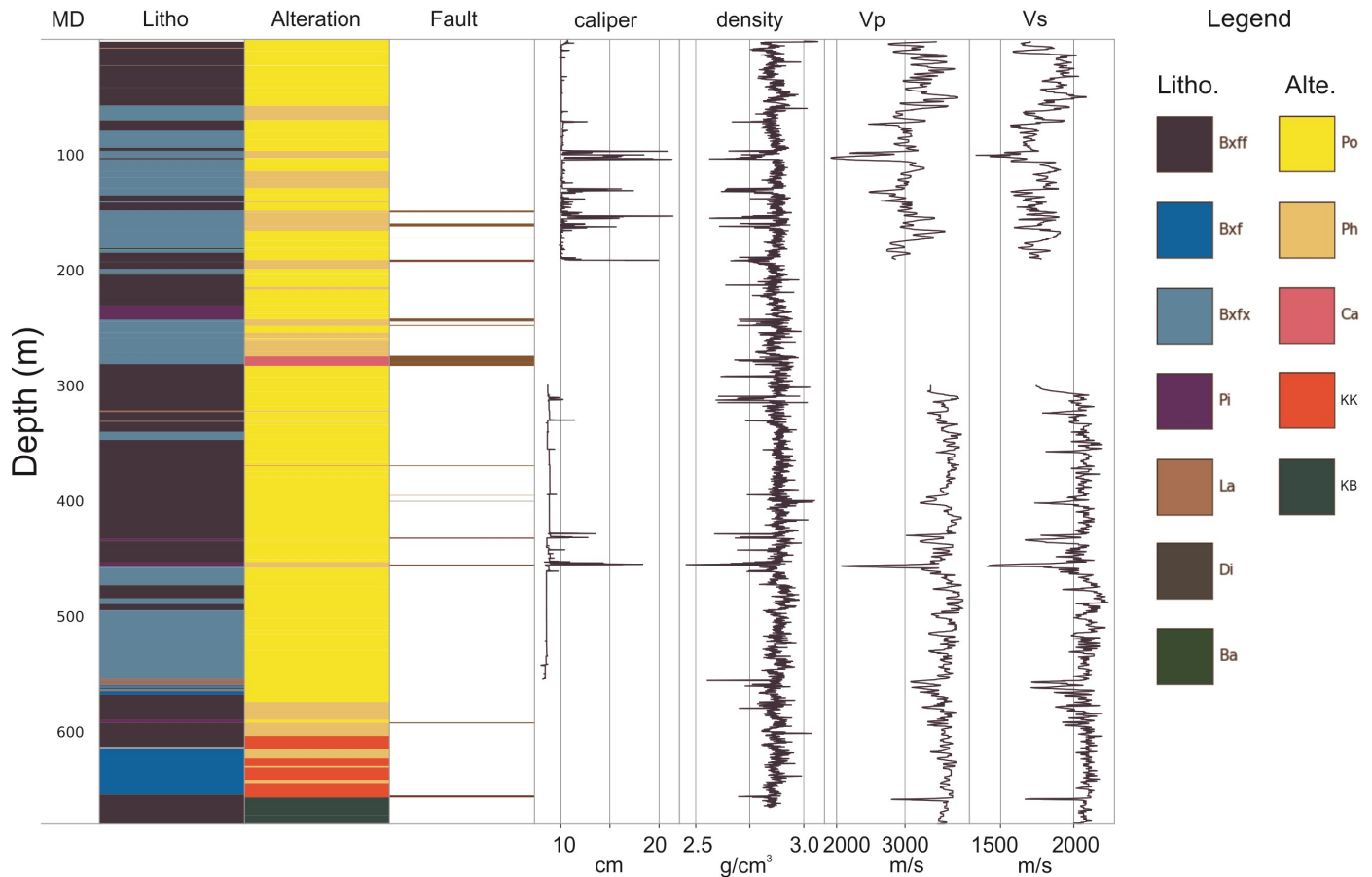
Figure 2. Wireline logging data in borehole EA17-197. Tracks from left to right show, meters, lithology, alteration, faults, calliper, density, P-wave and S-wave velocity. Bxf: volcanic fragmental; Bxfx: crystalline Bxf; Bxff: fragmental Bxf; Pi: picrite; La: latite; Di: diorite; Ba: basalt; Po: propylitic; Ph: phyllic; Ca: calcic; Kk: feldspar-dominant potassic; Kb: biotite-dominant potassic.
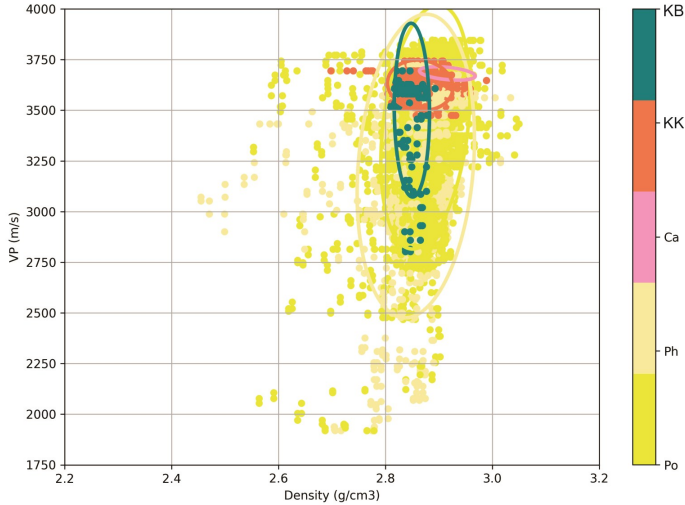
Figure 3. Velocity versus density for different types of altera-
tion in EA17-197. Main axis of ellipses represent two
standard deviations (from principal component analysis).

and minor axes of the ellipses correspond to two standard devi-
ations. Both propylitic and phyllic alteration zones have broad
distributions of density and velocity values. The feldspar-
dominant potassic zone (KK on Figure 3) is characterized by
higher P-wave velocities and relatively high densities. This
suggests that the feldspar-dominant potassic alteration zone
may be detectable on VSP data when juxtaposed against rocks
characterized with lower acoustic impedances. Logging data
presented in Figure 2 suggest this is a possibility in EA17-197
as rocks above the potassic zone have similar densities, but
slightly lower velocities.

VSP with distributed acoustic sensing

One technical objective of the survey was to compare VSP
results obtained with different types of fibre-optic cables and to
assess their relative merits for mineral exploration. The two
boreholes surveyed with wireline logs were also instrumented
with fibre-optic cables for VSP-DAS recording. The fibre-optic
cables comprised straight standard single mode fibre and
straight Constellation[TM] single mode fibre (hereafter referred to
as Constellation). In addition, a helically-wound single mode
fibre-optic cable comprising both types of fibre was installed in
borehole EA16-171. Standard fibre-optic cables placed in the
two boreholes were "daisy-chained" together to form an ap-
proximately 5 km long continuous fibre combining the straight
and helically-wound cables. The Constellation fibre-optic ca-
bles were also daisy-chained together. All fibre-optic cables
were cemented in boreholes to provide optimal coupling with
rock formations. DAS technology has been used previously for
oil and gas applications (Daley et al., 2014; Harris et al., 2016)
and for mineral exploration (Riedel et al., 2017; Urosevic et al.,
2017). Results from our survey at New Afton are the first VSP
data for mineral exploration obtained with straight and helical-

ly-wound Constellation fibre-optic cables. The latter was de-
ployed to ensure omnidirectional sensing capability of the vari-
ous potential wavefield modes and wave propagation direc-
tions.

Figure 4 shows a map of the survey area with locations of
shot points and surface projection of the two boreholes and the
main hypogene mineralized zone. The mine site has a variety
of infrastructure including mills, offices, subsidence zones, and
tailing pounds that restricted areas where seismic sources could
be deployed. The open pit of the old Afton mine was avoided
due to slope stability issues. In addition, the trans-Canada high-
way, two pipelines, numerous power lines, and concerns raised
to protect a vulnerable spadefoot toad species were addressed
during the planning of the survey. The survey included 50 shot
locations located in four clusters. Most shot points are located
in a cluster west of the open pit, which should contribute to
image the extent of lithological units and alteration zones west
of the two boreholes. Other shot locations will help define ve-
locities and also contribute to seismic imaging. At each source
location, one kilogram of pentolite explosive with two elec-
tronic detonators was placed in a 20 m deep shot hole. Each
shot hole was tamped with 90 kg of bentonite mixed with water
and drilling sand.

Two different distributed acoustic sensing recording sys-
tems were used for the VSP survey; one for the standard fibre-
optic cables (hereinafter referred to as V2) and one for the
Constellation fibre-optic cables (V3 – also referred to as the
Carina® sensing system). Constellation fibre-optic cable com-
bined with the V3 recording unit provides seismic data with
higher signal-to-noise ratio whereas the helically-wound fibre-
optic cable has enhanced transverse sensitivity relative to
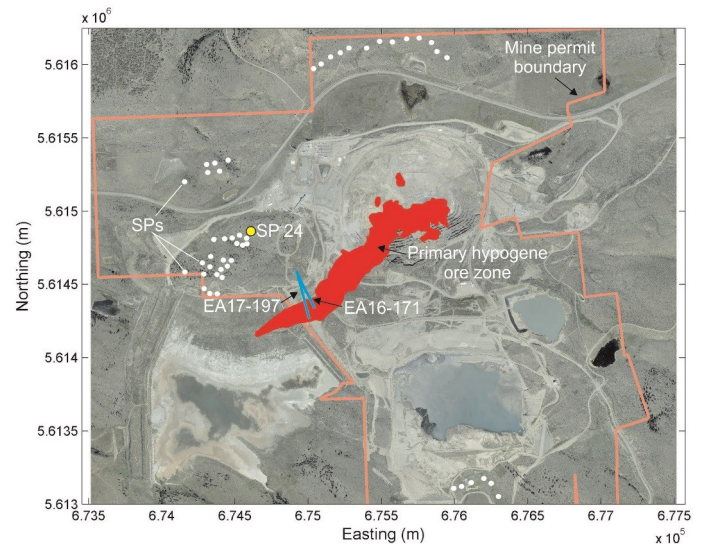
Figure 4. Map showing surface location of seismic shot points
(white dots), surface projection of two boreholes, and sur-
face projection of the hypogene mineralized zone (in red).
VSP data from shot point 24 are shown in Figure 5.
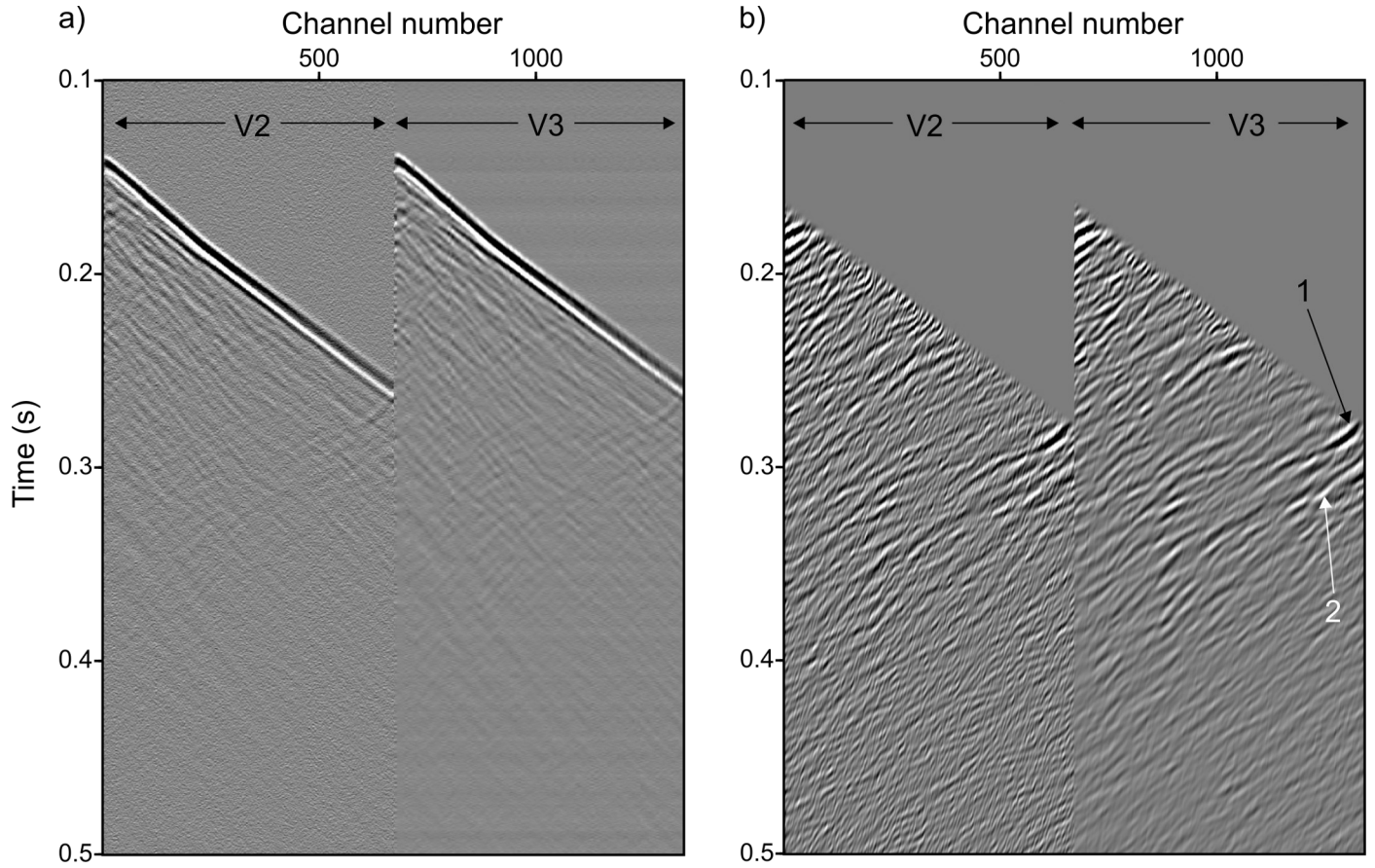
Figure 5. Comparison of V2 and V3 DAS data in EA17-197. a) Field data without any processing showing strong down going waves and some reflections. Both V2 and V3 data have the same gain for display. Signal-to-noise ratio is lower for the standard fibre-optic cable. b) Reflections and other up going signal after the application of a fk-filter and muting of first breaks. Arrows point to reflections discussed in the text. V2 data on this figure are sampled at 1 m interval (one channel corresponds to 1 m). The first channel is at 116 m above sea level, approximately 600 m below surface.

straight cable (Kuvshinov, 2016) which is most sensitive to wavefields that exert longitudinal strain on the fibre. Seismic waves generated at each source location were recorded every 0.25 m along the standard fibre-optic cable and every 1 m along the Constellation fibre-optic cable using a sampling rate of 0.5 ms. Synchronization between surface shots and underground DAS recording units was done with GPS time. A high-precision clock synchronized at surface with GPS time was brought underground and used to keep the time of continuous seismic records. At surface, the GPS time stamp was saved at the firing time of each shot point and served as the basis to extract shot gathers from continuous DAS recording. Three days of ambient noise were also recorded for seismic interferometry analysis prior to the survey with explosives. All VSP-DAS data were acquired in August 2017.

Figure 5 shows the field data acquired for the straight fibre-optic cable in borehole EA16-171 for shot point 24 (see Figure 4 for location of shot point). Figure 5a compares the field rec-

ords for both V2 and V3 systems (same gain for display). Both V2 and V3 data show clear down going waves and some reflections. Signal-to-noise ratio is significantly higher for V3 data. Figure 5b shows the same data after the application of an fk-filter to remove down going waves and first break muting. Several reflections are observed on both V2 and V3 data. V3 data show more detail and clearer reflections again due to the higher signal-to-noise ratio. Reflections 1 and 2 on Figure 5 are possibly associated with the potassic zone and the picrite unit located just below the bottom of the borehole. However, this is a tentative interpretation of preliminary data.

Discussion

Several factors complicated the acquisition of the borehole logging data and VSP-DAS data at New Afton. One of the most important complications was the instability of the boreholes that required the use of a drill rig. Open-hole deployment of any instrument over the entire length of the two boreholes

used in this work was simply not possible. The difficult borehole conditions increased the time required to complete the wireline logging program (by about three times). A VSP survey with a string of conventional geophones would have also required a significant amount of time. To this end, the utilisation of DAS simplified greatly the logistics and effort required to collect the VSP data. This also includes the use of only one dynamite charge per shot location, which reduced the cost of survey and simplified the permitting process to use explosives for seismic surveying on the mine site. For example, 58 shots per source location would have been required using a conventional wireline system with 12 levels to obtain data with receiver spacing similar to the V3 data shown in Figure 5.

Summary

Wireline logs and VSP data were acquired in two boreholes intersecting the Cu-Au New Afton porphyry deposit located near Kamloops, BC. Logging data provide physical rock properties for the propylitic, phyllic, and potassic alteration zones. Both propylitic and phyllic zones are characterized by a large distribution of density and P-wave velocities whereas the feldspar-dominant potassic alteration has similar densities but generally higher velocities. The VSP data used distributed acoustic sensing of fibre-optic cables cemented in two boreholes. Fibre-optic cables comprised standard and Constellation fibres in both straight and helically-wound configurations for comparison purposes. Seismic sources consisted of fifty shot points each loaded with one kilogram of pentolite explosive placed in a 20 m deep shot hole. VSP data from both types of fibre show clear down going waves and reflections although signal-to-noise ratio is significantly higher on the Constellation fibre-optic cable. A preliminary analysis of VSP data from one shot point shows reflections possibly associated with the potassic zone and the picrite unit located just below the bottom of the borehole.

Acknowledgments

References

Bergen, D., Krutzlmann, H., and Rennie, D.W., 2015. New Afton Project, Project #2400; New Gold Inc., Technical Report NI 43-101, 256 p.

Daley, T.M., White, D., Miller, D.E., Robertson, M., Freifeld, B.M., Herkenhoff, F., and Cocker, J., 2014. Simultaneous acquisition of distributed acoustic sensing VSP with multimode and single-mode fiber optic cables and 3-component geophones at the aquistore CO_2 storage site; SEG Technical Program Expanded Abstracts 2014, p. 5014–5018.

Harris, K., White, D., Melanson, D., Samson, C., and Daley, T., 2016, Feasibility of time-lapse VSP monitoring at the Aquistore CO_2 storage site using a distributed acoustic sensing system; International Journal of Greenhouse Gas Control, v. 50, p. 248–260.

Kuvshinov, B.N., 2016. Interaction of helically wound fibre-optic cables with plane seismic waves; Geophysical Prospecting, v. 64, p. 671–688.

Lipske, J. and Wade, D., 2014. Geological model of the New Afton copper and gold deposit, British Columbia; New Gold Inc., Internal Report, 53 p.

Riedel, M., Cosma, C., Komminaho, K., Enescu, N., Koivisto, E., Malinowski, M., Luhta, T., Juurela, S., and COGITO-MIN Working Group, 2017. Seismic imaging of the Kylylahti Cu-Au-Zn ore deposit using conventional and DAS VSP measurements supported by 3D full-waveform seismic modeling; *in* Proceedings of Exploration 17: Seismic Methods & Exploration Workshop, (ed.) G. Bellefleur and B. Milkereit; Decennial Mineral Exploration Conferences, Toronto, Ontario, p. 57–63.

Urosevic, M., Bona, A., Ziramov, S., Pevzner, R., Kepic, A., Egorov, A., Kinkela, J., Pridmore, D., and Dwyer, J., 2017. Seismic for mineral resources – a mainstream method of the future; *in* Proceedings of Exploration 17: Seismic Methods & Exploration Workshop, (ed.) G. Bellefleur and B. Milkereit; Decennial Mineral Exploration Conferences, Toronto, Ontario, p. 1–5.

Preliminary field observations at the Klaza deposit and nearby Kelly and Cyprus porphyry centres, Dawson Range, Yukon

W.-S. Lee[1], J.B. Chapman[2] and J.P. Richards[1]

[1]*Harquail School of Earth Sciences, Laurentian University, 935 Ramsey Lake Road, Sudbury, Ontario, P3E 2C6*
[2]*Geological Survey of Canada, 605 Robson Street, Vancouver, British Columbia, V6B 5J3*

Abstract

The Klaza deposit is a structurally controlled, polymetallic gold-silver-base metal intermediate sulphidation epithermal system, located within the Dawson Range Gold Belt, central Yukon. The Klaza deposit has four zones with varying vein complexity, ore grade and interaction with local porphyritic quartz-feldspar ('QFP') dykes. This study aims to develop a clear understanding of the genesis and fluid evolution of the Klaza deposit. Preliminary field observations include that the high gold-grade intervals of stockwork and sheeted quartz pyrite veins display two dominant structural orientations and phyllic (quartz-pyrite-sericite) alteration. Massive quartz-pyrite ± chalcopyrite gold-bearing veins cut the stockwork and sheeted veins. Silver-rich base metal sulfide veins at Central Klaza cut both vein types, indicating an early, high grade gold mineralization event followed by a later Ag-rich event. The main mineralization stage is followed by late stage carbonate veins, which are largely unmineralized in the Central Klaza zone, but contain euhedral sphalerite and galena in the Western BRX zone. High resolution re-logging of drill core revealed subtle textural and compositional differences between dykes previously logged as undifferentiated 'QFP' across the Central Klaza zone. Three types of dyke compositions are distinguishable in the field based on quartz phenocryst abundance and cross cutting relationships. A Type 1 mafic dyke is cut by Stage 1 early quartz-pyrite veinlets. The Type 2 felsic dykes are cut by Stage 4 base metal veins, while the Type 3 intermediate dyke is in contact with Type 2 dykes and is uncut by mineralization.

Introduction

The Klaza deposit is a polymetallic Au-Ag-base metal intermediate sulphidation epithermal system, located within the Dawson Range Gold Belt, central Yukon (Fig. 1). It comprises structurally controlled composite veins adjacent to porphyritic quartz feldspar ('QFP') dykes (Ross et al., 2016). The deposit consists of four zones: Central Klaza; Central BRX; Western Klaza; and Western BRX. Veins within the Klaza zone occur as multiple, braided to anastomosed, distributed arrays, with varying vein widths and sulphide mineralization. BRX veins are more intimately related to the QFP dykes and are generally less numerous, but wider, and have higher total metal grade than the Klaza veins. Mineralized veins in both zones dominantly trend north-northwest, dipping approximately 50° to the southwest. The western mineralized zones are separated from the main zones by strike-slip faults with significant apparent sinistral and unknown vertical displacement. The Western BRX zone contains the highest gold grades on the property, whereas the Western Klaza zone has the highest silver grades.

Metal zonation changes laterally across the property, with copper grades (and chalcopyrite-bornite abundance) increasing towards the southeast, leading to speculation that the magmatic source of this system may be related to the Kelly or the Cyprus porphyry centres, located within the adjacent Mount Nansen porphyry complex (Hart and Langdon, 1998).

The goal of this study on the Klaza Au-Ag-Pb-Zn-Cu deposit is: (i) to develop a clear understanding of the metallogeny, paragenesis and fluid evolution of the Klaza deposit; (ii) to better constrain the age of the QFP dykes, nearby intrusions (Kelly porphyry, Cyprus porphyry, Whitehorse suite granodiorite, Nansen suite granodiorite), the age of mineralization and the relationship of the intrusions to the Klaza mineralization in space and time; and (iii) to determine the tectonic setting of the Klaza deposit and if it is associated with other Au-Ag epithermal veins in the Mt. Nansen structural trend.

Building on preliminary work conducted in 2014 (Richards, 2014), 2015 (Main, 2015) and 2016 (Chapman, 2017), selected drill core was re-logged and sampled to provide clear characterization of the metallogeny, paragenesis and fluid evolution of the Central Klaza zone. During sampling, various dyke generations, breccia (barren and mineralized), and different generations of veins were examined. The majority of drillholes on the property are drilled at a dip azimuth of 037° and a dip of -50°.

Central Klaza zone veins and alteration

Regional propylitic alteration and chlorite veinlets

A pervasive regional scale alteration assemblage which comprises chlorite (Fig. 2a). This alteration affects the Whitehorse suite granodiorite host rock and is cut by all subsequent veins and alteration in the Central Klaza zone.
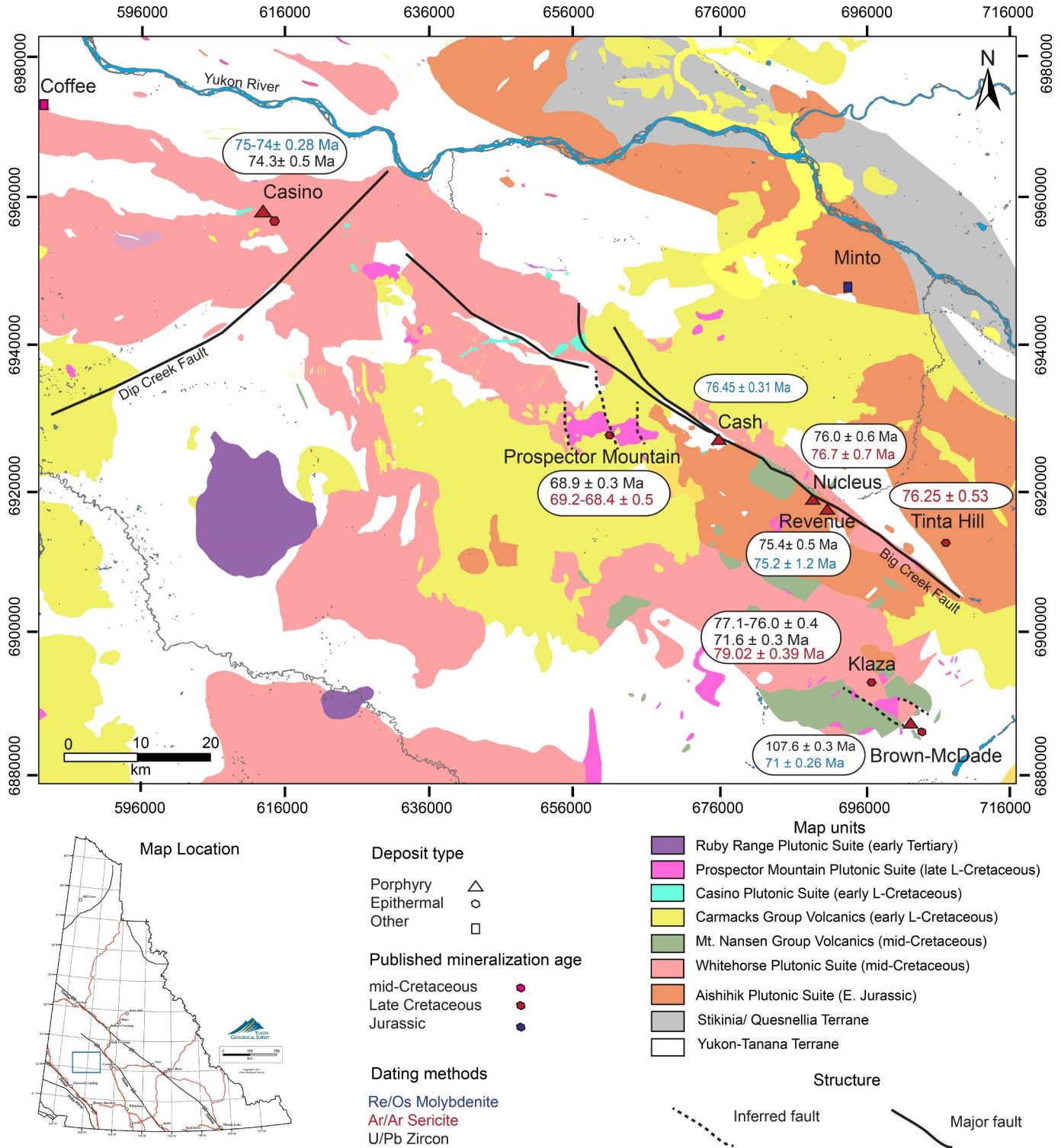
Figure 1. Simplified regional geology map of intrusive units and volcanic units with major faults superimposed. The location and ages of significant porphyry and epithermal deposits are also displayed. Bedrock geology modified from Yukon Geological Survey (2016). Inset map modified from Yukon Geological Survey (2011). Geochronology after Selby and Creaser, 2001a, b (Casino, Cash, Revenue, Prospector Mt., Brown McDade); Allan et al., 2013 (Nucleus, Revenue, Casino, Prospector Mt.); Bineli Betsi et al., 2013 (Tinta Hill, Revenue); Richards, 2014 (Klaza); Mortensen et al., 2016 (Klaza, Brown McDade).
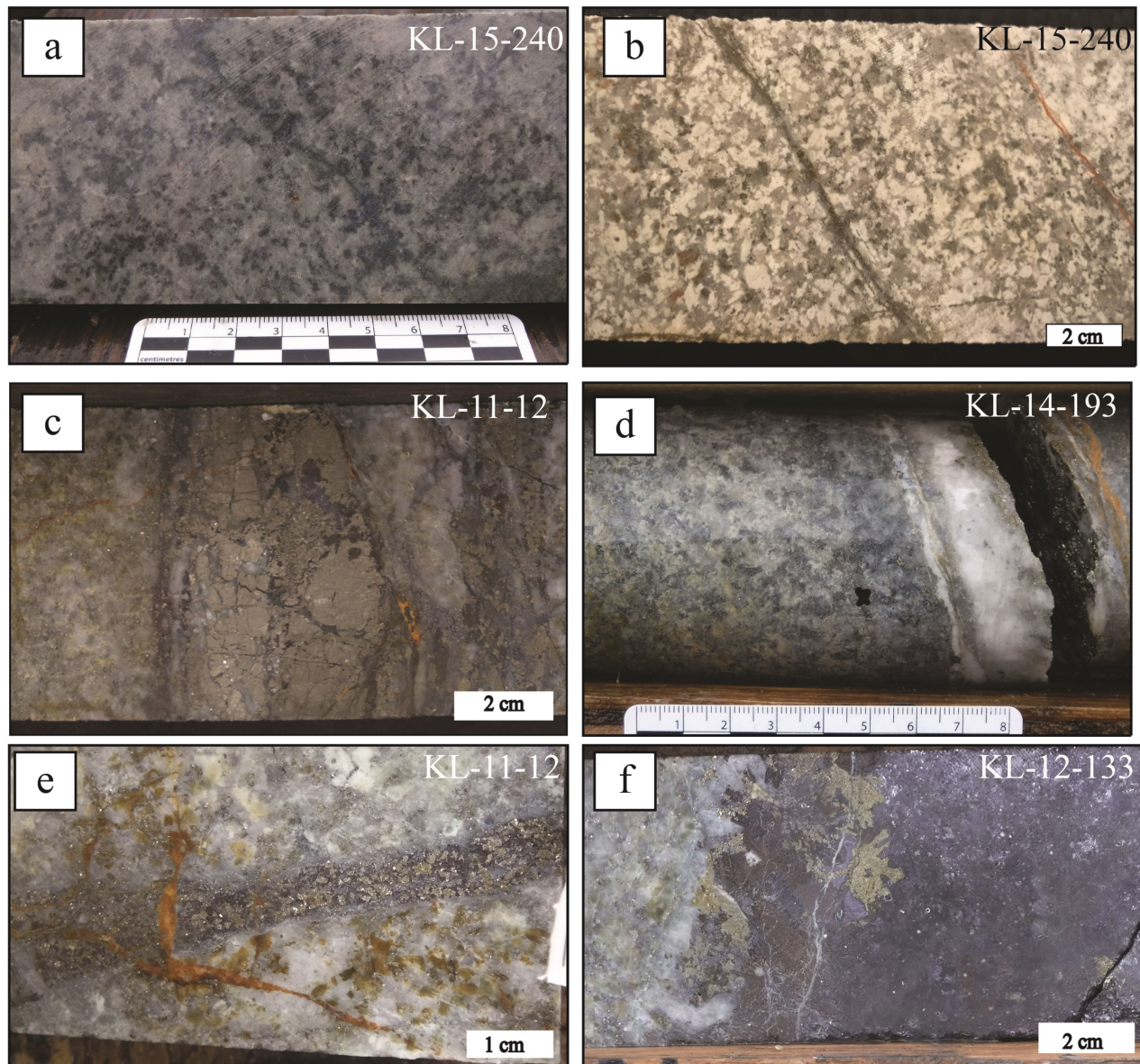
Figure 2. a) Regional propylitic alteration and chlorite veinlet b) Stage 1 sheeted quartz-pyrite veins and associated sericite-pyrite-quartz alteration. c) Stage 2 massive pyrite veins fractured by Stage 4 base metal veins. d) Stage 3 milky quartz-pyrite veins within epidote-chlorite altered host rock. e) Stage 4a quartz-sphalerite-pyrite-arsenopyrite vein cut by Stage 5 ankerite veinlet in epidote-carbonate altered host rock. f) Stage 4b smoky quartz-galena-sphalerite-chalcopyrite-pyrite vein in epidote altered host rock.

Stage 1 Early stockwork and sheeted quartz ± pyrite veins with phylic alteration

Stockwork and sheeted quartz-pyrite veins of hairline to 0.5 cm width were observed in drill core from the Central Klaza zone (Fig. 2b). The veins show two dominant structural orientations (60 to 70° to core axis (TCA) and complementary Riedel fracture sets) and display multiple crosscutting relationships and minimal offset. These stockwork pyrite veins are observed within a strongly phylic (sericite-quartz-pyrite) alteration halo of up to 10 cm wide.

The intervals containing these stockwork pyrite veins are often associated with high gold grade assays (e.g., KL-14-193 442.3 m: 23.5 g/t Au over 0.29 m). Sericite associated with the phyllic alteration of these veins was dated at 79.02 ± 0.39 Ma (Richards, 2014).

Stage 2 Massive pyrite veins

Massive aggregates of pyrite veins up to 15 cm wide are observed in the absence of quartz (Fig. 2c). This vein generation occupies a dominant structural orientation of 90° TCA.

17

This vein type is commonly fractured by and seen as clasts in Stage 3 and Stage 4 veins.

Stage 3 Euhedral quartz ± pyrite ± chalcopyrite veins

Cloudy euhedral quartz veins with massive pyrite ranging from 1cm to 10 cm wide are observed to occupy a dominant structural orientation of 90° TCA (Fig. 2d). Minor anhedral chalcopyrite is locally seen intergrown with massive pyrite. This vein generation cuts the early stockwork and sheeted veins but are not associated with an alteration halo.

Stage 4 Quartz-pyrite veins ± sphalerite ± galena ± arsenopyrite ± sulphosalts ± chalcopyrite with an epidote-chlorite-carbonate halo

Base metal veins (up to 40 cm wide) occupy a dominant structural orientation of 90° TCA and 60 to 70° TCA. This vein generation is commonly associated with pre-existing structures such as the early stockwork veins as well as rubbly fault zones. The base metal veins are further divided into two phases:

Stage 4a: Milky quartz-pyrite-arsenopyrite-sphalerite veins

This stage occurs as hairline veinlets up to 12 cm wide veins with blebby to massive sphalerite, arsenopyrite and pyrite intergrown with milky quartz (Fig. 2e). This early stage of base metal veins is cut by or adjacent to Stage 4b.

Stage 4b: Smoky quartz-galena-sphalerite-chalcopyrite ± sulfosalt veins

This stage occurs as massive, voluminous galena intergrown with smoky quartz up to 20 cm wide (Fig. 2f). Blebby sphalerite and chalcopyrite are also seen intergrown with acicular sulfosalts. Silver grades are highest in this vein generation, possibly associated with galena and sulfosalts.

A wide base metal vein proximal propylitic alteration (epidote-carbonate ± chlorite) 2 cm up to 5 m wide is seen overprinting the sheeted veins and their phyllic altered zones. This alteration is manifested as a thin (0.5 cm wide) chlorite halo grading into a wide epidote-carbonate alteration halo. The chlorite halo is not consistent due to the spatial correlation of base metal veins with other vein generations, which have made alteration assemblages challenging to differentiate. Further petrographic investigation will disentangle this relationship.

This vein generation occupies the same structures and structural trends a suite of porphyritic quartz-feldspar dykes. The dykes are commonly in contact with the base metal veins in the form of multiphase hydrothermal breccias up to 40 cm wide in the Central Klaza zone. Dykes in contact with the veins are bleached and highly carbonate altered.
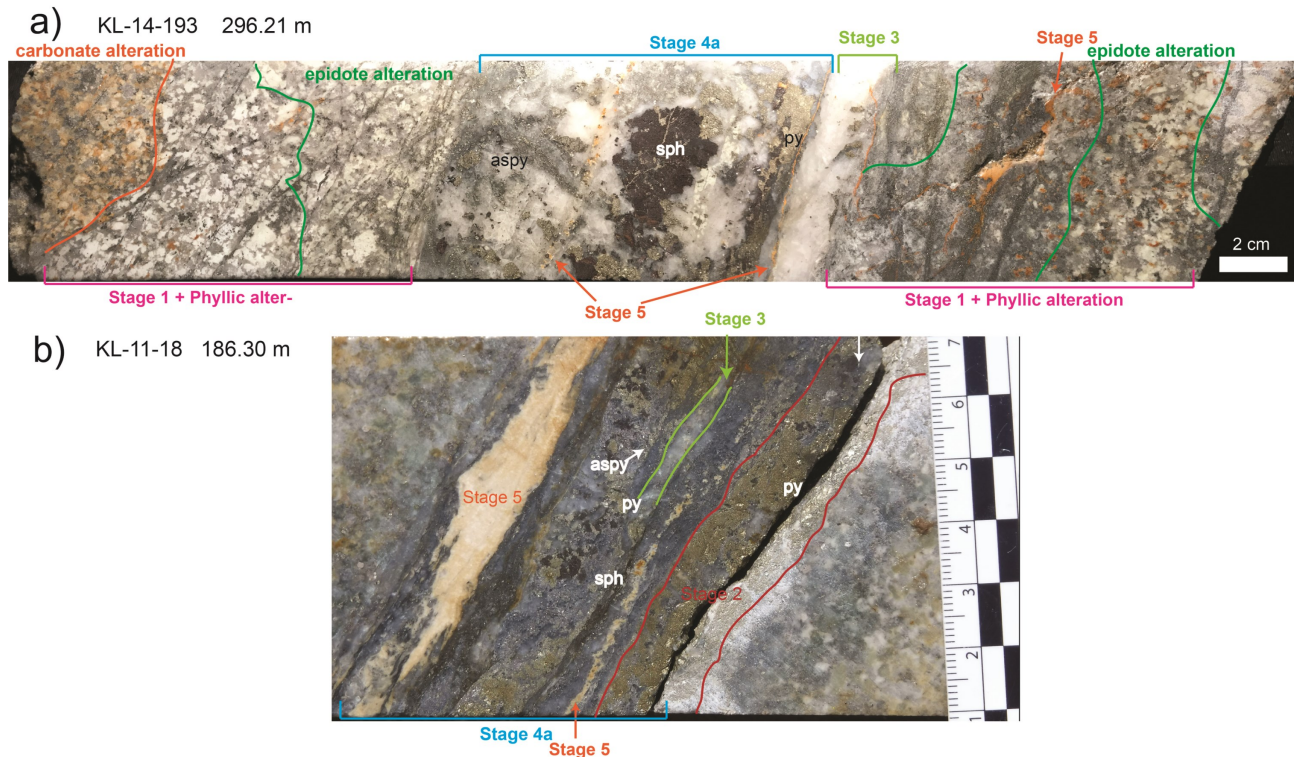
Figure 3. Representative cross cutting relationships between various vein generations and alteration types. a) A Stage 3 quartz-pyrite vein and Stage 4a base metal vein is seen cutting Stage 1 sheeted and stockwork quartz-pyrite veins in phyllic altered granodiorite. Epidote alteration is seen overprinting phyllic alteration. b) Stage 2 massive pyrite and Stage 1 quartz vein is seen brecciated by a Stage 4a base metal vein which is in turn cut by Stage 5 rhodochrosite veins. Epidote-chlorite-carbonate alteration is observed on the selvages of this composite vein. Abbreviations: py = pyrite, sph = sphalerite, aspy = arsenopyrite.

Stage 5 Late carbonate veinlets

Ankerite and rhodochrosite veins ranging from hairline width to 5 cm wide (Fig. 3). This vein generation cuts and is spatially associated to previous vein generations and has yet to be seen associated with any base metal or gold mineralization in the Central Klaza. However, euhedral sphalerite and galena are visible in ankerite/rhodochrosite veins in the Western BRX zone.

Supergene argillic alteration

Argillic alteration consisting of clay minerals post-date mineralization and overprint all alteration zones in close proximity to permeable fault structures such as gouge and fractures that have not been sealed by quartz veins. Argillic alteration halos are usually 10 to 20 cm wide, but can be up to 10 m wide near major fault structures.

Paragenesis

A paragenesis of the various vein generations in the Central Klaza zone is compiled based on field observations and crosscutting relationships in drill core (Fig. 4). The crosscutting relationships between vein generations are shown in Figure 3.

Klaza dyke suite

Mortensen et al. (2016) conducted a geochronological study on the Klaza dykes, which are currently aggregated together as quartz-feldspar porphyries (QFP). Mortensen et al. (2016) published five QFP dyke ages ranging from 77.1 ± 0.4 Ma to 76.0 ± 0.4 Ma, with one outlier at 71.6 ± 0.3 Ma, leading to an investigation into the drill holes in which these samples were collected. Closer inspection revealed subtle textural and compositional differences between dykes, as well as from different areas across the Central Klaza zone. Gradational and sharp contacts were observed between different dyke generations. Differentiating between dyke generations overprinted by alteration is challenging, although a relatively reliable tool for classifying the different units is quartz abundance. Field observations have been able to categorize dykes into four types:

- Type 1: aphanitic mafic dyke (Fig. 5a). This dyke generation has been observed to host quartz-pyrite veinlets with silicification and bleaching halos. This dyke was dated at 78.2 ± 1.0 Ma (Mortensen, 2016).

- Type 2: felsic composition quartz-feldspar porphyritic dyke (Fig. 5b). This dyke generation is quartz-rich and is observed to be cut by quartz-sulphide veinlets and breccias at the contact between dyke and granodiorite host rock.

- Type 3: intermediate composition (biotite-phyric), quartz-poor, feldspar porphyritic dyke (Fig. 5c). No mineralized veins have been observed to cut this dyke generation.

Dyke types 2 and 3 have previously both been logged as QFP; however, only the Type 2 dykes are actual QFPs. All dyke generations display intense bleaching and alteration at the

Figure 4. Paragenesis of vein generations in the Central Klaza zone in chronological order from left to right. *No native gold or silver has been observed in drill core. Gold occurs as refractory ore within arsenopyrite and arsenian pyrite, and is inferred to be present based on correlating assay grade intervals to drill core. Silver is inferred to be hosted in galena and sulfosalts based on assay grade and drill core correlation. Carbonates include ankerite, siderite and rhodochrosite.
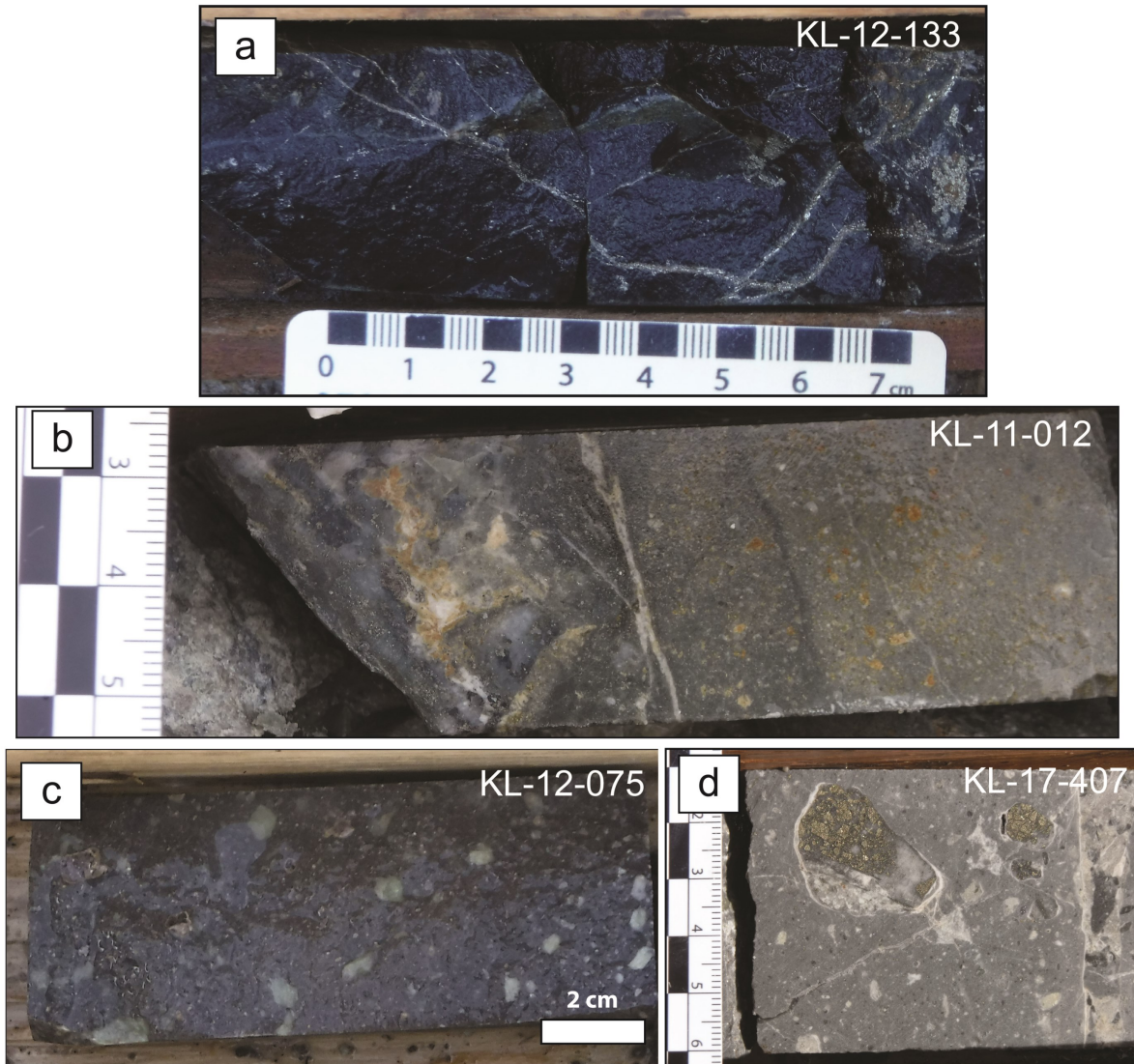
Figure 5. Dyke suite at Klaza with cross cutting relationships: a) Type 1 mafic dyke cut by Stage 1 pyrite veinlets; b) Stage 4 base metal vein in contact with Type 2 felsic dyke with a sulphidized halo in the dike. A late carbonate veinlet cuts through the contact between dyke and base metal vein; c) Type 3 dyke; d) Syn- to post-mineralization dyke observed to contain rounded clasts of phyllic and propylitic altered granodiorite in contact with Stage 2 pyrite veins.

contact between dyke and granodiorite host rock, but only Type 1 and 2 dykes are cut by mineralization or brecciation. One generation of dykes contains clasts of Stage 2 veins (Fig. 5d). This dyke does not fit the description of dykes described above.

Structural controls

Central Klaza zone mineralization displays composite quartz-pyrite-polymetallic veins and breccias occupying two dominant orientations (dips of 40° and 70° with dip directions ranging between 200 and 270°). Three types of breccia (Fig. 6) have been observed:

Fault breccia/pseudotachylite (Fig. 6a): dark, fine grained matrix with little to no mineralization. Carries large, angular clasts of granodiorite and dyke material; sometimes contains clasts of pyrite/vein material.

Hydrothermal breccia (Fig. 6b): quartz ± carbonate matrix with sub-angular clasts of mineralized material, phyllic-altered granodiorite, and dyke. Sometimes contains syn-brecciation disseminated pyrite/sulphides.

Magmatic breccia (Fig. 6c): Matrix supported monomict breccia. Rounded clasts of granodiorite host rock with minor matrix of igneous orthoclase, possibly from felsic dyke material.
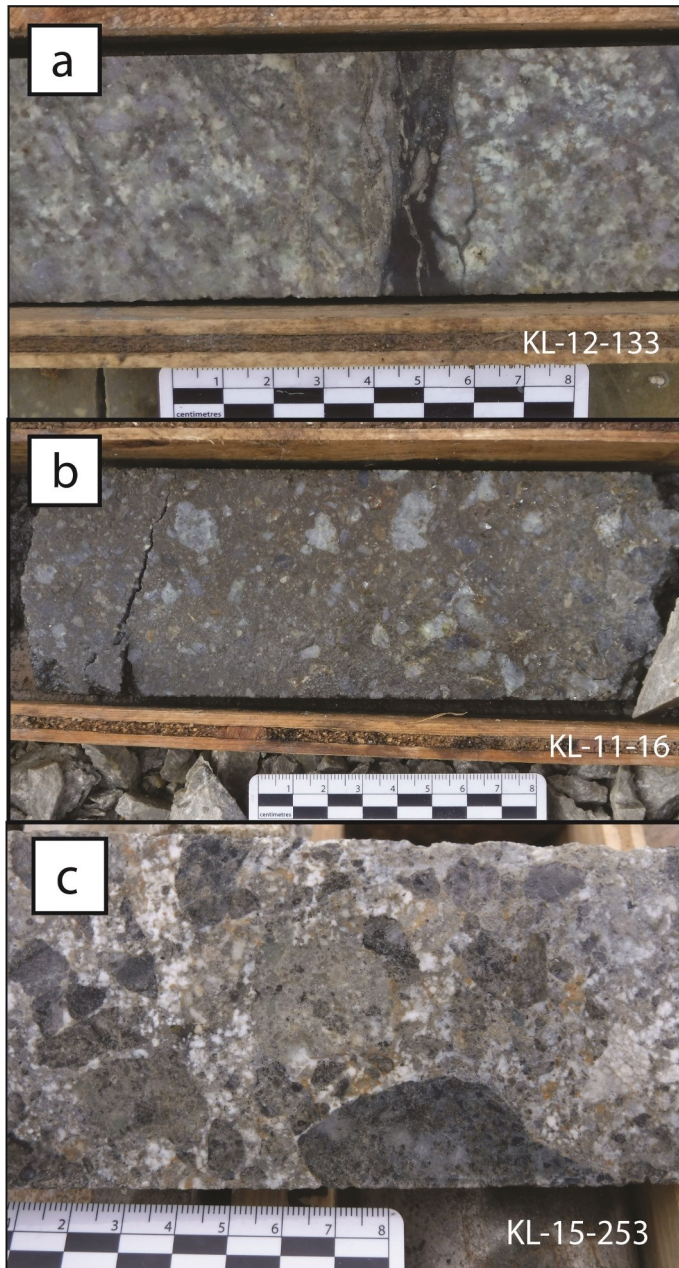
Figure 6. Breccia types in the Central Klaza zone: a) Pseudotachylite; b) Hydrothermal breccia; c) Magmatic breccia.

Structural control is evident in the intimate spatial association of veins, dykes, and breccias in the Central Klaza zone. The composite polymetallic veins display multiple extensional infill and brecciation events within the same fracture. Late ankerite veins and veinlets (Fig. 3) occupy the same structural weak points and appear adjacent to polymetallic veins or occur as infill veins cutting earlier vein generations.

Future analytical work

Initial analytical work will be directed towards classifying the various dyke generations based on age, chemistry and textures, dating host intrusive rocks, and determining the chemistry of various alteration assemblages associated with veins. Detailed petrographic studies will be conducted on vein samples to establish a paragenesis for the Central Klaza zone veins.

Acknowledgments

References

Allan, M.M., Mortensen, J.K., Hart, C.J.R., Bailey, L.A., Sánchez, M.G., Ciolkiewicz, W., McKenzie, G.G., and Creaser, R.A., 2013. Magmatic and metallogenic framework of west-central Yukon and eastern Alaska; *in* Tectonics, Metallogeny, and Discovery: The North American Cordillera and Similar Accretionary Settings, (ed.) M. Colpron, T. Bissig, B. Rusk and J. Thompson; Society of Economic Geologists, Special Publication 17, p. 111–168.

Bineli Betsi, T., Lentz, D., Chiaradia, M., Kyser, K., and Creaser, R.A., 2013. Genesis of the Au-Bi-Cu-As, Cu-Mo ± W, and base-metal Au-Ag mineralization at the Mountain Freegold (Yukon, Canada): Constraints from Ar-Ar and Re-Os geochronology and Pb and stable isotope compositions; Mineralium Deposita, v. 48, p. 991–1017.

Chapman, J.B., 2017. Deep mineralization processes within porphyry deposits of the Canadian Cordillera; *in* Targeted Geoscience Initiative – 2016 Report of Activities, (ed.) N. Rogers; Geological Survey of Canada, Open File 8199, p. 67–68.

Hart, C.J.R. and Langdon, M., 1998. Geology and mineral deposits of the Mount Nansen camp, Yukon; *in* Yukon Exploration and Geology 1997, Exploration and Geological Services Division, Yukon, Indian and Northern Affairs Canada, p. 129-138.

Main, D., 2015. Paragenesis and fluid inclusion characteristics of the Klaza gold-silver deposit, Yukon, Canada; B.Sc. thesis, University of Alberta, Edmonton, Alberta, 31 p.

Mortensen, J.K., Appel, V.L., and Hart, C.J.R., 2003. Geological and U-Pb age constraints on base and precious metal vein systems in the Mount Nansen area, eastern Dawson

Range, Yukon; *in* Yukon Exploration and Geology 2002, (ed.) D.S. Emond and L.L. Lewis; Exploration and Geological Services Division, Yukon Region, Indian and Northern Affairs Canada, p. 165–174.

Selby, D., and Creaser, R.A., 2001. Late and mid-Cretaceous mineralization in the northern Canadian Cordillera: Constraints from Re-Os molybdenite dates; Economic Geology, v. 96, p. 1461–1467.

Selby, D., Nesbitt, B.E., Creaser, R.A., Reynolds, P.H., and Muehlenbachs, K., 2001. Evidence for a nonmagmatic component in potassic hydrothermal fluids of porphyry Cu-Au-Mo Systems, Yukon, Canada; Geochimica et Cosmochimica Acta, v. 65, p. 571–587.

Richards, J.P., 2014. Report on field visit to the Klaza Gold-Silver deposit; Rockhaven Resources, internal report.

Ross, A.A., Martin, C.J., and Dumala, M.R., 2016. NI43-101 Technical Report: Geology and mineralization soil geochemical surveys diamond drilling summary diamond drilling specifications drill collar and down-hole surveys oriented core surveys; Rockhaven Resources 43-101 report, 91 p.

Yukon Geological Survey, 2011. Yukon bedrock terrane map; Yukon Geological Survey. <http://www.geology.gov.yk.ca/bedrock_terrane.html> [accessed November 13, 2017]

Yukon Geological Survey, 2016. Yukon digital bedrock geology; Yukon Geological Survey. <http://www.geology.gov.yk.ca/update_yukon_bedrock_geology_map.html> [accessed September 10, 2016]

Field mapping of the Eastern Highlands shear zone, Cape Breton Island, Nova Scotia

N. Piette-Lauzière[1], K.P. Larson[1] and D.A. Kellett[2]

[1]*Department of Earth and Environmental Science, University of British Columbia Okanagan, 3187 University Way, Kelowna, British Columbia, V1V 1V7*

[2]*Geological Survey of Canada, 1 Challenger Drive, Dartmouth, Nova Scotia, B3B 1A6*

Abstract

The Eastern Highlands shear zone (EHSZ) is located on Cape Breton Island where it separates rocks of the Bras-d'Or and Aspy terranes within Ganderia in the Appalachian accretionary belt. It records late Silurian to Early Devonian shear with east-over-west kinematics (D1) and a second deformation event (D2) with oblique dextral and west-over-east kinematics of unknown timing. Field mapping and thin section observations identified a third deformation event (D3) with brittle ductile fabrics, brecciation and hydrothermal alteration of a granite on the Aspy side of the EHSZ. These new mapping results contribute to our understanding of the later stages of deformation and their interplay with hydrothermal alteration. They also provide the framework for further studies attempting to reconstruct the post-orogenic reactivation of the EHSZ and the associated magmatic-hydrothermal processes that may have contributed to the mineral endowment of the orogen.

Introduction

The Eastern Highlands shear zone (EHSZ) is located in the Cape Breton Island portion of the Canadian Appalachians (Fig. 1). It is interpreted to separate Ordovician to Devonian rocks of the Aspy terrane to the west from Hadrian to Cambrian rocks of Bras d'Or terrane to the east (Barr and Raeside, 1989; Barr et al., 1998). Because at least part of its slip history is associated with abundant syn-deformation granite, the EHSZ provides a good location to investigate associations between faulting and the emplacement of mineralized and barren intrusions.

Here we present preliminary mapping and analysis on the tectono-metamorphic history of the EHSZ. One objective of the study is to resolve the style of deformation developed by the EHSZ and the potential of strain partitioning within the shear zone during the main episode(s) of deformation. Another objective is to define the structural history of the EHSZ region in respect to metamorphism and hydrothermal alteration. Finally this study should provide constraints on the role of inboard faults, such as the EHSZ, on emplacement and tectonic setting of post-accretionary intrusions, particularly those associated with polymetallic, porphyry-style mineralization.

Geological setting

The Lower Paleozoic closure of Iapetus and Rheic oceans, and associated successor basins (i.e. Tetagouche – Exploits back-arc basin) developed through the accretion of microcontinents (e.g. Dashwood, Ganderia, Avalonia and Meguma) and culminated in the Permian with the formation of the supercontinent Pangaea (van Staal et al., 2009). The Bras d'Or and Aspy terranes of Cape Breton Island are considered parts of the Ganderia microcontinent, where they have a basement – cover relationship (Lin, 1993). The Aspy terrane is dominated by supra-crustal volcano-sedimentary rocks with minor intrusive rocks, whereas the Bras d'Or terrane is dominated by Neoproterozoic to Cambrian intrusive felsic to intermediary rocks with minor metasedimentary rocks. The EHSZ is thus likely an internal structural discontinuity. It records a Late Silurian to Early Devonian east over west deformation event, D1, in response to the accretion of Avalonia during Acadian orogeny (Lin, 1995; van Staal et al., 2009). The second episode of deformation noted in the EHSZ, D2, records the opposite vergence, west-side up or east-side down, with a dextral strike-slip component (Lin, 1993). The timing of this episode has not been constrained by previous work.

Rock types, metamorphic assemblages and alteration

Preliminary petrographic analysis of the various rock types in the vicinity of the EHSZ (Fig. 1, 2) are described below. All ages are U-Pb zircon crystallization ages.

In the study area, the Black Brook granitic suite (375 +5/-4 Ma, Dunning et al., 1990) and the Park Spur Granite (379 ± 4 Ma, Dunning et al., 1990) are foliated and in foliation-parallel contact with the western side of the EHSZ (Fig. 1). The Park Spur granite is locally hematite altered and crosscut by millimetre to centimetre scale hematite veins oriented perpendicular to the main foliation.

A psammite unit occupies the western side of the EHSZ. Where present, garnet porphyroblasts are wrapped by the foliation and staurolite porphyroblasts mark a mineral shape linea-
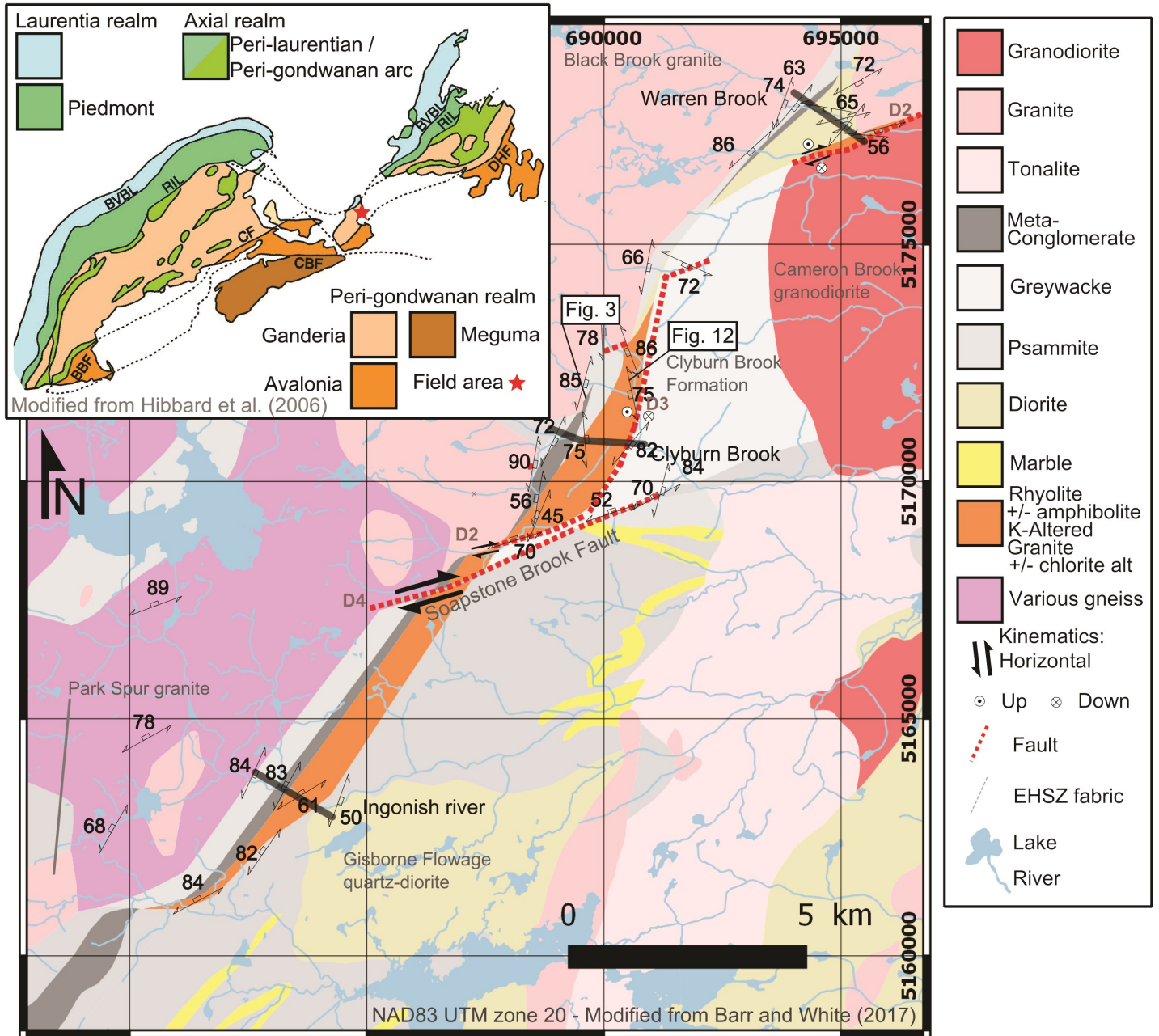
Figure 1. Geological map of the EHSZ with locations of the Figure 2 cross-sections (grey lines) and outcrops pictured in the report. Inset: Tectonic map of the Appalachian mountain belt and localization of the project (red star). Map modified from Barr and White (2017) and Hibbard et al. (2006).

tion. Albite-hornblende strata-bound alteration is common in the psammite near the contact with the intrusive rocks to the west. The hornblende grains are typically randomly oriented though some are locally aligned within the foliation.

A distinctive meta-conglomerate occurs internally within the psammite unit (Fig. 3); the contact between them appears to be gradational. This unit can be followed along strike across the mapped area, varying in width between a few meters in Roper Brook, to almost 500 m in Clyburn Brook and along the

Ingonish River (Fig. 2). The conglomerate is polymictic and pervasively strained. Individual intrusive rock pebbles are identifiable, but the background matrix is undifferentiated. In both metasedimentary units, centimetre to metre wide foliated granite dykes typically occur parallel to the foliation, but also locally cross-cut it.

A foliated diorite (Fig. 4) is in foliation-parallel contact with the psammite. This unit is restricted to the northern part of the EHSZ in Warren Brook and Roper Brook (Fig. 1, 2) and
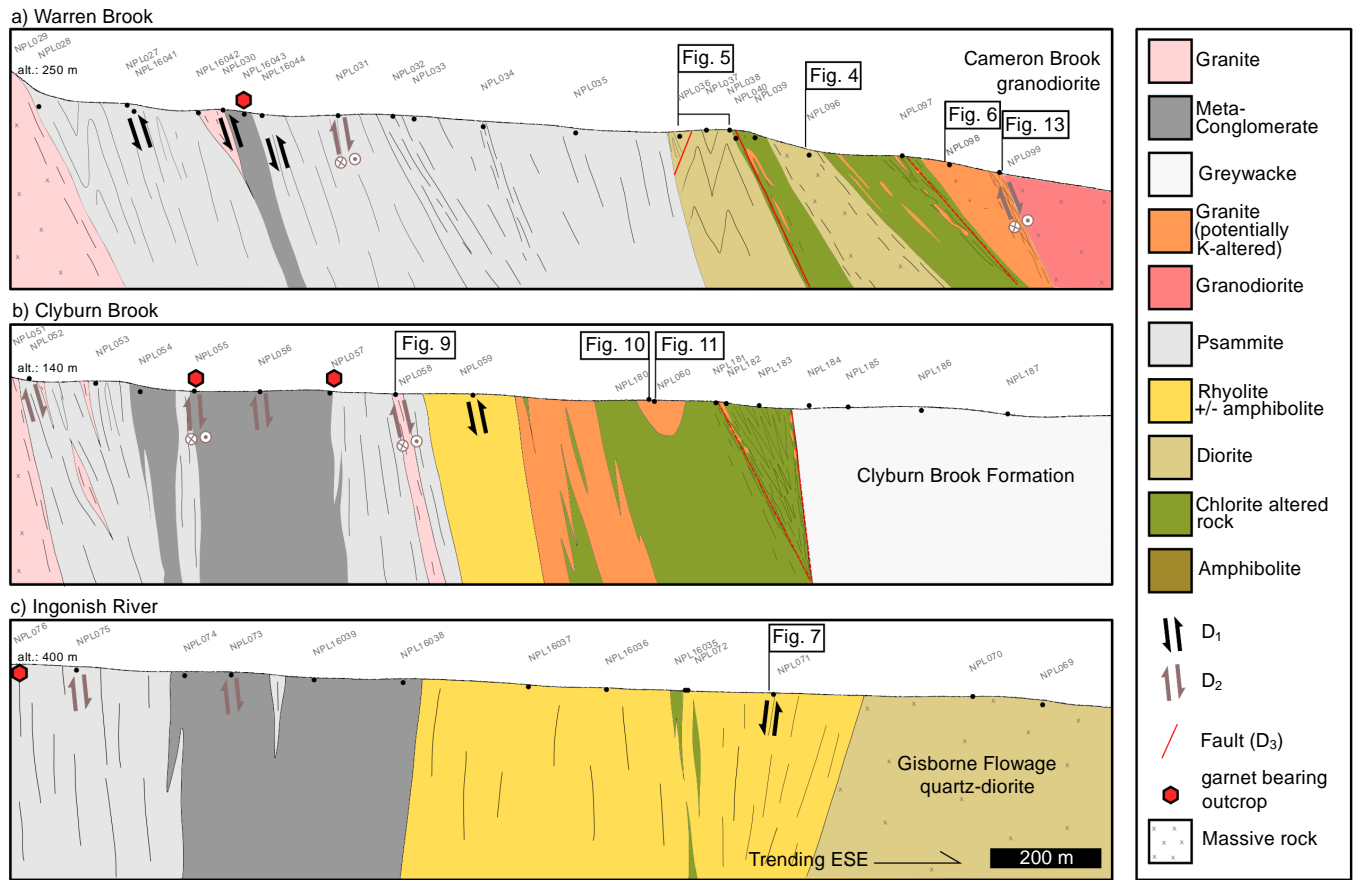
Figure 2. Cross-sections across the EHSZ along Warren Brook, Clyburn Brook and Ingonish River with location for the outcrops pictured in the report. Locations shown in Figure 1.

Figure 3. Outcrop KNA-17-NPL-063, strained meta-conglomerate.

Figure 4: Outcrop KNA-17-NPL-096, dioritic gneiss attributed to Roper Brook diorite (Fig. 2).

has been previously called the Roper Brook amphibolite (Raeside and Barr, 1992). Based on our observations in Warren Brook we refer to this unit as the Roper Brook diorite, as suggested by Lin (1993), to reflect the occurrence of quartz in the matrix (Fig. 5).

The easternmost unit deformed within the EHSZ is a variably-deformed massive to gneissic granite (Fig. 2). It commonly has a pink colour indicating potential hydrothermal alteration (Fig. 6). Towards the south, along the Ingonish River (Fig. 1, 2), a felsic crystal-tuff associated with a rhyolite has been identified and is also attributed to this unit (Fig. 7).

The eastern side of the EHSZ is bounded from north to south by the Cameron Brook granodiorite (Fig. 2; 402 ± 4 Ma, Dunning et al., 1990), low-grade greywacke of the Clyburn Brook Formation and quartz-rich, amphibolite-facies metasedimentary rocks of the McMillan Flowage Formation. The Clyburn Brook Formation includes greenschist-facies sedimentary and volcanic rocks. This unit has been attributed to Aspy ter-

Figure 6: Outcrop KNA-17-098, massive granite with possible K-alteration.

rane by Barr and Raeside (1998) (inferred age of 412 Ma), but is situated within Bras-d'Or terrane-related rocks. The Clyburn Brook and McMillan Flowage formations are separated by the Soapstone Brook Fault (Fig. 1). Based on its lack of foliation, the Cameron Brook granodiorite is interpreted to have an intrusive relationship with both the EHSZ and the Clyburn Brook Formation. However, Dunning et al. (1990) suggest that northern and southern boundaries of the Cameron Brook granodiorite are faulted along an eastern trend.

Deformation and hydrothermal alteration

Four generations of structures (D1–4) have been recognized by deformation style and crosscutting relationships. Two major alteration events have been identified and characterized with respect to those deformation events. D1 is associated with a north-northeast ductile fabric recorded in the metaconglomerate and the edges of the diorite unit. The lineation is steep and C/S fabrics and sigma- and delta-type clasts indicate
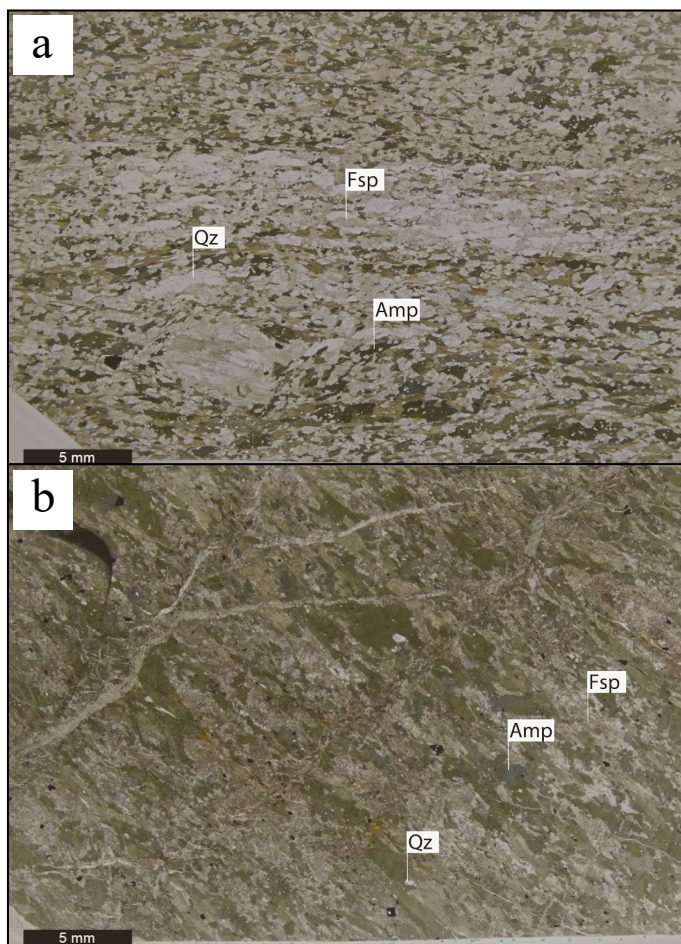
Figure 5: Plain polarized light photomicrograph of specimen KNA-17-NPL-036 (a) and 38B (b), respectively, of quartdiorite and diorite both attributed to Roper Brook diorite (Fig. 2). Qz - Quartz; Fsp - Feldspar; Amp - Amphibole.

Figure 7: Outcrop KNA-17-NPL-071, rhyolite band in a felsic crystal tuff.
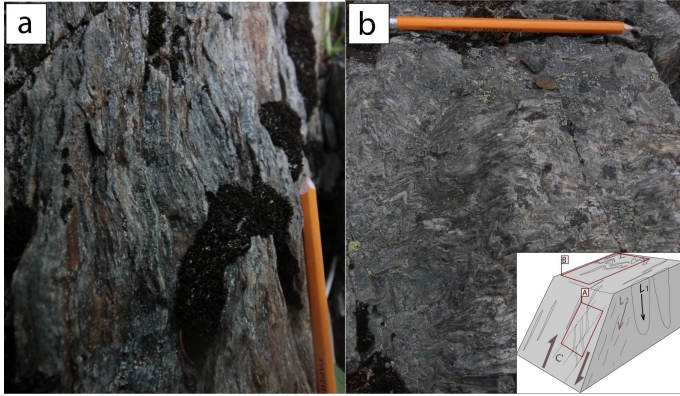
Figure 8. Outcrop KNA-17-NPL-142 of a meta-conglomerate with D2 C' shear bands cross-cutting D1 fabric. Lower-right cartoon shows pictures (a) and (b) in their respective orientations. The stretching lineation is defined by the pebble long axis (L1). L2 is defined by a muscovite shape lineation.

Figure 10. Plain polarized light photomicrograph of a brecciated granite specimen from outcrop KNA-17-NPL-60.

east-side-up kinematics. No strain gradient could be defined in the meta-conglomerate unit and the associated psammite.

D2 is associated with discrete shear zones oriented northeast with a mineral lineation that plunges moderately to the southwest. Associated C/S/C' fabrics were observed in all the units forming the EHSZ and indicate east-side-down dextral kinematics. Outcrop KNA-17-NPL-142 displays the main D1 fabric deformed by D2 (Fig. 8). Similar fabrics have been observed at both outcrop and thin section scales indicating that this event is regionally pervasive (Fig. 2). Muscovite is associated only with the D2 fabric (Fig. 9) indicating that the observed potassic alteration was syn-D2.

D3 is associated with a north trending brittle-ductile shear zone that is almost continuous along the eastern edge of the

EHSZ from Warren Brook to Clyburn Brook (Fig. 1, 2). Asymmetric boudins and drag folds indicate east-side-down kinematics. This structure is marked by brecciated rock that was likely previously potassic-altered (Fig. 10). The breccia matrix is amphibole- and chlorite-rich (Fig. 11). This alteration zone is exposed near continuously in a 500 m transect in Clyburn brook (Fig. 2) and outcropped regularly along strike (Fig. 1, 12, 13).

D4 is associated with east striking brittle strike-slip faults. Asymmetric chevron folds in the northern wall of the Soapstone Brook fault are consistent with dextral motion. The Soapstone Brook fault (Fig. 1) is the most prominent D4 structure observed, separating gneissic amphibolite-facies rocks to the south from lower greenschist-facies (chlorite-grade) sedimentary rocks to the north (Lin, 1993). These structures also appear to manifest as east oriented breccias within the meta-conglomerate and late-tectonic granite, associated with an al-

Figure 9. Cross-polarized (XPL) view of muscovite associated with D2 shear bands in a granite orthogneiss (KNA-17-NPL-058). Qz - Quartz; Mu - Muscovite; Fsp - Feldspar.
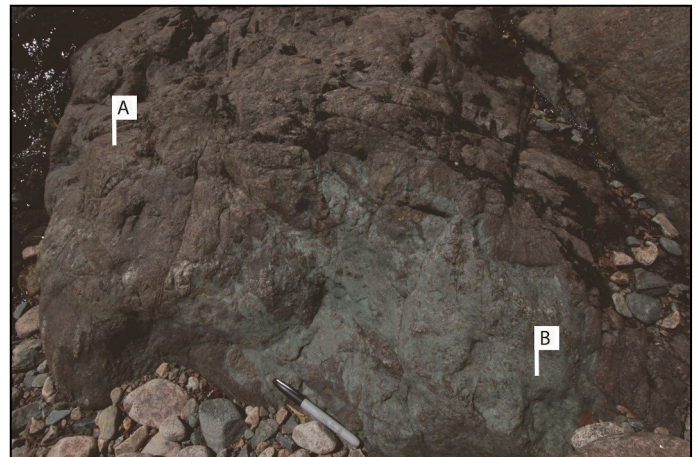
Figure 11. Field relationship between a brecciated granite (a) and a chlorite-amphibole rich rock (b) in outcrop KNA-17-NPL-060.
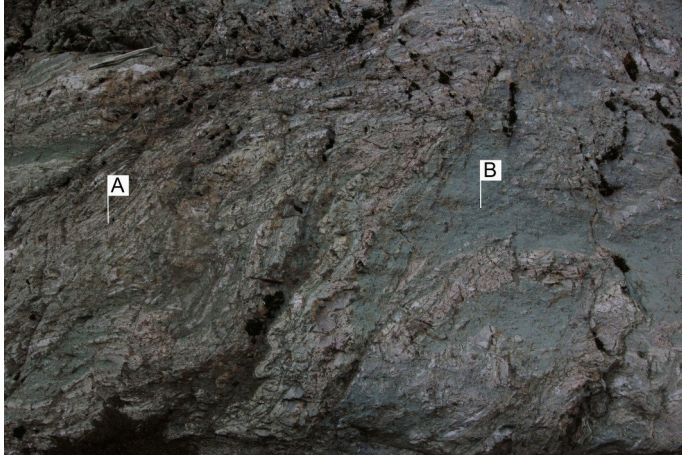
Figure 12. Field relationship between a brecciated granite (a) and a chlorite-amphibole rich rock (b) in outcrop KNA-17-NPL-133. Scratcher point for scale (upper left).

bite-rich matrix, hematite veins and brittle cleavage planes in the Park Spur granite.

Preliminary interpretations

The fabrics and hydrothermal alteration observed are inferred to occur sequentially during a retrograde cooling path. Ductile deformation is constrained along north-northeast trending fabrics with an east-side-up (D1) and a dextral-east-side-down (D2) kinematic, brittle-ductile deformation is limited to a north trending structure with an east-side down kinematic (D3) and brittle deformation by east trending strike-slip dextral faults (D4). Potassic and chlorite-amphibole alteration respectively interact with D2 and D3 fabrics. These alterations seem related to the post-orogenic and potential reactivation history of
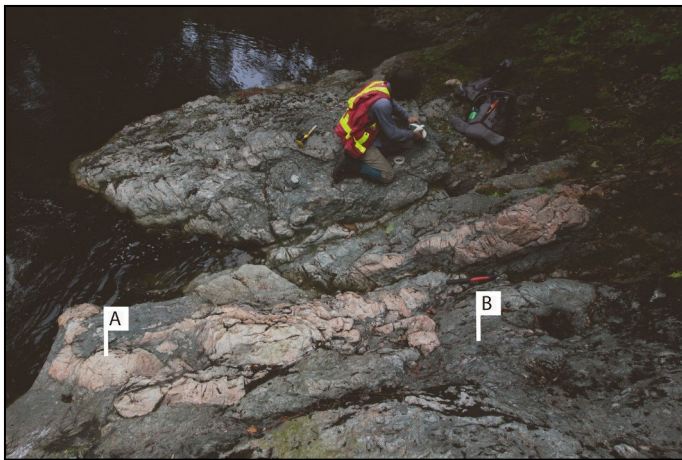
Figure 13. Outcrop KNA-17-NPL099 of a deformation zone at the edge of the K-altered granite of Figure 6. (a) K-altered granite boudinaged in a (b) chlorite-amphibole altered aphanitic rock.

the EHSZ. Future work will focus on better characterizing these alteration events.

Conclusion

The results presented here demonstrate the along strike continuity of the main units marking the EHSZ, with the exception of the Roper Brook diorite. Field mapping and thin section observations demonstrate the regional distribution of D2 fabrics and a zone of extensive brittle-ductile deformation attributed to D3. Moreover, it demonstrates direct ties of the post-D2 structural history of the EHSZ to a hydrothermal alteration system. Further work will build upon these observations to study how a shear zone can focus deformation and hydrothermal alteration across varying crustal levels. Additionally, the EHSZ may provide information on the role of accretion-related structures to continued outboard accretions, and even post-orogenic collapse of the Appalachian orogeny.

Acknowledgments

References

Barr, S.M. and Raeside, R.P., 1998. Petrology and tectonic implications of Silurian(?) metavolcanic rocks in the Clyburn Brook area and on Ingonish Island, northeastern Cape Breton Island, Nova Scotia; Atlantic Geology, v. 34, p. 27–37.

Barr, S.M. and Raeside, R.P., 1989. Tectono-stratigraphic terranes in Cape Breton Island, Nova Scotia: Implications for the configuration of the northern Appalachian orogen; Geology, v. 17, p. 822–825.

Barr, S.M., Raeside, R.P., and White, C.E., 1998. Geological

correlations between Cape Breton Island and Newfoundland, northern Appalachian orogen; Canadian Journal of Earth Sciences, v. 35, p. 1252–1270.

Barr, S.M. and White, C.E., 2017. Bedrock Geology Map of the Cheticamp River Area; Nova Scotia Department of Natural Resources, Map ME 2017-026, scale 1:50 000.

Dunning, G.R., Barr, S.M., Raeside, R.P., and Jamieson, R.A., 1990. U-Pb zircon, titanite, and monazite ages in the Bras-D'Or and Aspy terranes of Cape Breton Island, Nova Scotia – Implications for Igneous and Metamorphic History; Geological Society of America Bulletin, v. 102, p. 322–330.

Hibbard, J.P., van Staal, C.R., Rankin, D.W., and Williams, H., 2006. Lithotectonic map of the Appalachian Orogen (North), Canada – United States of America; Geological Survey of Canada, Map 02042A, scale 1:1 500 000.

Lin, S., 1993. Relationship between the Aspy and Bras d'Or "terranes" in the northeastern Cape Breton Highlands, Nova Scotia; Canadian Journal of Earth Sciences, v. 30, p. 1773–1781.

Lin, S., 1995. Structural evolution and tectonic significance of the Eastern Highlands shear zone in Cape Breton Island, the Canadian Appalachians; Canadian Journal of Earth Science, v. 32, p. 545–554.

Raeside, R.P. and Barr, S.M., 1992. Geology of the northern and eastern Cape Breton Highlands, Nova Scotia; Geological Survey of Canada, Paper 89-14, 39 p.

van Staal, C.R., Whalen, J.B., Valverde-Vaquero, P., Zagorevski, A., and Rogers, N., 2009. Pre-Carboniferous, episodic accretion-related, orogenesis along the Laurentian margin of the northern Appalachians; Geological Society, London, Special Publications, v. 327, p. 271–316.

Factors controlling intrusion-related mineralization in Cape Breton Island, Nova Scotia: A comparison of Silurian-Devonian plutons in Ganderia and Avalonia

A. Moning[1], S.M. Barr[1], C.E. White[2], G. Sombini dos Santos[1] and D. van Rooyen[3]

[1]*Department of Earth and Environmental Science, Acadia University, Wolfville, Nova Scotia, B4P 2R6*
[2]*Nova Scotia Department of Natural Resources, Halifax, Nova Scotia, B3J 2T9*
[3]*Department of Mathematics, Physics and Geology, Cape Breton University, Sydney, Nova Scotia, B1P 6L2*

Abstract

The Devonian Gillis Mountain granitoid pluton in the Avalonian Mira terrane of southern Cape Breton Island hosts porphyry-style copper-molybdenum mineralization. In contrast, plutons of assumed similar age and containing similar rock types in the Leonard MacLeod Brook area of the Ganderian Aspy terrane of northern Cape Breton Island are not known to be mineralized. Hence a comparison of features such as host rocks, depth of emplacement, mineralogy, and chemical composition between plutons in these two areas may provide insight about factors controlling porphyry-style mineralization. During the summer of 2017, existing samples from the Gillis Mountain pluton were re-analyzed to obtain a modern set of trace element data, and previously unstudied drill core from the pluton was sampled for petrological study. Plutons in the Leonard MacLeod Brook area were mapped and sampled for petrological studies and dating, now in progress.

Introduction

Cape Breton Island, Nova Scotia, consists of the Mira, Bras d'Or, and Aspy terranes and the Blair River Inlier (Fig. 1). These units represent distinct tectonic components in the accretionary collage that constitutes the Canadian Appalachians (Barr and Raeside, 1989; Hibbard et al., 2006). The Mira terrane is interpreted to be part of Avalonia, whereas the Bras d'Or and Aspy terranes are parts of Ganderia. Both Avalonia and Ganderia are interpreted to be peri-Gondwanan domains, whereas the Blair River Inlier is part of the Laurentian realm (Hibbard et al., 2006).

This project focuses on granitoid plutonic rocks in the Gillis Mountain area of the Mira terrane (Avalonia) and Leonard MacLeod Brook area of Aspy terrane (Ganderia). These areas were selected for study based on their tectonic affinity, the presence of economic porphyry-type mineralization in the Gillis Mountain area but apparently not in the Leonard MacLeod Brook area, and on the similar characteristics of the plutons (relatively shallow intrusions into country rocks at low-regional metamorphic grades; Barr and O'Beirne, 1991; O'Neill, 1996).

The purpose of the study is to compare plutonic rocks in the two areas in terms of field relations, host rocks, depth of emplacement, age, petrography, and major and trace element and isotopic composition. Similarities and differences in these features may provide information about factors which control the presence or absence of economic mineralization in high-level plutonic rocks.

Regional geology

The Mira terrane consists mainly of late Neoproterozoic volcanic, sedimentary, and plutonic rocks overlain in places by Cambrian to early Ordovician clastic sedimentary units (Fig. 1). These rocks were locally overprinted by post-Ordovician very low- to low-grade regional metamorphism and ductile deformation (McMullin et al., 2010; Willner et al., 2015). Only a few younger (Devonian) plutons are present in the Mira terrane, where they overprint the regional metamorphism and associated structures. These Devonian plutons are known to host widespread porphyry-type sulphide mineralization (Barr and O'Beirne, 1981; Barr et al., 1982; Barr and Macdonald, 1992).

In contrast to the Mira terrane, the Aspy terrane is mainly Paleozoic, although Neoproterozoic rocks are present in the western part of the terrane (e.g. Barr et al., 1992; Lin et al., 2007; Slaman et al., 2017). Volcanic and sedimentary rocks in the terrane were metamorphosed to greenschist and amphibolite facies in the late Silurian to early Devonian and intruded by plutons with ages ranging from ca. 442 to 365 Ma (Barr and Jamieson, 1991; Lin et al., 2007; Barr, 2010). In contrast to those in the Mira terrane, Devonian plutons in the Aspy terrane are not known to be associated with significant mineralization.

Geological setting: Gillis Mountain Pluton

The Gillis Mountain pluton is of special significance because of the presence of porphyry-style copper-molybdenum mineralization (Kirkham and Soregaroli, 1975; Hawkes, 1967;
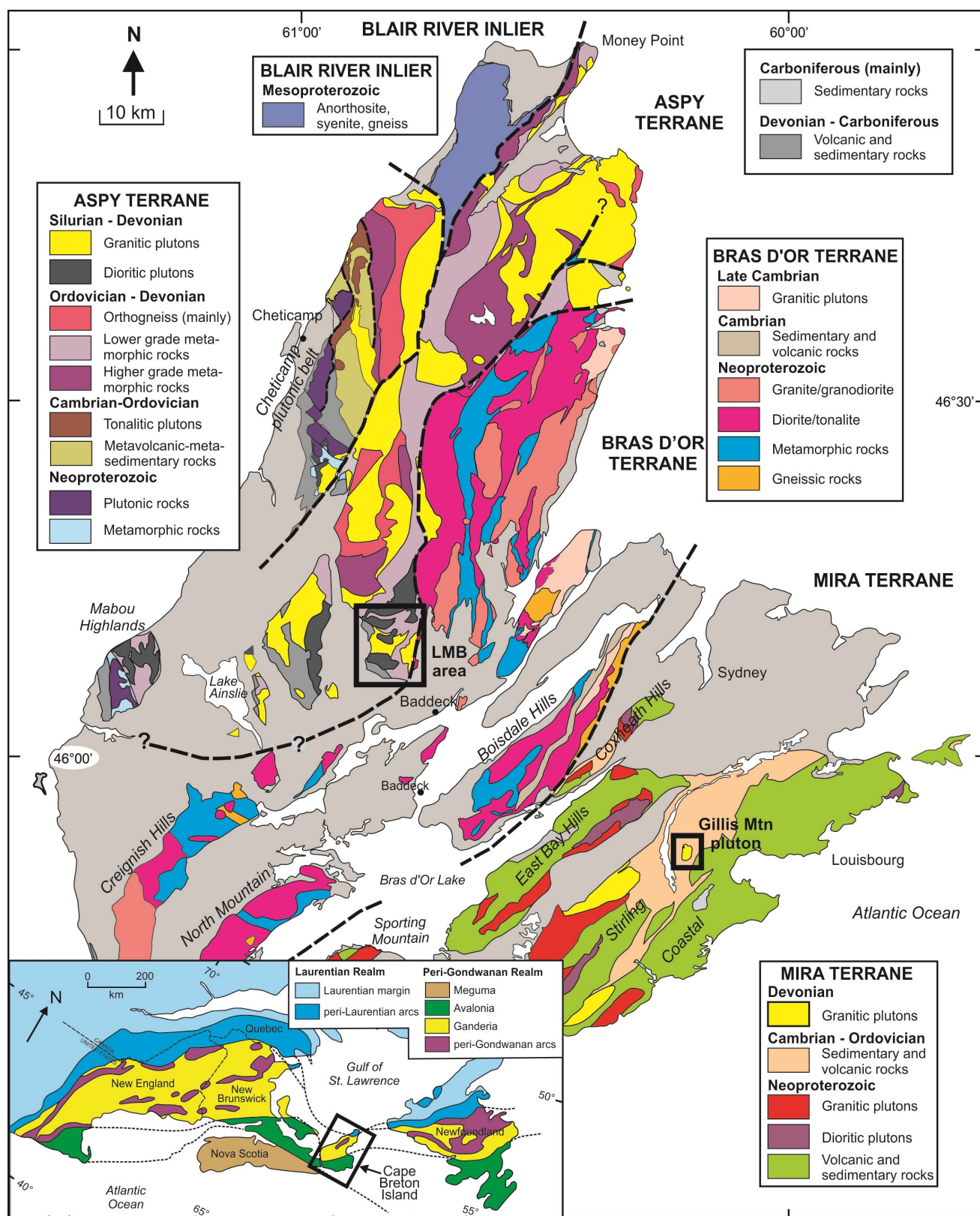
Figure 1. Simplified geological map of Cape Breton Island, modified after Barr (2010), showing the locations of the Gillis Mountain pluton and Leonard MacLeod Brook (LMB) area. Inset map showing divisions of the northern Appalachian orogen is from Hibbard et al. (2006).

MacKinnon, 2008). Significant mineralization (Cu-Mo-Bi-Ag) also occurs in association with a similar small granitic intrusion 10 km east of Gillis Mountain at Deep Cove (Barr et al., 1982; Dennis, 1988; Sheard, 2007), and polymetallic mineralization is present in hornfels and calc-silicate rocks (skarn) and associated dykes in the Blue Mountain area about 5 km northeast of Gillis Mountain (Macdonald and Barr, 1993). Together with the Salmon River rhyolite porphyry, these Devonian plutons appear to be related to one another and to have significant economic potential, both in the plutons themselves and in their host rocks (Macdonald and Barr, 1993).

As mapped by O'Beirne (1979), Barr and O'Beirne (1981) and Barr et al. (1982), the Gillis Mountain pluton consists of three main units: quartz monzodiorite, porphyritic granite, and fine-grained granite, as well as varied aplitic, granitic, and mafic dykes. Chalcopyrite and pyrite occur in all units but molybdenite is mainly in the porphyritic granite. The pluton is characterized by typical porphyry-type hydrothermal alteration, including hematitization and sericitization of feldspars and chloritization of mafic minerals (Barr and O'Beirne, 1981). The alteration is more moderate in the quartz monzodiorite, and more intense in the porphyritic granite and dykes of porphyritic granite and aplite (Barr and O'Beirne, 1981).

The Gillis Mountain pluton intruded Early to Middle Cambrian shale and siltstone. It is a typical high-level intrusion with sharp, strongly discordant contacts with the country rocks and structures relatively undisturbed. The contact metamorphic aureole is poorly exposed around the intrusion due to the swampy terrain, but where observed the hornfels contains cordierite and andalusite, consistent with shallow emplacement (O'Beirne, 1979). Recent dating of the Gillis Mountain pluton yielded a crystallization age of 369.7 ± 2.3 Ma (U-Pb zircon; C.E. White, work in progress, 2017), which is in broad agreement with a previous Rb-Sr determination of 384 ± 10 Ma (Cormier, 1979).

Geological setting: Leonard MacLeod Brook area

The Leonard MacLeod Brook area forms the southern tip of the central Cape Breton Highlands and includes the inferred shear-zone boundary between the Aspy and Bras d'Or terranes (Fig. 1). Jamieson et al. (1987) and Barr et al. (1992) included the volcanic and sedimentary rocks of the area in the Ordovician-Silurian Sarach Brook Metamorphic Suite. They also recognized a spatially associated Leonard McLeod Brook complex that included both metavolcanic rocks of the Sarach Brook Metamorphic Suite and fine-grained syenogranite that they inferred to be Devonian. The Sarach Brook Metamorphic Suite is intruded by the West Branch North River Granite (Barr et al., 1992), which includes the Bothan Brook pluton (O'Beirne-Ryan and Jamieson, 1986; Horne, 1995). The Bothan Brook pluton has a U-Pb zircon crystallization age of 376 ± 3 Ma (Horne et al., 2003).

O'Neill (1996) divided the Leonard MacLeod Brook complex of Barr et al. (1992) into the MacRae Brook formation,

Gillis Brook diorite, Easach Ban complex, and Leonard MacLeod Brook plutonic suite. He interpreted the plutonic units to be comagmatic and Middle to Late Devonian in age, whereas he assumed that the MacRae Brook formation is Ordovician to Silurian like the Sarach Brook Metamorphic Suite to the north. The Leonard MacLeod Brook plutonic suite ranges widely in composition from tonalite and alkali-feldspar granite to syenogranite and monzogranite (O'Neill, 1996). Angular to subrounded, xenoliths are attributed as Gillis Brook diorite (O'Neill, 1996).

Recent U-Pb zircon dating yielded an age of 436.4 ± 1.5 Ma for the Gillis Brook diorite, and 419.2 ± 2.2 Ma for Leonard MacLeod Brook suite syenogranite (D. van Rooyen, work in progress, 2017). Given the range in ages, additional U-Pb dating is needed to fully understand different dioritic and granitic units of the Leonard MacLeod Brook area.

The geological relations in the Leonard MacLeod Brook area are complicated by numerous shear zones, including the Highland Road, Southern Highlands, Captain Brook and Muskrat Brook shear zones (Jamieson and Doucet, 1983; Barr et al., 1992; Horne, 1995; O'Neill, 1996). O'Neill (1996) interpreted the shear zones to be Late Devonian and more or less synchronous. No significant mineral occurrences have been reported in the Leonard MacLeod Brook area.

Methods

Drill core from four holes in the Gillis Mountain pluton (MacKinnon, 2008) was logged and sampled for petrographic and chemical analyses. The deepest hole reached 363 m, and hence these data will provide insight into changes in the pluton with depth. In addition, the samples from O'Beirne (1979) will be re-analyzed to obtain a modern set of trace and rare earth elements, plus isotopic data for select samples.

New mapping has focused on the Leonard MacLeod Brook area where the geological units and relations have previously been relatively poorly defined.

Approximately 20 samples from the Gillis Mountain drill core and 200 samples from the Leonard MacLeod Brook area have been slabbed and stained for K-feldspar using the method of Hutchinson (1974) to assist with modal analysis. Thin sections have been made from most samples for petrographic descriptions. Slabs from the Leonard MacLeod Brook area were analyzed using a portable X-ray fluorescence instrument to provide an overview of their chemical composition. These data will aid in selecting a subset of about 40 samples for major, trace and rare earth element analysis. It is intended that Sm-Nd isotopic data will be obtained for about 5 samples, along with 3 to 4 additional radiometric age dates.

Preliminary results and future work

Initial examination of stained slabs and thin sections from the Gills Mountain pluton drill core show low-pressure contact

metamorphic mineral assemblages, consistent with high-level emplacement. Evidence of hydrothermal alteration is locally apparent adjacent to quartz veins and zones of copper sulphide mineralization (MacKinnon, 2008).

Mapping in the Leonard MacLeod Brook area during the summer of 2017 indicated that the rock types as described by O'Neill (1996) are broadly correct, but their distribution requires some revision. Volcanic rocks, especially pyroclastic rocks, occur throughout the area, and distinguishing the varied volcanic and sedimentary components of the Sarach Brook Metamorphic Suite, MacRae Brook formation, and MacMillan Mountain formation is problematic. At least two types of gabbroic to dioritic plutonic rocks occur in the area. Equigranular to porphyritic monzogranite characterizes the Leonard MacLeod Brook plutonic suite. O'Neill (1996) also included granophyric syenogranite in the Leonard MacLeod Brook suite; however, field relations indicate that it may be a younger unit and so is a target for dating. All these units are deformed in mylonitic shear zones (north-trending in the east; east-trending in the south and west). Granite of the Late Devonian Bothan Brook pluton is likely younger that any of the granitic units in the Leonard MacLeod Brook area, and was emplaced after deformation on the mylonitic shear zones. Sulphide mineralization (mainly pyrite) seems to be related to the shear zones, in contrast to the porphyry-style mineralization in the Gillis Mountain pluton. Absence of significant Cu, Pb, Mo or Zn mineralization in the Leonard MacLeod Brook area was confirmed by initial examination of the portable XRF analyses from sample slabs.

Future work will focus on using field observations, petrography, chemistry and U-Pb (zircon) dating to unravel the complex igneous events in the Leonard MacLeod Brook area for comparison to the much simpler history of the Gillis Mountain area.

Acknowledgments

References

Barr, S.M., 2010. Granites and terranes in Cape Breton Island; *in* Eurogranites 2010 Field Excursion Guidebook, Nova Scotia, (ed.) D.B. Clarke; Atlantic Geoscience Society Special Publication Number 37, p. 63–88.

Barr, S.M. and Jamieson, R.A., 1991. Tectonic setting and regional correlations of Ordovician – Silurian metavolcanic rocks of the Aspy Terrane, Cape Breton Island, Nova Scotia; Canadian Journal of Earth Sciences, v. 28, p. 1769–1779.

Barr, S.M. and Macdonald, A.S., 1992. Devonian plutonism and related mineralization in southeastern Cape Breton Island; Atlantic Geology, v. 28, p. 101–113.

Barr, S.M. and O'Beirne, A.M., 1981. Petrology of the Gillis Mountain pluton, Cape Breton Island, Nova Scotia; Canadian Journal of Earth Sciences, v. 18, p. 394–404.

Barr, S.M., O'Reilly, G.A., and O'Beirne, A.M. 1982. Geology and geochemistry of selected granitoid plutons of Cape Breton Island; Nova Scotia Department of Mines and Energy Paper 82-1, 176 p.

Barr, S.M., Jamieson, R.A., and Raeside, R.P., 1992. Geology of northern Cape Breton Island, Nova Scotia; Geological Survey of Canada, Map 1752A, scale 1:100 000.Cormier, R.F., 1979. Rubidium/strontium isochron ages of Nova Scotian granitoid plutons; Nova Scotia Department of Mines and Energy, Report 79-1, p. 143-147.

Dennis, F.A.R., 1988. Petrology and Mineralization of the Deep Cove Pluton, Gabarus Bay, Cape Breton Island, Nova Scotia; M.Sc. thesis, Acadia University, Wolfville, Nova Scotia, 209 p.

Dunning, G.R., Barr, S.M., Raeside, R.P., and Jamieson, R.A., 1990. U-Pb, zircon, titanite and monazite age in the Bras d'Or and Aspy Terranes of Cape Breton Island, Nova Scotia: Implications for igneous and metamorphic history; Geological Society of America Bulletin, v. 102, p. 322–330.

Hawkes, R.J., 1967. Exploration report on the McCormick Lake Granite, Noranda Exploration Campany; Nova Scotia Department of Mines, Report 13-C-66, 10 p.

Hibbard, J.P., van Staal, C.R., Rankin, D.W., and Williams, H. 2006. Lithotectonic map of the Appalachian Orogen, Canada – United States of America; Geological Survey of Canada, "A" Series Map 2096A, 2 sheets, scale 1:1 500 000.

Horne, R.J., 1995. Geology of the south-central Cape Breton Highlands, (Parts of NTS sheets 11K/07 and 11K/10), Inverness and Victoria Counties, Cape Breton Island, Nova Scotia; Nova Scotia Department of Natural Resources, Mineral and Energy Branch, Paper 95-2, 61 p.

Horne, R.J., Dunning, G., and Jamieson, R., 2003. U-Pb age data for Belle Cote Road orthogneiss, Taylors Barren pluton, and Bothan Brook pluton, southern Cape Breton Highlands (NTS 11K/07, 11K/10, 11K/11): Igneous ages and constraints on the age of host units and deformational history; *in* Mineral Resources Branch, Report of Activities 2002, Nova Scotia Department of Natural Resources Report 2003-1, pp 57-68.

Hutchinson, C.S., 1974. Laboratory handbook of petrographic techniques; Wiley Interscience, New York, New York, 527 p.

Jamieson, R.A. and Doucet, P., 1983. The Middle River – Crowdis Mountain area, southern Cape Breton Highlands; *in* Current research, Part A, Geological Survey of Canada, Paper 83-1A. p. 269–275.

Jamieson, R.A., Tallman, P., Marcotte, J.A., Plint, H.E., and

Connors, K.A., 1987. Geology of the Western-central Cape Breton Highlands, Nova Scotia; Geological Survey of Canada, Paper 87-13, 11 p.

Kirkham, R.V. and Soregaroli, A.E., 1975. Preliminary assessment of porphyry deposits in the Canadian Appalachians; Geological Survey of Canada, Paper 75-1, Part A, p. 249-252.

Lin, S., Davis, D.W., Barr, S.M., van Staal, C.R., Chen, Y., and Constantin, M., 2007. U-Pb geochronological constraints on the evolution of the Aspy terrane, Cape Breton Island: Implications for relationships between Aspy and Bras d'Or terranes and Ganderia in the Canadian Appalachians; American Journal of Science, v. 307, p. 371–398.

Macdonald, A.S. and Barr, S.M., 1993. The Blue Mountain polymetallic skarn and associated porphyry dykes, southeastern Cape Breton Island, Nova Scotia; *in* Mineral Deposit Studies in Nova Scotia v. II, (ed.) A.L. Sangster; Geological Survey of Canada Paper 91-9, p. 3–18.

MacKinnon, P., 2008. Gillis Mountain Drill Program 2008; Unpublished Assessment Report (Globex Mining Enterprises Inc.), Nova Scotia Department of Natural Resources, Report AR2008-234, 23 p plus appendices.

McMullin, D.W.A., Barr, S.M., and Raeside, R.P., 2010. Very low- and low-grade metamorphism of mafic volcanic rocks of the Mira terrane (Avalonia), southeastern Cape Breton Island, Nova Scotia; Atlantic Geology, v. 46, p. 95–126.

O'Beirne, A.M., 1979. Geology of the Gillis Mountain Pluton, Cape Breton Island, Nova Scotia; M.Sc. thesis, Acadia University, Wolfville, Nova Scotia, 168 p.

O'Beirne-Ryan, A.M. and Jamieson, R.A., 1986. Geology of the West Branch North River and the Bothan Brook plutons of the south-central Cape Breton Highlands, Nova Scotia; *in* Current research, Part B, Geological Survey of Canada, Paper 06-18, p. 191–200.

O'Neill, M., 1996. Geology of the Leonard MacLeod Brook area, southern Cape Breton Highlands, Nova Scotia; M.Sc. thesis, Acadia University, Wolfville, Nova Scotia, 203 p.

Sheard, E.R., 2007. Geology, mineralisation and alteration of the Deep Cove porphyry Cu-Mo deposit, Cape Breton Island, Nova Scotia; B.Sc. thesis, University of St. Andrews, Fife, Scotland, 129 p.

Slaman, L.R., Barr, S.M., White, C.E., and van Rooyen, D., 2017. Age and tectonic setting of granitoid plutons in the Cheticamp belt, western Cape Breton Island, Nova Scotia, Canada; Canadian Journal of Earth Sciences, v. 54, p. 88–109.

Willner, A.P., Barr, S.M., Glodny, J., Massonne, H.-J., Sudo, M., Thomson, S.N., van Staal, C.R., and White, C.E., 2015. Effects of fluid flow, cooling and deformation as recorded by $^{40}Ar/^{39}Ar$, Rb-Sr, and zircon fission track ages in very low- to low-grade metamorphic rocks in Avalonian SE Cape Breton Island (Nova Scotia, Canada); Geological Magazine, v. 152, p. 767–787.

New U-Pb (zircon and monazite) ages and Sm-Nd isotopic data from granitoid plutons in the Aspy and Bras d'Or terranes of Cape Breton Island, Nova Scotia: Implications for tectonic evolution and mineralization potential

D. van Rooyen[1], S.M. Barr[2] and C.E. White[3]

[1]*Department of Mathematics, Physics, and Geology, Cape Breton University, Sydney, Nova Scotia, B1P 6L2*
[2]*Department of Earth and Environmental Science, Acadia University, Wolfville, Nova Scotia, B4P 2R6*
[3]*Nova Scotia Department of Natural Resources, Box 698, Halifax, Nova Scotia, B3J 2T9*

Abstract

Granitoid plutons are widespread in the Ganderian Aspy and Bras d'Or terranes of Cape Breton Island and are diverse in composition, isotopic characteristics, and tectonic affinity. This study presents new U-Pb zircon ages from 10 previously undated plutons or their host rocks in the two terranes. The results range from Neoproterozoic (ca. 575 and 560 Ma in the Big Hill granodiorite and Price Point Formation), through Cambrian (ca. 515 and 510 Ma in Kellys Mountain diorite and granodiorite), Silurian (ca. 436 Ma in the Gillis Brook diorite, Gillanders Mountain granite, and ca. 420 Ma in the Leonard McLeod syenogranite), to Devonian (ca. 379 and 363 Ma in the Park Spur granite and Margaree pluton). Two samples were dated using U-Pb in monazite but the results for those were inconclusive and require further work. Overall the U-Pb zircon ages for samples presented here along with other recent work show a more complex magmatic history in the Bras d'Or and Aspy terranes than previously documented, and in particular more widespread Silurian magmatism. ƐNd data from this study shows that Bras d'Or and Aspy terrane rocks have negative ƐNd values characteristic of Ganderia. These results show Aspy and Bras D'Or terranes likely share similar basement rocks, and are both isotopically distinct from Avalonia, which has mainly positive ƐNd, and is represented in Cape Breton by the Mira terrane.

Introduction and project aims

Granitoid plutons constitute more than half of pre-Carboniferous rocks on Cape Breton Island and more than 120 different plutons, many of them composite, have been named, ranging from Mesoproterozoic to Late Devonian (Barr and White, 2017a). These plutons formed in a variety of tectonic settings, are compositionally varied, and display diversity in isotopic characteristics (e.g. Barr, 1990; Barr and Hegner, 1992; Potter et al., 2008). This diversity reflects the complex geology Cape Breton Island, which is made up of four lithotectonic divisions named (from north to south) the Blair River Inlier and Aspy, Bras d'Or and Mira terranes (Fig. 1). The Blair River Inlier is interpreted to be of Laurentian affinity whereas the terranes are peri-Gondwanan (Hibbard et al., 2006, 2007).

This study is focused on determining the distribution of Precambrian to Devonian plutons in the Bras d'Or and Aspy terranes. Many of these plutons have yet to be dated, and their relationships to each other are often obscure. Better geochronological context is essential in constructing an integrated understanding of tectonic significance and mineralization potential.

Methods

U-Pb geochronology

Most samples underwent electro-pulse disaggregation prior to zircon separation. Select grains were mounted, polished and imaged by cold cathodoluminescence (CL) to identify internal zoning and inclusions. These images were used to select ablation points (30 μm diameter), avoiding any visible inclusions, cracks, or other imperfections. Sample 11F16c-1115 was dated in situ from a polished thin section following methods described in Archibald et al. (2013).

U and Pb isotopic compositions were obtained by laser ablation – inductively coupled plasma – mass spectrometer (LA-ICP-MS) following the procedure outlined by McFarlane and Luo (2012) and Archibald et al. (2013). Data reduction was done using Iolite software (Paton et al., 2011) to process the laser output into data files, and further reduced for U–Pb geochronology using VizualAge (Petrus and Kamber, 2012). VizualAge outputs include uncorrected U–Pb ratios that were used to calculate ^{204}Pb-based corrections (Andersen, 2002) and ^{208}Pb-based corrections. Data were filtered using ^{204}Pb as a monitor. For grains with <80 counts/s ^{204}Pb, data are uncorrected; and for grains where the per cent error on the ^{204}Pb counts

---

Figure 1. Simplified geological map of Cape Breton Island modified after Barr et al. (1998) showing the locations of the dated samples and samples analyzed for Sm-Nd isotopes. Sample numbers and ages and ƐNd data are summarized in the inset tables at the bottom of the figure.

per second was <20%, we used a ^{204}Pb-based correction (Andersen, 2002). For grains where the per cent of radiogenic Pb (PB* in file) is less than 98.5% a ^{208}Pb-based correction (Petrus and Kamber, 2012). After these corrections were applied, data were sorted by per cent concordance (^{206}Pb/^{238}U versus ^{207}Pb/^{235}U), and by per cent radiogenic Pb in grains as calculated using VizualAge.

Concordia ages were calculated for clusters of three or more near-concordant points using Isoplot versions 3.75 and 4.15 (Ludwig, 2003, 2012). All ages are reported at 95% confidence, with decay-constant errors included in the calculations. Data points included in the Concordia calculations and reported here are grains that are 98 to 101% concordant and do not require a correction for common Pb (^{204}Pb < 80 counts per second). Because Concordia ages were calculated with as many grains as possible, the MSWD values and reported Probability of Concordance could in some cases be improved by using fewer grains. However, for consistency the approach of including as many grains as possible was followed throughout. In all cases the Concordia ages calculated overlap with the weighted mean ages for the samples using all near-concordant data. ^{206}Pb/^{238}U ages are used in all of the probability distribution calculations.

Concordia ages for standard FC1 during four separate runs were 1098.6 ± 3.7 Ma, 1098.7 ± 3.0 Ma, 1098.9 ± 2.9 Ma, and 1098.7 ± 2.4 Ma, respectively. Concordia ages for standard Plesovice during four separate runs were 339.5 ± 1.9 Ma, 339.5 ± 1.5 Ma, 339.0 ± 1.4 Ma and 334.18 ± 0.91 Ma. NIST610 glass was used as a concentration standard.

Monazite analyses data were filtered in a similar. For grains with <100 counts/s ^{204}Pb, data are uncorrected; and for grains where the per cent error on the ^{204}Pb counts per second was <20%, we used a ^{204}Pb-based correction (Andersen, 2002), and for grains where the per cent of radiogenic Pb (PB* in file) is less than 98.5% we used a ^{208}Pb-based correction (Petrus and Kamber, 2012). After these corrections were applied, data were sorted by per cent concordance (^{206}Pb/^{238}U versus ^{207}Pb/^{235}U), and by per cent radiogenic Pb in grains as calculated using VizualAge. Concordia age calculated for Monazite Standard 44069 was 425.9 ± 1.9 Ma with an MSWD (of concordance) of 5.5, and a probability (of concordance) of 0.019 and the Concordia age calculated for Monazite Standard 8153 was 510.61 ± 0.90 Ma with an MSWD (of concordance) of 7.2, and a probability (of concordance) of 0.007.

Whole rock Sm-Nd isotope analysis by TIMS

Whole rock powders were dissolved in Savilex© Teflon capsules using an 8 ml (4:1) mixture of 29 M HF – 15 M HNO$_3$. Prior to acid digestion, a mixed ^{150}Nd/^{149}Sm spike is added to each sample. After five days of acid digestion on a hotplate, the solution is then evaporated to dryness, taken back up in 6M HCl for 4 to 5 days. The sample is finally dried down and then re-dissolved in 2.5 M HCL. Samples are then loaded into a column containing cation exchange resin AG-50W-X8,

H$^+$ form, 200 to 400 mesh where a Sr fraction can be isolated followed by collection of bulk rare earth elements (REES). This bulk solution is then dried and taken up in 0.18 M HCl and loaded on a second column containing Eichrom© Ln resin (50–100 mesh) to isolate Sm and Nd separately from the other REEs. All reagents are purified in order to insure a low contamination level.

Sm and Nd concentrations and isotopic compositions are determined using a multi-collector Finnigan Mat 262 mass spectrometer in static mode for concentration determination, and dynamic mode for isotopic composition determination. Instrumental mass fractionation of Sm and Nd isotopes are corrected using a Raleigh law relative to ^{146}Nd/^{144}Nd of 0.7219 and ^{152}Sm/^{147}Sm of 1.783. The reported ^{143}Nd/^{144}Nd ratio is corrected for the deviation of repeated duplicates of the JNdi-1 standard from the accepted value of ^{143}Nd/^{144}Nd of 0.512115 (Tanaka et al., 2000). The 6 month mean value for Jndi-1 is ^{143}Nd/^{144}Nd of 0.512096 ± 14 (2SD, n=20).

Periodic analysis of USGS whole rock reference material BCR-2 ensured reproducibility with results of BCR-2 analyses over time in agreement with published results.

U-Pb geochronology samples

Twelve samples were selected for U-Pb zircon dating. These samples were chosen to cover some of the major igneous bodies in the Aspy and Bras d'Or terranes where robust ages were lacking. Samples and their locations are listed in Table 1, and also illustrated on the map in Figure 1.

CEW16-697 – Gillanders Mountain pluton (436.7 ± 2.6 Ma)

Sample CEW16-697 is medium-grained biotite monzogranite from the Gillanders Mountain pluton. This rock unit previously yielded a Devonian Rb-Sr age (French, 1985). The dated sample consists of approximately equal amounts of plagioclase, microcline and quartz, with less than 10% biotite. As is typical of the pluton (French, 1995), the quartz is interstitial and recrystallized into a mosaic of small anhedral grains. The zircon grains in this sample are mostly elongate euhedral crystals and bipyramidal terminations and a 3:1 to 5:1 aspect ratio. The grains are typically cloudy and stained brown. Ten grains yield a calculated Concordia age of 436.7 ± 2.6 Ma, interpreted as the main age of crystallization with an MSWD (of concordance) of 0.46, and probability (of concordance) of 0.50. A spread of younger ages (6 grains) do not make an overlapping cluster, and are interpreted as resulting from Pb loss.

The age of 436.7 ± 2.6 Ma is similar to Early Silurian ages reported by Slaman et al. (2017) for the MacLean Brook and Lavis Brook plutons in the Chéticamp plutonic belt to the north, and confirms that Silurian plutonic rocks are widespread in the Aspy terrane. It is somewhat older than the previously dated Silurian Gillanders Mountain diorite (428.6 ± 1.9 Ma; Lin et al., 2007), and is significantly older than rhyolite of the

Table 1: Samples for U-Pb zircon geochronology.

Terrane	Sample Number	Unit	Rock type	GZ	Easting	North-ing	Calculated Concordia age
Aspy	CEW16-519	Park Spur granite	granite	20T	671007	5163879	Concordia Age = 379.1 ±3.5 Ma
Aspy	CEW16-600	Dyke in JBMS on Cabot Trail	andesite	20T	658247	5176164	No zircons
Aspy	CEW16-697	Gillanders Mtn granite	granite	20T	651866	5121118	Concordia Age = 436.7 ±2.6 Ma
Aspy	CEW16-698	Leonard McLeod f.g. syenogranite	granite	20T	667595	5119757	Concordia Age = 420.9 ±2.8 Ma
Aspy	CEW16-699	Gillis Brook diorite	diorite	20T	664218	5114482	Concordia Age = 436.4 ±1.5 Ma
BdO	SMB16-216	Big Hill gd	granodiorite	20T	679335	5115865	Concordia Age = 559.4 ±1.8 Ma
Aspy	SMB16-218	Margaree Pluton	granite	20T	666347	5159009	Concordia Age = 363.1 ±1.6 Ma
BdO	SMB16-219	Kellys Mtn diorite (south side)	diorite	20T	697755	5117977	Concordia Age = 515.2 ±5.7 Ma
BdO	SMB16-220	Kellys Mtn bt gd (south side)	granodiorite	20T	691618	5122253	Concordia Age = 510.1 ±3.6 Ma
Aspy	SMB16-221	White Point	granite	20T	701919	5195291	Only high Th grains, no zircons
BdO	SMB16-222	Price Point Fm (St. Anns)	dacite	20T	689135	5134262	Concordia Age = 576.5 ±2.3 Ma
Aspy/BdO boundary	SMB16-224	granitic body in Gisborne Flowage	2-mica gt granite	20T	686570	5157674	Only high Th grains, no zircons

adjacent Fisset Brook Formation dated at 373 ± 4 Ma (Dunning et al., 2002).

Sample CEW16-699 – Gillis Brook diorite (436.1 ± 1.4 Ma)

The Gillis Brook diorite was mapped by O'Neill (1996) as a separate component within the Leonard MacLeod Brook complex of Barr et al. (1992). He described the unit as consisting of fine- to medium-grained dioritic rocks. The dated sample is from the southern part of the unit and is more gabbroic than dioritic. It consists of relict medium-grained plagioclase and clinopyroxene with abundant secondary minerals including biotite, chlorite, epidote, iron oxides/hydroxides, sericite and carbonate minerals.

Zircon grains in this sample are clear, mostly rounded and flat. Some are subhedral, but have clear facets. Some of the grains show brownish-red surface staining. In CL most grains show clear oscillatory zoning. Twenty-one grains yielded a calculated Concordia age of 436.1± 1.4 Ma, interpreted as the main age of crystallization with an MSWD (of concordance) of 1.05, and a probability (of concordance) of 0.31. The age of 436.1 ± 1.4 Ma shows that the diorite is Silurian, similar in age to the Lavis Brook diorite and MacLean Brook granite in the Chéticamp belt reported by Slaman et al. (2017) and somewhat older than the nearby diorite at Gillanders Mountain (428.6 ± 1.9 Ma; Lin et al., 2007). However, it is similar to the age of Gillanders Mountain monzogranite sample CEW16-697 (436.7 ± 2.6 Ma) mentioned above. It is significantly older than the Leonard MacLeod Brook monzogranite with which it is closely associated (see below), and 70 Ma older than the nearby Bothan Brook pluton dated at 376 ± 3 Ma (Horne et al., 2003).

CEW16-698 – Leonard MacLeod Brook monzoganite (420.9 ± 2.8 Ma)

Several types of granite occur in the enigmatic Leonard MacLeod Brook complex of Barr et al. (1992). O'Neill (1996) mapped and named the component plutons, as well as recognizing volcanic rocks which he assumed to be Silurian. Dated sample CEW16-698 is a fine-grained monzogranite from the Leonard MacLeod Brook plutonic suite of O'Neill (1996), which he inferred to be Devonian, like the 376 ± 3 Ma Bothan Brook pluton farther north (Horne et al., 2003). It is fine- to medium-grained mosaic of recrystallized K-feldspar and plagioclase; quartz is much less abundant than feldspar and is fine-grained and recrystallized in the interstices. Flakes of green biotite are also present, as well as scattered phenocrysts of plagioclase.

Zircon grains in this sample are all small, between 30 and 50 μm, and are short and stubby with euhedral shapes. About half are clear and colourless, and half are cloudy. The larger grains show oscillatory zoning in CL, but the smaller ones do not have distinct zones. Eleven grains yield a calculated Concordia age of 420.9 ± 2.8 Ma interpreted as the main age of crystallization with an MSWD (of concordance) of 0.96, and a Probability (of concordance) of 0.33.

This age shows that the granite is Silurian, not Devonian as previous assumed (O'Neill, 1996). It is younger than both the associated Gillis Brook diorite (436.1 ± 1.4 Ma) and the nearby diorite at Gillanders Mountain (428.6 ± 1.9 Ma; Lin et al., 2007), as well as monzogranite sample CEW16-697 (436.7 ± 2.6 Ma) from Gillanders Mountain. The Leonard MacLeod

Brook granite is also younger than the Taylors Barren pluton to the north that has an age of 430 ± 2 Ma (Horne et al., 2003). Thus, Silurian plutonism in this part of the Aspy terrane appears to be both more widespread and more protracted than previously recognized.

CEW16-519 – Park Spur Granite (379.1 ± 3.5 Ma)

The Park Spur granite is located in the Aspy terrane close to the Eastern Highlands Shear Zone, the boundary between Aspy and Bras d'Or terranes (Fig. 1). It was previously undated, but assumed mid-Devonian and related to the Black Brook Granitic Suite (Raeside and Barr, 1992). The dated sample is medium-grained monzogranite with minor (<5%) muscovite and biotite. Quartz is polygranular and interstitial to feldspar, which includes both plagioclase and microcline.

The sample contains few zircon grains and all possible grains were analyzed. Grains vary in shape from euhedral to rounded. In CL the grains do not show bright fluorescence, but zoning is visible in the larger grains. The calculated Concordia Age of 379.1 ± 3.5 Ma interpreted as the main age of crystallization with an MSWD (of concordance) of 0.084, with a Probability (of concordance) of 0.77. In this case there are only three grains in the Concordia age calculation, but they overlap, and make a peak in the frequency distribution. No other clusters occur in the dataset that includes very few concordant grains. The age of 379.1 ± 3.5 Ma confirms the previously proposed inferred mid-Devonian age (Raeside and Barr, 1992), and is within error of the U-Pb zircon (375 +5/-4 Ma) and monazite (372–373 Ma) ages from the Black Brook Granitic Suite (Dunning et al., 1990).

SMB16-218 – Margaree pluton (363.1 ± 1.6 Ma)

The Margaree pluton is the largest pluton in the Aspy terrane and consists mostly of distinctive megacrystic granite with plagioclase-rimmed K-feldspar (O'Beirne-Ryan et al., 1986). The pluton was previously dated by Rb-Sr and yielded a date of 353 ± 13 Ma (O'Beirne-Ryan et al., 1986). It was assumed to be the same age as the ca. 375 Ma rhyolite of the bimodal Fisset Brook Formation (Dunning et al., 2002) and the 365 +10/-5 Ma granite of the Salmon Pool pluton (Jamieson et al., 1986), and like them related to post-orogenic extension (Barr and Jamieson, 1991).

Sample SMB16-218 is medium-grained megacrystic granite with megacrysts of K-feldspar and smaller grains of quartz and plagioclase. Biotite forms 5% of the rock, and allanite is an accessory component. Zircon crystals in this sample are generally elongated euhedral to subhedral grains. The finer grained crystals in the sample (<100 μm) are mostly euhedral, showing bipyramidal terminations. Most grains are clear, but some show orange and black staining. Nineteen grains yielded a calculated Concordia age of 363.1 ± 1.6 Ma, which is interpreted as the main age of crystallization with an MSWD (of concordance) of 9.5, and probability (of concordance) of 0.002. The MSWD and probability of concordance could be improved by using fewer grains to calculate them, but this age is calculated with as many near-concordant grains as possible.

This is the youngest igneous age yet reported in the Aspy terrane, and is especially significant because of the large size of the Margaree pluton. The pluton straddles the prominent Aspy Fault, and also appears to "stitch" the shear zones that separate the Grenville-age Blair River Inlier from the rest of the highlands. The new age is within error as the age of 365 ± 2 Ma reported by Dunning et al. (2002) from rhyolite in the Lowland Cove Formation which overlies Grenvillian-age rocks of the Blair River Inlier. It is at the upper limit of the error range of an Rb-Sr date of 353 ± 13 Ma (O'Beirne-Ryan et al., 1986), and significantly younger than the Fisset Brook rhyolite. Hence the Late Devonian magmatic history of the Aspy terrane is more complex than previously known; the young events recorded in both the Aspy terrane and Blair River Inlier are consistent with the interpretation that those two areas were in proximity by that time.

CEW 16-600 – andesitic sill in the Jumping Brook Metamorphic suite (no age)

CEW16-600 is an andesitic sill in the Jumping Brook Metamorphic Suite (JBMS) in a new road cut on the Cabot Trail north of Chéticamp. The JBMS is a major lithological unit in the Aspy terrane but has been challenging to date. An age on this sill would have provided constraints on the deformation in the JBMS since it is deformed concordantly with the metamorphic country rock and could have provided a maximum age for the country rock. Unfortunately, no zircon grains or other dateable mineral phases were found in this sample.

SMB16-221 – Black Brook Granitic Suite (407.3 ± 1.5 Ma)

SMB16-221 is from White Point at the northern tip of the Black Brook Granitic Suite (BBGS). A biotite granite sample from the southern part of the BBGS previously yielded a U-Pb zircon age of 375 +5/-4 Ma and monazite ages of 372 to 373 Ma (Dunning et al., 1990). Due to the large size and important position of the BBGS in the Aspy-Bras d'Or boundary zone, dating a second sample from a different unit of this complex pluton (Yaowanoiyothin and Barr, 1991) seemed worthwhile. The dated sample is medium-grained muscovite-biotite monzogranite with allotriomorphic equigranular texture. The granite in this area contains abundant screens and enclaves of pelitic schist and other metamorphic rocks.

Sample SMB16-221 contains no zircon grains, but has a large number of high-thorium monazite grains. The dated crystals are high relief, euhedral grains with an elongated crystal habit and bipyramidal terminations. The crystals are slightly yellow under an optical microscope and under CL show blue-grey fluorescence but no oscillatory zoning.

The calculated Concordia age for this sample is 407.3 ± 1.5 Ma with an MSWD (of concordance) of 1.07, and a probability (of concordance) of 0.30 with 8 grains included in the calculation. This age suggests that this part of the BBGS is older than

the previously dated southern biotite monzogranite unit (Dunning et al., 1990). Alternatively, it is possible that the monazite grains could be inherited from the abundant xenolithic material in the granite. This interpretation is supported by the age of 379.1 ± 3.5 Ma for the Park Spur granite (CEW16-519 above), a muscovite and biotite-bearing granite that appears similar to the BBGS. In any case, additional dating is needed from the BBGS to better determine its age.

SMB16-224 – Muscovite-biotite pegmatitic granite (593.4 ± 3.2 Ma)

SMB16-224 is a pegmatitic granite body in the Gisborne Flowage quartz diorite, a magmatic epidote-bearing pluton (Farrow and Barr, 1992) previously dated by Dunning et al. (1990) at 564 ± 2 Ma (zircon) and 548 ± 2 Ma (titanite). The quartz diorite is intruded by abundant muscovite-bearing granitic, aplitic, and pegmatitic sheets, dykes, and small plutons (Raeside and Barr, 1992). The dated sample is from one of these muscovite-bearing granitic bodies to determine if they are similar in age to or younger than the host quartz diorite. The sample consists of medium-grained allotriomorphic inequigranular quartz, plagioclase, and microcline, with abundant garnet and muscovite and minor biotite. The sample contains no zircon grains, but has a large number of high-thorium monazite grains. The dated crystals are high relief, euhedral grains with an elongated crystal habit. The crystals are slightly yellow under an optical microscope and under CL show blue-grey fluorescence, but no oscillatory zoning.

The calculated Concordia age for this sample is 593.4 ± 3.2 Ma with an MSWD (of concordance) of 2.9, and a probability (of concordance) of 0.090 with 8 grains included in the calculation. This new age seems to suggest that the muscovite-bearing granitic bodies are older than their host rocks (previously dated at 564 Ma), which is impossible based on clear crosscutting field relations. Given that monazite from both the White Point sample and the Gisborne Flowage sample are ca. 30 Ma older than their field association suggests, we suspect a systemic problem with the monazite ages with inheritance in both units possibly contributing to the age discrepancy. Additional sampling is required to follow up on this problem.

SMB16-222 – Price Point Formation dacitic tuff (576.5 ± 2.3 Ma)

The Price Point Formation occurs in the southeastern Cape Breton Highlands and consists of mainly intermediate lithic and lithic-crystal tuff with minor andesitic and dacitic flows (Macdonald and Barr, 1985). The volcanic rocks were interpreted initially to be Devonian or Carboniferous, because of an inferred correlation with the Fisset Brook Formation (Kelley and Mackasey, 1965). However, Macdonald and Barr (1985) suggested a Neoproterozoic age based on interpreted intrusive contacts with plutonic rocks in the area, in particular the Indian Brook granodiorite that yielded a U-Pb titanite age of 564 ± 4 Ma interpreted to be the approximate crystallization age of the granodiorite (Dunning et al., 1990).

Sample SMB16-222 is a black dacitic lithic tuff. Most of the clasts in the tuff consist of plagioclase phenocrysts in very fine-grained quartzofeldspathic groundmass. Zircons in this sample are small, stubby grains and some are very rounded. Zircons are mostly clear with oscillatory zoning visible in CL, some have facets and are euhedral. It has a calculated Concordia Age of 576.5 ± 2.3 Ma interpreted as the main age of crystallization with an MSWD (of concordance) of 0.090, and a Probability (of concordance) of 0.76. This age includes 18 grains in the Concordia calculation.

This age supports the inferred co-magmatic relationship with the Indian Brook granodiorite and other plutonic units of the southeastern highlands (Grecco and Barr, 1999), although it is somewhat older than the dated plutons, which have ages between 570 Ma (Birch Plain granite; Barr et al., work in progress, 2017) and 555 Ma (Ingonish River tonalite; Dunning et al., 1990).

SMB16-216 – Big Hill Granodiorite (559.4 ± 1.8 Ma)

The Big Hill granodiorite is part of an elongate plutonic belt west of the belt containing the Price Point Formation, Indian Brook granodiorite and Birch Plain granite. Raeside and Barr (1992) included it in the Goose Cove pluton, but Barr and White (2017b) divided the area into a northern Goose Cove pluton and a southern Big Hill pluton, although they are probably of similar age. The pluton intruded the Glen Tosh Formation at Big Hill (Barr et al., 2013). It consists of hornblende-biotite granodiorite gradational to granite, locally with microcline megacrysts. The dated sample SMB16-216 is monzogranite with plagioclase and chloritized biotite enclosed in interstitial quartz and K-feldspar.

Zircons from this sample are mainly elongate crystals with bipyramidal terminations, although a few rounded grains are present. Grain size varies widely from 50 to 200 μm. The grains are slightly cloudy and about a quarter have a yellowish tint. In CL the grains show clear oscillatory zoning. The calculated Concordia Age of 559.4 ± 1.8 Ma interpreted as the main age of crystallization, with an MSWD (of concordance) of 1.3, and Probability (of concordance) of 0.25. This Concordia calculation includes 21 grains. A few near-concordant grains that could be old inherited grains occur at 1.3, 1.5 and 1.8 Ga, but these are single grains so do not provide unequivocal evidence of inheritance.

The Concordia age of 559.4 ± 1.8 Ma is slightly younger than the U-Pb titanite age from the Indian Brook granodiorite (Dunning et al., 1990), although the ages barely overlap within error. Like the ages from the Price Point Formation and Birch Plain Granite, this age supports the inferred broadly co-magmatic relationship among the volcanic rocks and plutons in the eastern highlands. Including the new data, these plutons are now represented by seven ages, the oldest of which is Price Point Formation at ca. 576 Ma, and youngest is Ingonish River tonalite at 555 Ma.

Table 2. Samples selected for Sm-Nd analysis.

Terrane	Sample number	Unit	Rock type	Zone	Easting	Northing	Age Ma
BdO	CBH88-7	Birch Plain granite	Granite	20T	697088	5155770	565
Aspy	CEW15-004	Lake Ainslie granite	Granite	20T	644527	5103843	440
Aspy	CEW15-014A	Grand Falaise K-feldspar granite	Granite	20T	656421	5171114	428
BdO	CH87-27	Creignish Hills granite	Granite	20T	624766	5068852	550
Aspy	CW14-121	French Mtn syenogranite	Syenogranite	20T	659307	5178443	366
Aspy	CW86-3587	Black Brook Granitic Suite	Granite	20T	693108	5187581	375
BdO	F15-1541	Boisdale Hills granodiorite	Granodiorite	20T	691080	5096079	542
Mira	F16c-1033	Gillis Mountain monzogranite	Monzogranite	20T	7130096	5085568	380
Aspy	SB86-3068	Glasgow Brook orthogneiss	Orthogneiss	20T	692693	5190472	411
BdO	SMB02-81	Chuggin Road orthogneiss	Orthogneiss	20T	642350	5094125	560

SMB16-219 and SMB16-220 – Kellys Mountain diorite and granodiorite (515.2 ± 5.7 Ma and 510.1 ± 3.6 Ma, respectively)

SMB16-219 is medium-grained diorite from the south side of Kellys Mountain in the Bras d'Or terrane (Fig. 1). It consists mostly of plagioclase and hornblende, the latter with relict cores of pyroxene. Quartz and biotite are minor interstitial components. The sample is zircon poor, and every grain that could be picked was analyzed. The zircon grains are subhedral to anhedral grains in the 20 to 100 μm range. The subhedral grains still display recognizable pyramidal terminations. In CL most grains show clear oscillatory zoning. The calculated for this sample is Concordia Age of 515.2 ± 5.7 Ma interpreted as the main age of crystallization with an MSWD (of concordance) of 0.051, and a Probability (of concordance) of 0.82. In this case there are only three overlapping grains in the Concordia calculation. There are no other clusters in the dataset, and there were very few concordant grains in this sample.

SMB16-220 is coarse-grained granodiorite/monzogranite from the south side of Kellys Mountain east of the dioritic unit represented by sample SMB16-219. Unlike the typical leucogranite that forms most of Kellys Mountain, sample SMB16-220 contains 10 to 15% biotite and minor hornblende. Plagioclase is the most abundant mineral, with quartz and perthitic orthoclase mainly interstitial. Zircon grains are euhedral and very fine grains in the 20 to 100 μm range. Grains display pyramidal terminations and prismatic shapes. Black rounded inclusions and red/orange staining is typical. In CL most grains show clear oscillatory zoning. This sample has a calculated Concordia Age of 510.1 ± 3.6 Ma interpreted as the main age

of crystallization with an MSWD (of concordance) of 1.3, and a probability (of concordance) of 0.26. It includes 9 grains in the Concordia calculation, and overlaps within error with the Kellys Mountain diorite (SMB-16-219 above).

The Cambrian ages of these samples are unexpected, as both rocks were previously assumed to be Neoproterozoic. The ages are similar to those of volcanic rocks and associated high-level granite in the Boisdale Hills to the south, assumed to be linked to separation of Ganderia from Gondwana (White et al., 1994). These ages are slightly older than the age of granite intrusion into the Kellys Mountain paragneiss, dated at 498 ± 2 Ma (Barr et al., 1990) and ca. 490 Ma (van Rooyen et al., 2017), suggesting a bimodal magmatic history in the Kellys Mountain area spanning ca. 20 Ma.

Sm-Nd isotopic data

Eleven samples from plutons with known U-Pb zircon ages were selected for Sm-Nd isotopic analysis. Sample locations are shown on Figure 1 and listed in Table 2.

The ƐNd data from the new samples are shown on Figure 2, plotted against the age of the unit. Also shown are previously existing ƐNd data for the Aspy, Bras d'Or and Mira terranes. The new data support the distinction between Avalonia and Ganderia, with mainly positive ƐNd in Avalonia igneous rocks and mainly negative ƐNd in Ganderian igneous rocks, as described in previous studies (e.g. Samson et al., 2000). Aspy and Bras d'Or samples are similar, supporting the interpretation that the Aspy terrane has a Bras d'Or terrane-like basement. However, data from units in the western part of the Aspy terrane
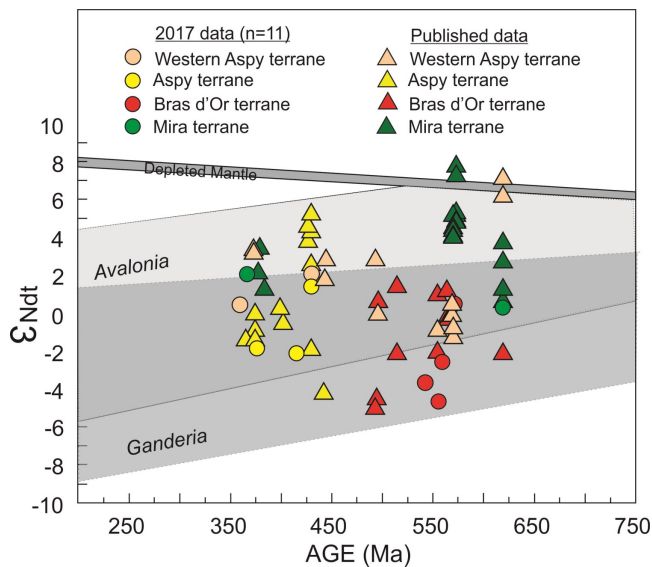
Figure 2. Plot of initial ƐNd versus age for igneous rocks from Cape Breton Island showing data obtained in this study (circles) and previously published data (triangles) Previously published data are from Barr and Hegner (1992), Barr et al. (1998), an and Slaman et al. (2017). Light grey shaded area indicates isotopic evolution of Neoproterozoic igneous samples from Avalonia estimated from Murphy (2002) and overlapping darker grey shaded area encloses the field for Neoproterozoic igneous samples in Ganderia estimated from Samson et al. (2000). Depleted mantle evolution curve is approximated from the model of DePaolo (1981).

tend to have positive ƐNd signatures (Fig. 2). It is apparent that more data is required to properly interpret the isotopic data, likely including the addition of Hf data from dated zircon.

Acknowledgments

References

Andersen, T., 2002. Correction of common lead in U–Pb analyses that do not report [204]Pb; Chemical Geology, v. 192, p. 59–79.

Archibald, D.B., Barr, S.M., Murphy, J.B., White, C.E., MacHattie, T.G., Escarraga, E.A., Hamilton, M.A., and McFarlane, C.R.M., 2013. Field relationships, petrology, age, and tectonic setting of the Ordovician West Barneys River Plutonic Suite, southern Antigonish Highlands, Nova Scotia, Canada; Canadian Journal of Earth Sciences, v. 50, p. 727–745.

Barr, S.M., 1990. Granitoid rocks and terrane characterization: An example from the northern Appalachian Orogen; Geological Journal, v. 25, p, 295–304.

Barr, S.M. and Hegner, E., 1992. Nd isotopic compositions of felsic igneous rocks in Cape Breton Island, Nova Scotia: Implications for petrogenesis and terrane analysis; Canadian Journal of Earth Sciences, v. 29, p. 650–657.

Barr, S.M. and Jamieson, R.A., 1991. Tectonic setting and regional correlation of Ordovician–Silurian rocks of the Aspy terrane, Cape Breton Island, Nova Scotia; Canadian Journal of Earth Sciences, v. 28, p. 1769–1779.

Barr, S.M. and White, C.E., 2017a. Overview map showing locations of bedrock geology maps for Cape Breton Island, Nova Scotia; Nova Scotia Department of Natural Resources, Geoscience and Mines Branch, Open File Map ME 2017-006, scale 1:220 000.

Barr, S.M. and White, C.E., 2017b. Bedrock geology map of the Whycocomagh area, NTS 11F/14, Inverness County, Nova Scotia. Nova Scotia Department of Natural Resources, Geoscience and Mines Branch, Open File Map ME 2017-013, scale 1:50 000.

Barr, S.M., Dunning, G.R., Raeside, R.P., and Jamieson, R.A., 1990. Contrasting U–Pb ages from plutons in the Bras d'Or and Mira terranes of Cape Breton Island, Nova Scotia; Canadian Journal of Earth Sciences, v. 27, p. 1200–1208.

Barr, S.M., Jamieson, R.A., and Raeside, R.P., 1992. Geology, Northern Cape Breton Island, Nova Scotia; Geological Survey of Canada, Map 1752A, scale 1:100 000.

Barr, S.M., Raeside, R.P., and White, C.E., 1998. Geological correlations between Cape Breton Island and Newfoundland, northern Appalachian orogen; Canadian Journal of Earth Sciences, v. 35, p. 1252–1270.

Barr, S.M., Pin, C., McMullin, D.W., and White, C.E., 2013. Whole-rock chemical and Sm-Nd isotopic composition of a Late Proterozoic metasedimentary sequence in Ganderia: Kellys Mountain, Bras d'Or terrane, Nova Scotia, Canada; Atlantic Geology, v. 49, p. 57–70.

Barr, S.M., van Rooyen, D, and White, C.E. Granitoid plutons in Cape Breton Island, Nova Scotia, Canada: new U-Pb (zircon) age constraints and implications for correlations with peri-Gondwanan terranes in Newfoundland and New Brunswick. Work in progress.

DePaolo, D.J. 1981. Neodymium isotopes in the Colorado front range and crust mantle-evolution in the Proterozoic. Nature, v. 291, p. 193–196.

Dunning, G.R., Barr, S.M., Raeside, R.P., and Jamieson, R.A.,

1990. U-Pb zircon, titanite, and monazite ages in the Bras d'Or and Aspy terranes of Cape Breton Island, Nova Scotia: Implications for magmatic and metamorphic history; Geological Society of America Bulletin, v. 102, p. 322–330.

Dunning, G.R., Barr, S.M., Giles, P.S., McGregor, D.C., Pe-Piper, G., and Piper, D.J., 2002. Chronology of Devonian to early Carboniferous rifting and igneous activity in southern Magdalen Basin based on U-Pb (zircon) dating; Canadian Journal of Earth Sciences, v. 39, p. 1219–1237.

Farrow, C.E.G. and Barr, S.M., 1992. Petrology of high-alumina hornblende and magmatic epidote-bearing plutons, southeastern Cape Breton Highlands, Nova Scotia; Canadian Mineralogist, v. 30, p. 377–392.

French, V.A., 1985. Geology of the Gillanders Mountain Intrusive Complex and satellite plutons, Lake Ainslie area, Cape Breton Island, Nova Scotia; M.Sc. thesis, Acadia University, Wolfville, Nova Scotia, 237 p.

Grecco, L. and Barr, S.M., 1999. Late Neoproterozoic granitoid and metavolcanic rocks of the Indian Brook area, southeastern Cape Breton Highlands, Nova Scotia; Atlantic Geology, v. 35, p. 43–57.

Horne, R.J., Dunning, G., and Jamieson, R., 2003. U-Pb age data for Belle Côte Road orthogneiss, Taylors Barren pluton and Bothan Brook pluton, southern Cape Breton Highlands (NTS 11K/07, 11K/10, 11K/11): Igneous ages and constraints on the age of host units and deformational history; *in* Mineral Resources Branch, Report of Activities 2002; Nova Scotia Department of Natural Resources, Report 2003-1, p. 57–68.

Jamieson, R.A., van Breemen, O., Sullivan, R.W., and Currie, K.L., 1986. The age of igneous and metamorphic events in the western Cape Breton Highlands, Nova Scotia; Canadian Journal of Earth Sciences, v. 23, p. 1891–1901.

Kelley, D.G. and Mackasey, W.O., 1965. Basal Mississippian volcanic rocks in Cape Breton Island; Geological Survey of Canada, Paper 64–34, 10 p.

Lin, S., Davis, D.W., Barr, S.M., van Staal, C.R., Chen, Y., and Constantin, M., 2007. U-Pb geochronological constraints on the evolution of the Aspy Terrane, Cape Breton Island: Implications for relationships between Aspy and Bras d'Or terranes and Ganderia in the Canadian Appalachians; American Journal of Science, v. 307, p. 371–398.

Ludwig, K.R., 2003. Isoplot 3.75: A Geochronological Toolkit for Microsoft Excel; Berkeley Geochronological Center. <http://www.bgc.org/isoplot_etc/isoplot/Isoplot3_75files.zip>

Ludwig, K.R., 2012. Isoplot 4.15: A Geochronological Toolkit for Microsoft Excel. Berkeley Geochronological Center. <http://www.bgc.org/isoplot_etc/isoplot/Isoplot4_15files.zip>

Macdonald, A.S. and Barr, S.M., 1985. Geology and age of polymetallic mineral occurrences in volcanic and granitoid rocks, St. Anns area, Cape Breton Island, Nova Scotia; *in*

Current research, Part B, Geological Survey of Canada Paper 85 1B, p. 117–124.

McFarlane, C.R.M. and Luo, Y., 2012. Modern analytical facilities: U-Pb geochronology using 193nm Excimer LA-ICP-MS optimized for in situ accessory mineral dating in thin sections; Geoscience Canada, v. 39, p. 158–172.

Murphy, J.B., 2002. Geochemistry of the Neoproterozoic metasedimentary Gamble Brook Formation, Avalon terrane, Nova Scotia: Evidence for a rifted-arc environment along the west Gondwanan margin of Rodinia; Journal of Geology, v. 110, p. 407–419.

O'Beirne-Ryan, A.M., Barr, S. M., and Jamieson, R.A., 1986. Contrasting petrology and age of two megacrystic granitoid plutons, Cape Breton Island, Nova Scotia; *in* Current research, Part B. Geological Survey of Canada, Paper 86-lB, p. 179–189.

O'Neill, M., 1996. Geology of the Leonard MacLeod Brook area, southern Cape Breton Highlands, Nova Scotia; M.Sc. thesis, Acadia University, Wolfville, Nova Scotia, 203 p., 1 map.

Petrus, J.A. and Kamber, B.S., 2012. VizualAge: A novel approach to laser ablation ICP-MS U- Pb geochronology data reduction; Geostandards and Geoanalytical Research, v. 36, p. 247–270.

Potter, J., Longstaffe, F.J., Barr, S.M., Thompson, M.D., and White, C.E., 2008. Altering Avalonia: Oxygen isotopes and terrane distinction; Canadian Journal Earth Sciences, v. 45, p. 815–825.

Raeside, R.P. and Barr, S.M. 1992. Geology of the northern and eastern Cape Breton Highlands, Nova Scotia; Geological Survey of Canada, Paper 89–14, 39 p.

Samson, S.D., Barr, S.M., and White, C.E., 2000. Nd isotopic characteristics of terranes within the Avalon zone, southern New Brunswick; Canadian Journal of Earth Sciences, v. 37, p. 1039-1052.

Slaman, L.R., Barr, S.M., White, C.E., and van Rooyen, D., 2017. Age and tectonic setting of granitoid plutons in the Chéticamp belt, western Cape Breton Island, Nova Scotia, Canada; Canadian Journal of Earth Sciences, v. 54, p. 88-109.

van Rooyen, D., Barr, S.M., and White, C.E., 2017. Proterozoic to Cambrian zircon geochronology in the Bras d'Or terrane on Cape Breton Island, Nova Scotia: Deciphering the infrastructure of Ganderia; Atlantic Geoscience Society Colloquium, Fredericton, New Brunswick. Atlantic Geology v. 53, p. 179.

White, C.E., Barr, S.M., Bevier, M.L., and Kamo, S., 1994. A revised interpretation of Cambrian and Ordovician rocks in the Bourinot belt of central Cape Breton Island, Nova Scotia; Atlantic Geology, v. 30, p. 123–142.

Yaowanoiyothin, W. and Barr, S.M., 1991. Petrology of the Black Brook Granitic Suite, Cape Breton Island, Nova Scotia; Canadian Mineralogist, v. 29, p. 499–515.

Ar/Ar thermochronology of the Aspy and Bras d'Or terranes, Cape Breton Island, Nova Scotia

D.A. Kellett[1], S.M. Barr[2], D. van Rooyen[3] and C.E. White[4]

[1]Geological Survey of Canada, 1 Challenger Drive, Dartmouth, Nova Scotia, B3B 1A6
[2]Department of Earth and Environmental Science, Acadia University, Wolfville, Nova Scotia, B4P 2R6
[3]Department of Mathematics, Physics, and Geology, Cape Breton University, Sydney, Nova Scotia, B1P 6L2
[4]Nova Scotia Department of Natural Resources, Box 698, Halifax, Nova Scotia, B3J 2T9

Abstract

The distribution of magmatic rocks through time within the Appalachian orogen suggests a tectonic control on magma generation. Cape Breton Island preserves a condensed yet complete record of the main tectonic units and magmatic suites of the Appalachian orogen. Here we present new ^{40}Ar/^{39}Ar cooling ages for muscovite from the Aspy terrane, a component of Ganderia preserved in western Cape Breton Island. The preliminary results show that this terrane cooled through muscovite closure temperatures during the Middle Devonian following regional metamorphism. Rocks from the southern Chéticamp plutonic belt of Aspy were not heated sufficiently during regional metamorphism to reset ^{40}Ar in muscovite. These results will contribute to a reconstruction of the tectonic and structural history of the Ganderian elements of the Appalachian orogen.

Introduction

The Aspy terrane of Cape Breton Island, Nova Scotia, is comprised of Neoproterozoic metamorphosed volcano-sedimentary units that are intruded by Late Neoproterozoic to Devonian intrusive rocks, and overlain by or faulted against Devonian to Carboniferous volcanic and sedimentary units (e.g. White et al., 2015; Fig. 1). It is juxtaposed against the Bras d'Or terrane along the Eastern Highlands shear zone. Though the Bras d'Or terrane also includes Neoproterozoic metamorphic and intrusive rocks, it notably lacks Silurian to Devonian intrusive rocks, suggesting a tectonic control on magma generation during the Silurian and Devonian. This coincides with the interpreted timing of slip along the Eastern Highlands shear zone (Lin, 1995), suggesting an association between regional orogenesis and granitoid magma generation and location.

^{40}Ar/^{39}Ar (Ar/Ar) geochronology is a valuable method for determining the post-metamorphic cooling history of medium- to high-metamorphic grade rocks. However, Ar/Ar dating of muscovite in particular can also be applied towards directly dating dynamic crystallization in shear zones (Kellett et al., 2016), as well as determining the crystallization age of low-grade metamorphic fabrics (Kellett et al., 2017a). A regional muscovite (+/- biotite, hornblende) Ar/Ar study in the Aspy and Bras d'Or terranes was initiated to determine age patterns across the Eastern Highlands shear zone. In the first phase of this study, we collected six samples in the Chéticamp region of the Aspy terrane (Kellett et al., 2017b), which has been a focus of recent mapping by the Nova Scotia Department of Natural Resources (White et al., 2015, 2016, 2017). These sequences, in which low- to high-metamorphic grade muscovite-bearing units are common, have not previously been dated by Ar/Ar (Fig. 1). Samples were selected to provide a regional distribution from lower (south) to higher (north) grade metamorphism, and to confirm earlier work demonstrating that Neoproterozoic plutonic rocks in the southern part of the Chéticamp plutonic belt did not experience sufficiently high metamorphic temperature during Silurian-Devonian regional metamorphism of the Aspy terrane to reset ^{40}Ar in muscovite (Reynolds et al., 1989; Fig. 1).

Samples were also collected from the Bras d'Or terrane, and along the Aspy/Bras d'Or terrane boundary. Although there have been two significant Ar/Ar studies covering the Bras d'Or region (Reynolds et al., 1989; Dallmeyer and Keppie, 1993; Fig. 1), they focused on hornblende- and biotite-bearing units, and presented few muscovite Ar/Ar ages. Further, for the dated muscovite the relationship between deformation and muscovite growth/recrystallization was not established to evaluate whether the ages represent cooling or deformation below the Ar closure temperature. Our sampling focused on obtaining a regional coverage of muscovite-bearing units, including sheared samples that will also be subjected to microstructural analysis.

Method

Muscovite (± biotite and hornblende) grains were separated by gentle hand crushing with mortar and pestle, washed and picked under a microscope. The mineral separates were irradi-
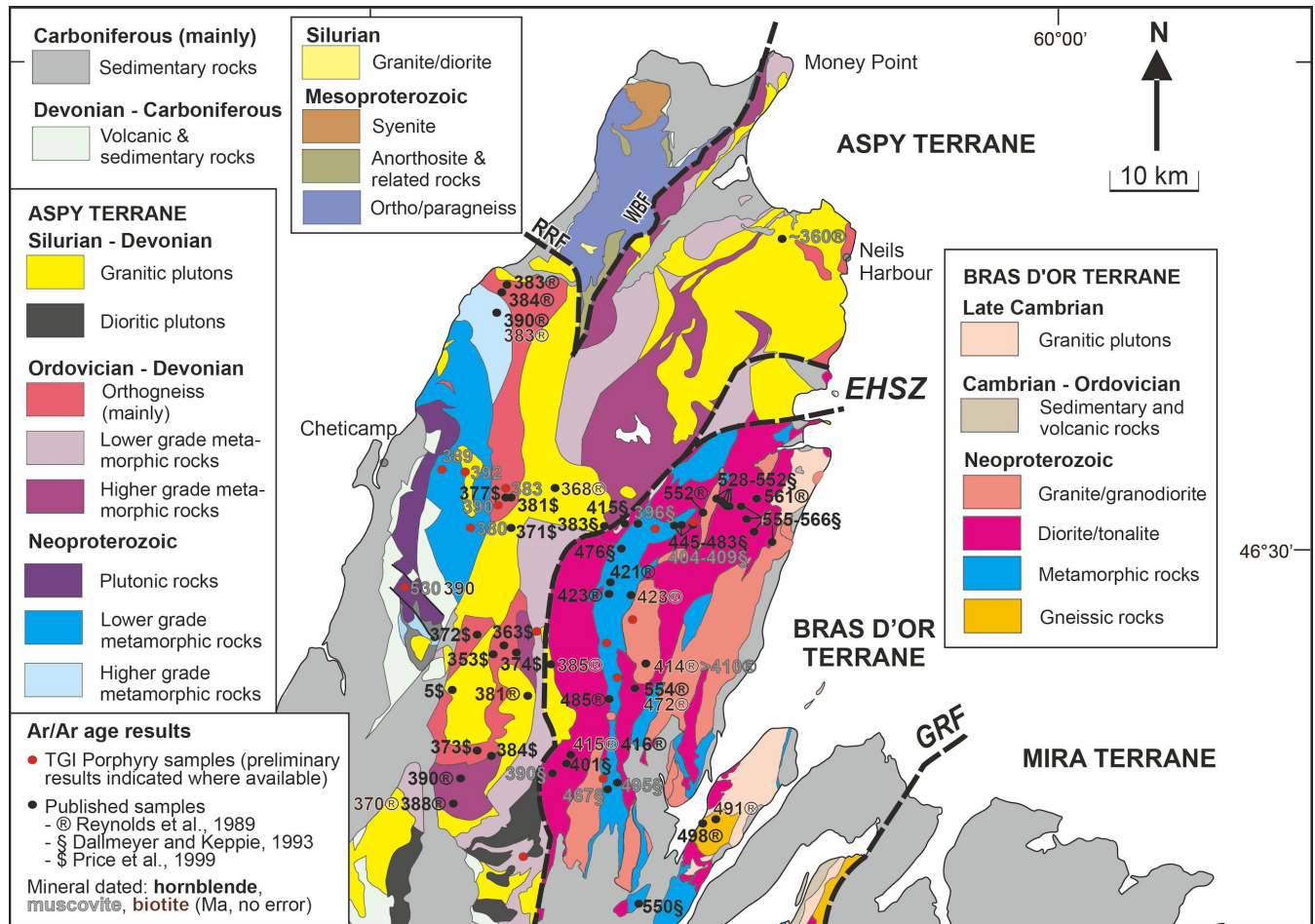
Figure 1. Simplified geological map of Cape Breton Island showing main geological units and terrane bounding faults and shear zones. Abbreviations: EHSZ - Eastern Highlands shear zone; GRF - Georges River fault; RRF - Red River fault; WBF - Wilkie Brook fault. Map is modified from Price et al. (1999) and Barr (2010).

ated, and then single grains were step heated under ultra-high vacuum and analyzed on a multicollector noble gas mass spectrometer housed at the Geological Survey of Canada in Ottawa.

Results and initial interpretations

Argon is an inert noble gas, and ^{40}Ar atoms produced from the radioactive decay of ^{40}K will diffuse out of the crystal lattice of K-bearing minerals, such as muscovite, at high temperature, but remain trapped within the crystal below a blocking, or 'closure' temperature. The ideal closure temperature of a mineral depends upon mineral dependent diffusion parameters, grain size and cooling rate, among other factors. The samples presented here will be compared to realistic diffusion forward models to determine appropriate mineral cooling ages. However, for the purposes of this report, we will consider nominal closure temperatures for Ar diffusion of 550, 400 and 300°C for hornblende, muscovite and biotite, respectively.

Preliminary new muscovite Ar/Ar ages are displayed in Figure 1, along with published muscovite, biotite and horn-

blende Ar/Ar ages (Reynolds et al., 1989; Dallmeyer and Keppie, 1993). Note that both published and new results are not distinguished according to plateau, inverse isochron or total gas ages. These data have yet to be evaluated regarding the geological significance of the resulting age data (e.g. cooling age, extraneous Ar, partial resetting), and errors and data quality are not shown. As this study evolves, the new and published age data will be critically evaluated as to its geological significance. Considering these caveats, there are some first order age patterns that can be extracted from this dataset.

Muscovite Ar/Ar ages from the central Chéticamp area range from 392 to 380 Ma, with a ca. 530 Ma age from the southern Chéticamp plutonic belt. Thus, our data concur with the pattern of Reynolds et al. (1989) for northwestern Aspy terrane, and recent U-Pb cooling ages of McCarron et al. (2016), that the Aspy terrane experienced post-metamorphic regional cooling or crystallization of muscovite during the Middle Devonian. Further, we confirm that Neoproterozoic rocks in the southern Chéticamp plutonic belt did not reach metamorphic conditions >400°C during the Silurian and Devo-

nian. Cambrian or older muscovite Ar/Ar ages in the south-westernmost Chéticamp plutonic belt and Middle Devonian hornblende Ar/Ar ages in the northeasternmost Chéticamp area are in agreement with the regional metamorphic field gradient observed across the Chéticamp area (White et al., 2016; McCarron et al., 2016).

In contrast to the Aspy terrane, available muscovite Ar/Ar ages from the Bras d'Or terrane are Early Devonian or older, as are the biotite Ar/Ar ages, despite the lower closure temperature for biotite. This indicates a clear contrast in cooling history between the Aspy and Bras d'Or terranes, which will be taken into account when reconstructing the slip history of the Eastern Highlands shear zone, and the tectonic setting of Silurian and Devonian "post-tectonic" granitoids.

Future work

Future work will involve obtaining Ar/Ar age data for the remaining muscovite-bearing samples identified in Figure 1 and a transect across the Eastern Highlands shear zone. Sample microstructure and metamorphic grade will be characterized, along with muscovite chemistry, where appropriate. Key samples will be prepared as thin rock slabs for in situ muscovite dating using a UV laser. Age interpretation will be performed by integrating mineral chemistry and microstructure, age data and forward models of Ar diffusion. Results should reveal the cooling history of the Aspy and Bras d'Or terranes, as well as provide constraints on the timing of the Eastern Highlands shear zone.

Acknowledgments

References

Barr, S.M., 2010. Granites and terranes in Cape Breton Island; in Eurogranites 2010 Field Excursion Guidebook, Nova Scotia, (ed.) D.B. Clarke; Atlantic Geoscience Society Special Publication Number 37, p. 63–88.

Dallmeyer, R.D. and Keppie, J.D., 1993. 40Ar/39Ar mineral ages from the Southern Cape Breton Highlands and Creignish Hills, Cape Breton Island, Canada: Evidence for a polyphaser tectonothermal evolution; Journal of Geology, v. 101, p. 467–482.

Kellett, D.A., Warren, C., Larson, K.P., Zwingmann, H., van Staal, C.R., and Rogers, N., 2016. Influence of deformation and fluids on Ar retention in white mica: Dating the Dover

Fault, Newfoundland Appalachians; Lithos, v. 254–255, p. 1–17.

Kellett, D.A., van Staal, C., Wilson, R.A., and Rogers, N., 2017a. The age of Salinic deformation constrained by 40Ar/39Ar dating of multiple cleavage domains: Bathurst Supergroup, New Brunswick Appalachians; American Journal of Science, v. 317, p. 338–368.

Kellett, D.A., Rogers, N., Barr, S., Kontak, D., Larson, K., Piette-Lauzière, N., van Rooyen, D., White, C., and Wilson, R., 2017b. Linking characteristics of post-orogenic, polymetallic porphyry-style ores to tectonically-driven temporal and spatial controls across an accretionary orogeny; in TGI Phase 5: Ore systems from source to deposit – 2016 Activity Report and Synthesis, (ed.) N. Rogers; Geological Survey of Canada Open File 8199, p. 75–78.

Lin, S., 1995. Structural evolution and tectonic significance of the Eastern Highlands shear zone in Cape Breton Island, the Canadian Appalachians; Canadian Journal of Earth Sciences, v. 32, p. 545–554.

McCarron, T., McFarlane, C, and Gaidies, F., 2016. P-T path of metamorphism for a garnet-zone schist in the western Cape Breton Highlands; Atlantic Geoscience Society 42nd Annual General Meeting, Program with Abstracts, Truro, Nova Scotia, p. 85.

Price, J.R., Barr, S.M., Raeside, R.P., and Reynolds, P.H., 1999. Petrology, tectonic setting and 40Ar/39Ar (hornblende) dating of the Late Ordovician – Early Silurian Belle Côte Road orthogneiss, western Cape Breton Highlands, Nova Scotia; Atlantic Geology, v. 35, p. 1–17.

Reynolds, P.H., Jamieson, R.A., Barr, S.M., and Raeside, R.P., 1989. An 40Ar/39Ar study of the Cape Breton Highlands, Nova Scotia: Thermal histories and tectonic implications; Canadian Journal of Earth Sciences, v. 26, p. 2081–2091.

White, C.E., Slaman, L., Barr, S.M., and Tucker, M., 2015. Preliminary geology and related economic mineralization potential of the Chéticamp area, Cape Breton Island, Nova Scotia; in Geoscience and Mines Branch, Report of Activities 2014; Nova Scotia Department of Natural Resources, Report ME 2015-001, p. 103–117.

White, C.E., Barr, S.M., van Rooyen, D., McCarron, T., Slaman, L.R., and Shute, J.M., 2016. New age controls on rock units in the Chéticamp area, western Cape Breton Island, Nova Scotia, Canada; in Geoscience and Mines Branch, Report of Activities 2015; Nova Scotia Department of Natural Resources, Report ME 2016-001, p. 131–142.

White, C.E., Shute, J., Sombini dos Santos, G., Barr, S.M. and van Rooyen, D., 2017. Progress report on geological and geochronological studies in the Chéticamp area, Aspy terrane, Cape Breton Island, Nova Scotia; in Geoscience and Mines Branch, Report of Activities 2016-17; Nova Scotia Department of Natural Resources, Report ME 2017-001, p. 89–93.

U-Pb geochronology of the South Mountain Batholith, Nova Scotia

L. Bickerton[1], D.J. Kontak[1], I.M. Samson[2], J.B. Murphy[3] and D.A. Kellett[4]

[1]*Harquail School of Earth Sciences, Laurentian University, Sudbury, Ontario, P3E 2C6*
[2]*Department of Earth and Environmental Sciences, University of Windsor, Windsor, Ontario, N9B 3P4*
[3]*Department of Earth Sciences, St. Francis Xavier University, Antigonish, Nova Scotia, B2G 2W5*
[4]*Geological Survey of Canada, 1 Challenger Drive, Dartmouth, Nova Scotia, B3B 1A6*

Abstract

The South Mountain Batholith (SMB) is a composite peraluminous intrusion in southwestern Nova Scotia and the largest granitoid body in the Appalachian Orogen. The batholith comprises early stage biotite-granodiorite to biotite-monzogranite and a later stage of leucomonzogranite to leucogranite plutons that are associated with numerous sub-economic to economic polymetallic (Sn, W, Mo, Cu, Ta, Nb, Zn) deposits, including East Kemptville, a past-producing Sn-Zn-Cu-Ag(-In) deposit.

The timing and duration of emplacement for intrusive phases that make up the SMB remain poorly constrained. The U-Pb zircon age results from Sensitive High-Resolution Ion Microprobe (SHRIMP) analyses in this study constrain the emplacement age of the early and later phases across the SMB, as well as provide insight into mineral potential in the intrusive complex. Zircons from five plutons in the batholith were analyzed; including one early phase granodiorite, to compliment previous U-Pb zircon dates from similar phases (ca. 381–373 Ma), and four late phase leucogranitic plutons. Results indicate the early granodiorite to be 380.9 ± 3.0 Ma and the later leucogranites to range between 376.0 ± 3.0 Ma and 372.8 ± 3.0 Ma. The ca. 15 Ma from oldest to youngest crystallization ages mark the beginning and end of SMB construction. Due to overlapping errors, more precise dating is necessary to determine whether the late stage polymetallic-mineralized plutons intruded as a discrete magmatic event to the early stage plutons, or as part of a protracted Late Devonian magmatism in the region.

Introduction

The South Mountain Batholith (SMB) in southwest Nova Scotia is one of the more extensively studied intrusive suites in the Canadian Appalachians, largely due to its size (largest pluton in the orogen at approximately 7300 km^2) and economic significance. The pluton is a composite body that hosts numerous sub-economic to economic polymetallic (Sn, W, Mo, Cu, Ta, Nb, Zn) mineral deposits (MacDonald et al., 1992; MacDonald, 2001), including the past producing East Kemptville Sn-Zn-Cu-Ag(-In) deposit. Emplaced at the terminal stages of regional deformation in the Meguma terrane, the batholith also records syn-emplacement deformation during the Neoacadian orogeny (e.g. Horne et al., 1992; Benn et al., 1997), which has relevance in the context of ore deposit formation (Bickerton et al., 2017, and references therein).

Although the petrology of the SMB has been extensively studied (e.g. Clarke et al., 2004, 2009; MacDonald and Clarke, 2017; and references therein), it is unclear whether its construction involved discrete intrusive events or a single protracted magmatic event. The emplacement history of the SMB remains to be comprehensively constrained by high-resolution dating (i.e. U-Pb zircon), which could provide significant insight into metallogeny of the batholith and further mineral exploration

potential. This study aims to constrain the timing of emplacement across the batholith, as well as further address processes of contamination and source influence on granite compositions (Clarke et al., 2004, 2009; MacDonald and Clarke, 2017) using a variety of in situ geochemical (e.g. REE) and isotopic (O, Lu-Hf) methods similar to that applied by Kemp et al. (2006, 2007) elsewhere on mineralized granitoid complexes.

Regional Geology

The Meguma terrane of southern Nova Scotia is predominantly underlain by metasedimentary and granitoid rocks. The former is represented by the extensive Meguma Supergroup, an Ediacaran to Early Ordovician sequence of interbedded metasandstones, metasiltstones and slate (White, 2010). This sequence was deformed during the Middle Devonian to Early Carboniferous Neoacadian orogeny (van Staal, 2007), which was accompanied by dextral oblique translation of the Meguma terrane along the eastern Laurentian margin (e.g. Hicks et al., 1999; Fig. 1). During the later stages of this orogenic event, the Meguma Supergroup was intruded by voluminous metaluminous to peraluminous granitoids; including the largest of these, the SMB. Field and geomagnetic studies indicate basement faults controlled the emplacement of the SMB and were also

---
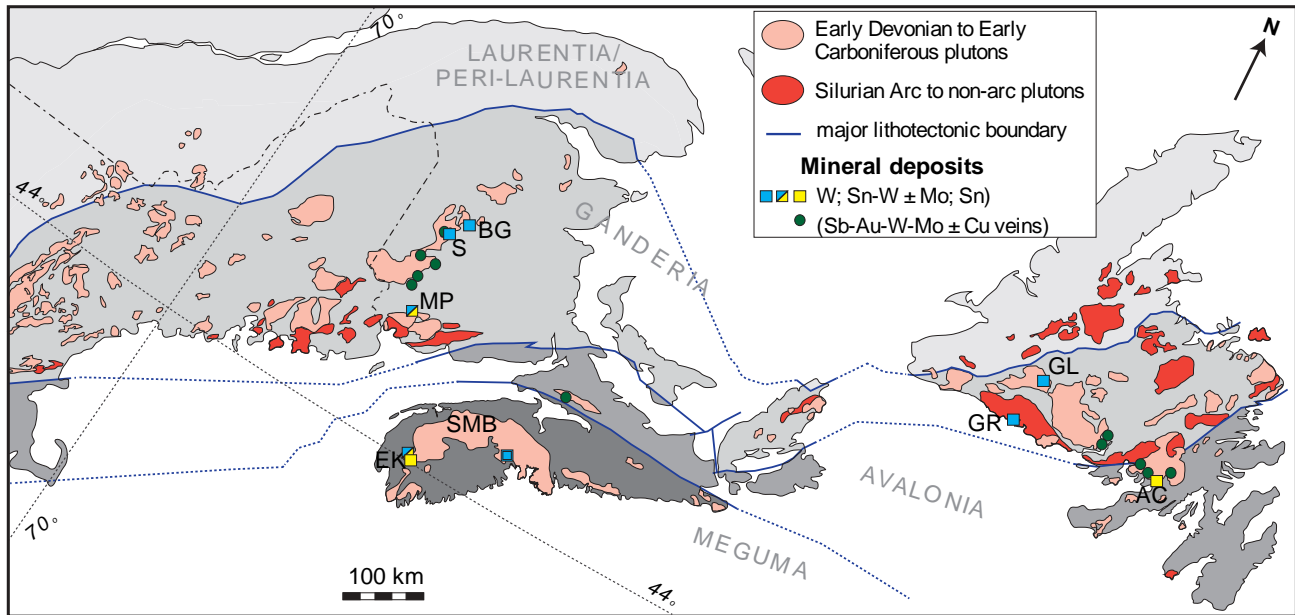
Figure 1. Tectonic setting of the northeast Appalachians. Terranes are shaded in grey with major Lithotectonic- bounding faults coloured blue. Paleozoic granitic magmatism in the region includes the South Mountain Batholith (SMB) in southwestern Nova Scotia. Polymetallic mineral deposits associated with the Paleozoic magmatism, include BG - Burnt Hill Granite, S - Sisson, MP - Mount Pleasant, GL - Granite Lake, GR - Grey River, AC - Ackley Granite, EK - East Kemptville. Modified after Hibbard et al. (2006) and van Staal (2007).

important conduits for focusing later mineralizing fluids (e.g. Horne et al., 1992; Kontak, 1994; Benn et al., 1997; MacDonald, 2001).

Detailed mapping of the SMB, as summarized and compiled in MacDonald (2001), revealed the composite batholith to be a multi-phase intrusive complex with an outer primitive zone of somewhat foliated granodiorite, as revealed by magnetic-fabric measurements (i.e. anisotropy of magnetic susceptibility (AMS) studies; Benn et al., 1997), that was intruded at multiple localities by more evolved leucogranitoid plutons lacking AMS fabrics. As depicted in Figure 2, the more evolved leucocratic bodies are, from west to east, the Davis Lake Pluton (DLP), the East Dalhousie Pluton (EDP), the New Ross Pluton (NRP), and the Halifax Pluton (HP).

Rare-metal and base-metal mineralization occurs in the SMB, although the only historically mined centre of any significance is the past-producing (1985–1992) East Kemptville (EK) Sn-Zn-Cu-Ag(-In) deposit, which is hosted by the most westerly intrusion, the approximately 800 km^2 DLP. Deposits like EK can be found in other similar-aged felsic intrusions in the Appalachians, such as at Mount Pleasant, NB, and the Ackley granite, NF (van Staal, 2007; see Kontak et al. (2013) for recent summary).

Analytical Techniques

Zircon grains were separated from several 9.1 to 11.3 kg rock samples by gravity and electromagnetic concentration.

Zircon grains were hand-picked and mounted in epoxy resin together with zircon standards. The grain mount was polished to reveal approximate zircon midsections, and imaged using optical and scanning electron microscopy (backscattered electrons (BSE) and cathodoluminescence (CL)). Abundances of U and Pb isotopes were measured by Sensitive High Resolution Ion Microprobe (SHRIMP) on individual zircon crystals from approximately 20 μm spots selected by evaluation of internal structures in the grains revealed in the BSE and CL images. Standard operating techniques for the SHRIMP II have been described by Stern (1997). All reported errors are at 2 sigma, and include the external long-term reproducibility of the standard of 0.8%.

Results

The five sets of analyses reported herein were collected from five different phases in the SMB; one sample from a central location in the batholith, representative of the less evolved granodiorite phase, and four that are representative of the more evolved leucocratic phases across the batholith (Fig. 2). The number of zircon grains recovered from sample concentrates ranges from >10 000 in the less evolved granodiorite sample, and approximately 5000 from each of the more evolved leucocratic samples. The size of the zircon grains in all samples range from 25 to 500 μm. The suite of samples has a spatial and character distribution that represents the petrogenetic evolution of the SMB.
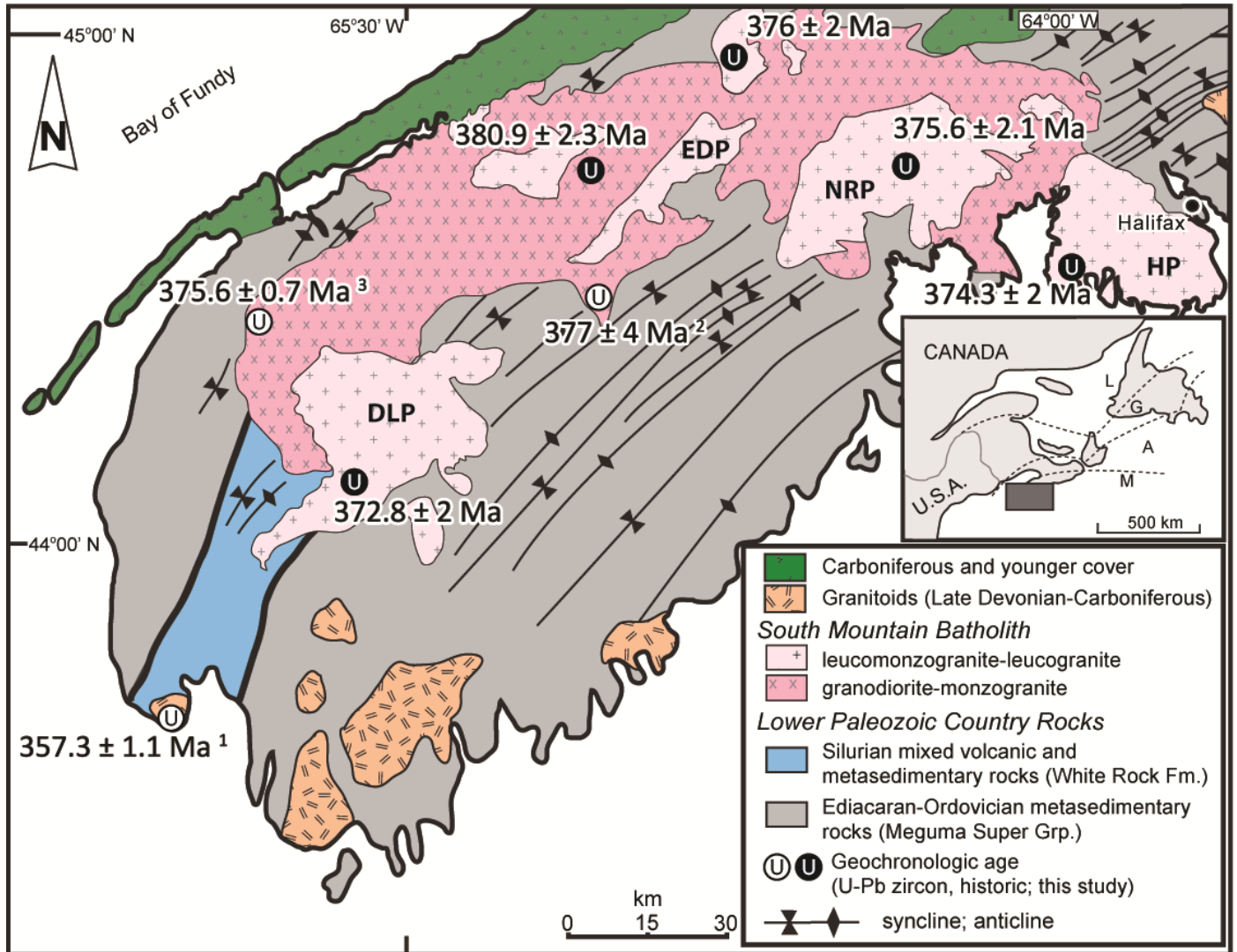
Figure 2. Close-up of regional bedrock geology in southwestern Nova Scotia. Pink granitoids are the various phases of the SMB, the darker being the less evolved granodiorite and the lighter being more evolved plutons (DLP: Davis Lake Pluton, EDP: East Dalhousie Pluton, NRP: New Ross Pluton, HP: Halifax Pluton). Inset shows regional tectonic boundaries: L - Laurentian margin, G - Ganderia, A - Avalonia, M - Meguma. U-Pb zircon geochronology samples outlined from this study (black symbols) and previous studies (white symbols: 1 - MacLean et al., 2004, 2 - Keppie et al., 1993, 3 - unpub. U-Pb data, 2015).

Central South Mountain Batholith (16-BIC-075; 380.9 ± 3.0 Ma)

The largest part of the SMB by area is underlain by the less evolved granodiorite phase which occurs across the entirety of the batholith. The sample collected (16-BIC-075) for dating is a massive, grey, medium-grained granodiorite that crops out along a road cut in the central part of the province (Fig. 2). Zircon grains from this sample range in size (50–500 μm) and morphology, from stubby resorbed to elongated prismatic grains, with a range of massive, chaotic, and fine oscillatory internal zonation. Inherited cores are commonly found in zircon from this sample. Thirty-three spots across 27 grains were

analyzed. The weighted mean ^{204}Pb-corrected ^{206}Pb/^{238}U age across the 20 youngest concordant data yields a date of 380.9 ± 3.0 Ma with a MSWD of 0.8.

East Dalhousie Pluton (16-BIC-084; 376.0 ± 3.0 Ma)

The EDP occurs along a NE-trending shear zone through the province and as a result has limited outcrop. The sample collected (16-BIC-084) for dating is a massive, pink- to buff-orange, coarse-grained to pegmatitic leucomonzogranite that crops out along the road near Lake George. Zircon grains range in size (25–400 μm) and typically have an equant prismatic morphology that is oscillatory zoned, with lesser stubby prismatic, massively-zoned crystals. Inherited cores are rare. Thirty

-two spots across 29 grains were analyzed. The weighted mean ^{204}Pb-corrected ^{206}Pb/^{238}U age across the 26 youngest concordant data yields a date of 376 ± 3.0 Ma with a MSWD of 1.4.

New Ross Pluton (16-BIC-081; 375.6 ± 3.0 Ma)

The NRP is the third largest phase of the SMB by area, and occurs in the New Ross area. The sample collected (16-BIC-081) for dating is a massive, pale, yellow-pink medium- to coarse-grained leucogranite that crops out along highway 14 near Sherwood. Zircon grains are small (25–250 μm) and have a morphology that is typically short, prismatic and oscillatory zoned, often with some resorption. Inherited cores are rare. Thirty-four spots across 30 grains were analyzed. The weighted mean ^{204}Pb-corrected ^{206}Pb/^{238}U age across the 24 youngest concordant data yields a date of 375.6 ± 3.0 Ma with a MSWD of 1.1.

Halifax Pluton (12105; 16-BIC-085; 374.3 ± 3.0 Ma)

The HP is the most eastern, evolved phase in the SMB and the best exposed due to its proximity to the southern coast. The sample collected (16-BIC-085) for dating is a massive, buff, medium-grained leucomonzogranite that occurs along a highway 333 road cut near Big Lake. Zircon grains range in size (50–400 μm) and are typically stubby prismatic to equant prismatic with fine to massive oscillatory zones. Inherited cores are relatively common in this sample. Thirty-four spots across 30 grains were analyzed. The weighted mean ^{204}Pb-corrected ^{206}Pb/^{238}U age across the 25 youngest data yields a date of 374.3 ± 3.0 Ma with a MSWD of 1.3.

Davis Lake Pluton: (16-BIC-072; 372.8 ± 3.0 Ma)

The DLP rarely outcrops on surface, but abundant sub-crop occurs northeast of East Kemptville. The sample (16-BIC-072) collected for dating is from a topographic high approximately 100 m from the roadside, where extensive sub-crop of massive, pale grey, coarse-grained feldspar-megacrystic leucogranite is present. Zircons range in size (25–500 μm), are stubby prisms with oscillatory zoning and have very few inherited (xenocrystic) cores. Thirty-one spots across 25 grains in this sample were analyzed (extra spots were used to determine core-rim relationship in some grains). The weighted mean ^{204}Pb-corrected ^{206}Pb/^{238}U age across the 25 youngest concordant data yields a date of 372.8 ± 3.0 Ma with a MSWD of 0.9.

Future Work

The zircon grains selected for SHRIMP spots in this study will be further analyzed using O and Lu-Hf isotope compositions to further understand the magmatic evolution of the SMB, following a similar approach as Kemp et al. (2006, 2007). The SHRIMP work completed during 2017 focused on dating each of the more evolved leucocratic phases. A follow-up study on the SMB will be conducted to characterize xenocrystic core ages in granodiorite across the SMB to constrain the basement and rocks assimilated by the batholith.

Conclusions

A variety of dating methods have been conducted on different parts of the SMB to constrain its magmatic evolution. Previous U-Pb zircon ages from the SMB include ages of 375.6 ± 0.7 Ma by thermal ionization mass spectrometry (D.J. Kontak, unpub. U-Pb data, 2015) and 377 ± 4 Ma by laser-ablation inductively coupled plasma mass spectrometry (Keppie et al., 1993). Other dating approaches applied to the SMB include: (i) Rb-Sr whole-rock (granodiorite) isochron ages of 374 ± 11 and 371.8 ± 2.2 Ma from the eastern part of the batholith (Clarke and Halliday, 1980); (ii) an ^{40}Ar/^{39}Ar muscovite cooling age of 381 ± 1 Ma that is thought to represent cooling through the approximate 350°C closure temperature of muscovite (Reynolds et al., 2004); and (iii) a molybdenite Re/Os mineralization age from pegmatites in the New Ross area of 371 ± 3 Ma (Carruzzo et al., 2003). The U-Pb data are similar, within error, to the range of SHRIMP ages obtained in this study, where less evolved phases are interpreted to have intruded at ca. 383 to 375 Ma and more evolved phases at ca. 380 to 370 Ma.

The nearly 15 Ma difference between oldest and youngest crystallization ages constrains the beginning and end of the SMB intrusive event. Given the ca. 5 Ma overlap in age errors across the different phases in the SMB and from each geochronological method, more precise dating is required to determine whether there is a pause of igneous activity between the less evolved and more evolved phases of the SMB.

Acknowledgments

References

Benn, K., Horne, R.J. Kontak, D.J., Pignotta, G.S., and Evans, N.G., 1997. Syn-Acadian emplacement model for the South Mountain Batholith, Meguma Terrane, Nova Scotia: Magnetic fabric and structural analyses; Geological Society of America Bulletin, v. 109, p. 1279–1293.

Bickerton, L., Kontak, D.J., Samson, I.M., and Murphy, J.B., 2017. A mesothermal greisen-hosted Sn-Zn-Cu-Ag-In deposit at East Kemptville, Nova Scotia, Canada; *in* Critical

and precious metal deposits: Theory, experiment and nature; 14th SGA biennial meeting 2017, vol. 4, p. 1273–1276.

Carruzzo, S., Kontak, D.J., Reynolds, P.H., Clarke, D.B., Dunning, G.R., and Selby, D., 2003. U/Pb, Re/Os, and Ar/Ar Dating of the South Mountain Batholith and its Mineral Deposits; Abstracts, *Geochimica* et Cosmochimica Acta, v. 67, Supplement 54.

Clarke, D.B. and Halliday, A.N., 1980. Strontium isotope geology of the South Mountain Batholith, Nova Scotia; *Geochimica* et Cosmochimica Acta, v. 44, p. 1045–1058.

Clarke, D.B., MacDonald, M.A., and Erdmann, S., 2004. Chemical variation in Al_2O_3-CaO-Na_2O-K_2O space: Controls on the peraluminosity of the South Mountain Batholith; Canadian Journal of Earth Sciences, v. 41, p. 785–798.

Clarke, D.B., Erdmann, S., Samson, H., and Jamieson, R.A., 2009. Contamination of the South Mountain Batholith by sulfides from country rocks; Canadian Mineralogist, v. 47, p. 1159–1176.

Hibbard, J.P., van Staal, C.R., Rankin, D.W., and Williams, H., 2006. Lithotectonic map of the Appalachian orogen (South), Canada – United States of America; Geological Survey of Canada Map 02096A, 2 sheets, scale 1:1 500 000.

Hicks, R.J., Jamieson, R.A., and Reynolds, P.H., 1999. Detrital and metamorphic $^{40}Ar/^{39}Ar$ ages from muscovite and whole-rock samples, Meguma Supergroup, southern Nova Scotia; Canadian Journal of Earth Sciences, v. 36, p. 23–32.

Horne, R.J., MacDonald, M.A., Corey, M.C., and Ham, L.J., 1992. Structure and emplacement of the South Mountain Batholith, soutlwestern Nova Scotia; Atlantic Geology, v. 28, p. 29–50.

Kemp, A.I.S., Hawkesworth, C.J., Paterson, B.A., and Kinny, P.D., 2006. Episodic growth of the Gondwana supercontinent from hafnium and oxygen isotopes in zircon; Nature, v. 439, p. 580-583.

Kemp, A.I.S., Hawkesworth, C.J., Paterson, B.A., Woodhead, J.D., Hergt, J.M., Gray, C.M., and Whitehouse, M.J., 2007. Magmatic and crustal differentiation history of granitic rocks from Hf-O isotopes in zircon; Science, v. 315, p. 980–983.

Keppie, J.D., Dallmeyer, R.D., Krogh, T.E., and Aftalion, M., 1993. Dating mineralization using several isotopic methods: An example from the South Mountain Batholith, Nova Scotia, Canada; Chemical Geology, v. 103, p. 251–270.

Kontak, D.J., 1994. Geological and geochemical studies of alteration processes in a Fluorine-rich environment: The East Kemptville Sn-(Zn-Cu-Ag) deposit, Yarmouth County, Nova Scotia, Canada; in Alteration and Alteration Processes associated with Ore-forming Systems, (ed.) D.R. Lentz; Geological Association of Canada, Short Course Notes, v. 11, p. 261–314.

MacDonald, M.A., Horne, R.J., Corey, M.C., and Ham, L.J., 1992. An overview of recent bedrock mapping and follow-up petrological studies of the South Mountain batholith, southwestern Nova Scotia, Canada; Atlantic Geology, v. 28, p. 7–28.

MacDonald, M.A., 2001. Geology of the South Mountain Batholith, southwestern Nova Scotia; Nova Scotia Department of Natural Resources Open File Report ME2001-2, 280p.

MacDonald, M.A. and Clarke, D.B., 2017. Occurrence, origin, and significance of melanogranites in the South Mountain Batholith, Nova Scotia; Canadian Journal of Earth Sciences, v. 54, p. 693–713.

MacLean, N.J., Barr, S.M., White, C.E., and Ketchum, J.W.F., 2004. New U-Pb (zircon) age and geochemistry of the Wedgeport pluton, Meguma terrane, Nova Scotia; Atlantic Geology, v. 39, p. 239–253.

Reynolds, P.H., Clarke, D.B., and Bogutyn, P.A., 2004. $^{40}Ar/^{39}Ar$ Laser dating of zoned white micas from the Lake Lewis leucogranite, South Mountain Batholith, Nova Scotia, Canada; Canadian Mineralogist, v. 42, p. 1129–1137.

Stern, R.A., 1997. A SHRIMP II Ion Microprobe at the Geological Survey of Canada; Geoscience Canada, v. 23, p. 73–76.

Stern, R.A., 2001. A new isotopic and trace element standard for the ion microprobe: Preliminary TIMS U-Pb and electron microprobe data; Radiogenic Age and Isotopic Studies Report 14, Geological Survey of Canada, Ottawa, Ontario, 11p.

van Staal, C.R., 2007. Pre-Carboniferous tectonic evolution and metallogeny of the Canadian Appalachians; in Mineral Deposits of Canada, (ed.) W.D. Goodfellow; Geological Association of Canada, Special Publication 5, p. 793–818.

White, C.E., 2010. Stratigraphy of the Lower Paleozoic Goldenville and Halifax groups in southwestern Nova Scotia; Atlantic Geology, v. 46, p. 136–154.

Mineral markers of porphyry copper mineralization: Work in progress at the Gibraltar deposit, British Columbia

A. Plouffe[1], C.H. Kobylinski[2], K. Hattori[2], L. Wolfe[2] and T. Ferbey[3]

[1]*Geological Survey of Canada, 601 Booth Street, Ottawa, Ontario, K1A 0E8*

[2]*Department of Earth and Environmental Sciences, University of Ottawa, 25 Templeton Street, Ottawa, Ontario, K1N 6N5*

[3]*British Columbia Geological Survey Branch, 1810 Blanshard Street, Victoria, British Columbia, V8T 4J1*

Abstract

Indicator minerals that can persist within glacial sediments offer the potential to be tracers towards buried porphyry mineralization. This study is examining the composition of epidote, rutile and zircon in till and bedrock from the Gibraltar copper-molybdenum porphyry deposit, British Columbia, to test their utility as indicators of mineralizing system fertility. Some rutile grains in till at Gibraltar have a composition comparable to rutile from the El Teniente porphyry copper deposit in Chile. Comparison of the composition of rutile in till and bedrock at Gibraltar is in progress. Other studies have indicated that high Ce/Ce* values in magmatic zircon are indicative of oxidizing conditions that are favourable for the formation of porphyry deposits. At Gibraltar, zircon from the mineralized phase of the intrusion yields high Ce/Ce* values (average of 133) relative to the barren intrusive phases. Epidote is more abundant in till in the region of the host intrusion. Such distribution was originally interpreted to be derived from the propylitic alteration related to porphyry mineralization. Detailed analysis of the epidote shows that epidote in till could be derived from the contact zone between the Granite Mountain batholith and the Nicola volcanic rocks.

Introduction

Significant interest is dedicated to the study of mineral chemistry indicative of fertile porphyry copper mineralization. For example, the compositions of zircon (Ballard et al., 2002; Lee et al., 2017a; Hattori et al., 2017; Zhang et al., 2017), epidote (Cooke et al., 2014; Jago et al., 2014), magnetite (Canil et al., 2016; Pisiak et al., 2017), apatite (Bouzari et al., 2016; Mao et al., 2016; Rukhlov et al., 2016), tourmaline (Baksheev et al., 2012; McClenaghan et al., 2017, 2018), titanite (Che et al., 2013; Celis et al., 2014; Celis, 2015; Kobylinski et al., 2016), plagioclase (Williamson et al., 2016) and chlorite (Wilkinson et al., 2015) have been investigated to understand the controls and ore formation processes related to mineral chemistry. The ultimate objective of this research is to be able to use these ore, magmatic and alteration minerals in rocks and/or sediments as indicators and vectors in mineral exploration for copper porphyry deposits.

This study aims to define a suite of minerals that are indicative of porphyry copper mineralization (e.g. zircon, epidote and rutile) and to test their utility in defining the fertility of porphyry systems within a glaciated landscape. The activity relies on till heavy mineral concentrates previously collected from four areas with porphyry copper mineralization in British Columbia (Ferbey et al., 2016; Plouffe and Ferbey, 2016; Plouffe et al., 2016). These sites include the Highland Valley Copper, Gibraltar and Mount Polley deposits and the Woodjam prospect (Fig. 1). The till sampling surveys completed around these copper porphyry systems revealed that a number of minerals recovered from till may be indicative of copper porphyry mineralization. Certain minerals such as chalcopyrite and jarosite are more abundant in till close to mineralization and generally decrease in abundance with increasing distance down ice from ore zones (Hashmi et al., 2015; Plouffe and Ferbey, 2015a; Plouffe et al., 2016). Other minerals that can be derived from a variety of rock types (e.g. apatite and magnetite) need to be chemically characterized to be linked to a porphyry copper source (Rukhlov et al., 2016; Pisiak et al., 2017; Plouffe and Ferbey, in press). Herein we report on work in progress on zircon, rutile and epidote composition in till and bedrock at the Gibraltar porphyry copper-molybdenum deposit in south-central British Columbia.

Background

The Gibraltar Mine is a calc-alkaline porphyry copper-molybdenum deposit hosted within the Late Triassic Granite Mountain batholith, which intruded volcanic and sedimentary rocks of the Upper Triassic to Lower Jurassic Nicola Group of the Quesnel Terrane (Fig. 1). At least three intrusive phases have been recognized in the Granite Mountain batholith including from west to east, the border, mine, and Granite Mountain phases (Fig. 2). The mine phase contains the economic copper-molybdenum porphyry mineralization. Including past production and current resources, the deposit represents 1.22 billion tonnes of ore with a Cu grade of 0.317% and an estimated Mo

---
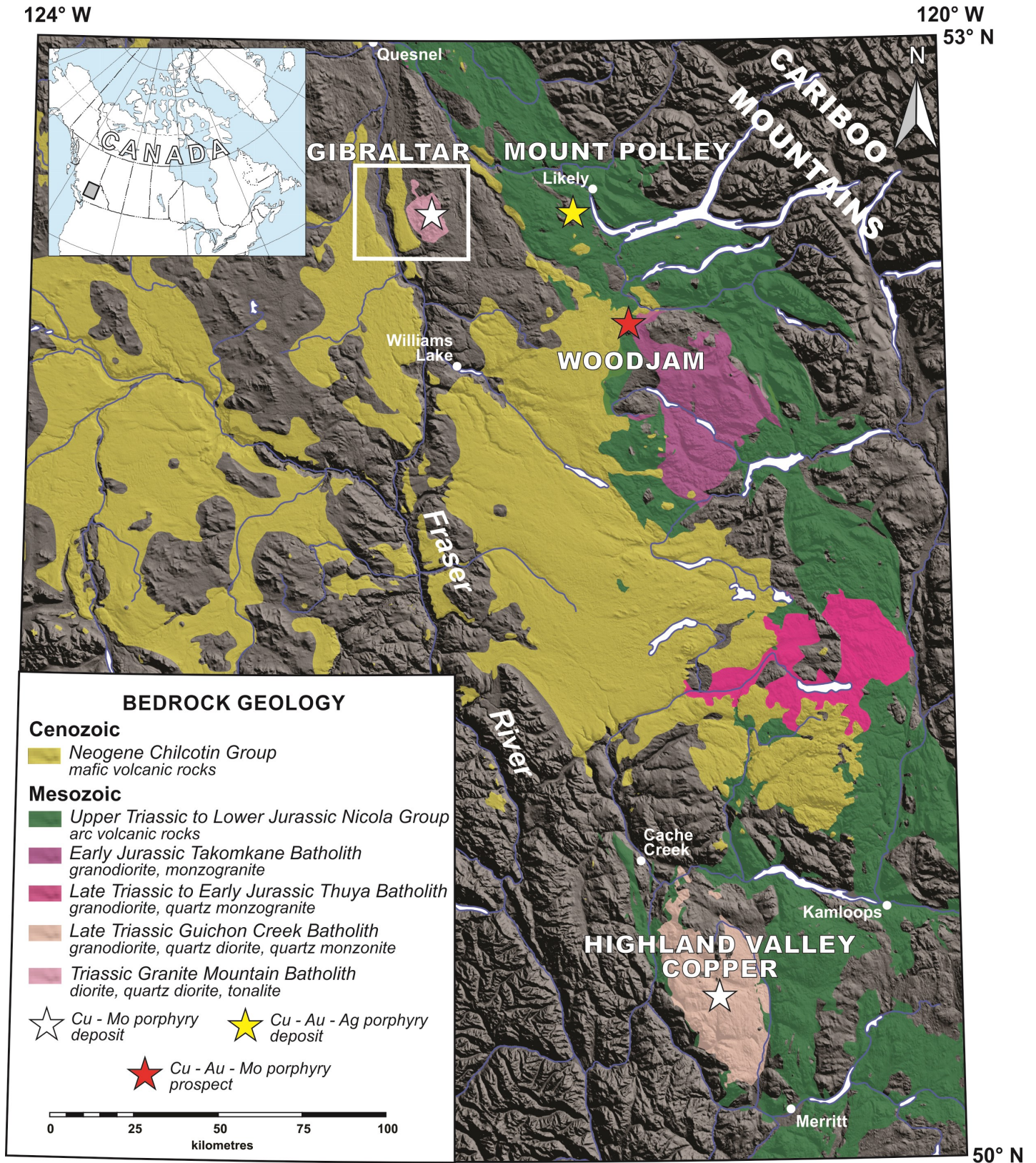
Figure 1. Location map of the Gibraltar and Highland Valley Copper porphyry copper-molybdenum deposits in British Columbia (modified from Plouffe et al., 2017). The white frame around Gibraltar represents the extent of Figures 2, 5, 6a and 8.

Figure 2. Rose zircon grain counts in the 0.25–0.5 mm, >3.2 SG fraction of till normalized to 10 kg sample weight at Gibraltar and distribution of samples collected for analysis. Figure modified from Plouffe and Ferbey (in press). Mineral grain count data is from Plouffe and Ferbey (2016). Till samples from which zircon grains were analyzed are labelled (e.g. 12P-MA522A01).

grade of 0.010% (van Straaten et al., 2013). The main ore minerals at Gibraltar are chalcopyrite, molybdenite and bornite. Propylitic hydrothermal alteration is present in the batholith extending outward at least 5 km from mineralization and includes epidote, chlorite and albite (Drummond et al., 1973, 1976; van Straaten et al., 2013; Kobylinski et al., 2017).

The Gibraltar region was last glaciated during the Late Wisconsin Fraser Glaciation (Clague and Ward, 2011). Most of the region is covered by till with lesser amounts of glaciofluvial sand and gravel deposits in valleys (Plouffe and Ferbey, 2015b). Three ice movements have been identified in the Gibraltar region: i) an initial local ice movement towards the southeast likely derived from a mountain ridge with cirques and arêtes located ca. 12 km north of the mine; ii) a regional movement to the southwest derived from the Cariboo Mountains; and iii) a third movement, likely the dominant one, towards the north to northwest, derived from an ice divide around 52° latitude (Plouffe et al., 2016). The till surface was marked by drumlins, flutings and crag-and-tails during this last event.

Analytical methods

Zircon, rutile and epidote compositions from till and bedrock were determined by a combination of laser ablation – inductively coupled plasma mass spectrometry (LA-ICP-MS), scanning electron microscopy - energy dispersive spectroscopy (SEM-EDS) and electron probe microanalyses (EPMA) at the University of Ottawa. Analyses were conducted on polished thin section (bedrock samples) and individual grains recovered from heavy mineral concentrates (till and bedrock samples).

Zircon composition

A number of studies point out the potential of zircon as a fertility indicator for porphyry mineralization (Ballard et al., 2002; Liang et al., 2006; Chapman et al., 2012; Dilles et al., 2015; Shen et al., 2015; Hattori et al., 2016, 2017; Lu et al., 2016; Lee et al., 2017a, b; Yang et al., 2017; Zhang et al., 2017). In summary, the rare earth element (REE) composition of magmatic zircon reflects melt oxidation state, which correlates with the potential of an intrusion to host porphyry-style mineralization. For example, in the above listed studies, magmatic zircons from fertile porphyry systems typically have higher ratios of Eu/Eu* (>0.3), Ce^{+4}/Ce^{+3} (typically >100), $10000(Eu/Eu*/Y)$ (>1), (Ce/Nd)/Y (>0.01) compared to zircons from barren intrusions. It is recognized that the presence of other REE-bearing minerals, such as titanite, can influence the REE composition of zircon, but even in such conditions the Eu/Eu* might remain a good proxy for fertile versus barren intrusions (Loader et al., 2017).

With this background knowledge at hand, we are testing zircon as a potential porphyry copper indicator mineral given its presence and regional distribution in till in the Gibraltar region (Fig. 2). In an oxidized magma potentially fertile for porphyry mineralization, Ce can occur in a +4 valence (Ce^{+4}) and substitute for Zr^{+4} in zircon, which can produce positive Ce anomalies in chondrites normalized rare earth element (REE) plots. The ratio Ce/Nd is a means of depicting the Ce enrichment in zircon and hence the relative oxidation state (and the fertility potential) of the magma (Hattori et al., 2017). The Ce/Nd ratio becomes useful when studying detrital zircon grains for which the Ce anomaly (Ce/Ce*; determined with La and Nd concentrations) cannot be calculated because the La concentrations are close or below the detection limit. At Gibraltar, zircon grains with the highest Ce anomaly are from the mine phase, which hosts the economic mineralization (Fig. 3a, b). Similar REE patterns are observed in zircon grains in till (Fig. 3c) but the Ce anomaly cannot be directly calculated for these grains, because the La concentrations are below detection limit or low
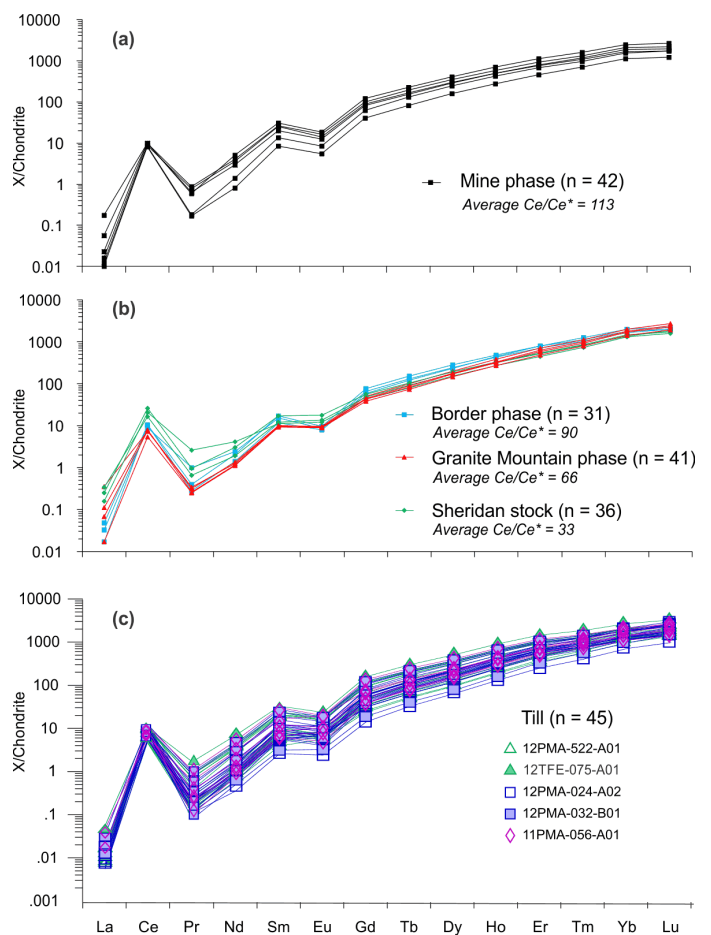
Figure 3. Chondrite-normalized rare earth element (REE) concentrations in zircon grains from: (a) the mine phase; (b) the border and Granite Mountain phases, and the Sheridan Creek stock; and (c) till. Till sample locations shown in Figure 2. Zircon from the mine phase (a), host of the copper-molybdenum mineralization, yields high Ce/Ce* values relative to the other intrusive phases. Samples taken from the barren Sheridan stock have low average Ce/Ce* (33). Chondrite values are from McDonough and Sun (1995).

and not precise. On the other hand, the Ce/Nd ratios in zircon grains from till provide an indication of the presence of a fertile intrusion. Till sample 11PMA024A02 located < 1 km from mineralization, contains three zircon grains with high Ce/Nd ratios (>18) which are indicative of more oxidizing magmatic conditions compared to the other grains (Fig. 4). Further investigation of the zircon rare earth element composition in intrusive rocks and till at Gibraltar is in progress.

Additionally, we have calculated the crystallization temperature of zircon grains in intrusive rocks and till at Gibraltar using the Ti in zircon thermometry method of Ferry and Watson (2007) assuming an activity of 0.7 for TiO_2 and 1.0 for SiO_2. This shows that the crystallization temperatures of the intrusive rocks at Gibraltar are generally hotter near mineralization (748–817°C) compared to distal sites (712–747°C) (Fig. 5). Similar temperatures have been calculated from zircon grains recovered from till (Fig. 4).

Rutile

We completed the analyses of red rutile grains obtained from five till samples located up- and down-ice of mineralization (Fig. 6a; Wolfe, 2017). Four out of five till samples contain at least one grain of rutile with a Mo and Sb content corresponding to the composition of rutile in the high- and low-grade ore at the El Teniente copper deposit in Chile (Fig. 6b; samples 11PMA024A02, 11PMA038A01, 12PMA042A01, and 12PMA536A01) (Rabbia et al., 2009; Wolfe et al., 2017).
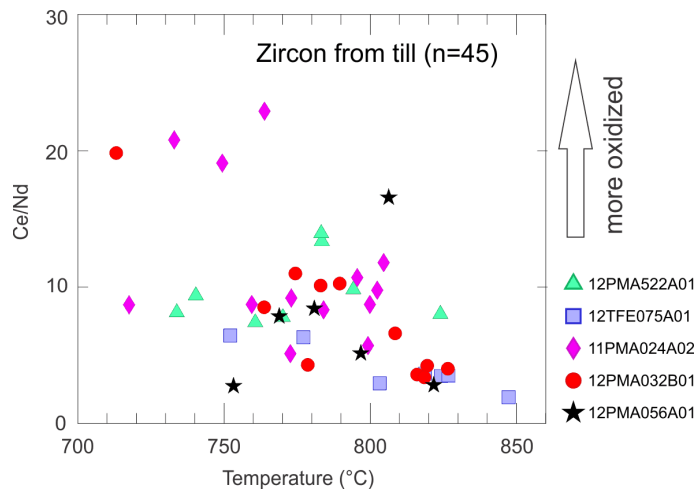
Figure 4. Ce/Nd ratio in zircon grains from till as a proxy to the Ce anomaly in zircon and hence the relative oxidation state of the magma (Hattori et al., 2017). Grains with the higher ratios are from more oxidized magma and could be indicative of fertility (e.g. Ballard et al., 2002). Sample 11PMA024A02 with three zircon grains characterized by an oxidized magma signature is located <1 km from mineralization. Modified from Wolfe et al. (2017). Sample locations are shown in Figure 2.
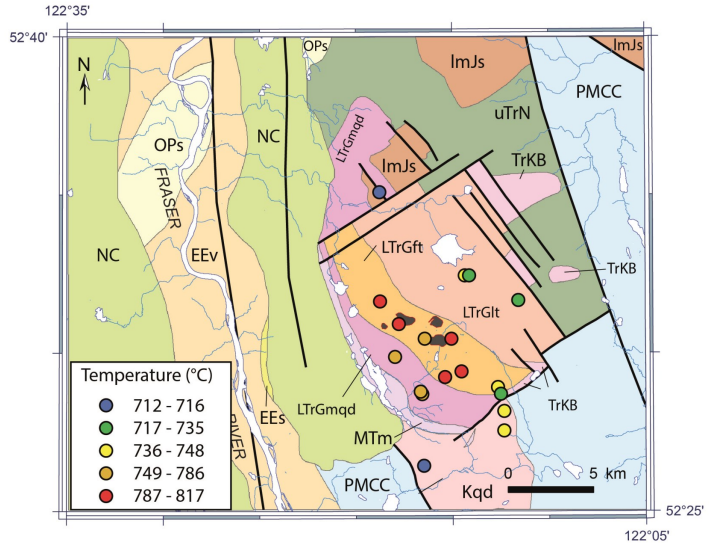
Figure 5. Distribution of zircon crystallization temperatures from the Granite Mountain batholith based on Ti in zircon thermometry (°C) calculated using the methodology of Ferry and Watson (2007), and assuming an activity of 0.7 for TiO_2 and 1.0 for SiO_2.

The only till sample with not a single grain of rutile within the El Teniente compositional field (12PMA056A01) is located approximately 7 km east (up-ice) from mineralization. Comparison of the rutile composition in till and bedrock at Gibraltar is in progress.

Epidote

Epidote is a common mineral in the hydrothermal alteration zones of copper porphyry deposits (e.g. Sinclair, 2007; Sillitoe, 2010) and has the potential to be a porphyry copper indicator mineral for exploration (e.g. Cooke et al., 2014). For instance, Hashmi et al. (2015), Plouffe et al. (2016), and Plouffe and Ferbey (in press) have suggested that the greater abundance of epidote in till (determined in the >3.2 specific gravity, 0.25–0.5 mm size, and 0.8–1 amp electromagnetic fraction) near porphyry copper mineralization compared to background regions could be derived from hydrothermal alteration related to the porphyry mineralization. However, a clear link between epidote abundance in till and a hydrothermal alteration source based on mineral attributes remains to be established. The challenge in developing epidote as a porphyry copper indicator mineral in the Canadian Cordilleran context is to differentiate epidote derived from alteration zones of fertile porphyry copper systems versus "background" epidote derived from: i) altered but non-fertile intrusions; ii) rocks of regional greenschist metamorphic facies; and iii) rocks from contact metamorphic aureoles such as the Nicola Group volcanic rocks of the Quesnel Trough, which are known to contain epidote (Campbell and Tipper, 1971).
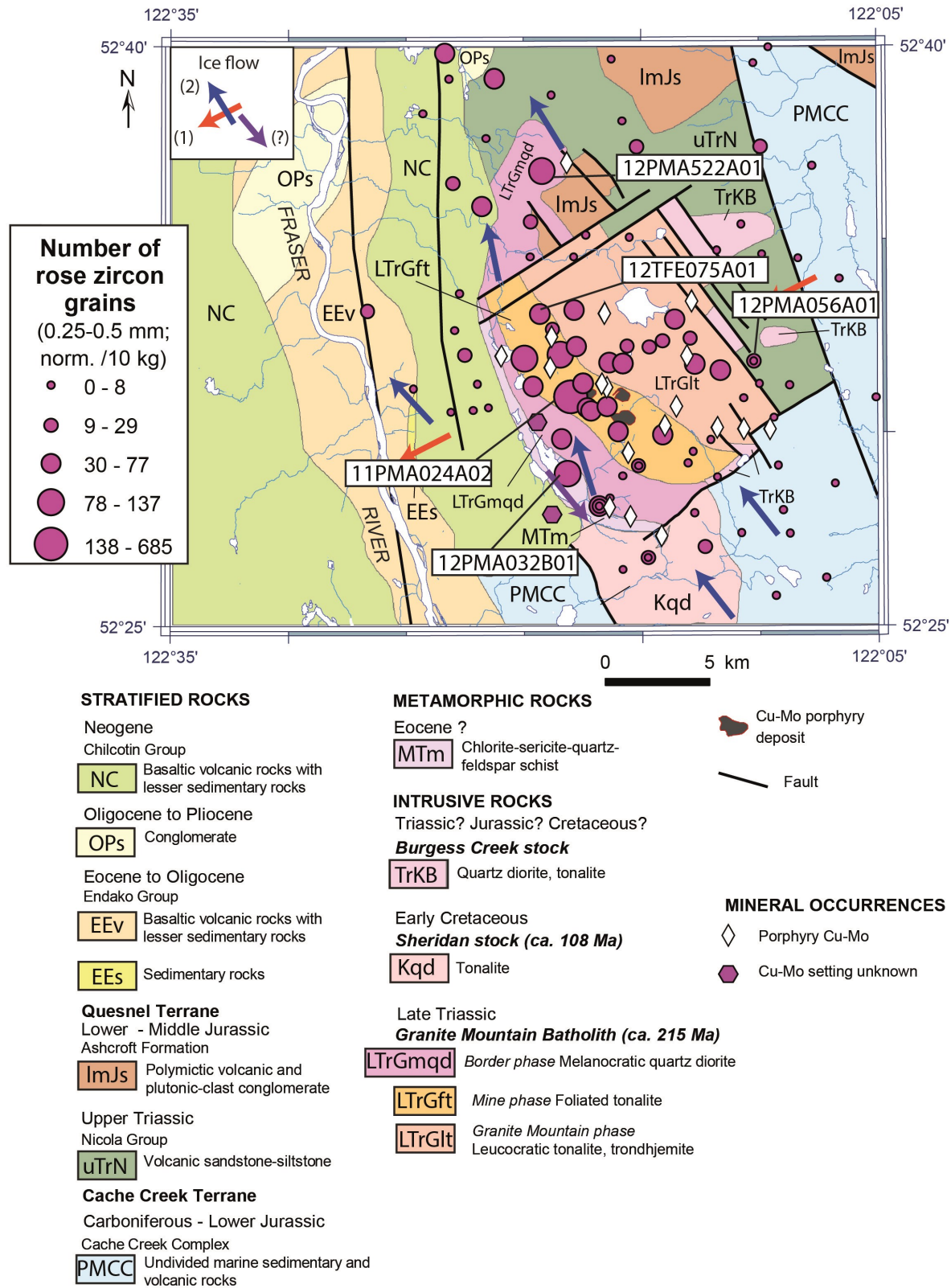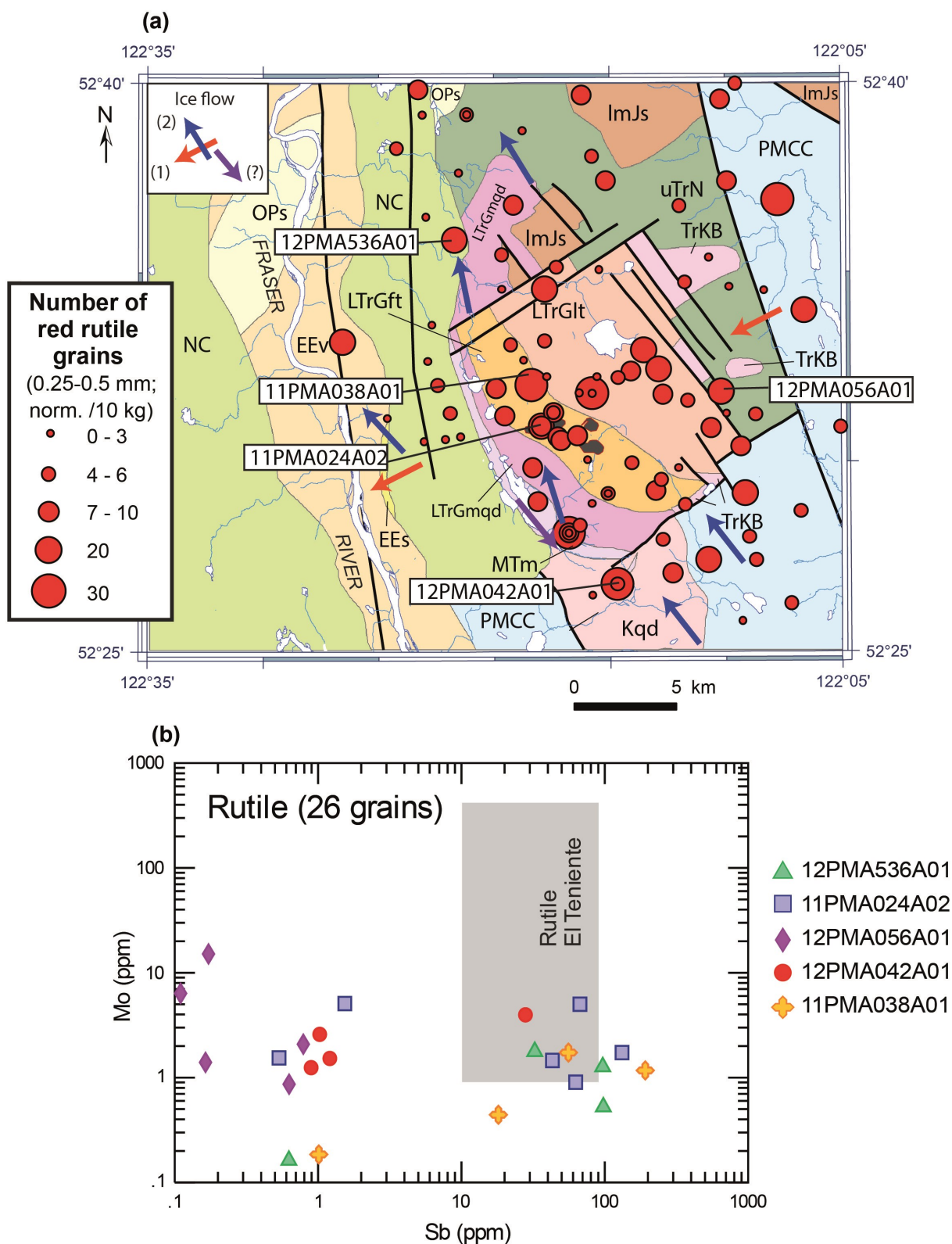
Figure 6. a) Red rutile grain counts in the 0.25–0.5 mm, >3.2 SG fraction of till normalized to 10 kg sample weight at Gibraltar. Figure modified from Plouffe and Ferbey (in press). Mineral grain count data is from Plouffe and Ferbey (2016). Till samples from which rutile grains were analyzed are labelled (e.g. 12PMA536A01). The bedrock legend is the same as Figure 2. b) Mo versus Sb content of rutile recovered from till. The grey field corresponds to the composition of rutile in the high- and low-grade ore at the El Teniente porphyry copper deposit in Chili (Rabbia et al., 2009). Figure modified from Wolfe et al. (2017).

Kobylinski et al. (2017) presented a detailed account of the form and composition of epidote within the Granite Mountain batholith and the intruded Nicola volcanic rocks. In summary, epidote occurs as aggregates, veins and veinlets, and disseminated and isolated grains within the various intrusive phases of the batholith. Most of the alteration epidote in the batholith shows a sharp zoning characterized by a Fe-poor core and Fe-rich rim. Kobylinski et al. (2017) set the Fe-rich / Fe-poor boundary at an Fe(t) / [Fe(t) + Al] ratio of 0.29 (Fig. 7). The zoning is interpreted to reflect the evolution in composition of hydrothermal fluids from an S-rich phase during growth of the epidote core, and S-poor phase during rim growth. The interpretation is that the Fe content of epidote is controlled by preferential precipitation of Fe into sulphides when there is excess S in the hydrothermal system. Furthermore, the rare earth element (REE) plus Y content of epidote varies from 0.01 to 21.7 weight % oxides. Some epidote grains contain >15 weight % REE oxides and therefore qualify as allanite (Kobylinski et al., 2017). Kobylinski et al. (2017) also investigated the composition of epidote in the Nicola volcanic rocks of the Gibraltar region. Epidote in the Nicola rocks does not show Fe zoning, commonly contains apatite and titanite inclusions, but has no detectable amount of REE. The abundance of epidote in the Nicola volcanic rocks is >40 volume % within 500 m of the contact with the batholith compared to <30 volume % at >500 m from the contact. The greater abundance of epidote in the Nicola rocks near the contact with the intrusion can be attributed to contact metamorphism or metasomatic alteration near the intrusion contact zone (Kobylinski et al., 2017).

A complementary study was conducted on the composition of 93 grains of epidote recovered from four of the till samples collected in the Gibraltar region (Fig. 8; Wolfe, 2017; Wolfe et al., 2017). The epidote grains in till have variable amounts of Ca (22–24 weight %), Fe$_2$O$_3$ (12–20 weight %), and Al$_2$O$_3$ (20
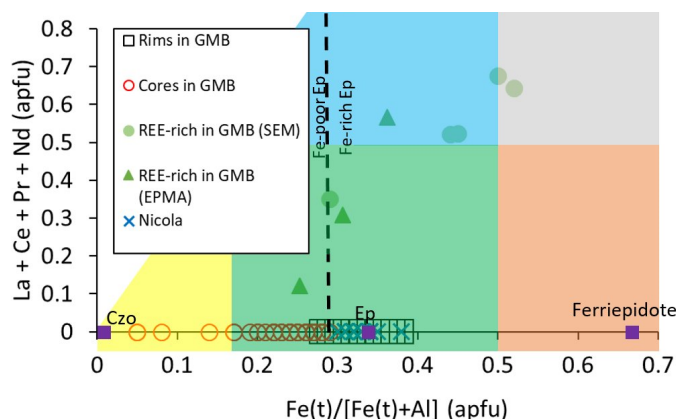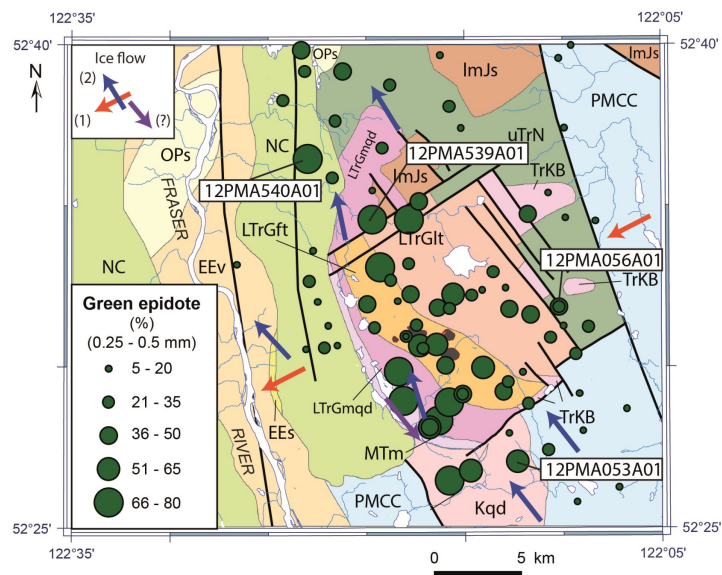
Figure 8. Percentage of green epidote in the 0.25–0.5 mm, >3.2 SG, 0.8–1 amp paramagnetic fraction of till at Gibraltar. Figure modified from Plouffe et al. (2016). Mineral grain count data is from Plouffe and Ferbey (2016). Till samples from which epidote grains were analyzed are labelled (e.g. 12PMA540A01). The bedrock legend is the same as Figure 2.

–25 weight %) (Fig. 9a, b). The distribution of Fe$_2$O$_3$ in epidote is not homogeneous and varies by 1 to 2 weight % within single grains following a complex texture. The epidote grains in till are not zoned. The REE content (Sc + Y + La + Ce) of epidote in till is low, attaining a maximum of 0.17 weight % (Fig. 9c). Mineral inclusions are common in the till epidote, including in decreasing abundance titanite, actinolite, zircon, apatite, quartz and magnetite. By comparing the composition, texture and mineral inclusions in epidote, Wolfe (2017) concluded that the epidote in till has more affinity to the epidote in the Nicola volcanic rocks as opposed to the Granite Mountain batholith. The greater abundance of epidote in till in the region of the Granite Mountain batholith could be related to the greater abundance of epidote in rocks of the Nicola Group near the contact with the intrusion.

This first set of results on epidote composition in till and rocks in the region of an economic porphyry copper deposit provides some insight as to the source of epidote in till, but also raises some questions still to be fully addressed:

- In which fraction of till is most of the Fe zoned, intrusion derived epidote present? Could it be present in a paramagnetic fraction other than the one separated at 0.8 to 1 amp? Could it be comminuted to a size fraction <0.25 mm? And, is it abundant enough in till heavy mineral concentrates to be efficiently detected in a 10 kg bulk sample?
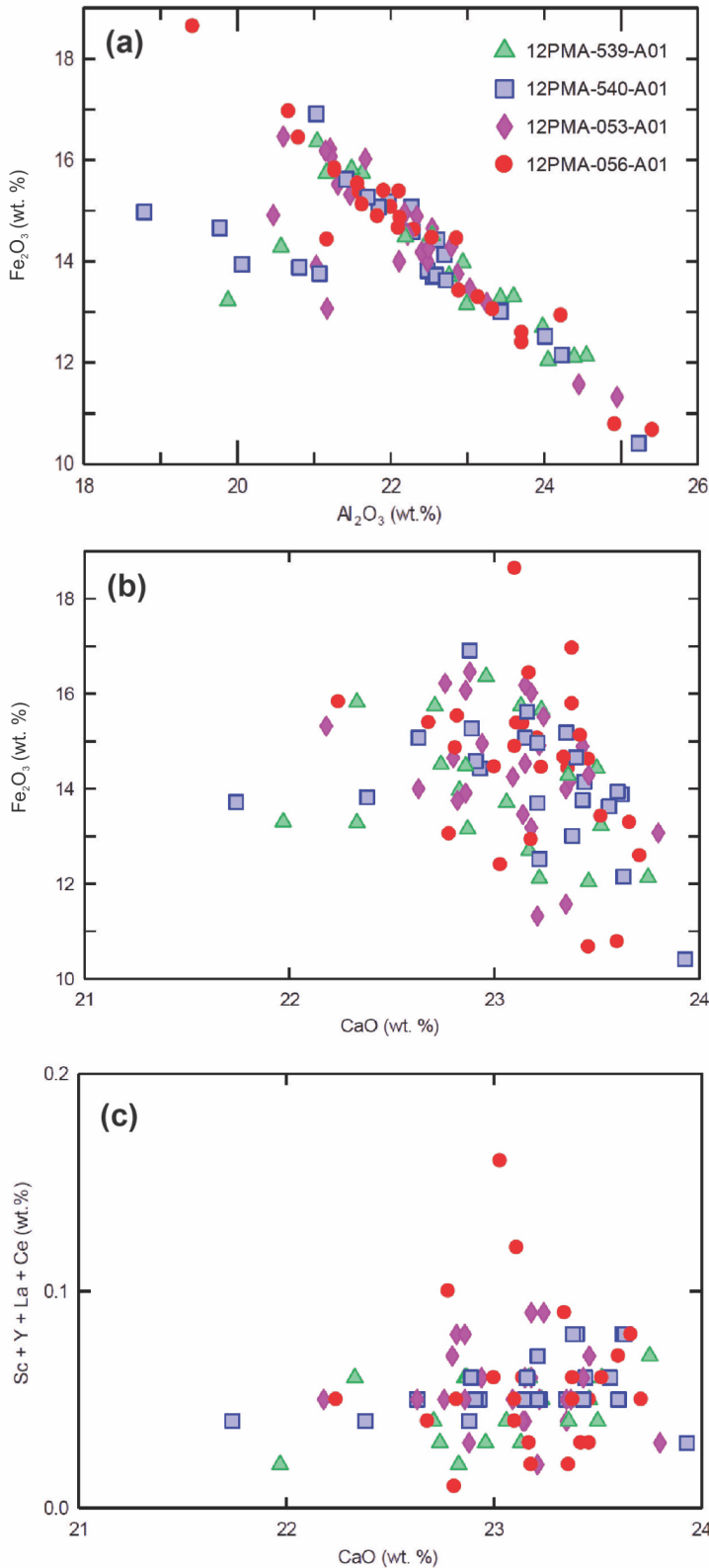
Figure 7. Epidote composition from the Gibraltar deposit. GMB - Granite Mountain batholith; SEM - scanning electron microscope; EPMA - electron probe microanalyses; apfu - atom per formula unit. Figure modified from Kobylinski et al. (2017).

- Is the Fe zoning observed in epidote at Gibraltar also present in epidote from other copper porphyry deposits, and if so, is the presence of zoning in epidote grains widely applicable as an indication of the presence of porphyry mineralizing processes in detrital sediments?

- Is the greater abundance of epidote in till near porphyry mineralization as outlined in Hashmi et al. (2015) and Plouffe et al. (2016) in large part derived from contact zones between the intrusion and host rocks?

- Can we establish criteria to distinguish between epidote derived from fertile and non-fertile intrusions?

Given that the hydrothermal alteration zones developed in porphyry copper deposits are much larger than the mineralized zones (Lowell and Guilbert, 1970; Sillitoe, 2010), they represent much larger exploration targets (Averill, 2011; Plouffe et al., 2016; Hickin and Plouffe, in press). Establishing hydrothermal alteration minerals (e.g. epidote) as porphyry copper indicator minerals could improve our efficiency at detecting buried porphyry deposits.

Concluding remark

The next generation of mineral deposits to be discovered is unlikely to be an "easy find" that is well exposed at surface. In a glaciated landscape, such as much of Canada, deposits to be discovered are likely covered by glacial and non-glacial sediments. Developing better mineral exploration strategies, including studies of mineral markers of copper porphyry deposits that persist within a glaciated environment will contribute to an improved capacity to detect buried ore that will respond to the needs of future generations.

Acknowledgments

References

Averill, S.A., 2011. Viable indicator minerals in surficial sediments for two major base metal deposit types: Ni-Cu-PGE and porphyry Cu; Geochemistry: Exploration, Environ-

Figure 9. a) $Fe_2O_3(t)$ versus Al_2O_3; b) $Fe_2O_3(t)$ versus CaO; and c) Sc+Y+La+Ce versus CaO in 91 epidote grains from till analyzed by EPMA. Modified from Wolfe (2017).

ment, Analysis, v. 11, p. 279–291.

Baksheev, I.A., Yu Prokof'ev, V., Zaraisky, G.P., Chitalin, A.F., Yapaskurt, V.O., Nikolaev, Y.N., Tikhomirov, P.L., Nagornaya, E.V., Rogacheva, L.I., Gorelikova, N.V., and Kononov, O.V., 2012. Tourmaline as a prospecting guide for the porphyry-style deposits; European Journal of Mineralogy, v. 24, p. 957–979.

Ballard, J.R., Palin, J.M., and Campbell, I.H., 2002. Relative oxidation states of magmas inferred from Ce(IV)/Ce(III) in zircon: application to porphyry copper deposits of northern Chile; Contributions to Mineralogy and Petrology, v. 144, p. 347–364.

Bouzari, F., Hart, C.J.R., Bissig, T., and Barker, S., 2016. Hydrothermal alteration revealed by apatite luminescence and chemistry: A potential indicator mineral for exploring covered porphyry copper deposits; Economic Geology, v. 111, p. 1397–1410.

Campbell, R.B. and Tipper, H.W., 1971. Geology of Bonaparte Lake map-area, British Columbia; Geological Survey of Canada, Memoir 363, 100 p.

Canil, D., Grondahl, C., Lacourse, T., and Pisiak, L.K., 2016. Trace elements in magnetite from porphyry Cu–Mo–Au deposits in British Columbia, Canada; Ore Geology Reviews, v. 72, p. 1116–1128.

Celis, M.A., 2015. Titanite as an indicator mineral for alkalic porphyry Cu-Au deposits in south-central British Columbia; M.Sc. thesis, University of British Columbia, Vancouver, British Columbia, 247 p.

Celis, M.A., Bouzari, F., Bissig, T., Hart, C.J.R., and Ferbey, T., 2014. Petrographic characteristics of porphyry indicator minerals from alkalic porphyry copper-gold deposits in south-central British Columbia (NTS 092, 093); in Geoscience BC Summary of Activities 2013, Geoscience BC, Report 2014-1, p. 53–62.

Chapman, J.B., Jackson, S.E., and Ryan, J.J., 2012. Anomalous zircon Ce^{4+}/Ce^{3+} ratios from early Jurassic plutons in Yukon: Implications for porphyry exploration potential; Abstracts, V.M. Goldschmidt Conference, Montréal, Quebec, v. 76, p. 1562.

Che, X.D., Linnen, R.L., Wang, R.C., Groat, L.A., and Brand, A.A., 2013. Distribution of trace and rare earth elements in titanite from tungsten and molybdenum deposits in Yukon and British Columbia, Canada; Canadian Mineralogist, v. 51, p. 415–438.

Clague, J.J. and Ward, B.C., 2011. Pleistocene glaciation of British Columbia; in Developments in Quaternary Science, Quaternary Glaciations - Extent and Chronology a Closer Look, Volume 15, (ed.) J. Ehlers, P.L. Gibbard and P.D. Hughes; Elsevier, Amsterdam, p. 563–573.

Cooke, D.R., Baker, M., Hollings, P., Sweet, G., Zhaoshan, C., Danyushevsky, L., Gilbert, S., Zhou, T., White, N., Gemmell, J.B., and Inglis, S., 2014. New advances in detecting the distal geochemical footprints of porphyry systems -

epidote mineral chemistry as a tool for vectoring and fertility assessments; in Building Exploration Capability for the 21st Century, (ed.) K.D. Kelley and H.C. Golden; Society of Economic Geologists, Special Publication 18, Littleton, Colorado, p. 127–152.

Dilles, J.H., Kent, A.J.R., Wooden, J.L., Tosdal, R.M., Koleszar, A., Lee, R.G., and Farmer, L.P., 2015. Zircon compositional evidence for sulphur-degassing from ore-forming arc magmas; Economic Geology, v. 110, p. 241–251.

Drummond, A.D., Tennant, S.J., and Young, R.J., 1973. The interrelationship of regional metamorphism, hydrothermal alteration and mineralization at the Gibraltar mines copper deposit in B.C.; Canadian Mining and Metallurgical Bulletin, v. 66, p. 48–55.

Drummond, A.D., Sutherland Brown, A., Young, R.J., and Tennant, S.J., 1976. Gibraltar - Regional metamorphism, mineralization, hydrothermal alteration and structural development; in Porphyry deposits of the Canadian Cordillera, (ed.) A. Sutherland Brown; Canadian Institute of Mining and Metallurgy, Special Volume 15, p. 195–205.

Ferbey, T., Plouffe, A., and Bustard, A.L., 2016. Geochemical, mineralogical, and textural data from tills in the Highland Valley Copper mine area, south-central British Columbia; British Columbia Geological Survey GeoFile 2016-11, Geological Survey of Canada Open File 8119, 1 zip file.

Ferry, J.M. and Watson, E.B., 2007. New thermodynamic models and revised calibrations for the Ti-in-zircon and Zr-in-rutile thermometers; Contributions to Mineralogy and Petrology, v. 154, p. 429–437.

Hashmi, S., Ward, B.C., Plouffe, A., Leybourne, M.I., and Ferbey, T., 2015. Geochemical and mineralogical dispersal in till from the Mount Polley Cu-Au porphyry deposit, central British Columbia, Canada; Geochemistry: Exploration, Environment, Analysis, v. 15, p. 234–249.

Hattori, K., Morfin, S., Baumgartner, R., Shen, P., and Petts, D., 2016. Fertility of igneous rocks related to porphyry copper deposits: indications from zircon compositions; Proceedings, XVIII Peruvian Geological Congress, 3 p.

Hattori, K., Wang, J., Baumgartner, R., Kobylinski, C., Morfin, S., and Shen, P., 2017. Zircon composition: indicator of fertile igneous rocks related to porphyry copper deposits; 14th Society for Geology Applied to Mineral Deposits Biennial meeting 2017, Québec, Quebec, v. 1, p. 295–298.

Hickin, A. and Plouffe, A., in press. Surficial sediment sampling for mineral exploration in the Canadian Cordillera: an historical perspective and review; in Indicator Minerals in Till and Stream Sediments of the Canadian Cordillera, (ed.) T. Ferbey, A. Plouffe and A. Hickin; Mineral Association of Canada, Topics in Mineral Sciences Volume 47, Geological Association of Canada, Special Paper 50.

Jago, C.P., Tosdal, R.M., Cooke, D.R., and Harris, A.C., 2014. Vertical and lateral variation of mineralogy and chemistry in the Early Jurassic Mt. Milligan alkalic porphyry Au-Cu

deposit, British Columbia, Canada; Economic Geology, v. 109, p. 1005–1033.

Kobylinski, C., Hatori, K., Smith, S., and Plouffe, A., 2016. Report on the composition and assemblage of minerals associated with the porphyry Cu-Mo mineralization at the Gibraltar deposit, south central British Columbia, Canada; Geological Survey of Canada, Open File 8025, 30 p.

Kobylinski, C., Hattori, K., Plouffe, A., and Smith, S., 2017. Epidote associated with the porphyry Cu-Mo mineralization at the Gibraltar deposit, south central British Columbia; Geological Survey of Canada, Open File 8279, 1 zip file.

Lee, R.G., Dilles, J.H., Tosdal, R.M., Wooden, J.L., and Mazdab, F.K., 2017a. Magmatic evolution of granodiorite intrusions at the El Salvador porphyry copper deposit, Chile, based on trace element composition and U/Pb age of zircons; Economic Geology, v. 112, p. 245–273.

Lee, R.G., Byrne, K., Alfaro, M., D'Angelo, M., Hart, C.J.R., Hollings, P., and Gleezon, S.A., 2017b. Assessing the zircon compositional evolution from the Guichon Creek Batholith and Highland Valley Copper deposit, south-central B.C.; 14th Society for Geology Applied to Mineral Deposits Biennial meeting 2017 Québec, Quebec, Volume 3, p. 1087–1090.

Liang, H.-Y., Campbell, I.H., Allen, C., Sun, W.-D., Liu, C.-Q., Yu, H.-X., Xie, Y.-W., and Zhang, Y.-Q., 2006. Zircon Ce^{4+}/Ce^{3+} ratios and ages for Yulong ore-bearing porphyries in eastern Tibet; Mineralium Deposita, v. 41, p. 152–159.

Loader, M.A., Wilkinson, J.J., and Armstrong, R.N., 2017. The effect of titanite crystallisation on Eu and Ce anomalies in zircon and its implications for the assessment of porphyry Cu deposit fertility; Earth and Planetary Science Letters, v. 472, p. 107–119.

Lowell, J.D. and Guilbert, J.M., 1970. Lateral and vertical alteration-mineralization zoning in porphyry ore deposits; Economic Geology, v. 65, p. 373–408.

Lu, Y.-J., Loucks, R.R., Fiorentini, M., McCuaig, T.C., Evans, N.J., Yang, Z.-M., Hou, Z.-Q., Kirkland, C.L., Parra-Avila, L.A., and Kobussen, A., 2016. Zircon composition as a pathfinder for porphyry Cu ± Mo ± Au deposits; *in* Tectonics and metallogeny of the Thetyan Orogenic Belt (ed.) J. Richard; Society of Economic Geologists, Special Publication No. 19, Littleton, Colorado, p. 329–347.

Mao, M., Rukhlov, A.S., Rowins, S.M., Spence, J., and Coogan, L.A., 2016. Apatite trace element compositions: a robust new tool for mineral exploration; Economic Geology, v. 111, p. 1187–1222.

McClenaghan, M.B., McDonald, A., Leybourne, M.I., Beckett-Brown, C., Chapman, J.B., Layton-Matthews, D., Lougheed, H.D., Plouffe, A., and Ferbey, T., 2017. Controls on the fertility of porphyry mineralizing systems recorded in indicator minerals; *in* Targeted Geoscience Initiative -2016 Report of Activities, (ed.) N. Rogers; Geological Survey of Canada, Open File 8199, p. 87–89.

McClenaghan, M.B., Beckett-Brown, C.E., McCurdy, M.W.,

McDonald, A.M., Leybourne, M.I., Chapman, J.B., Plouffe, A., and Ferbey, T., 2018. Mineral markers of porphyry copper mineralization: Progress report on the evaluation of tourmaline as an indicator mineral; *in* Targeted Geoscience Initiative: 2017 report of activities, volume 1, (ed.) N. Rogers; Geological Survey of Canada, Open File 8358, p. 69–77.

McDonough, W.F. and Sun, S.S., 1995. The composition of the Earth; Chemical Geology, v. 120, p. 223–253.

Pisiak, L.K., Canil, D., Lacourse, T., Plouffe, A., and Ferbey, T., 2017. Magnetite as an indicator mineral in the exploration of porphyry deposits: A case study in till near the Mount Polley Cu-Au deposit, British Columbia, Canada; Economic Geology, v. 112, p. 919–940.

Plouffe, A. and Ferbey, T., 2015a. Till composition near Cu-porphyry deposits in British Columbia: Highlights for mineral exploration; *in* TGI 4 - Intrusion Related Mineralisation Project: new vectors to buried porphyry-style mineralisation, (ed.) N. Rogers; Geological Survey of Canada, Open File 7843, p. 15–37.

Plouffe, A. and Ferbey, T., 2015b. Surficial geology, Granite Mountain area, British Columbia, parts of NTS 93-B/8 and 93-B/9; Geological Survey of Canada, Canadian Geoscience Map 223 (preliminary), British Columbia Geological Survey, Geoscience Map 2015-4, scale 1:50 000.

Plouffe, A. and Ferbey, T., 2016. Till geochemistry, mineralogy and textural data near four Cu porphyry deposits in British Columbia; Geological Survey of Canada Open File 8038 and British Columbia Geological Survey Geofile 2016 -10, 1 zip file.

Plouffe, A. and Ferbey, T., in press. Porphyry Cu indicator minerals in till: A method to discover buried mineralization; *in* Indicator Minerals in Till and Stream Sediments of the Canadian Cordillera, (ed.) T. Ferbey, A. Plouffe and A. Hickin; Mineral Association of Canada, Topics in Mineral Sciences Volume 47, Geological Association of Canada, Special Paper 50.

Plouffe, A., Ferbey, T., Hashmi, S., and Ward, B.C., 2016. Till geochemistry and mineralogy: Vectoring towards Cu porphyry deposits in British Columbia, Canada; Geochemistry: Exploration, Environment, Analysis, v. 16, p. 213–232.

Plouffe, A., Ferbey, T., Kobylinski, C.H., Hattori, K., Grenier, A., and McClenaghan, M.B., 2017. Deconvolution of complex spatial-temporal records of porphyry fertility recorded in till minerals; *in* Targeted Geoscience Initiative – 2016 Report of Activities, (ed.) N. Rogers; Geological Survey of Canada, Open File 8199, p. 79–85.

Rabbia, O.M., Hernández, L.B., French, D.H., King, R.W., and Ayers, J.C., 2009. The El Teniente porphyry Cu-Mo deposit from a hydrothermal rutile perspective; Mineralium Deposita, v. 44, p. 849–866.

Rukhlov, A.S., Plouffe, A., Ferbey, T., Mao, M., and Spence, J., 2016. Application of trace-element compositions of detrital apatite to explore for porphyry deposits in central Brit-

ish Columbia; *in* Geological Fieldwork 2015, British Columbia Ministry of Energy and Mines, British Columbia Geological Survey, Paper 2016-1, p. 145–179.

Shen, P., Hattori, K., Pan, H., Jackson, S., and Seitmuratova, E., 2015. Oxidation condition and metal fertility of granitic magmas: zircon trace-element data from porphyry Cu deposits in the central Asian orogenic belt; Economic Geology, v. 110, p. 1861–1878.

Sillitoe, R.H., 2010. Porphyry Copper Systems; Economic Geology, v. 105, p. 3–41.

Sinclair, W.D., 2007. Porphyry deposits; *in* Mineral Deposits of Canada: A synthesis of Major Deposit-Types, District Metallogeny, the Evolution of Geological Provinces, and Exploration Methods, (ed.) W.D. Goodfellow; Geological Association of Canada, Mineral Deposit Division, Special Publication No. 5, p. 223–243.

van Straaten, B.I., Oliver, J., Crozier, J., and Goodhue, L., 2013. A summary of the Gibraltar porphyry copper-molybdenum deposit, south-central British Columbia, Canada; *in* Porphyry systems of central and southern British Columbia: Tour of central British Columbia porphyry deposits from Prince George to Princeton, (ed.) J.M. Logan and T.G. Schroeter; Society of Economic Geologists, Field Trip Guidebook, Series 43, p. 55–66.

Wilkinson, J.J., Chang, Z., Cooke, D.R., Baker, M.J., Wilkinson, C.C., Inglis, S., Chen, H., and Gemmell, J.B., 2015. The chlorite proximitor: A new tool for detecting porphyry ore deposits; Journal of Geochemical Exploration, v. 152, p. 10–26.

Williamson, B.J., Herrington, R.J., and Morris, A., 2016. Porphyry copper enrichment linked to excess aluminium in plagioclase; Nature Geoscience, v. 9, p. 237–241.

Wolfe, L., 2017. Chemistry of refractory indicator minerals in tills around the Gibraltar porphyry copper deposit, south-central British Columbia; B.Sc. thesis, University of Ottawa, Ottawa, Ontario, 56 p.

Wolfe, L., Hattori, K., and Plouffe, A., 2017. Glacial dispersal of refractory minerals from the Gibraltar porphyry copper deposit, south central British Columbia, Canada; Geological Survey of Canada, Scientific Presentation 73, 1 poster.

Yang, Z., Yang, L.-Q., He, W.-Y., Gao, X., Liu, X.-D., Bao, X.-S., and Lu, Y.-G., 2017. Control of magmatic oxidation state in intracontinental porphyry mineralization: A case from Cu (Mo-Au) deposits in the Jinshajiang-Red River metallogenic belt, SW China; Ore Geology Reviews, v. 90, p. 827–846.

Zhang, C.-C., Sun, W.-D., Wang, J.-T., Zhang, L.-P., Sun, S.-J., and Wu, K., 2017. Oxygen fugacity and porphyry mineralization: A zircon perspective of Dexing porphyry Cu deposit, China; Geochimica et Cosmochimica Acta, v. 206, p. 343–363.

Mineral markers of porphyry copper mineralization: Progress report on the evaluation of tourmaline as an indicator mineral

M.B. McClenaghan[1], C.E. Beckett-Brown[2], M.W. McCurdy[1], A.M. McDonald[2], M.I. Leybourne[3], J.B. Chapman[4], A. Plouffe[1] and T. Ferbey[5]

[1]*Geological Survey of Canada, 601 Booth Street, Ottawa, Ontario, K1A 0E8*
[2]*Harquail School of Earth Sciences, Laurentian University, 935 Ramsey Lake Road, Sudbury, Ontario, P3E 2C6*
[3]*Department of Geological Sciences and Engineering, Queen's University, Kingston, Ontario, K7L 3N6*
[4]*Geological Survey of Canada, 605 Robson Street, Vancouver, British Columbia, V6B 5J3*
[5]*British Columbia Geological Survey Branch, 1810 Blanshard Street, Victoria, British Columbia, V8T 4J1*

Abstract

Tourmaline is considered a potential indicator of porphyry-style mineralization as it is a relatively common accessory mineral and has a broad range of compositions. The aim of this study is to test discrimination criteria for tourmaline in relation to porphyry copper mineralization. Work to date has focussed on the collection of tourmaline in bedrock samples from a broad range of known porphyry deposits, the detailed examination of tourmaline in archived till samples from the vicinity of the Woodjam deposit, and the collection of new bedrock and stream sediment samples in the area of the Casino deposit. Three different types of tourmaline were identified in bedrock from Casino: i) breccia-style; ii) vein-style; and iii) disseminated. A paragenetic analysis based on associated minerals and tourmaline textures indicates that tourmaline is one of the first hydrothermal minerals to form in the mineralized porphyry system. Diffusion-like textures found in some tourmaline grains from bedrock samples from other deposits is significant because chemical diffusion in tourmaline is considered to be virtually non-existent. Future work includes the completion of trace element analysis of tourmaline, comparison of tourmaline chemical signatures in bedrock to those recovered in till or stream sediments at the two test sites, and investigation of Fe^{2+}/Fe^{3+} using Raman spectroscopy.

Introduction

Indicator minerals are an established exploration tool in glaciated terrain for gold (e.g. Averill and Zimmerman, 1986; Averill, 2001; McClenaghan and Cabri, 2011) and diamonds (e.g. McClenaghan and Kjarsgaard, 2007), and more recently have been tested for porphyry copper deposits (e.g. Kelley et al., 2011; Hashmi et al., 2015; Plouffe et al., 2016). The objective of this research activity is to further develop the porphyry copper indicator mineral suite for both glaciated and unglaciated terrains through the detailed examination and testing of the mineral tourmaline. Discrimination criteria will be developed for identifying tourmaline in bedrock and unconsolidated sediments (i.e. till, stream sediments) that is indicative of fertile porphyry copper intrusions.

Sampling of GSC archives

Archived bedrock samples housed at Geological Survey of Canada's sample repository in Ottawa from a broad range of porphyry copper deposits and pegmatites that had been collected by R. Kirkham, D. Sinclair, R. Mulligan, A. Soregaroli and R. Boyle from British Columbia, Yukon, Ontario, Quebec, Nova Scotia, Chile and Mexico have been subsampled. At least half the subsamples selected for this study are from locations that are no longer accessible or represent upper parts of deposits that have been mined out. Tourmaline in these samples are being examined in polished thin section and/or heavy mineral concentrates to characterize textural relationships (grain size, mineral inclusions, colour, zonation, etc.), mineral chemistry (major, minor and trace) and isotopic ratios.

Figure 1. Brown tourmaline grains recovered from the mid-density fraction of till overlying mineralization at the Woodjam copper prospect, British Columbia.
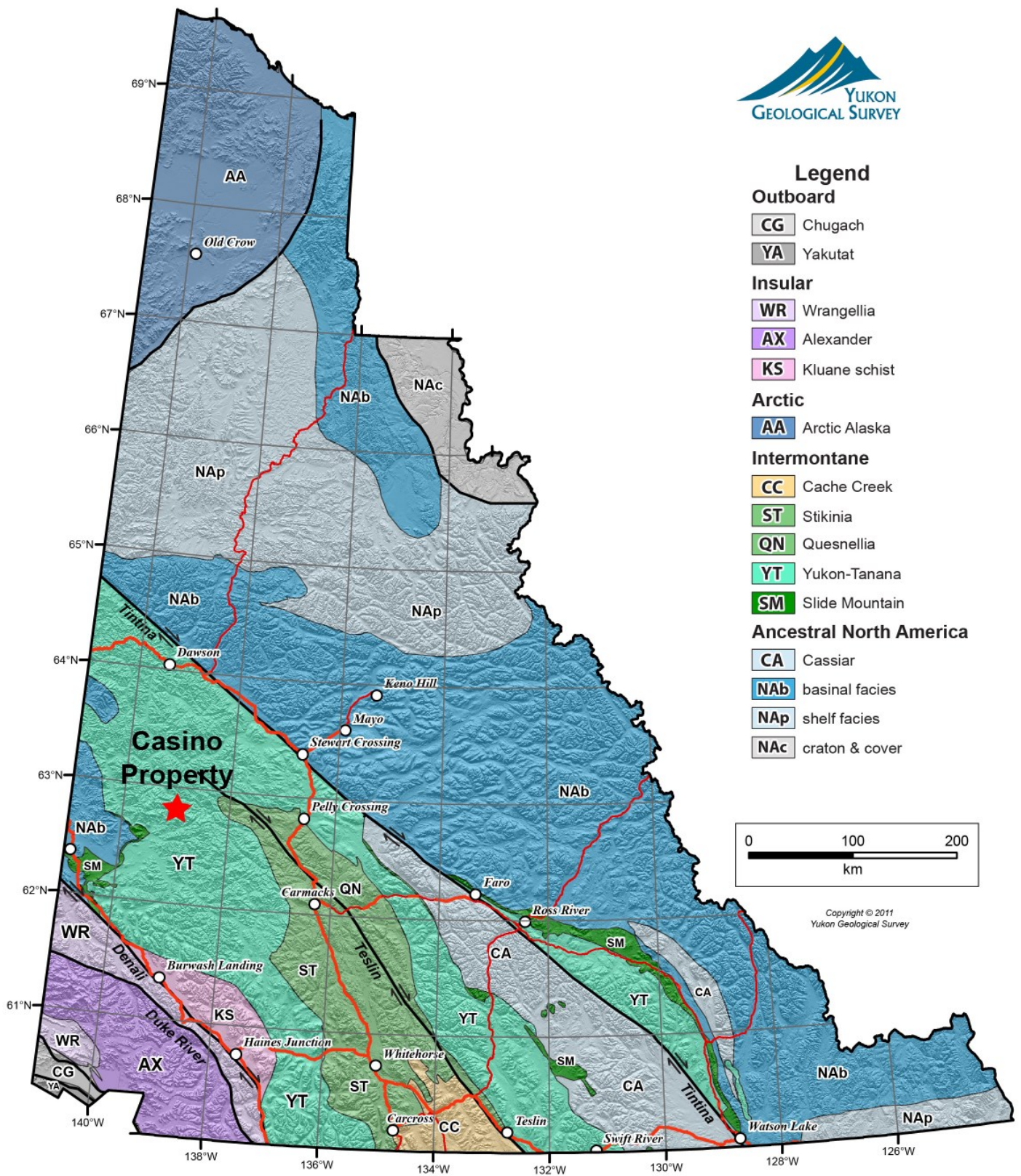
Figure 2. Terrane and geological map of Yukon showing the Casino property location. Modified after Colpron and Nelson (2011).

Woodjam tourmaline study

Mineral fractions of 91 archived till samples from a previous study of till indicator minerals down ice of the Woodjam copper-gold porphyry prospect, British Columbia (Plouffe et al., 2016) were re-examined. In particular, tourmaline (Fig. 1) was re-examined and recounted in both high (>3.2 SG) and mid-density (2.8–3.2 SG) fractions. The mineral chemistry and other features of tourmaline grains from four till samples up ice, overlying, and down ice of the deposit were initially examined by Chapman et al. (2015). Additional tourmaline grains from up ice, overlying, and at varying distances down ice of the deposit as well as newly acquired bedrock samples are currently being characterized, with special focus on understanding the differences in tourmaline recovered from the high- and mid-density mineral fractions.

Casino sampling

Bedrock and stream sediment samples were collected from the Casino copper-molybdenum-silver-gold porphyry deposit, 380 km northwest of Whitehorse, Yukon (Fig. 2). The deposit is a calc-alkalic porphyry and ore is hosted in quartz monzonite and associated breccias around the edge of the main intrusion (Casselman and Brown, 2017). Tourmaline occurs throughout the deposit in all rock types despite several different alteration types and styles (i.e. potassic, phyllic, propylitic and argillic). The Casino deposit was chosen for detailed study because of the abundance and widespread nature of tourmaline in the deposit, the availability of drill core from all parts of the deposit, and the relatively undisturbed nature of the deposit that was optimal for testing the effectiveness of tourmaline as an indicator mineral in surrounding stream sediments.

Thirty-eight bedrock samples were collected from drill core (Appendix 1). Surface bedrock sampling at the Casino deposit was not possible because of the thick cover of colluvium in this unglaciated terrain and the weathered bedrock masking hard competent bedrock. In addition to bedrock sampling, samples of stream sediment and water were collected at 22 sites (Fig. 3). At each site, two water samples, one stream silt sample, one bulk stream sediment sample for recovery of indicator minerals, and one pebble sample were collected following protocols described in Day et al. (2013).

Sand-size (<2 mm) bulk sample for indicator minerals

Samples were collected to determine the minerals that are indicative of porphyry copper mineralization. Material was
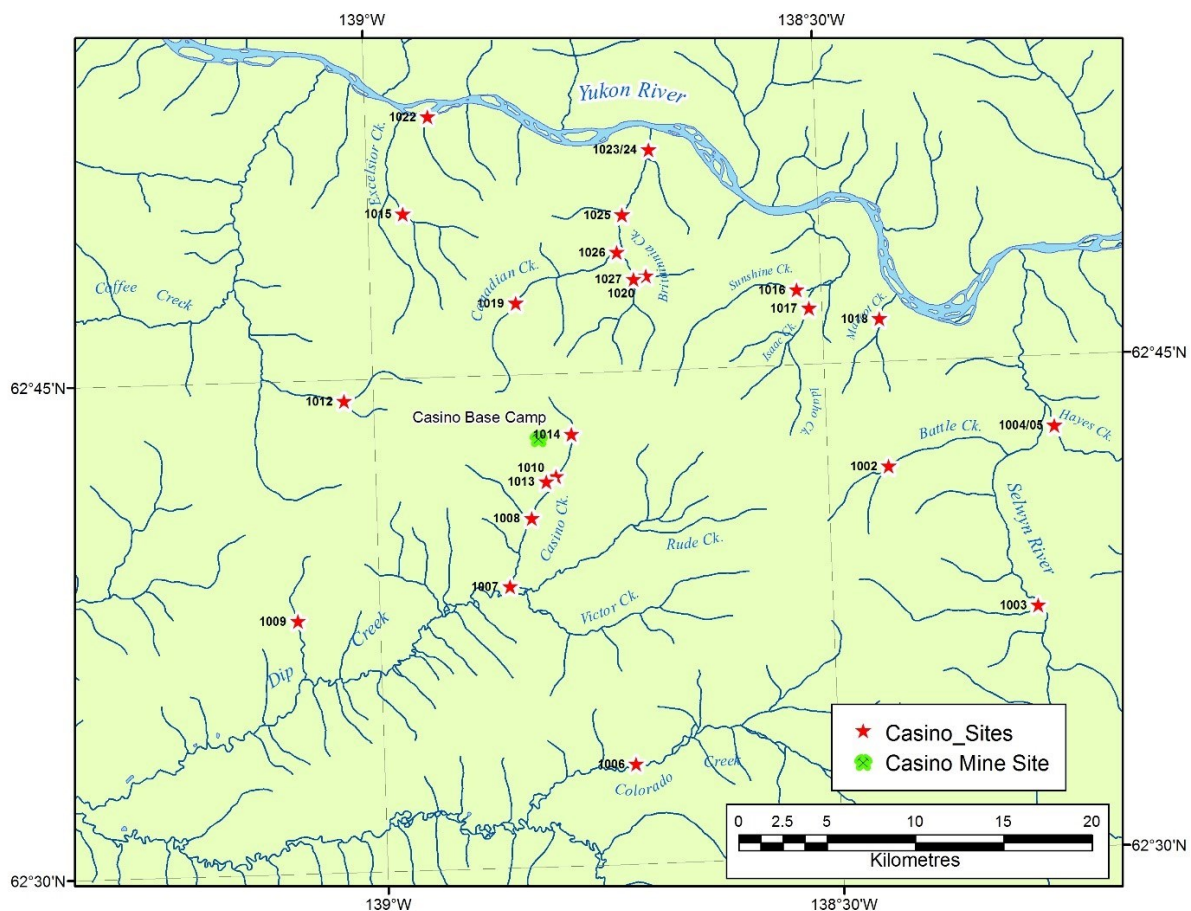
Figure 3. Location of stream sediment sample sites (red stars) around the Casino porphyry Cu deposit plotted on the digital topographic map for NTS 115J.

Table 1. Specifications for parameters measured in stream water samples collected around the Casino copper deposit.

	Range	Accuracy	Resolution	Units (Recorded)
Dissolved Oxygen (%)	0-500%	0 to 200% (±2% of reading or 2% air saturation, whichever is greater)	1% or 0.1% air saturation	%
Temperature	-5 to 70°C	±0.2°C	0.1°C	°C
Conductivity	0 to 200 mS/cm	±0.5% of reading or 0.001 mS/cm, whichever is greater	0 to 500 µS/cm=0.001; 501 to 5000 µS/cm=0.01	µS
pH	0 to 14 units	±0.2 units	0.01 units	pH units
Oxidation-Reduction Potential (ORP)	-1999 to +1999 mV	±20 mV in redox standards	0.1 mV	mV
Air Pressure	375 to 825 mmHg	±1.5 mmHg from 0 to 50°C	0.1 mmHg	kPa

collected from shovel holes dug at suitable sites (mid-channel bars, boulder or log traps, etc.) in the main channel of each stream (see Prior et al., 2009, for a full list of suitable sites). At each site, sediment was wet-sieved through a U.S. sieve series 12-mesh (1.68 mm) stainless steel sieve into a sample bag until a sample weight of 10-15 kg was collected. Bulk sediment samples for indicator minerals have been shipped to a commercial laboratory for heavy (>3.2 specific gravity) and moderate-density (2.8–3.2 specific gravity) fraction separation and identification of key indicator minerals (including tourmaline) of porphyry mineralization.

Stream sediments (silt)

At each site, a synthetic cloth bag was two-thirds filled with silt or fine sand collected from the active stream channel after collection of the water sample(s) and before the bulk sediment sample from various points in the active channel while moving upstream, over a distance of 5 to 15 m. If the stream channel consisted mainly of clay and coarse material or organic sediment was scarce or absent, trapped silt moss mats in the stream channel may have been collected. Field observations were digitally recorded on a tablet using a standard form developed jointly by the GSC and the Northwest Territories Geological Survey. Samples of stream silt collected around the Casino deposit are currently being dried at low temperatures (<40°C) at the GSC Sedimentology Laboratory, Ottawa. These samples will be sieved to recover the <177µm fraction and analyzed using modified aqua regia digestion /ICP-MS, instrumental neutron activation analysis, and portable XRF.

Stream waters

Stream water was collected at each site because it is a routine component of GSC stream sediment sampling protocols.

At each site the six variables listed in Table 1 were measured in stream waters. Two water samples were collected in the mid-channel of streams at each site: i) a filtered, acidified sample ('FA'); and ii) a filtered, un-acidified sample ('FU') by drawing stream water into a 60 ml plastic syringe and filtering into each HDPE bottle through a 0.45 µm disposable filter unit. One set of filtered stream water samples will be acidified with 0.5 ml 8M HNO_3. Groundwater samples collected from drill holes during the same time period by Western Copper and Gold staff have been shared with GSC. Filtered and acidified (FA) stream water samples will be analyzed for trace metal and major elements at GSC laboratories in Ottawa. Conductivity, pH and alkalinity will be measured in the filtered, un-acidified set of waters.

Tourmaline types

Three different types of tourmaline were identified in bedrock samples at Casino, these being classified as breccia-style, vein-style and disseminated (Fig. 4). The breccia-style consists of a tourmaline-dominant breccia matrix with associated quartz. Tourmaline grains form euhedral acicular radiating masses appearing black in hand sample, but under closer inspection, grains actually range in colour from black-brown to a pale-green, some being colour-zoned along their length (from nucleation to termination). The tourmaline morphology is consistent with that observed in other deposits examined in this study (e.g. Schaft Creek and Woodjam). However, the occurrence of lighter-coloured tourmaline in the breccia style is a new observation. The vein-style tourmaline is very fine-grained and commonly develops along the margins of quartz – sulphide veins (generally pyrite), but can also be observed as tourmaline-dominant veins that exhibit a pinch and swell texture. Tourmaline vein textures at Casino are similar to those observed at the

Figure 4. Casino deposit, Yukon, drill core samples: a) Hole 93-177 showing the breccia-style tourmaline (black matrix) surrounding mineralized fragments of Paton porphyry; b) Hole CAS-082 showing the vein-style tourmaline (black) forming along the rim of a pyrite vein; c) Hole CAS-084 showing the disseminated-style tourmaline (black).

found in a barren breccia close to the core of the deposit that has been overprinted by minor pyrite that formed much later. It is also observed to have been overgrown by sulphides and does not appear to have been modified or impacted by the various subsequent alteration styles (i.e. potassic, phyllic, propylitic, and argillic).

Ongoing tourmaline analysis

Polished thin sections of bedrock samples from the GSC archives have been examined by transmitted and reflected light microscopy, providing preliminary documentation of important mineral textures and associations. Select samples were then investigated using a scanning electron microscope (SEM) to collect major and minor chemical data by energy dispersive spectroscopy. An important observation during SEM analyses was the identification of what may be interpreted as diffusion-like textures in tourmaline (Fig. 5). This finding is significant as chemical diffusion in tourmaline is considered to be virtually non-existent (van Hinsberg et al., 2011), and thus this observation challenges our current state of knowledge regarding the mineral. It will therefore be important to be able to determine if: a) the observed textures do conform to solid state diffusion; and b) if so, the extent to which chemical diffusion may occur in the mineral. Understanding the potential for significant diffusion will be important when analyzing and interpreting distinct growth zones of tourmaline.

Preliminary laser-ablation work on samples has been conducted to establish protocols (e.g. ablation conditions, beam size, isotope list, internal and external standards) that will produce the best results for tourmaline trace element analyses. Preparation and mounting of tourmaline grains in epoxy pucks is
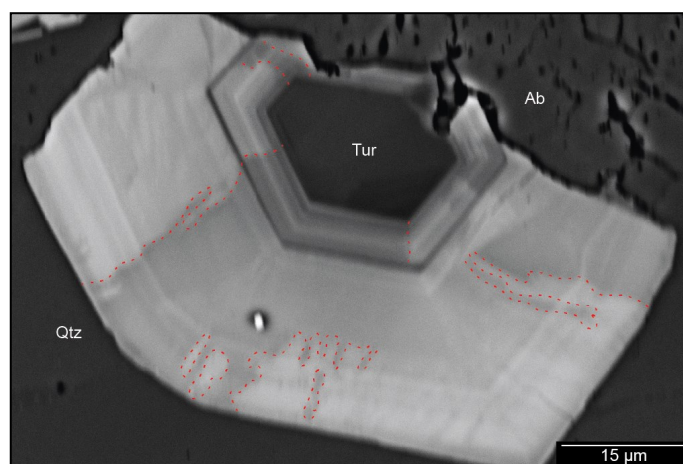
Figure 5. Backscattered electron image of a tourmaline (Tur) grain in quartz (Qtz) and albite (Ab) from a bedrock sample from the Highland Valley Cu deposit, British Columbia. Note the rhythmic oscillatory zonation which dominantly reflects changes in Fe:Mg:Al. Overprinting this zonation is what appears to be solid state diffusion, outlined by the dotted red lines for clarity.

other deposits in this study suggesting that they form from a similar process. Disseminated tourmaline is texturally similar to the breccia-style tourmaline (i.e. euhedral acicular radiating masses commonly infilled by quartz), but can also be observed overgrown by feldspars, sulphides, and clays and appears similar to that observed in other deposits in this study. A paragenetic analysis based on associated minerals and tourmaline textures indicates that tourmaline is one of the first hydrothermal minerals to form in the mineralized porphyry system. It is

ongoing for till samples collected at the Woodjam copper prospect as well as some other reference and background samples.

Future work includes the completion of trace-element analysis of tourmaline grains from the Schaft Creek and Woodjam copper deposits and other archived samples, the comparison of tourmaline chemical signatures to those recovered in till versus bedrock at Woodjam, investigation of Fe^{2+}/Fe^{3+} using Raman spectroscopy as a means of determining prevailing oxidation/reduction (fO_2) conditions, and the characterization of tourmaline in bedrock and stream sediments from the Casino deposit.

Acknowledgments

References

Averill, S.A., 2001. The application of heavy indicator minerals in mineral exploration with emphasis on base metal indicators in glaciated metamorphic and plutonic terrain; *in* Drift Exploration in Glaciated Terrain, (ed.) M.B. McClenaghan, P.T. Bobrowsky, G.E.M. Hall and S. Cook; Geological Society of London, Special Volume 185, p. 69–82.

Averill, S.A. and Zimmerman, J.R., 1986. The Riddle resolved: the discovery of the Partridge gold zone using sonic drilling in glacial overburden at Waddy Lake, Saskatchewan; Canadian Geology Journal of the Canadian Institute of Mining and Metallurgy, v. 1, p. 14–20.

Casselman, S.C. and Brown, H., 2017. Casino porphyry copper-gold-molybdenum deposit, central Yukon (Yukon MINFILE 115J 028); *in* Yukon Exploration and Geology Overview 2016, (ed.) K.E. MacFarlane; Yukon Geological Survey, p. 61–74, plus digital appendices.

Chapman, J.B., Plouffe, A., and Ferbey, T., 2015. Tourmaline: The universal indicator?; *in* Short Course 02 Application of Indicator Mineral Methods to Exploration, 27th International Applied Geochemistry Symposium, Tucson, Association of Applied Geochemists, p. 25–31.

Colpron, M. and Nelson, J.L., 2011. A Digital atlas of terranes for the northern Cordillera; <www.geology.gov.yk.ca> [accessed September 6, 2017]

Day, S.J A., Wodicka, N., and McMartin, I., 2013. Preliminary geochemical, mineralogical and indicator mineral data for heavy mineral concentrates and waters, Lorillard River area Nunavut (parts of NTS 56-A, -B, and -G); Geological Survey of Canada, Open File 7428.

Kelley, K.D., Eppinger, R.G., Lang, J., Smith, S.M., and Fey, D.L., 2011. Porphyry Cu indicator minerals in till as an exploration tool: Example from the giant Pebble porphyry Cu-Au-Mo deposit Alaska, USA; Geochemistry: Exploration, Environment, Analysis, v. 11, p. 321–334.

Hashmi, S, Ward, B.C., Plouffe, A., Leybourne, M.I., and Ferbey, T., 2015. Geochemical and mineralogical dispersal in till form the Mount Polley Cu-Au porphyry deposit, central British Columbia; Canada; Geochemistry: Exploration, Environment, Analysis, v. 15, p. 234–249.

McClenaghan, M.B. and Cabri, L.J., 2011. Gold and Platinum Group Element indicator minerals in surficial sediments; Geochemistry: Exploration, Environment, Analysis, v.11, p. 251–263.

McClenaghan, M.B. and Kjarsgaard, B.A., 2007. Indicator mineral and surficial geochemical exploration methods for kimberlite in glaciated terrain: Examples from Canada; *in* Mineral Deposits of Canada: A Synthesis of Major Deposit-Types, District Metallogeny, the Evolution of Geological Provinces, and Exploration Methods, (ed.) W.D. Goodfellow; Geological Association of Canada, Mineral Deposits Division, Special Publication No. 5, p. 983–1006.

Plouffe, A., Ferbey, T., Hashmi, S., and Ward, B.C., 2016. Till geochemistry and mineralogy: Vectoring towards Cu porphyry deposits in British Columbia, Canada; Geochemistry: Exploration, Environment, Analysis, v. 16, p. 213–232.

Prior, G.J., McCurdy, M.W., and Friske, P.W.B., 2009. Stream sediment sampling for kimberlite-indicator minerals in the Western Canada Sedimentary Basin: The Buffalo Head Hills survey, north-central Alberta; *in* Application of Till and Stream Sediment Heavy Mineral and Geochemical Methods to Mineral Exploration in Western and Northern Canada, (ed.) R.C. Paulen and I. McMartin; Geological Association of Canada Short Course Notes 18, p. 91–103.

van Hinsberg, V.J., Henry, J., and Marschall, R., 2011. Tourmaline: an ideal indicator of its host environment; Canadian Mineralogist, v. 49, p. 1–16.

Appendix 1. Casino copper deposit samples

Sample No.	Hole No.	Depth from (m)	Hole Collar Location (X,Y,Z), Azimuth, Dip	Brief Rock Description	Tourmaline Type	Tourmaline Description
CEBB001	93-147	29.00	610875.040, 6958325.680, 1370.700, 0.0, -90	Altered cap rock. Strong limonite alteration with other Fe-oxides.	Disseminated?	Fine-grained black grains that are not Fe-oxides. Too fine grained to definitively tell.
CEBB002	93-150	5.70	610963.040, 6958409.920, 1361.580, 0.0, -90	Milled breccia, with strong argillic and minor potassic alteration.	Vein, Disseminated	Tur found as clots and discontinuous veins. Tur forms as euhedral radial balls forming in association with quartz. Tur grains appear black in hand sample but are brownish up close.
CEBB003	93-177	189.00	610363.930, 6958203.960, 1331.580, 0.0, -90	Dawson range monolithic breccia with a Tur dominant matrix with phyllic alteration. Disseminated pyrite is observed both in the matrix and in the clasts and is likely later than the brecciation.	Breccia	Tur is forming the dominant phase in the breccia matrix. Tur forming as euhedral radial masses in the matrix, with significant quartz as the matrix colour is quite greyish.
CEBB004	93-177	191.82	610363.930, 6958203.960, 1331.580, 0.0, -90	Dawson range monolithic breccia with Tur dominant matrix with phyllic alteration. Disseminated pyrite is observed both in the matrix and in the clasts.	Breccia	Tur is forming the dominant phase in the breccia matrix as euhedral acicular radial masses. Some individual Tur grains observed are almost colourless.
CEBB005	93-177	200.33	610363.930, 6958203.960, 1331.580, 0.0, -90	Dawson range monolithic breccia with a Tur dominant matrix with phyllic alteration. Disseminated pyrite is observed both in the matrix and in the clasts.	Breccia	Tur is forming the dominant phase in the breccia matrix as radial masses. Some individual Tur grains are observed exhibiting an acicular habit which are almost colourless.
CEBB006	93-177	209.40	610363.930, 6958203.960, 1331.580, 0.0, -90	Dawson range monolithic breccia with Tur dominant matrix. Phyllic and argillic alteration. Disseminated pyrite is observed both in the matrix and in the clasts and is likely later than the brecciation.	Breccia	Tur is forming the dominant phase in the breccia matrix. Tur forming as radial masses in the matrix, with significant quartz as the matrix colour is quite greyish. Some individual almost colourless Tur grains are observed exhibiting an acicular habit. Breccia matrix appears greyish black but Tur grains themselves are quite light in colour.
CEBB007	93-177	217.81	610363.930, 6958203.960, 1331.580, 0.0, -90	Latite breccia. Breccia matrix is no longer dominated by Tur but appears to be a combination of milled material and minor disseminated Tur. Minor argillic and phyllic alteration.	Breccia	Tur is similar in textural style here forming as euhedral radial masses, but is less dominant in its abundance. Other disseminated grains of Tur are zoned with darker termination and lighter nucleation points.
CEBB008	93-177	218.95	610363.930, 6958203.960,1 331.580, 0.0, -90	Referred to as a "latite breccia". Dominated by a milled breccia matrix with roughly 5% breccia fragments. Minor kaolinite. Minor disseminated pyrite. Breccia fragments are strongly altered by Tur and pyrite.	Breccia	Tur forming as radial masses in the apparent breccia fragments. Colour at a distance appears black, but is actually quite light to even colourless at the nucleation point becoming black towards the termination.
CEBB009	93-177	225.84	610363.930, 6958203.960, 1331.580, 0.0, -90	Latite breccia dominated by a milled matrix with no more than 5% breccia fragments. Quartz-sericite-pyrite alteration with minor muscovite and kaolinite. Breccia fragments appear to be Paton porphyry.	Breccia, Disseminated	Tur forming as radial masses in the apparent breccia fragments. Colour at a distance appears black but is quite light to even colourless at the nucleation point becoming black towards the termination. Tur appears to be both within the breccia matrix as well as within the clasts.
CEBB010	93-177	226.69	610363.930, 6958203.960, 1331.580, 0.0, -90	Latite breccia dominated by a milled matrix with no more than 5% breccia fragments. Quartz-sericite-pyrite alteration with minor muscovite and kaolinite. Breccia fragments are apparently absent in this section.	Disseminated	Tur is forming as euhedral radial masses generally nucleating from another phase, either quartz or possibly pyrite. Tur appears black but is much more translucent under close observation.
CEBB011	93-177	155.63	610363.930, 6958203.960, 1331.580, 0.0, -90	Latite breccia dominated by a milled matrix. Breccia fragments contain Tur likely from earlier brecciation. Pyrite is dispersed throughout the sample. Alteration is dominated by quartz-sericite-pyrite and minor kaolinite.	Breccia	Tur again forming as euhedral radial masses. Colour appears black but is light to even colourless at the nucleation point and becomes black towards the terminus. Tur appears to be both within the breccia matrix as well as within the clasts.
CEBB012	CAS-035	153.92	609624.792, 6958755.792, 1222.899, 244, -70	Medium grained Dawson range batholith. Minor sericite, pyrite alteration not much quartz. Some late gypsum veins cross cutting the sample. Tur and chlorite forming in association.	Vein	Tur is forming in close association with chlorite and pyrite as irregular veins. Tur morphology is still in the form of radial aggregates of euhedral acicular Tur. Grains are strongly coloured appearing quite dark. Tur appears to overprint biotite in some places.
CEBB013	CAS-037	148.14	610561.858, 6958402.456, 1289.922, 0.0, -90	Paton Porphyry. Silica rich phyllic alteration with pitted plag phenos. Some kaolinite alteration and strong pyrite alteration. Some minor hematite alteration.	Disseminated	Tur forming as radial masses as euhedral grains. No apparent associations, observed within kaolinite, pyrite and with quartz and feldspar. Tur is quite a dominant phase despite it being disseminated in nature.
CEBB014	CAS-037	189.27	610561.858, 6958402.456, 1289.922, 0.0, -90	Paton Porphyry. Silica rich phyllic alteration with bleached yellow feldspar crystals. Some kaolinite alteration with strong pyrite alteration and minor hematite alteration. Minor chalcopyrite, covellite and bornite	Vein, Disseminated	Tur forming as radial masses of euhedral black grains. Found as blow out veins as well as disseminations. Disseminated grains seem to be in association with quartz.
CEBB015	CAS-040	87.20	610463.806, 6958398.500, 1282.253, 270, -45	Dawson Range Batholith. Texturally destructive phyllic alteration with some kaolinite alteration and significant Fe-oxide alteration.	Breccia?	Tur difficult to see due to pervasive Fe oxide alteration. Appears to be a breccia or infilling the matrix around the porphyritic feldspars.
CEBB016a	CAS-030	133.00	610165.755, 6958302.961, 1294.661, 90, -45	Paton porphyry. Pervasive argillic alteration in the form of kaolinite and some minor sericite. Some quartz-rich regions are still evident.	Disseminated	Tur is forming in dark regions of the sample. Forming as euhedral radial masses as brown black grains almost acicular in nature. Appears to be an association with quartz

Appendix 1. Casino copper deposit samples (cont.)

Sample No.	Hole No.	Depth from (m)	Hole Collar Location (X,Y,Z), Azimuth, Dip	Brief Rock Description	Tourmaline Type	Tourmaline Description
CEBB016b	CAS-030	140.96	610165.755, 6958302.961, 1294.661, 90, -45	Paton porphyry. Pervasive argillic alteration (kaolinite) with some minor sericite. Some indications this sample is a breccia, but the alteration is so intense it is difficult to tell.	Breccia?	Tur is forming within the dark regions in what appears to be the breccia matrix. Under close observation the Tur grains are quite light, almost a pale green-grey colour. Forming radial masses.
CEBB017	CAS-030	160.84	610165.755, 6958302.961, 1294.661, 90, -45	Paton porphyry. Intense phyllic alteration overprinted by argillic alteration.	Disseminated	Tur is forming as disseminated clots in the darker zones with chlorite. Tur is forming as radial acicular masses of euhedral grains. Seem to have grown in open space, minor quartz filling the interstitial space.
CEBB018	CAS-030	174.75	610165.755, 6958302.961, 1294.661, 90, -45	Paton porphyry. Intense phyllic alteration overprinted by argillic alteration. Some disseminated pyrite throughout the sample.	Disseminated	Tur is forming differently here, much darker than previous samples it seems. The radial masses of grains are much more solitary than being in clots. It is also accompanied by epidote.
CEBB019	CAS-030	185.05	610165.755, 6958302.961, 1294.661, 90, -45	Dawson range. Moderate argillic alteration. Sample seems to be dominated by a small quartz pyrite vein with a large alteration halo. Rimming the halo almost a cm away are some clots of Tur.	Disseminated	Tur is a similar colour here. Dark brown to black in colour. The Tur is still present as euhedral radial masses along the edge of a vein alteration halo in association with? epidote.
CEBB020	CAS-030	204.58	610165.755, 6958302.961, 1294.661, 90, -45	Paton porphyry with moderate argillic alteration (kaolinite) with some phyllic alteration. Quartz remains, but some increased barren sinuous quartz veins are observed.	Disseminated	Tur is forming as euhedral disseminated acicular radial masses. Grains are darker in colour than seen in the potentially breccia material. Grains appear to be infilling what was open space, which is now filled by kaolinite.
CEBB021	CAS-030	217.57	610165.755, 6958302.961, 1294.661, 90, -45	Paton porphyry with large regions of sulfides.	Not Tur	What was first thought to be Tur is likely chalcocite along the edge of pyrite veins.
CEBB022	CAS-062	76.77	609861.924, 9658599.958, 1239.461, 181, -59	Granodiorite. Intense phyllic alteration with some vuggy quartz. Disseminated pyrite and minor molybdenite. Two periods of brecciation. First was cemented by tourmaline the second is dominated by quartz.	Disseminated	Tur is forming as disseminated euhedral acicular radial masses and clots. Grains are dark-black to brown in colour with some lighter grains. Generally enveloped by kaolinite and sometimes quartz. Some epidote and chlorite appear in association.
CEBB023	CAS-070	80.77	610169.786, 6958300.703, 1301.965, 180, -60	Paton porphyry. Intense silica flooding in the form of quartz veins.	Vein?	Could be some Tur within the quartz-molybdenite veins but is too fine-grained to determine.
CEBB024	CAS-070	92.04	610169.786, 6958300.703, 1301.965, 180, -60	Paton porphyry. Lots of quartz veining with molybdenite.	Vein?	Lots of magnetite. Could be some Tur within the quartz-molybdenite veins but is too fine-grained to determine.
CEBB025	CAS-070	107.92	610169.786, 6958300.703, 1301.965, 180, -60	Paton porphyry. Lots of quartz veining with molybdenite.	Vein?	Lots of magnetite and epidote. Could be some Tur within the quartz-molybdenite veins but is too fine-grained to determine.
CEBB026	CAS-082	20.27	610562.693, 6958097.496, 1384.832, 0.0, -90	Granodiorite. Intense argillic alteration, textures are almost destroyed. Relict feldspars are bleached yellow. Lots of disseminated magnetite.	Disseminated	Tur forms eudral disseminated acicular radial masses. Grains are dark in colour with some masses have quartz cores.
CEBB027	CAS-082	34.18	610562.693, 6958097.496, 1384.832, 0.0, -90	Granodiorite. Intense argillic alteration, destroying most of the textures. Yellow bleaching of relict feldspars is present, with lots of silica flooding in the form of quartz veins.	Disseminated	Tur is forming as euhedral disseminated acicular radial masses. Grains are dark in colour with many of the grains in samples seemingly intergrown with quartz.
CEBB028	CAS-082	64.97	610562.693, 6958097.496, 1384.832, 0.0, -90	Granodiorite. Significant magnetite and hematite. Some phyllic alteration. Tourmaline-quartz-pyrite veins are observed throughout the sample.	Disseminated	Tur forming as euhedral acicular radial masses. Appearing as a black colour and very fine-grained. Tur is found in association with quartz and pyrite in veins.
CEBB029	CAS-082	140.33	610562.693, 6958097.496, 1384.832, 0.0, -90	Si flooded granodiorite. Phyllic alteration with quartz-pyrite veins.	Not Tur	After close observation it was determined to be fine-grained biotite not Tur.
CEBB030	CAS-082	170.66	610562.693, 6958097.496, 1384.832, 0.0, -90	Granodiorite. Increasing phyllic alteration with some intense Si flooding. Intense quartz-pyrite veins present with some possible chalcocite. Molybdenite is also present.	Disseminated	Tur is forming as acicular radial masses as very fine grained euhedral veins in association with quartz and pyrite.
CEBB031	CAS-082	177.13	610562.693, 6958097.496, 1384.832, 0.0, -90	Granodiorite. Less Si flooding and more intense phyllic alteration. Minor pyrite-quartz +/- tourmaline veins.	Vein, Disseminated	Tur is forming as both disseminations and within sulphide veins. Appearing as extremely fine-grained within veins. Tur grains within the veins appear darker in colour.
CEBB032	CAS-084	6.64	610660.692, 6958099.915, 1383.54, 0.0, -90	Granodiorite. Strong phyllic alteration with some argillic alteration likely the result of the proximity to surface. Lots of a black non-magnetic sulphide, tennantite-tetrahedrite? There is also some minor disseminated pyrite.	Disseminated	Tur is forming as acicular radial masses as brown-black euhedral grains. These masses are in close association and commonly overgrown by quartz.
CEBB033	CAS-084	21.02	610660.692, 6958099.915, 1383.54, 0.0, -90	Granodiorite. Part of the cap rock assemblage. Strong phyllic alteration with some overprinting argillic alteration. Apparent quartz tourmaline clots in this sample.	Disseminated	Tur is forming as acicular radial clots with quartz almost appearing as an intergrowth? Tur appears as black grains, but under close inspection they are almost transparent and light in colour.

Appendix 1. Casino copper deposit samples (cont.)

Sample No.	Hole No.	Depth from (m)	Hole Collar Location (X,Y,Z), Azimuth, Dip	Brief Rock Description	Tourmaline Type	Tourmaline Description
CEBB034	93-177	143.43	610363.930, 6958203.960, 1331.580, 0.0, -90	Sample consists of a milled breccia with phyllic alteration. Clasts appear to be granodioritic in composition. Some minor argillic alteration which seems to be concentrated within the clasts.	Disseminated	Tur forms acicular radial masses. Tur appears as black grains, but under close inspection they are almost transparent and light in colour.
CEBB035	94-270	100.25	610999.390, 6958549.090, 1351.080, 0.0, -90	Sample is a milled breccia of the granodiorite. Sample exhibits phyllic and minor argillic alteration. Matrix exhibits more alteration than the clasts.	Breccia	Tur is forming within the breccia clasts. Tur is forming as acicular radial clots. Grains are a grey-black in colour.
CEBB036	94-270	70.82	610999.390, 6958549.090, 1351.080, 0.0, -90	Sample is a milled breccia matrix with no visible clasts. Sample contains disseminated pyrite, and tourmaline. Matrix shows phyllic alteration overprinted by argillic alteration.	Disseminated	Tur forms radial masses. Grains are commonly found enveloped by quartz.
CEBB037	94-268	153.57	611141.100, 6958682.620, 1239.840, 315, -47.5	Fine grained granodiorite with minor phyllic alteration. Disseminated pyrite is evident throughout the sample.	Disseminated	Tur is forming as black radial masses comprised of acicular euhedral grains.

Structural style and timing of deformation on the Bathurst Fault (eastern Slave craton): Implications for basement fault-controlled fluid pathways

S. Ma[1], D.A. Kellett[2] and L. Godin[1]

*[1]Department of Geological Sciences and Geological Engineering, Queen's University,
36 Union Street, Kingston, Ontario, K7L 3N6*
[2]Geological Survey of Canada, 1 Challenger Drive, Dartmouth, Nova Scotia, B3B 1A6

Abstract

Crustal-scale basement faults persist as long-lived structures that localize deformation and enhance crustal permeability. The left-lateral Bathurst Fault in the eastern Slave craton intersects the 1.7 Ga Thelon Basin where unconformity uranium deposits are spatially associated with basement faults. Field observations, structural data, and U-(Th)-Pb and $^{40}Ar/^{39}Ar$ geochronological analyses are applied to characterize deformation on the Bathurst Fault in order to assess its potential as a conduit for uranium mineralization in the Thelon Basin. Highly-strained hornblende monzodiorite to granodiorite rocks are predominant along the Bathurst Fault, with quartz and feldspar microstructures showing deformation conditions above 500°C. Brittle fractures, cataclasis, and hydrothermal alteration overprint the ductile fabric in rocks adjacent to the fault trace. U-Th-Pb dates from syn-kinematic monazite suggest ductile shearing at ca. 1933 Ma and 1895 Ma, whereas zircon from a cross-cutting dyke constrains the onset of brittle deformation to ≤ 1839 ± 14 Ma. $^{40}Ar/^{39}Ar$ dates from fabric-defining minerals yield cooling ages of ca. 1900 Ma to 1850 Ma for hornblende and muscovite, and a maximum cooling age of ca. 1840 Ma for biotite. We interpret brittle deformation, occurring at or after ca. 1840 Ma, to have localized along an older, ca. 1935–1895 Ma, ductile high strain zone along the north-northwest trending Bathurst Fault trace. The timing of brittle faulting and heavy alteration of primary host rock minerals, including disturbed U-Th-Pb systematics in monazite, support the inference that the Bathurst Fault behaved as permeable basement structure with the capacity to channel fluids into the adjacent Thelon Basin.

Introduction

Faults are inherent zones of weakness in the rigid continental crust and can be prone to reactivation during successive tectonic events (Holdsworth et al., 1997). Long-lived, deep-seated structures influence rock permeability, and control the architecture of orogenic belts, the formation of sedimentary basins and the distribution of petroleum and ore resources (Sibson, 2001; Bense et al., 2013). Such basement faults are key components of world-class unconformity-associated uranium deposits in the Athabasca Basin, where uranium mineralization is structurally-controlled along the intersection of basement faults with overlying sandstone strata (Jefferson et al., 2007). Thus, this close spatial relationship between high-grade uranium deposits and basement faults adjacent to Proterozoic intracontinental basins (e.g. Athabasca, Hornby Bay, and Thelon basins; Fig. 1a) are exploration targets (Jefferson et al., 2007 and references therein).

The Bathurst Fault is a basement structure that underlies the Thelon Basin, a frontier basin with multiple uranium occurrences. However, the tectonic evolution of the crustal-scale fault is poorly understood. The objective of this study is to constrain the structural evolution of the fault by establishing a deformation-time history at different crustal-levels. In order to

achieve this goal, field relationships, petrography, microstructural analysis, U-Pb geochronology, and $^{40}Ar/^{39}Ar$ thermochronology have been applied to the Bathurst Fault study area (Fig. 1b).

Regional geology

Tectonic framework

The north-northwest trending Bathurst Fault is situated within the northwestern Canadian Shield, which exposes the Slave, Rae, Hearne and Superior cratons (Fig. 1a). The fault offsets the Thelon tectonic zone (TTZ), a Paleoproterozoic orogen that forms the boundary between the Slave and Rae cratons (Fig. 1a, b). The TTZ is expressed as a north trending curvilinear magmatic belt of granulite-facies metamorphic rocks. The Slave province west of the TTZ is dominated by variably-deformed Archean supracrustal rocks, including the Yellowknife Supergroup volcano-sedimentary rocks and successor granitoids (Isachsen and Bowring, 1994). East of the TTZ, the western Rae craton comprises Meso- and Neoarchean upper amphibolite- to granulite-facies gneiss and supracrustal rocks of the Queen Maud block (Schultz et al., 2007).

The Bathurst Fault trace extends for over 400 km in the eastern Slave craton from the Coronation Gulf coast to the The-

---
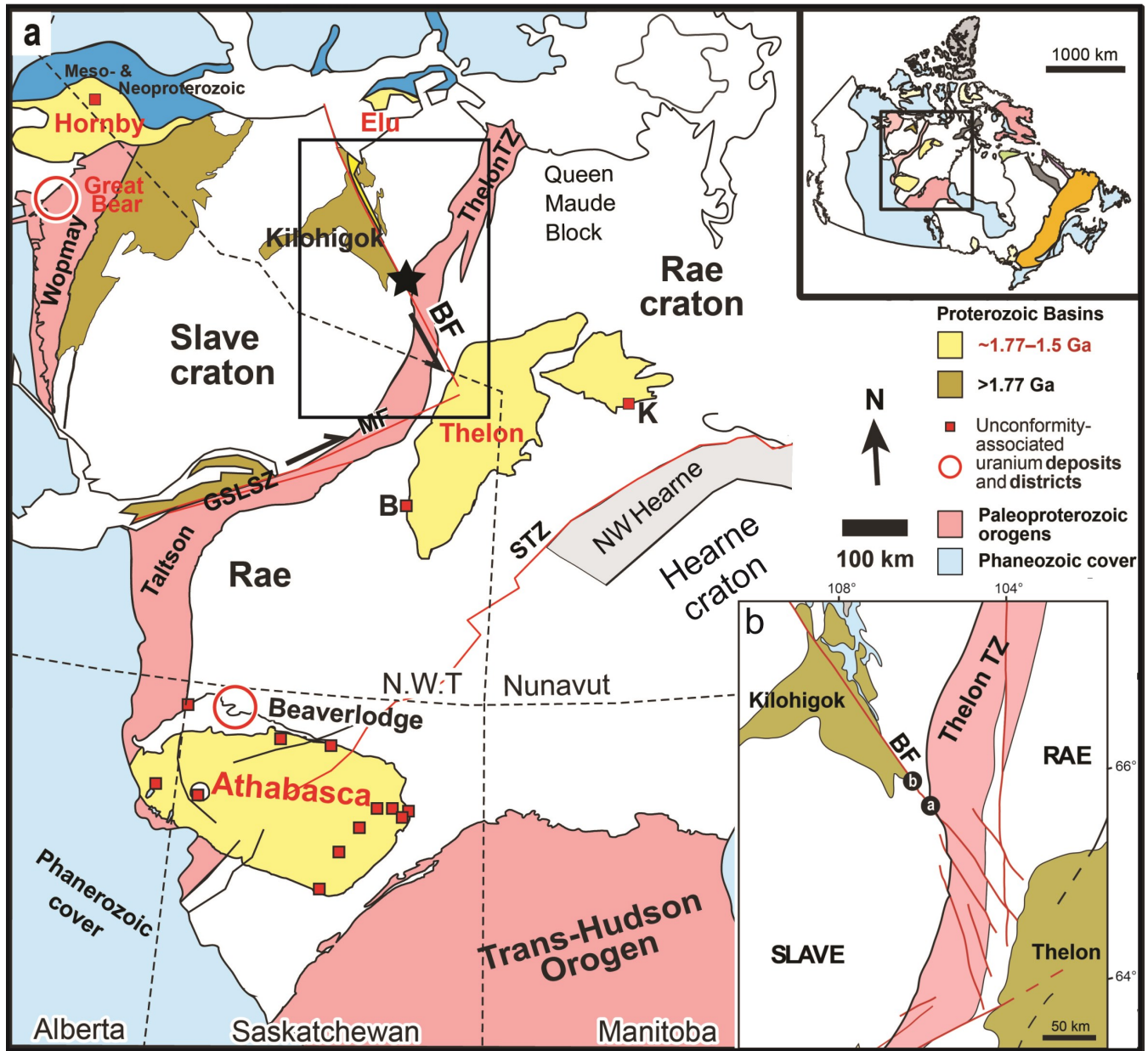
Figure 1. Regional tectonic map; a) Distribution of crustal-scale basement faults in Archean cratons, Proterozoic orogens, and intracratonic basins in the Canadian Shield. Unconformity-type uranium prospects in Thelon Basin include Boomerang Lake (B) and Kiggavik (K). The boxed area is shown in (b); b) The locations of the two transects in this study: (a) southern transect and (b) northern transect, corresponding to Fig. 2. BF - Bathurst Fault; MF - MacDonald Fault; GSLSZ - Great Slave Lake shear zone; STZ - Snowbird tectonic zone; TZ - tectonic zone. Figure modified after Jefferson et al. (2007).

lon Basin. The fault left-laterally offsets the TTZ and the 1.9 Ga Kilohigok Basin, with an estimated displacement of up to 110 km (Frith, 1982; Henderson et al., 1990). Previous researchers have suggested episodic slip along the Bathurst Fault based on the offset of stratigraphic markers (Campbell and Cecile, 1981). The Bathurst Fault is overlain by segments of the Elu and Thelon basins, two of several late Paleoproterozoic fluvial-dominated intracontinental basins that formed during

periods of relative tectonic quiescence subsequent to microcontinent amalgamation (Hoffman, 1988).

The Bathurst Fault together with the MacDonald Fault to the south form a conjugate system that transects the northeastern and southwestern margins of the Slave craton, respectively (Fig. 1a). This crustal-scale conjugate fault system led Gibb (1978) to propose a wedge indentation model for the Slave-Rae

collision, in which the rigid Slave craton has indented into the weaker TTZ on the western flank of the Rae craton.

Basement faults and the Thelon Basin

Uranium mineralization that is deposited near basal unconformities are thought to form by the mixing of an oxidizing fluid circulating in basinal sandstones with a reducing fluid emanating from basement rocks near or at the unconformity (Cuney and Kyser, 2009). The 1.7 Ga Thelon Basin is an intracratonic flat-lying basin east of the TTZ in the Rae province (Fig. 1a) predominantly made up of fluvial conglomeratic sandstone. The Thelon Basin has an analogous tectonic setting to the better-known Athabasca Basin and represents an area with a high potential for unconformity-associated uranium discoveries (Jefferson et al., 2007). Uranium occurrences are spatially associated with reactivated basement faults in the Kiggavik deposit and Boomerang Lake prospect of the northeastern and southwestern Thelon Basin, respectively (Tschirhart et al., 2016; Beyer et al., 2010). Based on regional-scale relationships, deformation on the Bathurst Fault occurred between ca. 1.9 and 1.6 Ga, which coincides with sedimentation and early mineralization in the Athabasca and Thelon basins (Jefferson et al., 2007 and references within).

This research focuses on a central segment of the Bathurst Fault located approximately 160 km south-southeast of the settlement of Bathurst Inlet. Two across-strike structural transects were conducted to map the fault zone and collect rock samples for microstructural analysis and geochronology (Fig. 1b).

Geology of the Bathurst Fault

The Bathurst Fault juxtaposes supracrustal rocks of the Kilohigok Basin and low metamorphic grade Slave rocks to the west against reworked high metamorphic grade Slave or Thelon rocks to the east (Fig. 2a, b). In the southeastern portion of the study area, low metamorphic grade Yellowknife Supergroup metavolcanic rocks and minor syenogranite lie west of the Bathurst Fault (Fig. 2a). The mapped fault trace is unconformably overlain by Ellice Formation conglomerate. The main Bathurst Fault trace manifests as a prominent, 100 m high ridge of granitoid that is in contrast to the lower relief Yellowknife Supergroup rocks. The dominant lithology east of the fault is a hornblende-bearing, quartz-poor monzodiorite to granodiorite (plagioclase + hornblende + alkali feldspar + quartz ± epidote, chlorite, ilmenite) with minor phyllosilicate-rich layers (Fig. 3a, b). This unit is cross-cut by pegmatitic granite dykes (Fig. 3c). East of the monzodiorite and granodiorite, biotite monzogranite is interlayered with sillimanite-garnet pelitic schist (quartz + microcline + plagioclase + biotite + garnet + sillimanite; Fig. 3d). In the north-northwest portion of the study area, quartz to lithic arenite and carbonate of the Kilohigok Basin are exposed in the west-southwest wall of the fault. East of the fault lies hornblende monzogranite that hosts a discrete chlorite-muscovite phyllonite unit (Fig. 3e, f).

The main hornblende-bearing monzodiorite to granodiorite units that form the east-northeast wall of the Bathurst Fault within both transects show a shape-preferred linear fabric defined by feldspar and hornblende aggregates, locally resembling L-tectonite. Mineral elongation lineations are steeply plunging to the north-northwest or south-southeast and the pervasive foliation is subvertical and strikes north-northwest (Fig. 2a). Foliation is defined by phyllosilicate layers as weak schistosity or gneissosity, the latter of which is more prominent towards the east. Shear sense indicators are sparse and where present display ambiguous northwest- or southeast-directed shear (e.g. Fig. 3b). The cross-cutting pegmatitic granite dyke does not exhibit a ductile deformation fabric. The sillimanite-garnet pelitic schist and biotite monzogranite have southeast-striking sub-horizontal foliation (Fig. 2a). Sillimanite needles define a north trending, near-horizontal mineral elongation lineation. Garnet porphyroblasts have sigmoidal wings with occasional asymmetry showing top-to-the-north shear (e.g. Fig. 3d). The main foliation has been gently folded, with folds showing shallowly south-plunging fold hinges.

The Kilohigok Basin rocks in the northern transect display basin-scale open folds and minor axial planar slaty cleavage development. The chlorite-muscovite phyllonite displays a south-southeast striking schistosity that is steeply dipping towards the west-southwest (Fig. 2b).

Brittle features are ubiquitous along the main Bathurst Fault trace and become rare away from the fault. Macroscopic brecciation or cataclasis in granitoid rocks coincides with high chlorite content (Fig. 3a, g). Multiple generations of veins are present. Brittle fractures locally form fracture networks, interpreted as Riedel shear fractures, with main slip joints oriented parallel to the Bathurst trend and showing left-lateral offset.

On the basis of structural trends and minor lithological changes, we have identified three structural domains. Domain I includes a high strain zone that is adjacent and parallel to the Bathurst Fault plane, overprinted by pervasive brittle deformation; Domain II includes high strain rocks east of Domain I that show limited to no brittle deformation; and, Domain III includes deformation recorded by the muscovite-chlorite phyllonite unit in the northern transect.

Microstructures and deformation conditions

In Domain I, rocks display a characteristic linear fabric of lenticular feldspar aggregates. Within the feldspar aggregates, interlobate to polygonal grain boundary geometry is indicative of grain boundary migration and static recrystallization, respectively, indicating high temperature deformation above feldspar plasticity (about 500°C; Evans, 1988). Dynamic recrystallization is not evident in quartz due to its low modal abundance; grains are usually polygonal suggesting post-deformation static recrystallization. Ductile fabrics have been overprinted by brittle fractures in and cataclasis of feldspar, both involving formation of retrograde chlorite. Zones of cataclasis are character-
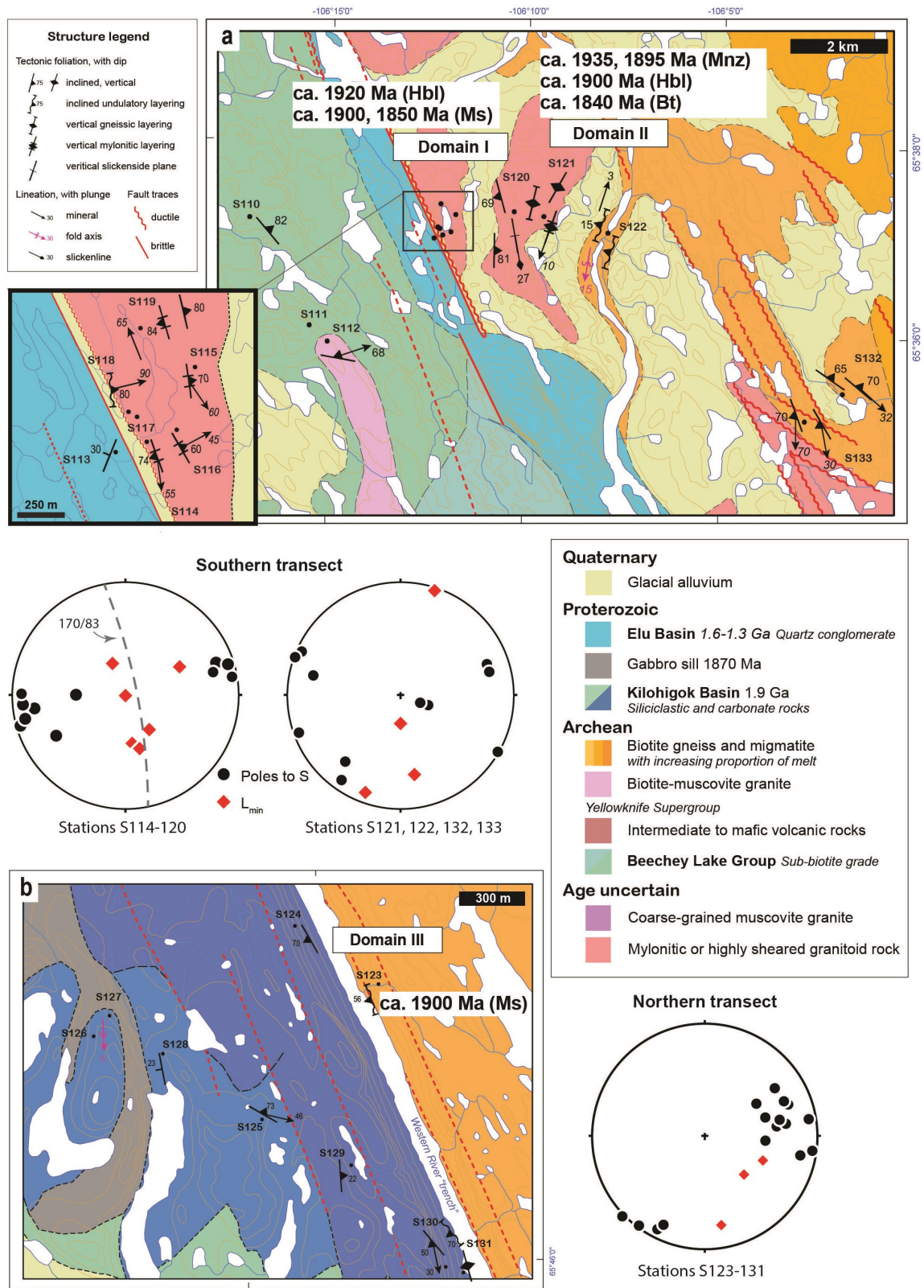
Figure 2. Detailed geological map with stereographic projections of structural measurements from the study areas shown in Figure 1b; lithological units and contacts from Frith (1982); a) Southern transect; b) Northern transect adjacent to the Kilohigok Basin. Dots indicate sample locations. Age dating results are indicated with the dated mineral in parentheses; mineral abbreviations after Whitney and Evans (2010).
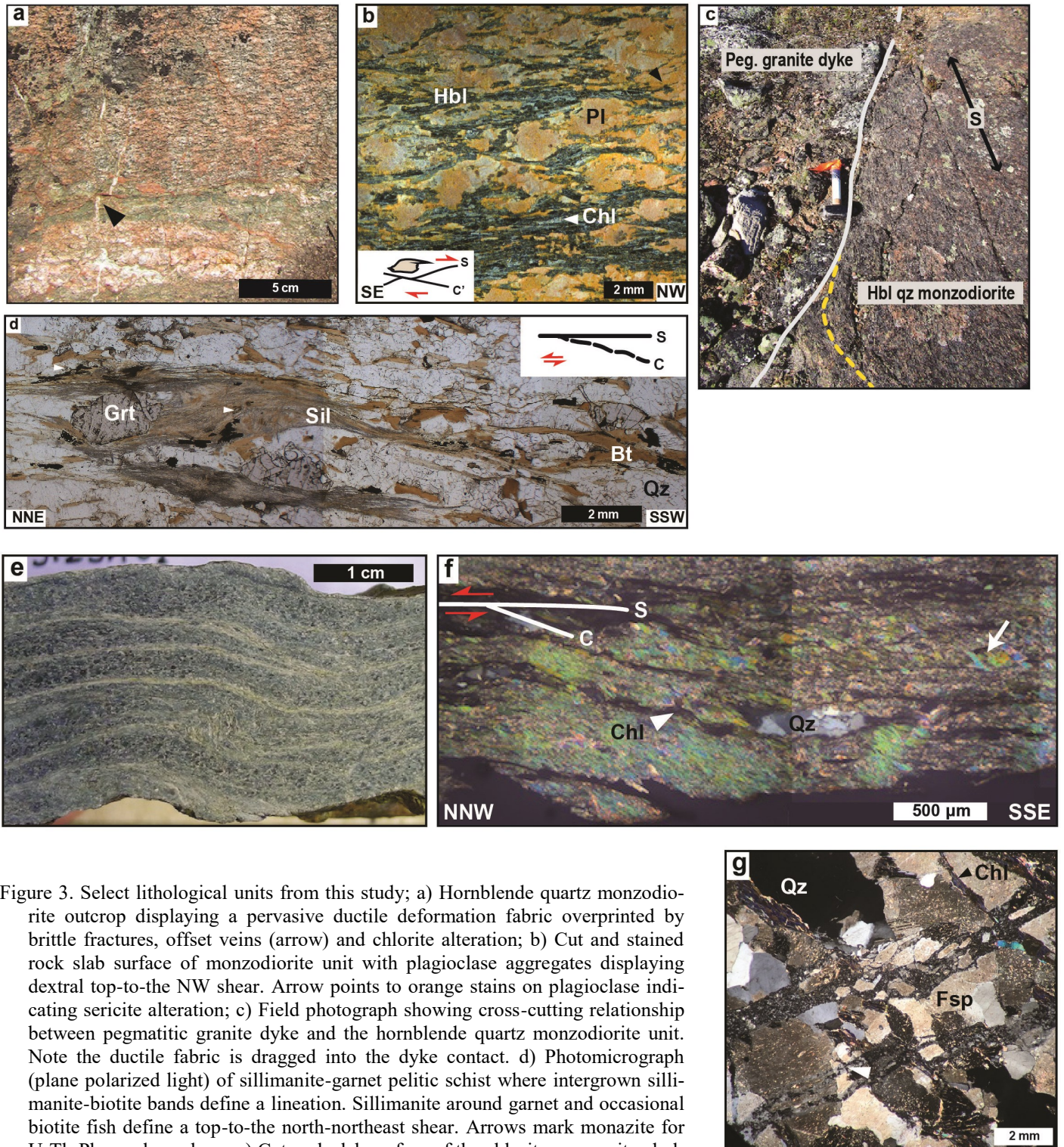
Figure 3. Select lithological units from this study; a) Hornblende quartz monzodiorite outcrop displaying a pervasive ductile deformation fabric overprinted by brittle fractures, offset veins (arrow) and chlorite alteration; b) Cut and stained rock slab surface of monzodiorite unit with plagioclase aggregates displaying dextral top-to-the NW shear. Arrow points to orange stains on plagioclase indicating sericite alteration; c) Field photograph showing cross-cutting relationship between pegmatitic granite dyke and the hornblende quartz monzodiorite unit. Note the ductile fabric is dragged into the dyke contact. d) Photomicrograph (plane polarized light) of sillimanite-garnet pelitic schist where intergrown sillimanite-biotite bands define a lineation. Sillimanite around garnet and occasional biotite fish define a top-to-the north-northeast shear. Arrows mark monazite for U-Th-Pb geochronology; e) Cut rock slab surface of the chlorite-muscovite phyllonite unit adjacent to the Kilohigok Basin. Phyllosilicate (muscovite and chlorite) layers and quartzofeldspathic bands define alternating wavy microlithons; f) In phyllosilicate microlithons of the phyllonite, chlorite seams define a C-S fabric and muscovite foliation fish (arrow) are inclined, both suggesting left-lateral or top-to-the north-northwest shear; g) Photomicrograph (cross-polarized light) of cataclasis texture in a monzogranite with overprinting feldspar-rich fractures (arrow).

ized by angular feldspar clasts within a fine grained recrystallized feldspar ± quartz matrix (Fig. 3g).

Domain II rocks show distinct porphyroclast development in granodiorite gneiss and biotite monzogranite, which implies feldspar recrystallization below feldspar plasticity. The syn-kinematic metamorphic mineral assemblage of syn-kinematic fibrolite sillimanite + K-feldspar, muscovite absent in the pelitic schist suggests upper amphibolite-facies metamorphic conditions during deformation (about 600°C). Quartz shows interlobate and pinning microstructures indicative of grain boundary migration typical above 500°C; this further supports high temperature deformation conditions. Domain II rocks rarely show brittle microstructures and retrograde alteration minerals are minimal.

In Domain III, the muscovite-chlorite phyllonite shows a left-lateral shear fabric in phyllosilicate microlithons and pinning microstructures in quartz. The quartz underwent grain boundary migration recrystallization at high temperature conditions (>500°C), whereas the shear fabric is interpreted to have developed or persisted during retrograde conditions since it is defined by chlorite that partially replaces muscovite in phyllosilicate microlithons. Brittle fractures in feldspar and high chlorite content in the phyllonite suggests deformation at low temperature conditions.

In summary, rocks across the three domains in the study area experienced similar high temperature ductile deformation conditions (about 500–600°C), with brittle overprint and retrograde alteration localized adjacent to the Bathurst Fault. The results presented here suggest that the Bathurst Fault is developed within and parallel to a pre-existing high strain zone, but clear evidence for a pre-existing ductile shear zone is lacking.

Geochronology

We applied geochronology methods to constrain the ductile to brittle evolution of rocks within the Bathurst Fault zone. Total U-Th-Pb dating of syn-kinematic monazite was used to establish the timing of high temperature ductile deformation. Isotopic U-Pb dating of zircon from a cross-cutting pegmatitic dyke provides a minimum age for the ductile Bathurst-trend fabric. $^{40}Ar/^{39}Ar$ dating of hornblende, muscovite, and biotite characterizes cooling and exhumation through the brittle-ductile transition. Table 1 summarizes a working interpretation of the structural and geochronology results from this study.

Monazite geochronology

Total U-Th-Pb dating of in-situ monazite was performed on grains in polished thin sections using the Cameca SX100 Ultrachron microprobe at the University of Massachusetts following the analytical protocol of Williams et al. (2006). Multiple ages were obtained from fourteen monazite grains in two samples (S122A and S114A). Microprobe dating achieves excellent spatial resolution as it is capable of sampling compositional domains as small as 5 μm in diameter, and permits the simultaneous acquisition of trace element data, including rare earth elements. Ages were calculated by iteration of the Montel age equation, processed and statistically evaluated within Williams' in-house DatCon software.

Monazite grains in sample S122A, a sillimanite-garnet pelitic schist, are 80 to 150 μm in diameter and occur adjacent to major silicate phases in the matrix and locally enclosed within fibrolite-biotite bands (Fig. 3d). Compositional zoning with respect to Th and Y is patchy to irregular and shows limited overgrowth textures. Twenty analyses from eight monazite grains yield dates ranging ca. 1965 to 1843 Ma (Fig. 4a). Compositional domains within multiple grains show two population clusters with weighted mean dates at 1933 ± 4.0 Ma (n = 10, MSWD = 1.07) and 1895 ± 11 Ma (n = 6, MSWD = 3.0). Trends from REE analysis suggest that the older monazite population is coeval with garnet growth, whereas the younger population may have grown during garnet breakdown (Engi, 2017). Since these grains are situated within or aligned to the fibrolite linear fabric, the ca. 1933 Ma age is interpreted as syn-kinematic monazite that formed coeval to fabric development.

Table 1. Geochronology results and interpretations.

Geochronometer	Approx. Age (Ma)	Mineral	Structural context	Interpretation of age
U-Th-Pb	1933 ± 4, 1895 ± 11	Monazite	Oriented parallel to foliation in matrix and within sillimanite bands	Syn-kinematic monazite growth. Ages suggest dominant periods of high temperature deformation coeval to fabric development in pelitic schist (Domain II)
U-Pb ($^{207}Pb/^{206}Pb$)	1839 ± 14	Zircon	Magmatic zircon from brittlely deformed granite dyke	Crystallization age represents a minimum age of the pervasive ductile fabric along the fault trace, and the onset of brittle deformation
$^{40}Ar/^{39}Ar$	1900	Hornblende	Defines ductile linear fabric	Age approximates timing of feldspar plasticity and the ductile fabric. A cooling age through ~500°C.
	1900-1850	Muscovite	Defines ductile planar fabric, or recrystallized secondary alteration mineral	Cooling age through ~430°C, or if of secondary origin, recrystallization age below closure temperature
	1890-1840	Biotite	Defines ductile planar fabric	A maximum cooling age through ~300°C; maximum age due to presence of excess Ar.
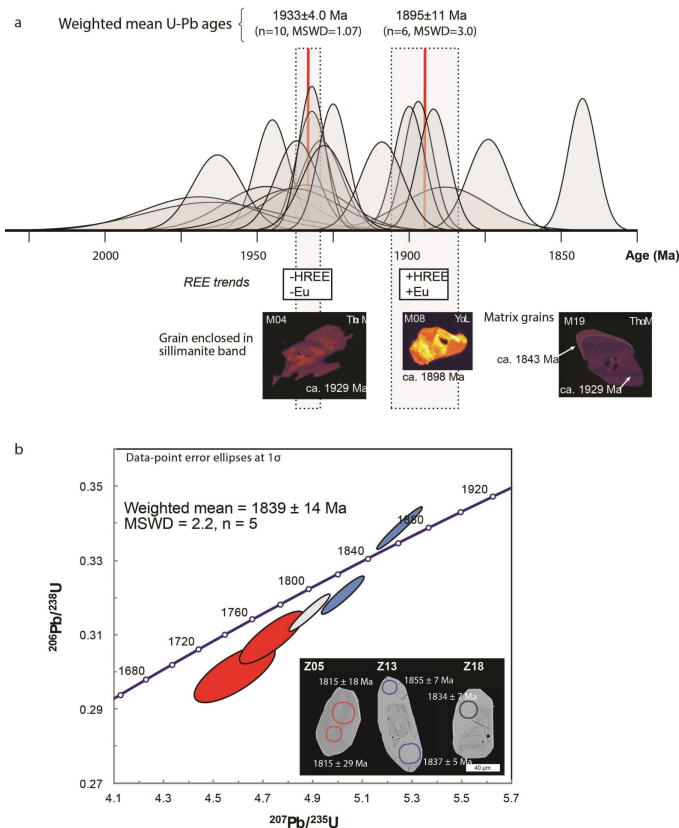
Figure 4. Summary of U-(Th)-Pb geochronology. Sample locations shown in Figure 2: a) Probability density plot of monazite electron microprobe ages, showing age clusters at ca. 1933 and 1895 Ma. Errors reported at 2σ. Y-axis is relative probability. Th and Y chemical maps show zoning in select grains b) Concordia plot and weighted mean age for zircon from pegmatitic granite dyke (see Fig. 4e). BSE images of zircon grains showing analytical spots and resulting ^{207}Pb/^{206}Pb ages. Colours correspond to analyses shown on concordia plot.

The younger ca. 1895 Ma period may reflect continued syn-kinematic or post-kinematic monazite growth primarily in the matrix.

Monazite grains in sample S114A, a sheared quartz monzonite, are very coarse (100–400 μm), occur adjacent to feldspar aggregates, and coincide with fractures and cataclasis zones. Monazite grains are highly altered and appear sponge-like, with resorbed grain boundaries, grain-scale fractures and inclusions of alteration products. Likewise, chemical grain maps show highly disturbed mottled or patchy composition zoning with respect to Th, U and Y. The analyses produced scattered and imprecise dates. Eight analyses from four monazite grains yield 360 to 2180 Ma, with this range of dates occurring within a single grain. The monazite grain morphology, compositional zoning patterns, presence of alteration products and spurious

age dates strongly suggest disturbed U-Th-Pb systematics. Considering the microstructural context of monazite in this sample, it is very likely that fluid-assisted alteration led to Th, U or Pb remobilization (e.g. Williams et al., 2011; Seydoux-Guillaume et al., 2012), which invalidates the basic assumption of closed system behaviour for radiogenic dating.

Zircon geochronology

Zircon grains from sample S119B, a pegmatitic granite dyke, were analyzed with the sensitive high resolution ion microprobe (SHRIMP) at the Geological Survey of Canada in Ottawa, Ontario. Zircon grains were limited and are dominated by inherited Archean grains. Five analyses on three grains interpreted to be representative of the crystallization of the granite dyke yield a mean ^{207}Pb/^{206}Pb date of 1839 ± 14 Ma (MSWD = 2.2; Fig. 4b). Microscopically, the granite dyke exhibits intracrystalline brittle deformation such as grain-scale faulting in feldspar, and localized zones of cataclasis. Since this dyke cross-cuts Domain I rocks, 1839 ± 14 Ma represents a minimum age of the ductile deformation fabric, and a maximum age for brittle deformation in this study area.

^{40}Ar/^{39}Ar thermochronology

^{40}Ar/^{39}Ar dating was performed at the Noble Gas Laboratory at the Geological Survey of Canada in Ottawa, Ontario using a Nu Instruments Noblesse multicollector mass spectrometer. ^{40}Ar/^{39}Ar measurements involve single grain step-heating experiments. All target minerals (hornblende, muscovite and biotite) define a ductile linear or planar deformation fabric in their respective host rocks.

Preliminary interpretations of the step heat spectra are presented here (Fig. 5). Hornblende produced an inverse isochron age of ca. 1916 Ma in Domain I and plateau and integrated ages of ca. 1900 Ma in Domain II. Muscovite from phyllosilicate-rich sections of Domain I produced a plateau age of ca. 1903 Ma, and integrated ages of ca. 1850 Ma. Similarly, muscovite of the phyllonite (Domain III) yields an integrated age of ca. 1900 Ma. In Domain II, biotite from the granodiorite gneiss produced a plateau age ca. 1838 Ma while biotite in the pelitic schist produced integrated ages of ca. 1890 Ma. Step-heating age spectra and inverse isochron data show varying degrees of excess Ar and Ar loss, especially apparent in biotite analyses.

Implications

The pervasive veining and chlorite overprint on ductilely deformed rocks, in addition to intensely altered monazite grains that reveal U, Th or Pb remobilization suggest these rocks experienced low temperature fluid-assisted alteration event(s). Brittle deformation was likely most prevalent during exhumation through the ductile-brittle transition (approximately 350°C), where faults typically evolve to higher fluid fluxes owing to the low temperature and pressure circulation of meteoric fluids in the shallow crust (Parry, 1998). Brittle fault damage zones create fluid pathways through otherwise
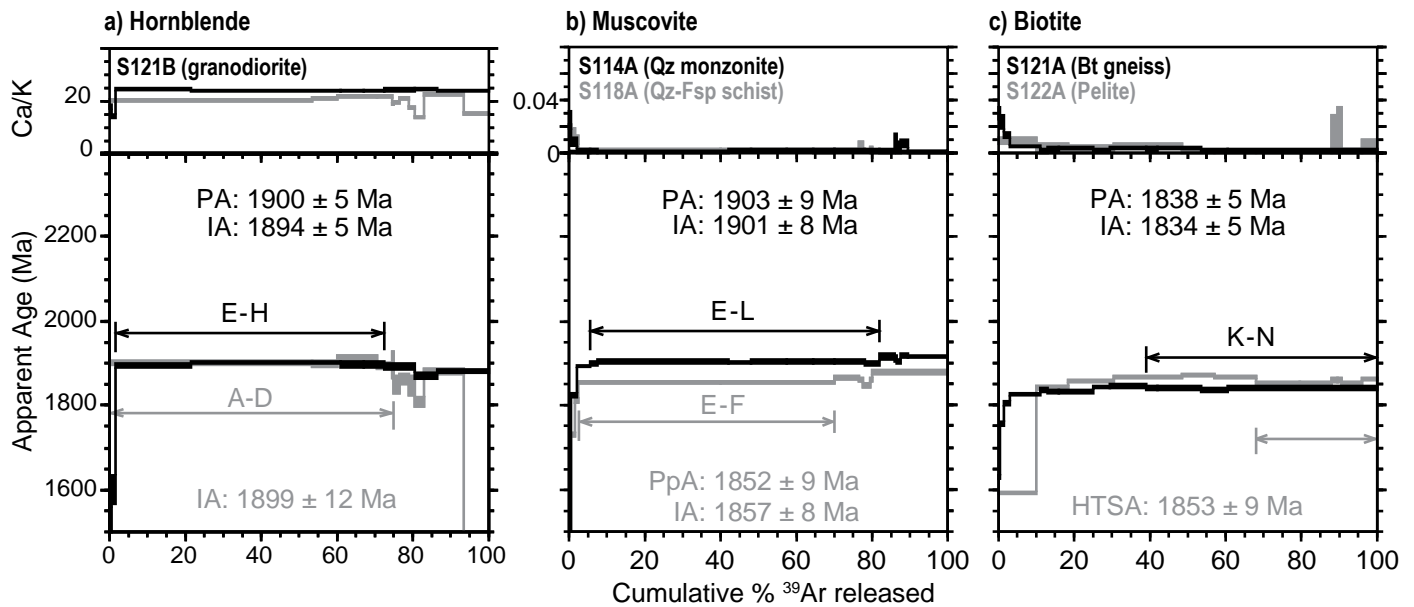
Figure 5. Representative $^{40}Ar/^{39}Ar$ step-heating age spectra and Ca/K plots for: a) hornblende; b) muscovite; c) biotite. Sample locations shown in Figure 2. PA - plateau age; IA - integrated age; PpA - pseudoplateau age; HTSA - age of last high temperature, which approach the true cooling age (for biotite). Grey plots and ages are either a repeated aliquot or another sample.

impermeable basement rocks. Brittle fault failure provides a mechanism for enhanced along-fault fluid flow, which enables fluid redistribution potentially leading to ore mineralization (Sibson, 2001).

Geochronology results provide a maximum age constraint on brittle deformation. The zircon U-Pb crystallization age from the granite dyke and biotite $^{40}Ar/^{39}Ar$ maximum cooling ages suggest that brittle deformation along the Bathurst Fault had initiated by ca. 1840 Ma, indicating that the fault-fluid network was in place since the Paleoproterozoic. Uranium mineralization in the Thelon Basin has been dated at ca. 1650 and 1250 Ma, while in the Athabasca Basin, regional hydrothermal activity including pre-ore alteration minerals occurred ca. 1670 to 1620 Ma, followed by episodic ore-related events from 1600 to 1350 Ma (Jefferson et al., 2007 and references therein).

The structural style of deformation, degree of hydrothermal alteration within the fault zone, and geochronological constraints on the Bathurst Fault supports its potential as a pathway for fluid flow during the late Paleoproterozoic and Mesoproterozoic in the otherwise impermeable crystallization basement.

Acknowledgments

References

Bense, V.F., Gleeson, T., Loveless, S.E., Bour, O., and Scibek, J., 2013. Fault zone hydrogeology; Earth Science Reviews, v. 127, p. 1–22.

Beyer, S.R., Kyser, K., Hiatt, E.E., and Fraser, I., 2010. Geological evolution and exploration geochemistry of the Boomerang Lake unconformity-type uranium prospect, Northwest Territories, Canada; Society of Economic Geologists, Special Publication v. 15, p. 675–702.

Campbell, F.A. and Cecile, M.P., 1981. Evolution of the Early Proterozoic Kilohigok Basin, Bathurst Inlet – Victoria Island, Northwest Territories; *in* Proterozoic Basins of Canada, (ed.) F.H.A. Campbell; Geological Survey of Canada, Paper 81-10, p. 103–131.

Cuney, M. and Kyser, K., 2009. Unconformity-related deposits; *in* Recent and Not-so-recent Developments in Uranium Deposits and Implications for Exploration, (ed.) Cuney, M. and Kyser, K.; Mineralogical Association of Canada Short Course Series, v. 39, p. 161–219.

Davidson, G.I. and Gandhi, S.S., 1989. Unconformity-related U-Au mineralization in the middle Proterozoic Thelon Sandstone, Boomerang Lake Prospect, Northwest Territories, Canada; Economic Geology, v. 84, p. 143–157.

Engi, M., 2017. Petrochronology based on REE-minerals: Monazite, allanite, xenotime, apatite; Reviews in Mineralogy & Geochemistry, v. 83, p. 365–418.

Evans, J.P., 1988. Deformation mechanisms in granitic rocks at shallow crustal levels; Journal of Structural Geology, v. 10, p. 437-443.

Frith, R.A., 1982. Geology, Beechey Lake – Duggan Lake, District of Mackenzie; Geological Survey of Canada, Open File 851, map, scale 1:125 000.

Gibb, R.A., 1978. Slave-Churchill collision tectonics; Nature, v. 271, p. 50–53.

Henderson, J.B., McGrath, P.H., Theriault, R.J., and van Breemen, O., 1990. Intracratonic indentation of the Archean Slave Province into the early Proterozoic Thelon tectonic zone of the Churchill Province, northwestern Canadian Shield; Canadian Journal of Earth Sciences, v. 27, p. 1699–1713.

Hoffman, P.F., 1988. United Plates of America, the birth of a craton – Early Proterozoic assembly and growth of Laurentia; Annual Review of Earth and Planetary Sciences, v. 16, p. 543–603.

Holdsworth, R.E., Butler, C.A., and Roberts, A.M., 1997. The recognition of reactivation during continental deformation; Journal of the Geological Society, London, v. 154, p. 73–78.

Isachsen, C.E. and Bowring, S.A., 1994. Evolution of the Slave craton; Geology, v. 22, p. 917–920.

Jefferson, C.W., Thomas, D.J., Gandhi, S.S., Ramaekers, P., Delaney, G., Brisbin, D., Cutts, C., Quirt, D., Portella, P., and Olson, R.A., 2007. Unconformity-associated uranium deposits of the Athabasca Basin, Saskatchewan and Alberta; *in* Mineral Deposits of Canada: A Synthesis of Major Deposit-Types, District Metallogeny, the Evolution of Geological Provinces, and Exploration Methods, (ed.) W.D. Goodfellow; Geological Association of Canada, Mineral Deposits Division, Special Publication No. 5, p. 273–305.

Parry, W.T., 1998. Fault-fluid compositions from fluid-inclusion observations and solubilities of fracture-sealing minerals; Tectonophysics, v. 290, p. 1–26.

Schultz, M.E., Chacko, T., Heaman, L.M., Sandeman, H.A., Simonetti, A., and Creaser, R.A., 2007. Queen Maud block: A newly recognized Paleoproterozoic (2.4-2.5 Ga) terrane in northwest Laurentia; Geology, v. 35, p. 707–710.

Seydoux-Guillaume, A.-M., Montel, J.-M., Bingen, B., Bosse, V., de Parseval, P., Paquette, J.-L., Janots, E., and Wirth, R., 2012. Low-temperature alteration of monazite: Fluid mediated couple dissolution-precipitation, irradiation damage, and disturbance of the U–Pb and Th–Pb chronometers; Chemical Geology, v. 330-331, p. 140–158.

Sibson, R.H., 2001. Seismogenic framework for hydrothermal transport and ore deposition; Society of Economic Geologists Reviews, v. 14, p. 25–50.

Tschirhart, V., Jefferson, C.W., and Morris, W.A., 2016. Basement geology beneath the northeast Thelon Basin, Nunavut: Insights from integrating new gravity, magnetic and geological data; Geophysical Prospecting, v. 65, p. 617–636.

Whitney, D.L. and Evans, B.W., 2010. Abbreviations for names of rock-forming minerals; American Mineralogist, v. 95, p. 185–187.

Williams, M.L., Jercinovic, M.J., Goncalves, P., and Mahan, K., 2006. Format and philosophy for collecting, compiling, and reporting microprobe monazite ages; Chemical Geology, v. 225, p. 1–15.

Williams, M.L., Jercinovic, M.J., Harlov, D.E., Budzyń, B., and Hetherington, C.J., 2011. Resetting monazite ages during fluid-related alteration; Chemical Geology, v. 283, p. 218–225.

Reactivated basement faults and uranium-rich fluid pathways in the Athabasca Basin: New insights from the Patterson Lake corridor, northwestern Saskatchewan

V. Tschirhart[1], E.G. Potter[1], J.W. Powell[1], D. Johnstone[2], M. Rabiei[2], K.M. Bethune[2], G. Chi[2] and C.L. Duffett[2]

[1]Geological Survey of Canada, 601 Booth Street, Ottawa, Ontario, K1A 0E8
[2]University of Regina, 3737 Wascana Parkway, Regina, Saskatchewan, S4S 0A2
[3]Carleton University, 1125 Colonel By Drive, Ottawa, Ontario, K1S 5B6

Abstract

This report summarizes the 2017 field investigations and on-going research in the Patterson Lake corridor, northwestern Saskatchewan, an area hosting recently discovered, high-grade uranium deposits. 2017 activities included acquisition and release of a new aeromagnetic survey and derivative map products, sampling and structural measurements on industry drill core. Samples will be analyzed for magnetization, petrographic, geochronologic, fluid inclusion and stable isotopes. Together these analyses will provide information on the ore genesis, alteration and structural reactivation history of the region to inform on-going exploration and challenge existing ore deposit models.

Introduction

The Athabasca Basin is the primary exploration target for uranium deposits in Canada. Within this Proterozoic basin and surrounding basement rocks, known uranium deposits are spatially associated with structural trends and/or intersections of crustal-scale faults that were likely the main fluid conduits during formation of unconformity-related uranium deposits (Jefferson et al., 2007). Many of these structures show evidence of multiple periods of deformation (e.g. brittle fabrics overprinting ductile fabrics) and alteration (new mineral growth: clay minerals, tourmaline, aluminium-phosphate-sulphate minerals, hematite, etc.), which is reflected in their petrophysical characteristics, and geophysical and isotopic signatures.

This activity investigates the role reactivated faults played in the formation of unconformity-related uranium deposits and aims to quantify expressions of fertile alteration along such fluid pathways. In order to achieve these goals this activity is focused in the Patterson Lake corridor (PLC) of northwestern Saskatchewan (Fig. 1). The PLC hosts recently discovered deposits (e.g. Triple R, Arrow) in reactivated basement structures outside and along the southwestern margin of the Athabasca Basin, with ore lenses situated well below the regional unconformity in host rocks that are atypical when compared to the uranium deposits elsewhere in the Athabasca Basin. Although hosted in reactivated fault structures, the location of these recent discoveries challenge the standard unconformity-related deposit model, and thus warrants further investigation.

Key activity highlights

A new, modern aeromagnetic survey was released (Fig. 2; Kiss and Tschirhart, 2017a–o) covering the PLC and stretching into northeastern Alberta, where previously there was only regional legacy magnetic data available. In addition to residual total field magnetic data, supplementary geophysical products include the first vertical derivative (Kiss and Tschirhart, 2017f–j), tilt angle (Kiss and Tschirhart, 2017k–o) and Keating Correlation Coefficient results (Kiss and Tschirhart, 2017f–j). The Keating Correlation Coefficient identifies roughly circular magnetic anomalies (Keating, 1995), which might correspond to kimberlite bodies or possibly carbonatite intrusions. The survey highlights several exploration targets and reveals previously unrecognised details on the regional geology, such as where the PLC is truncated by a broad ~15 km magnetic high corresponding to the Clearwater Domain (Fig. 2), and the trend of the PLC northwards under the Athabasca Basin and west of the Clearwater Domain, where a similar magnetic character is observed. During 2017 fieldwork, detailed magnetic susceptibility measurements (every 0.5–1 m) were conducted on key industry drill holes in the PLC and on sparsely distributed regional drill holes (Fig. 2). These measurements will serve to constrain magnetic susceptibility characteristics of the basement rocks and alteration expressions during subsequent geophysical data analysis (i.e. forward and inverse modelling).

Drill core samples have been collected from Forum Uranium's Clearwater project, Purepoint Uranium Group's Spitfire Zone and Fission Uranium Corporation's Triple R deposit.
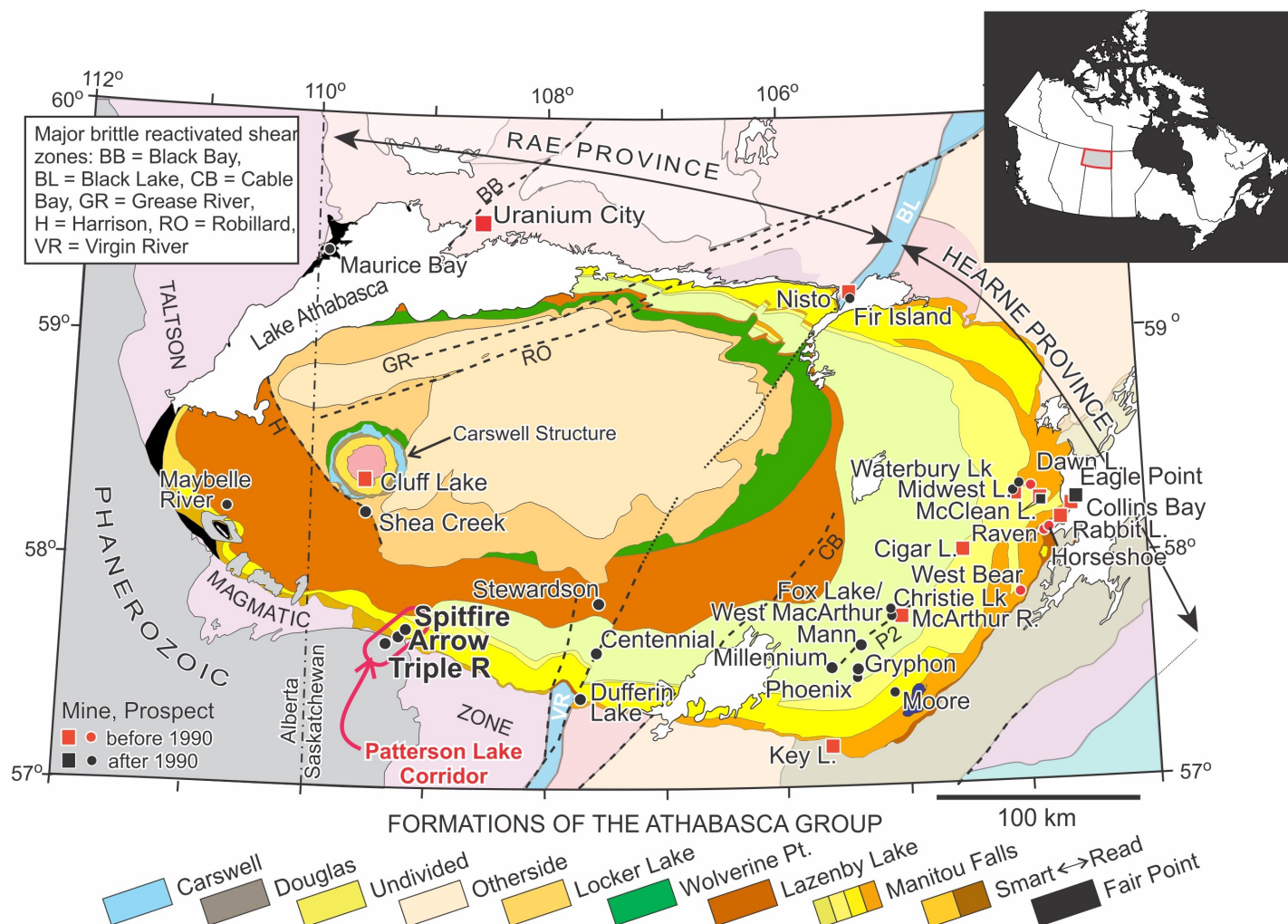
Figure 1. Location of the Patterson Lake Corridor along the southwestern margin of the Proterozoic Athabasca Basin. Modified from Jefferson et al. (2007). Deposits discussed in the text are labelled.

These samples are being processed for petrographic, geochronologic, fluid inclusion and stable isotope analysis. Ultimately, the resulting data will provide a new level of understanding to the ore genesis, alteration mineralogy, timing of structural events and composition of the ore-bearing fluids associated with the style of mineralization developed in the PLC.

Unusual features present in the PLC include: i) undeformed carbonatite dykes (Card and Noll, 2016); ii) abundant graphite and sulphide minerals that post-date pervasive silicification but pre-date uranium mineralization; and iii) complex paragenetic sequences characterized by dateable mineral phases, such as coarse-grained micas, clays, sulphides, uraninite and specular hematite (Fig. 3). The carbonatite dykes are of particular interest, as their association with ultramafic-mafic and anorthosite host rocks at the Spitfire Zone occurrence suggest a deep, crustal-scale fault system. Assessing the timing of dyke emplacement relative to mineralization is a priority, as the carbonatites are a potential heat source for the circulation of uranium-

bearing fluids and a source of carbon for the hydrothermal graphite within fault zones.

Next Steps

Samples collected for paleomagnetic studies have been shipped to the Paleomagnetism and Petrophysics Laboratory at GSC Pacific. These samples will provide information on the magnetization (induced and remnant components) of the PLC rocks and will further constrain 3D modelling and interpretations products from the new aeromagnetic survey.

Thin section preparation has begun on a subset of the samples collected in the 2017 field program. Following petrographic analysis, samples representative of the alteration assemblages and paragenetic history of the PLC will be selected for further geochronology, clay mineralogy (X-ray diffraction and shortwave infrared studies) and stable isotope analysis. Fluid inclusions from various generations of quartz will be examined
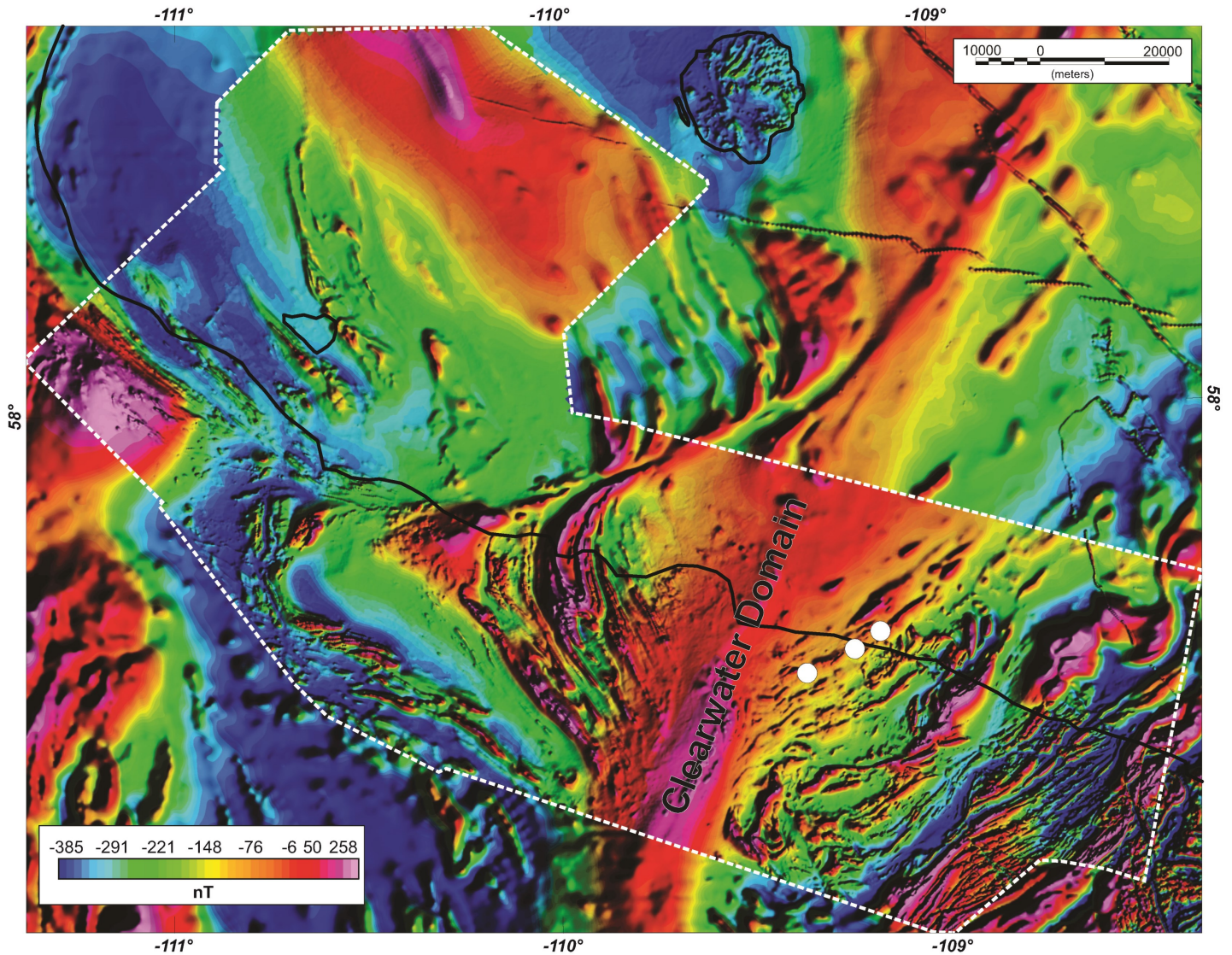
Figure 2. Marguerite River aeromagnetic survey outlined by white dashed line; black lines denotes Athabasca Basin outline. White circles are uranium deposits and occurrences in the PLC discussed in text.

to characterize the composition and pressure-temperature condition of fluids involved in different stages in the development of the basement and basin.

References

Bosman. S.A., Card, C.D., MacKnight, S.G., and Boulanger, S., 2012. The Athabasca Basin ore-systems project: an update on geochemistry, spectral data, and core logging; *in* Summary of Investigations 2012, Volume 2, Saskatchewan Geological Survey, Saskatchewan Ministry of the Economy, Miscellaneous Report 2012-4.2, Paper A-5, 10p.
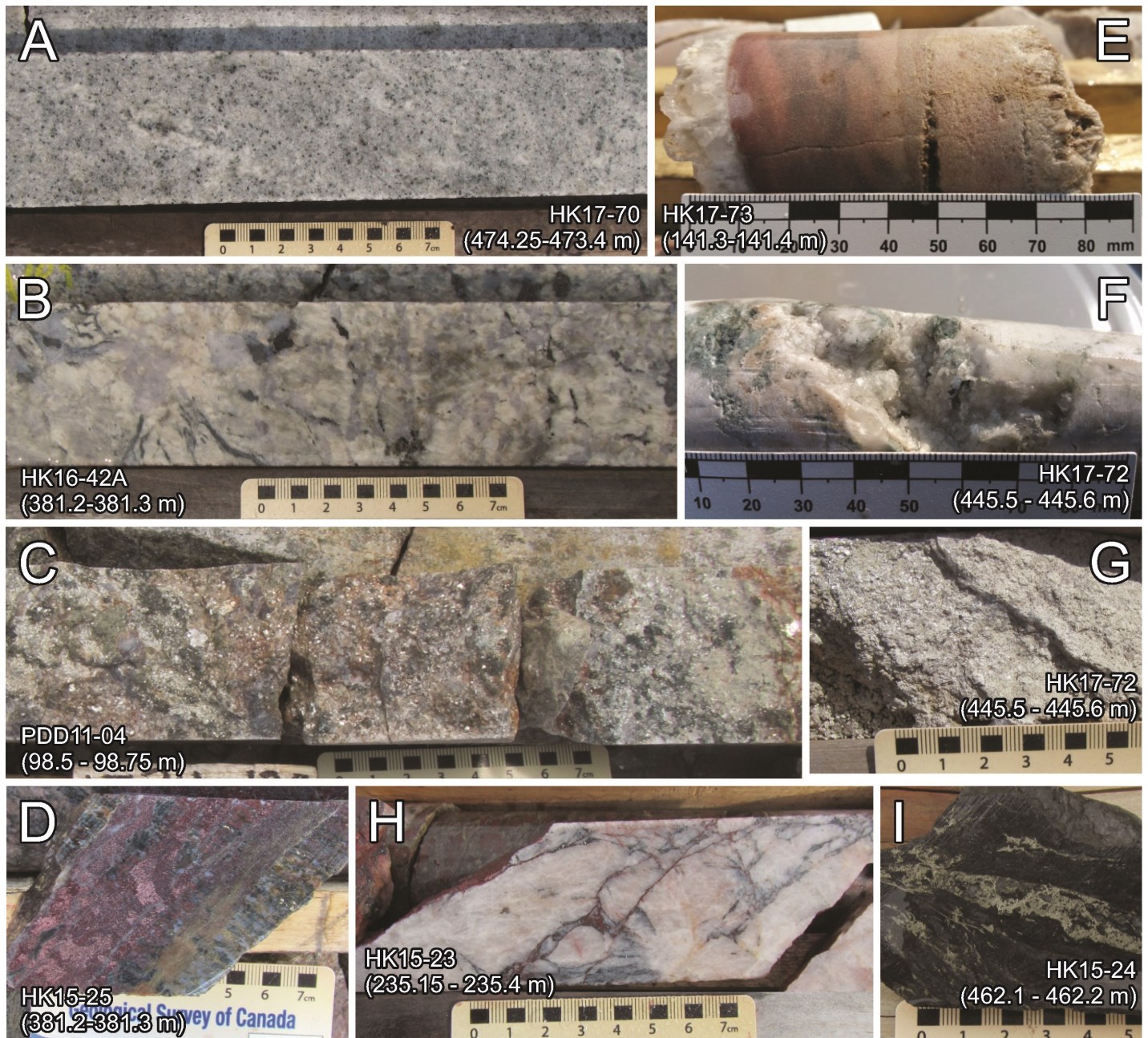
Figure 3. Representative drill core imageS of: a) carbonatite dike intruded into alteratered monzodiorite gneiss ; b) silicified anorthosite; c) coarse-grained muscovite; d) fine- to medium-grained hematite alteration of silicified gneiss; e) sub-horizontal druzy quartz in Read Formation sandstone; f) sub-vertical druzy quartz in silicified basement rocks; g) medium-grained muscovite grains in fine-grained, clay-rich alteration; h) fracture-controlled hematite and specular hematite cross-cutting silicified gneiss; and i) pyrite and chalcopyrite in sheared, graphite-rich basement rocks). The diamond drill hole ID and depth interval are displayed along with each image and follow company nomenclature (HK = Hook Lake; PDD = Patterson Lake south).

Card, C.D. and Noll, J. 2016. Host-rock protoliths, pre-ore metasomatic mineral assemblages and textures, and exotic rocks in the western Athabasca Basin: ore-system controls and implications for the unconformity-related uranium model; *in* Summary of Investigations 2016, Volume 2, Saskatchewan Geological Survey, Saskatchewan Ministry of the Economy, Miscellaneous Report 2016-4-2, Paper A-8, 19 p.

Jefferson, C.W., Thomas, D.J., Gandhi, S.S., Ramaekers, P., Delaney, G., Brisbin, D., Cutts, C., Portella, P., and Olson, R.A., 2007. Unconformity-associated uranium deposits of the Athabasca Basin, Saskatchewan and Alberta; *in* EXTECH IV: Geology and uranium EXploration TECHnology of the Proterozoic Athabasca Basin, Saskatchewan and Alberta, (ed.) C.W. Jefferson and G. Delaney; Geological Survey of Canada, Bulletin v. 588, p. 23–68.

Kiss, F. and Tschirhart, V., 2017a. Residual total magnetic field, aeromagnetic survey of the Marguerite River area, Alberta, parts of NTS 74-L north and 74-L south; Geological Survey of Canada, Open File 8259, 2017; 1 sheet, 1:100 000.

Kiss, F. and Tschirhart, V., 2017b. Residual total magnetic field, aeromagnetic survey of the Marguerite River area, Alberta, parts of NTS 74-E north and 74-E south; Geological Survey of Canada, Open File 8260, 2017; 1 sheet, 1:100 000.

Kiss, F. and Tschirhart, V., 2017c. Residual total magnetic field, aeromagnetic survey of the Marguerite River area, Saskatchewan, parts of NTS 74-F south; Geological Survey of Canada, Open File 8261, 2017; 1 sheet, 1:100 000.

Kiss, F. and Tschirhart, V., 2017d. Residual total magnetic field, aeromagnetic survey of the Marguerite River area, Saskatchewan, parts of NTS 74-F north; Geological Survey of Canada, Open File 8262, 2017; 1 sheet, 1:100 000.

Kiss, F. and Tschirhart, V., 2017e. Residual total magnetic field, aeromagnetic survey of the Marguerite River area, Saskatchewan, parts of NTS 74-K south; Geological Survey of Canada, Open File 8263, 2017; 1 sheet, 1:100 000.

Kiss, F. and Tschirhart, V., 2017f. First vertical derivative of the magnetic field, aeromagnetic survey of the Marguerite River area, Alberta, parts of NTS 74-L north and 74-L south; Geological Survey of Canada, Open File 8264, 2017; 1 sheet, 1:100 000.

Kiss, F. and Tschirhart, V., 2017g. First vertical derivative of the magnetic field, aeromagnetic survey of the Marguerite River area, Alberta, parts of NTS 74-E north and 74-E south; Geological Survey of Canada, Open File 8265, 2017; 1 sheet, 1:100 000.

Kiss, F. and Tschirhart, V., 2017h. First vertical derivative of the magnetic field, aeromagnetic survey of the Marguerite River area, Saskatchewan, parts of NTS 74-F south; Geological Survey of Canada, Open File 8266, 2017; 1 sheet, 1:100 000.

Kiss, F. and Tschirhart, V., 2017i. First vertical derivative of the magnetic field, aeromagnetic survey of the Marguerite River area, Saskatchewan, parts of NTS 74-F north; Geo-

logical Survey of Canada, Open File 8267, 2017; 1 sheet, 1:100 000.

Kiss, F. and Tschirhart, V., 2017j. First vertical derivative of the magnetic field, aeromagnetic survey of the Marguerite River area, Saskatchewan, parts of NTS 74-K south; Geological Survey of Canada, Open File 8268, 2017; 1 sheet, 1:100 000.

Kiss, F. and Tschirhart, V., 2017k. Tilt angle of the magnetic field, aeromagnetic survey of the Marguerite River area, Alberta, parts of NTS 74-L north and 74-L south; Geological Survey of Canada, Open File 8269, 2017; 1 sheet, 1:100 000.

Kiss, F. and Tschirhart, V., 2017l. Tilt angle of the magnetic field, aeromagnetic survey of the Marguerite River area, Alberta, parts of NTS 74-E north and 74-E south; Geological Survey of Canada, Open File 8270, 2017; 1 sheet, 1:100 000.

Kiss, F. and Tschirhart, V., 2017m. Tilt angle of the magnetic field, aeromagnetic survey of the Marguerite River area, Saskatchewan, parts of NTS 74-F south; Geological Survey of Canada, Open File 8271, 2017; 1 sheet, 1:100 000.

Kiss, F. and Tschirhart, V., 2017n. Tilt angle of the magnetic field, aeromagnetic survey of the Marguerite River area, Saskatchewan, parts of NTS 74-F north; Geological Survey of Canada, Open File 8272, 2017; 1 sheet, 1:100 000.

Kiss, F. and Tschirhart, V., 2017o. Tilt angle of the magnetic field, aeromagnetic survey of the Marguerite River area, Saskatchewan, parts of NTS 74-K south; Geological Survey of Canada, Open File 8273, 2017; 1 sheet, 1:100 000.

Keating, P., 1995. A simple technique to identify magnetic anomalies due to kimberlite pipes; Exploration and Mining Geology, v. 4, p. 121–125.

Wheeler, J.O., Hoffman, P.F., Card, K.D., Davidson, A., Sanford, B.V., Okulitch, A.V., and Roest, W.R., 1996. Geological Map of Canada: Geological Survey of Canada, Map 1860A, 3 sheets; 1 CD-ROM.

Controls on the distribution, style, composition and timing of the gold-bearing mineralized zones of the Horne 5 deposit, Abitibi greenstone belt, Quebec

A. Krushnisky[1], P. Mercier-Langevin[2], P.-S. Ross[1], J. Goutier[3],
V.J. McNicoll[4], L. Moore[5], C. Pilote[6] and C. Bernier[6]

[1]*Institut national de la recherche scientifique, Centre Eau Terre Environnement,
490 rue de la Couronne, Québec, Quebec, G1K 9A9*

[2]*Geological Survey of Canada, 490 rue de la Couronne, Québec, Quebec, G1K 9A9*

[3]*Ministère de l'Énergie et des Ressources naturelles du Québec, 70 avenue Québec,
Rouyn-Noranda, Quebec, J9X 6R1*

[4]*Geological Survey of Canada, 601 Booth Street, Ottawa, Ontario, K1A 0E8*

[5]*McGill University, 3450 University Street, Montréal, Quebec, H3A 0E8*

[6]*Falco Resources Ltd., 161 avenue Murdoch, Rouyn-Noranda, Quebec, J9X 1E3*

Abstract

The gold-bearing Horne 5 VMS deposit is located in the Archean Blake River Group of the Abitibi greenstone belt. Hosted within steeply-dipping, north-facing felsic volcaniclastic units, the deposit is fault-bounded and within the boundaries of the Horne block. Mineralization consists of a series of stacked massive to semi-massive sulphide lenses alternating with disseminated and stringer sulphide zones in coarse felsic volcaniclastic units which often contain massive sulphide clasts. Results from this study show: i) gold and silver are associated with a sulphide assemblage composed dominantly of pyrite and lesser sphalerite, chalcopyrite and magnetite; ii) gold appears to be hosted in sulphide grains and electrum was only rarely observed as tiny blebs associated with remobilized chalcopyrite and near recrystallized pyrite grains, suggesting local remobilization due to metamorphism and deformation; iii) gold-bearing mineralization is partly controlled by the primary permeability of the host volcanic units and formed mostly by replacement of the host rocks under the paleo-seafloor. The Horne 5 deposit represents an opportunity to better understand ore-forming processes in large Archean synvolcanic gold systems.

Introduction

The Archean Horne gold-rich volcanogenic massive sulphide (VMS) deposit is the largest of its type, having produced, largely from the H orebodies, 53.7 Mt of ore grading at 6.1 g/t Au for a total of 327.6 t, or 11.6 Moz, of gold produced (Kerr and Mason, 1990; Mercier-Langevin et al., 2011). The deposit is in the 2704 to 2695 Ma Blake River Group (McNicoll et al., 2014) of the Abitibi greenstone belt, Superior Province, an extremely well-endowed region in terms of VMS and gold-rich VMS deposits. The Horne 5 deposit, lying downdip and stratigraphically slightly above the H orebodies, contains combined resources that amount to 112.7 Mt at 1.44 g/t Au for a total of 172.6 t, or 5.55 Moz of gold (Falco Resources Ltd., 2017).

Objectives of this study are threefold: i) document the mineralization style, mineralogy and geochemistry of the Horne 5 gold-bearing zones; ii) determine the spatial and temporal relationships between mineralization, deformation and metamorphism; and iii) establish controls on gold distribution. Research methods include drill core logging, geochemical characterization, petrography and micro-analysis of sulphides, trace ore-related minerals and alteration phases.

Horne 5 deposit geology

The gold-bearing zones of the Horne 5 deposit are hosted within steeply dipping, north-facing felsic volcaniclastic units, comprising felsic lapilli tuff, breccia and minor finely bedded tuff facies, intruded by a swarm of barren mafic dykes (Sinclair, 1971). These volcanic units are part of the Horne structural block that is bounded by the Horne Creek and Andesite faults (Fig. 1). Gold and silver are spatially associated with a sulphide assemblage of pyrite and lesser sphalerite, chalcopyrite and magnetite (Krushnisky et al., 2017a). Two broad styles of mineralization are present: a series of stacked massive to semi-massive sulphide lenses (Fig. 2a); and large intercalated zones of disseminated and stringer sulphides (Fig. 2b). Massive sulphide clasts of variable sizes are also present at several intervals in the mineralized zone (Fig. 2c), and occasionally form parts of the massive sulphide lenses.
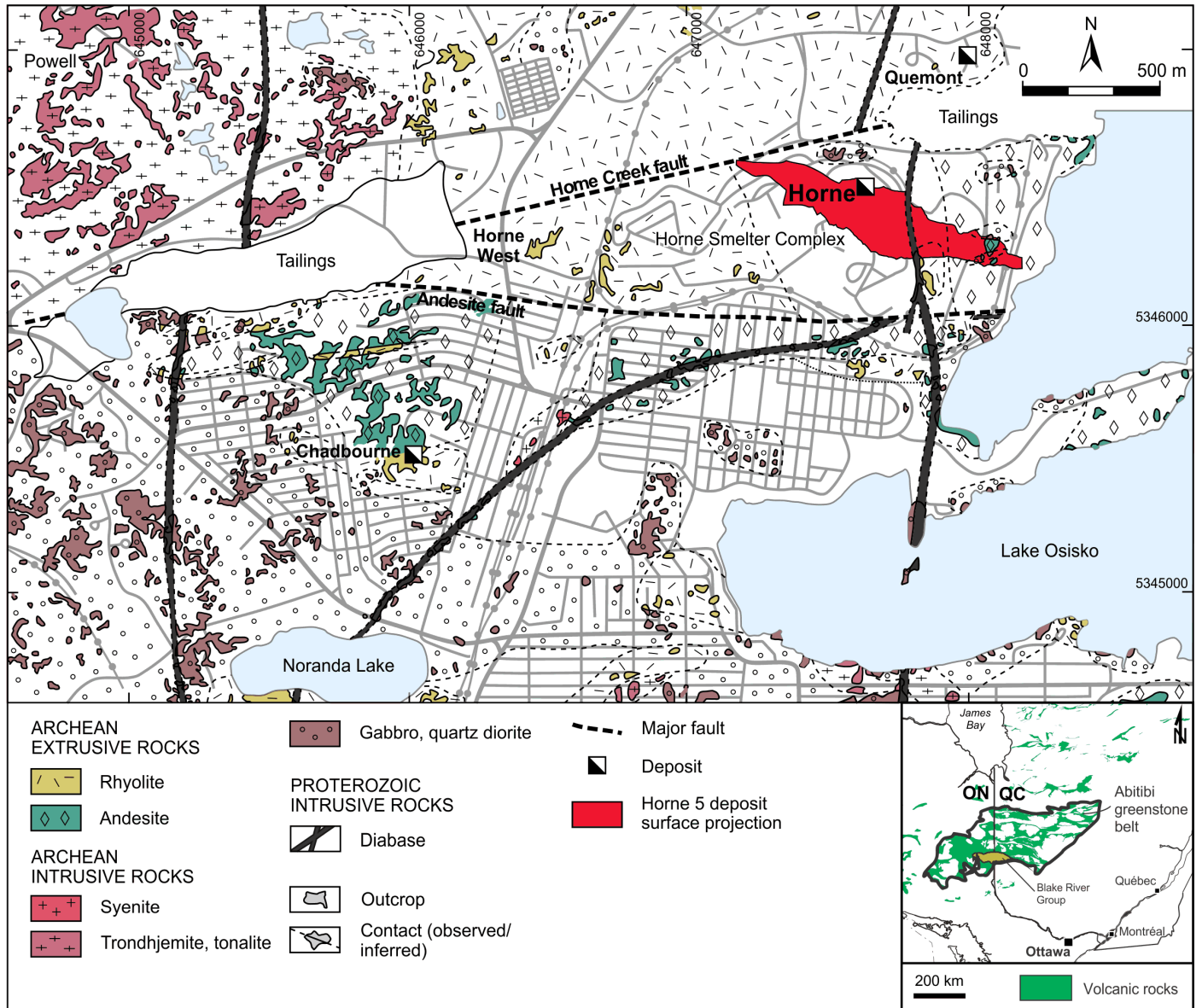
Figure 1. Geological map of the Horne Block and its surroundings within the Blake River Group (modified from Monecke et al., 2008). Surface projection of the Horne 5 deposit is shown in red between the Horne Creek and Andesite faults. Inset shows location of Blake River Group in the Abitibi greenstone belt, straddling the border between Québec and Ontario.

Sulphide mineralization is generally composed of fine-grained recrystallized pyrite with associated sphalerite (generally ≤5%, locally up to 10–30%; Fig. 2d) and chalcopyrite (generally ≤1%, locally up to 5%). Massive to semimassive pyrite is often granoblastic (usually ≤1 mm) and variably fractured. Sphalerite occurs as finely disseminated grains in the matrix of the volcaniclastic rocks and within massive pyrite, and is locally massive where it is associated with bands of fine-grained pyrite. Chalcopyrite is usually remobilized along fractures crosscutting pyrite and along grain boundaries (Fig. 2e). Fine- to coarse-grained magnetite, associated with chalcopyrite mineralization, appears mainly in the top section of the

Horne 5 deposit. Electrum is very rare and was observed with remobilized chalcopyrite in massive pyrite (Fig. 2f), along sulphide grain margins (Fig. 2g) and as inclusions in pyrite. Other secondary mineral phases, present mostly as inclusions in pyrite and along grain boundaries, include pyrrhotite, galena, stannite, cassiterite, and Pb-, Bi-, Ag- and Au-bearing tellurides.

Detailed mapping of the volcanic facies and mineralized zones from drill core to date show that host volcanic succession primary permeability contrasts control gold and sulphide distribution (Krushnisky et al., 2017b). Volcanic textures indicate that most of the mineralization was emplaced by infilling of
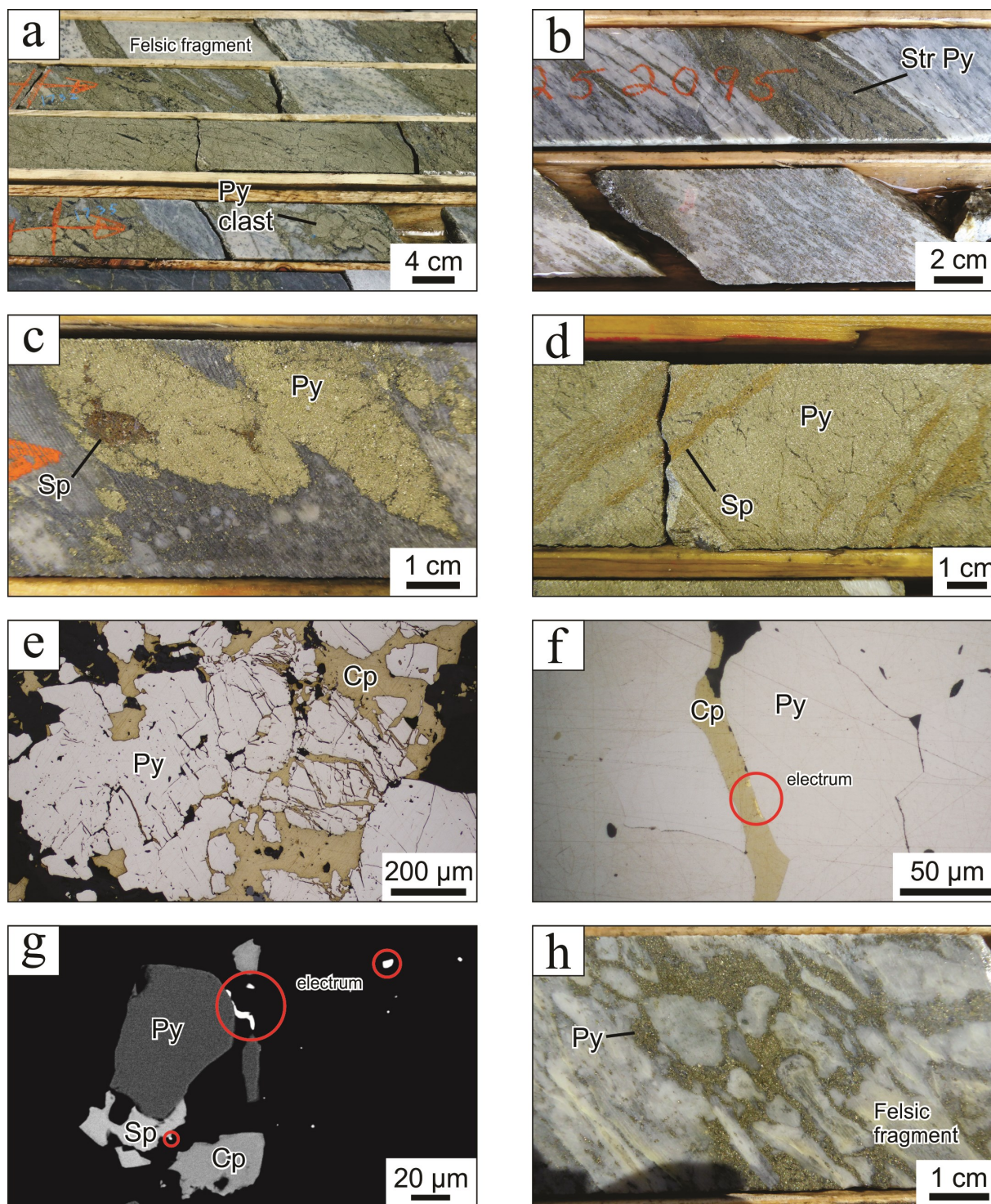
Figure 2. a) Replacement-style massive to semi-massive sulphide lens, containing relict felsic fragments from host rocks and several massive sulphide clasts. b) Stringer and disseminated pyrite zone, located stratigraphically below a massive sulphide body. c) Massive sulphide fragments composed of pyrite and clusters of sphalerite. Fragments are flattened into the main foliation. d) Fine-grained massive pyrite with pale orange sphalerite bands. e) Fractured pyrite porphyroblasts in a matrix of remobilized chalcopyrite. f) Remobilized chalcopyrite between pyrite grains containing specks of electrum, within a massive sulphide vein. g) Very fine-grained electrum occurring at margins of sulphide grains within massive sulphide sample (backscattered electron image). h) Replacement of margins of felsic fragments with fine-grained pyrite. Cp = chalcopyrite, Py = pyrite, Sp = sphalerite, Str = stringer.

primary pore spaces in the host volcaniclastic units and by partial to complete replacement of host rocks (Fig. 2a, h). High-grade gold zones, corresponding mostly to massive, semi-massive and stringer sulphide mineralization, coincide with coarser-grained, more permeable volcaniclastic facies (tuff breccia to breccia). The presence of overlying, fine-grained graded beds and coherent felsic units also influenced the distribution of the mineralization by acting as impermeable cap to ascending hydrothermal fluids, focusing them along specific horizons. The extent of deformation-induced gold remobilization, likely only affecting the distribution on a local scale, remains to be established. Some of the synvolcanic gold may have been remobilized to form higher-grade intersections associated with late quartz veins along high strain zones near the sulphide lenses.

Expected outcomes and future work

Continuing work on the Horne 5 deposit will focus on documenting the precise nature of the gold mineralization, and will include laser-ablation inductively coupled plasma mass spectrometry analysis of sulphide phases, 3-D modelling of metal distribution/alteration and U-Pb zircon geochronology. Coupled with petrography, geochemistry, scanning electron microscope and microprobe data, it is anticipated these data will constrain the genesis and timing of formation of the gold-bearing zones.

Acknowledgments

References

Falco Resources Ltd., 2017. Falco announces positive feasibility study results on Horne 5 gold project; Falco Resources Ltd. <http://www.falcores.com/English/news/news-details/2017/Falco-Announces-Positive-Feasibility-Study-Results-on-Horne-5-Gold-Project/default.aspx> [accessed December 11, 2017]

Kerr, D.J. and Mason, R., 1990. A re-appraisal of the geology and ore deposits of the Horne mine complex at Rouyn-Noranda, Quebec; Canadian Institute of Mining and Metallurgy, Special Volume 43, p. 153–165.

Krushnisky, A., Mercier-Langevin, P., Ross, P.-S., McNicoll, V.J., Goutier, J., Moore, L., Pilote, C., and Bernier, C., 2017a. Au-Ag-Cu-Zn-bearing mineralized zones at the Horne 5 Deposit, Rouyn-Noranda, Quebec - new observations and preliminary results; Geological Survey of Canada, Scientific Presentation 62, 1 sheet.

Krushnisky, A., Mercier-Langevin, P., Ross, P.-S., McNicoll, V.J., Goutier, J., Moore, L., Pilote, C., and Bernier, C., 2017b. Controls on gold distribution at the Horne 5 VMS deposit, Abitibi greenstone belt, Québec; *in* Proceedings of the 14th SGA Biennial Meeting, Québec, Quebec, p. 163–166.

McNicoll, V.J., Goutier, J., Dubé, B., Mercier-Langevin, P., Ross, P.-S., Dion, C., Monecke, T., Legault, M., Percival, J., and Gibson, H., 2014. U-Pb Geochronology of the Blake River Group, Abitibi Greenstone Belt, Quebec, and Implications for Base Metal Exploration; Economic Geology, v. 109, p. 27–59.

Mercier-Langevin, P., Hannington, M.D., Dubé, B., and Bécu, V., 2011. The gold content of volcanogenic massive sulfide deposits; Mineralium Deposita, v. 46, p. 509–539.

Monecke, T., Gibson, H.L., Dubé, B., Laurin, J., Hannington, M.D., and Martin, L., 2008. Geology and volcanic setting of the Horne deposit, Rouyn-Noranda, Quebec: initial results of a new research project; Geological Survey of Canada, Current Research 2008-9, 16 p.

Sinclair, W.D., 1971. A Volcanic Origin for the No. 5 Zone of the Horne Mine, Noranda, Quebec; Economic Geology, v. 66, p. 1225–1231.

Volcanic, hydrothermal and structural controls on the nature and distribution of base and precious metals at the B26 project, Brouillan volcanic complex, Abitibi, Quebec

Q. Fayard[1,2], P. Mercier-Langevin[3], R. Daigneault[1] and S. Perreault[2]

[1]*Université du Québec à Chicoutimi, 555 Boulevard de l'Université, Chicoutimi, Quebec, G7H 2B1*
[2]*SOQUEM Inc., 1740 Chemin Sullivan, Val-d'Or, Quebec, J9P 7H1*
[3]*Geological Survey of Canada, 490 rue de la Couronne, Québec, Quebec, G1K 9A9 X*

Abstract

The B26 project located in the northern Abitibi greenstone belt, a few kilometres south of the past producing Selbaie mine, consist of transposed, gold-rich chalcopyrite veins associated with porphyritic felsic volcanic rocks overlain by newly discovered lenses of semi-massive to massive, Zn-Ag-rich sulphide lenses higher up in the stratigraphy. Diffuse and remobilized Ag-rich zone are present in the hanging-wall rocks. The mineralized zones and host rocks have undergone major shortening, producing the steeply south-dipping S2 penetrative planar fabric. The mineralized zones have also been subjected to stretching, indicated by a well-developed 55–60° plunge towards the west on the schistosity. This deformation and the accompanying metamorphism are responsible for some remobilization. Although similar to other Archean volcanogenic massive sulphide deposits in terms of overall geometry, the B26 deposit is locally enriched in precious metals and shows a few unusual characteristics that suggest specific ore-forming conditions that may have played a role on the precious-metal budget and distribution.

Introduction

The B26 copper-zinc-silver-gold exploration project is located 5 km south of the past producing Selbaie mine and about 90 km west of Matagami, Quebec (Fig. 1). The B26 property is located in the Northern Volcanic Zone of the Archean Abitibi greenstone belt, within the Brouillan – Matagami volcanic arc (Fig. 1) in the southwest part of the Brouillan volcanic complex. Recent exploration has seen the discovery of copper- and gold-rich zones (10.7 Mt at 1.25% Cu and 0.41 g/t Au; Paiement, 2016) and of zinc- and silver-rich semi-massive to massive sulphide zones higher in the stratigraphy.

The nearby Matagami district is host to numerous zinc-rich volcanogenic massive sulphide (VMS) deposits associated with ca. 2725–2724 Ma felsic volcanic rocks (Ross et al., 2014) that are presumed coeval with those of the B26 prospect area (Fig. 1). These VMS deposits are separated spatially with no major deposits known between the Matagami district and the Selbaie mine. Selbaie mine mineralization is interpreted as epithermal overprinting a barren massive pyrite lens (Faure et al., 1996). The large Brouillan synvolcanic complex is considered to be a potential driver for the hydrothermal activity in the area, which may explain the high prospectivity of the area for base and precious metals.

The objectives of this study are to: i) characterize the various styles of mineralization and the metallic associations; ii) determine the relative role and importance of factors controlling the distribution and geometry of the precious metal zones; and iii) define the original geometry of the hydrothermal system and its influence on gold and silver mineralization.

B26 exploration project

The B26 deposit is hosted by south-facing, transitional, felsic to intermediate volcanic rocks attributed to the Brouillan Group, near the contact with Enjalran Group tholeiitic mafic units to the south (Fig. 2). There are few age constraints in the area, but the Brouillan volcano-plutonic rocks has been dated at 2726 ±3 Ma (Barrie and Krogh, 1996), and correlated with the VMS-rich 2734 to 2724 Ma Deloro volcanic episode (Thurston et al., 2008). The B26 mineralized zones and host rocks have undergone major shortening, producing the steeply south-dipping S2 penetrative planar fabric. The mineralized zones have also been subjected to stretching, indicated by a well-developed 55–60° plunge towards the west on the schistosity.

The B26 mineralization consists of both lower Cu-(Au) and upper Zn-(Ag-Pb) zones that are typical of Archean VMS systems. These zones are separated by a few tens of metres of mostly barren, altered rhyolite, which is not a typical VMS feature. Also, the upper zinc-rich portion of the deposit is enriched in silver relative to other Archean VMS deposits. As the lower portion includes some very high-grade gold intersections, this deposit provides an excellent opportunity to investigate Archean silver-gold enrichment processes.
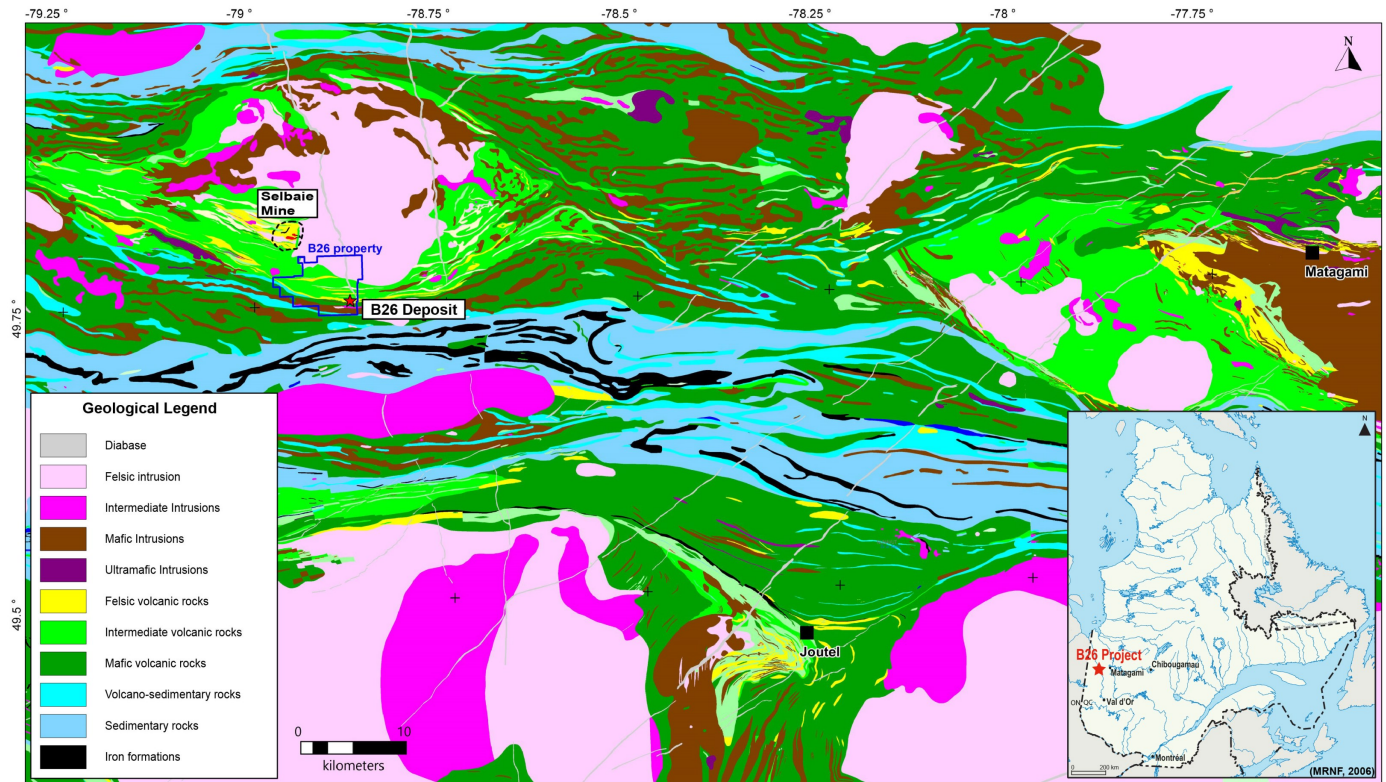
Figure 1. Regional geological map (1:400 000) of the Brouillan-Matagami volcanic arc showing the location of the B26 property. Modified after Faure (2015)

Interim observations

B26 mineralization is strongly zoned, with centimetre to decimetre wide, semi-massive to massive chalcopyrite ± pyrite veins (Fig. 3) defining the copper-gold zone at the base (north) of the system. These chalcopyrite veins are strongly deformed and transposed into the main schistosity. They are located at or very near the contact between a quartz-porphyry rhyolite (footwall) and an aphyric rhyolite (hanging wall; Figs. 2 and 3). There is a strong chlorite alteration halo in the vein selvages, the intensity of which gradually decreases away from the veins and is replaced by white mica. A few tens of metres higher in the stratigraphy, a massive (0.5–3.5 m thick), but laterally discontinuous, Zn-Pb-(Ag)-rich sulphide lens (Fig. 3) overlies a strongly sericitized alteration zone. Aphyric rhyolite caps this mineralized horizon, and is locally partially replaced by sphalerite (Fig. 3) and pyrite. This rhyolite is also cut by late sulphide and quartz veins (Fig. 3) that commonly contain significant but variable amounts of sphalerite, galena and native silver. These veins are at an angle with the main schistosity and are interpreted as partly transposed piercement structures (cf. Marshall et al., 1989). These late veins are generally strongly enriched in silver relative to the underlying stratiform and strat-abound replacement sulphide zones.

Expected outcomes and future work

Observations to date suggest B26 mineralization having a synvolcanic origin, followed by polyphase local remobilization of the precious metals during syn- to late-main deformation. The presence of intensely altered rhyolite between the Cu and Zn zones suggest that the zonation and physical separation between both ore styles is primary. Precise U-Pb zircon dating of the various rhyolites will constrain timing and enable regional correlation.

Since the entire study area is covered by 40 m of overburden data is restricted to drill core. Future work will include compiling available data (e.g. assays, lithogeochemistry and drill logs) to help resolve the hydrothermal system geometry. Collected samples are to be analyzed for whole-rock lithogeochemistry that will be combined with petrography and microanalytical studies using LA-ICP-MS and SEM.

Acknowledgments

LEGEND

Proterozoïc

Diabase

Archean

Enjalran-Bapst Group (2734-2724 Ma)

Basalt / Gabbro

Brouillan-Fénélon Group (2734-2724 Ma)

Graphitic argilite

Ankeritized sediments

Quartz-crystal felsic tuff

Aphyric rhyolite

Quartz-porphyry rhyolite

Andesite

Undifferentiated felsic tuff

Quartz-Feldspaths Intrusion

Quartz-porphyry rhyolite

Cu-Au

Zn-Ag

Mineralized envelopes (Copper = red ; Zinc = blue)
(light shade 0.5 <Zn-Cu <1%, dark shade Zn-Cu> 1%)

Séricite +/- chlorite strongly altered zone

HW / FW   *Footwall-Hangingwall* contact
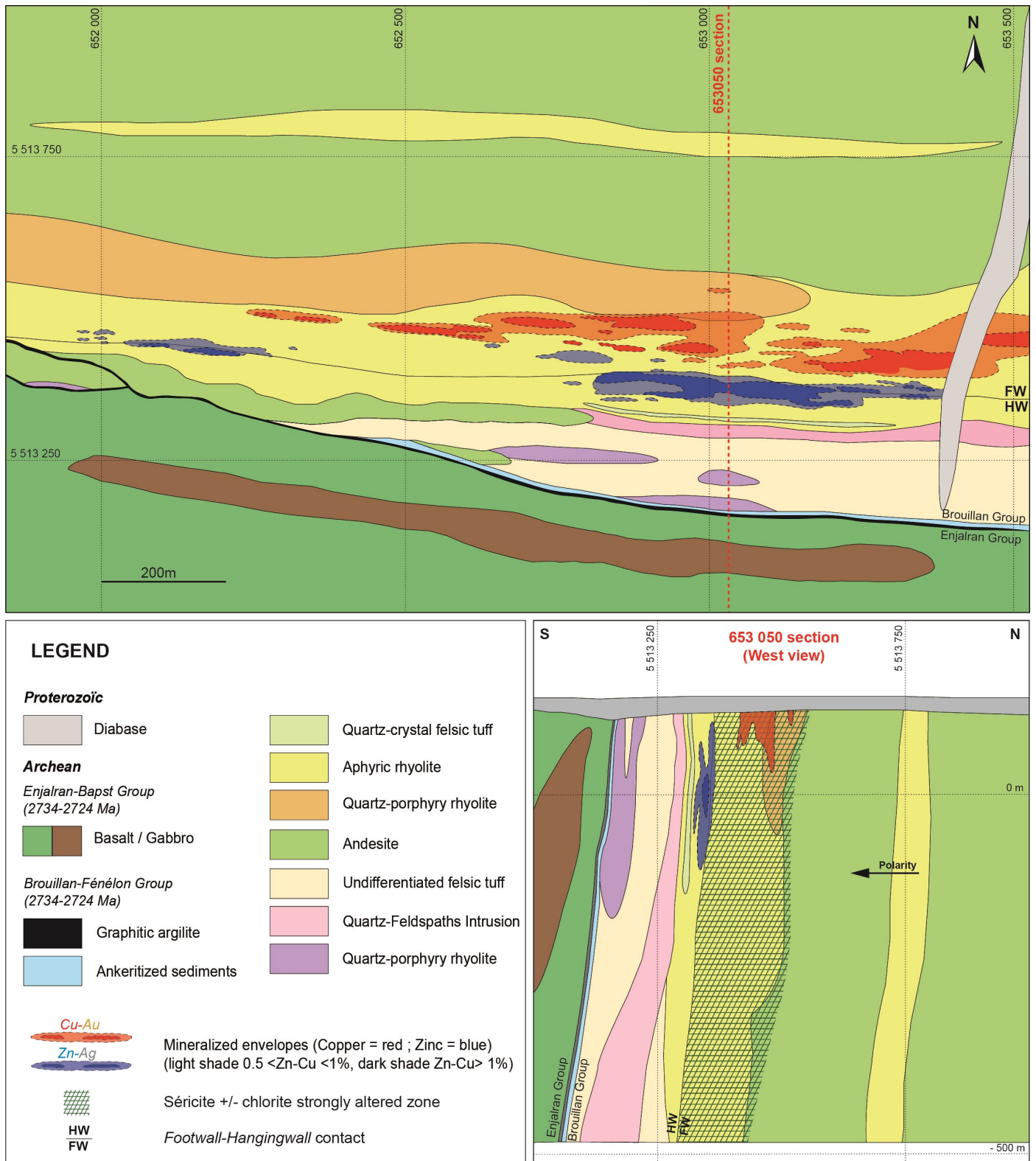
Figure 2. Geological map and section of the B26 deposit interpreted from drilling data. The mineralized envelopes, which plunge 60 degrees to the west, have been projected on surface.
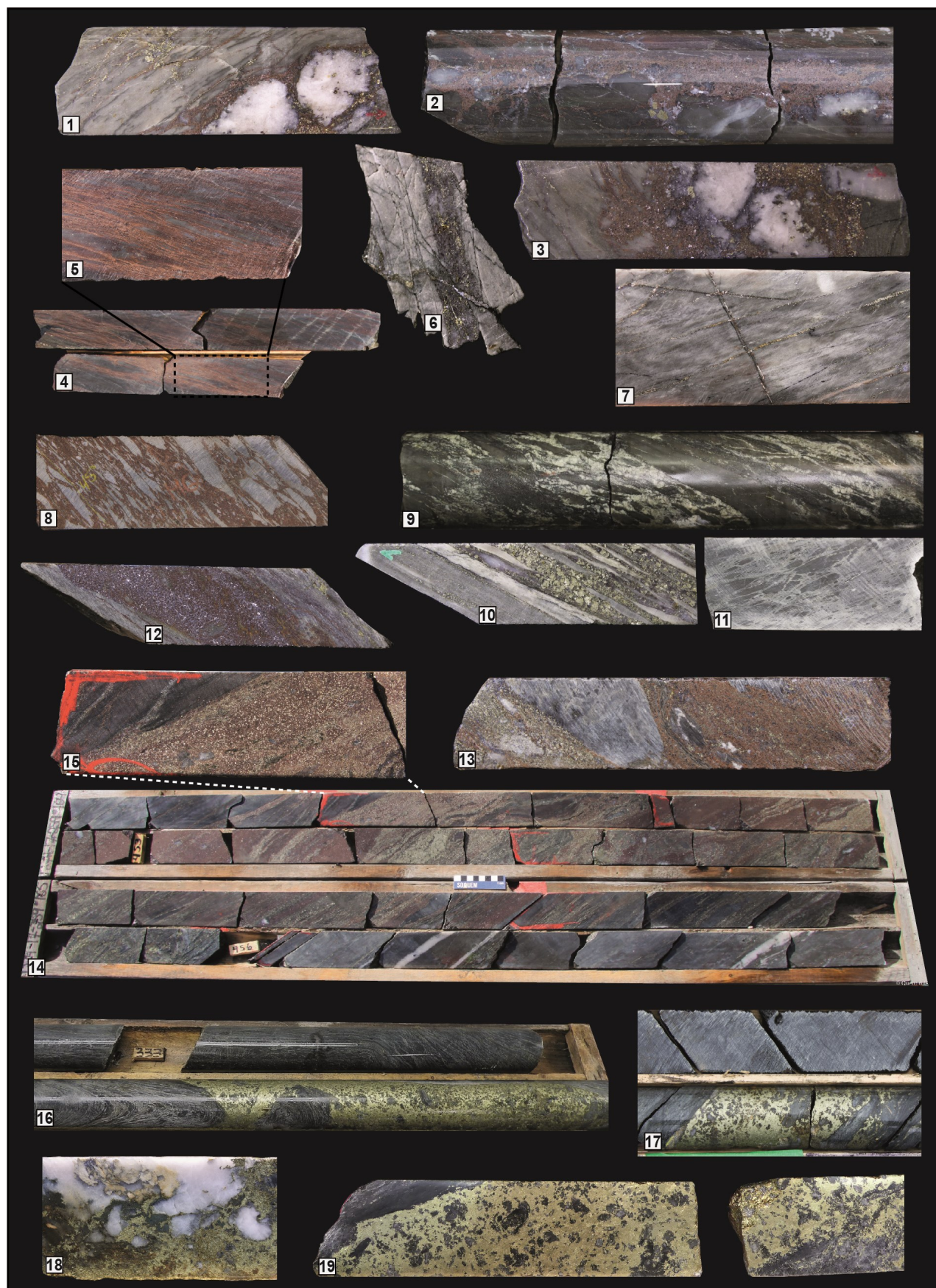
101

References

Barrie, C.T. and Krogh, T.E., 1996. U-Pb Zircon Geochronology of the Selbaie Cu-Zn-Ag-Au Mine, Abitibi Subprovince, Canada; Economic Geology, v. 91, p. 563–575.

Faure, S., 2015. Prolongement de la faille Sunday Lake (mine Detour Gold, Ont.) au Québec et son potentiel pour les minéralisations aurifères et en métaux de base; Unpublished report, CONSOREM Project 2013-02, 41 p.

Faure, S., Jébrak, M., and Angelier, J., 1996. Structural evolution of Les Mines Selbaie, northern Abitibi, Québec, Canada; Exploration and Mining Geology, v. 5, p. 215–230.

Marshall, B. and Gilligan, L.B., 1989. Durchbewegung structure, piercement cusps, and piercement veins in massive sulfide deposits; formation and interpretation; Economic Geology, v. 84, p. 2311–2319.

Paiement, J.-P., 2016. Rapport technique NI 43-101: Estimation des ressources, Projet B26, Québec, SOQUEM Inc. – SGS Canada Inc.; Internal Report, SOQUEM Inc., 129 p.

Ross, P.-S., McNicoll, V.J., Debreil, J.-A., and Carr, P., 2014, Precise U-Pb geochronology of the Matagami mining camp, Abitibi greenstone belt, Quebec: Stratigraphic constraints and implications for volcanogenic massive sulfide exploration; Economic Geology, v. 109, p. 89–101.

Thurston, P.C., Ayer, J.A., Goutier, J., and Hamilton, M.A., 2008. Depositional gaps in Abitibi greenstone belt stratigraphy: A key to exploration for syngenetic mineralization; Economic Geology, v. 103, p. 1097–1134.

Figure 3 (opposite). Examples of mineralized intervals. Photos 1, 2 and 3 show silver-rich hanging-wall piercement quartz veins with sphalerite-galena-chalcopyrite-piercement. These veins are partly transposed and boudinaged into the main schistosity. Photos 4 and 5 show diffuse sphalerite replacement of a volcanoclastic unit. Photos 6 and 7 show veinlets of native silver at high angle with the main schistosity. Photos 8 and 9 show ankerite-magnetite breccias present in the hanging wall of the B-26 zinc lenses. The breccia contains fragments of aphyric rhyolite. Photo 10 shows a tuff unit with quartz crystals and lapilli that is partially to totally replaced by pyrite and local sphalerite stringers. Photo 11 shows rhyolitic breccia flow texture located just above the massive sulphide lens. Photo 12 shows strongly deformed massive sphalerite and galena with late slip planes. This interval grades 542 ppm Ag over 0.3 m. Photos 13, 14 and 15 show examples of massive sulphide (sphalerite-pyrite) mineralization. The presence of fragments of the wall rocks is due to deformation of the massive sulphides. The footwall of the VMS (close-up photo 15) presents a veinlet that shows the onset of mechanical brecciation. All sulphides have undergone recrystallization during metamorphism. Photos 16, 17 and 19: Massive gold-bearing chalcopyrite veins. The intersection shown on Photo 17 grades 52 ppm Au over 0.5m. The veins are deformed, with the development of classical Durchbewegung textures (cf. Marshall et al., 1989). A halo of intense chlorite alteration is present around those Cu-Au-rich veins. Photo 18 shows a gold-rich vein of quartz-chalcopyrite-ankerite.

Nature and significance of deformation zones on gold mineralization in the Detour Lake area: Implications for exploration in Ontario and Quebec

S. Castonguay[1], B. Dubé[1], P. Mercier-Langevin[1], V.J. McNicoll[2],
A. DeLazzer[3] and K. Malcolm[3]

[1]*Geological Survey of Canada, 490 rue de la Couronne, Québec, Quebec, G1K 9A9*
[2]*Geological Survey of Canada, 601 Booth Street, Ottawa, Ontario, K1A 0E8*
[3]*Detour Gold Corp., Detour Lake Mine, 86 2nd Street, P.O. Box 1325, Cochrane, Ontario, P0L 1C0*

Abstract

The Detour Lake gold mine and Lower Detour zones (e.g. Zone 58N and Zone 75) are located in the northwestern part of the Abitibi greenstone belt and are hosted in a volcanic sequence of the 2.73 to 2.72 Ga Deloro assemblage or in altered feldspar porphyry intrusive(s). Mineralization consists of low-grade disseminated quartz-sulphide zones and silicified high-grade zones, including laminated quartz-tourmaline-carbonate veins and stockworks. Ore zones are commonly oriented sub-parallel to a series of high-strain zones occurring co-planar and in the hanging wall to the regional-scale Sunday Lake and Lower Detour deformation zones. The latter zone has a close spatial relationship with polymictic conglomerates and intermediate to felsic intrusive rocks, which is analogous to major fault systems of the Timmins-Porcupine area and associated syn-orogenic Timiskaming conglomerates. The focus of this study is to examine the relationships between gold mineralization and deformation in the Detour Lake region and in Quebec and compare these with those of the southern Abitibi.

Introduction

The Detour Lake gold mine (approximately 25 Moz Au) and Lower Detour zones are located in the northwestern part of the Abitibi greenstone belt (Marmont, 1986; Oliver et al., 2012; Detour Gold Corporation, 2017; Fig. 1, 2). Auriferous zones of the Detour Lake gold deposit are hosted in a sequence of pillowed and massive basaltic and altered ultramafic rocks, both as low-grade disseminated quartz-sulphide zones and as silicified high-grade zones. Ore zones are commonly oriented sub-parallel to a series of high-strain zones occurring co-planar and in the hanging wall to the regional-scale Sunday Lake deformation zone (SLDZ; Fig. 2, 3). According to Thurston et al. (2008), Ayer et al. (2010), and Oliver et al. (2012), the SLDZ juxtaposes 2.73 to 2.72 Ga volcanic rocks of the Deloro assemblage over the 2.70 Ga Caopatina turbititic sedimentary assemblage. The Lower Detour area lies 7 km south of the SLDF, across the Caopatina belt (Fig. 2), and comprises the Lower Detour deformation (LDDZ) zone and related splays. The latter are associated with recently discovered significant gold zones (e.g. Zone 58N and Zone 75) hosted in altered feldspar porphyry intrusive(s) and/or volcanic units of the Deloro assemblage (Fig. 4, 5; Malcolm et al., 2015). The SLDF and LDDZ can be traced for more than 25 km on the Detour property and extend eastward into Quebec where they are also known to be prospective for gold (Fig. 1, 2; e.g. Faure, 2015).

The primary focus of this study is to examine the relationship between Detour Lake region gold mineralization and deformation, with an emphasis on the recently uncovered Lower Detour area. In concert with this aim is a secondary objective to compare these deformation corridors with those of the southern Abitibi, such as the Porcupine-Destor deformation zone (Fig. 1).

Detour Lake gold zones

The Detour Lake gold mine comprises high grade zones commonly hosted by the 'Chert Marker Horizon' (CMH), which occurs at the boundary between the mafic-dominated volcanic rocks of the upper Detour Lake formation and ultramafic-dominated lower Detour Lake formation (Fig. 3, 6a; Oliver et al., 2012). The CMH is not a primary chert, but rather a fine-grained felsic volcanoclastic unit (Oliver et al., 2012) and/or a series of intensely silicified and sulphidized mafic volcanic rocks and intermediate sills and/or dykes. Examined intervals previously described as CMH contain silicified fine-grained intermediate intrusives, with grades reaching up to 1 g/t Au (Fig. 6b), whereas the silicified and sulphidized mafic volcanic intervals, which have up to 15% sulphide stringer and quartz veins, contain 1 to 10 g/t Au (Fig. 6c). In the hanging wall (north) of the CMH, potassic-altered, biotite-rich, massive and pillowed mafic volcanic rocks are injected by millimetre to centimetre wide quartz-carbonate veins and 0.5 to 5% pyrrho-

---
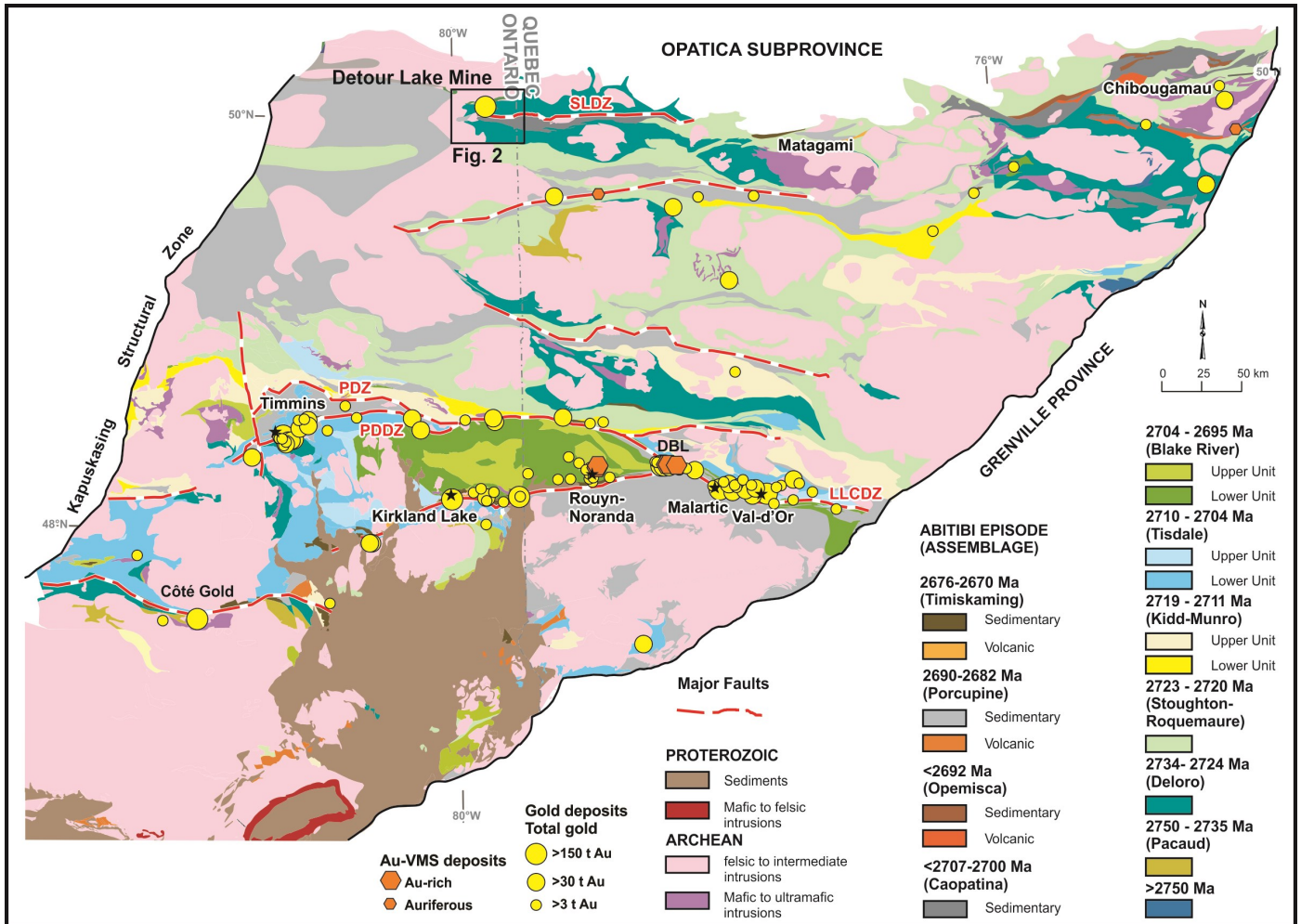
Figure 1. Generalized geological map of the Abitibi subprovince showing the main lithotectonic assemblages and location of major gold deposits, including the Detour Lake Mine. Modified from Ayer et al. (2010). Data for major gold and gold-rich VMS deposits modified from Gosselin and Dubé (2005) and Mercier-Langevin et al. (2011). DBL - Doyon-Bousquet-Laronde camp; LLCDZ - Larder Lake-Cadillac deformation zone; PDDZ - Porcupine-Destor deformation zone; PDZ - Pipestone deformation zone; SLDZ - Sunday Lake deformation zone.

tite-pyrite±chalcopyrite stringers that grade between 1 and 5 g/t Au (Fig. 6d). In general, the auriferous quartz veins are part of a series of sub-vertical high strain zones that are parallel the SLDF (Fig. 3). Several mineralogical types of veins, with various relative timing relationships (pre- to post-main deformation) comprise the ore zones. Dubosq et al. 2017) documented evidence for late gold remobilization associated with pyrite recrystallization. Gold associated with sulphides also occurs in the footwall of the CMH in strongly sheared serpentinized and talcose ultramafic rocks in a zone historically termed the 'talc zone' (Fig. 3; Detour Gold Corporation, 2017).

The Lower Detour area is underlain by volcanic units correlated with the Detour Lake formation that occurs to the north (Fig. 2). These units are juxtaposed to the clastic units of the

Caopatina assemblage along the Lower Detour and Massicotte deformation zones (Detour Gold Corporation, 2017). Deformed and locally carbonatized polymictic conglomerate beds occur northward in the immediate footwall of the LDDZ. The polymictic conglomerate beds are poorly sorted, with clasts variably flattened and stretched (Fig. 7a), locally forming an L-S tectonite. Locally altered, intermediate feldspar porphyritic dykes commonly obscure the tectonic contact between the volcanic and sedimentary assemblages in the LDDZ.

Gold in the Lower Detour area mainly occurs in two steeply south-dipping zones (Fig. 5). Zone 75 is hosted in silicified, biotite-sericite altered mafic volcanic rocks (Fig. 7b) and very occasionally in intermediate feldspar porphyry rocks. The sulphide content reaches up to 20% as mainly pyrite, and lesser
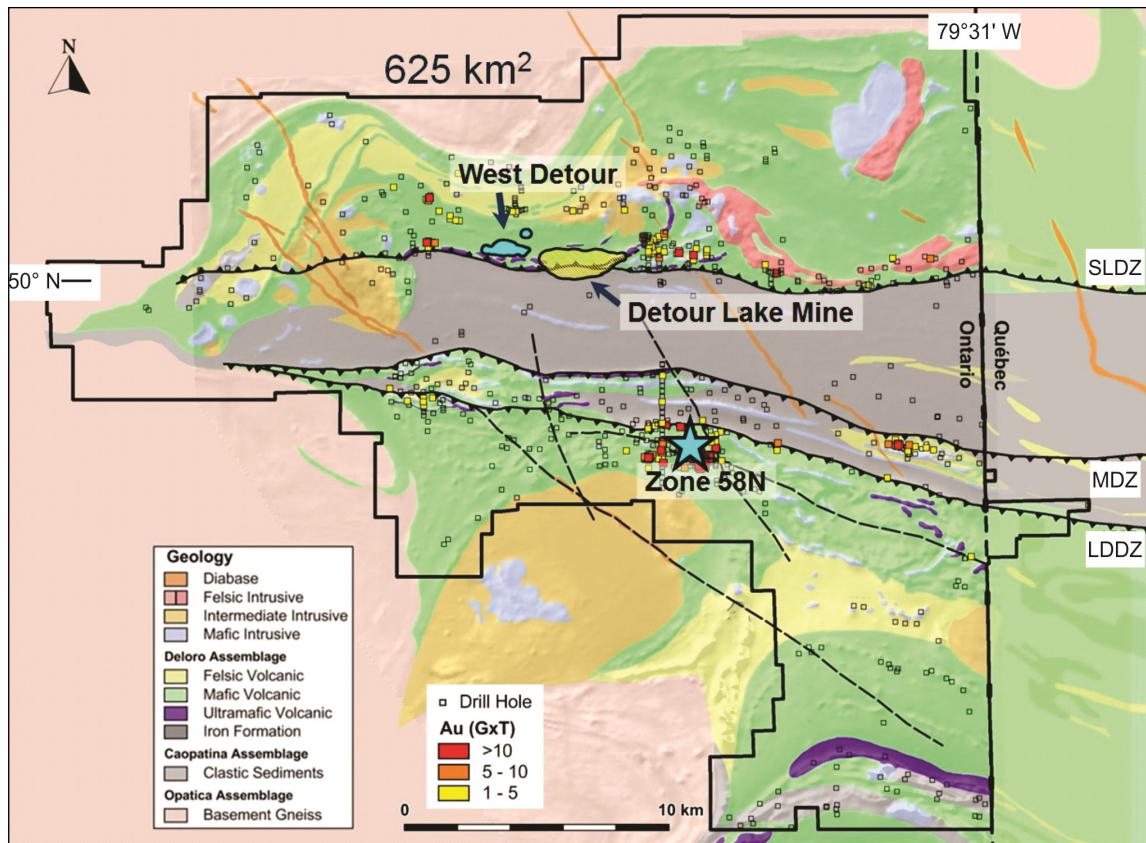
Figure 2. Simplified regional geological map of the Detour Lake mine area, with the location of the Detour Lake mine, Lower Detour mineralized zones (Zone 58N), drill holes and outline of the Detour Lake Corp property (modified from Detour Gold Corporation, 2017). LDDZ - Lower Detour deformation zone (Zone 58N); MDZ - Massicotte deformation zone; SLDZ - Sunday Lake deformation zone.
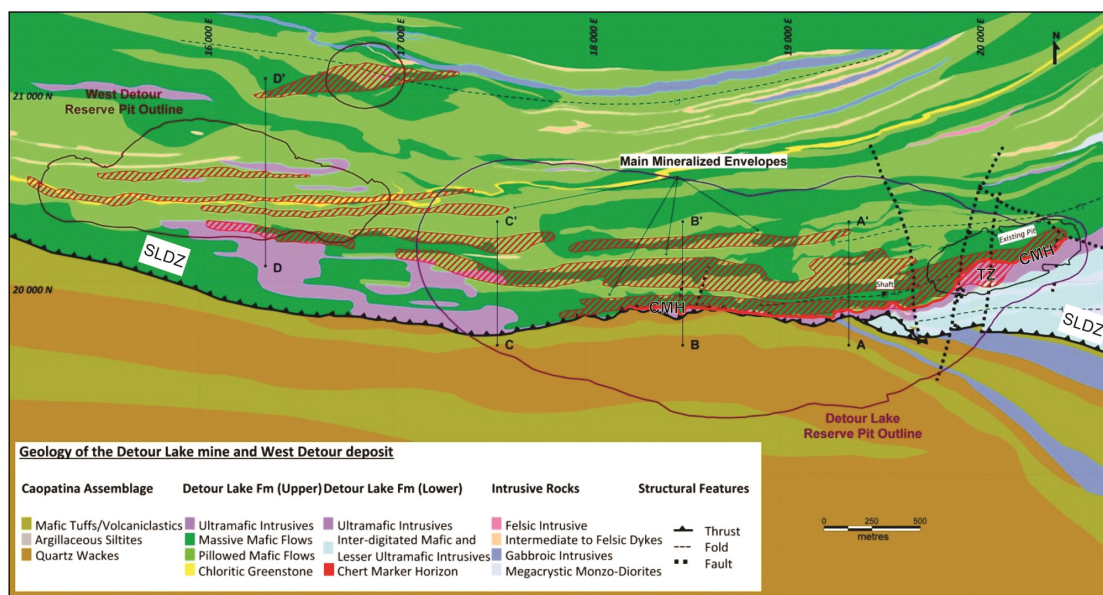
Figure 3. Simplified geological map of the Detour Lake deposit area, with location of the main mineralized zones and historical and future pit outlines (modified from Oliver et al., 2012 and Detour Gold Corporation, 2017). CMH: Chert marker horizon; SLDZ: Sunday Lake deformation zone; TZ; Talc zone.
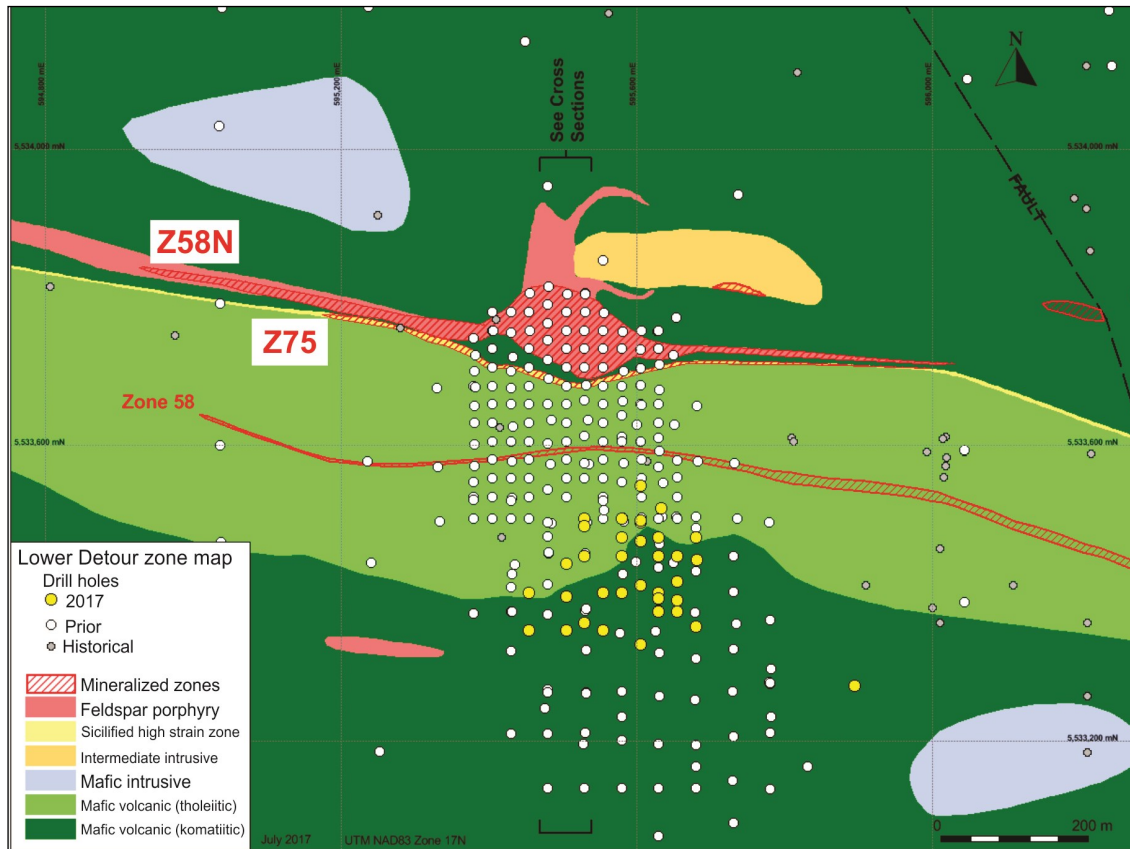
Figure 4. Simplified geological map of the Lower Detour (Zone 58N) area extrapolated from drill core data, with location of the main mineralized zones (modified from Malcolm et al., 2015; Detour Gold Corporation, 2017).
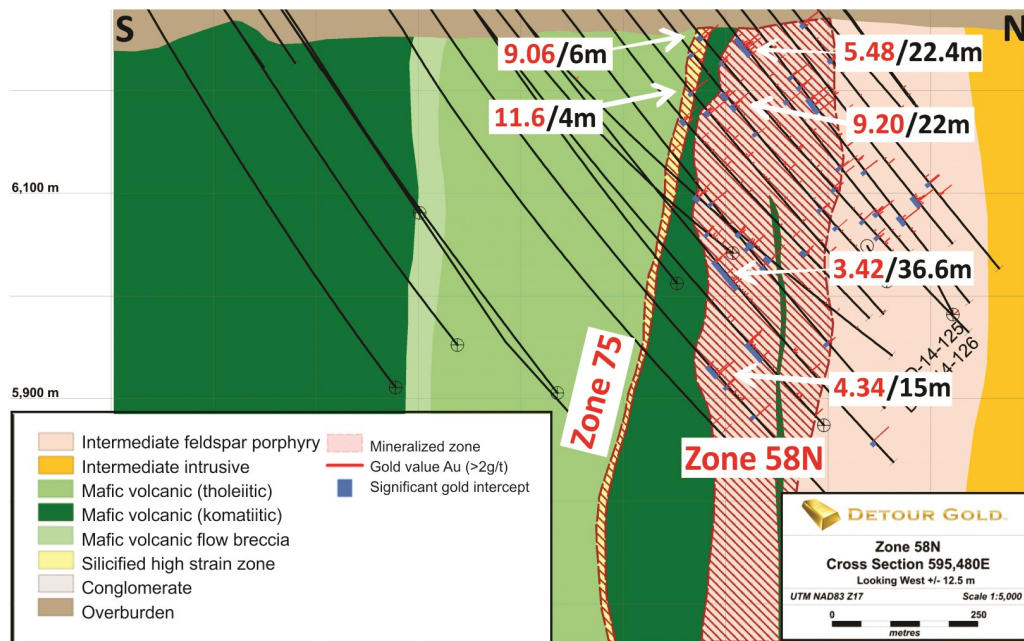
Figure 5. Simplified geological cross section of the Lower Detour zones 75 and 58N with representative gold intercepts (modified from Malcolm et al., 2015; Detour Gold Corporation, 2017).

108
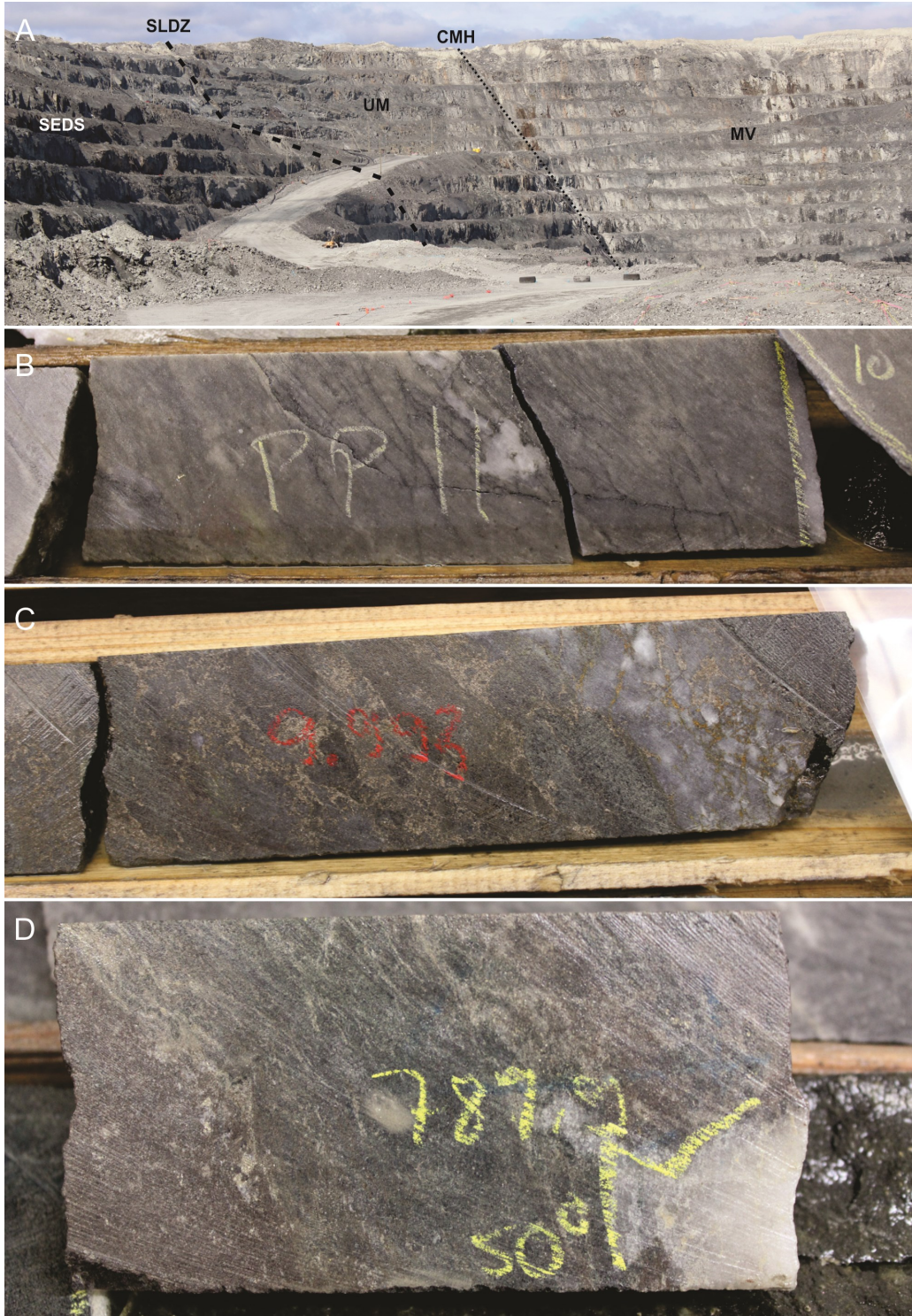
Figure 6. Detour Lake mine. a) View to the west of the Detour Lake mine pit (southwest part); CMH; approximate trace of the "chert Marker horizon"; MV: Mafic volcanic flow; SEDS: volcanoclastic and quartz wacke units of the Caopatina assemblage; UM; sheared ultramafic rocks; SLDF; approximate trace of the Sunday Lake deformation zone. b) Medium grey fine-grained feldspar-phyric intermediate intrusive rock associated with the CMH; cut by quartz-tourmaline veinlets. c) Strongly silicified mafic volcanic rock (originally described as chert) with 5 to 20% pyrrhotite-pyrite stringers and locally visible gold (interval is 10 g/t Au); d) Biotite-altered mafic volcanic, locally pillowed, cut by quartz veins with pyrite-pyrrhotite blebs at veins contacts (Hanging wall of the CMH).
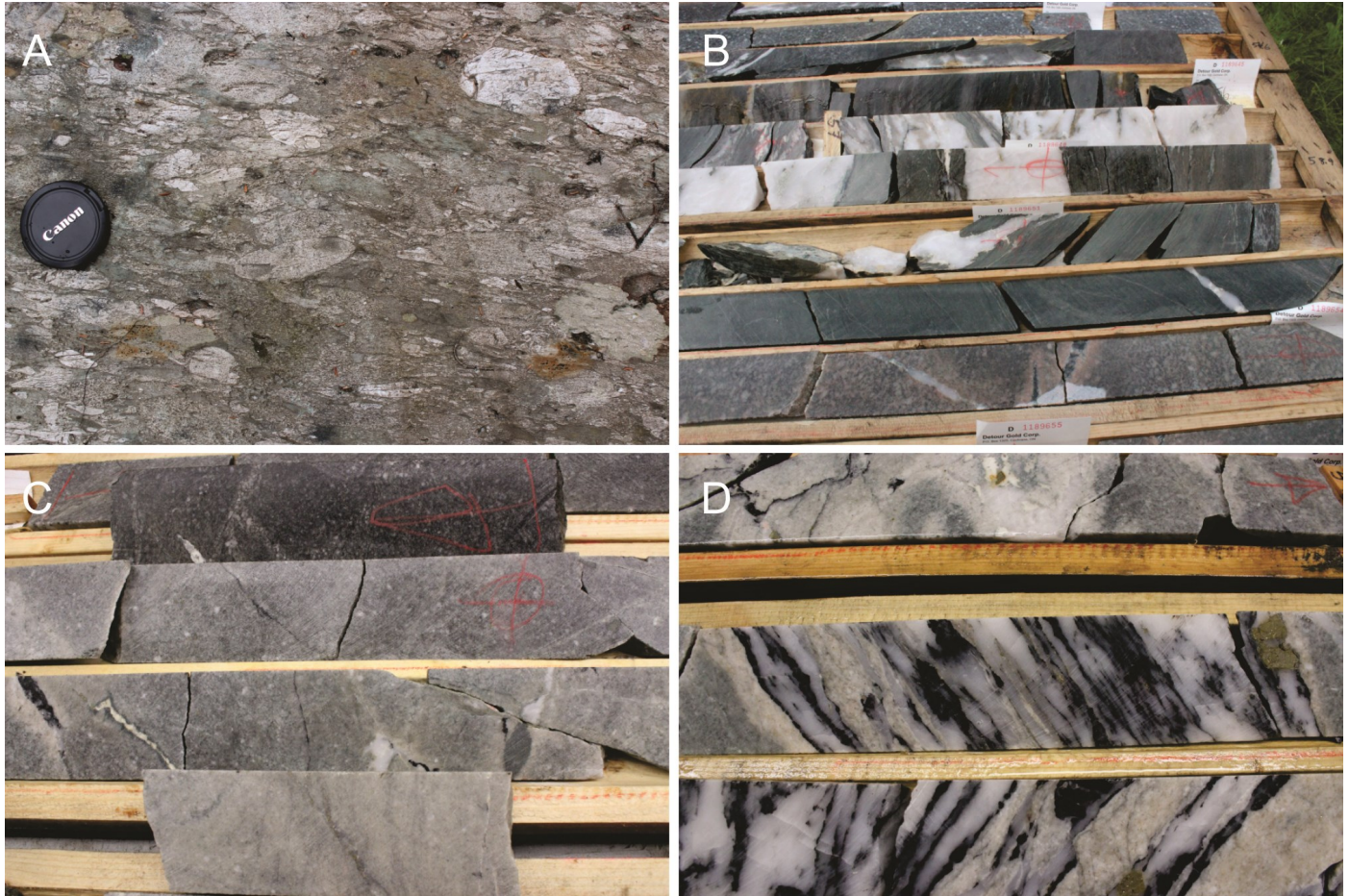
Figure 7. Lower Detour area: a) Foliated and lineated (down dip) polymictic conglomerate occurring in the structural footwall of the Lower Detour deformation zone; b) Typical zone 75 host rock, with quartz ± tourmaline veins cutting silicified strongly foliated mafic volcanic and weakly-foliated potassic altered intermediate feldspar porphyritic dyke (Mafic volcanic interval is 1.5 to 28 g/t Au); c) Series of drill core from the hanging wall of Zone 58N showing the progressive (top to bottom) bleaching caused by sericite alteration; some quartz-tourmaline veins; d) Typical zone 58N, with laminated quartz-tourmaline veins in silica-sericite altered intermediate feldspar porphyry with trace to 2% coarse pyrite along vein contacts with the feldspar porphyry (interval is 34.9 g/t over 1 m).

pyrrhotite, chalcopyrite and sphalerite. Zone 58N is hosted in a swarm of intermediate feldspar porphyritic dykes and bodies, and is associated with laminated quartz-tourmaline-carbonate veins and stockworks with visible gold. The veins are associated with a decimetre wide sericite, silica and biotite alteration zone (Fig. 7c, d). Sulphide abundance varies significantly, but is generally between 0.5 and 5%. The sulphides typically occur as disseminated pyrite within the veins or their selvages, along with trace amounts of sphalerite and chalcopyrite.

Discussion and future work

The Detour Lake mine area has very limited exposure and is underexplored compared to the southern Abitibi. Preliminary investigations have raised the following questions and observations:

- What is the first order structure in the Detour Lake mine area? The SLDZ is generally considered the main regional fault zone. However, the LDDZ also has characteristics of a first order structure, such as a close spatial relationship with polymictic conglomerates and intermediate to felsic intrusive rocks. These relationships are analogous to Timmins-Porcupine area major fault systems and associated synorogenic Timiskaming conglomerates (e.g. Bleeker, 2015).

- Most of the Lower Detour auriferous zones occur at, or very near, the contact between mafic and ultramafic volcanic units, which corresponds with the lithological succession (lower and upper Detour Lake formation) hosting the high-grade zones at the Detour Lake mine. If such a correlation

is confirmed, this type of contact may represent a key prospective setting.

- The Lower Detour zones are hosted in sheared and silicified mafic volcanic rocks (Zone 75) and in intermediate feldspar porphyritic rocks (Zone 58N) associated with quartz ± tourmaline - carbonate laminated veins and stockworks. These share characteristics (e.g. vein network geometry, alteration and setting) with the prolific Sigma-Lamaque deposit (e.g. Robert, 1990) and Goldex mine of the Val d'Or district, in Quebec.

Geochemical and geochronological analyses are underway to document the lithotectonic setting of the Lower Detour zones (75 and 58N) and constrain the timing of deformation, magmatism, sedimentation and mineralization. Investigations are intended to extend into the Quebec portion of the belt. Both the Sunday Lake and Lower Detour deformation zones extend eastward, where they are also spatially associated with significant gold mineralization.

Acknowledgments

References

Ayer, J.A., Goutier, J., Thurston, P.C., Dubé, B., and Kamber, B.S., 2010. Tectonic and metallogenic evolution of the Abitibi and Wawa subprovinces; Summary of fieldwork and other activities 2010, Ontario Geological Survey, Open Files Report 6260, p. 3-1–3-6.

Bleeker, W., 2015. Synorogenic gold mineralization in granite-greenstone terranes: The deep connection between extension, major faults, synorogenic clastic basins, magmatism, thrust inversion, and long-term preservation; *in* Targeted Geoscience Initiative 4: Contributions to the Understanding of Precambrian Lode Gold Deposits and Implications for Exploration; Geological Survey of Canada, Open File 7852, p. 25–47.

Detour Gold Corporation, 2017. Detour Lake operation Ontario, Canada: NI 43-101 Technical Report; Detour Gold Corporation, 304 p. <http://s22.q4cdn.com/327131108/files/doc_news/archive/DGC-PR-17-03-22-LOM-Plan.pdf> [accessed October 31, 2017].

Dubosq, R., Schneider, D., Lawley, C.J.M., Jackson, S.E., and Yang, Z., 2017. Deciphering sulfide recrystallization and Au remobilization through 2D chemical mapping and microstructural analysis, Detour Lake mine, Superior Province; Proceedings of the 14th SGA Biennial Meeting, Québec, Quebec, p. 127–130.

Faure, S., 2015. Prolongement de la faille Sunday Lake (mine Detour Gold, Ont.) au Québec et son potentiel pour les minéralisations aurifères et en métaux de base; CONSOREM Project Report 2013-02, 41 p.

Gosselin, P. and Dubé, B., 2005. Gold deposits of Canada: distribution, geological parameters and gold content; Geological Survey of Canada, Open File 4896, 105 p., 1 CD-ROM.

Oliver, J., Ayer, J., Dubé, B., Aubertin, R., Burson, M., Panneton, G., Friedman, R., and Hamilton, M., 2012. Structure, Stratigraphy, U-Pb Geochronology, and Alteration Characteristics of Gold Mineralization at the Detour Lake Gold Deposit, Ontario, Canada; Exploration and Mining Geology, v. 20, p.1–30.

Malcolm, K.J., Kontak, D.J., Tinkham, D.k., Ayer, J.A., and MacGillivray, G., 2015. The Lower Detour Lake Au Discovery, Ontario, Canada: A High-Grade Oxidized Intrusion-Related Au Deposit; AGU-GAC-MAC-CGU Joint Assembly, Montréal, Quebec, p.302–303.

Marmont, S., 1986. The geological setting of the Detour Lake gold mine, Ontario, Canada; Proceedings of Gold '86 symposium, Toronto, p. 3–22.

Mercier-Langevin, P., Hannington, M., Dubé, B., McNicoll, V., Goutier, J., and Monecke, T., 2011. Geodynamic influences on the genesis of Archean world-class gold-rich VMS deposits: examples from the Blake River Group, Abitibi greenstone belt, Canada; *in* Proceedings 11th Biennial SGA meeting, Antofagasta, Chile, p. 85–87.

Robert, F., 1990. Structural setting and control of gold-quartz veins of the Val d'Or area, southeastern Abitibi subprovince; *in* Gold and base-metal mineralization in the Abitibi subprovince, Canada, with emphasis on the Quebec segment, University of Western Australia, Publication No. 24, p. 167–210.

Thurston, P.C., Ayer, J.A., Goutier, J., and Hamilton, M.A., 2008. Depositional gaps in Abitibi greenstone belt stratigraphy: A key to exploration for syngenetic mineralization; Economic Geology, v. 103, p. 1097–1134.

Structural controls and relative timing of events at the orogenic Island Gold deposit, Michipicoten greenstone belt, Wawa, Ontario

K.M. Jellicoe[1], S. Lin[1], T.J. Ciufo[1], C. Yakymchuk[1] and P. Mercier-Langevin[2]

[1]*University of Waterloo, 200 University Ave W, Waterloo, Ontario, N2L 3G1*
[2]*Geological Survey of Canada, 490 rue de la Couronne, Québec, Quebec, G1K 9A9*

Abstract

The Goudreau Lake Deformation Zone (GLDZ) transects the Michipicoten greenstone belt and hosts multiple gold deposits, most notably the Island Gold deposit. This structural study aims to determine the deformation history of the deposit and surrounding area, and to improve current exploration models. The GLDZ strikes east-northeast, sub-parallel to regional stratigraphy and foliation, and is centred along the contact of two metavolcanic assemblages. The Island Gold deposit is located in the southern metavolcanic assemblage, to the south of the trondhjemitic Webb Lake Stock. The main Island Gold deposit forms a mineralized corridor comprising steeply south-dipping ore zones. The Goudreau zone occurs to the north of the main deposit and contains tightly folded sub-horizontal ore veins. Two generations of deformation and multiple vein generations have been identified in the study area on the basis of overprinting and cross-cutting relationships. Mineralization is interpreted to have occurred during D1 sinistral north-side-up transpression.

Introduction

Gold mining in the Michipicoten greenstone belt of the Wawa subprovince has been ongoing for more than a century (Sage, 1994). Recent discoveries have reignited interest in the area and generated the need for enhanced knowledge to vector toward additional prospective areas. The richest deposits of the Michipicoten greenstone belt occur along the Goudreau Lake Deformation Zone (GLDZ), which transects the belt north of the Goudreau Anticline. The GLDZ is part of a regionally continuous fault zone that hosts multiple gold deposits, most notably the high-grade Island Gold deposit near Dubreuilville, Ontario. It has been correlated with the gold-rich Cadillac-Larder Lake Fault Zone of the Abitibi greenstone belt, across the Kapuskasing Structural Zone (Leclair et al., 1993), and also lies in proximity to the prolific Hemlo gold camp located to the northwest. The Island Gold deposit presents a unique opportunity to observe the western extension of an economically important regional fault zone.

This structural study is focused on the Island Gold deposit and the GLDZ immediately surrounding it. The aims are to resolve the deformation history of the area, as well as improving exploration models, by: i) establishing and characterizing the episodes of deformation in the GLDZ; ii) defining the generations of veining in the Island Gold deposit; iii) constraining the relative and absolute timing of the deformation and mineralizing events; and iv) determining the structural controls on mineralization.

Methods

Surface and in-mine underground mapping have been conducted with samples collected for gold assay, petrographic analysis and U-Pb geochronology. Structural and lithologic mapping records the planar and linear fabrics, kinematic indicators and crosscutting relationships between the various fabrics to decipher the complex polyphase deformation. Petrographic analysis is conducted in conjunction with mapping to identify kinematic indicators and identify compositional variation between vein generations.

Regional and Island Gold deposit geology

The GLDZ is up to 4.5 km wide and strikes east-northeast for at least 30 km. It is subparallel to regional stratigraphy and foliation, and is centred at the contact between the Michipicoten Iron Formation, which caps the 2750 Ma Wawa assemblage and the mafic volcanics of the 2700 Ma Catfish assemblage (Heather and Arias, 1992). The Island Gold deposit forms a mineralized corridor in the intermediate to felsic volcanics of the upper Wawa assemblage, south of the mafic-hosted past-producing Kremzar gold mine and east of the Webb Lake Stock-hosted Magino gold mine. The deposit is comprised of the Island Gold, Island Deep, Lochalsh, and Extension 1 and 2 Zones, which lie along the same strike, and the Goudreau Zone that lies to the north (Fig. 1). The Island and Extension Zones are hosted in intermediate to felsic volcanic rocks and consist of six subparallel ore zones with an average strike of 060° and

---
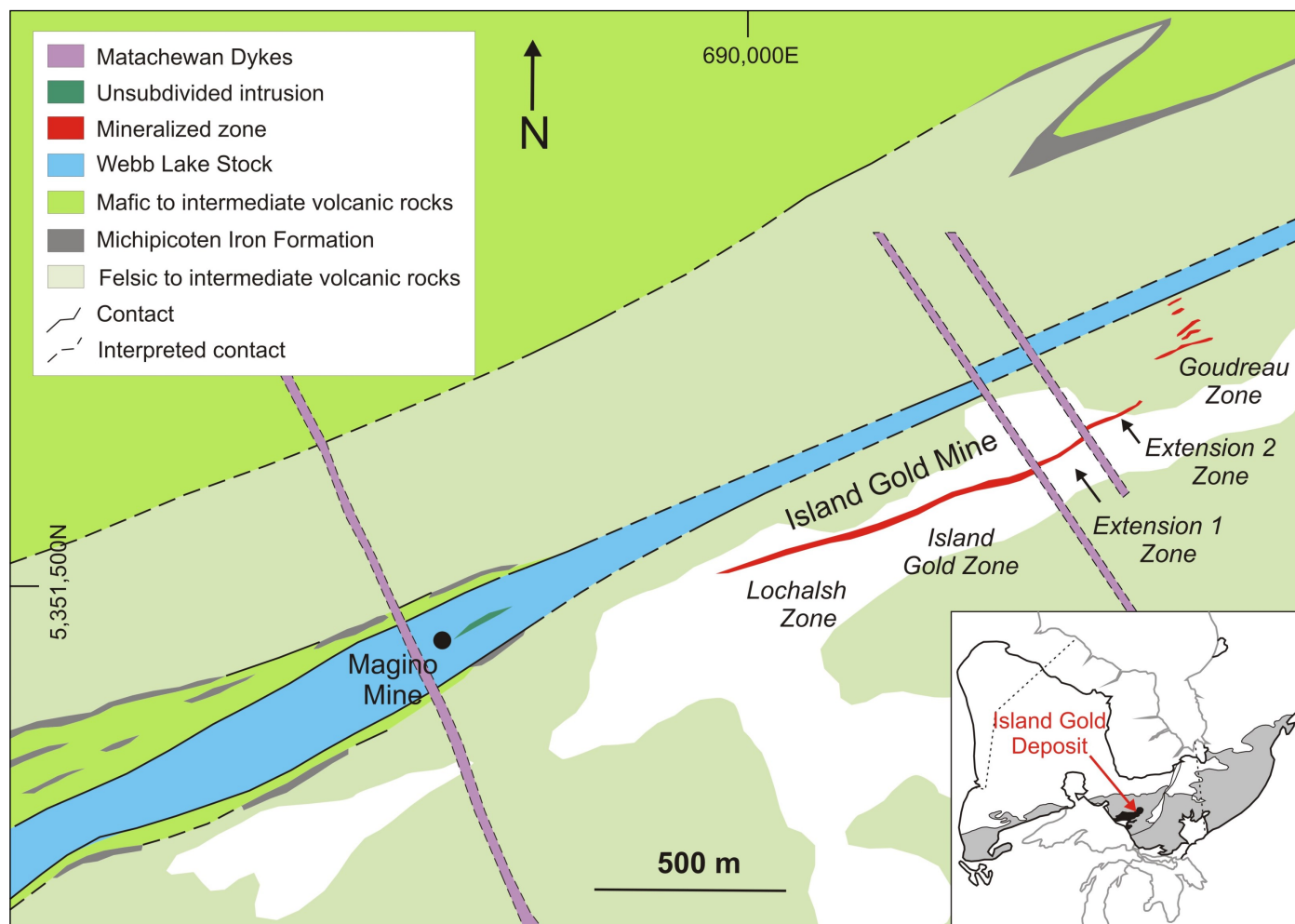
Figure 1: Camp-scale simplified geological map of study area showing surface traces of Island Gold ore zones (in red) and Webb Lake Stock intrusion (in blue). Inset map shows Wawa-Abitibi sub-province in grey and Michipicoten greenstone belt in black. Inset map modified from Card (1990).

dip of 80° to the south. The C zone is the most continuous and consistently high-grade of these ore zones and is the main economic target. The Goudreau Zone, which consists of tightly folded horizontal ore veins and several steeply dipping ore zones, is hosted by both intermediate to felsic volcanic rocks and dioritic intrusions.

Interim structural interpretations

At least two generations of deformation have been identified in the study area. The earlier generation, D1, is associated with sinistral, north-side-up transpression (Fig. 2a), while D2 is associated with dextral, south-side-up transpression (Fig. 2b). The main Island Gold zones occur along strike and sub-parallel to the long arm of a bend in the Webb Lake Stock at depth, which suggests that the geometry of the stock may have played an important role in the formation of the deposit and location of the mineralized veins., Cross-cutting relationships define a

preliminary timing sequence for the multiple vein generations identified. V1a extensional mineralized veins, V1b mineralized shear veins (Fig. 2c, d), and V1c weakly mineralized crack-seal veinlets (Fig. 2c) were emplaced during progressive D1. V2 veins (Fig. 2c) were emplaced during late D1 and overprint V1b and V1c veins. Barren sub-horizontal V3 extensional veins are associated with D2 and cut the ore zone, but do not significantly affect mineralization. Late V4+ quartz-tourmaline veins overprint and crosscut all previous vein generations.

Future work

Future work will include the compilation of structural observations and a comprehensive analysis of the deformation and veining history at the Island Gold deposit. Differentiating and characterizing generations of veins and their crosscutting relationships, on surface and underground, allows us to characterize the generations of deformation that they are associated
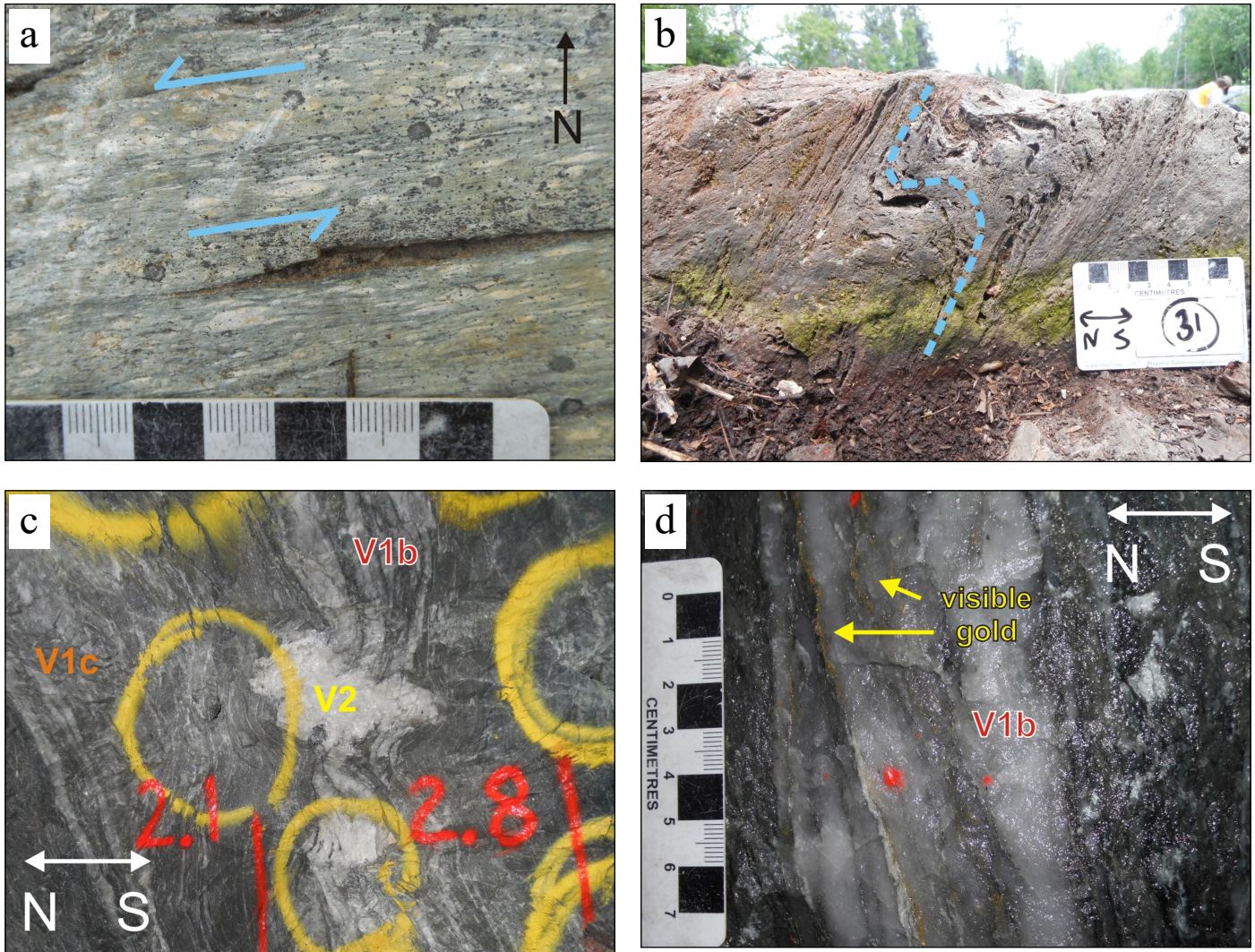
Figure 2: Photographs of outcrops and drift faces at Island Gold deposit: a) Plan-view of D1-related planar fabric in porphyritic tuff, showing a sinistral component of shearing; b) Vertical face showing D1-related foliation (blue dashed line) folded by later deformation suggesting an apparent normal motion (south-side-up); c) Vertical blasting face in mining drift showing sub-vertical, smoky grey quartz ore veins (V1b) and sub-parallel crack-seal veinlets (V1c) cut by later, weakly mineralized milky white quartz veins (V2); d) Close-up of visible gold in smoky grey quartz ore vein (V1b).

with. This allows mineralization, which occurs in specific vein sets, to be correlated with episodes of deformation. U-Pb dating of the Webb Lake Stock, which is mineralized, will place an older age limit on the absolute timing of mineralization and the associated generation of deformation, while dating an intrusion which cross-cuts the mineralization will give a younger age limit on the mineralizing system.

References

Card, K.D., 1990. A review of the Superior Province of the Canadian Shield, a product of Archean accretion; Precam-

brian Research, v. 48, p. 99–156.

Heather, K.B. and Arias, Z., 1992. Geological and structural setting of gold mineralization in the Goudreau-Lochalsh area, Wawa gold camp; Ontario Geological Survey, Open File Report 5832.

Leclair, A.D., Ernst, R.E., Hattori, K., 1993, Crustal-scale auriferous shear zones in the central Superior province, Canada; Geology, v. 21, p. 399–402.

Sage, R.P., 1994. Geology of the Michipicoten greenstone belt; Ontario Geological Survey, Open File Report 5888.

Hydrothermal alteration and vectors at the orogenic Island Gold deposit, Michipicoten greenstone belt, Wawa, Ontario

T.J. Ciufo[1], C. Yakymchuk[1], S. Lin[1], K. Jellicoe[1] and P. Mercier-Langevin[2]

[1]*University of Waterloo, 200 University Ave West, Waterloo, Ontario, N2L 3G1*
[2]*Geological Survey of Canada, 490 rue de la Couronne, Québec City, Québec, G1K 9A9*

Abstract

The orogenic Island Gold deposit, located in the Michipicoten greenstone belt, is part of the Goudreau-Lochalsh gold district. Preliminary results indicate that gold is hosted in multiple subparallel mineralized zones along well-defined shear zones that generally strike east-northeast with a steep southerly dip. The alteration envelope is a combination of silicification, sericitization, carbonatization, pyritization and chloritization. Quartz "flooding" (silicification) as well as quartz veins are often present at the core of these alteration envelopes and commonly contain visible gold. Alteration quickly decreases in intensity away from the veins and deformation corridors. Ongoing work aims at further characterizing the alteration styles and compare with other orogenic gold deposits and at constraining the source of the gold-bearing fluid and conditions of gold mineralization. Achieving these objectives will aid in exploration efforts to expand resources and find new deposits as well as contribute to the understanding of orogenic gold deposits.

Introduction

Greenstone belts of the Superior Province host many world-class orogenic gold deposits and are significant economic drivers for many communities (Goldfarb et al., 2001). The Goudreau-Lochalsh gold district in the Michipicoten greenstone belt hosts a number of orogenic gold deposits and is being actively mined and explored. These deposits are located in or associated with the Goudreau Lake Deformation Zone (GLDZ) (Fig. 1; Adam et al., 2015). In this study, the alteration at the Island Gold deposit will be investigated and compared to the alteration at well-studied orogenic gold deposits in other areas. This aim will be undertaken by establishing the geochemical and petrographical signature of the alteration associated with the auriferous zones. This will contribute to the development of a comprehensive model for the geological history of the deposit. The principal objectives are to: i) characterize the alteration envelope associated with various gold-bearing quartz veins and compare this alteration to those in other orogenic gold deposits; ii) establish mineralogical and textural indicators for gold mineralization; iii) determine the protoliths of the altered lithologies; iv) determine the source of the gold-bearing fluid and conditions of gold mineralization; and v) determine the age(s) of gold mineralization and protoliths.

Methods

In order to study each part of the alteration envelope, samples were taken moving progressively outward from an ore zone, moving from strongly to less altered rock. Multiple transects were conducted across ore zones at varying depths, locations along the strike of the GLDZ, and within different host lithologies. To identify the protoliths of altered lithologies within the GLDZ, samples of less-altered rocks were also taken from outside the deformation zone that are equivalent to the altered lithologies within the GLDZ. Samples were selected for whole-rock geochemistry and polished thin sections. Detailed petrographic and scanning electron microscope energy-dispersive X-ray spectroscopic analysis, including point-counting to determine mineral concentrations, is ongoing. Mineralogy and textures are correlated with gold grade to investigate possible gold mineralization indicators. Elemental and isotopic mapping of pyrite grains may also be conducted by Laser Ablation Inductively Coupled Plasma Mass Spectrometry to elucidate the relative timing of auriferous pyrite growth. Geochemical data is used to establish the protoliths of altered rocks, study bulk chemical changes moving outward from the ore zone, and establish alteration indexes to classify the degree of hydrothermal alteration (weak, moderate or strong).

Sulphur isotope analyses (Δ^{33}S and δ^{34}S) will provide constraints on the gold-bearing fluid source and geothermometry. Gold inclusions are common within the pyrite grains from the Island Gold deposit. As there is an intimate association of sulphide minerals (mainly pyrite) with the ore zones, it is suspected that sulphur and gold were introduced into the system together. The δ^{34}S and Δ^{33}S values define whether sulphur (and by extension gold) is derived from a magmatic, sedimentary or meteoric source (Ohmoto and Rye, 1979; Lambert et al., 1984; Xue et al., 2013). Sulphur isotopes may also be used to approximate temperature of mineralization using the equations of Ohmoto and Rye (1979).

To determine the age(s) of gold mineralization at the Island Gold deposit, U-Pb geochronology will be performed on zir-

---
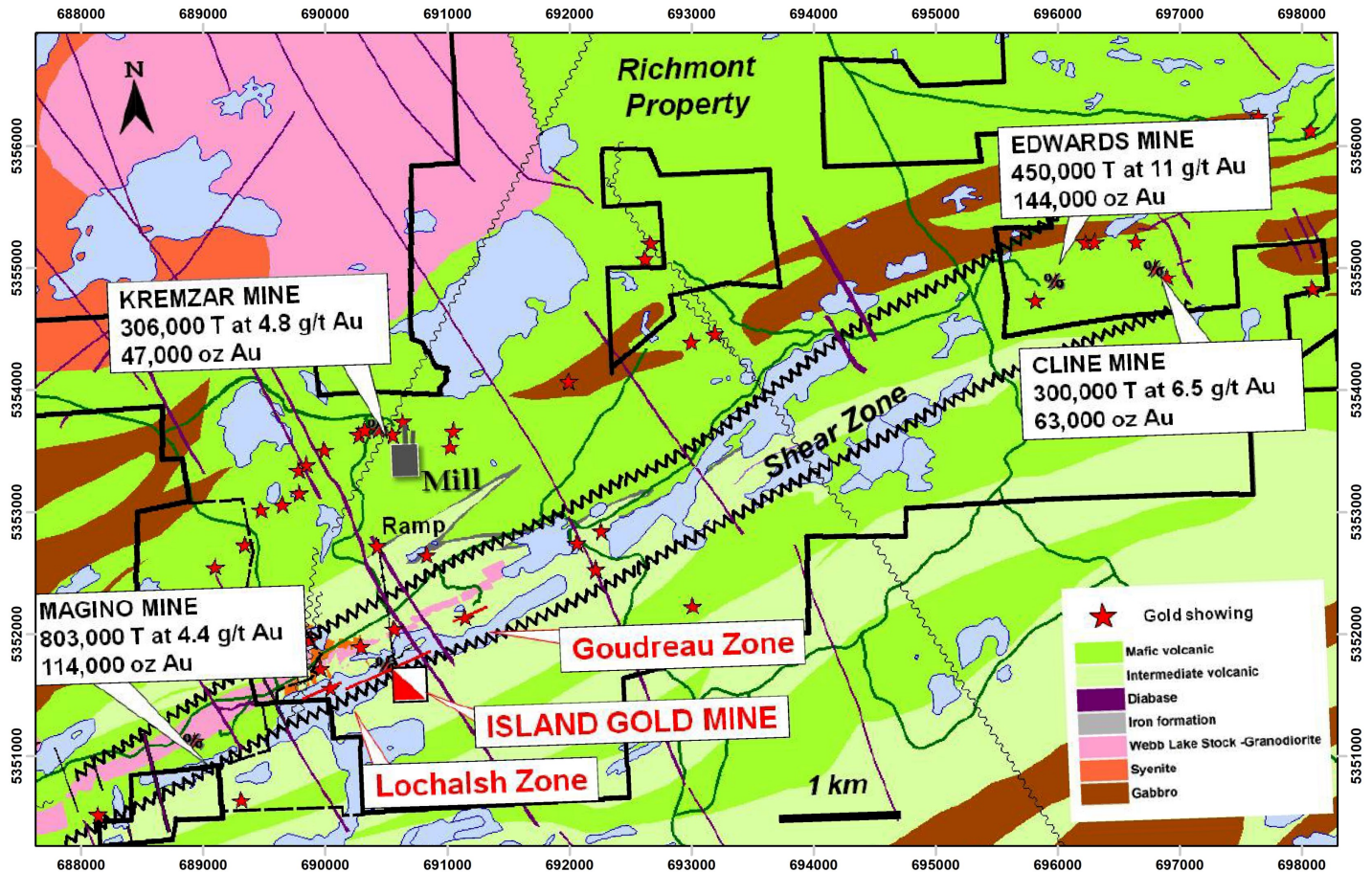
Figure 1. Local geology map of the Island Gold deposit with locations of other mines, gold showings, and zones of gold mineralization. The coordinate system used is NAD 1983 UTM Zone 16N. Past production and resource estimates from these non-operational mines are from Adam et al. (2015) and may not be NI43-101 compliant. Modified from Adam et al. (2015).

cons from an intensely altered dacitic tuff in an ore zone and a relatively unaltered dacitic tuff nearby. Zircon from the unaltered sample will be used to determine the age of the protolith. Zircons from the altered sample may show evidence of recrystallization or lead loss, which can be used to constrain the age of alteration and hence bracket the timing of gold mineralization (Schneider et al., 2012). Cathodoluminescence imaging will be used to characterize zircon morphology and zoning.

Island Gold regional and deposit geology

The Island Gold deposit, in addition to other gold deposits in the Goudreau-Lochalsh gold district, is closely tied to a large deformation corridor known as the Goudreau Lake Deformation Zone (GLDZ; Fig. 1) and its fault splays (Heather and Arias, 1987). Rocks within the GLDZ have been metamorphosed to greenschist facies and subject to various degrees of deformation and hydrothermal alteration. The Island Gold deposit is primarily hosted within felsic to intermediate volcanic rocks that were interpreted by Sage (1994) to have been generated during the region's second cycle of volcanism. A variety of mafic to felsic intrusive units are identified at the Island Gold deposit, but their protoliths are typically obscured by metamorphism, deformation and hydrothermal alteration. Gold is hosted in multiple subparallel mineralization zones that generally strike east-northeast with a steep southerly dip (Adam et al., 2015). These shear-hosted zones consist of an envelope of alteration and strain that decreases in intensity moving outwards (Fig. 2a). The alteration envelope consists of a combination of silicification, sericitization, carbonatization, pyritization and chloritization. Quartz "flooding" as well as quartz veins are often present at the core of these alteration envelopes and commonly contain visible gold (Fig. 2b).

Acknowledgments
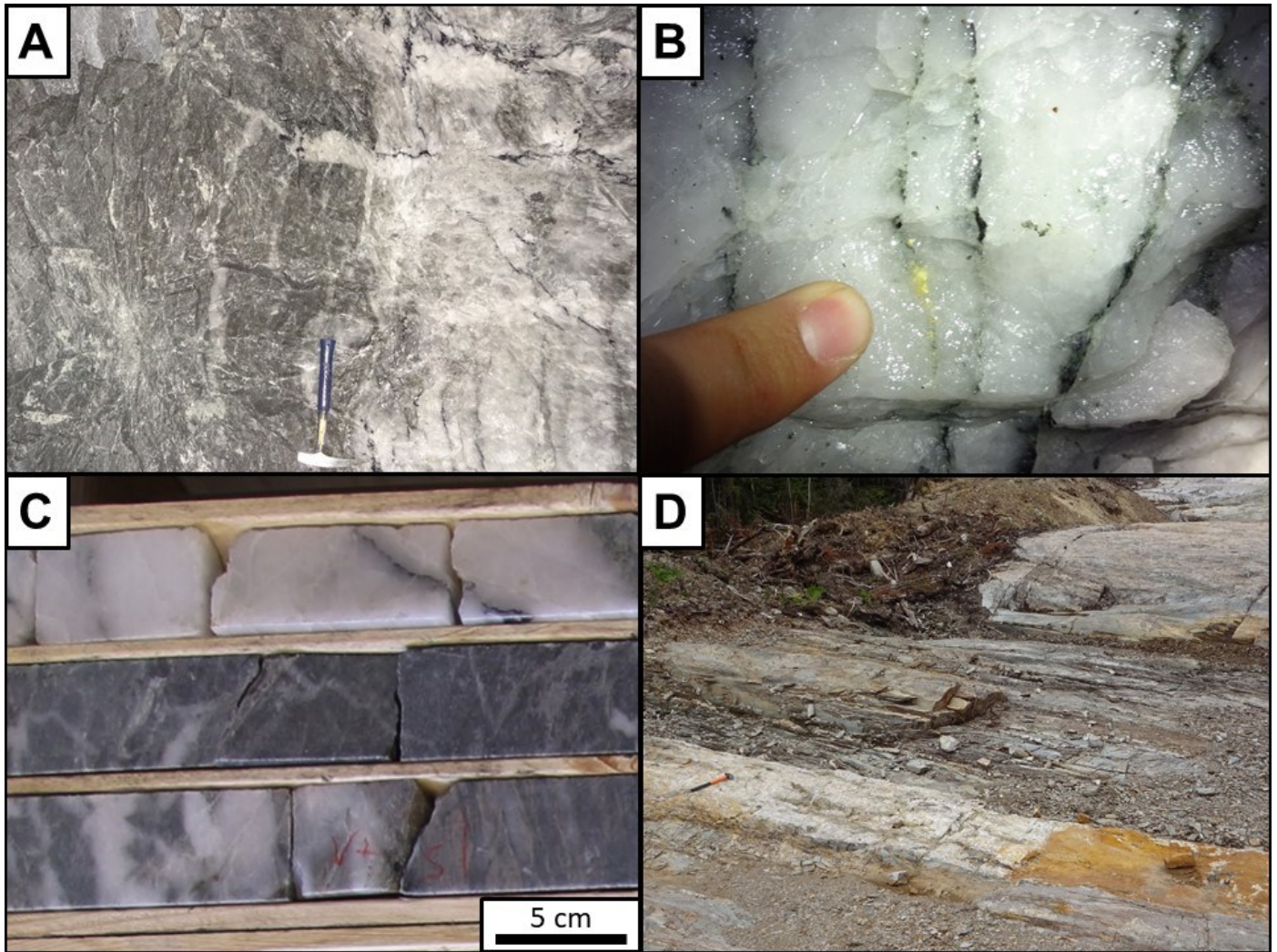
Figure 2. Photographs of quartz veins and their alteration envelopes: a) Visible gold-bearing quartz vein (right) and strongly hydrothermally altered volcanic rock (left) observed underground; b) Quartz vein with tourmaline and visible gold; c) Drill core composed of gold-bearing quartz veins with tourmaline seams as well as altered dacitic volcanic rock; d) Quartz vein and associated alteration envelope exposed on surface. The quartz vein and altered volcanic rocks in the bottom left of the photo distinctly transition into less altered volcanic rocks moving towards the upper right of the photo (away from the quartz vein).

References

Adam, D., Bastien, J., Bélisle, M., and Poirier, S., 2015. Technical report and preliminary economic assessment for the Island Gold Lower Zones (according to National Instrument 43-101 and Form 43-101F1); Richmont Mines Inc., Rouyn-Noranda, Quebec, p. 58–72.

Goldfarb, R.J., Groves, D.I., and Gardoll, S., 2001. Orogenic gold and geologic time: a global Synthesis; Ore Geology Reviews, v. 18, p. 1–75.

Heather, K.B. and Arias, Z.G., 1987. 024: Geological setting of gold mineralization in the Goudreau-Lochalsh area, District

of Algoma; *in* Summary of Field Work and Other Activities 1987, (ed.) R.B. Barlow, M.E. Cherry, A.C. Colvine, B.O. Dressler and O.L. White; Ontario Geological Survey, Miscellaneous Paper 137, p. 155–162.

Lambert, I.B., Phillips, G.N., and Groves, D.I., 1984. Sulfur isotope compositions and genesis of Archaean gold mineralization, Australia and Zimbabwe; *in* Gold '82: The Geology, Geochemistry and Genesis of Gold Deposits, (ed.) R.P. Foster. Geological Society of Zimbabwe Special Publication 1, p. 373–387.

Ohmoto, H. and Rye, R., 1979. Isotopes of sulfur and carbon; *in* Geochemistry of Hydrothermal Ore deposits, 2nd edition, (ed.) H.L. Barnes; Wiley, New York, p. 509–567.

Sage, R.P., 1994. Geology of the Michipicoten Greenstone Belt; Ministry of Northern Development and Mines, Ontario Geological Survey, Open File Report 5888, p. 22-34, 168–171.

Schneider, D.A., Bachtel, J., and Schmitt, A.K., 2012. Zircon alteration in wall Rock of Pamour and Hoyle Pond Au deposits, Abitibi Greenstone Belt: Constraints on timescales of fluid flow from depth-profiling techniques; Economic Geology, v. 107, p. 1043–1072.

Xue, Y., Campbell, I., Ireland, T.R., Holden, P., and Armstrong, R., 2013. No mass-independent sulfur isotope fractionation in auriferous fluids supports a magmatic origin for Archean gold deposits; Geology, v. 41, p. 791–794.

Geology of the Éléonore gold mine and adjacent gold showings, Superior Province, northern Quebec

A. Fontaine[1], B. Dubé[2], M. Malo[1], V.J. McNicoll[3], N. Prud'homme[4], C. Beausoleil[4] and J. Goutier[5]

[1]*Institut national de la recherche scientifique, Centre Eau Terre Environnement, 490 rue de la Couronne, Québec, Quebec, G1K 9A9*

[2]*Geological Survey of Canada, 490 rue de la Couronne, Québec, Quebec, G1K 9A9*

[3]*Geological Survey of Canada, 601 Booth Street, Ottawa, Ontario, K1A 0E8*

[4]*Goldcorp Inc., Éléonore Mine, 853, boulevard Rideau, Rouyn-Noranda, Quebec, J9Y 0G3*

[5]*Ministère de l'Énergie et des Ressources naturelles du Québec, 70, avenue Québec, Rouyn-Noranda, Quebec, J9X 6R1*

Abstract

Located in the northeastern part of the Superior Province, the Éléonore mine had mineral reserves of 4.57 Moz (23.44 Mt at 6.07 g/t Au), measured and indicated gold mineral resources of 0.93 Moz (5.14 Mt at 5.66 g/t Au) and inferred mineral resources of 2.35 Moz (9.73 Mt at 7.52 g/t Au). Predominantly hosted by metamorphosed and deformed turbiditic rocks of the La Grande subprovince, the deposit is located 1.5 km south of the tectonometamorphic boundary with the Opinaca subprovince. Subparallel ore zones composed an envelope with a width of 70 to 80 m and vertical extension of >1.4 km. Associated with potassic, boron- and calcium-rich alteration assemblages and Au-As-Sb-Bi-W metallic signature, gold mineralization is associated with disseminations of arsenopyrite, pyrrhotite and löllingite. Various mineralization styles include veins and hydrothermal breccia, replacement zones, stockwork of quartz veins and veinlets composed of quartz, dravite, microcline, phlogopite, actinolite, diopside, hedenbergite, muscovite and schorl. Recent activities include field and underground mapping on the Éléonore, Éléonore South and Cheechoo properties. Gold mineralization also occurs within the Cheechoo tonalite/granodiorite, pegmatites and paragneiss (Cheechoo and Moni prospects). At Cheechoo and Moni, gold mineralization is structurally-controlled and associated with the presence of quartz-feldspar-(biotite-arsenopyrite-scheelite) sheeted veinlets in association with silicification albitization and 1 to 2% of arsenopyrite, pyrrhotite, pyrite and visible gold. This emerging gold district shares analogies with hypozonal orogenic gold deposits and reduced intrusion-related gold systems and illustrates the potential of an area affected by a high metamorphic gradient near a subprovince boundary.

Introduction

It has become apparent that there is a greater diversity of gold mineralization in the Superior Province than had been considered (Dubé et al., 2015). Gold mineralization in high-grade metamorphic terrains is frequently labelled as 'atypical'. Critically reassessing these so-called atypical deposits may lead to new deposit models that will open-up additional areas to exploration. The Éléonore mine (Roberto gold deposit) is a metamorphosed sediment-hosted stockwork-disseminated ore (Dubé et al., 2015), an emerging deposit type in Archean greenstone belts (i.e. Canadian Malartic; De Souza et al., 2015). The Roberto deposit is located approximately 1.5 km south of the boundary between the Opinaca and La Grande subprovinces. The ca. 2612 Ma tonalite/granodiorite hosted Cheechoo and Moni showings, 12 km southeast of Éléonore, present an opportunity to study the potential role of magmatism on gold mineralization (Fontaine et al., 2017a). To resolve the evolution of this deposit, it is critical to establish whether the mineralizing system results from multiphase or distinct auriferous event(s), if gold is metamorphic and/or magmatic in origin, and if the main mineralizing event is pre- or syn-peak metamorphism.

Éléonore mine geology

The Éléonore mine is located in the Eeyou Istchee James Bay municipality, northern Quebec (Fig. 1). The deposit is mainly hosted by Archean metasedimentary rocks of the Low Formation (Bandyayera and Fliszár, 2007). The Low Formation is a turbiditic sequence composed of, a basal polymictic conglomerate and a thick turbiditic sequence including arenite, wacke and mudstone (Bandyayera and Fliszár, 2007; Bandyayera et al., 2010). The Éléonore property straddles the boundary between the Opinaca Subprovince (paragneiss, migmatites and syn- to post-tectonic intrusions) and the La Grande Subprovince (reworked Meso- to Neoarchean volcano-sedimentary sequences with syn- to late-tectonic intrusions).
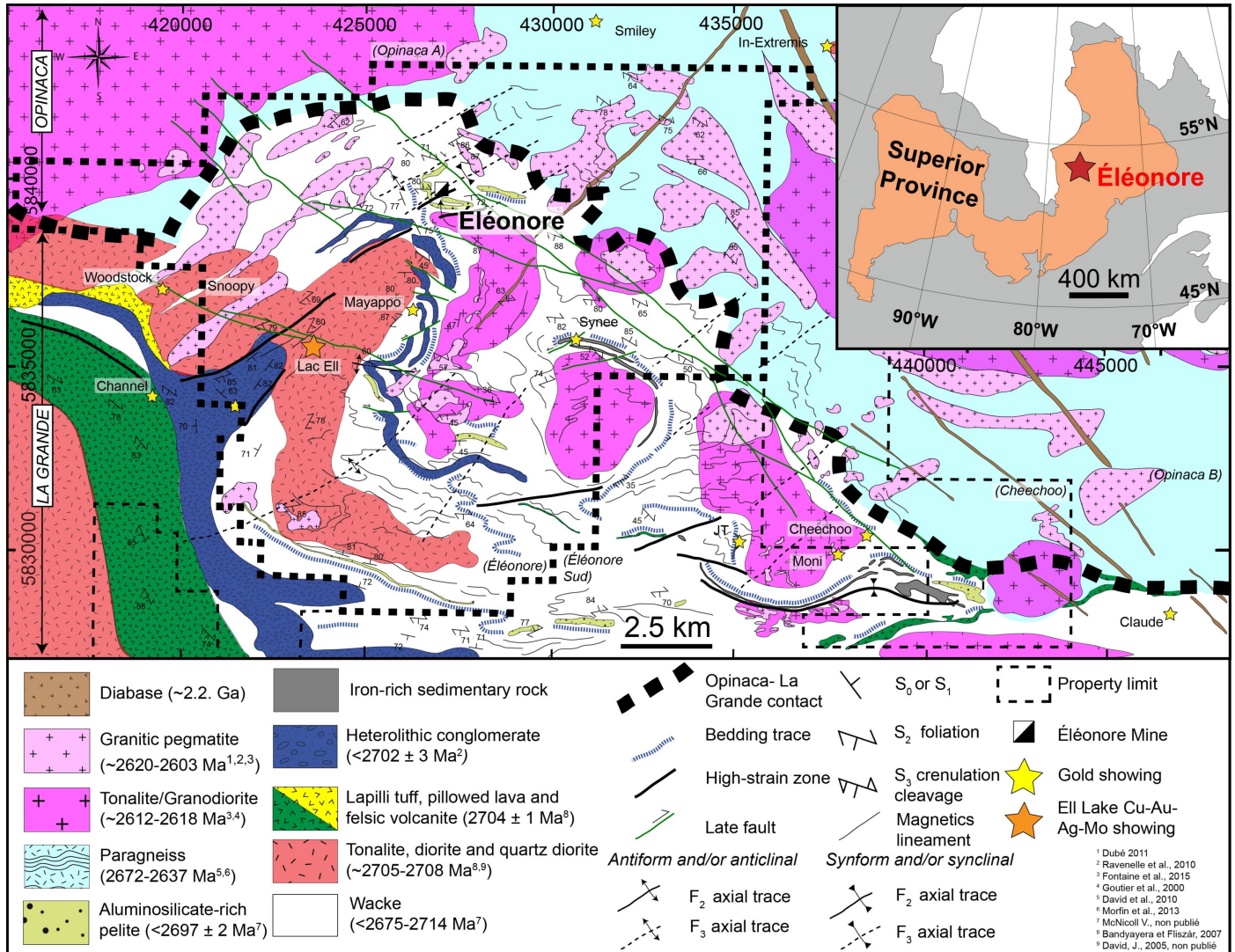
Figure 1. Regional geology of the Éléonore mine area. Modified after Bandyayera and Fliszár, (2007), Bandyayera et al. (2010), David et al. (2010), Ravenelle et al. (2010), Dubé et al. (2011), Morfin et al. (2013), Fontaine et al. (2015, 2017a, b).

Underground and surface mapping at the Éléonore mine and adjacent gold showings indicate a diversity of mineralization styles and settings (Fig. 2; Fontaine et al., 2015, 2017a, b). Auriferous zones occur as veins and replacements mainly hosted in metasedimentary rocks (Fig. 2a–c), quartz-rich diorite (Fig. 2d), the Cheechoo tonalite/granodiorite (Fig. 2e) and also locally pegmatites, amphibolite schist (Fig. 2f) or dykes (including lamprophyre). Field studies on the Cheechoo showing indicate structural control on the distribution and geometry of auriferous sheeted quartz and quartz-feldspar-(biotite-arsenopyrite-scheelite) veins and veinlets within the Cheechoo tonalite/granodiorite. The veinlets are spatially associated with pegmatite dykes and are commonly more abundant towards the contact with the surrounding chloritized wacke. Visible gold also occurs in some folded sheeted quartz-(feldspar) veins.

Disseminated arsenopyrite and pyrrhotite occurs along vein selvages in the 'silicified' tonalite, in association with albite, actinolite and diopside.

Summary

The Éléonore mine is an important Archean example of a deformed orogenic gold deposit being overprinted, at least in part, by high-grade metamorphism (Dubé et al., 2015, 2017; Fontaine et al., 2015, 2017a, b). This is well illustrated by the metamorphosed ore zones present at depth. Detailed underground mapping suggests that pegmatites cut the bulk of the gold mineralization within the mine (Fontaine et al., 2017a, b). However, pegmatite dykes are locally gold bearing and transitional to quartz-feldspar auriferous veins and veinlets (Ravenelle, 2013).
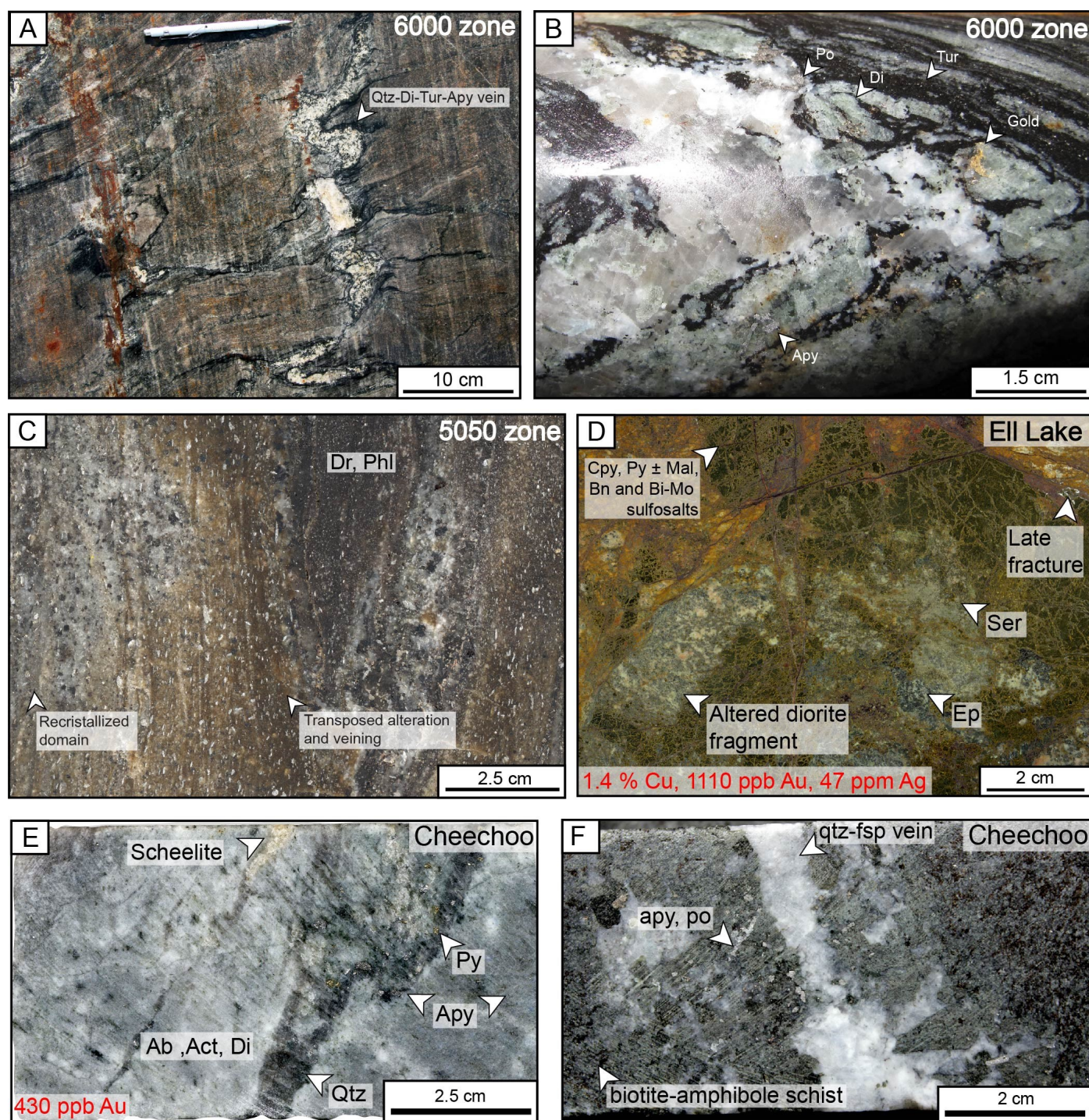
Figure 2. Examples of gold ore from the Éléonore deposit, Ell Lake and Cheechoo showings: a) Folded quartz-diopside-arsenopyrite-schorl vein; b) Quartz-diopside-schorl-arsenopyrite-pyrrhotite-visible gold vein; c) Deformed and metamorphosed Roberto zone; d) Chalcopyrite-rich Ell Lake zone with altered fragment of the ca. 2705 Ma Ell Lake diorite; e) Quartz-pyrite-arsenopyrite-scheelite vein within altered and foliated, ca. 2612 Ma Cheechoo tonalite/granodiorite; f) Quartz-feldspar-arsenopyrite vein within amphibole-biotite schist near the contact between Cheechoo tonalite/granodiorite and surrounding metasedimentary rocks. Abbreviations: Ab = albite; act = actinote; apy = arsenopyrite; Bn = bornite; Cpy = chalcopyrite; Di = diopside; Dr = dravite; Ep = epidote; fsp = feldspar; Mal = malachite; Qtz = quartz; Phl = phlogopite; Po = pyrrhotite; Py = pyrite; Ser = sericite; Tur = tourmaline.

Overall, this emerging gold district shares strong similarities with hypozonal orogenic gold deposits (Kolb et al., 2015) as well as more locally with reduced intrusion-related gold systems (Thompson and Newberry, 2000; Goldfarb et al., 2005; Hart, 2007). However, to decipher the setting of this deposit, the timing of gold introduction and potential role of magmatism need to be further investigated. Thus, further work is targeting these aspects through a multidisciplinary approach combining field and underground mapping, U-Pb geochronology, lithogeochemistry and petrographic observations.

Acknowledgments

References

Bandyayera, D. and Fliszár, A., 2007. Géologie de la région de la baie Kasipasikatch (33C09) et du lac Janin (33C16); Ministère des Ressources naturelles et de la Faune, Quebec, RP 2007-05, 15 p., 2 maps.

Bandyayera, D., Rhéaume, P., Maurice, C., Bédard, É., Morfin, S., and Sawyer, E., 2010. Synthèse géologique du secteur du réservoir Opinaca, Baie-James; Ministère des Ressources naturelles et de la Faune, Quebec, RG 2010-02, 46 p., 1 map.

Card, K. and Ciesielski, A., 1986. Subdivisions of the Superior Province of the Canadian shield; Geoscience Canada, v. 13, p. 5–13.

David, J., Vaillancourt, D., Bandyayera, D., Simard, M., Dion, C., Goutier, J., and Barbe P., 2010. Datations U-Pb effectuées dans les sous-provinces d'Ashuanipi, de La Grande, d'Opinaca et d'Abitibi en 2008–2009; Ministère des Ressources naturelles et de la Faune, Quebec, RP 2010-11, 37 p.

De Souza, S., Dubé, B., McNicoll, V.J., Dupuis, C., Mercier-Langevin, P., Creaser R., and Kjarsgaard I., 2015. Geology, hydrothermal alteration, and genesis of the world-class Canadian Malartic stockwork-disseminated Archean gold deposit, Abitibi, Quebec; *in* Targeted Geoscience Initiative 4: Contributions to the Understanding of Precambrian Lode Gold Deposits and Implications for Exploration, (ed.) B. Dubé and P. Mercier-Langevin; Geological Survey of Canada, Open File 7852, p. 113–126.

Dubé, B., Fontaine, A., Ravenelle, J.-F., McNicoll, V.J., Malo, M., Beausoleil, C., and Goutier, J., 2017. Le gisement aurifère Éléonore, Eeyou Istchee Baie-James, Province du Supérieur: un système hydrothermal fertile et complexe dans un environnement hypozonal; Abstracts, Quebec Mines 2017, Québec, Quebec. <http://mern.gouv.qc.ca/events/gisement-aurifere-eleonore-eeyou-istchee-baie-james-province-superieur-systeme-hydrothermal-fertile-complexe-environnement-hypozonal/> [accessed December 14, 2017]

Dubé, B., Mercier-Langevin, P., Castonguay, S., McNicoll, V.J., Bleeker, W., Lawley, C.J.M., De Souza, S., Jackson S.E., Dupuis, C., Gao, J., Bécu, V., Pilote, P., Goutier, J., Beakhouse, G., Yergeau, D., Oswald, W., Janvier, V., Fontaine, A., Pelletier, M., Beauchamp, A.-M., Malo, M., Katz, L., Kontak, D., Tóth, Z., Lafrance, B., Gourcerol, B., Thurston, P., Creaser, R., Enkin, R., El Goumi, N., Grunsky, E., Schneider, D., Kelly, C., and Lauzière, K., 2015. Precambrian lode gold deposits – A summary of TGI-4 contributions to the understanding of lode gold deposits, with an emphasis on implications for exploration; *in* Targeted Geoscience Initiative 4: Contributions to the understanding of Precambrian lode gold deposits and implications for exploration, (ed.) P. Mercier-Langevin and B. Dubé; Geological Survey of Canada, Open File 7852, p. 1–24.

Dubé, B., Ravenelle, J-F., McNicoll, V.J., Malo, M., Creaser, R., Nadeau, L., and Simoneau, J., 2011. The world-class Roberto gold deposit, Éléonore property, James Bay area, Québec: Insights from geology and geochronology; Joint Annual Meeting of the GAC-MAC-SEG-SGA 2011 Abstracts, Geological Association of Canada, p. 55–56.

Fontaine, A., Dubé, B., Malo, M., McNicoll, V.J., Brisson, T., Doucet, D., and Goutier J., 2015. Geology of the metamorphosed Roberto gold deposit (Éléonore mine), Baie-James region, Québec: diversity of mineralization styles in a polyphase tectono-metamorphic setting; *in* Targeted Geoscience Initiative 4: Contributions to the understanding of Precambrian lode gold deposits and implications for exploration, (ed.) P. Mercier-Langevin and B. Dubé; Geological Survey of Canada, Open File 7852, p. 209–225.

Fontaine, A., Dubé, B., Malo, M., McNicoll, V.J, Jackson, S.E., Beausoleil, C., Layne, G.D, and Goutier, J., 2017a. Geology and insights on the genesis of the world-class Éléonore gold mine, Eeyou Istchee Baie-James, Superior Province, Quebec, Canada; *in* Proceeding of the 14th Biennial SGA Meeting, Québec, Quebec, p. 31–34.

Fontaine, A., Dubé, B., Malo, M., Ravenelle, J.-F., Fournier, E., McNicoll, V.J., Beausoleil, C., Prud'homme, N., and Goutier, J., 2017b. The Éléonore gold mine: Exploration, Discovery and Understanding of an emerging gold district in Eeyou Istchee James Bay, Superior Province, Northern Québec,

Canada; *in* Proceedings of Exploration 17: Sixth Decennial International Conference on Mineral Exploration, (ed.) V. Tschirhart and M.D. Thomas; Decennial Minerals Exploration Conferences, Toronto, Ontario, p.601-617.

Goldfarb, R.J., Baker, T., Dubé, B., Groves, D.I., Hart, C.J., and Gosselin, P., 2005. Distribution, character, and genesis of gold deposits in metamorphic terranes; Economic Geology, 100th anniversary volume 40, p. 407–450.

Hart, C.J., 2007. Reduced intrusion-related gold systems; *in* Mineral Deposits of Canada: A synthesis of Major deposit types, district metallogeny, the Evolution of geological provinces, and exploration methods, (ed.) W.D. Goodfellow; Geological Association of Canada, Mineral Deposits Division, Special Publication 5, p. 95–112.

Kolb, J., Dziggel, A., and Bagas, L., 2015. Hypozonal lode gold deposits: A genetic concept based on a review of the New Consort, Renco, Hutti, Hira Buddini, Navachab, Nevoria and The Granites deposits; Precambrian Research, v. 262, p. 20–44.

Morfin, S., Sawyer, E., and Bandyayera, D., 2013. Large volumes of anatectic melt retained in granulite facies migmatites: An injection complex in northern Quebec; Lithos, v. 168, p. 200–218.

Percival, J.A., 2007. Geology and metallogeny of the Superior Province, Canada; in Mineral Deposits of Canada: A synthesis of Major deposit types, district metallogeny, the Evolution of geological provinces, and exploration methods, (ed.) W.D. Goodfellow; Geological Association of Canada, Mineral Deposits Division, Special Publication 5, p. 903–928.

Ravenelle, J.-F. 2013. Amphibolite facies gold mineralization: An example from the Roberto deposit, Eleonore property, James Bay, Quebec; Ph.D. thesis, Université du Québec, Institut national de la recherche scientifique, Québec, Quebec, 325 p.

Ravenelle, J.-F., Dubé, B., Malo, M., McNicoll, V.J., Nadeau, L., and Simoneau, J., 2010. Insights on the geology of the world-class Roberto gold deposit, Éléonore property, James Bay area, Quebec; Geological Survey of Canada, Current Research 2010-1, 26 p.

Thompson, J. and Newberry, R., 2000. Gold deposits related to reduced granitic intrusions; Reviews in Economic Geology, v. 13, p. 377–400.

Preliminary geochemical results on mantle metal mobility

C.J.M. Lawley[1], B.A. Kjarsgaard[1], A. Zagorevski[1], G. Pearson[2], P. Waterton[2], D. Savard[3], S.E. Jackson[1], Z. Yang[1], S. Zhang[4] and V. Tschirhart[1]

[1]*Geological Survey of Canada, 601 Booth St., Ottawa, Ontario, K1A 0E8*

[2]*Department of Earth and Atmospheric Sciences, University of Alberta, Edmonton, Alberta, T6G 2E3*

[3]*Universite du Quebec a Chicoutimi, 555 Boulevard de l'Université , Chicoutimi, Quebec, G7H 2B1*

[4]*Department of Earth Sciences, Carleton University, 1125 Colonel By Drive, Ottawa, Ontario, K1S 5B6*

Abstract

Processes operating within mantle source regions likely impact the fertility of ore-bearing melts, although the precise link between mantle conditioning and ore genesis remain poorly understood. New fieldwork and isotopic (Re-Os and Pb-Pb) results for ultramafic samples from young (Mesozoic), ophiolitic mantle near Atlin British Columbia, document ancient (i.e. Paleoproterozoic and younger), refractory mantle domains hosted within variably depleted harzburgite. The metal endowment of these distinct mantle segments and the microscale distribution of gold, platinum group elements and base metals are the focus of on-going study.

Field-based research at Atlin complements chemical analysis of kimberlite-hosted mantle olivine and clinopyroxene xenocrysts. These mantle fragments provide a snapshot of the ancient, sub-continental lithospheric mantle beneath the Neoarchean Abitibi sub-province (Kirkland Lake kimberlite field). Geochemical depth profiles, based on preliminary in situ geochemical results of the least-altered xenocrysts, suggest that high temperature olivine is a significant silicate mineral host for some of the so-called chalcophile elements at depth (e.g. Cu and Zn). Other metals, including a rare subset of xenocrysts that yield concentrations for gold and platinum at or above the analytical detection limit (1 –5 ppb), occur as micro-inclusions. The distribution of metal-bearing mineral phases within the mantle and, the micro-scale setting of metals within those phases (e.g. mineral inclusions versus lattice substitution), may control the variable metallic endowment of mantle-derived melts in ancient and modern settings.

Introduction

Mantle-derived melts and their derivatives, such as ultramafic to mafic magmatic rocks, in modern and ancient settings (e.g. Archean greenstone belts) are important host rocks for gold, nickel-copper and platinum group element ore deposits. The fertility of these rocks is related, at least in part, to processes that operate within the mantle source regions, although the precise links between ore genesis and mantle conditioning remain unclear. Mantle processes can be examined via ophiolites, mantle-derived xenoliths and xenocrysts, or indirectly imaged by deep geophysical techniques. As ophiolites are not available for the Archean, mantle xenoliths and xenocrysts entrained within younger volcanic rocks such as kimberlites represent the only opportunity to study, date and elucidate mantle processes related to ore deposit genesis during the Archean and earliest Proterozoic.

This study has two parts that seek to document the distribution of base- and precious-metals within variably melted and re-fertilized mantle rocks, and to explore their role in the genesis of metal-rich melts that go on to host and/or serve as source rocks for gold, nickel-copper and platinum group element ore deposits. The first component focuses on modern ophiolitic sections where young oceanic mantle contains trapped mantle melts and re-fertilized mantle domains that can be observed directly. This aspect is targeting ultramafic rocks in and around Atlin, British Columbia, where excellent exposures enable the investigation into the impact of melting and re-fertilization on the mobility and distribution of base- and precious-metals within a highly-depleted segment of Phanerozoic mantle (Fig. 1, 2). The second component is lab-based and focuses on the ancient, Superior Province lithospheric mantle through in situ geochemical analysis of clinopyroxene and olivine xenocrysts sampled from the Kirkland Lake kimberlite field (Fig. 3, 4). These kimberlites erupted through one of the largest gold districts, providing an opportunity to investigate whether the exceptional metal endowment of the Abitibi Subprovince can be linked to its mantle heritage. The distribution of metals within mantle minerals (e.g. mineral inclusions versus lattice substitution) may ultimately explain the variable metallic endowment of mantle-derived melts in ancient and modern settings.

Inferences on mantle metal mobility from oceanic mantle

A Mesozoic ophiolite belt exposed around Atlin, British Columbia (Fig. 1; Zagorevski et al., 2015; 2017; McGoldrick et al., 2016), contains a variety of mantle lithologies, including

---
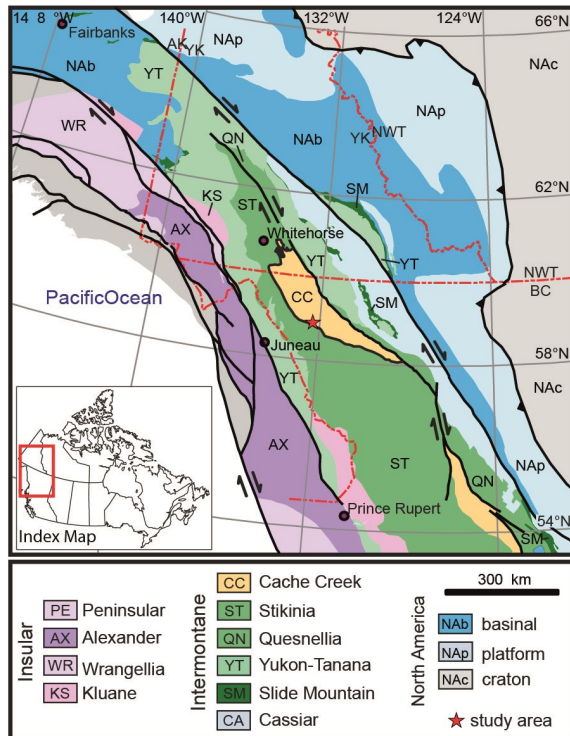
Figure 1. Terranes of the Northern Cordillera (modified from Colpron and Nelson, 2011).

dunite, olivine websterite and orthopyroxenite dykes that cut spinel-bearing harzburgite and rare lherzolite (Fig. 2a, b). These diverse mantle lithologies and cross cutting relationships document a complex magmatic history that is also supported by conventional whole rock, unconventional ultra-low concentration trace element and in situ laser ablation inductively coupled plasma mass spectrometry (LA-ICP-MS) geochemical analyses. New whole-rock Pb and Os isotope analysis (Lawley et al., work in progress, 2017) point to a protracted melt history that likely extends to the Paleoproterozoic, i.e. approximately 2 Ga prior to the main Triassic melting event (ca. 252 Ma; Zagorevski et al., 2015). The meso- to micro-scale occurrence and distribution of gold and other metals within these ancient, refractory mantle domains compared to more recently (Phanerozoic) depleted mantle-segments is the focus of further study. Despite this long-lived melt history and evidence for ultra-depleted harzburgite ($\geq 20\%$ partial melting), a rare sulphide and metal assemblage of pentlandite [$(Fe,Ni)_9S_8$], pyrrhotite ($Fe_{1-x}S$), Cu-Fe-bearing sulphides, awaruite (Ni_2Fe to Ni_3Fe), and native Fe and Cu was observed. These minerals are concentrated within the interstices of serpentinized olivine and orthopyroxene crystals. Pentlandite may represent a relict mantle sulphide phase that escaped complete recrystallization and de-sulphidation during serpentinization (Fig. 2c), with the awaruite and native Fe and Cu de-sulphidized equivalents. If correct, these sulphide mineral phases and native elements
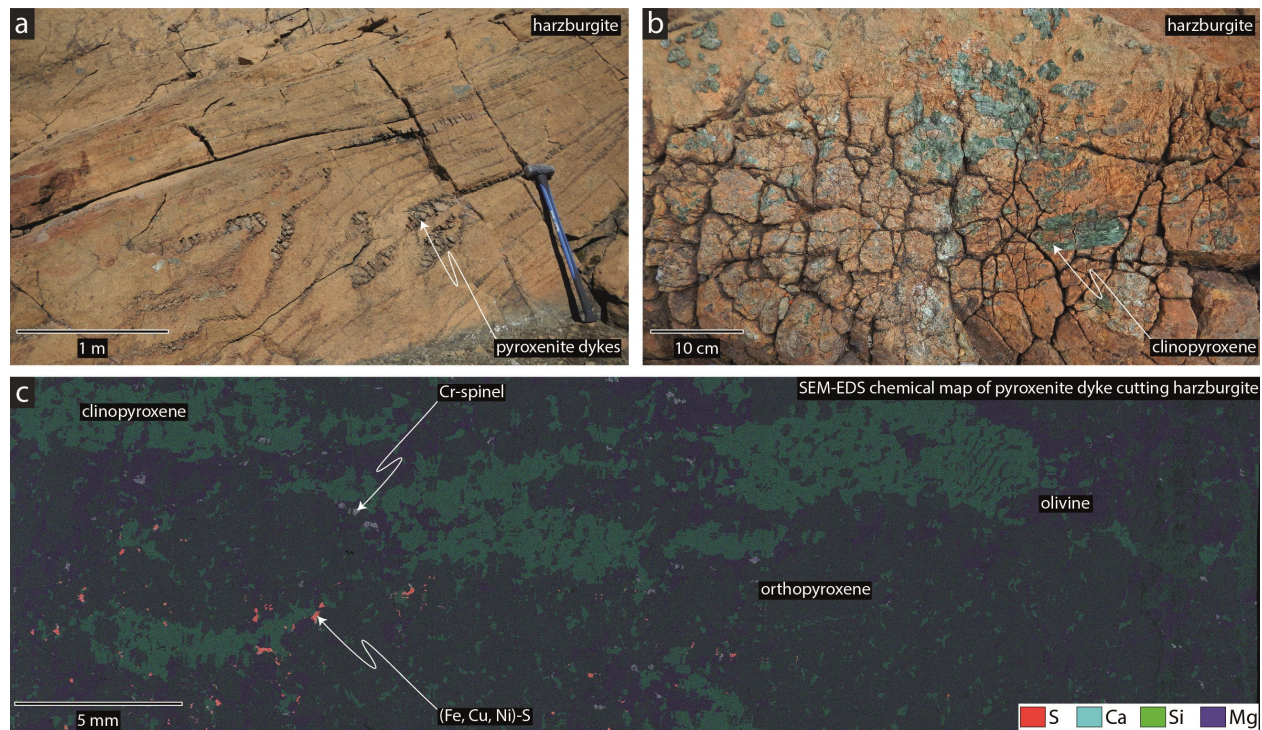
Figure 2. a) Pyroxenite dykes cut harzburgite on Monarch Mountain; b) Clinopyroxene megacrysts on olivine websterite dyke surface, which cuts harzburgite; c) Scanning electron microscope energy dispersive X-ray spectroscopy (SEM-EDS) chemical map of pyroxenite dyke, which cuts harzburgite. Note rare sulphides and natural metal alloys associated with clinopyroxene and spinel.
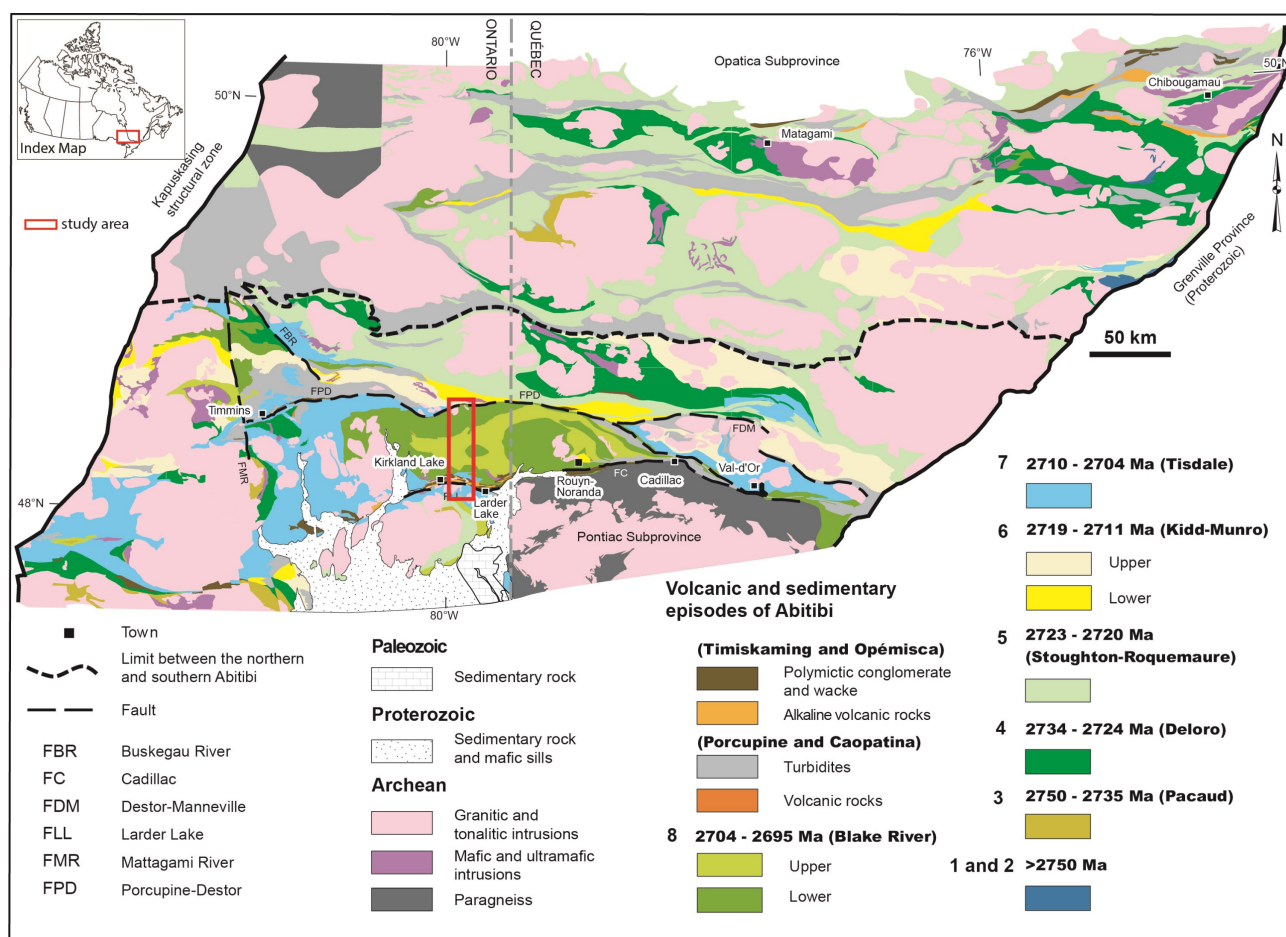
Figure 3. Simplified geological map of the Abitibi Subprovince (modified from Thurston et al., 2008).

could represent an important host for base- and precious-metals within the depleted and/or serpentinized mantle. Primary (e.g. olivine and clinopyroxene) and secondary (e.g. partially preserved mantle sulphides) mantle minerals will thus be the focus of on-going in situ trace element geochemistry in order to document the occurrence and distribution of metals within 'modern' oceanic mantle.

Indicators for metal mobility in Archean lithospheric mantle

Clinopyroxene and olivine xenocrysts were separated from four Abitibi kimberlite samples using electronic pulse disaggregation, with representative suites (by morphology and colour) of clinopyroxene and olivine mounted and analyzed by Electron Probe Microanalyser (EPMA) and LA-ICP-MS. Initial robust principle component analyses (PCA) of major and trace element compositions of olivine and clinopyroxene xenocrysts (Lawley et al., work in progress, 2017) suggest that pitted, barite-bearing, metasomatized xenocryst rims and fractures are associated with a distinct, large ion lithophile element as-

semblage that is likely related to carbohydrothermal fluids circulating during kimberlite emplacement (Fig. 4a, b, d, e). On-going trace element mapping of clinopyroxene and olivine xenocrysts suggest that these late, fractures and rims are relatively metal rich (e.g. Cu, Pb, Ag, Sn, Sb; Fig. 4c, f) and thus spot LA-ICP-MS analyses with this alteration signature are not being pursued. Least altered, garnet peridotite-derived clinopyroxene and mantle-derived olivine xenocrysts are being classified geochemically (Nimis, 1998; Nimis and Taylor 2000; Bussweiler et al., 2017) and fitted to geotherms using single-grain clinopyroxene and olivine thermobarometry (Nimis and Taylor 2000; Bussweiler et al., 2017), and previously published garnet peridotite xenolith data (Meyer et al., 1994; Vicker, 1997). Depth estimates of least-altered, garnet peridotite derived clinopyroxene and olivine xenocrysts are enabling the construction of a series of chemical depth profiles through the Abitibi lithospheric mantle for each kimberlite. These chemical depth profiles are documenting compositional changes within the xenocryst suite and highlight variably melted and re-fertilized regions of the Abitibi lithospheric mantle. The distribution of metals within these regions is the focus of continued study, however, depth

129
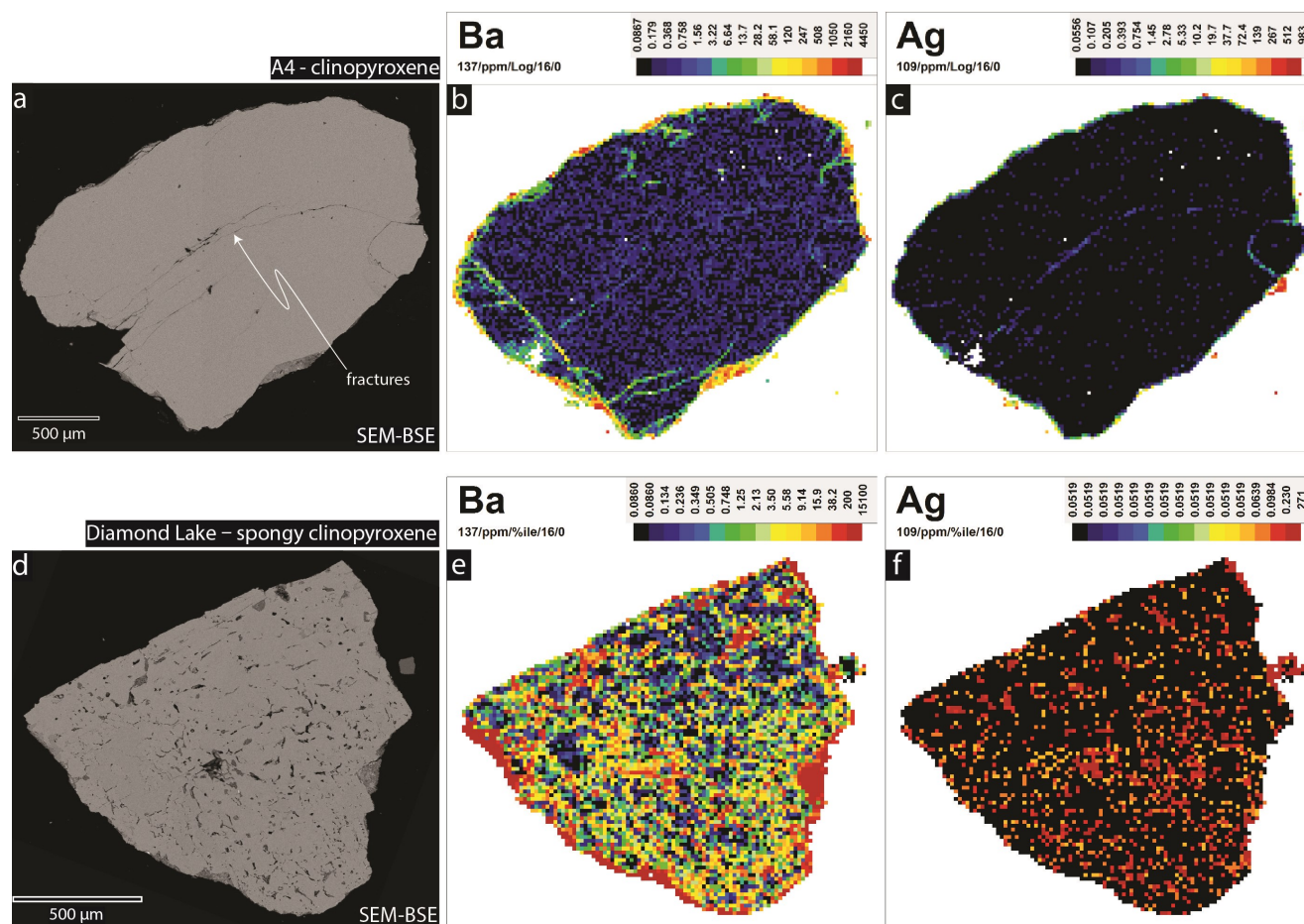
Figure 4. Scanning electron microscope backscattered electron image (SEM-BSE) of clinopyroxene xenocryst from the A4 (a) and Diamond Lake kimberlite (d) and LA-ICP-MS trace element maps (b, c and e, f). Note clinopyroxene rims and fractures are metal-rich and hydrothermally altered. These hydrothermally altered domains were excluded prior to the construction of chemical depth profiles.

profiles for some chalcophile and siderophile elements (e.g. Cu and Zn) points to the importance of high temperature olivine as a metal-bearing phase at depth. Statistical analysis of the time-resolved LA-ICP-MS spectra further suggests that these minor- and trace-element signatures occur as a combination of substitution with mineral-forming major-elements and, for some elements (e.g. Cu and Zn), as sub-micron inclusions. A small proportion of analyses (<15%) also yield gold and platinum element concentrations at, or slightly above, the LA-ICP-MS analytical detection limit (1–5 ppb). The significance of these results requires further study as silicate phases likely represent a rare host for precious metals within the mantle and may point to the role of trapped, metal-bearing inclusions hosted by silicate minerals within the lithospheric mantle at depth.

Expected outcomes and future work

Sample preparation for geochemical and isotopic analyses of Atlin area ultramafic rock samples (e.g. harzburgite, dunite, orthopyroxenite and olivine websterite) is underway. New whole rock and in situ analytical protocols for the ultra-trace determination precious- and base-metals will be used to map and document the trace element distribution of gold and other metals at the meso- to micro-scales.

Acknowledgments

References

Bussweiler, Y., Brey, G.P., Pearson, D.G., Stachel, T., Stern, R.A., Hardman, M.F., Kjarsgaard, B.A., and Jackson, S.E., 2017. The aluminium-in-olivine thermometer for mantle

peridotites — Experimental versus empirical calibration and potential applications; Lithos, v. 272-273, p. 301–314.

Colpron, M. and Nelson, J.L., 2011. A Digital Atlas of Terranes for the Northern Cordillera; BC GeoFile 2011-11.

McGoldrick, S., Zagorevski, A., Canil, D., Corriveau, A.-S., Bichlmaier, S., and Carroll, S., 2016. Geology of the Cache Creek terrane in the Peridotite Peak–Menatatuline Range area, northwestern British Columbia (parts of NTS104K/15, /16); *in* Geoscience BC Summary of Activities 2015, Geoscience BC, Report 2016-1, p. 149–162.

Meyer, H.O.A., Waldman, M.A., and Garwood, B.L., 1994. Mantle xenoliths from kimberlite near Kirkland Lake, Ontario; Canadian Mineralogist, v. 32, p. 295–306.

Nimis, P., 1998. Evaluation of diamond potential from the composition of peridotitic chromian diopside; European Journal of Mineralogy, v. 10, p. 505–519.

Nimis, P. and Taylor, W.R., 2000. Single clinopyroxene thermobarometry for garnet peridotites. Part 1. Calibration and testing of Cr-in-Cpx barometer and an enstatite-in-Cpx thermometer; Contributions to Mineralogy and Petrology, v. 139, p. 541–554.

Thurston, P.C., Ayer, J.A., Goutier, J., and Hamilton, M.A., 2008. Depositional gaps in Abitibi Greenstone Belt stratigraphy: A key to exploration for syngenetic mineralization; Economic Geology, v. 103, p. 1097–1134.

Vicker, P.A., 1997. Garnet peridotite xenoliths from kimberlite near Kirkland Lake, Canada; MSc thesis, University of Toronto, Toronto, Ontario, 138 p.

Zagorevski, A., Corriveau, A.-S., McGoldrick, S., Bédard, J.H., Canil, D., Golding, M.L., Joyce, N., and Mihalynuk, M.G., 2015. Geological framework of ancient oceanic crust in northwestern British Columbia and southwestern Yukon, GEM 2 Cordillera; Geological Survey of Canada, Open File 7957, 12 p.

Zagorevski, A., Bedard, J.H., Bogatu, A., Coleman, M., Golding, M., Joyce, N., 2017. Stikinia Bedrock Report of Activities, British Columbia and Yukon: GEM2 Cordillera; Geological Survey of Canada, Open File 8329, 13 p.

Age relationships and preliminary U-Pb zircon geochronology results from the Lynn Lake greenstone belt

C.J.M. Lawley[1], D. Schneider[2], E. Yang[3], W.J. Davis[1], S.E. Jackson[1], Z. Yang[1], S. Zhang[4] and D. Selby[5]

[1]Geological Survey of Canada, 601 Booth St., Ottawa, Ontario, K1A 0E8

[2]Department of Earth and Environmental Sciences, University of Ottawa, 120 University, Ottawa, Ontario, K1N 6N5

[3]Manitoba Geological Survey, 360-1395 Ellice Avenue, Winnipeg, Manitoba, R3G 3P2

[4]Department of Earth Sciences, Carleton University, 1125 Colonel By Drive, Ottawa, Ontario, K1S 5B6

[5]Department of Earth Sciences, Durham University, Durham, DH1 3LE, UK

Abstract

Evaluating the genetic link between gold, faulting and metamorphism remains a significant challenge at orogenic gold deposits in the absence of precise geochronological constraints with clear paragenetic context. Here we report new field observations and preliminary U-Pb zircon age results from gold deposits hosted within the Paleoproterozoic Lynn Lake greenstone belt. New zircon ages from a faulted, hydrothermally altered and metamorphosed diorite sample intruding the southern edge of the past-producing open-pit constrain the timing of gold, deformation and metamorphism at the Gordon gold deposit to ≤1854 Ma. Auriferous veining thus significantly post-dates the age of the volcano-sedimentary host rocks, which are constrained to 1879 to 1892 Ma based on new zircon age dating from two granitic intrusions south of the Gordon gold deposit. Gold thus clearly post-dates some of the earliest deformation events recognized in the La Ronge - Lynn Lake segments of the Trans-Hudson orogeny (ca. 1.87 Ga). The temporal relationship between gold, peak metamorphism and a major deformation phase at ca. 1.81 Ga will be the focus of on-going Re-Os pyrite and arsenopyrite geochronology of auriferous veins.

Introduction

The tectonic triggers and drivers of gold mineralization within ancient greenstone belts have proven difficult to define due to the challenge of directly dating gold deposition and the multiple, overprinting tectono-thermal events that characterize these complex geologic settings. The Paleoproterozoic Lynn Lake greenstone belt, Manitoba, hosts multiple gold occurrences (including three past producing mines) with contrasting styles of mineralization. Thus, this greenstone belt is an ideal area to investigate the timing of gold deposition in relation to Paleoproterozoic orogenesis (Fig. 1). In addition to gold mineralization, the Lynn Lake greenstone belt hosts past-producing volcanogenic massive sulphide and orthomagmatic nickel mines. The absolute age relationship between these disparate deposit types are currently poorly constrained, but if resolved should provide significant insight into the metallogenic evolution of Proterozoic greenstone belts from volcanism to burial and metamorphism.

Lynn Lake greenstone belt geochronology

Herein we report three preliminary U-Pb zircon ages from the Gordon gold deposit (formally known as the Farley Lake deposit; Fig. 1). Samples were analyzed by the Sensitive High Resolution Ion Microprobe (SHRIMP) following the approach of Stern (1997) and Stern and Amelin (2003). Weighted average zircon ages were calculated using Isoplot v. 3.00 (Ludwig, 2003).

Foliated diorite (sample 16CL08071035: 1854 ± 2 Ma)

Dioritic to gabbroic dykes and plutons intrude mafic volcanic and intercalated banded iron formation (BIF) at the southern edge of the Gordon gold deposit. A chloritized, silicified, sulphidized, veined (veins were removed during sample preparation) and locally foliated diorite sample (16CL08071035; Fig. 2a; Table 1) from this locality (NAD83 UTM 14N: 6307760, 412565) yielded prismatic, oscillatory zoned zircons crystals and a unimodal age population. Concordant zircons (± 5%) from this sample yield a weighted average $^{207}Pb/^{206}Pb$ age at 1854 ± 2 Ma (MSWD = 1.0, n = 26).

Farley Lake monzogranite (sample 16CL08071215: 1879 ± 4 Ma)

Zircons from a monzogranite sample (16CL08071215; NAD83 UTM 14N: 6306256, 412104; Fig. 2b; Table 2) were oscillatory zoned with prismatic to stubby crystal shapes. Dat-
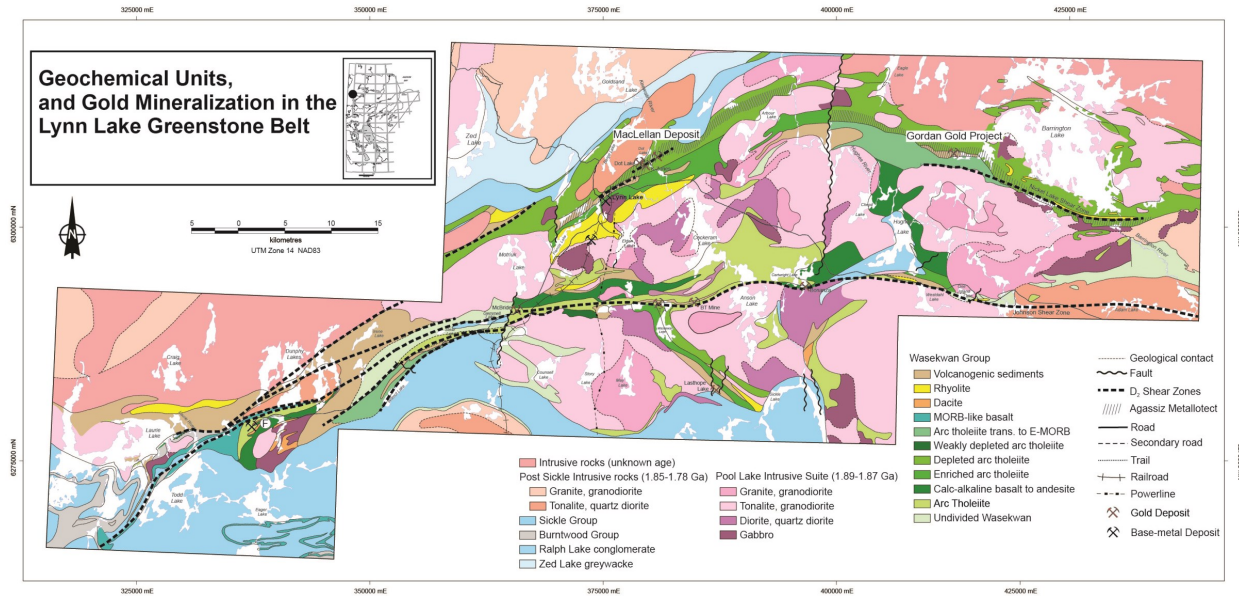
Figure 1. Regional geology map of the Lynn Lake greenstone belt (modified from Zwanzig et al., 1999; Beaumont-Smith et al., 2006; Yang and Beaumont-Smith, 2015).

ed zircon show no inheritance or younger rims. Concordant zircons (± 5% concordant) yield a weighted average ^{207}Pb/^{206}Pb age of 1879 ± 4 (MSWD = 1.2, n = 27).

Farley Lake syenogranite (sample 16CL08071336: 1873 ± 3 Ma)

Variably metasomatized and complexly zoned zircon crystals from a reduced-I type (Yang and Beaumont-Smith, 2015) syenogranite sample (16CL08071336; NAD83 UTM 14N: 6301541, 411204; Fig. 2c; Table 3). The zircon age population is unimodal with no evidence for zircon inheritance or younger

rims, as suggested by complex growth zoning and metasomatic domains within the dated zircons. Concordant zircons (± 5% concordant) yield a weighted average ^{207}Pb/^{206}Pb age of 1873 ± 3 Ma (MSWD = 0.8, n = 18).

Age relationships in the Lynn Lake greenstone belt

Relative timing relations between veining, metamorphism and deformation were investigated at the MacLellan deposit (Fig. 1, 3). Early quartz veins are pre- to syn-deformational,

Table 1 - U-Pb isotope results for diorite sample 16CL08071035.

										Isotope Ratios										Apparent Ages (Ma)			
Spot Name	U (ppm)	Th (ppm)	Th/U	Yb (ppm)	Hf (ppm)	^{206*}Pb (ppm)	^{204}Pb/^{206}Pb	1s (%)	f(206)^{204} %	^{208*}Pb/^{206*}Pb	1s (%)	^{207*}Pb/^{235}U	1s (%)	^{206*}Pb/^{238}U	1s (%)	Corr Coeff	^{207*}Pb/^{206*}Pb	1s (%)	^{206}Pb/^{238}U	1s (abs)	^{207}Pb/^{206}Pb	1s (abs)	Disc. (%)
11995-001.1	398	141	0.37	368	6805	109	1.41E-05	57.7	2.45E-02	0.107	2.23	5.030	1.13	0.3205	1.07	0.944	0.1138	0.373	1792	17	1862	7	4.3
11995-010.1	311	108	0.36	310	7071	90	5.53E-06	100.0	9.58E-03	0.106	2.39	5.226	1.16	0.3357	1.09	0.939	0.1129	0.396	1866	18	1847	7	-1.2
11995-016.1	705	390	0.57	663	7566	198	5.12E-06	70.7	8.87E-03	0.169	1.29	5.104	1.14	0.3267	1.11	0.972	0.1133	0.269	1822	18	1853	5	1.9
11995-023.1	285	83	0.30	274	7059	79	-1.29E-05	70.7	-2.23E-02	0.089	2.80	5.031	1.18	0.3217	1.10	0.930	0.1134	0.434	1798	17	1855	8	3.5
11995-029.1	743	391	0.54	610	7934	209	2.01E-05	35.4	3.48E-02	0.156	4.16	5.094	1.29	0.3274	1.21	0.939	0.1128	0.442	1826	19	1846	8	1.3
11995-030.1	389	132	0.35	356	6970	110	2.81E-05	40.8	4.87E-02	0.104	2.25	5.139	1.14	0.3298	1.07	0.941	0.1130	0.386	1837	17	1849	7	0.7
11995-036.1	693	400	0.60	667	7635	198	7.72E-06	57.7	1.34E-02	0.178	1.27	5.189	1.07	0.3320	1.04	0.967	0.1134	0.272	1848	17	1854	5	0.4
11995-037.1	360	116	0.33	328	7151	103	1.50E-05	57.7	2.61E-02	0.099	3.82	5.226	1.15	0.3341	1.08	0.942	0.1134	0.386	1858	17	1855	7	-0.2
11995-045.1	449	229	0.53	406	6952	125	1.64E-05	50.0	2.85E-02	0.151	2.84	5.054	1.12	0.3246	1.06	0.947	0.1129	0.360	1812	17	1847	7	2.2
11995-054.1	86	16	0.19	108	8209	25	8.41E-05	50.0	1.46E-01	0.052	7.45	5.148	1.61	0.3330	1.32	0.819	0.1121	0.925	1853	21	1834	17	-1.2
11995-056.1	449	180	0.41	421	7331	128	7.76E-06	70.7	1.34E-02	0.125	1.85	5.190	1.11	0.3316	1.06	0.954	0.1135	0.333	1846	17	1856	6	0.6
11995-058.1	389	143	0.38	353	7046	111	4.61E-06	100.0	8.00E-03	0.105	2.18	5.184	1.26	0.3332	1.21	0.958	0.1128	0.362	1854	19	1846	7	-0.5
11995-067.1	588	279	0.49	525	7703	166	-1.27E-05	50.0	-2.20E-02	0.146	1.53	5.177	1.35	0.3290	1.26	0.933	0.1141	0.486	1833	20	1866	9	2.0
11995-073.1	405	141	0.36	361	7061	113	9.21E-06	70.7	1.60E-02	0.105	2.17	5.066	1.13	0.3241	1.07	0.946	0.1134	0.365	1810	17	1854	7	2.8
11995-074.1	458	198	0.45	425	6937	129	4.11E-06	100.0	7.12E-03	0.125	1.89	5.174	1.27	0.3288	1.23	0.964	0.1141	0.339	1832	20	1866	6	2.1
11995-078.1	445	198	0.46	428	7046	128	-1.20E-05	57.7	-2.08E-02	0.136	2.88	5.237	1.12	0.3346	1.06	0.951	0.1135	0.346	1861	17	1856	6	-0.3
11995-088.1	309	114	0.38	306	7609	89	5.62E-06	100.0	9.74E-03	0.111	2.38	5.221	1.29	0.3338	1.11	0.861	0.1134	0.656	1857	18	1855	12	-0.1
11995-090.1	237	128	0.56	234	9056	66	7.54E-06	100.0	1.31E-02	0.163	2.25	5.039	1.21	0.3256	1.12	0.923	0.1122	0.466	1817	18	1836	8	1.2
11995-090.2	206	88	0.44	164	9469	56	1.83E-05	70.7	3.18E-02	0.133	2.78	4.967	1.26	0.3199	1.14	0.908	0.1126	0.528	1789	18	1842	10	3.3
11995-091.1	974	422	0.45	663	8692	275	1.88E-06	100.0	3.26E-03	0.137	1.22	5.159	1.21	0.3286	1.18	0.982	0.1139	0.229	1832	19	1862	4	1.9
11995-093.1	631	359	0.59	607	7528	180	1.20E-05	50.0	2.07E-02	0.176	1.37	5.191	1.08	0.3320	1.04	0.962	0.1134	0.296	1848	17	1855	5	0.4
11995-094.1	393	160	0.42	377	7641	113	1.37E-05	57.7	2.37E-02	0.128	1.99	5.238	1.13	0.3354	1.07	0.946	0.1133	0.367	1865	17	1852	7	-0.8
11995-099.1	544	248	0.47	505	7960	153	3.46E-06	100.0	6.00E-03	0.138	1.66	5.137	1.10	0.3282	1.05	0.959	0.1135	0.312	1829	17	1857	6	1.7
11995-100.1	684	358	0.54	543	7569	194	-2.63E-06	100.0	-4.56E-03	0.161	1.34	5.154	1.14	0.3294	1.11	0.971	0.1135	0.271	1835	18	1856	5	1.3
11995-115.1	801	495	0.64	596	7411	228	2.23E-05	100.0	3.87E-03	0.191	1.13	5.179	1.06	0.3313	1.03	0.972	0.1134	0.249	1845	17	1854	5	0.6
11995-115.2	370	120	0.33	324	7172	103	5.07E-06	100.0	8.80E-03	0.101	2.34	5.081	1.14	0.3245	1.08	0.943	0.1135	0.378	1812	17	1857	7	2.8

Notes (see Stern, 1997):
Spot name follows the convention x-y.z; where x = sample number, y = grain number and z = spot number. Multiple analyses in an individual spot are labelled as x-y.z.z
Uncertainties reported at 1s
f(206)^{204} refers to mole percent of total ^{206}Pb that is due to common Pb, calculated using the 204Pb-method; common Pb composition used is the surface blank (4/6: 0.05770; 7/6: 0.89500; 8/6: 2.13840)
* refers to radiogenic Pb (corrected for common Pb)
Disc.: Discordance given as difference between measured ^{206*}Pb/^{238}U ratio and the expected ^{206*}Pb/^{238}U ratio at t=^{207}Pb/^{206*}Pb age, in percent.
Calibration standard 6266; U = 910 ppm; Age = 559 Ma; 206Pb/238U = 0.09059
Error in ^{206}Pb/^{238}U calibration 1.0% (included);spot size 17x23 mm.
Standard Error in Standard calibration was 0.34% (not included in above errors but required when comparing data from different mounts).

isoclinally folded and host coarse visible gold. Associated to these are fine- to ultra-fine-grained arsenopyrite alteration halos hosted in amphibolite facies metamorphosed mafic volcanic and intercalated sedimentary successions (Fig. 3a). The contacts between quartz-biotite (± plagioclase ± garnet) schist and amphibole-plagioclase-biotite (± garnet) schist are locally mineralized, suggesting that auriferous fluids were focused along primary rock contacts. Although galena, sphalerite, chalcopyrite, pyrite and pyrrhotite occur in some of the highest grade auriferous veins (Fig. 3b), the relationship base metal mineralization appears to be, at least locally, unrelated to gold. High-grade gold ore zones and coarse, visible gold also occurs within the interstices of decussate textured actinolite porphyroblasts (Fig. 3d), which were devoid of veining and associated alteration. The absence of veining within some gold ore zones distinguish the MacLellan deposit from other gold occurrences within the Lynn Lake greenstone belt (Beaumont-Smith and Böhm, 2003). For instance, ore zones at the Gordon gold deposit are almost entirely hosted within quartz veins (Fig. 3c) and related sulphide replacement zones overprinting BIF.

The new age determination of foliated diorite from near the Gordon gold deposit at 1854 ± 2 Ma, which is consistent with late-stage Pool Lake intrusive suite rocks elsewhere, provides a maximum age for the main deformation fabric (D2; Beaumont-Smith and Böhm, 2002), as well as the pre- to syn-deformation quartz veins at the Gordon gold deposit. Similar aged rocks are observed adjacent to the MacLellan deposit (e.g. ca. 1857 Ma Burge Lake; Beaumont-Smith et al., 2006), suggesting a broadly comparable lithologic setting for these two deposits along the inferred continuation of the Nickel Lake shear zone (Fig. 1). Our new results are also consistent with the inferred timing of regional deformation and peak metamorphism ca. 1814 Ma (Beaumont-Smith and Böhm, 2002), which is expected to postdate the Sickle Group at ≤1830 Ma (Beaumont-Smith et al., 2006) and late-stage, ca. 1815 Ma pegmatitic dykes that cut post-Sickle intrusive rocks (Beaumont-Smith and Böhm, 2002).

The foliated and hydrothermally altered diorite sample is distinctly younger than the Farley Lake granodiorite to monzogranite pluton to the south of the Gordon gold deposit. Their ages are consistent with the main-stage of the Pool Lake intrusive suite (Beaumont-Smith and Böhm, 2002) and suggest that mafic volcanic and BIF host rocks at the Gordon gold deposit were deposited ≥1879 Ma. The inferred timing of mafic volcanism is slightly younger than the regions oldest dated rhyolitic volcanism at ca. 1892 Ma (Beaumont-Smith and Böhm, 2002), suggesting rapid burial after mafic volcanism and BIF deposition.

Expected outcomes and future work

Future work will be directed at comparing the age and isotopic characteristics of the Gordon and MacLellan deposits to constrain the evolution of distinct gold mineralization styles during orogenesis. Part of this work includes trace element and
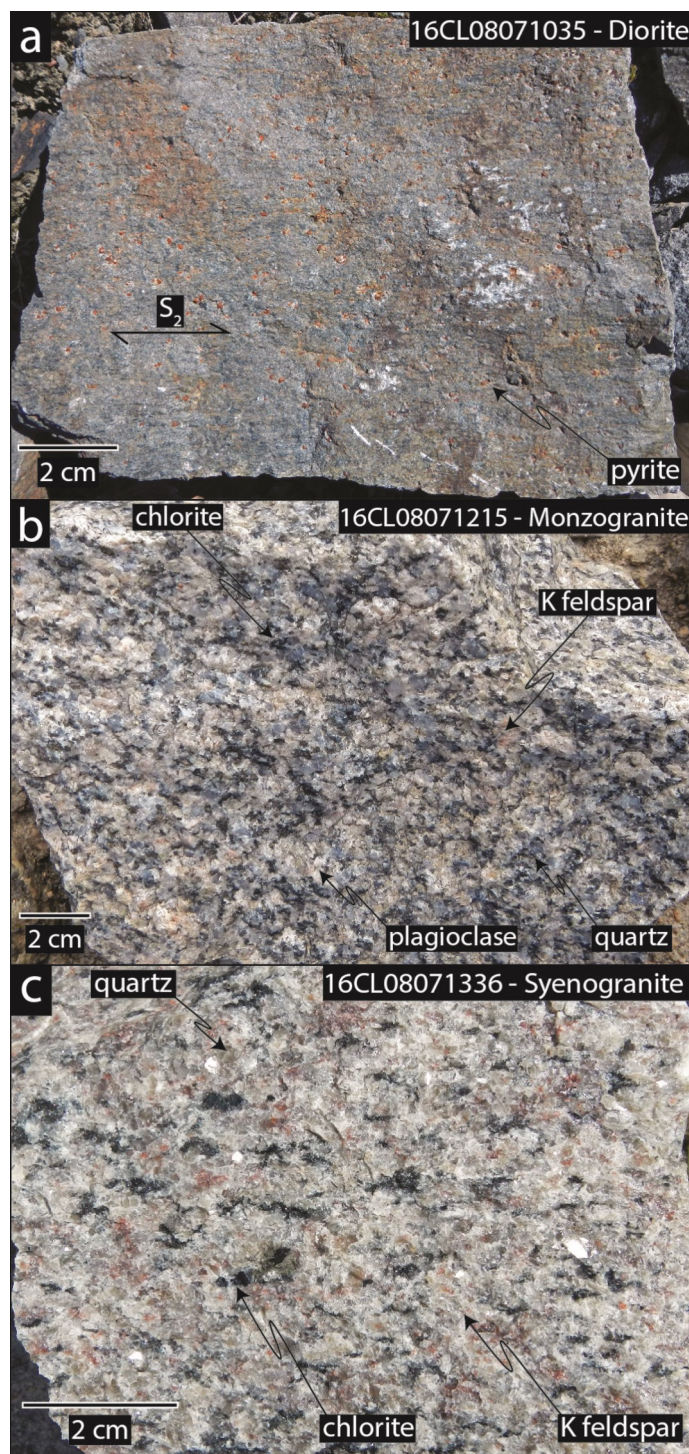
Figure 2. Field photos of intermediate to felsic intrusive phases dated around the Gordon gold deposit: a) Foliated diorite (sample 16CL08071035: 1854 ± 2 Ma); b); Farley Lake monzogranite (sample 16CL08071215: 1879 ± 4 Ma); c) Farley Lake syenogranite (sample 16CL08071336: 1873 ± 3 Ma).

Table 2 - U-Pb results for monzogranite sample (16CL08071215).

| Spot Name | U (ppm) | Th (ppm) | Th/U | Yb (ppm) | Hf (ppm) | ^{206*}Pb (ppm) | Isotope Ratios | | | | | | | | | | | | Apparent Ages (Ma) | | | | |
							^{204}Pb/^{206}Pb	1s (%)	f(206)^{204} %	^{208*}Pb/^{206*}Pb	1s (%)	^{207*}Pb/^{235}U	1s (%)	^{206*}Pb/^{238}U	1s (%)	Corr Coeff	^{207*}Pb/^{206*}Pb	1s (%)	^{206*}Pb/^{238}U Age	1s (abs)	^{207*}Pb/^{206*}Pb Age	1s (abs)	Disc. (%)
11996-014.1	187	52	0.29	401	8458	54	-2.73E-05	58	-4.72E-02	0.085	3.44	5.373	1.27	0.3378	1.15	0.909	0.1154	0.530	1876	19	1886	10	0.6
11996-015.1	218	45	0.21	385	8723	62	9.04E-06	100	1.57E-02	0.061	4.07	5.262	1.25	0.3319	1.15	0.914	0.1150	0.509	1848	18	1880	9	2.0
11996-017.1	188	56	0.31	393	8184	56	9.24E-06	100	1.60E-02	0.095	3.35	5.491	1.26	0.3450	1.15	0.914	0.1155	0.512	1910	19	1887	9	-1.4
11996-019.1	206	83	0.42	476	8470	62	6.79E-14	9999	1.18E-10	0.126	2.75	5.582	1.57	0.3518	1.49	0.951	0.1151	0.483	1943	25	1881	9	-3.8
11996-020.1	226	98	0.45	551	8420	67	3.27E-14	9999	5.67E-11	0.134	2.62	5.482	1.42	0.3460	1.34	0.942	0.1149	0.474	1915	22	1879	9	-2.3
11996-029.1	158	42	0.28	360	8248	45	2.49E-05	71	4.32E-02	0.086	4.08	5.333	1.35	0.3337	1.20	0.888	0.1159	0.619	1856	19	1894	11	2.3
11996-029.2	155	47	0.31	254	9837	45	-5.95E-05	45	-1.03E-01	0.093	3.88	5.380	1.35	0.3361	1.19	0.880	0.1161	0.643	1868	19	1897	12	1.7
11996-030.1	220	85	0.40	540	8233	64	-8.16E-06	100	-1.41E-02	0.121	2.73	5.363	1.23	0.3381	1.13	0.920	0.1151	0.482	1877	18	1881	9	0.2
11996-034.1	189	41	0.22	365	8220	56	4.68E-05	45	8.11E-02	0.068	4.11	5.441	1.29	0.3437	1.16	0.899	0.1148	0.564	1904	19	1877	10	-1.7
11996-035.1	277	110	0.41	513	7765	81	3.26E-05	45	5.64E-02	0.119	2.50	5.375	1.31	0.3392	1.11	0.842	0.1149	0.708	1883	18	1879	13	-0.3
11996-036.1	300	98	0.34	554	7976	88	1.22E-05	71	2.12E-02	0.096	2.64	5.413	1.28	0.3420	1.10	0.858	0.1148	0.657	1896	18	1877	12	-1.2
11996-047.1	175	74	0.43	438	8541	50	-4.01E-14	9999	-6.96E-11	0.127	2.94	5.310	1.28	0.3348	1.16	0.912	0.1150	0.523	1862	19	1880	9	1.1
11996-047.2	109	35	0.33	210	9511	32	-7.72E-05	45	-1.34E-01	0.100	4.24	5.411	1.46	0.3402	1.25	0.855	0.1153	0.759	1888	20	1885	14	-0.2
11996-048.1	183	71	0.40	425	9293	53	2.95E-05	58	5.11E-02	0.109	3.18	5.292	1.28	0.3353	1.16	0.901	0.1145	0.557	1864	19	1872	10	0.5
11996-051.1	179	76	0.44	470	8333	53	8.14E-14	9999	1.41E-10	0.128	2.94	5.396	1.28	0.3458	1.17	0.910	0.1132	0.532	1915	19	1851	10	-4.0
11996-051.2	205	89	0.45	535	8194	60	1.88E-05	71	3.25E-02	0.131	2.83	5.358	1.27	0.3384	1.15	0.908	0.1148	0.532	1879	19	1877	10	-0.1
11996-054.1	220	97	0.45	540	8245	66	5.90E-05	38	1.02E-01	0.127	2.77	5.453	1.26	0.3468	1.14	0.900	0.1140	0.551	1919	19	1865	10	-3.4
11996-055.1	186	61	0.34	385	8230	55	1.02E-05	100	1.78E-02	0.099	3.39	5.449	1.28	0.3433	1.17	0.907	0.1151	0.542	1903	19	1881	10	-1.3
11996-072.1	180	73	0.42	469	8079	53	-3.95E-14	9999	-6.85E-11	0.121	3.00	5.401	1.27	0.3401	1.16	0.913	0.1152	0.519	1887	19	1883	9	-0.3
11996-073.1	212	56	0.27	416	8089	61	-9.47E-06	100	-1.64E-02	0.083	3.61	5.333	1.27	0.3351	1.15	0.911	0.1154	0.522	1863	19	1886	9	1.4
11996-087.1	145	57	0.40	336	8676	42	3.82E-05	58	6.62E-02	0.114	3.58	5.299	1.37	0.3384	1.21	0.882	0.1136	0.648	1879	20	1858	12	-1.3
11996-088.1	78	14	0.19	140	8166	23	-2.32E-05	100	-4.02E-02	0.053	7.38	5.374	1.65	0.3361	1.40	0.847	0.1160	0.878	1868	23	1895	16	1.7
11996-089.1	246	106	0.45	603	8322	71	-6.09E-14	9999	-1.06E-10	0.131	2.50	5.392	1.21	0.3365	1.12	0.927	0.1162	0.454	1870	18	1899	8	1.8
11996-089.2	240	105	0.45	500	6897	70	3.21E-05	50	5.57E-02	0.143	2.53	5.315	1.53	0.3379	1.44	0.943	0.1141	0.510	1876	23	1866	9	-0.7
11996-090.1	182	55	0.31	326	8117	53	4.82E-05	45	8.36E-02	0.098	3.44	5.327	1.49	0.3360	1.37	0.922	0.1150	0.574	1867	22	1880	10	0.8
11996-092.1**	145	30	0.21	343	8243	43	7.39E-05	41	1.28E-01	0.060	8.79	5.280	1.39	0.3415	1.21	0.867	0.1121	0.693	1894	20	1834	13	-3.8
11996-092.2**	153	56	0.38	346	9235	42	2.57E-21	9999	4.46E-18	0.113	3.43	5.151	1.49	0.3226	1.19	0.798	0.1158	0.900	1802	19	1893	16	5.5
11996-108.1	184	43	0.24	354	8191	53	1.03E-05	100	1.78E-02	0.076	3.89	5.319	1.29	0.3352	1.16	0.906	0.1151	0.544	1863	19	1881	10	1.1
11996-109.1	231	90	0.41	541	8061	69	4.73E-05	41	8.19E-02	0.113	2.87	5.512	1.24	0.3489	1.13	0.909	0.1146	0.519	1929	19	1873	9	-3.5

Table 3 - U-Pb isotope results for Reduced-I type syenogranite sample (16CL08071336).

| Spot Name | U (ppm) | Th (ppm) | Th/U | Yb (ppm) | Hf (ppm) | ^{206*}Pb (ppm) | Isotope Ratios | | | | | | | | | | | | Apparent Ages (Ma) | | | | |
							^{204}Pb/^{206}Pb	1s (%)	f(206)^{204} %	^{208*}Pb/^{206*}Pb	1s (%)	^{207*}Pb/^{235}U	1s (%)	^{206*}Pb/^{238}U	1s (%)	Corr Coeff	^{207*}Pb/^{206*}Pb	1s (%)	^{206*}Pb/^{238}U Age	1s (abs)	^{207*}Pb/^{206*}Pb Age	1s (abs)	Disc. (%)
11997-002.1	262	116	0	380	6246	75	2.66E-05	50	4.61E-02	0.135	4.01	5.258	1.20	0.3356	1.11	0.924	0.1136	0.458	1865	18	1858	8	-0.4
11997-012.1	694	298	0	1595	7198	206	4.10E-04	13	7.11E-01	0.153	1.86	5.457	1.25	0.3455	1.04	0.830	0.1146	0.700	1913	17	1873	13	-2.5
11997-015.1	322	119	0	855	6598	92	2.82E-05	45	4.89E-02	0.109	2.42	5.242	1.17	0.3308	1.09	0.933	0.1149	0.421	1842	17	1879	8	2.2
11997-018.1**	231	123	1	737	6369	62	1.93E-04	20	3.35E-01	0.126	2.82	4.916	1.29	0.3143	1.12	0.866	0.1134	0.647	1762	17	1855	12	5.8
11997-019.1	703	244	0	736	7495	202	2.54E-06	100	4.41E-03	0.102	1.64	5.275	1.07	0.3347	1.04	0.969	0.1143	0.266	1861	17	1869	5	0.5
11997-025.1	2267	743	0	1753	9884	672	1.59E-14	9999	2.76E-11	0.097	0.95	5.446	1.02	0.3452	1.01	0.989	0.1144	0.148	1912	17	1871	3	-2.5
11997-031.1	1396	462	0	1459	10819	403	1.20E-05	33	2.07E-02	0.103	1.19	5.313	1.03	0.3363	1.02	0.982	0.1146	0.197	1869	16	1873	4	0.3
11997-034.1**	443	219	1	1082	6617	95	1.60E-03	10	2.77E+00	0.126	8.68	3.804	3.80	0.2491	1.58	0.416	0.1107	3.454	1434	20	1812	63	23.2
11997-034.2	268	114	0	767	6401	74	2.43E-04	19	4.22E-01	0.116	3.05	5.043	1.32	0.3233	1.11	0.843	0.1131	0.711	1806	18	1850	13	2.7
11997-041.1	145	58	0	504	6427	41	2.60E-05	71	4.51E-02	0.113	6.71	5.167	1.65	0.3273	1.65	0.932	0.1145	0.642	1825	26	1872	12	2.9
11997-041.2	155	41	0	280	7668	46	-3.37E-05	58	-5.84E-02	0.077	4.08	5.478	1.32	0.3479	1.18	0.892	0.1142	0.599	1925	20	1867	11	-3.5
11997-043.1	478	197	0	1099	6911	135	4.47E-05	29	7.74E-02	0.124	1.86	5.163	1.12	0.3280	1.06	0.948	0.1142	0.356	1829	17	1867	6	2.3
11997-063.1	312	109	0	550	6502	90	4.22E-05	38	7.32E-02	0.104	2.59	5.273	1.19	0.3347	1.10	0.926	0.1142	0.450	1861	18	1868	8	0.4
11997-064.1**	168	58	0	417	6211	46	1.84E-21	9999	3.19E-18	0.106	3.39	5.082	1.53	0.3213	1.17	0.765	0.1147	0.988	1796	18	1875	18	4.8
11997-069.1	1378	422	0	1177	10048	395	6.57E-06	45	1.14E-02	0.093	1.24	5.282	1.03	0.3336	1.02	0.982	0.1148	0.193	1856	16	1877	3	1.3
11997-073.1**	253	62	0	597	6546	68	1.21E-04	25	2.10E-01	0.075	3.71	4.855	1.26	0.3119	1.12	0.884	0.1129	0.590	1750	17	1847	11	6.0
11997-083.1	493	212	0	1157	6879	140	1.49E-05	50	2.59E-02	0.131	1.79	5.280	1.11	0.3320	1.06	0.954	0.1147	0.332	1848	17	1875	6	1.7
11997-088.1	600	130	0	598	11071	173	1.93E-04	13	3.35E-01	0.073	2.49	5.343	1.12	0.3363	1.04	0.929	0.1152	0.416	1869	17	1883	7	0.9
11997-090.1	390	187	0	1106	5927	111	2.28E-05	45	3.96E-02	0.144	3.44	5.214	1.07	0.3305	1.07	0.944	0.1144	0.375	1841	17	1871	7	1.8
11997-090.2	389	182	0	1126	6090	112	9.74E-06	71	1.69E-02	0.140	1.95	5.306	1.39	0.3357	1.34	0.963	0.1146	0.374	1866	22	1874	7	0.5
11997-092.1	327	93	0	539	6835	92	5.45E-06	100	9.45E-03	0.086	2.62	5.167	1.27	0.3268	1.21	0.952	0.1147	0.391	1823	19	1875	7	3.2

lead isotopic analysis of pressed-powder micro-pellets of pyrite and arsenopyrite minerals separates, which will complement Re-Os analysis of the same sample suite. Isolation of other dateable mineral phases within auriferous veins (e.g. apatite) and hydrothermal alteration halos is on-going.

Acknowledgments

References

Beaumont-Smith, C.J. and Böhm, C.O., 2002. Structural analysis and geochronological studies in the Lynn Lake greenstone belt and its Au-bearing shear zones (NTS 64C10, 11, 12, 14, 15 and 16), Manitoba; *in* Report of Activities 2002, Manitoba Industry, Trade and Mines, Manitoba Geological Survey, p. 159–170.

Beaumont-Smith, C.J. and Böhm, C.O., 2003. Tectonic evolution and Au metallogeny of the Lynn Lake greenstone belt, Manitoba (NTS 64C10, 11, 12, 14, 15 and 16); *in* Report of

Figure 3. Core photos of MacLellan and Gordon ore zones: a) Coarse to ultrafine disseminated arsenopyrite associated with silicified and biotitized biotite-amphibole schist at MacLellan; b) Galena and sphalerite are locally good visual indicators of gold grade, however, Pb- and Zn-rich zones at the deposit scale are not co-spatial with the highest gold grades; c) Coarse visible gold at the margin of quartz vein, which cuts diorite at the south end of the Farley Lake pit; d) Visible gold intergrown with coarse actinolite porphyroblast within amphibole schist.

Activities 2003, Manitoba Industry, Trade and Mines, Manitoba Geological Survey, p. 39–49.

Beaumont-Smith, C.J., Machado, N., and Peck, D.C., 2006. New uranium-lead geochronology results from the Lynn Lake greenstone belt, Manitoba (NTS 64C11-16); Geoscientific Paper, Manitoba Mineral Resources, Manitoba Geological Survey, 16 p.

Ludwig, K.R., 2003. Isoplot; A Plotting and Regression Program for Radiogenic Isotope Data, Version Ex/3.00; Berkeley Geochronology Center. <http://www.bgc.org/isoplot_etc/isoplot/Isoplot3_75files.zip> [accessed November 17, 2017]

Stern, R.A., 1997. The GSC Sensitive High Resolution Ion Microprobe (SHRIMP): Analytical Techniques of Zircon U–Th–Pb Age Determinations and Performance Evaluation; Current Research 1997-F, Geological Survey of Canada, pp. 1–31.

Stern, R.A. and Amelin, Y., 2003. Assessment of errors in SIMS zircon U–Pb geochronology using a natural zircon standard and NIST SRM 610 glass; Chemical Geology, v. 197, p. 111–146.

Yang, X.M. and Beaumont-Smith, C.J., 2015. Geological investigations of the Keewatin River area, Lynn Lake greenstone belt, northwestern Manitoba (parts of NTS 64C14, 15); *in* Report of Activities 2015, Manitoba Mineral Resources, Manitoba Geological Survey, p. 52–67.

Zwanzig, H.V., Syme, E.C., and Gilbert, H.P., 1999, Updated trace element geochemistry of ca. 1.9 Ga metavolcanic rocks in the Paleoproterozoic Lynn Lake Belt; Manitoba Industry, Trade and Mines, Geological Services, p. 46.

Gold along Cordilleran faults: Key characteristics and analogies between Phanerozoic and Archean settings

S. Castonguay[1], L. Ootes[2], P. Mercier-Langevin[1] and F. Devine[3]

[1]*Geological Survey of Canada, 490 rue de la Couronne, Québec, Quebec, G1K 9A9*
[2]*British Columbia Geological Survey, 1810 Blanshard Street, Victoria, British Columbia, V8T 4J1*
[3]*Merlin Geoscience Inc., 178 6th Street, Atlin, British Columbia, V0W 1A0*

Abstract

Several gold deposits and prospects in the Canadian Cordillera of British Columbia and Yukon are associated, at least spatially, to major fault zones. The Llewellyn fault and Tally Ho shear zone region of northwestern British Columbia and southern Yukon is the locus of a series of vein-hosted gold prospects and deposits, including the past-producing Engineer and Mount Skukum mines. Many of these gold occurrences have epithermal polymetallic signatures, although some are considered mesothermal-orogenic, as such related to first-order crustal breaks and synchronous magmatism. However, the temporal and genetic relationships between the orogenic- and epithermal-style systems along the Llewellyn fault and Tally Ho shear zone remain to be clearly established. Reconnaissance work has underlined a three-part relationship between these large-scale structures, gold mineralization and Eocene magmatic complexes. Characterization of Llewellyn fault zone in the Bennett Plateau and Tagish Lake area of British Columbia, and of the Tally Ho shear zone in the Tally Ho Mountain, Gold Hill and Mount Hodnett areas of Yukon, and of their spatially associated gold mineralization, aims to test this model and ultimately draw comparisons with the much older, structurally controlled gold deposits of the Archean and Paleoproterozoic.

Introduction

A significant number of gold deposits and prospects in the Canadian Cordillera of British Columbia and Yukon are associated, at least spatially, to major fault zones. The intension of this study is to investigate the extent to which these types of mineralization are comparable to the much older, structurally controlled gold deposits of the Archean and Paleoproterozoic. Research has focused on the Llewellyn fault (Mihalynuk, 1999) and Tally Ho shear zone (e.g. Hart and Radloff, 1990; Tizzard et al., 2009) region of northwestern British Columbia and southern Yukon (Fig. 1). This area is the locus of a series of vein-hosted gold prospects and deposits that are spatial related to faults, including the past-producing Engineer and Mount Skukum mines (Fig. 1, 2). Many of these gold occurrences have epithermal polymetallic signatures (see Nesbitt et al., 1986; Love, 1989; Millonig et al., 2017), although some, like those at Montana Mountain are considered mesothermal (Hart and Pelletier, 1989). The apparent relationship between structure, mineralization, and magmatism points to the intrusion-related, epizonal, endmember of the orogenic gold deposit model, as such deposits are typically related to first-order crustal breaks and synchronous magmatism (Goldfarb et al., 2005). However, the temporal and genetic relationships between the orogenic- and epithermal-style systems along the fault zones remain to be clearly established.

The study area shares some common traits with metallogenically well-endowed Archean belts (e.g. Abitibi, Yellowknife), such as multiple lithotectonic settings and intrusive suites that are affected by major long-lived faults (Fig. 2, 3). Thus, it represents an ideal test site to examine which features are conducive to gold mineralization and if they can be incorporated into advanced exploration strategies that are independent of the age of deposition.

Reconnaissance work (Castonguay et al., 2017; Ootes et al., 2017) has underlined that gold mineralization at the Engineer and Mount Skukum deposits is both spatially and temporally coincident with Eocene magmatism. These first order observations gave rise to a three-part model between large-scale structures, gold mineralization and Eocene magmatism. Traverses were undertaken across the Llewellyn fault zone in the Bennett Plateau and Tagish Lake area of British Columbia, and across the Tally Ho shear zone in the Tally Ho Mountain, Gold Hill and Mount Hodnett areas of Yukon (Fig. 2, 3) to test this model.

Llewellyn fault and Tally Ho shear zone geology

The Llewellyn fault extends from the Tulsequah area, in the south, to Bennett Lake at the British Columbia – Yukon border. Northward, across Bennett Lake, the Tally Ho shear zone occurs on strike, possibly representing the northern extension of the Llewellyn fault (Mihalynuk, 1999; Tizzard et al., 2009).

The Llewellyn fault is a northwest trending, steeply dipping deformation zone that displays an early ductile history overprinted by brittle fabrics (Mihalynuk, 1999). The ductile defor-
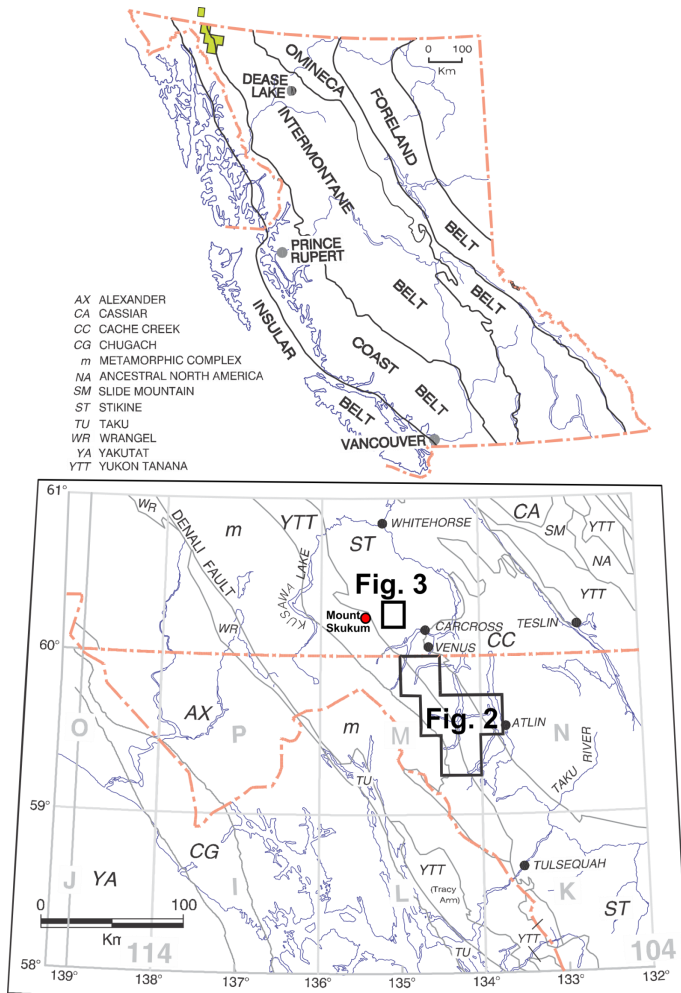
Figure 1. Location map and regional geography and terranes (modified from Mihalynuk, 1999).

mation is mostly expressed to the west of the fault, in presumed Triassic or older schists of the Boundary Ranges metamorphic suite (Fig. 2). East of the Llewellyn fault are the Triassic to Jurassic rocks of the Stuhini and Laberge groups. Several generations of Triassic to Eocene plutons and minor volcanic complexes occur on both sides of the fault (Mihalynuk, 1999). Eocene (ca. 55 Ma) volcano-plutonic centres, assigned to the Sloko Group (Mihalynuk, 1999), are preserved adjacent to the trace of Llewellyn fault along its strike length (Fig. 2). In the study area, these magmatic centres generally cap older units, such as at Engineer Mountain and Teepee Peak in British Columbia (Fig. 2; (Mihalynuk, 1999) or the Bennett Lake and Mount Skukum volcanic complexes in the Yukon (Hart and Radloff, 1990).

Exposure of the Llewellyn fault is rare as it mainly occurs along deep valleys and under lakes. Some exposures and trenching were examined south of the Engineer mine, along the southeastern shore of the Tagish Lake (Fig. 2). One section

across the west side of the Llewellyn fault zone shows moderately to locally strongly-foliated granodiorite to quartz diorite (Aishihik plutonic suite; Fig. 4a) structurally interleaved with chlorite-amphibole and biotite-garnet schists of the Boundary Range metamorphic suite ((Mihalynuk, 1999). Sigmoidal pressure-shadows of plagioclase porphyroblasts (Fig. 4a) and shear and extensional veins (Fig. 4b) suggest apparent northeast-directed and sinistral motions along the main fabric. Gossanous zones locally mark brittle-ductile high strain zones with quartz and sulphide veins (Fig. 4c). To the east, near the Wann River, trenches expose an 80 cm wide quartz vein, sub-parallel to the main fabric, with pyrite, chalcopyrite, tetrahedrite and malachite (Fig. 4d, e). The vein is associated with an alteration front marked by silicification, sulphidization and bleaching of Stuhini Group mafic schists (Fig. 4f).

The Tally Ho shear zone is a southeast trending package of mylonitic to schistose rocks, metabasalt, and minor marble (Hart and Radloff, 1990; Tizzard et al., 2009; Fig. 3) that extends 40 km north of the Yukon – British Columbia border, after which the sequences are covered by Neogene basalt flows. Rock units in the shear zone footwall are variably deformed and include augite phenocrystic basalt, volcaniclastic and sedimentary rocks. Megacrystic granite, granodiorite, quartz diorite and numerous subvolcanic rhyolite dykes intrude or are in fault contact with most units.

The better-exposed section across the Tally Ho shear zone is at Mount Hodnett (Fig. 3). From west to east, exposed units include weakly to moderately foliated granodiorite in sheared contact with steeply west-dipping mylonitic and strongly foliated metabasalt (Fig. 5a) and folded marble (Fig. 5b). Kinematic indicators suggest east-directed motion. Mylonitic basalt structurally interlayered with moderately foliated monzodiorite occur along the eastern side of the shear zone. This juxtaposition is the result of sub-vertical brittle high strain zones marked by cataclasites that overprint the mylonitic fabric in the metabasalt. Some of these cataclastic zones are characterized by a distinctive rusty weathered, iron carbonate alteration (Fig. 5c). All units are intruded by unfoliated feldspar porphyritic andesitic to rhyolitic dykes (Fig. 5d).

To complement ongoing Targeted Geoscience Initiative and Geoscience for Energy and Minerals research, NRCan commissioned a high-resolution aeromagnetic survey in spring of 2017. The data was recently published as maps and derived products (Boulanger and Kiss, 2017a–f). This survey fills a gap in high-resolution aeromagnetic coverage of northern British Columbia and southern Yukon, and will directly benefit future research and mineral exploration.

Discussion and future work

Tentative interpretations are that the Llewellyn and Tally Ho fault zones followed a two stage structural evolution marked by early (Lower Jurassic?) ductile shearing and late (Eocene?) brittle-ductile faulting; each of which are associated with distinct mineralization styles. The discrete late fault zones
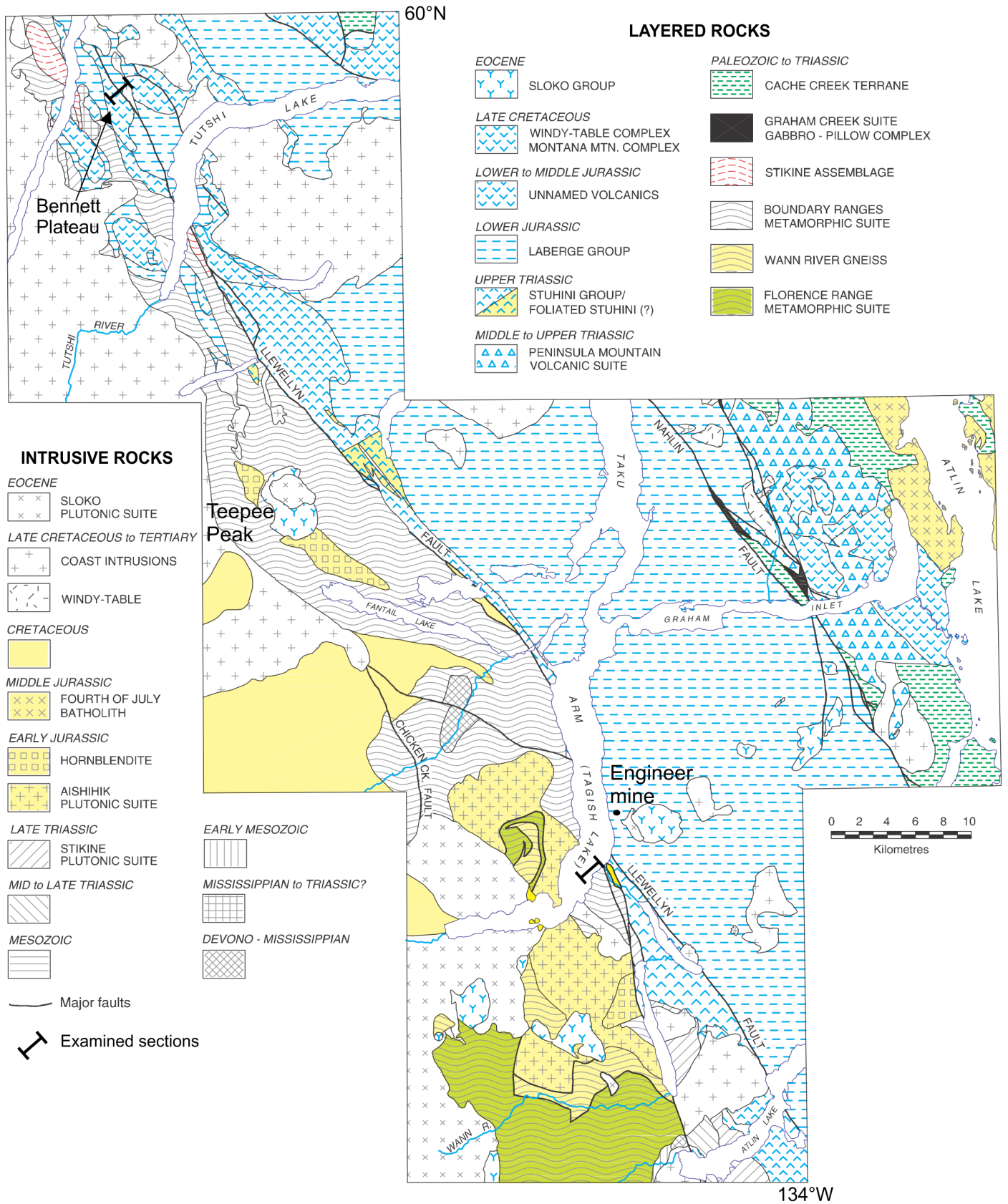
Figure 2. Generalized geology of the Tagish Lake area (modified from Mihalynuk, 1999).
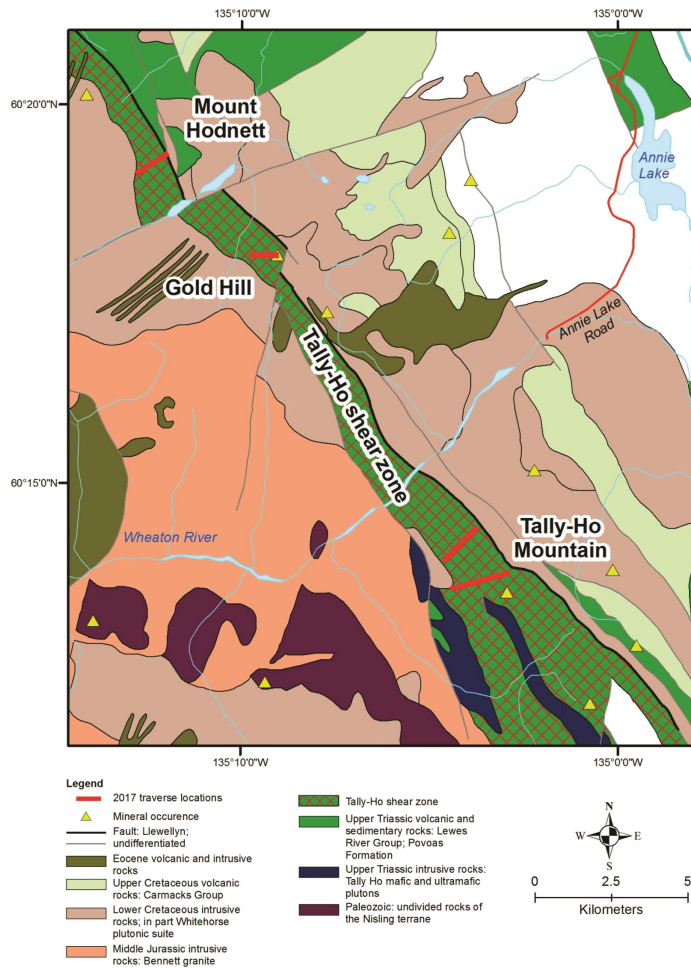
Figure 3. Generalized geology of the Tally Ho shear zone in the Wheaton valley area (modified from Tizzard et al., 2009).

spatially overprint the early, more diffuse shear zones, but both systems may not be tectonically related.

The highly strained schists of the (western) footwall of the Llewellyn fault and that of the Tally Ho shear zone have similar structural and kinematic characteristics. Both structures are also marked by overprinting discrete brittle high strain zones and cataclasites, such as those occurring along the eastern part of the Tally Ho shear zone, at the same structural position as the Llewellyn fault sensu stricto.

Some vein-hosted and skarn-like gold and base metal mineralization is correlated to the early-ductile deformation phase. This early phase is associated with early- to syn-main foliation quartz-amphibole veins hosted predominantly in metamorphic rocks, such as those at Bennett Plateau (e.g. Skarn Zone; Ootes et al., 2017), and the occurrences to the west of the Llewellyn Fault on the south shore of Tagish Lake (Wann River area).

Vein and high strain zone hosted precious metal mineralization consists of gold bearing quartz carbonate veins in splays

and second-order structures related to the Llewellyn fault and spatially associated with Eocene volcanic centres. The principal ore assemblage of the Engineer Mine veins precipitated during a hydrothermal event at ca. 50 Ma (Millonig et al., 2017), which although slightly younger than the Sloko Group magmatism (ca. 55 Ma; (Mihalynuk, 1999), corroborate a genetic link between faulting, Eocene magmatism and epithermal mineralization.

A suite of samples has been collected for radiometric age determinations to constrain the timing of movement(s) along the Llewellyn and Tally Ho faults, magmatism and mineralization. To further investigate the postulated link between faulting, Eocene magmatism and epithermal mineralization, follow up work at the Blackdome epithermal gold deposit of south-central British Columbia is envisioned. Mineralization at Blackdome mine is hosted by ca. 50 Ma volcanic rocks and spatially related to the Fraser fault (Mahoney et al., 2013). The Fraser fault is reported to have undergone dextral strike-slip in the early Eocene, linked to the Cordillera-wide strike-slip and extensional deformation at that time (Mathews and Rouse, 1984; Coleman and Parrish, 1991). A similar style and evolution of gold mineralization at the Blackdome mine and at deposits along the Llewellyn fault zone could substantiate a Cordillera-wide Eocene gold event.

Acknowledgments

References

Boulanger, O. and Kiss, F., 2017a. Residual total magnetic field, aeromagnetic survey of the Llewellyn area, NTS 104-M/8 and parts of 104-M/1,2,6,7, British Columbia; Geological Survey of Canada, Open File 8287, 1 sheet.

Boulanger, O. and Kiss, F., 2017b. Residual total magnetic field, aeromagnetic survey of the Llewellyn area, NTS 104-M/9, 10, 15, 16 and parts of 104-M/11, 14, British Columbia; Geological Survey of Canada, Open File 8288, 1 sheet.

Boulanger, O. and Kiss, F., 2017c. Residual total magnetic field, aeromagnetic survey of the Llewellyn area, NTS 105-D/1, 2, 3 and parts of 105-D/6, 7, 8, Yukon; Geological Survey of Canada, Open File 8289, 1 sheet.
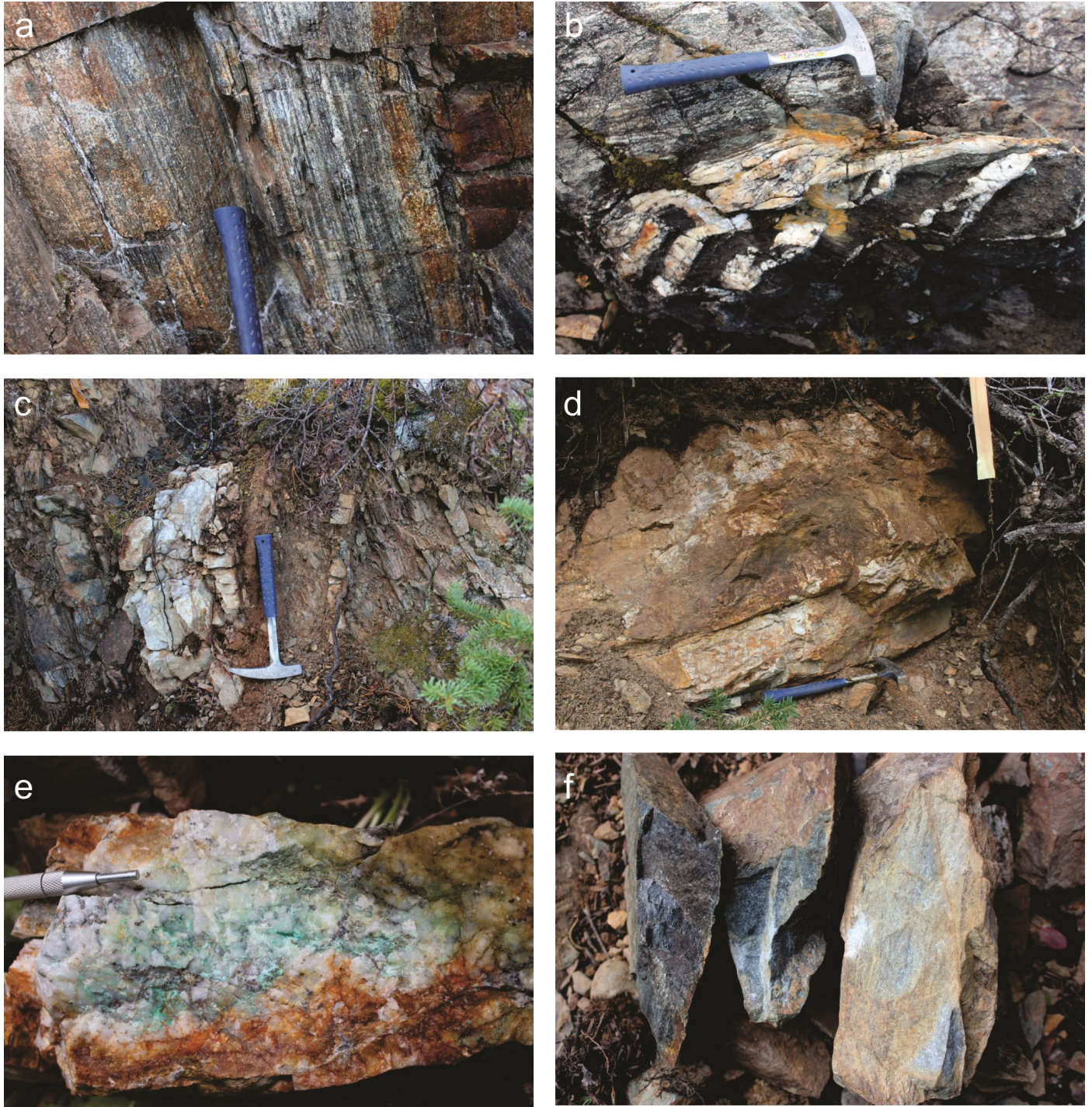
Figure 4. Llewellyn fault section: a) Strongly-foliated quartz diorite of Aishihik plutonic suite; SW of Llewellyn fault on the SE shore of Tagish Lake (view to the east-southeast); b) sheared contact between quartz diorite and amphibole-chlorite-garnet schists with shear and extensional quartz veins at suggesting apparent northeast-directed and sinistral motions along the main fabric; southwest of Llewellyn fault on the SE shore of Tagish Lake (view to the southwest); c) Gossanous zones locally mark brittle-ductile high strain zones with quartz-sulphides veins (view to the east-southeast); d) 80 cm-wide polymetallic quartz vein, sub-parallel to the main fabric (view to the west); e) Piece of the veins with pyrite-chalcopyrite-tetrahedrite and malachite; f) Three rock samples showing the (left to right) alteration front approaching the vein, marked by increasing silicification, sulphidization and bleaching of mafic schists of the Stuhini Group.
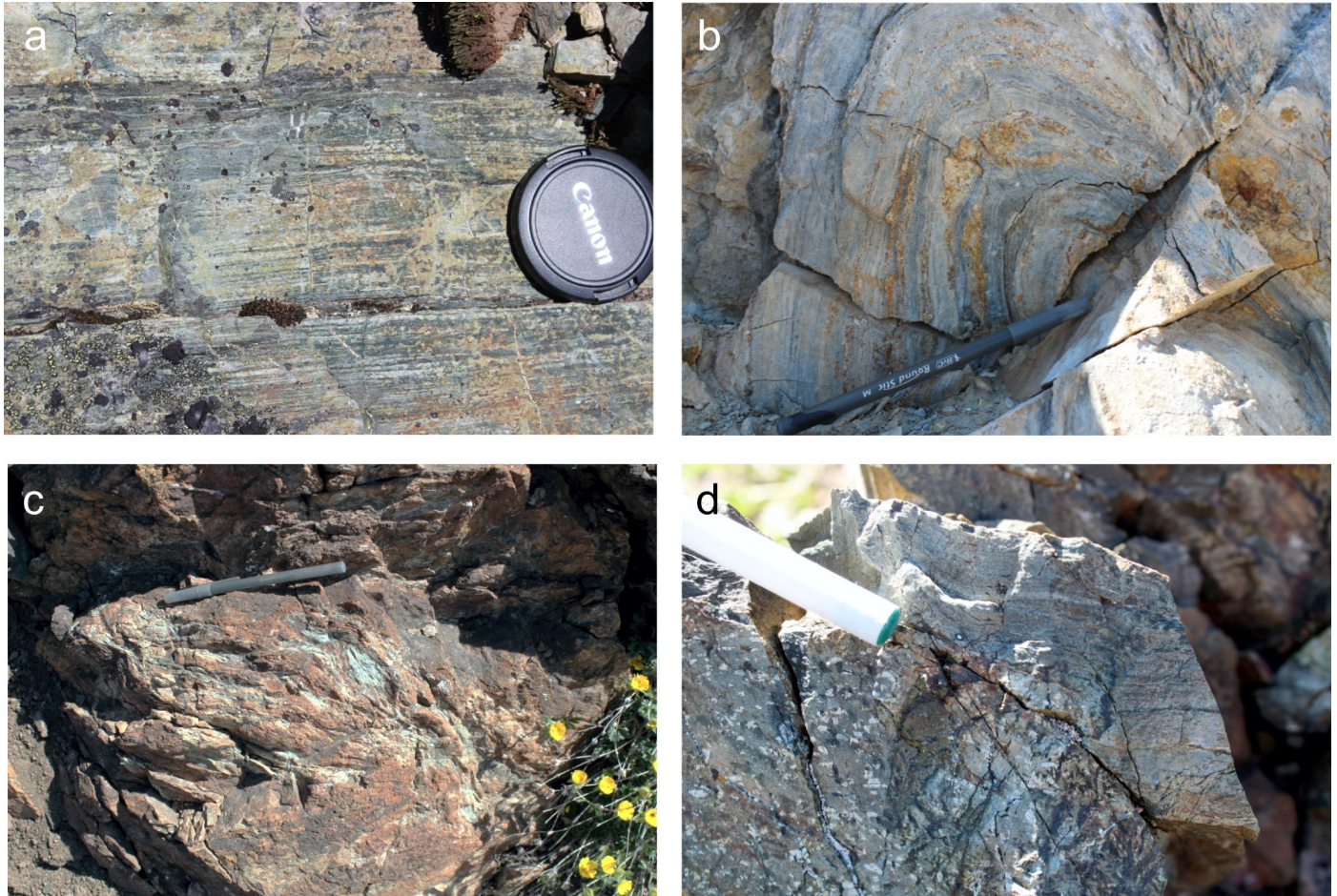
Figure 5. Tally Ho shear zone section at Mount Hodnett: a) strongly foliated to mylonitic mafic schist (view to the northeast); b) Shallow north-northwest-plunging fold in marble; axial-planar main fabric locally visible in more argillaceous beds (view to the north-northwest); c) Altered cataclastic high strain zone in mafic schist (view to the north-northeast); d) Unfoliated feldspar-porphyritic dacitic dyke intruding strongly foliated metabasalt (view to the west-northwest).

Boulanger, O. and Kiss, F., 2017d. First vertical derivative of the magnetic field, aeromagnetic survey of the Llewellyn area, NTS 104-M/8 and parts of 104-M/1,2,6,7, British Columbia; Geological Survey of Canada, Open File 8290, 1 sheet.

Boulanger, O. and Kiss, F., 2017e. First vertical derivative of the magnetic field, aeromagnetic survey of the Llewellyn area, NTS 104-M/9, 10, 15, 16 and parts of 104-M/11, 14, British Columbia; Geological Survey of Canada, Open File 8291, 1 sheet.

Boulanger, O. and Kiss, F., 2017f. First vertical derivative of the magnetic field, aeromagnetic survey of the Llewellyn area, NTS 105-D/1, 2, 3 and parts of 105-D/6, 7, 8, Yukon; Geological Survey of Canada, Open File 8292, 1 sheet.

Castonguay, S., Ootes, L., Mercier-Langevin, P., Rowins, S.M., and Devine, F., 2017. Orogenic gold along Cordilleran faults: Key characteristics and analogies between Phanerozoic and Archean settings; *in* Targeted Geoscience Initiative – 2016 Report of Activities, (ed.) N. Rogers; Geological Survey of Canada, Open File 8199, p. 35–37.

Coleman, M.E. and Parrish, R.R., 1991. Eocene dextral strike-slip and extensional faulting in the Bridge River terrane, southwest British Columbia; Tectonics, v. 10, p. 1222–1238.

Goldfarb, R.J., Baker, T., Dubé, B., Groves, D.I., Hart, C.J.R., and Gosselin, P., 2005. Distribution, character, and genesis of gold deposits in metamorphic terranes; *in* Economic Geology 100th Anniversary Volume, (ed.) J.W. Hedenquist, J.F.H. Thompson, R.J. Goldfarb and J.P. Richards, p. 407–450.

Hart, C.J.R. and Pelletier, K.S., 1989. Geology of Carcross (105D/2) and Part of Robinson (105D/7) Map Areas; Indian and Northern Affairs Canada, Yukon Geological Survey Open File 1989-1, 84p.

Hart, C.J.R. and Radloff, J.K., 1990. Geology of Whitehorse, Alligator Lake, Fenwick Creek, Carcross and part of Robinson map areas (105D/11, 6, 3, 2, & 7); Indian and Northern Affairs Canada, Open File 1990-4, p.1–113.

Love, D.A., 1989. Geology of the epithermal Mount Skukum gold deposit, Yukon Territory; Geological Survey of Canada, Open File 2123, 47p.

Mahoney, J.B., Hickson, C.J., Haggart, J.W., Schiarizza, P., Read, P.B., Enkin, R.J., van der Heyden, P., and Israel, S., 2013. Geology, Taseko Lakes, British Columbia; Geological Survey of Canada, Open File 6150, 5 sheets.

Mathews, W.H. and Rouse, G.E., 1984. The Gang Ranch – Big Bar area, south-central British Columbia: stratigraphy, geochronology, and palynology of the Tertiary beds and their relationship to the Fraser Fault; Canadian Journal of Earth Sciences, v. 21, p. 1132–1144.

Mihalynuk, M.G., 1999. Geology and mineral resources of the Tagish Lake area (NTS 104M/8, 9, 10E, 15 104N/12W), northwestern British Columbia; British Columbia Ministry of Energy, Mines & Petroleum Resources, Bulletin 105, scale, 1: 100 000, 217p.

Millonig, L.J., Beinlich, A., Raudseppa, M., Devine, F., Archibald, D.A., Linnen, R.L., and Groat, L.A., 2017. The Engineer Mine, British Columbia: An example of epithermal Au-Ag mineralization with mixed alkaline and subalkaline characteristics; Ore Geology Reviews, v. 83, p. 235–257.

Nesbitt, B.E., Murowchick, J.B., and Muehlenbachs, K., 1986. Dual origins of lode gold deposits in the Canadian Cordillera; Geology, v. 14, p. 506–509.

Ootes, L., Elliott, J.M., and Rowins, S.M., 2017. Testing the relationship between the Llewellyn fault, gold mineralization, and Eocene volcanism in northwest British Columbia: A preliminary report; *in* Geological Fieldwork 2016, British Columbia Ministry of Energy and Mines, British Columbia Geological Survey Paper 2017-1, p. 49–59.

Tizzard, A.M., Johnston, S.T., and Heaman, L.M., 2009. Arc imbrication during thick-skinned collision within the northern Cordilleran accretionary orogen, Yukon, Canada; Geological Society, London, Special Publications 318, p.309–327.

Lithologic controls on Paleoproterozoic BIF-hosted/associated gold: Overview of Re-Os geochronology and Pb isotopes preliminary results

P. Mercier-Langevin[1], M. Valette[2], S. De Souza[2], R.A. Creaser[3], V.J. McNicoll[4],
P. Grondin-LeBlanc[5], B. St.Pierre[5], M.-C. Lauzon[6], M. Malo[5], O. Côté-Mantha[7]
and M. Simard[8]

[1]*Geological Survey of Canada, 490 rue de la Couronne, Québec, Quebec, G1K 9A9*

[2]*Université du Québec à Montréal, 201 Avenue du Président Kennedy, Montréal, Quebec, H2X 3Y7*

[3]*University of Alberta, 116th Street and 85th Avenue, Edmonton, Alberta, T6G 2R3*

[4]*Geological Survey of Canada, 601 Booth Street, Ottawa, Ontario, K1A 0E8*

[5]*Institut national de la recherche scientifique, Centre Eau Terre Environnement,
490 rue de la Couronne, Québec, Quebec, G1K 9A9*

[6]*Université Laval, 2325 rue de l'Université, Québec, Quebec, G1V 0A6*

[7]*Agnico Eagle Mines Limited, Exploration Division, 765 chemin de la mine Goldex, Val-d'Or, Quebec, J9P 4N9*

[8]*Agnico Eagle Mines Limited, Regional - Technical Services Division, 10 200 route de Preissac,
Rouyn-Noranda, Quebec, J0Y 1C0 X*

Abstract

Eastern Nunavut represents an excellent site to study BIF-hosted gold deposits. Many examples of this type of deposit are present in this region that is largely underlain by Neoarchean rocks that were deformed at Archean and Paleoproterozoic times. Recent research indicates that what was previously considered to be a simple Early Proterozoic gold metallotect associated with the Trans-Hudson orogen at ca. 1.9 to 1.8 Ga rather appears to be a long, multiphase hydrothermal history associated with a number of distinct orogenic events. Preliminary Re-Os analyses on ore-associated arsenopyrite from the Amaruq deposit suggest a major time span with the youngest model ages at ca. 2250 and the oldest at ca. 2650 Ma. Such a long ore-forming history is in agreement with results obtained in the Meliadine district where arsenopyrite Re-Os ages range from 2.3 Ga to 1.8 Ga. The oldest model ages suggest that the Archean basement and host rocks may have played an active role in forming the Paleoproterozoic gold systems.

Introduction

Banded iron-formation (BIF)-hosted gold deposits generally consist of complex, varied styles of gold mineralization that are completely to partially hosted in BIF units (Kerswill, 1993; Dubé and Mercier-Langevin, 2015). Many gold deposits and prospects of eastern Nunavut are hosted or associated with Neaoarchean BIF, but display a diversity and complexity of styles largely related to Paleoproterozoic structures, making this region a prime site to study the lithotectonic controls on BIF-hosted/associated gold (Fig. 1; Mercier-Langevin et al., 2017a). For instance, at Meliadine gold is associated with a crustal-scale fault and its splays (Carpenter and Duke, 2004; Carpenter et al., 2005; Lawley et al., 2015a–c, 2016). In contrast the Portage and Goose deposits of the Meadowbank mine are associated with intensely poly-deformed BIFs (Sherlock et al., 2004; Janvier et al., 2015; Janvier, 2016), as is the case for

the Three Bluffs exploration project (Davies et al., 2010). At Amaruq folded BIFs are associated with steeply-dipping high-strain zones and associated(?) shallowly-dipping vein systems (Côté-Mantha et al., 2015, 2017; Valette et al., 2017a, b, 2018), whereas BIF-hosted gold at the Vault deposit is associated with shallow-dipping sericite-carbonate shears (Mercier-Langevin et al., 2017b). Although gold zones are controlled by Paleoproterozoic structures (e.g. Hrabi et al., 2003; Pehrsson et al., 2013), it is hosted in Neoarchean rocks. Therefore, there is a possibility for an Archean heritage on the gold budget. Recent research indicates a more complex, or at least longer (older) hydrothermal history, than a simple ca. 1.85 Ga gold event in some of these systems (e.g. Meliadine; Lawley et al., 2015a). Important aspects of gold metallogenesis in Nunavut being tackled by this study are the timing of gold introduction, its source, and the age and nature of the major ore-forming events in the region (i.e. Archean versus Paleoproterozoic); specifically determin-
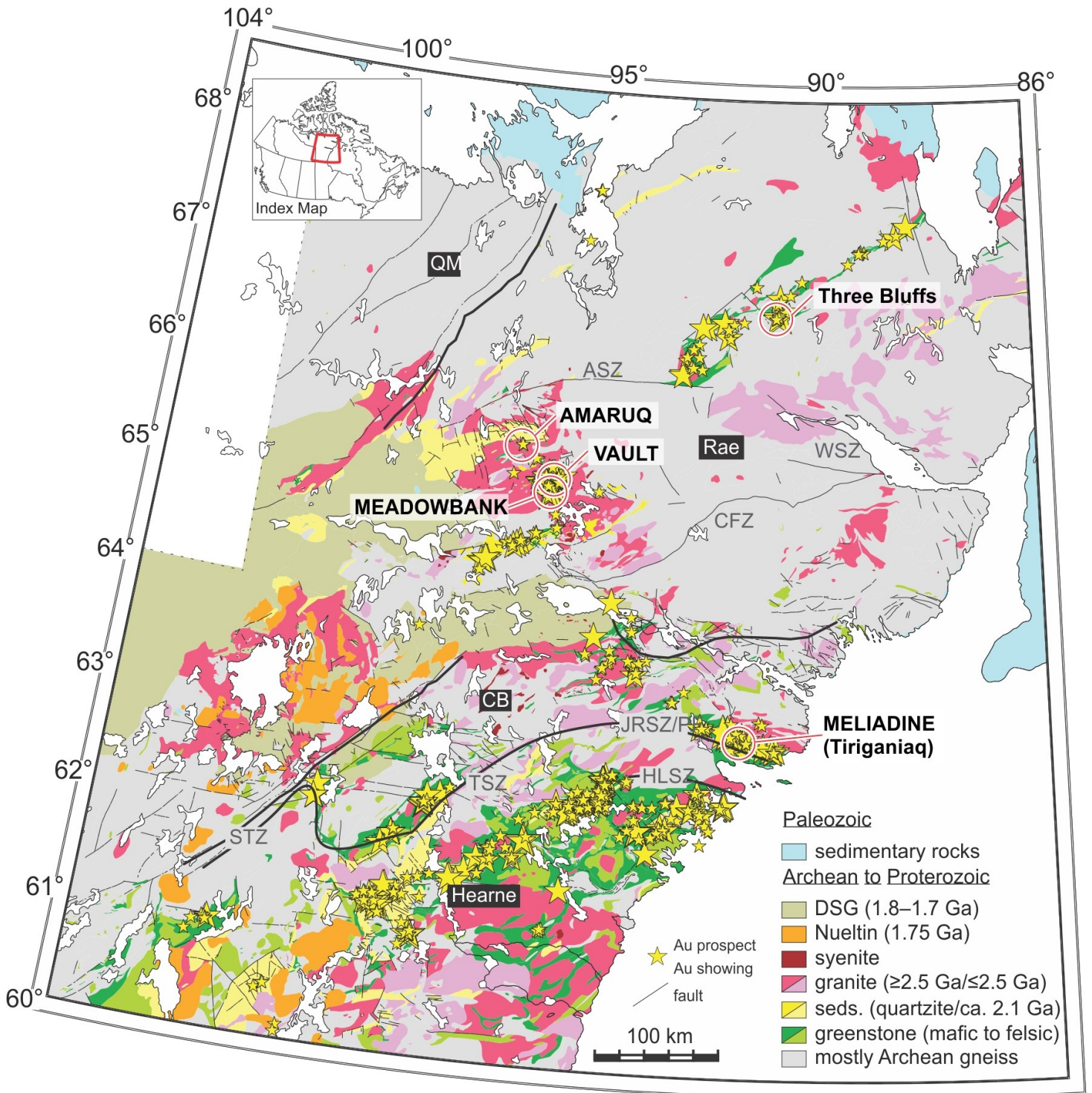
Figure 1. Regional geologic map of the Western Churchill Province (taken from Lawley et al., 2015a). The map shows the distribution of the gold occurrences, including the Amaruq project, and the Vault, Meadowbank and Tiriganiaq deposits. Abbreviations: ASZ = Amer shear zone, CB = Chesterfield block, CFZ = Chesterfield fault zone, DSG = Dubawnt Supergroup, HLSZ = Happy Lake shear zone, JRSZ = Josephine River shear zone, PF = Pyke fault, QM = Queen Maud block, STZ = Snowbird tectonic zone, TSZ = Tyrrell shear zone, WSG = Wager Bay shear zone.
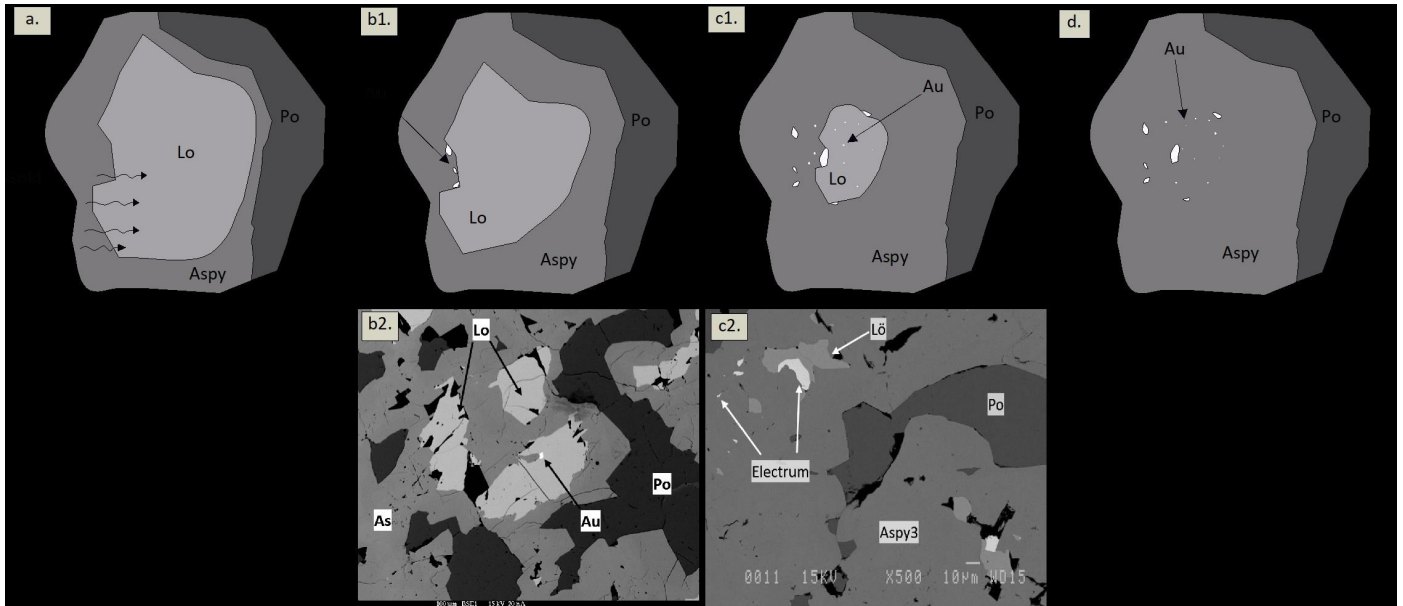
Figure 2. Scanning electron microscope backscatter images (bottom) of arsenopyrite, pyrrhotite, loellingite, and electrum from the Whale Tail zone at Amaruq, and schematic evolution of these phases at peak metamorphism (a: gold diffusion into loellingite) and during retrograde metamorphism (b1, c1 and d: top). From Lauzon et al. (2017).

ing whether gold was introduced into the system during the Archean and remobilized afterwards, or introduced at the Paleoproterozoic.

Four sites were selected to work on resolving those problems (Fig. 1): i) the Amaruq gold project (Côté-Mantha et al., 2015, 2017), 50 km northwest of the Meadowbank mine in the Neoarchean Woodburn Lake group (Grondin-LeBlanc et al., 2016, 2017; Lauzon, 2017; Lauzon et al., 2016, 2017; Mercier-Langevin et al., 2017a; Valette et al., 2016, 2017a, b, 2018); ii) the Vault deposit (Mercier-Langevin et al., 2017b); iii) the Tiriganiaq mine in the Meliadine district (St.Pierre et al., 2018); and iv) Meadowbank mine (Janvier et al., 2015; Janvier, 2016).

Initial results

Ongoing work at Amaruq includes structural mapping at deposit scale, drill core logging, geochemical characterization of the host rocks and mineralized zones, U-Pb ID-TIMS/SHRIMP geochronology on zircon, Re-Os geochronology on sulphides and radiogenic and stable isotope analyzes. The arsenopyrite at Amaruq is generally coarse grained and present in quartz veins, strongly silicified chert bands and amphibole-rich layers in cherts (Lauzon et al. 2017). Arsenopyrite is also associated with varying amounts of pyrrhotite, and locally some loellingite, in response to amphibolite grade metamorphism (Lauzon, 2017: Fig. 2). Detailed petrography shows that early arsenopyrite and pyrrhotite underwent prograde metamorphism to amphibolite conditions to form an assemblage of loellingite-pyrrhotite-arsenopyrite with gold incorporated into the loellingite structure, Loellingite was then retrograded back to

arsenopyrite and pyrrhotite, liberating gold that could not be incorporated in the arsenopyrite structure as shown in Figure 2. The coarse arsenopyrite is often in contact with pyrrhotite, or contains pyrrhotite inclusions (Fig. 3). Gold is mostly found as electrum in association with arsenopyrite and pyrrhotite (Fig. 2), or relatively uniformly distributed in arsenopyrite (Fig. 3).

Rhenium is generally very low in most Amaruq samples analyzed to date and no precise isochron age can be obtained. The following samples all come from the Whale Tail zone of
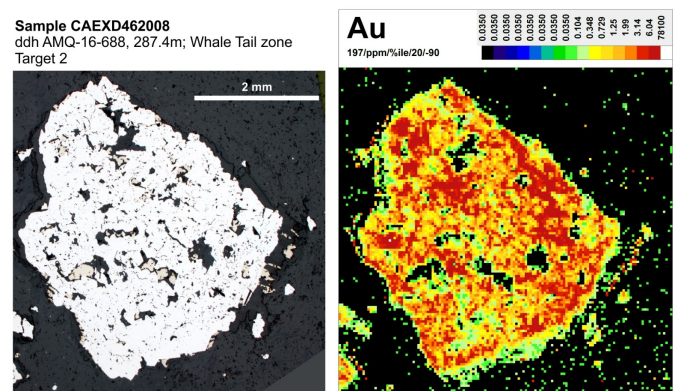
Figure 3. LA-ICP-MS map for CAEXD462008: (left) photomicrograph in reflected light of a large arsenopyrite grain made of smaller grains with pyrrhotite inclusions. (right) Element (gold) map (logarithmic concentration scale in ppm) showing that gold is mostly concentrated in the fine-grained arsenopyrite while the pyrrhotite and late granoblastic rim are devoid of gold.

Amaruq have yielded some provisional data. CAEXD288986 (ddh IVR-14-158 at 84.2 m) contains very little common osmium and yielded preliminary individual model ages between 2490 to 2550 Ma and a preliminary weighted average model age of 2523 Ma (Mercier-Langevin et al., work in progress, 2017). CAEXD462004 (ddh AMQ-16-668 at 53.2 m) gave preliminary model ages ranging from 2465 to 2552 Ma, with the preliminary weighted average model age of 2516 Ma (Mercier-Langevin et al., work in progress, 2017). CAEXD462007 (ddh AMQ-16-688 at 286.6 m) shows an age distribution between 2250 and 2550 Ma, with the three oldest fractions yielding a preliminary weighted average model age of 2549 Ma (Mercier-Langevin et al., work in progress, 2017). CAEXD462008 (ddh AMQ-16-688 at 287.4 m) provided a distribution of ages between ca. 2470 and 2650 Ma, with the older model ages yielding a preliminary weighted average model age of 2626 Ma (Mercier-Langevin et al., work in progress, 2017). In addition to the Amaruq analyses, sample GSC-MBK-12-001 from the Meadowbank deposit (open pit, Portage South mine) has a preliminary model ages ranging from 1830 to 1913 Ma, and a weighted average model age of 1899 Ma (Janvier, 2016).

These interim results need refinement and additional analyses are in progress, but preliminary results suggest a major time span with the youngest model ages at ca. 2250 and the oldest at ca. 2650 Ma. Similarly, Lawley et al. (2015a) obtained model ages varying between 1.8 and 2.3 Ga on arsenopyrite from the Meliadine district. Except for the Meadowbank sample, ca. 1.85 Ga Trans-Hudson orogen ages (Pehrsson et al., 2013) were not yet been obtained in this study.

Most of the lead isotope analyzes are still pending. However, based on preliminary and partial data (Mercier-Langevin et al., work in progress, 2017), there is large spread in the $^{206}Pb/^{204}Pb$ and $^{207}Pb/^{204}Pb$ ratios. This suggests source mixing and heritage. Further work (e.g. initial Pb correction, in situ measurements) is necessary before more detailed interpretations are possible.

Expected outcomes and future work

Preliminary results on Re-Os geochronology and Pb isotope analyzes suggest a long, protracted hydrothermal history and/or mixed source for the metals in the western Churchill. This agrees with the work of Lawley et al. (2015a) in the Meliadine district that demonstrated that the Paleoproterozoic gold metallotect (cf. Miller et al., 1994) comprises multiple, temporally distinct gold events.

Further work and analyzes (Re-Os and Pb isotopes) are expected to shed more light on the timing of events and potential metal sources in the area. Detailed petrography and microanalyzes (scanning electron microscope and laser ablation inductively-coupled plasma mass spectrometry) will help refine textural relationships and strengthen any correlation between, Re-Os ages, Pb-Pb signatures and geological events. In order to constrain the genesis of the sulphide zones and their associated gold, sulphur isotopes will also be incorporated into the data analysis.

Ultimately, integrated studies at Amaruq, Vault, Meadowbank and Tiriganiaq are expected to contribute to resolving the role of Archean basement and host rocks on Paleoproterozoic gold systems.

References

Carpenter, R.L. and Duke, N.A., 2004. Geologic setting of the West Meliadine gold deposits, Western Churchill Province, Nunavut, Canada; Exploration and Mining Geology, v. 13, p. 49–65.

Carpenter, R.L., Duke, N.A., Sandeman, H.S., and Stern, R., 2005. Relative and absolute timing of gold mineralization along the Meliadine trend, Nunavut, Canada: Evidence for Paleoproterozoic gold hosted in an Archean greenstone belt; Economic Geology, v. 100, p. 567–576.

Côté-Mantha, O., Gosselin, G., Vaillancourt, D., and Blackburn, A., 2015. Amaruq: A new gold discovery in Nunavut, Canada; NewGenGold 2015 meeting, Extended Abstracts volume, p. 41–56.

Côté-Mantha, O., Gosselin, G., Vaillancourt, D., Blackburn, A., 2017. The Amaruq deposits – Building a customized toolset and using a flexible geomodel: Optimization from discovery to mine development; *in* Proceedings of Exploration 17: Sixth Decennial International Conference on Mineral Exploration 2017, p. 553–567.

Davies, T., Richards, J.P., Creaser, R.A., Heaman, L.M., Chacko, T., Simonetti, A., Williamson, J., and McDonald,

D.W., 2010. Paleoproterozoic age relationships in the Three Bluffs Archean iron formation-hosted gold deposit, Committee Bay greenstone belt, Nunavut, Canada; Exploration and Mining Geology Journal, v. 19, p. 55–80.

Dubé, B. and Mercier-Langevin, P. (ed.), 2015. Targeted Geoscience Initiative 4: Contributions to the Understanding of Lode Gold Deposits, with an Emphasis on Implications for Exploration; Geological Survey of Canada, Open File 7852, 293 p.

Grondin-LeBlanc, P., Mercier-Langevin, P., Malo, M., Côté-Mantha, O., Simard, M., Barbe, P., Valette, M., and De Souza, S., 2016. Contrôles structuraux principaux sur la nature et la distribution de l'or dans les successions volcanosédimentaires précambriennes polytectonisées – exemple de la zone Whale Tail du projet Amaruq; Abstracts, Quebec Mines 2016, Québec, DV2016-03, p. 93.

Grondin LeBlanc, P., Mercier-Langevin, P., Malo, M., Côté-Mantha, O., Simard, M., Barbe, P., Valette, M., and De Souza, S., 2017. Structural controls on the nature and distribution of gold in polytectonized Precambrian volcano-sedimentary successions: an example from the Whale Tail Zone, Amaruq project, Nunavut; Geological Survey of Canada, Scientific Presentation 63, 1 sheet.

Hrabi, R.B., Barclay, W.A., Fleming, D., and Alexander, R.B., 2003. Structural evolution of the Woodburn Lake group in the area of the Meadowbank gold deposit, Nunavut: Geological Survey of Canada, Current Research 2003-C27, 10 p.

Janvier, V., 2016. Géologie du gisement d'or Meadowbank encaissé dans des formations de fer rubannées, Nunavut, Canada; Ph.D. thesis, Institut national de la recherche scientifique – Centre Eau, Terre et Environnement, Québec, Quebec, 472 p.

Janvier, V., Castonguay, S., Mercier-Langevin, P., Dubé, B., Malo, M., McNicoll, V.J., Creaser, R.A., De Chavigny, B., and Pehrsson, S.J., 2015. Geology of the banded iron formation-hosted Meadowbank gold deposit, Churchill Province, Nunavut; *in* Targeted Geoscience Initiative 4: Contributions to the understanding of Precambrian lode gold deposits and implications for exploration, (ed.) B. Dubé and P. Mercier-Langevin; Geological Survey of Canada, Open File 7852, p. 255–269.

Kerswill, J.A., 1993. Models for iron-formation-hosted gold deposits; *in* Mineral Deposits Modeling, (ed.) R.V. Kirkham, W.D. Sinclair, R.I. Thorpe and J.M. Duke; Geological Association of Canada, Special Paper 40, p. 171–199.

Lauzon, M.-C., 2017. Empreinte minéralogique et géochimique des minéralisations aurifères de la zone Whale Tail du projet Amaruq; B.Sc. thesis, Université Laval, Québec, Quebec, 48 p.

Lauzon, M.-C., Mercier-Langevin, P., Beaudoin, G., Valette, M., De Souza, S., Côté-Mantha, O., and Simard, M., 2016. Empreinte minéralogique et géochimique des minéralisations aurifères de la zone Whale Tail du projet Amaruq et

applications à la définition de vecteurs d'exploration; Abstracts, Quebec Mines 2016, Québec, DV2016-03, p. 94.

Lauzon, M.-C., Mercier-Langevin, P., Beaudoin, G., Côté-Mantha, O., Simard, M., Valette, M., and de Souza, S., 2017. Mineralogy and geochemistry of the Whale Tail zone, Amaruq gold project, Nunavut; Geological Survey of Canada, Scientific Presentation 61, 2017; 1 sheet.

Lawley, C.J.M., Creaser, R.A., Jackson, S., Yang, Z., Davis, B., Pehrsson, S., Dubé, B., Mercier-Langevin, P., and Vaillancourt, D., 2015a. Unravelling the Western Churchill Province Paleoproterozoic gold metallotect: constraints from Re-Os arsenopyrite and U-Pb xenotime geochronology and LA-ICP-MS arsenopyrite trace element chemistry at the BIF-hosted Meliadine gold district, Nunavut, Canada; Economic Geology, v. 110, p. 1425–1454.

Lawley, C.J.M., Dubé, B., Mercier-Langevin, P., Kjarsgaard, B., Knight, R., and Vaillancourt, D., 2015b. Defining and mapping hydrothermal footprints at the BIF-hosted Meliadine gold district, Nunavut, Canada; Journal of Geochemical Exploration, v. 155, p. 33–55.

Lawley, C., Dubé, B., Mercier-Langevin, P., McNicoll, V., Creaser, R., Pehrsson, S., Castonguay, S., Blais, J.-C., Simard, M., Davis, B., and Jackson, S., 2015c. Setting, age, and hydrothermal footprint of the emerging Meliadine gold district, Nunavut; *in* Targeted Geoscience Initiative 4: Contributions to the understanding of Precambrian lode gold deposits and implications for exploration, (ed.) B. Dubé and P. Mercier-Langevin; Geological Survey of Canada, Open File 7852, p. 99–111.

Lawley, J.M.C., McNicoll, V., Sandeman, H., Pehrsson, S., Simard, M., Castonguay, S., Mercier-Langevin, P., and Dubé, B., 2016. Age and geological setting of the Rankin Inlet greenstone belt and its relationship to the gold endowment of the Meliadine gold district, Nunavut, Canada; Precambrian Research, v. 275, p. 471–795.

Mercier-Langevin, P., Valette, M., De Souza, S., McNicoll, V.J., Grondin-LeBlanc, P., Creaser, R.A., Côté-Mantha, O., Simard, M., and Malo, M., 2017a. Lithologic and tectonic controls on Paleoproterozoic BIF-hosted/associated gold; *in* Targeted Geoscience Initiative – 2016 Report of Activities, (ed.) N. Rogers; Geological Survey of Canada, Open File 8199, p. 39–42.

Mercier-Langevin, P., Janvier, V., McNicoll, V., Castonguay, S., Dupuis, C., Dubé, B., de Chavigny, B., and Côté-Mantha, O., 2017b. Géologie du gisement d'or Vault et implications pour l'exploration aurifère dans les ceintures de roches vertes précambriennes; Geological Survey of Canada, Scientific Presentation 64, 1 sheet.

Mercier-Langevin, P., Rogers, N., Dubé, B., Bleeker, W., Castonguay, S., McNicoll, V.J., Chapman, J.B., Lawley, C.J.M., Bellefleur, G., Houlé, M.G., Pinet, N., Jackson, S., Davis, B., Bécu, V., Peter, J.M., Paradis, S., Potter, E.G., Bjerkelund, C., Villeneuve, M.E., and Evans, R., 2017c. Targeted Geoscience Initiative: 2016 Report of Activities –

an overview; *in* Targeted Geoscience Initiative 2016 Report of Activities, (ed.) N. Rogers; Geological Survey of Canada Open File 8199, p. 7–16.

Miller, A.R., Balog, M.J., Barham, B.A., and Reading, K.L., 1994. Geology of the Early Proterozoic gold metallotect, Hurwitz Group in the Cullaton-Griffin lakes area, central Churchill Structural Province, Northwest Territories; Geological Survey of Canada, Current Research 1994-C, p. 135–146.

Pehrsson, S.J., Berman, R.G., and Davis, W.J., 2013. Paleoproterozoic orogenesis during Nuna aggregation: A case study of reworking of the Rae craton, Woodburn Lake, Nunavut; Precambrian Research, v. 232, p. 167–188.

Sherlock, R., Pehrsson, S., Logan, A.V., Hrabi, R.B., and Davis, W.J., 2004. Geological setting of the Meadowbank gold deposit, Woodburn Lake Group, Nunavut; Exploration and Mining Journal, v. 13, p. 67–107.

St.Pierre, B., Mercier-Langevin, P., Simard, M., Côté-Mantha, O., Malo, M., and Servelle, G., 2018. Structural and lithologic controls on the nature and distribution of gold in the BIF-associated 1150 and 1250 lode series at Tiriganiaq, Meliadine district, Rankin Inlet greenstone belt, Nunavut; *in* Targeted Geoscience Initiative: 2017 report of activities, volume 1, (ed.) N. Rogers; Geological Survey of Canada, Open File 8358, p. 157–161.

Valette, M., De Souza, S., Mercier-Langevin, P., Côté-Mantha, O., Simard, M., McNicoll, V., and Barbe, P., 2016. Géologie du projet aurifère Amaruq – résultats préliminaires et implications pour l'exploration des gisements d'or associés aux formations de fer en terrain archéens et protérozoïques; Abstracts, Quebec Mines 2016, Québec, DV2016-03, p. 93.

Valette, M., De Souza, S., Mercier-Langevin, P., Côté-Mantha, O., Simard, M., McNicoll, V., and Barbe, P., 2017a. Geology of the 4.2 Moz Au Amaruq project, Nunavut; Proceedings of the 14th Biennial SGA meeting, Québec, Society for Geology Applied to Mineral Deposits, p. 199–202.

Valette, M., De Souza, S., Mercier-Langevin, P., Côté-Mantha, O., Simard, M., McNicoll, V., Barbe, P., 2017b. Geology of the 130 t (4.2 Moz) Au, banded iron-formation-hosted Amaruq project, Nunavut; Geological Survey of Canada, Scientific Presentation 60, 1 sheet.

Valette, M., De Souza, S., Mercier-Langevin, P., McNicoll, V., Grondin-LeBlanc, P., Côté-Mantha, O., Simard, M., and Malo, M., 2018. Lithological, hydrothermal, structural and metamorphic controls on the style, geometry and distribution of the auriferous zones at Amaruq, Churchill Province, Nunavut; *in* Targeted Geoscience Initiative: 2017 report of activities, volume 1, (ed.) N. Rogers; Geological Survey of Canada, Open File 8358, p. 153–156.

Lithological, hydrothermal, structural and metamorphic controls on the style, geometry and distribution of the auriferous zones at Amaruq, Churchill Province, Nunavut

M. Valette[1], S. De Souza[1], P. Mercier-Langevin[2], V.J. McNicoll[3], P. Grondin-LeBlanc[4], O. Côté-Mantha[5], M. Simard[5] and M. Malo[4]

[1]*Université du Québec à Montréal, 201 Avenue du Président- Kennedy, Montreal, Quebec, H2X 3Y7*
[2]*Geological Survey of Canada, 490 rue de la Couronne, Québec, Quebec, G1K 9A9*
[3]*Geological Survey of Canada, 601 Booth Street, Ottawa, Ontario, K1A 0E8*
[4]*Institut national de la Recherche scientifique, Centre Eau Terre Environnement,*
490 rue de la Couronne, Québec, Quebec, G1K 9A9
[5]*Agnico Eagle Mines limited, Exploration Division, 765 chemin de la mine Goldex, Val-d'Or, Quebec, J9P 4N9 X*

Abstract

The Amaruq gold project is part of the Woodburn Lake group of the Rae Domain, in the western Churchill Province. Exploration for BIF-hosted gold deposits in this region has led to an emerging gold district, which comprises the Meliadine, Meadowbank and Amaruq deposits. In the Amaruq area, the Woodburn Lake group comprises a 250 m thick Neoarchean volcano-sedimentary sequence intercalated with chert and silicate facies iron formations. The two main ore zones (i.e. Whale Tail and IVR) exhibit different ore and alterations styles related to distinct geochemical and structural traps. The Whale Tail zone is primarily characterized by stratabound pyrrhotite-arsenopyrite-loellingite -gold replacement type mineralization in chert and iron formation. The ore zones at IVR consist of gold-bearing quartz-carbonate veins developed at, or near contacts between favourable units or reverse fold fault zones. In both ore zones, the geometry and style of the ore are controlled by at least the two Paleoproterozoic phases of deformation, and crosscutting relationships between folded sedimentary rocks and quartz-carbonate veins indicate protracted hydrothermal activity.

Introduction

This study is intended to advance understanding of the lithotectonic controls on banded iron formation (BIF)-hosted gold deposits by examining the recently discovered Amaruq deposit, Nunavut. Previous research has clearly indicated that BIF-hosted gold deposits are characterized by varied mineralization styles related to a number of factors including complex geological histories (Kerswill, 1995). Algoma-type BIFs are iron rich rocks, initially chemically precipitated from water close to a volcanic centre, which are generally intensely deformed especially when associated to gold mineralization (Kerswill, 1995; Gross, 2009).

The Kivalliq region of Nunavut contains the Meliadine, Meadowbank and Amaruq BIF-hosted gold deposits projects (Côté-Mantha et al., 2015; Mercier-Langevin et al., 2017a). BIF-hosted or associated gold zones in eastern Nunavut are structurally controlled by Paleoproterozoic crustal-scale faults, shear zones, and/or polydeformed Neoarchean BIFs, which have created conduits and traps for gold mineralization (see Mercier-Langevin et al., 2017a and references therein). Early work on the Amaruq property shows that the mineralized zones have a complex geometry, are structurally and stratigraphically controlled, and are hosted in complexly folded and faulted Neoarchean volcanic and sedimentary rocks, including chert and silicate-facies BIFs (Côté-Mantha et al., 2015; Valette et al., 2017a). Examination of the Amaruq deposit will elucidate the principal controls on gold mineralization in silicate facies BIF-bearing successions and test the hypothesis of an Archean influence on the Paleoproterozoic ore-forming events (Mercier-Langevin et al., 2017b).

Ongoing research at Amaruq is focused on establishing the principal lithological, hydrothermal, structural and metamorphic controls on ore genesis and gold distribution. This enhanced knowledge will contribute to more robust exploration models for BIF-hosted/associated gold deposits in similar settings elsewhere.

Amaruq gold deposit geology

The Amaruq gold deposit is located 120 km north of Baker Lake and 50 km to the northwest of the Meadowbank mine (Fig. 1a). Two main gold zones of contrasting styles are present in the Amaruq area: the Whale Tail and IVR zones (Fig. 1b).
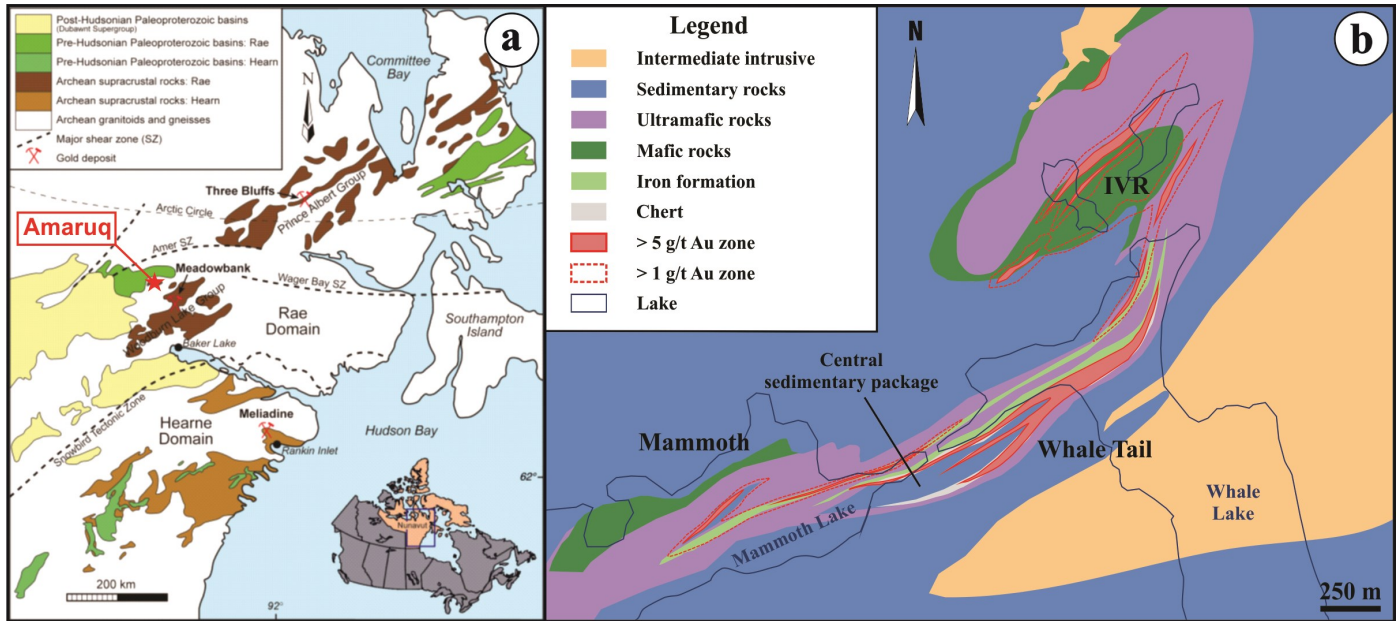
Figure 1. a) Simplified geological map of the Rae and Hearne domains of the western Churchill Province with the location of the Amaruq gold project in the Woodburn Lake greenstone belt (modified from Davies et al., 2010). b) Simplified geological map of the Amaruq area showing the location of the Whale tail and IVR zones (modified from Agnico Eagle Mines Ltd., 2016).

The mineralized zones are underlain by the Neorchean supra-crustal rocks of the Woodburn Lake group (ca. 2.71 Ga), within the Rae Domain of the western Churchill Province (Zaleski, 2005; Pehrsson et al., 2013; Jefferson et al., 2015). On the Amaruq property, the Woodburn Lake group includes a 250 m thick volcano-sedimentary sequence composed of mafic to ultramafic volcanic rocks and greywacke interlayered with chert and silicate-facies iron-formation (Fig. 1b). This narrow volcano-sedimentary band is bounded to the north and south by thick greywacke successions that are cut by large dioritic to granodioritic intrusions. Preliminary U-Pb zircon dating indicate that the bounding sedimentary sequences are younger than ca. 2650 Ma, with the central, ore-hosting panel having a younger heritage than the two bounding panels (McNicoll, work in progress, 2017), suggesting a much smaller source region and more local source and/or local sub-basin. The bounding sedimentary panels are older than ca. 2600 Ma, the preliminary age of a crosscutting diorite (McNicoll, work in progress, 2017).

Geochemical signatures determined by whole rock analysis and portable XRF lithotyping indicate that the ultramafic rocks to the north of the central sedimentary package are tholeiitic, whereas those to the south are transitional (Côté-Mantha et al., 2017). The two packages of ultramafic rocks are folded and pinch-out east-northeast of the IVR zone (Fig. 1b). Whether there is continuity between the Whale Tail and IVR zones is currently under investigation.

The Whale Tail zone is mainly characterized by strata-bound to discordant pyrrhotite-arsenopyrite-loellingite-gold replacement-style ore, 'silica flooding' and veining in iron-formation and chert layers (Fig. 2a, b; Grondin-Leblanc et al., 2016; Lauzon et al., 2017). High-grade gold zones are preferentially developed along lithological contacts and in open fold hinge zones. In the IVR area, gold is primarily associated with several sets of quartz ± carbonate veins (Fig. 2c) preferentially developed in the hinge zone of a shallow plunging fold (Valette et al., 2017b). The observed main auriferous quartz ± carbonate gold veins appear to be deformed and recrystallized. At least two phases of Paleoproterozoic deformation control the geometry of the mineralized zones (Fig. 2d–f), with peak metamorphic conditions varying from upper greenschist to lower amphibolite facies.

Both the main auriferous quartz ± carbonate veins of the IVR zone and the replacement-style and vein orebodies of the Whale Tail zone are deformed and have shallowly east-plunging ore shoots. Crosscutting relationships between these auriferous veins and other vein sets suggest the possibility of a multiphase or protracted hydrothermal history. Correlations between these contrasting ore styles, timing of mineralization and any genetic relationship between the gold-bearing and other vein sets are still being examined.

Future work

Future work will include petrological and geochemical characterization of the host rocks and alteration zones to help establish the stratigraphy on the Amaruq property and define the ore forming conditions. In addition, microprobe, scanning

154
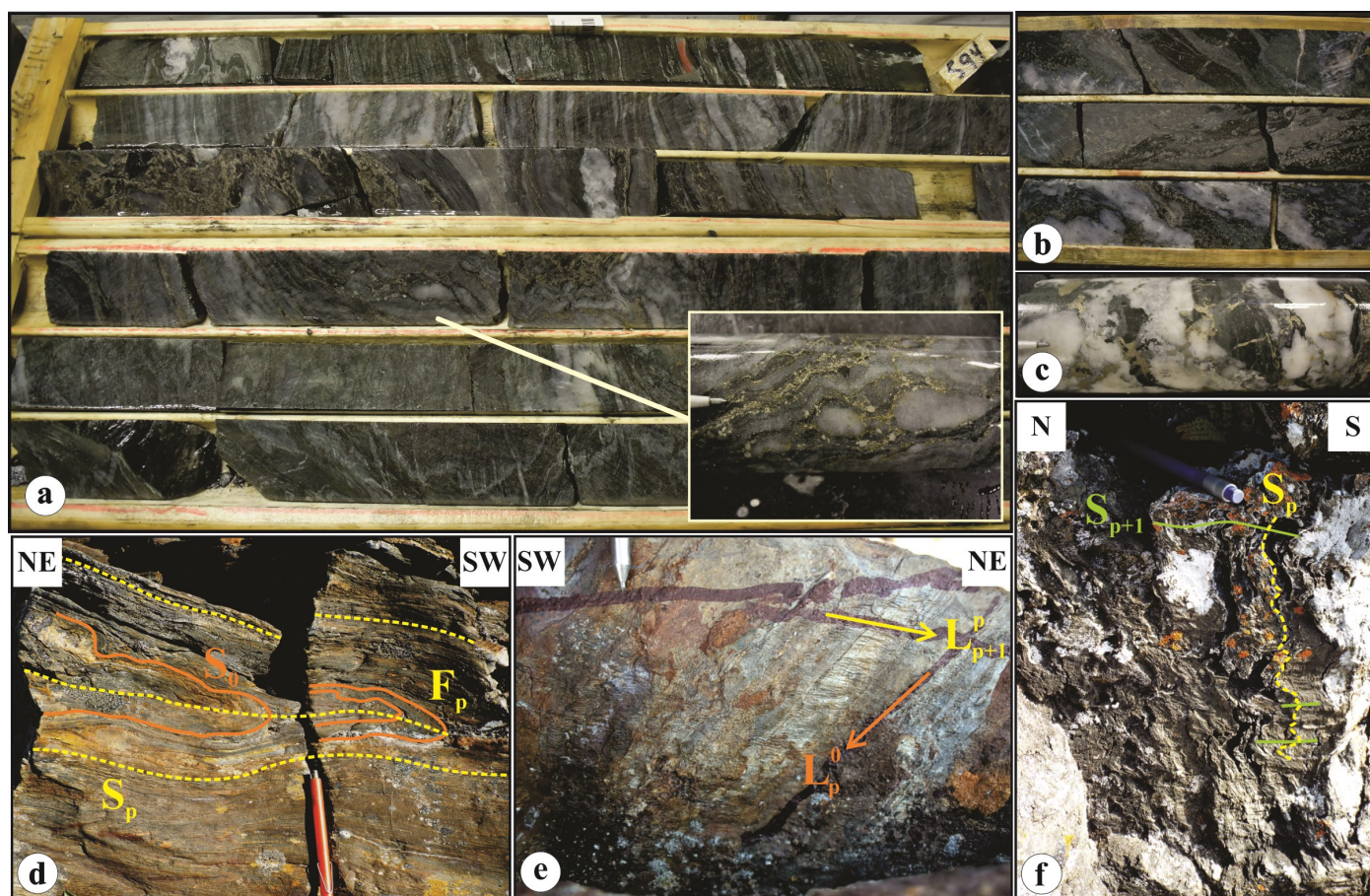
Figure 2. Photographs of mineralized and hydrothermally altered rocks and veins of the Whale Tail and IVR zones, Amaruq deposit. a) Interval of mineralized chert and iron formation interlayered with sericitized greywacke cut by the main auriferous set of veins. The inset shows the layering partially obliterated by silica flooding in a fold hinge zone. b) Stratabound to locally discordant disseminated pyrrhotite characterizing the replacement-type mineralization of iron formation. c) Chert and iron formation are cut by quartz ± carbonate-biotite-chlorite-pyrrhotite veins, which corresponds to the second auriferous set of veins. d) Isoclinally folded (F_p) stratification (S_0) with axial planar cleavage (S_p). e) Intersection lineations between S_0/S_p and S_p/S_{p+1}. F) S_p schistosity affected by subhorizontal S_{p+1} crenulation cleavage.

electron microscope, laser ablation inductively coupled plasma mass spectrometry, and U-Pb zircon geochronology, are underway or planned to constrain the relative and absolute timing of events, as well as the mineralogical and chemical composition of the ore.

Acknowledgments

References

Côté-Mantha, O., Gosselin, G., Vaillancourt, D., and Blackburn, A., 2015. Amaruq: A new gold discovery in Nunavut, Canada; NewGenGold 2015 meeting, Extended Abstracts volume, p. 41–56.

Davies, T., Richards, J.P., Creaser, R.A., Heaman, L.M., Chacko, T., Simonetti, A., Williamson, J., and McDonald, D.W., 2010. Paleoproterozoic age relationships in the Three Bluffs Archean iron formation-hosted gold deposit, Committee Bay greenstone belt, Nunavut, Canada; Exploration and Mining Geology Journal, v. 19, p. 55–80.

Grondin-LeBlanc, P., Mercier-Langevin, P., Malo, M., Côté-Mantha, O., Simard, M., Barbe, P., Valette, M., and De Souza, S., 2016. Contrôles structuraux principaux sur la nature et la distribution de l'or dans les successions volcanosédimentaires précambriennes polytectonisées – Exemple de la zone Whale Tail du projet Amaruq; Aabstracts, Quebec Mines 2016, Québec, DV2016-03, p. 93.

Gross, G.A., 2009. Iron Formation in Canada, Genesis and Geochemistry; Geological Survey of Canada, Open File 5987, 164 p.

Jefferson, C.W., White, J.C., Young, G.M., Patterson, J., Tschirhart, V., Pehrsson, S.J., Calhoun, L., Rainbird, R.H., Peterson, T.D., Davis, W.J., Tella, S., Chorlton, L.B., Scott, J.M.J., Percival, J.A., Morris, W.A., Keating, P., Anand, A., Shelat, Y., and MacIsaac, D., 2015. Outcrop and remote predictive geology of the Amer Belt and basement beside and beneath the northeast Thelon Basin, in parts of NTS 66-A, B, C, F, G and H, Kivalliq Region, Nunavut; Geological Survey of Canada, Open File 7242, 1 sheet.

Kerswill, J.A., 1995. Iron-formation-hosted stratabound gold; *in* Geology of Canadian Mineral Deposit, (ed.) O.R. Eckstrand, W.D. Sinclair and R.I. Thorpe; Geological Survey of Canada, Geology of Canada, no. 8, p. 367–382.

Lauzon, M.-C., Mercier-Langevin, P., Beaudoin, G., Côté-Mantha, O., Simard, M., Valette, M., and de Souza, S., 2017. Mineralogy and geochemistry of the Whale Tail zone, Amaruq gold project, Nunavut; Geological Survey of Canada, Scientific Presentation 61, 2017; 1 sheet.

Mercier-Langevin, P., Rogers, N., Dubé, B., Castonguay, S., McNicoll, V.J., Lawley, C.J.M., Bleeker, W., Bellefleur, G., Chapman, J.B., Pinet, N., Jackson, S.E., Davis, W.J., Bécu, V., Peter, J.M., Paradis, S., Potter, E.G., Bjerkelund, C., Villeneuve, M.E., and Evans, R., 2017a. Targeted Geoscience Initiative: 2016 Report of Activities – An Overview; *in* Targeted Geoscience Initiative – 2016 Report of Activities, (ed.) N. Rogers; Geological Survey of Canada, Open File 8199, p. 7–16.

Mercier-Langevin, P., Valette, M., De Souza, S., McNicoll, V.J., Grondin-LeBlanc, P., Creaser, R.A., Côté-Mantha, O., Simard, M., and Malo, M., 2017b. Lithologic and tectonic controls on Paleoproterozoic BIF-hosted/associated gold; *in* Targeted Geoscience Initiative – 2016 Report of Activities, (ed.) N. Rogers; Geological Survey of Canada, Open File 8199, p. 39–42.

Pehrsson, S.J., Berman, R.G., and Davis, W.J., 2013. Paleoproterozoic orogenesis during Nuna aggregation: A case study of reworking of the Rae craton, Woodburn Lake, Nunavut; Precambrian Research, v. 232, p. 167–188.

Valette, M., De Souza, S., Mercier-Langevin, P., Côté-Mantha, O., Simard, M., McNicoll, V.J, Barbe, P., 2017a. Geology of the 130 t (4.2 Moz) Au, banded iron-formation-hosted Amaruq project, Nunavut; Geological Survey of Canada, Scientific Presentation 60, 1 sheet.

Valette, M., De Souza, S., Mercier-Langevin, P., Côté-Mantha, O., Simard, M., McNicoll, V.J, and Barbe, P., 2017b. Geology of the 4.2 Moz Au Amaruq project, Nunavut; Proceedings of the 14th Biennial SGA meeting, Québec, Society for Geology Applied to Mineral Deposits, p. 199–202.

Zaleski, E., 2005. Meadowbank River area, Nunavut; Geological Survey of Canada, Map 2068A, scale 1:50 000.

Structural and lithologic controls on the nature and distribution of gold in the BIF-associated 1150 and 1250 lode series at Tiriganiaq, Meliadine district, Rankin Inlet greenstone belt, Nunavut

B. St.Pierre[1], P. Mercier-Langevin[2], M. Simard[3], O. Côté-Mantha[3], M. Malo[1] and G. Servelle[3]

[1]*Institut national de la Recherche scientifique, Centre Eau Terre Environnement,*
490 rue de la Couronne, Québec, Quebec, G1K 9A9

[2]*Geological Survey of Canada, 490 rue de la Couronne, Québec, Quebec, G1K 9A9*

[3]*Agnico Eagle Mines limited, Exploration Division, 765 chemin de la mine Goldex, Val-d'Or, Quebec, J9P 4N9*

Abstract

The Meliadine gold project is located within the Rankin Inlet greenstone belt, Nunavut; one of Canada's largest emerging gold districts. A large part of the 1000 and 1100 ore zones or 'lodes' at the Tiriganiaq mine are closely associated with the moderately to steeply north-dipping Lower fault and are characterized by decimetre to metre wide laminated, fault-fill veins and associated deformed extensional veins. Other ore zones such as the 1150 and 1250 lodes, north of the 1000 and 1100 lodes, appear to have a more complex geometry. Preliminary research indicates that the main controls on gold distribution within the 1150 lode series are Lower fault parallel, narrow north-dipping reverse shears that overprint the slightly steeper, north-dipping main foliation and associated axial planar tight folds. Shallowly south-dipping extension veins associated with the shear zones and related fault-fill veins are preferentially developed in tightly folded decimetre to metre thick BIF layers around the moderately north-dipping reverse shears.

Introduction

Deformed banded iron formation (BIF)-hosted deposits are classified into two descriptive groups: i) large deposits in which the ore is mainly hosted in Algoma-type BIFs; and ii) deposits where only part of the mineralization is hosted in BIF (Dubé and Mercier-Langevin, 2015). The Meliadine gold district, located within the Rankin Inlet greenstone belt, Nunavut (Fig. 1), is one of Canada's largest BIF-hosted gold districts. Meliadine district deposits are closely associated with the crustal-scale Pyke fault and its splays and so are assigned to the partly BIF-hosted group (Dubé and Mercier-Langevin, 2015; Lawley et al., 2015a). One of principal deposits of the district (Tiriganiaq) largely consist of decimetre to metre thick laminated fault-fill veins and associated extensional veins with coarse arsenopyrite replacement of magnetite-rich BIF units along vein selvages (Carpenter et al., 2005; Lawley et al., 2015 a-c, 2016).

This study aims at documenting the geometry of the Tiriganiaq vein systems and at defining their evolution relative to the deformation events, and at evaluating the potential role played by some lithologies (e.g. BIF) on vein and gold grades distribution. Ongoing underground developments at the Tiriganiaq mine facilitate observation and documentation of the structural style and lithologic controls. This information is used to document and study the nature and complexities of partly BIF-hosted gold deposits, which will contribute at enhancing exploration efficiency in this district and elsewhere.

Specific objectives of this study include: i) documenting the geometry and structural style of the mineralized quartz ± carbonate veins through underground mapping and logging drill holes; ii) characterizing the different sets of quartz ± carbonate veins based on their geometry, composition and evolution relative to deformation; iii) identifying which systems or generation of quartz ± carbonate veins are related to gold; iv) integrating the observations, results and interpretation with existing exploration models; v) expand upon the overall metallogenic model for the district and for orogenic/BIF-hosted gold deposits in general.

Tiriganiaq deposit geology

The Tiriganiaq deposit, located in the central part of the Meliadine district, just north of the Pyke fault, consists of a series of ore zones, or 'lodes' that are stacked from south to north in the Pyke fault hanging wall. Most of the ore is hosted in the Upper Oxide formation (Fig. 2) and closely associated with the Lower fault, west-trending subsidiary splay of the Pyke fault. The main ore zones (i.e. lodes 1000 and 1100), are directly associated with the moderately to steeply north-dipping Lower fault with decimetre to metre wide laminated, fault-fill veins and associated deformed extensional veins. Oth-

Figure 1. Regional geology map and location of the Meliadine gold district, and the Tiriganiaq deposit (Number 2 on the map). Modified from Lawley et al. (2016).

er ore zones such as the 1150 and 1250 lodes, north of the 1000 and 1100 lodes, have a more complex geometry, which suggests secondary controls on ore distribution. The structural and lithologic controls on some of the vein systems in the 1150 and 1250 lodes, and gold distribution in these systems, are currently not well established.

Preliminary results

Preliminary results indicate that there are multiple parallel narrow, decimetre to metre wide shear zones acting as a first order control of mineralization at ore zone scale (Fig. 3). These shear zones, which dip moderately to the north and are parallel to the Lower fault to the south, control the location of vein corridors (deformed fault-fill/shear veins). Extensional quartz ± carbonate veins are associated with the shear veins and are particularly well mineralized in BIF units, forming stratabound zones of coarse arsenopyrite replacement of magnetite layers

along vein margins (Fig. 4a, b). The mineralized extensional veins dip shallowly to the south in north dipping units. The veins appear to be late- to post-folding, and syn- to late-shearing. The shear zones have a slightly shallower dip than the main foliation (270°/55° and 270°/60°, respectively; Fig. 3). Shearing appears to overprint the foliation although both may be part of a protracted deformation event. The main foliation is axial planar to folding, and all units are folded, although folding is most prominent in decimetre to metre thick BIF units. Lithologic contacts are generally parallel with the main foliation at drift scale, except in hinge zones. Kinematic indicators almost uniformly show reverse motion in the shear zones. There are rare, relatively late discrete cataclasites (north dipping) that cut both the foliation and the shear fabrics and have normal movement.

Shallowly south-dipping extension veins associated with the shear zones are clearly preferentially developed in tightly

158
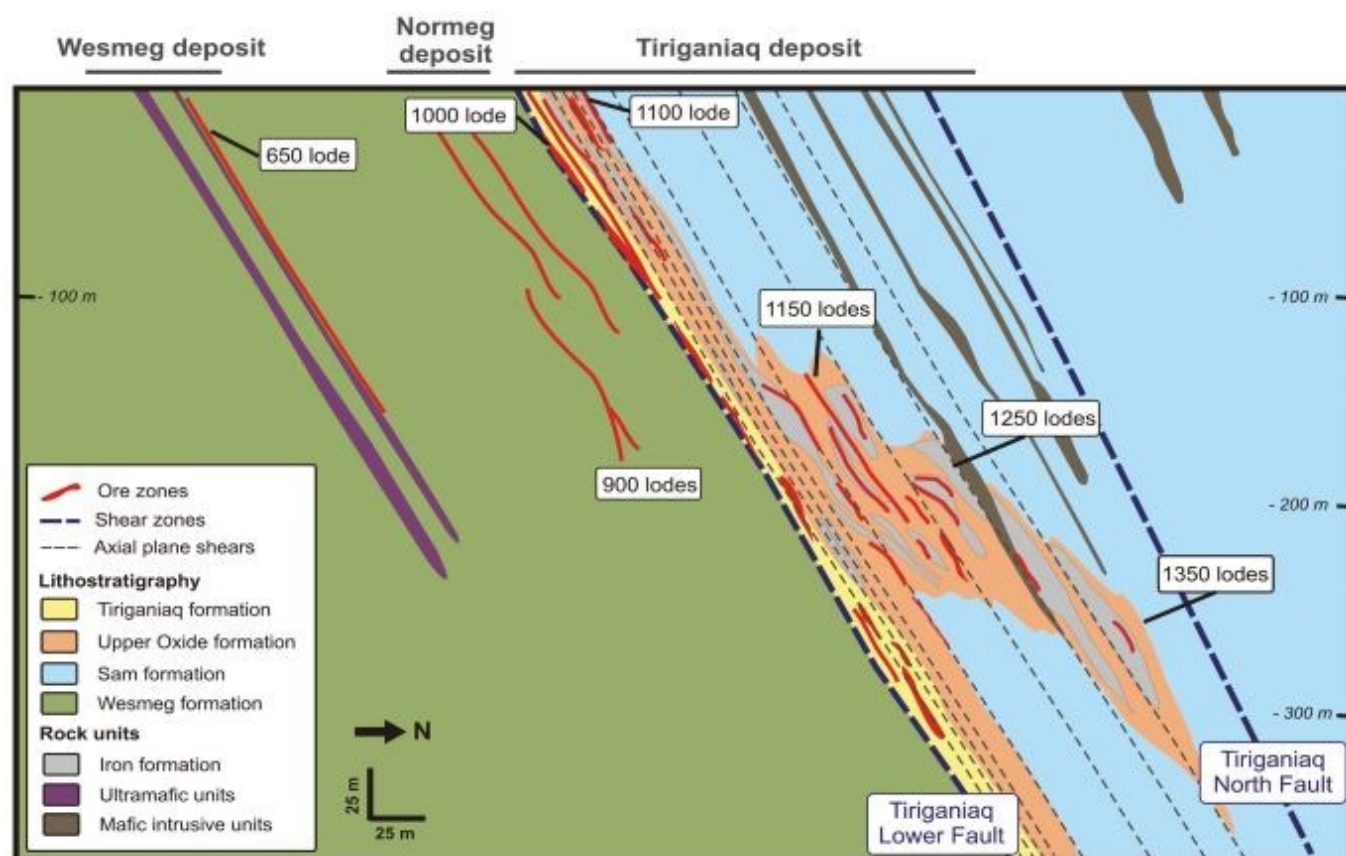
Figure 2. Schematic cross-section 9770E of the Tiriganiaq, Normeg and Wesmeg deposits in the central part of the Meliadine gold district. This section shows the planar nature of the 1000 and 1100 lode series in comparison to the structurally complex 1150 and 1250 lode series in the Tiriganiaq deposit (after Lawley et al., 2015a).

folded decimetre to metre thick BIF layers around the moderately north-dipping reverse shears. These shears and the related fault-fill veins are however better developed in the altered siltstones at the contact with the BIF units.

Future work

Ongoing work includes further underground mapping of relevant exposures, geochemical characterization of the host rocks and mineralized zones, and microstructural analysis of key fabrics registered by the host rocks using thin section microscopy. Underground mapping of new exposures (1150 and 1250 lode series) will help in unravelling the controls on the distribution and density of the south dipping extension veins, i.e. if these south-dipping extension veins are more abundant in large hinge zones, or along attenuated fold limbs. Establishing whether there is a higher density of extension veins in the hanging wall or footwall of shears will be done by looking at the larger scale geometry of the ore zones and high-grade gold intercepts in section, plan view, and longitudinal view.

Geochemical characterization of the host rocks and mineralized zones will be used to further assess lithologic controls on gold grades and distribution. The results from this study may directly contribute at developing improved exploration models by providing key information on the structural controls (conduits and traps) on orogenic gold deposits.

Acknowledgments

Figure 3. a) Large quartz-carbonate-arsenopyrite vein controlled by a moderately north-dipping shear, along with extension quartz ± carbonate veins that are transposed into the main, slightly steeper foliation, indicating a component of reverse motion (north over south) on the ore-controlling shear corridor. Also shows a refracted, shallowly south-dipping quartz-carbonate-arsenopyrite vein and bedding-parallel replacement zone in the BIF in the footwall of the shear corridor. Looking west. b) Same as 3a with main units and features schematized. A = Large quartz-carbonate-arsenopyrite vein controlled by a moderately north-dipping shear. B = extensional quartz ± carbonate veins that are transposed into the main foliation. C = refracted, shallowly south-dipping quartz – carbonate – arsenopyrite vein and bedding-parallel replacement zone in the BIF in the footwall of the shear corridor.
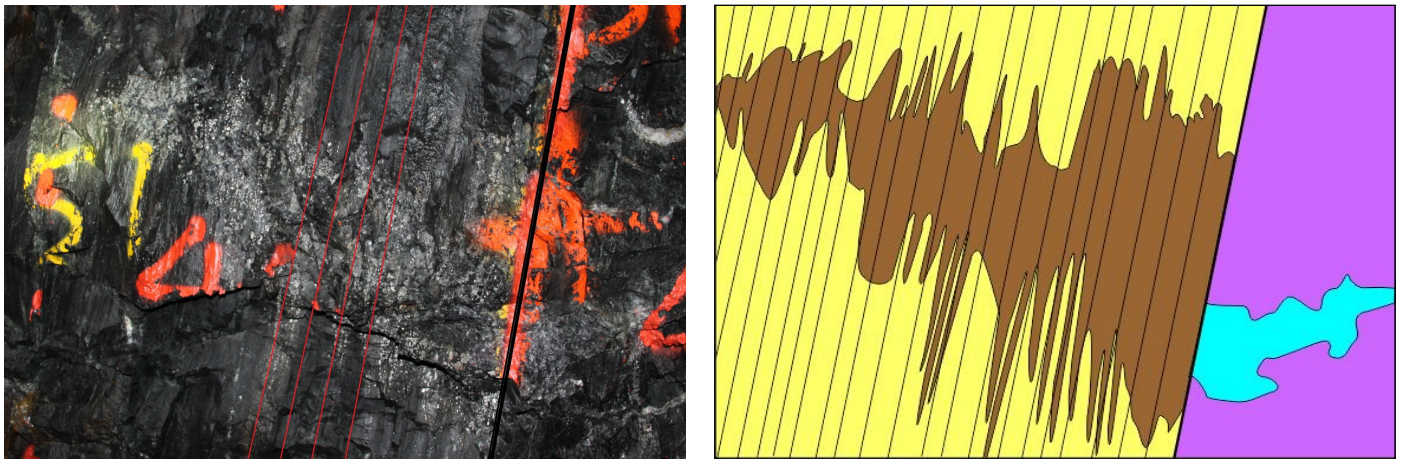
Figure 4. a) Right wall of CC300-152 (looking east). The solid black line represents the contact between BIF (left) and a chloritic siltstone (right). Shallowly south-dipping extensional quartz ± carbonate veins forming stratabound zones of coarse arsenopyrite replacement of magnetite layers along vein margins. The red lines represent the orientation of bedding and the main foliation (dip of approximately 70° to the north). Note the presence of the vein in the siltstone but the absence of arsenopyrite replacement. b) Illustration of Figure 4a. Shows a shallowly south-dipping quartz-carbonate with minimal arsenopyrite extensional vein extend into a BIF unit forming stratabound zones of coarse arsenopyrite replacement of magnetite layers along vein margins. The fine black lines within the BIF represent the orientation of the bedding and the main foliation (dip of approximately 70° to the north). Note the presence of the vein in the siltstone but the absence of major arsenopyrite replacement.

References

Carpenter, R.L., Duke, N.A., Sandeman, H.S., and Stern, R., 2005. Relative and absolute timing of gold mineralization along the Meliadine trend, Nunavut, Canada: Evidence for Paleoproterozoic gold hosted in an Archean greenstone belt; Economic Geology, v. 100, p. 567−576.

Dubé, B. and Mercier-Langevin, P., 2015. Targeted Geoscience Initiative 4: Contributions to the understanding of Precambrian lode gold deposits and implications for exploration; Geological Survey of Canada, Open File 7852, p. 1–24.

Lawley, C.J.M., Dubé, B., Mercier-Langevin, P., McNicoll, V.J., Creaser, R.A., Pehrsson, S., Castonguay, S., Blais, J.-C., Simard, M., Davis, W.J., and Jackson, S.E., 2015a. Setting, age, and hydrothermal footprint of the emerging Meliadine gold district, Nunavut; in Targeted Geoscience Initiative 4: Contributions to the understanding of Precambrian lode gold deposits and implications for exploration, (ed.) B. Dubé and P. Mercier-Langevin; Geological Survey of Canada, Open File 7852, p. 99–111.

Lawley, C.J.M., Creaser, R.A., Jackson, S., Yang, Z., Davis, W.J., Pehrsson, S., Dubé, B., Mercier-Langevin, P., and Vaillancourt, D., 2015b. Unravelling the Western Churchill Province Paleoproterozoic gold metallotect: Constraints from Re-Os arsenopyrite and U-Pb xenotime geochronology and LA-ICP-MS arsenopyrite trace element chemistry at the BIF-hosted Meliadine gold district, Nunavut, Canada; Economic geology, v. 110, p. 1425–1454.

Lawley, C.J.M., Dubé, B., Mercier-Langevin, P., Kjarsgaard, B.A., Knight, R., and Vaillancourt, D., 2015c. Defining and mapping hydrothermal footprints at the BIF-hosted Meliadine gold district, Nunavut, Canada; Journal of Geochemical Exploration, v. 155, p. 33–55.

Lawley, C.J.M., McNicoll, V.J., Sandeman, H., Pehrsson, S., Simard, M., Castonguay, S., Mercier-Langevin, P., and Dubé, B., 2016. Age and geological setting of the Rankin Inlet greenstone belt and its relationship to the gold endowment of the Meliadine gold district, Nunavut, Canada; Precambrian Research, v. 275, p. 471–795.

Breccia styles and controls on carbonate replacement-type ('Carlin-type') gold zones, Rackla belt, east-central Yukon

N. Pinet[1], P.J. Sack[2], P. Mercier-Langevin[1], D. Lavoie[1], B. Dubé[1], J. Lane[3] and V. Brake[1]

[1]*Geological Survey of Canada, 490 rue de la Couronne, Québec, Quebec, G1K 9A9*
[2]*Yukon Geological Survey, 102-300 Main Street Whitehorse, Yukon, Y1A 2B5*
[3]*ATAC Resources Ltd., 1016-510 West Hastings Street, Vancouver, British Columbia, V6C 0B3*

Abstract

Drillhole logging of the three main Carlin-type prospects of eastern Rackla belt (north-central Yukon) demonstrates the diversity of ore styles and the frequent association of mineralization with several types of brecciated intervals formed through sedimentary, hydrothermal and/or tectonic processes. This attests to the opportunistic nature of mineralizing fluids that exploit permeable pathways, regardless of their origin.

Introduction

Carlin-type deposits are sedimentary-hosted gold deposits characterized by submicron ('invisible') gold contained in the arsenical rims of pyrite grains (Cline et al., 2005). The deposit type is named after the Carlin mine, Nevada, the first large deposit of this type discovered in the southwest United States.

In the type districts of Nevada, this broad definition masks a plethora of ore styles that vary from one deposit to the other, or even within the same deposit. These marked changes include, and partly result from, the relative importance of stratigraphic and structural controls (Teal and Jackson, 2002). In the broad spectrum of Carlin-type deposits, the original Carlin deposit represents the stratigraphically-controlled end-member, whereas the Deep Star deposit (Heitt et al., 2003) is a structurally-controlled end-member.

The occurrence of several Carlin-type gold prospects in a relatively small area (< 50 km^2) of north-central Yukon provides an opportunity to document their key characteristics and study the variability of sediment-hosted mineralization outside Nevada, with the broader aim of identifying the main controls on location, geometry and grade of mineralized zones.

Rackla belt carbonate-replacement type gold zones

The Rackla belt in north-central Yukon is a 5 to 15 km wide east-trending zone (bounded to the south by the Dawson Thrust and to the north by the Kathleen Lakes Fault) that marks the northern boundary of the Selwyn Basin in this region (Fig. 1). The regional geology of the Rackla belt was mapped by Colpron et al. (2013) and Moynihan (2016), with the main characteristics of Carlin-type prospects summarized by Tucker et al. (2012), Tucker (2015), Beaton (2015), Palmer and Kuiper (2016) and Pinet et al. (2017a, b).

Drill hole logging of eastern Rackla belt main prospects (Conrad, Sunrise and Anubis; Fig. 1) has confirmed several previously ascribed mineralization characteristics, including: i) the general association of realgar and orpiment with gold mineralized intervals (these minerals are commonly good visual guides for mineralization); ii) a partial to complete decarbonatization of mineralized intervals; iii) the local silicification or argillitization within or close to mineralized intervals; and iv) the occurrence of several generations of cross-cutting vein sets of varying composition (including one set characterized by a calcite and realgar infill that is commonly found close to mineralized zones).

Despite these common traits, there is a clear diversity in styles of gold mineralization and a frequent association of mineralization with brecciated intervals. Such characteristics are well known for the Nevada Carlin-type deposits, but are not well documented for Yukon prospects. Breccia is used herein as a broad generic term for a rock composed of angular to subangular rock fragments held together by a mineral cement or in a fine-grained matrix. In the Conrad, Sunrise and Anubis prospects, many breccias are not auriferous, but many mineralized intervals occur in brecciated rocks. Thus, understanding the origin(s) of the breccias and their specific association (or lack of) to mineralization is of prime importance.

Breccia types

Several types of mineralized breccia are recognized and their formation interpreted as related to sedimentary, hydrothermal and/or tectonic processes (Fig. 2). In some cases, multiple breccia events and processes are identified within a single breccia interval. Furthermore, preliminary interpretations on the origin of some intervals remain uncertain due to complicating factors such as intense/complex mineralization and alteration. That mineralization preferentially occurs in brecciated
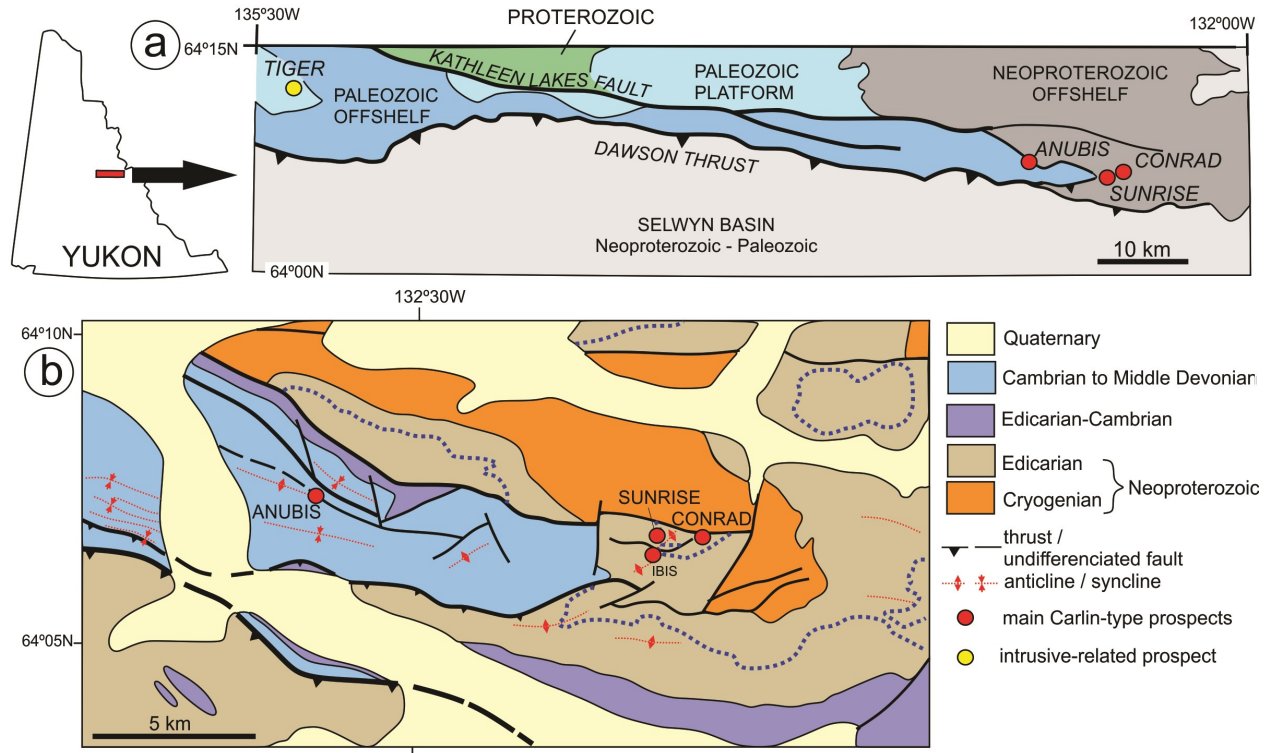
Figure 1. a) Geological setting of the Rackla belt in east-central Yukon (modified from Colpron et al., 2013). b) Geological map of the eastern Rackla belt (simplified from Moynihan, 2016). The blue dotted line is a marker horizon corresponding to the contact between the Nadaleen and Gametrail formations.
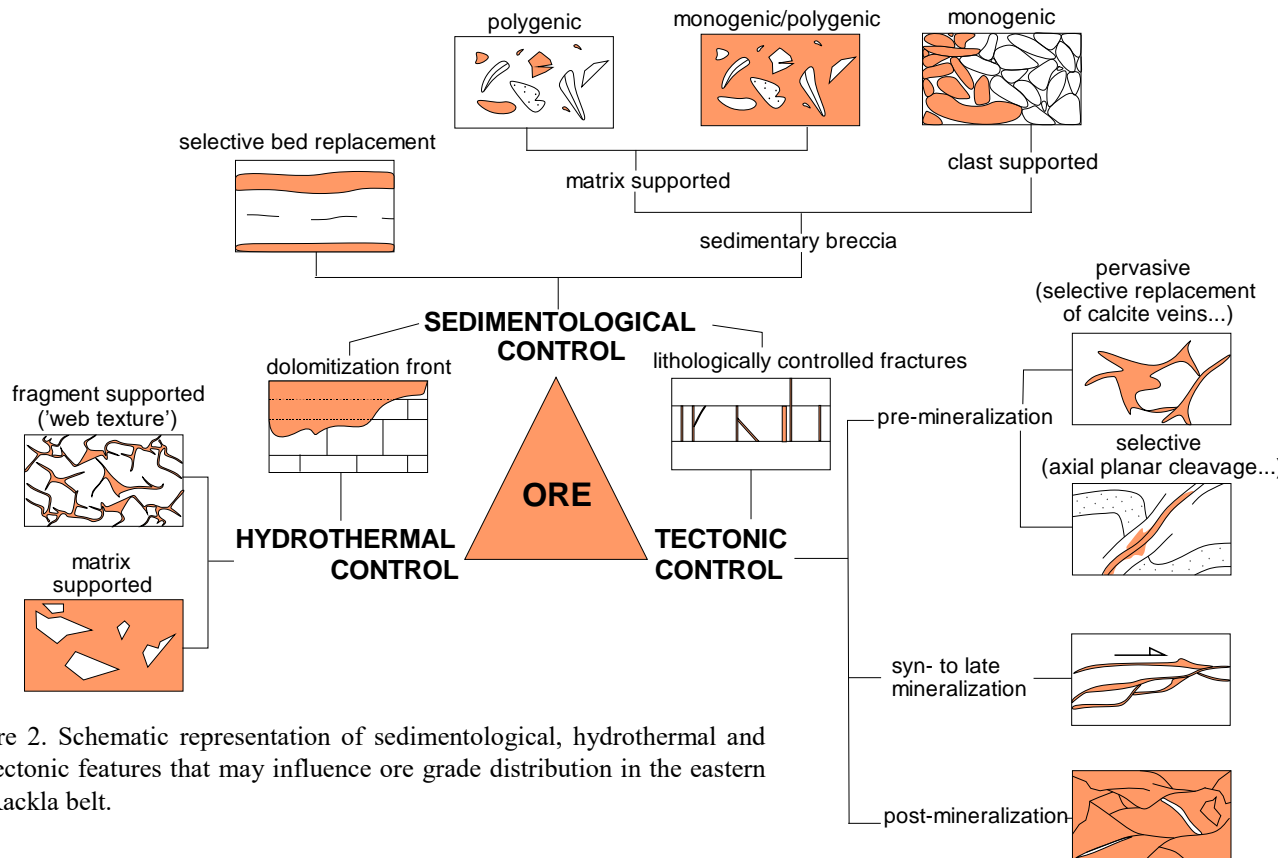
Figure 2. Schematic representation of sedimentological, hydrothermal and tectonic features that may influence ore grade distribution in the eastern Rackla belt.

intervals formed through different processes attests to the opportunistic nature of mineralizing fluids that exploit permeable pathways, regardless of their origin.

Mineralized sedimentary breccias, which are commonly bedding parallel and locally have erosive bases are interpreted as having formed in slope environments and comprise the following types (Fig. 2):

1) Matrix-supported to locally clast-supported polygenic breccia in which mineralization preferentially occurs in certain clast types (Fig. 3a and b). Clasts are commonly either: i) dark grey elongated impure fine-grained limestone fragments of local (i.e. slope) derivation; or ii) pale grey micrite clasts possibly derived from up-slope facies. Clasts are generally angular to sub-angular with visible bedding, and occasionally soft-
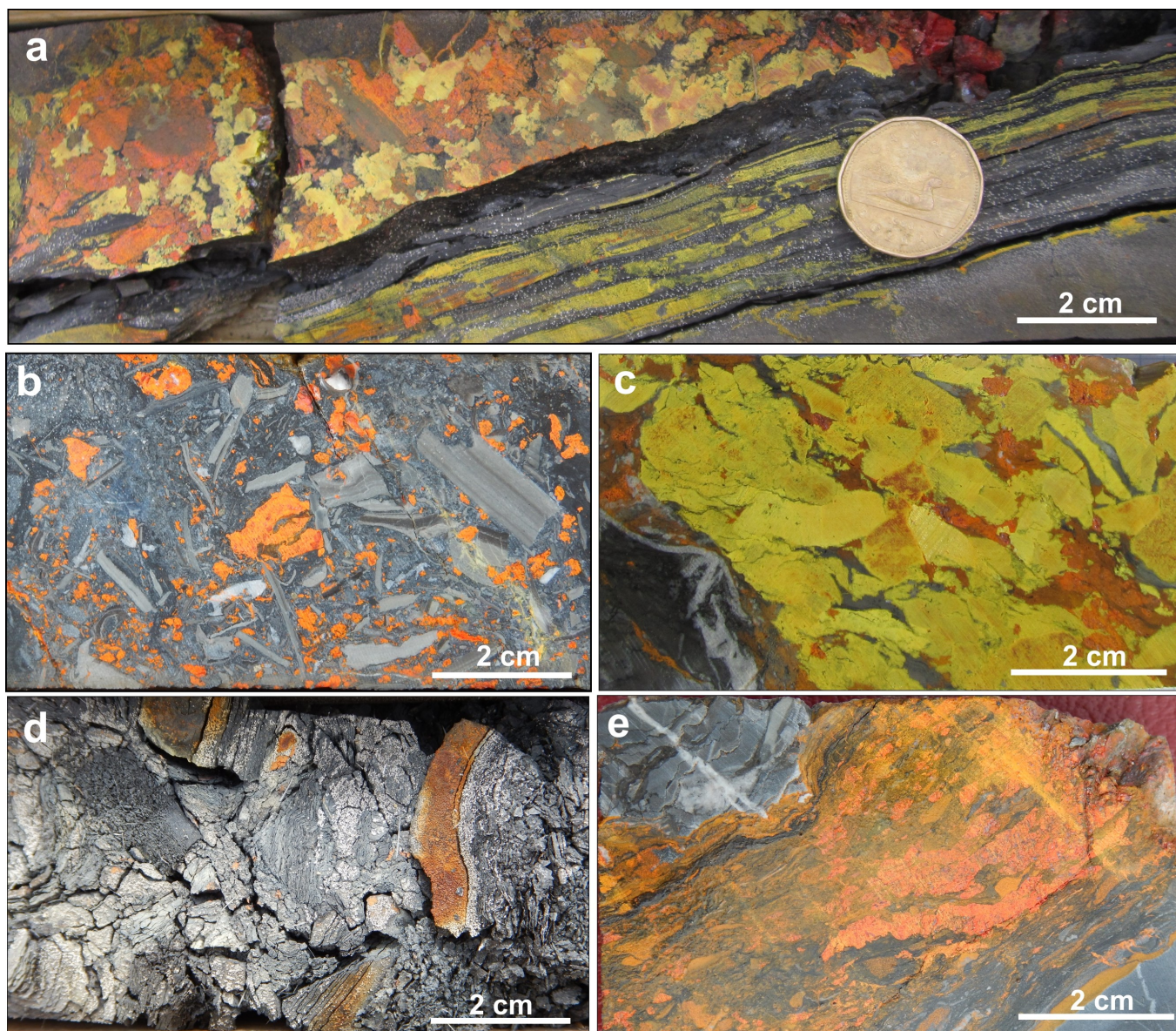
Figure 3. Examples of mineralized sedimentary breccias. a) Orpiment replacement of selective centimetre scale beds (bottom) and orpiment-realgar replacement of a clast-supported sedimentary breccia. Note that some clasts have a yellow colour associated with the presence of orpiment, whereas others may have an orange colour due to realgar, likely related to several stages of mineral emplacement and/or fluid evolution. b) Selective realgar replacement of clasts in a sedimentary breccia. c) Orpiment (and realgar) replacement of clasts in a monogenic-clast-supported sedimentary breccia. d) Mineralization and alteration (decarbonatization and argillitization) of a probable polygenic matrix-supported sedimentary breccia. Note that some fragments are almost indistinguishable from the matrix whereas others remain clearly defined. e) Mineralization of a matrix supported sedimentary breccia (bottom). Note that the monogenic clast-supported conglomerate in the upper left of the picture is not mineralized.

sediment deformation features (i.e. slumping). Clasts have no clear preferred orientation, represent a variable percentage of the rock and are variably decarbonatized. In some cases the clasts are composed of earlier breccias or veins.

2) Clast-supported sedimentary breccia in which the majority of clasts are mineralized. This association suggests that the fragments were originally quite uniform in terms of porosity and composition and the breccia was probably monogenic (Fig. 3c)

3) Matrix-supported breccia in which mineralization preferentially occurs in the matrix and in certain clast types (Fig. 3d). In this breccia type, the matrix is generally silty with some intervals where the sand-sized granular matrix is locally laminated. In high-grade intervals, the matrix is often decarbonatized, and can exhibit an argillic staining. Clasts are subangular to sub-rounded and show no preferred orientation. Some fragments have a colour and grain size similar to the matrix suggesting that the later may formed almost in-situ, likely from remobilisation of little compacted and cemented slope facies units.

Sedimentary breccias of types 1 and 2 are interpreted as debris flow units resulting from the platform margin erosion and downslope transport. As noted by Cook (2015) for the Carlin-type deposits of Nevada, these debris flows are favourable host-rocks given that they can maintain relatively high porosity, contain abundant limestone clasts, are rheologically weaker than the enclosing strata, and can be easily partly dissolved by even slightly acidic hydrothermal fluids. An interpretation on the forming mechanism of type 3 sedimentary breccias remains to be firmly established.

Interpreted hydrothermal breccias are characterized by a highly variable matrix-fragment ratio (Fig. 4). They are commonly realgar-rich and the texture varies from an irregular mineralized vein set ('crackle breccia') to matrix-supported breccia characterized by angular fragments. The latter type are divided between those for which the fragments maintain a 'jigsaw fit' ('mosaic breccia') and those that do not ('rotated breccia'). Cement is typically realgar and/or calcite, though orpiment and, to a lesser extent, fluorite also occur.

Brecciated intervals related to tectonic processes show a wide spectrum of styles and, in some cases, the distinction between pre-, syn- and late-mineralization is challenging. At the metre scale, pre-mineralization tectonic breccias form a pervasive network of brittle fractures or veins mainly filled by barren calcite (and/or, quartz or dolomite). They may also be restricted to specific deformation corridors, such as fault zones or narrow-spaced axial planar cleavage zones associated with folding. In several cases, hydrothermal fluids used pre-mineralization fractures/faults and tectonic breccia as pathways, dissolving and replacing earlier calcite veins (Fig. 5a, b). Syn-mineralization deformation involved brittle faulting, cataclasite and gouge development that contribute to the development of pathways for mineralizing fluids (Fig. 5c). Fault planes with realgar slickenlines attest to such syn- to late-
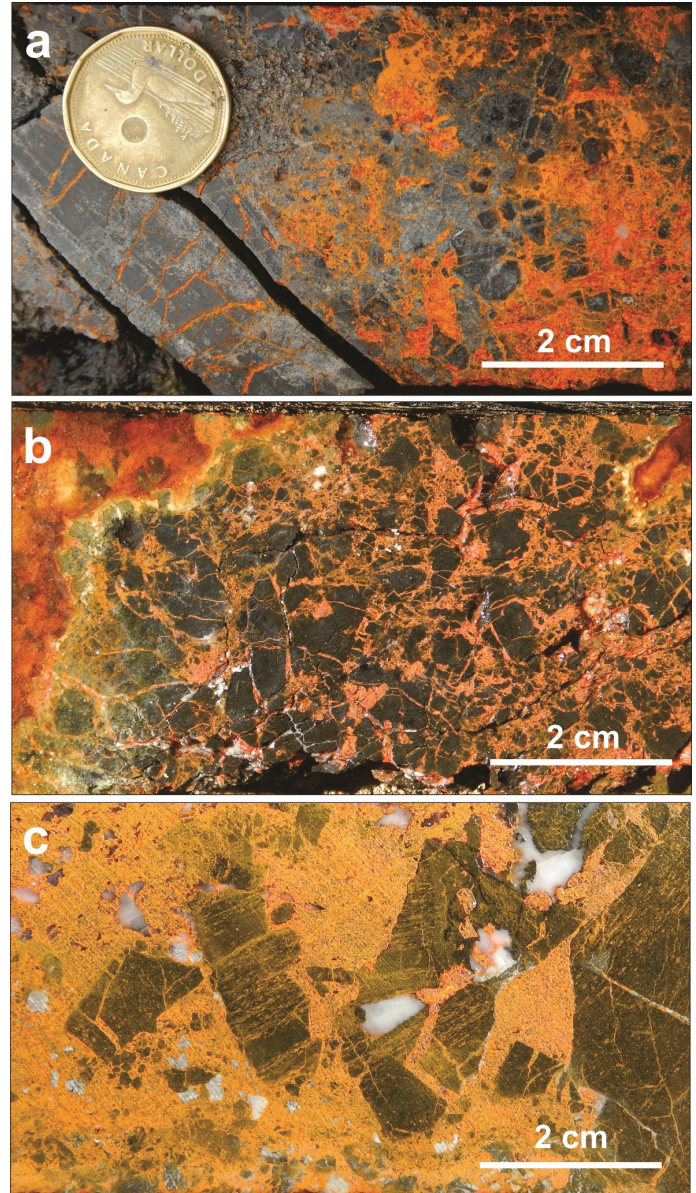
Figure 4. Examples of mineralized hydrothermal breccias. The matrix-fragment ratio increases from a to c. Note the change from a crackle breccia texture (right) to bedding perpendicular fractures (left) in a and the mosaic to rotated texture in c.

mineralization deformation. Late brecciation of mineralized intervals has been documented in a few cases (Fig. 5d).

Next Steps

Although the variability of mineralization styles has been documented at mineralized interval scale (1–10 m), its significance at the prospect scale (100s of metres) remains to be firmly established. The development of reliable conceptual models will need to take into account not only the abundance and vari-

166
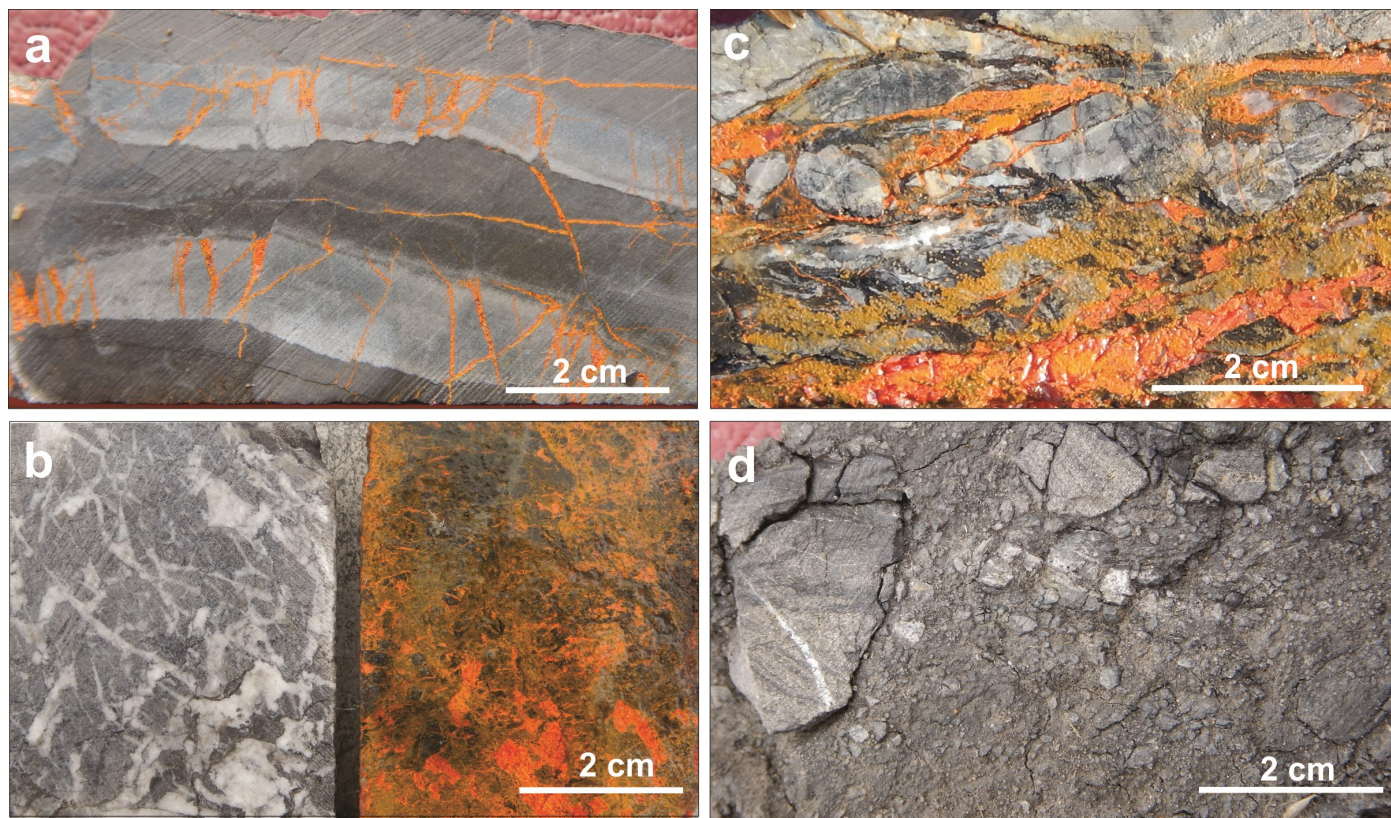
Figure 5. Examples of mineralized tectonic breccias: a) Mineralization along mainly bedding perpendicular fractures that may correspond to joints or fractures formed before the mineralizing event; b) Comparison of unmineralized breccia characterized by irregular calcite veins (left) and mineralized breccia (right) suggesting that realgar selectively replaces calcite; c) Realgar occurring in a sheared interval suggesting that mineralization emplacement is syn-deformation; d) Cataclasite within a decarbonatized interval suggesting late to post-mineralization brittle deformation.

ety of ore-bearing breccias, but also their complex chronology relative to deformation and fluid flow events.

References

Beaton, N.I., 2015. Diagenetic controls on hydrothermal fluid flow in the Osiris, Isis and Isis East Carlin-type showings, Nadaleen Trend, Yukon; M.Sc. Thesis, University of Alberta, Edmonton, Alberta, 180 p.

Cline, J.S., Hofstra, A.H., Muntean, J.L., Tosdal, R.M., and Hickey, K.A., 2005. Carlin-type gold deposits in Nevada: critical geologic characteristics and viable models; Economic Geology, 100th Anniversary volume, (ed.) J.W. Hedenquist, J.F.H. Thompson, R.J. Goldfarb and J.P. Richards, p. 451–484.

Colpron, M., Moynihan, D., Israel, S., and Abbott, G., 2013. Geologic map of the Rackla belt, east-central Yukon (NTS 106C/1-4, 106D/1); Yukon Geological Survey, Open File 2013-13, 5 maps, scale 1:50 000.

Cook, H.E., 2015. The evolution and relationship of the western North American Paleozoic carbonate platform and basin depositional environments to Carlin-type gold deposits in the context of carbonate sequence stratigraphy; *in* New Concepts and Discoveries: GSN 2015 Symposium Proceedings, (ed.) W.M. Pennell and L.J. Garside; DEStech Publications Inc., Lancaster, Pennsylvania, p. 1–80.

Heitt, D.G., Dunbar, W.W., Thompson, T.B., and Jackson, R.G., 2003. Geology and geochemistry of the Deep Star Gold Deposit, Carlin Trend, Nevada; Economic Geology, v.

98, p. 1107–1135.

Moynihan, D., 2016. Bedrock geology compilation of the eastern Rackla Belt, NTS 105N/15, 105N/16, 105O/13, 106B/4, 106C/1, 106C/2, east-central Yukon; Yukon Geological Survey Open File 2016-2, scale 1:75 000.

Palmer, J.C. and Kuiper, Y.D., 2016. Structural geology of the eastern Nadaleen trend, Yukon Territory, Canada: Implications for recently discovered sedimentary rock-hosted gold; Ore Geology Reviews, v. 80, p. 48–60.

Pinet, N., Mercier-Langevin, P., Dubé, B., Brake, V., Lane, J., and Colpron, M., 2017a. Geological characteristics of Carlin-type gold mineralization prospects in a 'frontier' area, Rackla belt, Yukon, Canada; Proceedings of the 14th SGA Biennial Meeting, Québec, Quebec, p. 179–182.

Pinet, N., Mercier-Langevin, P., Dubé, B., Colpron, M., Lane, J., and Asselin, E., 2017b. Lithotectonic controls on the genesis and distribution of carbonate re-placement-type ("Carlin-type") gold zones, east-central, Yukon; *in* Targeted Geoscience Initiative – 2016 Report of Activities, (ed.) N. Rogers; Geological Survey of Canada, Open File 8199, p. 43–45.

Teal, L. and Jackson, M., 2002. Geologic overview of the Carlin Trend gold deposits; *in* Gold deposits of the Carlin Trend, Nevada Bureau of Mines and Geology, Bulletin 111, p. 9–19.

Tucker, M.J., 2015. Geology, mineralization and geochronology of the Conrad zone Carlin-type prospect, east-central Yukon Territory, Canada; M.Sc. Thesis, University of British Columbia, Vancouver, British Columbia, 160 p.

Tucker, M.J., Hart, C.J.R., and Carne, R.C., 2012. Geology, alteration, and mineralization of the Carlin-type Conrad zone, Yukon; *in* Yukon Exploration and Geology 2012, (ed.) K.E. MacFarlane, M.G. Nordling and P.J. Sack; Yukon Geological Survey, p. 163–178.

Investigation of ultramafic to mafic komatiitic units within the Raglan Block within the Cape Smith Belt, Nunavik, northern Quebec

D.J. McKevitt[1], M.G. Houlé[2] and C.M. Lesher[1]

[1]*Harquail School of Earth Sciences, Laurentian University, 935 Ramsey Lake Road, Sudbury, Ontario, P3E 2C6*
[2]*Geological Survey of Canada, 490 rue de la Couronne, Québec, Quebec, G1K 9A9*

Abstract

The Circum-Superior large igneous province that extends for over than 2500 km along the margin of the Superior Province hosts two of Canada's most important magmatic Ni-Cu-PGE districts: the Thompson (northern Manitoba) and the Raglan (Nunavik, northern Quebec) nickel belts. The vast majority of the Ni-Cu-(PGE) mineralization in the Raglan belt occurs within a series of thick (50–200 m) lava channels and channelized sheet flows facies along the contact between the early Proterozoic Povungnituk and younger Chukotat groups. This geological contact appears to be repeated in the 'Northern Permits' area located north of active mining area, however, although it contains lithologically similar ultramafic-mafic units, it lacks significant mineralization. The overall metal endowment of these two panels is disparate; this research seeks to understand why the metal endowment is significantly different between these two areas.

Introduction

Two of Canada's most important magmatic Ni-Cu-PGE districts are the Thompson (northern Manitoba) and Raglan (Nunavik, northern Quebec) nickel belts, which form part of the approximately 2500 km long Circum-Superior large igneous province that occurs along the northern margin of the Superior craton. The overall metal endowment is disparate, not only at the scale of the entire Circum-Superior belt, but also at the district scale. The critical parameters that control the distribution of endowment are poorly understood at present.

The Cape Smith segment of the Circum-Superior belt in northern Quebec hosts several magmatic Ni-Cu-(PGE) sulphide deposits, occurring predominantly within two main trends known as the 'Main trend' (i.e. Raglan formation) and the 'South trend' (i.e. Expo-Ungava trend) (Fig. 1). The mafic-ultramafic flows/intrusions of these trends have been interpreted as coeval and comagmatic (Mungall, 2007), however the emplacement (e.g. extrusive versus intrusive), mineralization styles (e.g. massive versus disseminated; Ni-Cu-PGE versus Cu-Ni-PGE) and metal endowments are significantly different between the two trends. The bulk of the Ni-Cu-(PGE) mineralization occurs in the Raglan formation within a series of thick (50–200 m) primarily ultramafic complexes. This Main trend mineralization outcrops discontinuously along the contact between the Proterozoic Chukotat and Povungnituk groups between Cross Lake and Raglan Lake in the east-central part of the Cape Smith Belt (Lesher, 2007; Lesher and Houlé, 2017).

The Chukotat – Povungnituk contact is duplicated in this area by north directed thrusting (Fig. 1; St-Onge and Lucas, 1993; see also Bleeker and Ames, 2017). However, it is not clear whether the gabbro/peridotite and peridotite bodies near that contact in the northern panel (known locally as the 'Northern Permits') are part of the highly prospective Raglan formation or part of the sills in the upper part of the Povungnituk Group (considered less prospective). This study revisits the volcanic to subvolcanic architecture of the komatiitic magmatism along the Raglan formation and compares it with the poorly-endowed Northern Permits.

Physical volcanology of the Raglan formation (Main trend)

Detailed descriptions of the mafic and ultramafic rocks in the Raglan formation are given in Lesher (1999, 2007) and Lesher and Houlé (2017). Early workers interpreted these units as very high level sills that fed overlying komatiitic basalts (e.g. Francis and Hynes, 1979; Barnes et al., 1982; Francis et al., 1981, 1983; Bédard et al., 1983; Giovenazzo et al., 1989) or as flows that evolved into sills during the evolution of the volcanic pile (Albino, 1984). More recently, they have been reinterpreted as lava ponds (Barnes and Barnes, 1990), lava channels (Lesher et al., 1991; Gillies, 1993; Thacker, 1995; Stilson, 1999) or invasive flows (e.g. Lévesque and Lesher, 2002). Some debate still exists regarding whether these units are extrusive, invasive (shallowly burrowing), and/or subvolcanic

---
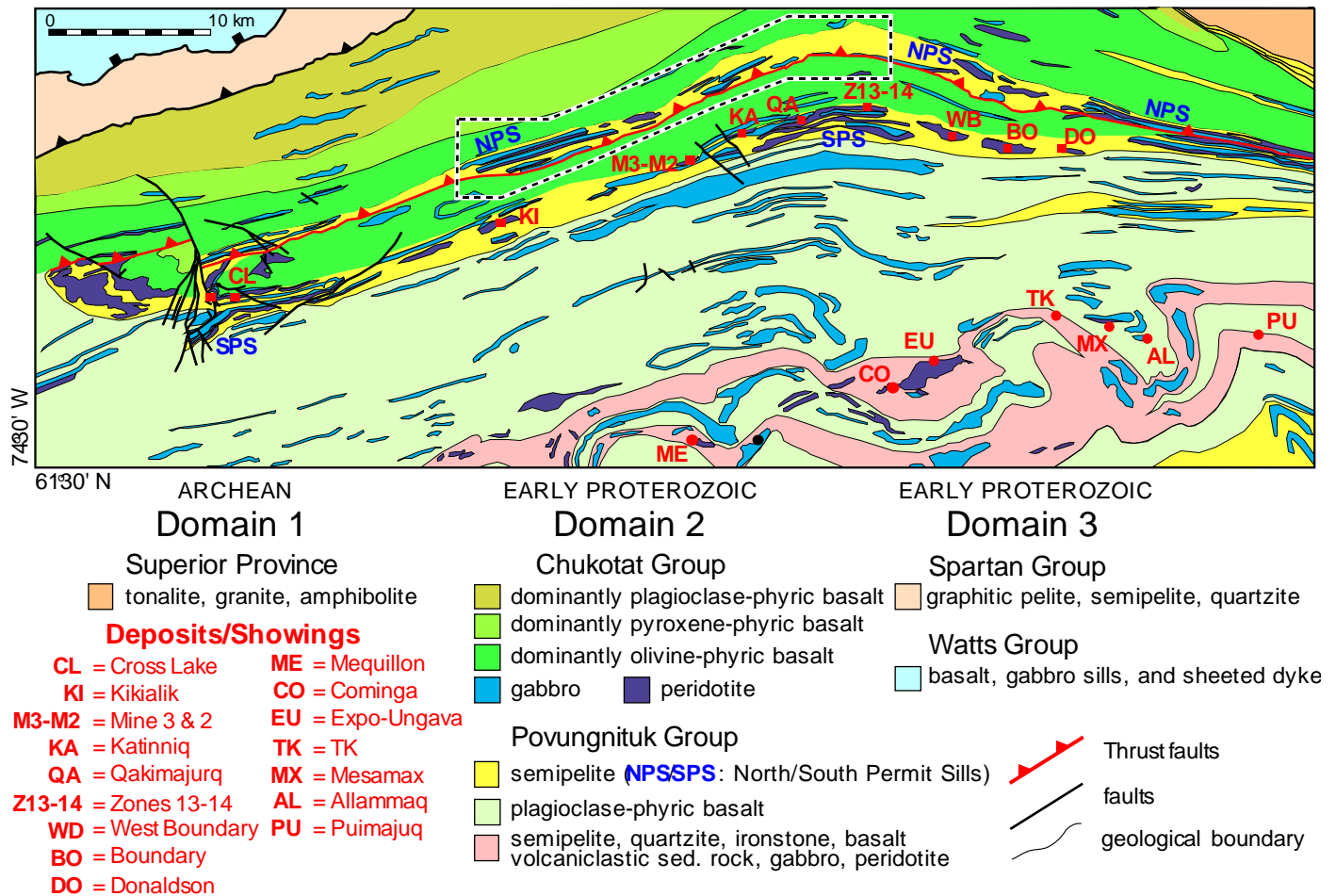
Figure 1. Geological compilation map of the Raglan area (modified from St-Onge and Lucas, 1993), showing the locations of the main Ni-Cu-(PGE) deposits in the 'Main trend' and 'South trend'. The area of the field investigation with the 'Northern Permits' is outline by the dashed black box.

intrusive. Lesher (2007) and Lesher and Houlé (2017) demonstrated unequivocally that at least part of the mineralized units are lava flows based upon the presence of volcanic features (e.g. the Katinniq ultramafic unit and many other sites are locally capped by polyhedral flow-top breccias). Other units in the Cape Smith belt are thought to be coeval and comagmatic with the Raglan formation mineralized bodies, but they have been interpreted as both intrusive (i.e. the Expo-Ungava South trend area; Mungall, 2007) and extrusive (i.e. the Raglan West area located approximately 80 km along strike west of Katinniq; Dionne-Foster, 2007). The connection between these areas and the overall architecture of the entire ore system in the Cape Smith belt remains undefined.

The ultramafic complexes of the Raglan block comprise two principal facies assemblages: i) the conduit facies assemblages that are laterally restricted and composed primarily of peridotite; and ii) the channelized sheet facies assemblages where conduit facies peridotite is flanked by extensive sheets of massive gabbro or differentiated peridotite-gabbro. Mineral-ization occurs exclusively within conduit facies, with the largest deposits occurring within the larger conduit facies assemblages.

Field investigation in the Northern Permits on the Raglan Block

Most historic and current exploration, academic research, and most mining activity have focused on the approximately 70 km-long Main trend of the Raglan formation. The Northern Permits area hosts what appears to be a repetition of the Main trend located 3 to 4 km to the north; however, although it contains lithologically similar mafic-ultramafic units, it lacks significant mineralization. This component seeks to understand why the metal endowment is significantly different between these two parts of the belt.

The mafic and ultramafic units composed of peridotite, olivine pyroxenite, pyroxenite, melagabbro to leucogabbro were examined along approximately 23 km of the Northern

Permits, centred north of active mining along the Main trend (Fig. 1). These units consist of three main types of mafic to ultramafic units: i) mafic-dominated; ii) ultramafic-dominated; and iii) differentiated ultramafic to mafic. Field observations across these units highlight abundant igneous structures that could be typical of shallow intrusions or lava flows such as columnar jointing and locally possible flow-top breccia (McKevitt et al., 2017). Trends in olivine cumulate textures, oikocrysts, and internal load-casted contacts exhibit some similarities with those described in komatiitic basalt flows on Gilmour Island in Hudson Bay (e.g. Arndt, 1982). These field observations highlight some similarities (e.g. unit types: mafic-dominated, ultramafic-dominated, and differentiated units; igneous/volcanic structures: columnar jointing, flow-top breccia; igneous textures: olivine cumulate, oikocrystic textures), but also some differences (e.g. most are not at the Povungnituk-Chukotat boundary; well-differentiated units are much more abundant; most appeared to be mainly barren) suggesting that the Northern Permits units are unlikely to be a simple structural duplication of the Main Trend. The variations between these two panels might reflect significant differences in their physical volcanology (e.g. proximal versus distal facies) and also reflect the disparity in their respective metal endowment. However, further geochemical and textural analyses in conjunction with a proper physical volcanology assessment will help resolve whether they have potential for Ni-Cu-(PGE) mineralization.

Future work

On-going regional-scale geochemical compilation, at the scale of the entire belt, is currently underway to compare the geochemical signatures of barren and mineralized ultramafic to mafic units throughout the Main trend and the Northern Permits within the Raglan Block area but also with other sectors of the belt. Samples collected during the last field season will be examined, characterized petrographically and geochemically in order to established their petrogenesis and their emplacement within the Northern Permits area.

Acknowledgments

References

Albino, G.V., 1984. Petrology, geochemistry, and mineralization of the Boundary ultramafic complex, Quebec, Canada; M.Sc. thesis, Colorado State University, Fort Collins, Colorado, 220 p.

Arndt, N.T., 1982. Proterozoic spinifex-textured basalts of Gilmour Island, Hudson Bay; Current Research, Part A, Geological Survey of Canada, Paper 82-1A, p. 137–142.

Barnes, S.J. and Barnes, S.-J., 1990. A new interpretation of the Katinniq nickel deposit, Ungava, northern Quebec; Economic Geology, v. 85, p. 1269–1272.

Barnes, S.J., Coats, C.J.A., and Naldrett, A.J., 1982. Petrogenesis of a Proterozoic nickel sulfide-komatiite association: the Katinniq sill, Ungava, Quebec; Economic Geology, v. 77, p. 413–429.

Bédard, J.H., Francis, D.M., and Hynes, A.J., 1983. Fractionation in the feeder system at a Proterozoic rifted margin; Canadian Journal of Earth Sciences, v. 21, p. 489–499.

Dionne-Foster, C., 2007. Géologie et indices de Ni-Cu-ÉGP de la Zone Frontier dans la ceinture de Cape Smith, Nouveau Québec; M.Sc. thesis, Université du Québec à Chicoutimi, Chicoutimi, 320 p.

Bleeker, W. and Ames, D.E., 2017. System-scale and deposit-scale controls on Ni-Cu-PGE mineralization in cratonic areas and their margins; *in* Targeted Geoscience Initiative – 2016 Report of Activities, (ed.) N. Rogers; Geological Survey of Canada, Open File 8199, p. 47–53.

Francis, D.M. and Hynes, A.J., 1979. Komatiite-derived tholeiites in the Proterozoic of New Quebec; Earth and Planetary Science Letters, v. 44, p. 473–481.

Francis, D.M., Hynes, A.J., Ludden, J.N., and Bédard, J., 1981. Crystal fractionation and partial melting in the petrogenesis of a Proterozoic high-MgO volcanic suite, Ungava, Quebec; Contributions to Mineralogy and Petrography, v. 78, p. 27–36.

Francis, D.M., Ludden, J.N., and Hynes, A.J., 1983. Magma evolution in a Proterozoic rifting environment; Journal of Petrology, v. 24, p. 556–582.

Gillies, S.L., 1993. Physical Volcanology of the Katinniq Peridotite Complex and associated Fe-Ni-Cu-(PGE) mineralization, Cape Smith Belt, Northern Quebec; M.Sc. thesis, University of Alabama, Tuscaloosa, Alabama, 146 p.

Giovenazzo, D., Picard, C., and Guha, J., 1989. Tectonic setting of Ni-Cu-PGE deposits in the central part of the Cape Smith Belt; Geoscience Canada, v. 16, no. 3, p. 134–136.

Lesher, C.M., (ed.), 1999. Komatiitic Peridotite-Hosted Fe-Ni-Cu-(PGE) Sulphide Deposits in the Raglan Area, Cape Smith Belt, New Québec; Guidebook Series 2, Mineral Exploration Research Centre, Laurentian University, Sudbury, 205 p.

Lesher, C.M., 2007, Ni-Cu-(PGE) Deposits in the Raglan Area, Cape Smith Belt, New Québec; *in* Mineral Resources of Canada: A Synthesis of Major Deposit-types, District Metallogeny, the Evolution of Geological Provinces, and Exploration Methods, (ed.) W.D. Goodfellow; Geological Survey of Canada and Mineral Deposits Division of the Geological Association of Canada Special Publication 5, p. 351–386.

Lesher, C.M. and Houlé, M.G. (ed.), 2017. Geology, physical volcanology, and Ni-Cu-(PGE) deposits of the Raglan area, Cape Smith Belt, Nunavik, Québec, Canada: A Field Trip to the 14th Biennial SGA Meeting; Geological Survey of Canada, Open File 8350, 110 p.

Lesher, C.M., Thacker, J.L., Thibert, F., Tremblay, C., and Dufresne, M.W., 1991. Physical volcanology of Proterozoic komatiitic peridotites in the Chukotat Group, Cape Smith Belt, New Quebec. Geological Association of Canada - Mineralogical Association of Canada Annual Meeting, Program with Abstracts, p. A74.

Lévesque, M. and Lesher, C.M., 2002. Invasive features of mafic-ultramafic rocks at the Zone 3, Zone 2, and Katinniq Ni-Cu-(PGE) deposits, Raglan Formation, Cape Smith Belt, Nouveau-Québec; 9th International Platinum Symposium, Billings, Montana, p. 257–260.

McKevitt, D.J., Lesher, C.M., and Houlé, M.G., 2017. Geology and geochemistry of mafic-ultramafic sills in the northern permits, Raglan Ni-Cu-(PGE) District, Cape Smith Belt, Nunavik, Québec; Abstracts of oral presentations and posters, Québec Mines 2017; Ministère des Ressources naturelles du Québec.

Mungall, J.E., 2007. Crustal contamination of picritic magmas during transport through dikes: The Expo Intrusive Suite, Cape Smith Fold Belt, New Québec; Journal of Petrology, v. 48, p. 1021–1039.

Stilson, C.M., 1999. Geology of the boundary ultramafic complex and genesis of associated Fe-Ni-Cu-(PGE) sulfide mineralization, Cape Smith Belt, New Québec; M.Sc. thesis, University of Alabama, Tuscaloosa, Alabama, 258 p.

St-Onge, M.R. and Lucas, S.B., 1993. Geology of the eastern Cape Smith belt: parts of the Kangiqsujuaq, Cratère du Nouveau-Quebec, and Lacs Nuvilik map areas, Quebec; Geological Survey of Canada Memoir 438, 110 p.

Thacker, J.L., 1995. Geology of the 5-8 gabbro-peridotite complex, Cape Smith Belt, New Québec; M.Sc. thesis, University of Alabama, Tuscaloosa, Alabama, 173 p.

Reconnaissance thallium isotope study of zinc-lead SEDEX mineralization and host rocks in the Howard's Pass district, Selwyn Basin, Yukon: Potential application to paleoredox determinations and fingerprinting of mineralization

J.M. Peter[1], M.G. Gadd[1], D. Layton-Matthews[2] and A. Voinot[2]

[1]*Geological Survey of Canada, 601 Booth Street, Ottawa, Ontario, K1A 0E8*
[2]*Department of Geological Sciences and Geological Engineering, Queen's University,*
36 Union Street, Kingston, Ontario, K7L 3N6

Abstract

The commonly accepted genetic model for sedimentary exhalative (SEDEX) lead-zinc deposits requires a marine basin with anoxic (no oxygen) and euxinic (free H_2S) conditions, in order to provide sulphur to bond with the metals. Recent work on the largest SEDEX district in Canada, the Howard's Pass district, Selwyn Basin, Yukon, has cast doubt on the universality of this model, as the water column may have been suboxic during mineralization. Paleoredox indicators based on bulk geochemical compositions can be contradictory or equivocal. Developments in non-traditional metal stable isotope analysis have shown the potential of certain isotope systems (e.g. molybdenum, uranium, thallium) as paleoredox indicators.

We have conducted a bulk geochemical and thallium isotopic traverse through a mineralized intersection (and immediate stratigraphic footwall and hanging wall) from the Anniv East vent-distal SEDEX deposit, Howard's Pass district. The $\varepsilon^{205}Tl$ values range from -7.5 to -4.0 for unmineralized samples and -3.6 to -2.6 for mineralized ones. There is good general agreement between certain redox sensitive elements, venerable redox indicators and $\varepsilon^{205}Tl$ for the unmineralized host rocks (reflecting suboxic or oxic conditions for the most negative values). Thus, the application of thallium isotopes as a redox indicator in seafloor hydrothermal deposits in sedimentary (or volcano-sedimentary) settings shows great promise. The heaviest values are for mineralized samples, likely reflecting contributions of isotopically heavy thallium from the mineralizing fluids. Preliminary data indicate that thallium isotopes as a redox indicator in mineralized samples is untenable, but it has the potential to fingerprint sulphides precipitated by various processes.

Introduction and background

The commonly accepted genetic model for sedimentary exhalative (SEDEX) lead-zinc deposits requires a marine basin with anoxic (no oxygen) and euxinic (free H_2S) conditions, in order to provide sulphur to bond with the metals. Goodfellow and Jonasson (1984) and Goodfellow and Lydon (2007) identified anoxia (no oxygen in the water column) as a critical control on SEDEX formation, whereas other researchers have suggested that it plays only a passive/casual role (e.g. Taylor and Beaudoin, 2000; Saez et al., 2011; Magnall et al., 2015). Recent work on the Howard's Pass district, Selwyn Basin, Yukon (Canada's largest SEDEX district), using microscale sulphur isotopes and rare earth elements (REE) suggests that neither anoxia nor euxinia are requisite to the SEDEX mineralizing processes (e.g. Gadd et al., 2016a, b, 2017; Magnall et al., 2016), a finding that is in stark contrast to the commonly accepted SEDEX deposit genetic model. Corroborating or discounting the role of anoxia in these deposits has the strong likelihood to revolutionize genetic and exploration models for SEDEX deposits.

Paleo-redox indicators based on bulk geochemical compositions (e.g. V, Mo, Re/Mo, Ni/Co, V/Cr, U/Th, Mo/TOC (total organic carbon), and Ce/Ce*$_{SN}$; Jones and Manning, 1994; Tribovillard et al., 2006) are intended to resolve between suboxic (0.2–2 ml O_2/L H_2O), dysoxic (<0.2 ml O_2/L H_2O), anoxic (0 ml O_2/L H_2O) and euxinic (>0 ml H_2S/L H_2O) depositional conditions. However, the various bulk geochemical indicators commonly contradict each other, making the determination of paleoredox conditions equivocal (e.g. Saez et al., 2011). For this reason, there has been much effort directed towards the development of other independent and more robust indicators.

Recent advancements in stable isotope analysis of non-traditional, redox-sensitive metals (e.g. Ni, Mo, Se, U) by multicollector-inductively coupled plasma-mass spectrometer (MC-ICP-MS) in geological materials (Anbar and Rouxel, 2007) indicate that some of these metal isotope systems may be use-

ful as paleoredox proxies (e.g. chromium - Frei et al., 2009; molybdenum - Anbar and Gordon, 2008). It has been recently shown that thallium isotopes can serve as a reliable proxy to track redox (reduction-oxidation) processes in an oceanic water column (e.g. Nielsen et al., 2011; Ostrander et al., 2017; Owens et al., 2017). Few previous studies have employed thallium isotopes in a mineral deposit environment (e.g. Baker et al., 2010; Hettmann et al., 2014; Wickham, 2014), and none on seafloor-hydrothermal deposits. Herein, we present the results of a reconnaissance study on the application of thallium isotope analyses as a potential redox indicator in a lead-zinc SEDEX deposit environment. To do this we conducted a bulk geochemical and thallium isotopic drillhole traverse through a mineralized intersection (plus its immediate stratigraphic footwall and hanging wall) from the Anniv East vent-distal lead-zinc SEDEX deposit in the Howard's Pass district.

Prevailing SEDEX model

The long-standing genetic model for SEDEX deposits (e.g. Goodfellow and Lydon, 2007) is that metal-bearing sedimentary basinal fluids rise along growth faults in second- or third-order marine basins and vent into anoxic (no free O_2 present) and euxinic (free H_2S present) waters (Fig. 1). The H_2S results from bacterial reduction of seawater sulphate. Metals in the venting fluids (Fe, Zn, Pb) are fixed by the H_2S in the water column upon mixing, and the precipitated pyrite, sphalerite and galena are then settled to the seafloor in layers. A key implication of this model to exploration is the presence of reduced, fine-grained marine strata (black shales).

Thallium geochemistry

Thallium is redox active and has two oxidation states (Tl^{1+} and Tl^{3+}) that have dramatically different geochemical characteristics. In oxic (>2 mL O_2/L H_2O) and anoxic (0 mL O_2/L H_2O) aqueous systems (Tribovillard et al., 2006), thallium occurs predominantly as Tl(I), whereas Tl(III) is present only under extremely oxidizing and highly alkaline conditions (Kaplan and Mattigod, 1998). Speciation calculations indicate that Tl^{1+} is the salient species in most natural waters, but in seawater thallium can also exist as $TlCl^0$ (Kaplan and Mattigod, 1998). The average thallium content of seawater is 12 to 14 ppb, where its residence time in the oceans is ca. 18.5 ka. (Flegal and Patterson, 1985). Tl(I) is adsorbed onto hydrous Mn oxide phases of ferromanganese minerals (particularly in ferromanganese nodules in the marine environment), oxidized, and precipitated as Tl_2O_3 (Iskowitz et al., 1982; Bidoglio et al., 1993; Rehkämper and Nielsen, 2004; Jacobson et al., 2005). Thallium also has a strong affinity for organic matter (Wade and Banister, 1973).

During magmatic processes, thallium is highly incompatible, and has chemical behaviour similar to that of large ion lithophile elements such as rubidium, cesium and potassium, which is the result of similarities in ionic radii (Lee, 1971). Thallium can also be integrated as a monovalent cation in K-

bearing minerals, such as micas, illite and similar phyllosilicates, where it is incorporated into interlayer sites (Matthews and Riley, 1970; Kaplan and Mattigod, 1998). Thallium is highly mobile within hydrothermal fluids (e.g. Heinrichs et al., 1980). Indeed, thallium can also behave as a chalcophile element, and substitute for S in pyrite (e.g. Wickham, 2014) (see below). Due to its volatile nature, thallium can be mobilized from mineralization outward into adjacent host rocks and surficial materials in response to metamorphism and deformation, and is a potential pathfinder element in the wall rocks (so-called 'leakage halos') of some SEDEX deposits, as documented by Large and McGoldrick (1998).

Thallium isotope systematics and fractionation processes

Thallium has two naturally occurring stable isotopes: ^{203}Tl and ^{205}Tl, with abundances of 29.5% and 70.5%, respectively (e.g. Nielsen and Rehkämper, 2011). The two isotopes can be fractionated according to the relative proportions of the oxidation states, the heavier isotope (^{205}Tl) being enriched in the species having the lowest electronic density at the nucleus, Tl (III) (Bigeleisen, 1996; Schauble, 2007). Both mass-dependent and mass-independent fractionation of thallium isotopes can potentially occur in nature, but changes of redox state (Tl^{1+} to Tl^{3+} and vice versa) can potentially lead to the most significant isotopic fractionation (Yang and Liu, 2015).

Thallium isotope compositions of the samples are reported as ε^{205}Tl, which is the deviation of ^{205}Tl/^{203}Tl in parts per 10 000 relative to the isotopic standard NIST 997, a high purity thallium metal (May and Watters, 2004), according to the following equation:

$$\varepsilon^{205}Tl_{sample} = \left(\frac{\left. ^{205}Tl \middle/ _{^{203}Tl} \right._{sample}}{\left. ^{205}Tl \middle/ _{^{203}Tl} \right._{NIST997}} - 1 \right) \times 10\,000$$

The two isotopes of thallium display a wide range of fractionation in terrestrial and marine environments of about 35 (see Nielsen et al., 2017). In general, though, there are not large redox potentials in most environments on Earth, and therefore there is limited thallium isotope fractionation (Nielsen and Rehkämper, 2011). River waters, high-temperature seafloor hydrothermal vent fluids, volcanic volatiles and solids have nearly invariant ε^{205}Tl compositions of approximately -2, identical to continental crust and upper mantle (see compilation in Table 1 and Figure 2).

However, several sample types deviate significantly from this common value of -2. The highest known ε^{205}Tl (+10 to +14) have been measured in ferromanganese nodules, in which thallium (Tl^{1+}) in seawater is adsorbed onto the reactive iron-manganese oxides (and oxidized to Tl^{3+}) (Rehkämper et al., 2002). The remaining thallium fraction in seawater will thus be
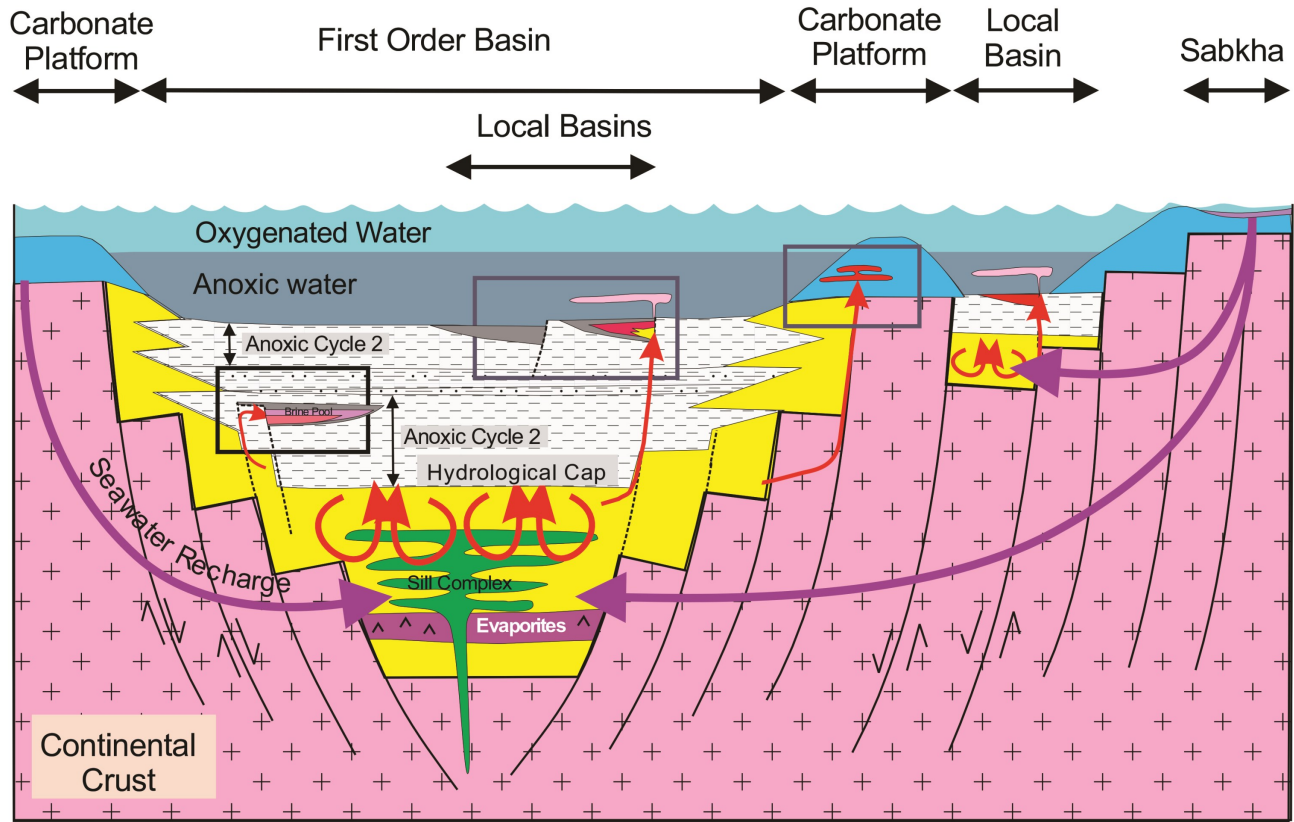
Figure 1. Generalized, schematic model for formation of SEDEX deposits (modified from Goodfellow and Lydon, 2007).
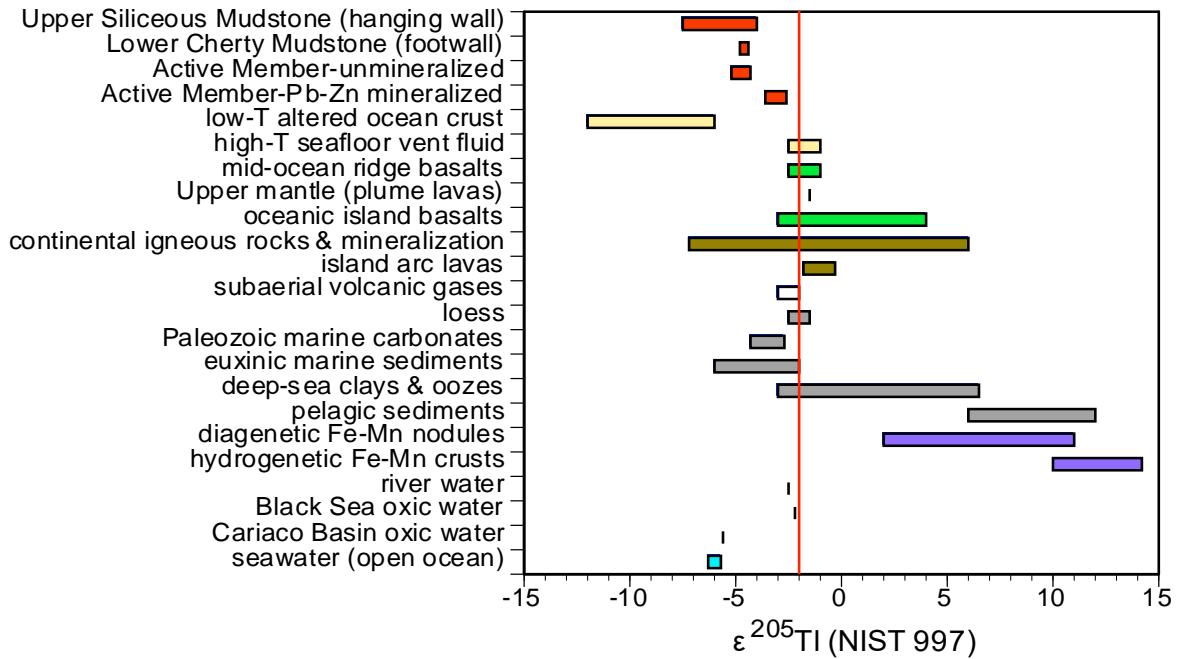
Figure 2. Synthesis of natural thallium isotope variations within various reservoirs on Earth, together with data from the present study. Dashed vertical red line is the inferred composition of continental crust and upper mantle. Modified from Kersten et al., 2014, and additional data sources listed in Table 1.

Table 1. Thallium isotope compositions of various reservoirs, together with references for data values.

Material	ε^{205}Tl
Global seawater (open ocean)[1,2,3,4]	-6.3 to -5.7
Carico Basin oxic water[4]	-5.6
Black Sea oxic water[4]	-2.2
Rivers[5,6]	-2.5
Hydrogenetic Fe-Mn crusts[7,8]	+10 to +14.2
Diagenetic Fe-Mn nodules[3]	+2 to +11
Pelagic clays[1,7,9]	+6 to +12
Euxinic marine sediments[4]	-6 to -2
Paleozoic marine carbonates[10]	-4.3 to -2.7
Loess[11]	-2.5 to -1.5
Subaerial volcanic gases[12]	-2
Island arc lavas[13]	-1.8 to -0.3
Continental igneous rocks & mineralization[6,12,14]	-7.2 to +6
Oceanic island basalts[15]	-3 to +4
Upper mantle (plume lavas)[15]	-1.5
Mid-ocean ridge basalts[2]	-2.5
High-T seafloor hydrothermal fluids[2]	-2.5
Low-temperature altered ocean crust[1,2,16]	-8.5

[1]Rehkämper and Nielsen, 2004

[2]Nielsen et al., 2006b

[3]Rehkämper et al., 2002

[4]Owens et al., 2017

[5]Rehkämper and Nielsen, 2004

[6]Nielsen et al., 2005

[7]Rehkämper et al., 2004

[8]Nielsen et al., 2006a

[9]Nielsen and Rehkämper, 2011

[10]Wickham, 2014

[11]Cloquet et al., 2005

[12]Baker et al., 2009

[13]Prytulak et al., 2013

[14]Hettmann et al., 2014

[15]Nielsen et al., 2007

[16]Coggon et al., 2014

significantly lighter at ε^{205}Tl -5.8 ± 0.6 (Nielsen and Rehkämper, 2011). Isotopic studies of ancient iron-manganese crusts show that the thallium isotope composition of seawater has changed with time, and is possibly controlled by variations in riverine and benthic input rates (Rehkämper et al., 2004). Sedimentary rocks precipitated from seawater are expected to have significantly lower ε^{205}Tl values than igneous rocks or detrital sedimentary rocks (e.g. ε^{205}Tl -4.3 to -2.7 for Paleozoic carbonates; Wickham, 2014). The lowest known ε^{205}Tl values

(as low as -16) have been measured in low-temperature hydrothermally altered oceanic crust; in contrast, high-temperature hydrothermally altered ocean crust is similar to MORB glass, and both display minimal fractionation (ε^{205}Tl -1.9) similar to mantle rocks (Nielsen et al., 2006a), and high temperature (endmember) seafloor hydrothermal vent fluids (ε^{205}Tl -1.9 ± 0.6; Nielsen et al., 2006b).

Geology

The Howard's Pass district of the Selwyn Basin (Fig. 3) is a metallogenic province known for its world-class Zn-Pb (±Ag±Ba) SEDEX deposits (Fig. 4). The Selwyn Basin is a continental margin basin consisting of thick sequences of Lower Ordovician to Lower Devonian fine-grained siliciclastic rocks with calcareous intercalations (Fig. 3; Goodfellow and Jonasson, 1986). The geology of the Howard's Pass district is detailed in Gadd et al. (2016a), with the stratigraphy summarized in Figure 5 (modified after Gordy and Anderson, 1993).

Mineralization in the Howard's Pass district is restricted to the Ordovician to Silurian Duo Lake Formation of the Road River Group (Fig. 5), which comprises carbonaceous siliceous and calcareous mudstone, cherty mudstone, and minor limestone. The Duo Lake Formation has been informally subdivid-
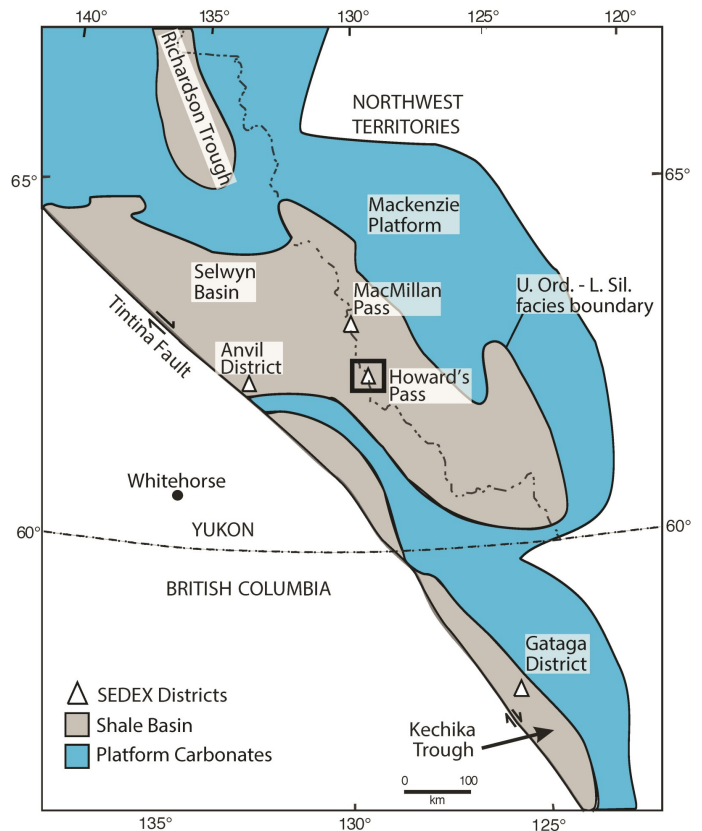
Figure 3. General geological map of the Selwyn basin and Mackenzie platform with major SEDEX Zn-Pb-(Ag-Ba) districts labelled (Goodfellow, 2007).

LEGEND

CRETACEOUS
🟥 Quartz monzonite and granite

TRIASSIC
TRS Sandstone

CARBONIFEROUS
Cp Shale

SELWYN BASIN
DEVONIAN AND MISSISSIPPIAN
EARN GROUP
Shale and sandstone
Shale and chert

ORDOVICIAN AND SILURIAN
ROAD RIVER GROUP
Shale and chert

MACKENZIE CARBONATE PLATFORM
CAMBRIAN, ORDOVICIAN, SILURIAN
AND DEVONIAN
🟦 Dolomite and limestone

ORDOVICIAN AND CAMBRIAN
🟦 Limestone

CAMBRIAN AND NEOPROTEROZOIC
🟪 Shale and sandstone
○ SEDEX deposits

Figure 4. Geological map of the Howard's Pass district, showing locations of SEDEX deposits (modified from Goodfellow, 2004). 1: XY zone (XY, XY Central and XY West deposits); 2: Brodel deposit; 3: HC zone (HC and HC West deposits); 4: Don zone (Don and Don East deposits); 5: Anniv Zone (Anniv and Anniv East deposits); 6: OP deposit; 7: Pelly North deposit. Red dashed line is Yukon - Northwest Territories border.

ed into several members at Howard's Pass (Morganti, 1979). These are the Pyritic Siliceous Mudstone member (PSMS), Lower Cherty Mudstone member (LCMS) and Calcareous Carbonaceous Mudstone member (CCMS) that constitute the immediate stratigraphic footwall to the mineralization (Fig. 6a), Active Member (ACTM) that hosts the mineralization (Fig. 6b, c), and the Upper Siliceous Mudstone member (USMS) which is the immediate stratigraphic hanging wall to the mineralization (Fig. 6d).

Conodonts recovered from the ACTM place the time of formation near Lower to Middle Llandoverian (443–439 Ma) time (Norford and Orchard, 1985). The PSMS member (2–10

m thick) is the basal unit of the Duo Lake Formation in the Howard's Pass district and consists of grey to black pyritic, carbonaceous shale. The CCMS (50–100 m thick) overlies the PSMS member and consists of highly carbonaceous mudstone with variable amounts of intercalated limestone and carbonate concretions. Minor wispy pyrite and calcite veins, 2.5 mm to 1 cm, occur locally. The LCMS (15–30 m thick) consists of highly carbonaceous and siliceous mudstone. The CCMS and LCMS have similar appearances in that they are massive and monotonous, highly carbonaceous cherty mudstones with variable contents of calcite. The ACTM (0–60 m thick, and typically 20–30 m) hosts the Zn-Pb mineralization at Howard's Pass. The USMS (20–90 m thick) consists of carbonaceous and cherty mudstones with minor to abundant laminations (0.5–1.5 cm thick) of carbonate-rich fluorapatite and locally abundant carbonate concretions. Pyrite is a widespread, but minor constituent in all of the members.

Mineralization in the Howard's Pass district occurs along what is termed the 'Zinc Corridor', a 38 km long, northwest trending series of 14 lead-zinc SEDEX deposits that contain an estimated 400.7 Mt grading 4.5% Zn and 1.5% Pb (Kirkham et al., 2012). All of these deposits are located along the same 20 to 30 m thick Llandoverian horizon that is composed dominantly of massive and semi-massive sphalerite and galena hosted in calcareous and cherty mudstones; pyrite is a minor (approx. 5.5 weight %) part of the mineralization (e.g. Fig. 6c). The Anniv East zone has an indicated resource of 16.92 Mt grading 1.2 weight % Pb and 4.15 weight % Zn, and an in-

Figure 5. Stratigraphic section of the Howard's Pass district. The Zn-Pb mineralization is hosted entirely within the ACTM (modified from Gordey and Anderson, 1993).

177
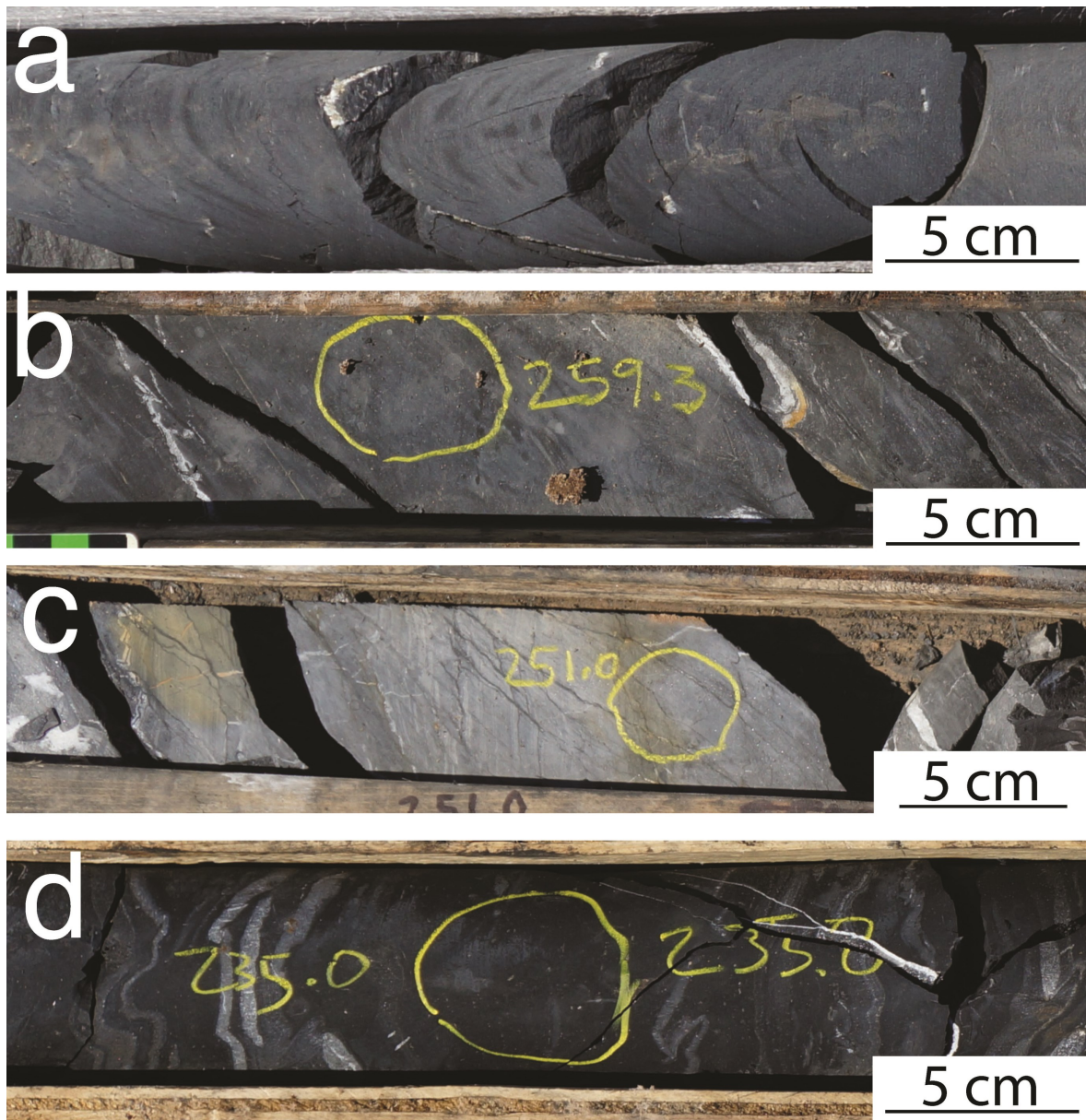
Figure 6. Representative photographs of drill core samples from ANE-108 used in this study. a) LCMS - downhole depth 284.0 m; b) unmineralized ACTM - downhole depth 259.3 m; c) Pb-Zn mineralized ACTM - downhole depth 251.0 m; d) USMS - downhole depth 235.0 m. Diameter of drill core is 4.8 cm for all photographs.

ferred resource of 16.05 Mt grading 1.08 weight % Pb and 4.04 weight % Zn (Kirkham et al., 2012). Anniv East has a strike length of 2.6 km and is interpreted to be an antiform (Yukon Geological Survey, 2014).

Sampling

Twelve samples were collected from drillhole ANE-108 (UTM E 475413, UTM N 6935877, NAD 83, Zone 9) that cored a complete stratigraphic section through the Anniv East mineralized horizon. The samples span a stratigraphic interval from 225.6 to 284.0 m downhole depth. Three samples are from the LCMS, six from the ACTM and three from the USMS (Table 2).

Methods

Bulk geochemistry

Drill core samples were crushed, pulverized in a ceramic mill, and analyzed by the following methods (see Table 3): Method 4B) lithium metaborate/tetraborate fusion, 5% HNO_3 dissolution and analysis by inductively coupled plasma-mass

Table 2. Thallium isotope and bulk geochemical compositions of samples of drill core ANE-108 from the Duo Lake Formation at the Anniv East deposit.

Drillhole	Depth (m)	Unit	$\varepsilon^{205}Tl$	2-sigma
ANE-108	225.6	USMS	-4.0	1.1
ANE-108	235	USMS	-4.9	2.0
ANE-108	244.9	USMS	-7.5	4.4
ANE-108	251	ACTM	-3.4	0.4
ANE-108	252.5	ACTM	-4.6	1.3
ANE-108	259.3	ACTM	-5.2	1.0
ANE-108	262.2	ACTM	-3.6	0.6
ANE-108	271.5	ACTM	-2.6	1.1
ANE-108	273	ACTM	-4.3	1.2
ANE-108	275.2	LCMS	-4.8	1.2
ANE-108	281.6	LCMS	-4.4	0.8
ANE-108	284	LCMS	-4.6	1.0

spectrometer (ICP-MS); Method 1F30) ultra-trace, 4 acid (HF, HNO_3, $HClO_4$, HCl) near-total digestion and analysis by ICP-MS; Method LOI) sintering at 1000°C; Method G806) digestion with sulphuric and hydrofluoric acid, indicator solution added and titrated using potassium dichromate; Method 2A F) fusion and analysis by specific ion electrode; Method TC001 and TC002) ignition in induction furnace and measurement by adsorption in an infrared spectrometric cell; Method 2A-C) leaching with dilute HCl, followed by ignition at 500°C and analysis of residue by Leco; Method 2A11) leach sample with perchloric acid, and measurement of CO_2 gas evolved into LECO analyzer; Method organic C) by difference (= total C – inorganic C – graphite C).

Precision and accuracy were monitored using laboratory in-house standards, as well as by replicate analysis of certified reference material standards. Detection limits are listed in Table 3. For plotting purposes, ½ the detection limits were used for non-reporting elements as follows: Au 0.1 ppb, Be 0.5 ppm, Bi 0.01 ppm, C org 0.01 weight %, Cd 0.005 ppm, Ga 0.25 ppm, Ge 0.05 ppm, Hf 0.05 ppm, In 0.01 ppm, Na 0.0005 weight %, Pd 5 ppb, Pt 1 ppb, Sn 0.5 ppm, Ta 0.05 ppm, Ti 0.0005 weight %, W 0.25 ppm, H_2O+ 0.005 weight %. For three analyses of mineralized ACTM, upper detection limits of 10 000 ppm were exceeded, and a value of 10 000 was used for plotting purposes.

Chemical treatment, separation and mass spectrometry of thallium

High purity reagents were used for the digestion and dissolution of thallium from the samples in this study, and were either obtained through Seastar (Baseline H_2SO_4 and H_2O_2) or distilled from technical grade acids (HNO_3 and HCl).

About 50 mg of pulverized sample and in-house standard reference materials (NIST 997 and PTC-1) were weighed into PerFluoroAlkoxy (PFA - Savillex Corporation) digestion vessels. Both the NIST 997 and PTC-1 standards were also run through the entire procedure, to ensure that no contamination or fractionation occurred. Individual sample weights were adjusted to the minimum Tl contents provided by previous studies (Gadd, 2015). Four millilitres of aqua regia (molar ratio of 1:3 HNO_3:HCl) were added to each container and put on a hotplate to digest overnight at 180°C. Samples were then centrifuged at 3500 rpm for 10 minutes, and the liquid residue was evaporated to dryness at 85°C. Two millilitres of 0.2 M HBr (2% v/v Br_2) were then added to the evaporated sample before being undergoing thallium separation. Samples were loaded onto a 100 µL AG1-X8 column (Bio Rad), following the method developed by Rehkämper and Halliday (1999).

After elution of the thallium from the columns into clean PFA digestion vessels, the samples were put on the hotplate to dry overnight at 70°C. One drop (approximately 40 µL) of H_2O_2 and one drop of HNO_3 were added to the residue and put to evaporate to almost complete dryness. Two millilitres of 2% HNO_3 were then added to each sample. Samples were measured using a Standard-Sample Bracketing method, using NIST 997 (May and Watters, 2004) as a reference material. Samples were measured on a Thermo-Finnigan Neptune MC-ICP-MS, using a desolvating interface (ESI Apex Q) with a 20 µL/min take-up line. Because of the significant amount of H_2SO_4 remaining in solution at the end of the chemical purification procedure (Rehkämper and Halliday, 1999), all solutions used during the measurement (wash, blank, NIST 997 bracketing standard) were prepared in a 2% HNO_3 with 0.1% v/v H_2SO_4 to match the matrix of the samples (Nielsen et al., 2004). Overall procedure blanks, from sample digestion to measurement on the MC-ICP-MS, were below detection limit on the MC-ICP-MS faraday cups (< 20 pg Tl). Drift between consecutive NIST 997 standards was controlled throughout the sequence with a variability ±0.1 $\varepsilon^{205}Tl$. The PTC-1 $\varepsilon^{205}Tl$ value was within error from the average value typically measured for that reference material in QFIR (-5.8 ± 0.5 $\varepsilon^{205}Tl$, n = 10).

Data analysis and statistics

Several REE ratios were calculated from the bulk geochemical data. All were normalized to average post-Archean Australian Shale (PAAS; Taylor and McLennan, 1985) and designated as shale-normalized (SN) as follows:

$Ce/Ce*_{SN} = 2Ce_{SN}/(La_{SN}+Pr_{SN})$

$Eu/Eu*_{SN} = 2Eu_{SN}/(Sm_{SN}+Gd_{SN})$

$Gd/Gd*_{SN} = Gd_{SN}/((Sm_{SN})^{0.33} \times (Tb_{SN})^{0.67})$

Non-parametric Spearman's rank correlations were used rather than Pearson Product-Moment, as the latter is very susceptible to the effects of outliers, particularly in small sample sizes (n = 12 in this study). Correlation coefficients are expressed as r_s.

Table 3. Summary of geochemical data for samples analyzed for thallium isotopic composition in this study. Ranges (minimum to maximum) are given for LCMS, unmineralized ACTM, mineralized ACTM, and USMS. Also shown are lower limits of detection and analytical methods used (see text for details).

Element	Detection Limit	Unit	LCMS Range	Unmin. ACTM Range	Min ACTM Range	USMS Range	Analytical Method Code
Ag	2	ppb	1069 - 2227	196 - 1000	547 - 1256	265 - 1182	1F30
Al	0.01	wt %	0.43 - 0.57	0.07 - 0.13	0.05 - 0.10	0.43 - 1.37	1F30
As	0.1	ppm	21.6 - 36.1	16.3 - 23.5	12.0 - 28.3	3.2 - 38.9	1F30
Au	0.2	ppb	0.1 - 0.4	0.1	0.1	0.1 - 0.3	1F30
B	1	ppm	10 - 14	3 - 4	2 -3	14 - 40	1F30
Ba	0.5	ppm	687 - 875	52 - 468	50 - 276	2053 - 3784	4B
Be	0.1	ppm	2 - 5	0.5 - 5	0.5 - 4	0.5 - 11	1F30
Bi	0.02	ppm	0.19 - 0.36	0.01 - 0.12	0.01 - 0.08	0.12 - 0.16	1F30
CO_2	0.02	wt %	0.02 - 0.66	0.08 - 28.43	0.21 - 26.59	0.94 - 3.27	2A11
C tot	0.02	wt %	3.75 - 9.37	6.16 - 13.12	3.04 - 10.71	6.74 - 12.76	2A LECO
C org	0.02	wt %	3.54 - 9.33	3.65 - 6.14	1.84 - 3.01	6.46 - 11.67	2A-C
Ca	0.01	wt %	0.61 - 0.98	0.25 - 31.49	0.83 - 32.03	2.55 - 3.91	1F30
Cd	0.01	ppm	0.07 - 6.53	1.01 - 4.82	46.29 - 68.83	0.005 - 0.20	1F30
Ce	0.1	ppm	50.3 - 64.1	4.7 - 23.9	10.5 - 20.2	20.5 - 60.6	1F30
Co	0.1	ppm	10.9 - 14.3	1.4 - 6.4	0.8 - 3.5	5.4 - 11.1	1F30
Cr	0.5	ppm	13.3 - 30.0	6.2 - 17.0	4.8 - 19.5	20.0 - 64.6	1F30
Cs	0.02	ppm	2.5 - 7.1	0.3 - 0.8	0.2 - 0.5	1.6 - 7.3	1F30
Cu	0.01	ppm	47.66 - 82.67	12.81 - 105.05	20.59 - 24.84	43.15 - 48.61	1F30
Dy	0.05	ppm	3.5 - 7.13	1.15 - 3.23	0.91 - 1.72	1.86 - 2.99	4B
Er	0.03	ppm	2.63 - 4.61	0.47 - 2.36	0.68 - 1.16	1.95 - 3.91	4B
Eu	0.02	ppm	1.0 - 1.78	0.14 - 0.72	0.26 - 0.44	0.45 - 1.68	4B
F	10	ppm	1096 - 1764	286 - 740	223 - 323	220 - 1604	2A-F
Fe tot	0.01	wt %	1.61 - 2.93	0.48 - 0.85	0.79 - 1.82	0.58 - 1.11	G806
Ga	0.5	ppm	14.1 - 18.3	0.25 - 4.7	0.25 - 1.4	4.1 - 10.8	1F30
Gd	0.05	ppm	3.83 - 8.68	0.96 - 4.11	1.33 - 1.84	1.83 - 8.82	4B
Ge	0.1	ppm	0.05	0.05	0.1 - 0.3	0.05 - 0.10	1F30
Hf	0.02	ppm	3.4 - 4.6	0.05 - 0.6	0.05 - 0.5	1.6 - 5.2	1F30
Hg	5	ppb	195 - 239	102 - 160	1271 - 1772	77 - 136	1F30
Ho	0.02	ppm	0.81 - 1.51	0.16 - 0.77	0.2 - 0.4	0.5 - 1.45	4B
H_2O+	0.01	wt %	9.04 - 13.94	2.28 - 7.85	0.005 - 5.64	8.15 - 14.94	LOI
In	0.02	ppm	0.01 - 0.03	0.01	0.01 - 0.05	0.01	1F30
K	0.01	wt %	0.28 - 0.38	0.05 - 0.09	0.03 - 0.06	0.28 - 0.76	1F30
La	0.5	ppm	33.5 - 37.6	1.7 - 22.2	4.2 - 12.2	16.2 - 51.8	1F30
Li	0.1	ppm	1.7 - 4.3	0.6 - 2.0	0.3 - 1.1	3.3 -28.5	1F30
LOI	0.1	wt %	10.5 - 15.1	8.8 - 37.4	5.8 - 32.0	9.5 - 19.3	LOI
Lu	0.01	ppm	0.40 - 0.58	0.08 - 0.31	0.05 - 0.19	0.26 - 0.53	4B
Mg	0.01	wt %	0.05 - 0.14	0.03 - 0.08	0.01 - 0.06	0.07 - 1.51	1F30
Mn	1	ppm	29 - 77	36 - 433	81 - 437	33 -110	1F30

Table 3. Cont.

Element	Detection Limit	Unit	LCMS Range	Unmin. ACTM Range	Min ACTM Range	USMS Range	Analytical Method Code
Mo	0.01	ppm	3.27 - 57.15	9.5 - 50.63	5.34 - 16.26	1.92 - 38.23	1F30
Na	0.001	wt %	0.0005	0.0005 - 0.003	0.0005 - 0.002	0.0005 0.002	1F30
Nb	0.02	ppm	13.9 - 25.5	0.9 - 5.9	0.6 - 2.3	5.2 - 10.5	1F30
Nd	0.3	ppm	24.6 - 39.8	3.9 - 16.0	5.9 - 12.2	11.0 - 41.7	4B
Ni	0.1	ppm	100.8 - 192.1	32.2 - 79.7	18.5 - 47.8	75.2 - 91.3	1F30
P	0.001	wt %	0.08 - 0.44	0.03 - 0.25	0.05 - 0.06	0.04 - 1.24	1F30
Pb	0.01	ppm	37.46 - 49.26	104.73 - 113.08	3699.21 - >10000	11.07 - 17.07	1F30
Pd	10	ppb	5 - 18	5 - 12	5	5	1F30
Pr	0.02	ppm	6.89 - 9.54	0.85 - 4.11	1.33 - 2.71	3.26 - 10.92	4B
Pt	2	ppb	1 - 8	1 - 3	1 - 3	1 - 6	1F30
Rb	0.1	ppm	103.7 - 150.1	8.0 - 28.7	6.0 - 15.2	64.0 - 122.5	1F30
Re	1	ppb	17 - 77	14 - 79	3 - 23	20 - 28	1F30
S	0.02	wt %	1.84 - 3.29	0.52 - 0.95	1.76 - 3.30	0.66 - 1.09	1F30
S tot	0.02	wt %	1.91 - 3.42	0.60 - 1.04	2.04 - 3.43	0.73 - 1.25	2A LECO
Sb	0.02	ppm	3.12 - 9.08	1.68 - 3.47	3.55 - 7.94	1.82 - 2.06	1F30
Sc	0.1	ppm	2.0 - 4.0	0.5 - 1.4	0.3 - 1.2	1.4 - 4.3	1F30
Se	0.1	ppm	5.9 - 8.8	0.7 - 2.3	1.0 - 5.4	4.3 - 7.6	1F30
Sm	0.05	ppm	3.91 - 7.86	0.77 - 3.56	1.06 - 1.69	1.67 - 8.11	4B
Sn	0.1	ppm	1.0 - 2.0	0.5	0.5	0.5 - 2.0	1F30
Sr	0.5	ppm	16.1 - 27.9	5.8 - 229.6	10.1 - 209.0	50.8 - 78.4	1F30
Ta	0.05	ppm	0.9 - 1.8	0.05 - 0.3	0.05 - 0.2	0.3 - 0.6	1F30
Tb	0.01	ppm	0.61 - 1.29	0.16 - 0.61	0.18 - 0.33	0.27 - 1.26	4B
Te	0.02	ppm	0.1 - 1.24	0.04 - 0.12	0.03 - 0.09	0.07 - 0.17	1F30
Th	0.1	ppm	7.8 - 10.7	0.5 - 2.8	0.6 - 1.3	6.4 - 9.9	1F30
Ti	0.001	wt %	0.004 - 0.005	0.001 - 0.002	0.0005 - 0.001	0.005 - 0.027	1F30
Tl	0.02	ppm	0.35 - 1.12	0.26 - 0.40	0.81 - 3.14	0.07 - 0.16	1F30
Tm	0.01	ppm	0.40 - 0.62	0.09 - 0.36	0.07 - 0.21	0.27 - 0.59	4B
U	0.1	ppm	10.4 - 29.7	3.2 - 51.0	2.6 - 4.2	9.6 - 12.8	1F30
V	2	ppm	273 - 1674	281 - 974	168 - 275	125 - 750	1F30
W	0.1	ppm	0.9 - 1.1	0.25 - 0.9	0.25	0.25 - 1.4	1F30
Y	0.01	ppm	22.5 - 52.5	6.2 - 27.8	6.5 - 14.7	19.4 - 61	1F30
Yb	0.05	ppm	2.14 - 3.71	0.66 - 1.89	0.46 - 1.06	2.11 - 3.08	4B
Zn	0.1	ppm	30.4 - 654.4	251.1 - 780.7	>10000	5.0 - 18.7	1F30
Zr	0.1	ppm	119.5 - 165.2	11.7 - 27.2	7.2 - 19.6	70 - 144.3	1F30

Results

Bulk geochemical compositions

Table 3 gives the elemental ranges for LCMS, unmineralized ACTM, mineralized ACTM, and USMS. USMS has the lowest Tl contents (0.07–0.16 ppm), followed by unmineralized ACTM (0.26–0.40 ppm) and LCMS (0.35–1.12 ppm).

Mineralized ACTM has the highest Tl contents at 0.81 to 3.14 ppm.

Thallium isotopic compositions

Thallium isotope compositions and their 2σ standard deviations are shown in Table 2 and ε^{205}Tl ranges from a low of -7.5 to a high of -2.6. The highest ε^{205}Tl value (-2.6) is near the base

of the mineralized ACTM, whereas the lowest value (ε^{205}Tl -7.5) occurs in USMS of the immediate hanging wall to the mineralized ACTM. There is a systematic increase upwards within the USMS (ε^{205}Tl to -4.0). Thallium isotope compositional ranges for the different units are as follows: LCMS (ε^{205}Tl -4.8 to -4.4), ACTM overall (ε^{205}Tl -5.2 to -2.6), unmineralized ACTM (ε^{205}Tl -5.2 to -4.3) mineralized ACTM (ε^{205}Tl -3.6 to -2.6) and USMS (ε^{205}Tl -7.5 to -4.0). Samples with higher thallium abundances have lower relative standard deviations with respect to their ε^{205}Tl compositions. Similarly, the most negative ε^{205}Tl value also has the highest uncertainty (ε^{205}Tl -7.5 ± 4.4), with the high standard deviation related to the very low thallium abundance of this sample (0.07 ppm).

Discussion

Mineralogical residence site of thallium

A key question is what are the mineralogical residence(s) of thallium in the rocks and mineralization at Anniv East? Our bulk geochemical data show positive correlations for Tl-As (r_s = +0.37, two-tailed P = 0.2356; plot not shown), Tl-Hg (r_s = +0.93, two-tailed P = <0.0001; plot not shown), Tl-Sb (r_s = +0.85, two-tailed P = 0.0005; plot not shown), together with excellent positive Tl-Fe (r_s = +0.35, two-tailed P = 0.2652; plot not shown) and Tl-S (r_s = +0.66, two-tailed P = 0.0202; plot not shown) that collectively indicate that pyrite is by far the largest mineralogical residence site for thallium.

Both Gadd et al. (2016a) and Liu (2017) show that pyrite within Howard's Pass district mineralization and host rocks contain abundant Tl (up to about 800 ppm) though average values are far lower: LCMS – framboidal pyrite range 7 to 800 ppm, mean 50 ppm, and recrystallized diagenetic pyrite range 4 to 500, mean 15 ppm; ACTM – framboidal pyrite range 12 to 180 ppm, mean 75 ppm, and recrystallized diagenetic pyrite range 10 to 250, mean 30 ppm; USMS – framboidal pyrite 9 to 350 ppm, mean 250 ppm, and recrystallized diagenetic pyrite range 2 to 30, mean 7 ppm. Gadd et al. (2016a) showed that for pyrite in mineralization and host rocks of the Howard's Pass district Tl groups together with Zn, Pb, Mn, As, Ag, and Sb,

and indicated that they were delivered with the SEDEX mineralizing fluids.

In addition to pyrite, thallium can reside in sphalerite (Cook et al., 2009; Graham et al., 2009) and galena (Deditius et al., 2011; George et al., 2015). There is no correlation between Tl and Pb (r_s = -0.25, two-tailed P = 0.0045; plot not shown), but there is a correlation between Tl and Zn (r_s = +0.85, two-tailed P = 0.00054; plot not shown). Note there is no Tl-Zn correlation for unmineralized samples, but the statistics are strongly influenced by three mineralized samples that have concomitant high zinc and thallium contents. These relationships indicate thallium is not resident in galena, but is present in sphalerite.

As noted by Peter et al. (2015), there is white mica present within the ACTM, which contains up to 112.7 ppm Tl (Liu, 2017), where it likely substitutes for potassium (Heinrichs et al., 1980; Kaplan and Mattigod, 1998). There is a negative correlation between Tl and K (r_s = -0.60, two-tailed P = 0.0396; plot not shown), indicating that white mica is a sink for thallium, though not in the mineralized samples. In summary, pyrite contents far exceed white mica contents in the samples, and, together with the low thallium contents of mineralized samples collectively indicates that pyrite is, by far, the dominant sink for thallium in our samples.

Bulk geochemical paleoredox indicators

In order to assess the potential viability of thallium isotopes as a paleoredox indicator in Canadian Paleozoic SEDEX settings, it is instructive to first evaluate the bulk geochemical paleoredox indicators for comparison purposes. A caveat is that the redox conditions of bottom waters may not be reflective of redox conditions of pore waters in the sediments and (and immediately below) the seafloor (e.g. oxic bottom waters overlying sediments with anoxic and/or sulphidic pore waters). Indeed, this scenario is what is proposed for the Howard's Pass SEDEX deposits (Gadd et al., 2016b, 2017). Table 4 is a compilation of some selected (least problematic or contradictory) geochemical paleoredox proxies from literature, and the redox conditions for the LCMS, unmineralized ACTM, mineralized ACTM and USMS.

Table 4. Summary of selected (least problematic, viable) bulk geochemical paleoredox proxies and salient references. Shown are the value ranges (minimum to maximum) for each of each of these by LCMS, unmineralized ACTM, mineralized ACTM and USMS.

Paleoredox Proxy:	V	Mo	Re/Mo	Ni/Co	V/Cr	U/Th	Mo/TOC	Ce/Ce* PAAS norm
LCMS Range	273–1674 ppm	3.3–57.1 ppm	0.0012–0.0052	8.0–16.7	20.6–76.0	1.0–3.8	0.9–6.1	0.74–0.78
LCMS Redox	e (i)	e (i)	a (i) to s (i)	a & s (p)	a & s (p)	a (i) to d (i)	a	s (p)
Unmin. ACTM Range	281–974 ppm	9.5–50.6 ppm	0.0013–0.0016	12.4–23.0	37.5–72.7	6.4–34.0	2.6–9.4	0.62–0.90
Unmin. ACTM Redox	?	e (i)	a (p)	a & s (p)	a & s (p)	a & s (p)	a	s (p)
Min. ACTM Range	168–275 ppm	5.3–16.3 ppm	0.00025–0.0015	13.7–23.1	9.7–57.3	2.8–4.3	2.9–5.4	0.70–1.02
Min. ACTM Redox	?	e (p porewater)	a (i) to s (i)	a & s (p)	a & s (p)	a & s (p)	a	s (i) and a (i)
USMS Range	125–750 ppm	1.9–38.2 ppm	0.0007–0.015	6.8–16.4	5.9–19.5	1.3–1.6	0.3–3.3	0.59–0.84
USMS Redox	?	e (p porewater; i water)	a (i) to s (i)	a & s (p)	a & s (p)	a & s (p)	a	s (p)
References	Breit & Wanty, 1991; Scott et al., 2013	Scott & Lyons, 2012	Ross & Bustin, 2009; Crusius et al., 1996	Ross & Bustin, 2009; Jones & Manning, 1994	Ross & Bustin, 2009; Jones & Manning, 1994	Ross & Bustin, 2009; Jones & Manning, 1994	Algeo & Lyons 2006; Algeo & Rowe, 2012	Wright et al., 1987; Tribovillard et al., 2006

o oxic (>2 ml O_2/L H_2O); s suboxic (0.2 to 2 ml O_2/L H_2O); d dysoxic (<0.2 ml O_2/L H_2O); a anoxic (<0 ml O_2/L H_2O); e euxinic (>0 ml H_2S/L H_2O); i intermittent; p permanent

Cerium and europium are the only REE that can have valence states other than +3 (III). Cerium has two oxidation states (Ce^{3+} and Ce^{4+}) that are strongly redox dependent, and cerium is fractionated from it neighboring REE according to redox state (e.g. De Baar et al., 1988). In oxygenated marine waters, Ce^{4+} predominates and this is scavenged onto highly reactive iron-manganese oxyhydroxides, leaving the oxic seawater depleted in cerium (Elderfield and Greaves, 1982). The magnitude of the Ce anomaly Ce/Ce*) varies with water depth in the modern oceans; it is absent (i.e. Ce/Ce* = 1) in surface waters, but in becomes increasingly negative with depth due to oxidative scavenging onto the Fe-Mn oxyhydroxides in the water column (Alibo and Nozaki, 1999). The iron-manganese oxyhydroxides capture Ce^{4+} (and have Ce/Ce* >1). In anoxic marine settings, cerium occurs as Ce^{3+} (same valence state as the other REE), and nil (Ce/Ce* = 1) to weakly positive anomalies occur. Thus, the magnitude of cerium anomalies can serve as a proxy for oxygen levels (e.g. Wright et al., 1987).

Values of Ce/Ce* vary widely from 0.58 to 1.02 in our samples. Most of the cerium anomalies are real, based on a plot of Pr/Pr* versus Ce/Ce* (plot not shown), following Bau and Dulski (1996). The Ce/Ce* anomalies are shown in Figure 7, a PAAS normalized REE plot, with samples classified into LCMS, unmineralized ACTM, mineralized ACTM, and USMS. Cerium anomalies between 0.4 and 0.9 are taken to indicate deposition under suboxic conditions (i.e. 0.2–2 mL O_2/L H_2O; Tribovillard et al., 2006), and most of our analyses fall within this range. Our analyses also have gadolinium anomalies (Gd/Gd*) that range from 1.02 to 1.30, and are indicative of seawater influence (Alibo and Nozaki, 1999; Gadd et al., 2016b).

Total organic carbon (TOC) contents themselves are not diagnostic of anoxia, as there is too much overlap between anoxic and oxic settings (e.g. Raiswell et al., 1988). Ni/Co that was previously proposed to be an effective redox indicator (e.g. Jones & Manning, 1994; Ross and Bustin, 2009), displays a

positive correlation with TOC (r_s = -0.41, two-tailed P = 0.12826), whereas V/Cr and U/Th, both of which have been cited as effective redox indicators (e.g. Jones & Manning, 1994), show no correlation with TOC (V/Cr r_s = +0.02, two-tailed P-0.9484; U/Th r_s = -0.31, two-tailed P = 0.33059). However, there is good positive correlation between V and TOC (r_s = +0.63, two-tailed P = 0.02832; plot not shown). The two uppermost samples of CCMS have V>1000 ppm, indicative of hyper-sulphidic conditions, according to Scott et al. (2013).

Molybdenum contents of sediments are considered a robust paleoredox proxy (Mo <25 ppm is indicative of euxinic conditions within pore waters; Mo >100 ppm signifies permanently euxinic conditions within the water column itself; and Mo between 25 and 100 ppm indicates an intermittently euxinic water column; Scott and Lyons, 2012). According to these criteria, LCMS, ACTM and USMS were deposited in conditions that varied between euxinic pore waters and an intermittently euxinic water column. The two uppermost LCMS samples have Mo contents of 46 and 57 ppm, indicative of intermittently euxinic (i.e., anoxic and sulphidic) conditions (see Slack et al., 2017).

The ratio of molybdenum (in ppm) to TOC (in weight %) (Mo/TOC) has also been proposed as a potential redox indicator (e.g. Algeo and Lyons, 2006; Algeo and Rowe, 2012). Our data (Mo/TOC = 0.3 to 9.4) are in the range of modern anoxic basins. Further, based on the residence time of molybdenum in seawater (ca. 730 ka; Algeo, 2004), and comparison with deepwater renewal times of modern anoxic basins, the LCMS experienced a deepwater renewal time of ca. 400 years, whereas at the base of the ACTM this decreased to ca. 200 years (see Figure 3 of Algeo and Rowe, 2012).

According to Crusius et al. (1996) and Ross and Bustin (2009), Re/Mo between 0.0008 and 0.004 indicate anoxic conditions, Re/Mo greater than 0.004 indicate suboxic conditions, whereas Re/Mo similar to seawater (0.0008) indicate deposition under euxinic conditions. Re/Mo ratios for Anniv East samples are very low) and suggest anoxic to sulphidic depositional conditions: LCMS 0.0012 to 0.005 (indicate anoxic), ACTM mineralized 0.0002 to 0.0014 (euxinic to anoxic), ACTM barren 0.0013 to 0.0016 (indicate anoxic), USMS 0.0007 to 0.015 (anoxic to suboxic). Furthermore, there is excellent negative correlation between Re/Mo and Ce/Ce*.

Although the Anniv East deposit is about 20 km northwest of the XY Central deposit where Slack et al. (2017) conducted their bulk geochemical paleoredox studies, our paleoredox indicators show similar trends, supporting the proposition that all the deposits/zones along the Zinc Corridor formed within the same water column and/or (early diagenetic) sedimentary environment.

Thallium isotopic compositions as paleoredox indicators?

The utility of thallium isotopes as paleoredox proxies is tested through correlations between the aforementioned various

Figure 7. PAAS normalized REE plot, with samples classified into LCMS, unmineralized ACTM, mineralized ACTM, and USMS.

Figure 8. ε^{205}Tl versus various elemental values and ratios: a) Pb; b) Zn; c) S total; d) Mn; e) Tl; f) Ge; g) Eu/Eu*$_{SN}$, h) Ni; i) TOC; j) Re/Mo; k) Ba; l) Ce/Ce*$_{SN}$.

elements, element ratios and geochemical redox indicators, and thallium isotopic compositions for the same samples (Fig. 8). ε^{205}Tl values correlate negatively with Ni (r_s = -0.58, two-tailed P = 0.04786; Fig. 8h), TOC (r_s = -0.51, two-tailed P = 0.08991; Fig. 8i), Re/Mo (r_s = -0.59, two-tailed P = 0.0446; Fig. 8j) and Ba (r_s = -0.51, two-tailed P = 0.08991; Fig. 8k). Nickel, rhenium, and molybdenum are redox sensitive elements present in seawater. In oxic marine settings, nickel is complexed with organic matter in the water column and sedimented, leading to enrichments in the sediments (Algeo and Maynard, 2004). Evidence for this in the Anniv East samples is the excellent positive correlation between Ni and TOC (r_s = +0.66, two-tailed P = 0.02019; plot not shown). In reducing sediments, nickel is mobilized from sediment into the overlying water column. Re/Mo vs ε^{205}Tl relations show that higher ε^{205}Tl values indicate anoxic conditions, whereas the lowest values indicate suboxic conditions. High barium in sediments is typically an indication of high paleoproductivity (Liguori et al., 2016), with barium originating from decaying organic matter (Falkner et al., 1993), and the oxidation of organic sulphur producing dissolved sulphate, which is then fixed as barite (Griffith and Paytan, 2012). Evidence for this in our samples is the good negative correlation between Ba and TOC (r_s = -0.51, two-tailed P = 0.08991; plot not shown).

Finally, there is a positive correlation between ε^{205}Tl and Ce/Ce* (r_s = +0.37, two-tailed P = 0.2356; Fig. 8l) and between Eu/Eu* and Ce/Ce* (r_s = +0.36; two-tailed P = 0.2551; plot not shown). The negative Ce/Ce* ratios indicate oxidation of Ce^{3+} to Ce^{4+} and removal by adsorption onto the reactive surfaces of iron-manganese oxyhydroxides, and burial thereof, leaving the (oxygenated) ocean water cerium depleted with respect to adjacent REE. Cerium anomalies approaching unity or slightly >1 are the hallmark of anoxic conditions, and these have the most positive ε^{205}Tl. Collectively, the above correlations show that the most negative ε^{205}Tl indicate the most oxic conditions, whereas the most positive ε^{205}Tl indicate anoxic conditions; furthermore, the latter (anoxic) conditions coincide with systematically larger (positive) europium anomalies, likely due to the precipitation of hydrothermal sulphides.

Mineralizing fluid control on thallium isotopic compositions

There are no systematic correlations between ε^{205}Tl and Rb, Cs, or K (plots not shown), indicating that incorporation in phyllosilicates (or clays) is not the main controlling factor on the thallium isotopic compositions. However, ε^{205}Tl correlates positively with Pb (r_s = +0.59, two-tailed P = 0.0446; Fig. 8a), Zn (r_s = +0.63, two-tailed P = 0.0292; Fig. 8b), S tot (r_s = +0.50, two-tailed P = 0.1006; Fig. 8c), Mn (r_s = +0.69, two-tailed P = 0.0130; Fig. 8d), Tl (r_s = +0.64, two-tailed P = 0.0261; Fig. 7e), Ge (r_s = +0.58, two-tailed P = 0.0502; Fig. 8f), as well as Cd (r_s = +0.66, two-tailed P = 0.0199) and Hg (r_s = +0.60, two-tailed P = 0.0386) (plots not shown for both). These correlations indicate strong control by sulphides. Indeed, samples with (Pb+Zn) < 1000 ppm and low Tl have ε^{205}Tl val-

ues that range from -5.2 and -4.0, whereas mineralized samples (>10 000 Pb+Zn) have ε^{205}Tl values from -3.6 to -2.6. Furthermore, there is a positive correlation between ε^{205}Tl and Eu/Eu* (r_s = +0.63, two-tailed P = 0.0283; Fig. 8g). Values of Eu/Eu* range from 0.76 to 1.20, but all mineralized (Zn+Pb > 10 000 ppm) samples displaying Eu/Eu* > 1, indicative of hydrothermal input (e.g. Peter and Goodfellow, 1996; Peter, 2003; Slack et al., 2017).
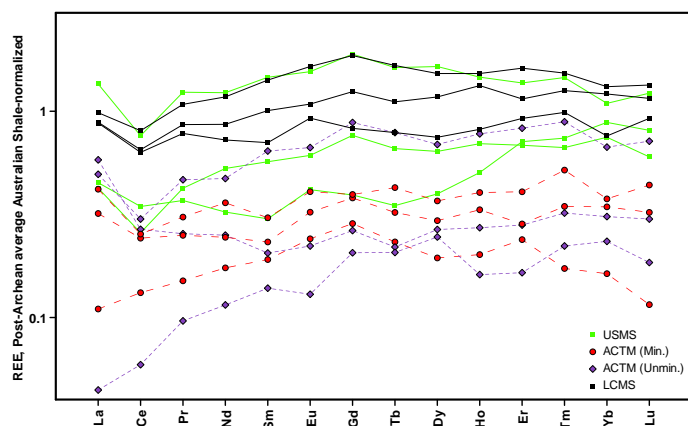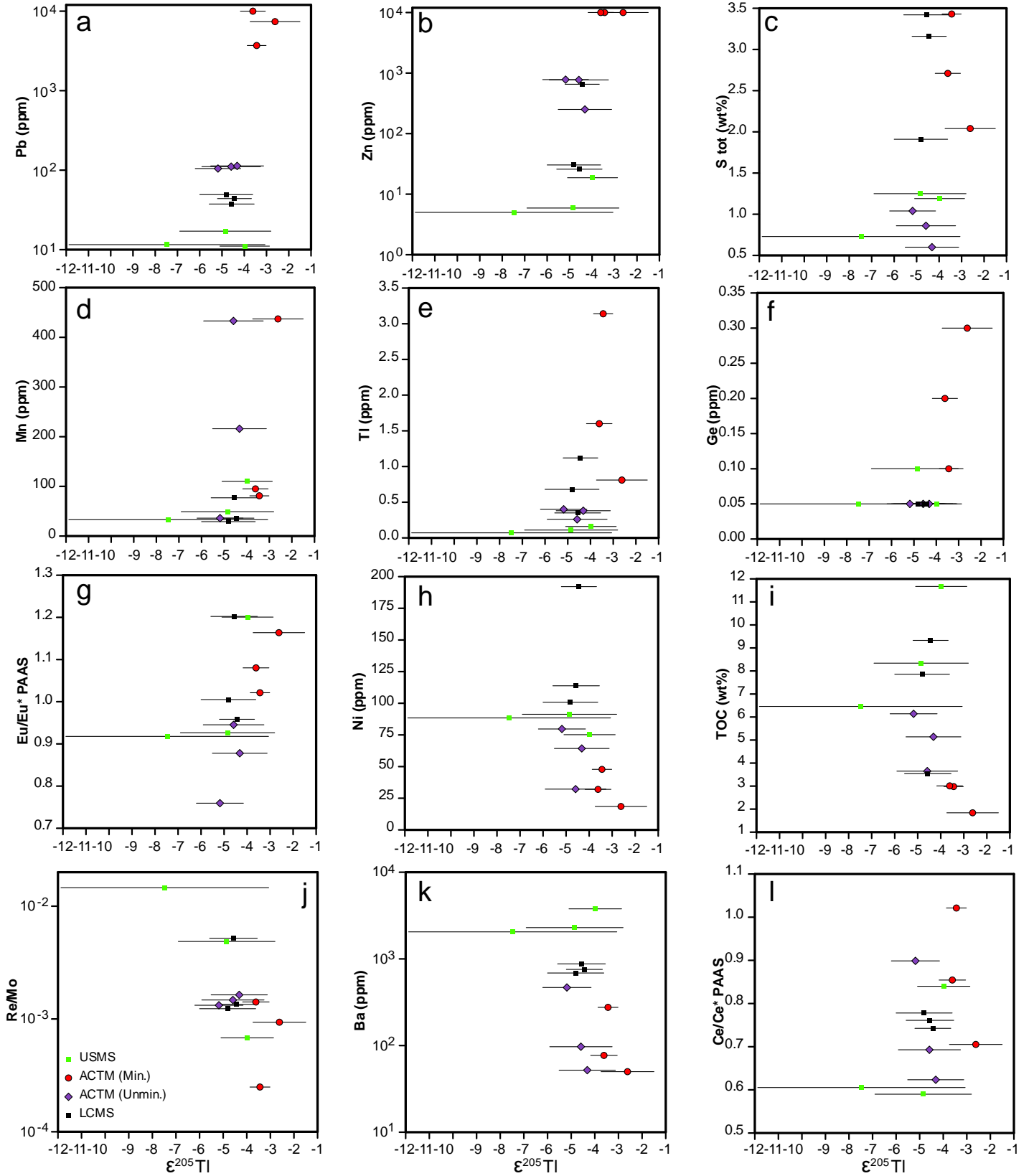
The REE systematics are depicted in Figure 7, a PAAS-normalized REE plot, with samples classified into LCMS, unmineralized ACTM, mineralized ACTM, and USMS. Positive europium anomalies occur sporadically not only in the ACTM, but also in LCMS and USMS, similar to the observations of Slack et al. (2017) at the XY Central deposit, also in the Howards Pass District, and along the Zinc Corridor (see Fig. 4). Collectively, these data indicate that "ore" sulphides (galena, sphalerite, syn-ore pyrite) precipitated from mineralizing fluid (dense brine, as suggested by Gadd et al., 2016a, 2017), represent the highest ε^{205}Tl value (-3.6 to -2.6) endmember. Further, this fluid was of sufficient temperature and pH to mobilize Eu^{2+} and form subtle positive europium anomalies. One possible mechanism for the high(er) ε^{205}Tl values in the mineralized samples is that low temperature manganese oxyhydroxides (a major sink for ^{205}Tl —see above) may have been leached by the mineralizing fluid/brine, contributing isotopically heavy thallium to the mineralized samples.

Comparison with other ore deposits

Metallic mineral deposit types for which thallium isotope data are available in the literature are Mississippi Valley (MVT), Alpine metamorphic polymetallic, magmatic copper-arsenic and Carlin gold (Table 5). Mineralized ACTM samples range between ε^{205}Tl -3.6 and -2.6, a range of only one. These values are more negative than most of the reported data, but do overlap with the MVT, Alpine metamorphic and magmatic copper-arsenic deposits.

Wickham (2014) reports relatively heavy ε^{205}Tl values (-1.5 to -2.5) for Neoproterozoic clastic metasedimentary rocks underlying Carlin gold deposits in Nevada and suggests that these rocks are a viable metal source for the mineralization, based on isotopic similarities between ore-stage pyrite and these metasedimentary rocks. The rocks of the Howard's Pass district were deposited on the same Laurentian margin during the early Paleozoic, and depositional environments of the Northern and Southern Cordillera are interpreted as similar (Turner et al., 1989). Lydon (2015) demonstrates that clastic sedimentary rocks such as these can be fertile because their metals are readily leachable by hydrothermal fluids. The ε^{205}Tl values for Anniv East mineralized ACTM samples fall within the range for Paleozoic marine carbonates, modern euxinic marine sediments and continental igneous rocks (and presumably their detrital sedimentary equivalents) (Fig. 2; Table 1). This is not unexpected, given that the (rift basinal sedimentary) rocks that the hydrothermal fluids circulated through (and leached elements

Table 5. Summary of thallium isotopic data for ore deposits available in the literature. See text for further details.

Deposit/Showing Name	Deposit Type	Sample Type	ε^{205}Tl	References
Anniv East	Vent Distal SEDEX Pb-Zn	bulk mineralization	-3.6 to -2.6	this study
Wiesloch	Mississippi Valley Type Pb-Zn	sphalerite, galena	-1.4 to -2.7	Hettmann et al., 2014
Lengenbach Quarry	Alpine Metamorphic Pb-As-Tl-Zn	various "ore" minerals	-4.1 to +1.1	Hettmann et al., 2014
Pizzo Cervandone	Magmatic Cu-As	fahlore, asbecasite	-3 to +0.1	Hettmann et al., 2014
Turquoise Ridge	Carlin Type Au	pyrite	-1.3	Wickham, 2014
Getchell	Carlin Type Au	realgar	-2.1	Wickham, 2014

from) would impart their thallium isotopic composition with negligible fractionation (Nielsen and Rehkämper, 2011).

Lithologic and stratigraphic variation in thallium isotopic compositions

The highest ε^{205}Tl value (-2.6), which occurs within the mineralized ACTM, near its base, approaches an average crustal value/range (approximately -2; Nielsen and Rehkämper, 2011), and all 3 mineralized ACTM samples have the highest ε^{205}Tl values (range -3.6 to -2.6) obtained in this study (Fig. 9). It is likely that the thallium isotope systematics of the mineralized samples are perturbed by isotopically heavy thallium within the mineralizing fluids compared with those of unmineralized shales and calcareous shales. Indeed, the three non-mineralized samples within the ACTM show significantly lower ε^{205}Tl values (range -5.2 to -4.3; Fig. 9), potentially indicating variable redox controls/conditions. This is in agreement with the observation of Slack et al. (2017) who concluded that the unmineralized ACTM was deposited under diverse redox conditions, ranging from suboxic to sulphidic. The lowest ε^{205}Tl value (-7.5; Fig. 9) occurs in USMS of the immediate hanging wall to the mineralized ACTM and falls well within the field for oxic seawater (Nielsen and Rehkämper, 2011); the upwards systematic increase within the USMS (to -4.0; Fig. 9) likely reflects an increased influence from continental detritus, which would be expected to be higher (ε^{205}Tl = -2?). The ε^{205}Tl values for LCMS (range -4.8 to -4.4; Fig. 9) are intermediate between the lightest and heaviest values, and similar to most of the USMS and unmineralized ACTM, likely indicating intermediate redox conditions between anoxic (during deposition of mineralized ACTM) and suboxic (during deposition of USMS).

Conclusions

We have conducted a bulk geochemical and thallium isotopic stratigraphic traverse through a mineralized intersection (and immediate stratigraphic footwall and hanging wall) in a single drillhole from the Anniv East vent-distal Pb-Zn SEDEX deposit in the Howard's Pass district of the Selwyn Basin, Yukon. Bulk geochemical redox proxies commonly accepted to have the least problems (V, Mo, Re/Mo, Ni/Co, V/Cr, U/Th, Mo/TOC, and Ce/Ce*$_{SN}$), though somewhat contradictory amongst each other, generally show that redox conditions var-

ied between suboxic, anoxic, and euxinic (intermittently to permanently). Given the sample density, we cannot place constraints on the durations that these disparate conditions existed. We can conclude, however, that conditions were not static over the stratigraphic interval sampled.

Thallium isotope compositions vary from ε^{205}Tl -7.5 to -2.6. The lightest ε^{205}Tl value (an outlier from the rest of the data, and with the largest uncertainty) is more negative than present day seawater (approximately -6). The heaviest value is within the range for modern oceanic clays, continental igneous rocks and Paleozoic carbonates. Comparison of the bulk geochemical paleoredox indicators with ε^{205}Tl (for the same sample) indicate that the most negative values reflect deposition under suboxic or oxic conditions. Although the most positive values (ε^{205}Tl > -4; all mineralized ACTM samples) are consistent with sulphide deposition under anoxic conditions, they may only reflect contributions of hydrothermal, heavy thallium to the mineralizing environment, and therefore would provide no marine sedimentary redox information. Thus, redox information can only be extracted from thallium isotopic data for non-mineralized, marine chemical sedimentary (limestone) and fine-grained detrital sedimentary rocks in seafloor hydrothermal deposit settings (e.g. SEDEX and volcano-sedimentary massive sulphides). For mineralized samples, thallium isotopes show great promise for fingerprinting various sulphides precipitated by various processes (e.g. pyrite and other sulphides deposited from ore-forming fluids versus those precipitated from diagenetic fluids).

Future work

Recent work using selective extractions targeted at specific phases has shown there are differences in the thallium isotopic compositions of authigenic pyrite versus silicates, and versus bulk sample (e.g. Owens et al., 2017). We aim to examine such an approach for SEDEX systems at Howard's Pass and elsewhere. Furthermore, we will integrate our thallium isotope work with other metal isotope systems (e.g. molybdenum and uranium) that have proven useful in redox determinations. Molybdenum and thallium isotopes fractionate in opposite directions with respect to manganese oxide burial, and comparison of data for these two systems may provide additional insights into redox conditions and processes.
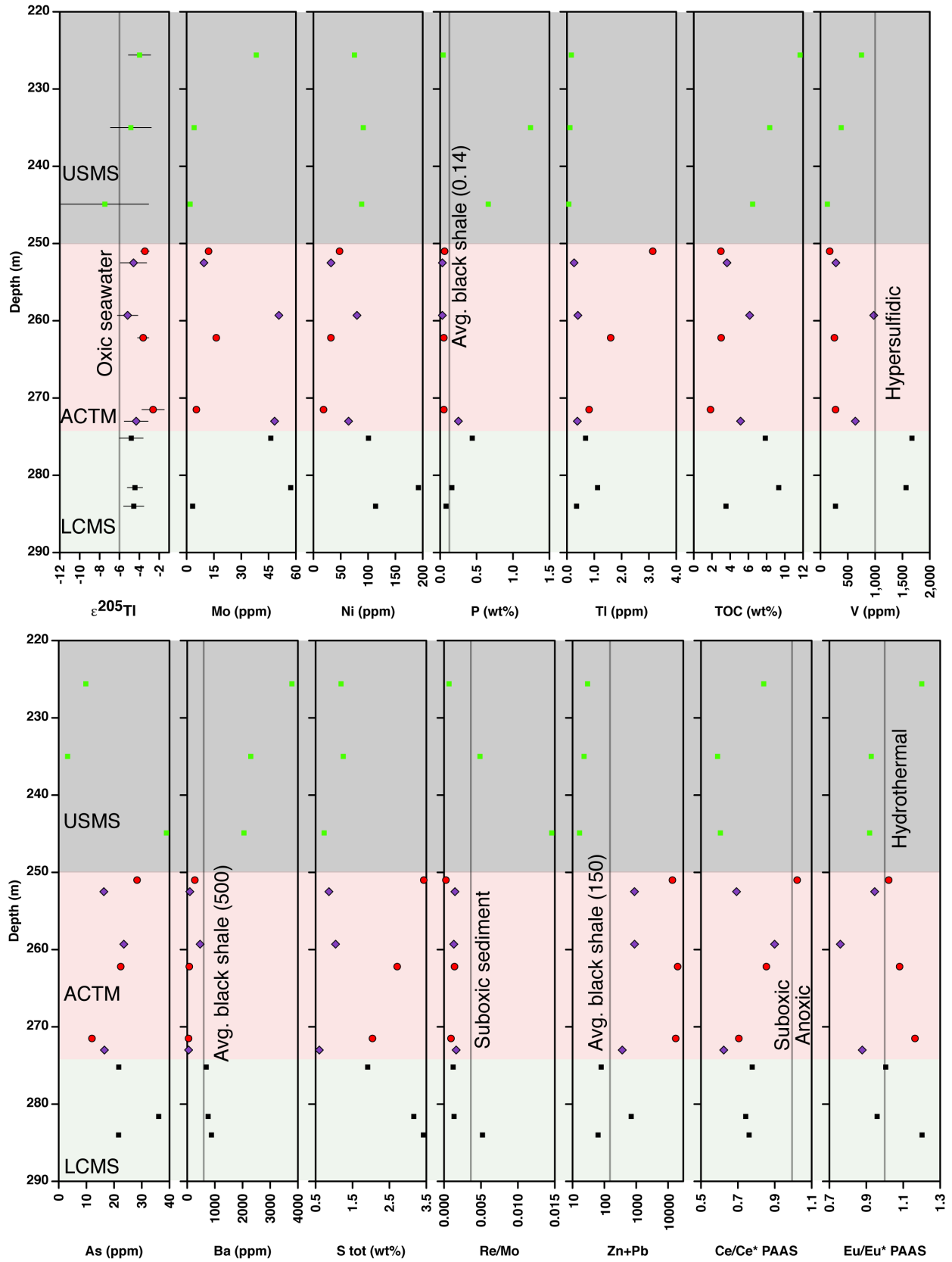
Figure 9. Stratigraphic thallium isotope and bulk geochemical profiles for samples from drillhole ANE-108. Refer to Figure 7 for the meaning of the markers.

Acknowledgments

References

Algeo, T.J., 2004. Can marine anoxic events draw down the trace-element inventory of seawater?; Geology, v. 32, p. 1057–1060.

Algeo, T.J. and Lyons, T., 2006. Mo-total organic carbon co-variation in modern anoxic marine environments: Implications for analysis of paleoredox and paleohydrographic conditions; Paleoceanography, v. 21, 16 p.

Algeo, T.J. and Maynard, J.B., 2004. Trace-element behaviour and redox facies in core shales of Upper Pennsylvanian Kansas-type cyclothems; Chemical Geology, v. 206, p. 289–318.

Algeo, T.J. and Rowe, H., 2012. Paleoceanographic applications of trace-metal concentration data; Chemical Geology, v. 324-325, p. 6–18.

Alibo, D.S. and Nozaki, Y., 1999. Rare earth elements in seawater; particle association, shale-normalization, and Ce oxidation; Geochimica et Cosmochimica Acta, v. 63, p. 363–372.

Anbar, A.D. and Rouxel, O., 2007. Metal stable isotopes in paleoceanography; Annual Review of Earth and Planetary Sciences, v. 35, p. 717–746.

Anbar, A. D. and Gordon, G. W., 2008. Redox renaissance; Geology, v. 36, p. 271–272.

Baker, R.G.A., Rehkämper, M., Hinkley, T.K., Nielsen, S.G., and Toutain, J.P., 2009. Investigation of thallium fluxes from subaerial volcanism—Implications for the present and past mass balance of thallium in the oceans; Geochimica et Cosmochimica Acta, v. 73, p. 6340–6359.

Baker, R.G.A., Rehkämper, M., Ihlenfeld, C., Oates, C.J., and Coggon, R., 2010. Thallium isotope variations in an ore-bearing continental setting: Collahuasi Formation, northern Chile; Geochimica et Cosmochimica Acta, v. 74, p. 4405–4416.

Bau, M. and Dulski, P., 1996. Distribution of yttrium and rare-earth elements in the Penge and Kuruman iron-formations, Transvaal Supergroup, South Africa; Precambrian Research, v. 79, p. 37–55.

Bidoglio, G., Gibson, P.N., O'Gorman, M., and Roberts, K.J., 1993. X-ray absorption spectroscopy investigation of surface redox transformations of thallium and chromium on colloidal mineral oxides; Geochimica Cosmochimica Acta, v. 57, p. 2389–2394.

Bigeleisen, J., 1996. Nuclear size and shape effects in chemical reactions. Isotope chemistry of the heavy elements; Journal of the American Chemical Society, v. 118, p. 3676–3680.

Breit, G.N. and Wanty, R.B., 1991. Vanadium accumulation in carbonaceous rocks: a review of geochemical controls during deposition and diagenesis: Chemical Geology, v. 91, p. 83–97.

Cloquet, C., Rouxel, O., Carignan, J., and Libourel, G., 2005. Natural cadmium isotopic variations in eight geological reference materials (NIST SRM 2711, BCR 176, GSS-1, GXR-1, GXR-2, GSD-12, Nod-P-1, Nod-A-1) and anthropogenic samples, measured by MC-ICP-MS; Geostandards and Geoanalytical Research, v. 29, p. 95–106.

Coggon, R.M., Rehkämper, M., Attecka, C., Teagle, D.A.H., Alt, J.C., and Cooper, M.J., 2014. Controls on thallium uptake during hydrothermal alteration of the upper ocean crust; Geochimica et Cosmochimica Acta, v. 144, p. 25–42.

Cook, N.J., Ciobanu, C.L., Pring, A., Skinner, W., Shimizu, M., Danyushevsky, L., Saini-Eidukat, B., and Melcher, F., 2009. Trace and minor elements in sphalerite; A LA-ICPMS study; Geochimica et Cosmochimica Acta, v. 73, p. 4761–4791.

Crusius, J., Calvert, S., Pedersen, T., and Sage, D., 1996. Rhenium and molybdenum enrichments in sediments as indicators of oxic, suboxic and sulfidic conditions of deposition; Earth and Planetary Science Letters, v. 145, p. 65–78.

De Baar, H.J.W., German, C.R., Elderfield, H., and Van Gaans, P., 1988. Rare earth element distributions in anoxic waters of the Cariaco Trench; Geochimica et Cosmochimica Acta, v. 52, p. 1203–1219.

Deditius, A., Utsunomiya, S., Reich, M., Kesler, S., Ewing, R., Hough, R., and Walshe, J.L., 2011. Trace metal nanoparticles in pyrite; Ore Geology Reviews, v. 42, p. 32–46.

Elderfield, H. and Greaves, M. J., 1982. The rare earth elements in seawater; Nature, v. 296, p. 214–218.

Falkner, K.K., Klinkhammer, G.P., Bowers, T.S., Todd, J.F., Lewis, B.L., Landing, W.M., and Edmond, J.M., 1993. The behavior of barium in anoxic marine waters; Geochimica et Cosmochimica Acta, v. 57, p. 537–554.

Flegal, A.R. and Patterson, C.C., 1985. Thallium concentrations in seawater; Marine Chemistry, v. 15, p. 327–331.

Frei, R., Gaucher, C., Poulton, S.W., and Canfield, D.E., 2009. Fluctuations in Precambrian atmospheric oxygenation recorded by chromium isotopes; Nature, v. 461, p. 250–254.

Gadd, M.G., 2015. The world-class Howard's Pass District of SEDEX Zn-Pb deposits, Yukon: ambient redox conditions and timing of mineralization revealed by LA-ICP-MS and SIMS, Ph.D. thesis, Queen's University, Kingston, Ontario, 204 p.

Gadd, M.G., Layton-Matthews, D., Peter, J.M., and Paradis, S.J., 2016a. The world-class Howard's Pass SEDEX Zn-Pb district, Selwyn Basin, Yukon. Part I. trace element compositions of pyrite record input of hydrothermal, diagenetic, and metamorphic fluids to mineralization; Mineralium Deposita, v. 51, p. 319–342.

Gadd, M.G., Layton-Matthews, D., and Peter, J.M., 2016b. Non-hydrothermal origin of apatite in SEDEX mineralization and host rocks of the Howard's Pass district, Yukon, Canada; American Mineralogist, v. 101, p. 1061–1071.

Gadd, M.G., Layton-Matthews, D., Peter, J.M., Paradis, S., and Jonasson, I.R., 2017. The world-class Howard's Pass SEDEX Zn-Pb district, Selwyn Basin, Yukon. Part II. The roles of thermochemical and bacteria sulphate reduction in metal fixation; Mineralium Deposita, v.52, p. 405–419.

George, L., Cook, N., Ciobanu, C., and Wade, B., 2015. Trace and minor elements in galena: A reconnaissance LA-ICP-MS study; American Mineralogist, v. 100, p. 548–569.

Goodfellow, W.D., 2004. Geology, genesis and exploration of SEDEX deposits, with emphasis on the Selwyn Basin, Canada; in Sediment-hosted lead-zinc sulphide deposits, (ed.) M. Deb and W.D. Goodfellow; Narosa, New Delhi, p. 24–99.

Goodfellow, W.D., 2007. Base metal metallogeny of the Selwyn Basin, Canada; in Mineral Resources of Canada: A Synthesis of Major Deposit-types, District Metallogeny, the Evolution of Geological Provinces, and Exploration Methods, (ed.) W.D. Goodfellow; Mineral Deposits Division, Geological Association of Canada, Special Publication 5, p. 553–579.

Goodfellow, W.D. and Jonasson, I.R., 1984. Ocean stagnation and ventilation defined by δ34S values in pyrite and barite, Selwyn Basin, Yukon; Geology, v. 12, p. 583–586.

Goodfellow, W.D. and Jonasson, I.R., 1986. Environment of formation of the Howards Pass (XY) Zn-Pb deposit, Selwyn Basin, Yukon; in Mineral Deposits of Northern Cordillera, (ed.) J.A. Morin; Canadian Institute of Mining and Metallurgy, p.19–50.

Goodfellow, W.D. and Lydon, J.W., 2007. Sedimentary-exhalative (SEDEX) deposits; in Mineral Deposits of Canada: A Synthesis of Major Deposit-types, District Metallogeny, the Evolution of Geological Provinces, and Exploration Methods, (ed.) W.D. Goodfellow; Mineral Deposits Division, Geological Association of Canada Special Publication 5, p. 163–183.

Gordey, S.P. and Anderson, R.G., 1993. Evolution of the Northern Cordillera Miogeocline, Nahanni map area (105I), Yukon and Northwest Territories; Geological Survey of Canada Memoir 428, 214 p.

Graham, G.E., Kelley, K.D., Slack, J.F., and Koenig, A.E.,

2009. Trace elements in Zn-Pb-Ag deposits and related stream sediments, Brooks Range Alaska, with implications for Tl as a pathfinder element; Geochemistry: Exploration, Environment, Analysis, v. 9, p. 19–37.

Griffith, E.M. and Paytan, A., 2012. Barite in the ocean – Occurrence, geochemistry, and palaeoceanographic applications; Sedimentology, v. 59, p. 1–19.

Heinrichs, H., Schulz-Dobrick, B., and Wedepohl, K.H., 1980. Terrestrial geochemistry of Cd, Bi, Tl, Pb, Zn and Rb; Geochimica Cosmochimica Acta, v. 44, p. 1519–1533.

Hettmann, K., Kreissig, K., Rehkämper, M., Wenzel, T., Mertz-Kraus, R., and Markl, G., 2014. Thallium geochemistry in the metamorphic Lengenbach sulfide deposit, Switzerland: Thallium-isotope fractionation in a sulfide melt; American Mineralogist, v. 99, p. 793–803.

Iskowitz, J., Lee, J., and Zeitlin, H., 1982. Determination of thallium in deep-sea ferromanganese nodules; Marine Mining, v. 3, p. 285–295.

Jacobson, A.R., McBride, M.B., Baveye, P., and Steenhuis, T.S., 2005. Environmental factors determining the trace-level sorption of silver and thallium to soils; Science of the Total Environment, v. 345, p. 191–205.

Jones, B. and Manning, D.A.C., 1994. Comparison of geochemical indices used for the interpretation of palaeoredox conditions in ancient mudstones; Chemical Geology, v. 111, p. 111–129.

Kaplan, D.I. and Mattigod, S.V., 1998, Aqueous geochemistry of thallium; in Thallium in the Environment, (ed.) J. Nriagu; New York, New York, John Wiley and Sons, p. 15–29.

Kersten, M., Xiao, T., Kreissig, K., Brett, A., Coles, B.J., and Rehkämper, M., 2014. Tracing anthropogenic thallium in soil using stable isotope compositions; Environmental Science and Technology, v. 48, p. 9030–9036.

Kirkham, G., Dunning, J., and Schleiss, W., 2012. Update for Don deposit mineral resource estimate, Howard's Pass property, eastern Yukon; Selwyn Resources Ltd., NI 43–101 Technical Report. 145 p.

Large, R.R. and McGoldrick, P.J., 1998. Lithogeochemical halos and geochemical vectors to stratiform sediment hosted Zn-Pb-Ag deposits; 1, Lady Loretta Deposit, Queensland; Journal of Geochemical Exploration, v. 63, p. 37–56.

Lee, A.G., 1971. The Chemistry of Thallium; Amsterdam, Elsevier, 336 p.

Liguori, B.T.P., de Almeida, M.G., and de Rezende, C.E., 2016. Barium and its importance as an indicator of (paleo) productivity; Anais da Academia Brasileira de Ciências (Annals of the Brazilian Academy of Sciences), v. 88, p. 2093–2103.

Liu, M., 2017. Residence of thallium in the hanging wall of the Howard's Pass district SEDEX deposits: B.Sc. thesis, Queen's University, Kingston, Ontario, 47 p.

Lydon, J.W., 2015. The leachability of metals from sedimen-

tary rocks; *in* Targeted Geoscience Initiative 4: Sediment-hosted Zn-Pb Deposits: Processes and Implications for Exploration, (ed.) S.J. Paradis; Geological Survey of Canada Open File 7838: Ottawa, Ontario, p. 11–42.

Magnall, J.M., Stern, R., Gleeson, S.A., and Paradis, S., 2015, Widespread euxinic conditions are not a prerequisite for sediment-hosted base metal (Pb-Zn-Ba) mineralization at Macmillan Pass, Yukon; *in* Targeted Geoscience Initiative 4: Sediment-hosted Zn-Pb Deposits: Processes and Implications for Exploration, (ed.) S.J. Paradis; Geological Survey of Canada Open File 7838: Ottawa, Ontario, p. 43–57.

Magnall, J.M., Gleeson, S.A., Stern, R.A., Newton, R.J., Poulton, S.W., and Paradis, S., 2016. Open system sulphate reduction in a diagenetic environment – Isotopic analysis of barite (δ^{34}S and δ^{18}O) and pyrite (δ^{34}S) from the Tom and Jason Late Devonian Zn–Pb–Ba deposits, Selwyn Basin, Canada; Geochimica et Cosmochimica Acta, v. 180, p. 46–163.

Matthews, A.D. and Riley, J.P., 1970. The occurrence of thallium in sea water and marine sediments; Chemical Geology, v. 6, p. 149–152.

May, W.E. and Watters, R.L., 2004. National Institute of Standards & Technology Certificate of Analysis Standard Reference Material 997 Isotopic Standard for Thallium, 2 p. <https://nemo.nist.gov/srmors/certificates/997.pdf> [accessed November 27, 2017]

Morganti, J.M. 1979. The geology and ore deposits of the Howards Pass area, Yukon and Northwest Territories: The origin of basal sedimentary stratiform sulphide deposits; Ph.D. thesis, University of British Columbia, Vancouver, British Columbia, 351 p.

Nielsen, S.G. and Rehkämper, M., 2011. Thallium isotopes and their application to problems in earth and environmental science; *in* Handbook of Environmental Isotope Geochemistry, (ed.) M. Baskaran; Advances in Isotope Geochemistry: Berlin, Germany, Springer-Verlag, p. 247–269.

Nielsen, S.G., Rehkämper, M., Baker, J. and Halliday, A.N., 2004. The precise and accurate determination of thallium isotope compositions and concentrations for water samples by MC-ICPMS; Chemical Geology, v. 204, p. 109–124.

Nielsen, S.G., Rehkämper, M., Porcelli, D., Andersson, P., Halliday, A.N., Swarzenski, P.W., Latkoczy, C., and Günther, D., 2005. Thallium isotope composition of the upper continental crust and rivers – An investigation of the continental sources of dissolved marine thallium; Geochimica et Cosmochimica Acta, v. 19, p. 2007–2019.

Nielsen, S.G., Rehkämper, M., Norman, M.D., Halliday, A.N., and Harrison, D., 2006a. Thallium isotopic evidence for ferromanganese sediments in the mantle source of Hawaiian basalts; Nature, v. 439, p. 314–317.

Nielsen, S.G., Rehkämper, M., Teagle, D.A.H., Butterfield, D., Alt, J.C., and Halliday, A.N., 2006b. Hydrothermal fluid fluxes calculated from the isotopic mass balance of thallium in the ocean crust; Earth and Planetary Science Letters, v.

251, p. 120–133.

Nielsen, S.G., Rehkämper, M., Brandon, A.D., Norman, M.D., Turner, S., and O'Reilly, S.Y., 2007. Thallium isotopes in Iceland and Azores lavas – Implications for the role of altered crust and mantle geochemistry; Earth and Planetary Science Letters, v. 264, p. 332–345.

Nielsen, S.G., Goff, M., Hesselbo, S.P., Jenkyns, H.C., Larowe, D.E., and Lee, C.-T.A., 2011. Thallium isotopes in early diagenetic pyrite – A paleoredox proxy?; Geochimica et Cosmochimica Acta, v. 75, p. 6690–6704.

Nielsen, S.G., Rehkämper, M., and Prytulak, J., 2017. Investigation and application of thallium isotope fractionation; Reviews in Mineralogy and Geochemistry, v. 82, p. 759–798.

Norford, B. and Orchard, M., 1985. Early Silurian age of rocks hosting lead-zinc mineralization at Howards Pass, Yukon Territory and District of Mackenzie; Geological Survey of Canada Paper 83-18, 35 p.

Ostrander, C.M., Owens, J.D., and Nielsen, S.G., 2017. Constraining the rate of oceanic deoxygenation leading up to a Cretaceous Oceanic Anoxic Event (OAE-2: ≈94 Ma); Science Advances, v. 3, e1701020, 5 p.

Owens, J.D., Nielsen, S.G., Horner, T.J., Ostrander, C.M., and Peterson, L.C., 2017. Thallium-isotopic compositions of euxinic sediments as a proxy for global manganese-oxide burial; Geochimica Cosmochimica Acta, v. 213, p. 291–307.

Peter, J.M., 2003. Ancient iron-rich metalliferous sediments (iron formations): their genesis and use in the exploration for stratiform base metal sulphide deposits, with examples from the Bathurst Mining Camp; *in* Geochemistry of Sediments and Sedimentary Rocks: Secular Evolutionary Considerations to Mineral Deposit-Forming Environments, (ed.) D.R. Lentz; Geotext v. 4: St. John's, Geological Association of Canada, p. 145–173.

Peter, J.M., Layton-Matthews, D., Gadd, M.G., Gill, S., Baker, S., Plett, S., and Paradis, S.J., 2015. Application of Visible-Near Infrared and Short Wave Infrared Spectroscopy to SEDEX Deposit Exploration in the Selwyn Basin, Yukon; *in* Targeted Geoscience Initiative 4: Sediment-hosted Zn-Pb (±Ag, ±Ba) Deposits: Processes and Implications for Exploration, (ed.) S.J. Paradis; Geological Survey of Canada Open File, v. 7838, p. 152–172.

Peter, J.M. and Goodfellow, W.D., 1996. Mineralogy, bulk and rare earth element geochemistry of massive sulphide-associated hydrothermal sediments of the Brunswick Horizon, Bathurst Mining Camp, New Brunswick; Canadian Journal of Earth Sciences, v. 33, p. 252–283.

Prytulak, J., Nielsen, S.G., Plank, T., Barker, M., and Elliott, T., 2013. Assessing the utility of thallium and thallium isotopes for tracing subduction zone inputs to the Mariana arc; Chemical Geology, v. 345, p. 139–149.

Raiswell, R., Buckley, F., Berner, R.A., and Anderson, T.F., 1988. Degree of pyritization of iron as a paleoenvironmental indicator of bottom-water oxygenation; Journal of Sedi-

mentary Petrology, v. 58, p. 812–819.

Rehkämper, M. and Halliday, A.N., 1999. The precise measurement of Tl isotopic compositions by MC-ICPMS: Application to the analysis of geological materials and meteorites; Geochimica et Cosmochimica Acta, v. 63, p. 935–944.

Rehkämper, M. and Nielsen, S.G., 2004. The mass balance of dissolved thallium in the oceans; Marine Chemistry, v. 85, p. 125–139.

Rehkämper, M., Frank, M., Hein, J.R., Porcelli, D., Halliday, A.N., Ingri, J., and Liebetrau, V., 2002. Thallium isotope variations in seawater and hydrogenetic, diagenetic and hydrothermal ferromanganese deposits; Earth and Planetary Science Letters, v. 197, p. 65–81.

Rehkämper, M., Frank, M., Hein, J.R., and Halliday, A.N., 2004. Cenozoic marine geochemistry of thallium deduced from isotopic studies of ferromanganese crusts and pelagic sediments; Earth and Planetary Science Letters, v. 219, p. 77–91.

Ross, D.J.K. and Bustin, R.M., 2009. Investigating the use of sedimentary geochemical proxies for paleoenvironment interpretation of thermally mature organic-rich strata: examples from the Devonian-Mississippian shales, western Canada sedimentary basin; Chemical Geology, v. 260, p. 1–19.

Saez, R., Moreno, C., González, F., and Amodódovar, G., 2011. Black shales and massive sulfide deposits: causal or casual relationships? Insights from Rammelsberg, Tharsis, and Draa Sfar; Mineralium Deposita, v. 46, p. 585–614.

Schauble, E.A., 2007. Role of nuclear volume in driving equilibrium stable isotope fractionation of mercury, thallium, and other very heavy elements; Geochimica et Cosmochimica Acta, v. 71, p. 2170–2189.

Scott, C. and Lyons, T., 2012. Contrasting molybdenum cycling and isotopic properties in euxinic versus non-euxinic sediments and sedimentary rocks: refining the paleoproxies; Chemical Geology, v. 324-325, p. 9–27.

Scott, C., Slack, J.F., and Kelley, K., 2013. The origin of vanadium hyper-enriched black shales; Geological Society of America Abstracts and Program, v. 45, p. 427.

Slack, J.F., Falck, H., Kelley, K.D., and Xue, G.G., 2017. Geochemistry of host rocks in the Howards Pass district, Yukon-Northwest Territories, Canada: implications for sedimentary environments of Zn-Pb and phosphate mineralization; Mineralium Deposita, v. 52, p. 565–593.

Taylor, B. and Beaudoin, G., 2000. Sulphur isotope stratigraphy of the Sullivan Pb-Zn-Ag deposit, B.C.: Evidence for hydrothermal sulphur, and bacterial and thermochemical sulphate reduction; *in* The Geological Environment of the Sullivan deposit, British Columbia, (ed.) J. Lydon, T. Höy, J. Slack and M. Knapp; Mineral Deposits Division, Geological Association of Canada, p. 696–719.

Taylor, S.R. and McLennan, S.M., 1985. The Continental Crust: Its Composition and Evolution; Oxford, Blackwell Scientific Publications, 312 p.

Tribovillard, N., Algeo, T., Lyons, T., and Riboulleau, A., 2006. Trace metals as paleoredox and paleoproductivity proxies: An update; Chemical Geology, v. 232, p. 12–32.

Turner, R.J.W., Madrid, R.J., and Miller, E.L., 1989. Roberts Mountain Allochthon: Stratigraphic comparison with lower Paleozoic outer continental margin strata of the northern Canadian Cordillera; Geology, v. 17, p. 341–344.

Wade, K. and Banister, A.J., 1973. The Chemistry of Aluminum, Gallium, Indium, and Thallium, Pergamon Texts in Inorganic Chemistry, v. 12; New York, NY, Pergamon Press, 214 p.

Wickham, K., 2014. Thallium isotope implications for the metalliferous source of Carlin-type deposits in northern Nevada; M.Sc. thesis, University of Nevada, Reno, Nevada, 49 p.

Wright, J., Schrader, H., and Holser, W.T., 1987. Paleoredox variations in ancient oceans recorded by rare earth elements in fossil apatite; Geochimica et Cosmochimica Acta, v. 51, p. 631–644.

Yang, S. and Liu, Y., 2015. Nuclear volume effects in equilibrium stable isotope fractionations of mercury, thallium and lead; Scientific Reports, v. 5, paper 12626, 12 p.

Yukon Geological Survey, 2014. Yukon Minfile 105I 037; Yukon Geological Survey. <http://data.geology.gov.yk.ca/Occurrence/DownloadOccurrenceDirect/13393> [accessed December 18, 2017]

Field observations, mineralogy and geochemistry of Middle Devonian Ni-Zn-Mo-PGE hyper-enriched black shale deposits, Yukon

M.G. Gadd and J.M. Peter

Geological Survey of Canada, 601 Booth Street, Ottawa, Ontario K1A 0E8

Abstract

Hyper-enriched black shale (HEBS) deposits are a globally significant repository of base, strategic and precious metals. Some of the best examples of this deposit type are hosted within Devonian shales in northern Yukon. Hyper-accumulations of Ni-Zn-Mo-platinum group elements (PGE) occur in a thin (<10 cm) stratiform and stratabound layer that is widespread geographically (10 000s km^2). Despite decades of research, basic questions surrounding the precious metal mineral host(s), age and process(es) responsible for hyper enrichment remain unresolved.

Preliminary laser ablation-inductively coupled plasma-mass spectrometry data for the various base metal sulphide minerals within the HEBS mineralization reveal that vaesite is the principal PGE host (up to 10 ppm Pd, Pt) at the Nick deposit, whereas the fine-grained pyritic matrix hosts PGE (up to 3 ppm Pd and 10 ppm Pt) at the Peel River locality. Conodont biostratigraphy, determined using x-ray microcomputed tomography, gives a Givetian (late Middle Devonian) age that compares well with the regional stratigraphic framework, and is the first ever reported for the HEBS mineralization in Yukon. Finally, recent fieldwork has revealed the occurrence of up to three discrete stacked stratigraphic HEBS layers.

Collectively, these data indicate an ambient paleoenvironment in which highly efficient scavenging of metals and metalloids from seawater operated in tandem with extremely low rates of clastic sedimentation and highly efficient organic matter remineralization. Similar topologies between continental crust-normalized PGE patterns for seawater and HEBS layers support the conclusion that metals and metalloids predominantly originated from ambient seawater.

Introduction

Hyper-enriched black shales (HEBS), also referred to as polymetallic metalliferous shales, are an important global repository for Zn, Ni, Cu, Mo, Se, U, V, ± Cr, Co, Ag, Au, platinum group elements (PGE) and rare earth elements (REE) (Jowitt and Keays, 2011). These deposits are thin (<10 cm) and laterally widespread, covering 10 000s of km^2 (e.g. Cambrian, Yangtze Platform, China; Devonian, Mackenzie Platform, Yukon). Canada hosts some of the best examples globally (e.g. Nick deposit, Yukon; Hulbert et al., 1992) and there is significant potential for the further discovery and development of such deposits. The Nick deposit was discovered in 1981 by Cominco geologists by following up a Geological Survey of Canada stream sediment survey (Garrett et al., 1977; Carne, 1989). The nickel sulphide horizon is very thin (3–10 cm) and discontinuously crops out over a strike length of 100 km (Carne, 1989). This style of mineralization has been recognized in many localities across northern Yukon (Fig. 1). Exploration is currently hindered by a lack of understanding of how these deposits formed. Current genetic models are myriad, including seafloor hydrothermal, ambient seawater/phosphogenesis/high organic productivity, and impact-related (Hulbert et al., 1992; Lehmann et al., 2007; Goodfellow et al., 2010). Basic questions that are being addressed by us for Yukon HEBS deposits include the age and duration of the mineralizing event(s) and the host phase(s) of PGE. The goal of our research is to develop a cogent, internally consistent genetic model for HEBS deposits using robust field observations, together with bulk and micro-analytical geochemical data.

Regional geology

The HEBS deposits are located within Paleozoic basinal strata of the Richardson trough (Fig. 1). This tectonic depression is bound to the east by the Mackenzie platform and to the west by the Yukon Stable Block, which for much of the early Paleozoic was a stable shelf feature (Morrow, 1999). The sedimentary rocks within the Richardson trough are characterized by >100 m-thick succession of fine-grained, carbonaceous siliciclastic rocks of the Late Cambrian to Early Devonian Road River Group (Fig. 2a; Morrow, 1999). The Canol Formation overlies Road River Group sedimentary rocks, and consists of up to approximately 220 m of Middle Devonian to early Late Devonian siliceous carbonaceous shale (Hutchison and Fraser, 2015). The nature of the contact between the Road River Group and overlying Canol Formation has been documented as both conformable and unconformable (Pugh, 1983; Hutchison and Fraser, 2015). A thin (1–10 cm thick) Ni-Zn-PGE-rich HEBS layer at this contact is documented in many localities throughout northern Yukon (Fig. 2). The Late Devonian Imperial Formation, a deep-water shale interbedded with turbiditic sandstones, overlies the Canol Formation (Lane, 2007).
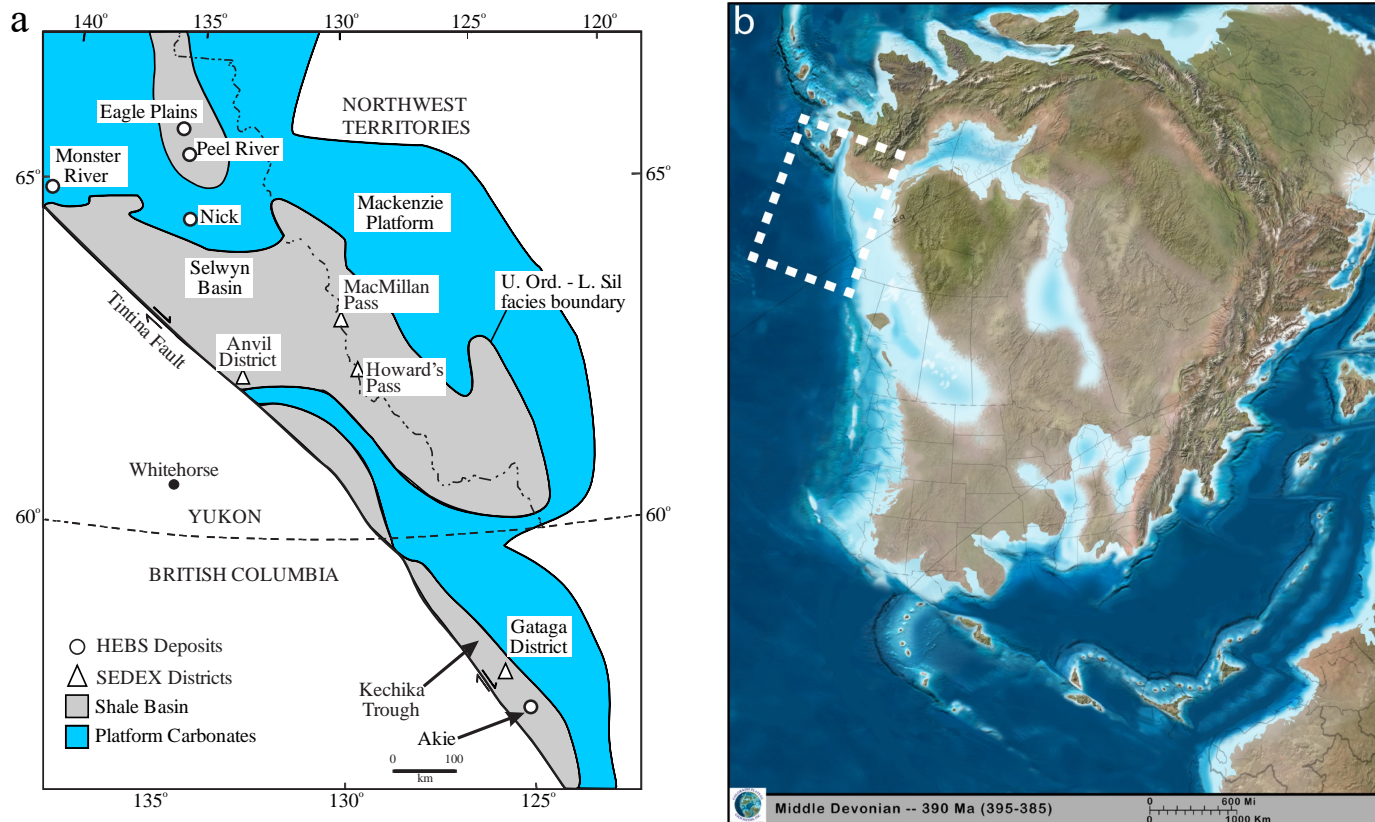
Figure 1. a) Map of ancestral North American passive continental margin displaying locations of key HEBS deposits and SEDEX districts. b) Middle Devonian paleogeographic reconstruction of North America at ca. 390 Ma with Selwyn basin outlined in dashed box (Blakey, 2013).

Stratigraphy

The stratigraphy of each of the HEBS deposits is nearly identical. From the base upward (Fig. 2), a typical section comprises: 1) a 2 to 20 m thick carbonaceous shale with 1 to 1.5 m diameter calcareous concretions termed the "limestone ball member". Shale beds drape around concretions, and bedding is preserved within some concretions; 2) an up to 120 cm thick siliceous, carbonaceous shales with centimetre scale barite and calcite nodules; 3) a 1 to 10 cm thick stratabound, stratiform semi-massive Ni-Zn-Fe-sulphide HEBS layer; 4) carbonaceous, siliceous shale to black-cherty shale that is in sharp contact with the underlying HEBS mineralization.

Previously published data (Hulbert et al., 1992; Goodfellow et al., 2010) for the HEBS layers across northern Yukon indicate striking enrichments in a broad suite of elements relative to the enclosing sedimentary rocks (Fig. 3). The data are summarized in Table 1. The HEBS mineralization was previously thought to occur as a single (discrete) layer within the host stratigraphic succession (Hulbert et al., 1992; Goodfellow et al., 2010). However, in 2017, we identified three discrete (i.e. not structurally repeated), stacked HEBS layers at the north bank of Peel River and two discrete HEBS layers at the south bank locality (about 5 km to the east). Only one nickeliferous

horizon was identified at the Eagle Plains showing (referred to as the Rich showing by Dumala, 2007), but at least two discrete 1 cm thick pyritic (not Ni-bearing, as revealed by field-portable x-ray fluorescence) massive sulphide layers underlie this horizon. Moreover, 1.96 m (true stratigraphic thickness) of mineralization containing 1.31 weight % Ni and approximately 500 ppb Au + Pt + Pd was intersected in drill core by Southampton Ventures at this locality (Dumala, 2007). This thick accumulation of HEBS mineralization was not encountered in the field, and other diamond-drill holes in the area encountered only centimetre scale thicknesses of HEBS mineralization at the Eagle Plains showing (Dumala, 2007), similar to what we documented in outcrop.

Methods

Laser ablation-inductively coupled plasma-mass spectrometry (LA-ICP-MS) element concentration mapping was conducted at the Geological Survey of Canada. The system consists of a Teledyne Photon Machines Analyte G2 excimer laser ablation system ($\lambda = 193$ nm) with HelEx ablation cell and an Agilent 7700x ICP-MS equipped with a second rotary vacuum pump that improves instrument sensitivity across the mass range by 2 to 3 times (Cabri and Jackson, 2011). Collision cell technology, with He as the collision gas, was used to reduce
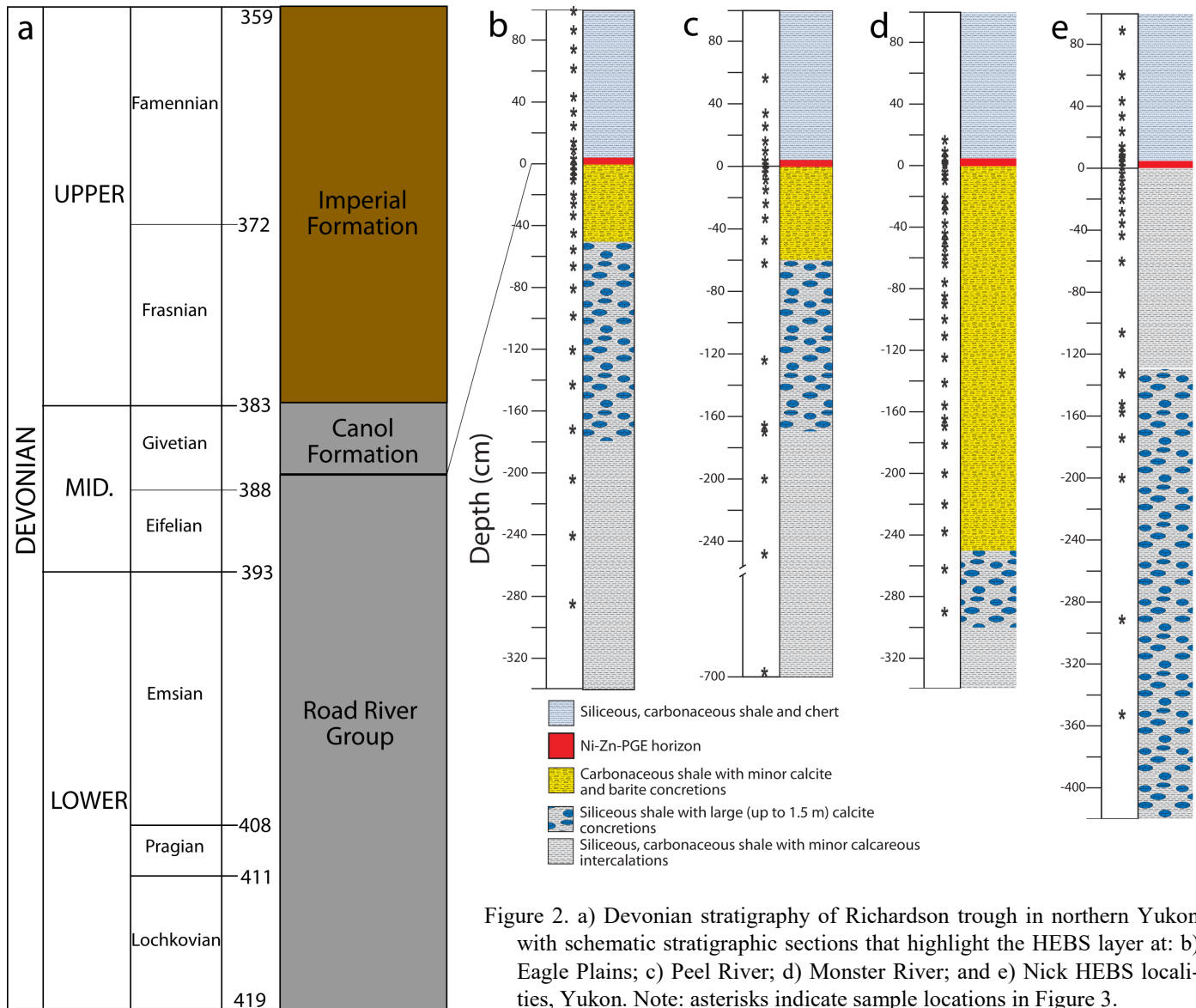
Figure 2. a) Devonian stratigraphy of Richardson trough in northern Yukon with schematic stratigraphic sections that highlight the HEBS layer at: b) Eagle Plains; c) Peel River; d) Monster River; and e) Nick HEBS localities, Yukon. Note: asterisks indicate sample locations in Figure 3.

transition metal argide interferences on the light PGE (Ru, Rh and Pd).

Element mapping was accomplished by sampling the target mapping areas utilizing multiple parallel line scans. Each line was rapidly pre-ablated to remove surface contamination. USGS doped basaltic glass GSE-1G (Guillong et al., 2005), doped synthetic pyrrhotite reference material Po726 (Sylvester et al., 2005), and National Mineral Collection calcite were used for standardization. These standards were analyzed every 20 lines of sample analysis. Details of the operating parameters are given in Table 2.

Mineralogy and mineral chemistry

The mineralogy among the different HEBS localities studied is relatively uniform. Broadly, the sulphide mineralogy comprises pyrite, nickel-sulphides—millerite (NiS), vaesite (NiS_2) and gersdorffite (NiAsS)—and sphalerite, whereas non-sulphide minerals are predominantly quartz, barite, apatite, pyrobitumen and trace to minor hyalophane (Ba-K feldspar) and K feldspar (Table 3). The mineralization is about 60% sulphide minerals and 40% non-sulphide gangue minerals (Hulbert et al., 1992). Vaesite is the main nickel sulphide mineral at Nick, whereas millerite predominates at the Peel River, Monster River and Eagle Plains localities.

At the Nick deposit, vaesite is anhedral and forms encrustations on and is interstitial to pyrite (Fig. 4a, b). Electron probe microanalysis (EPMA) indicates that the average (n = 14) major and minor element composition of vaesite is 44.8 ± 1.3 weight % Ni, 50.1 ± 0.6 weight % S and 1.5 ± 0.6 weight % Se, <0.1 to 0.95 weight % As, 0.6 to 1.8 weight % Fe, <0.1 to 0.26 weight % Cu, and 0.15 to 0.26 weight % Tl. Millerite at the
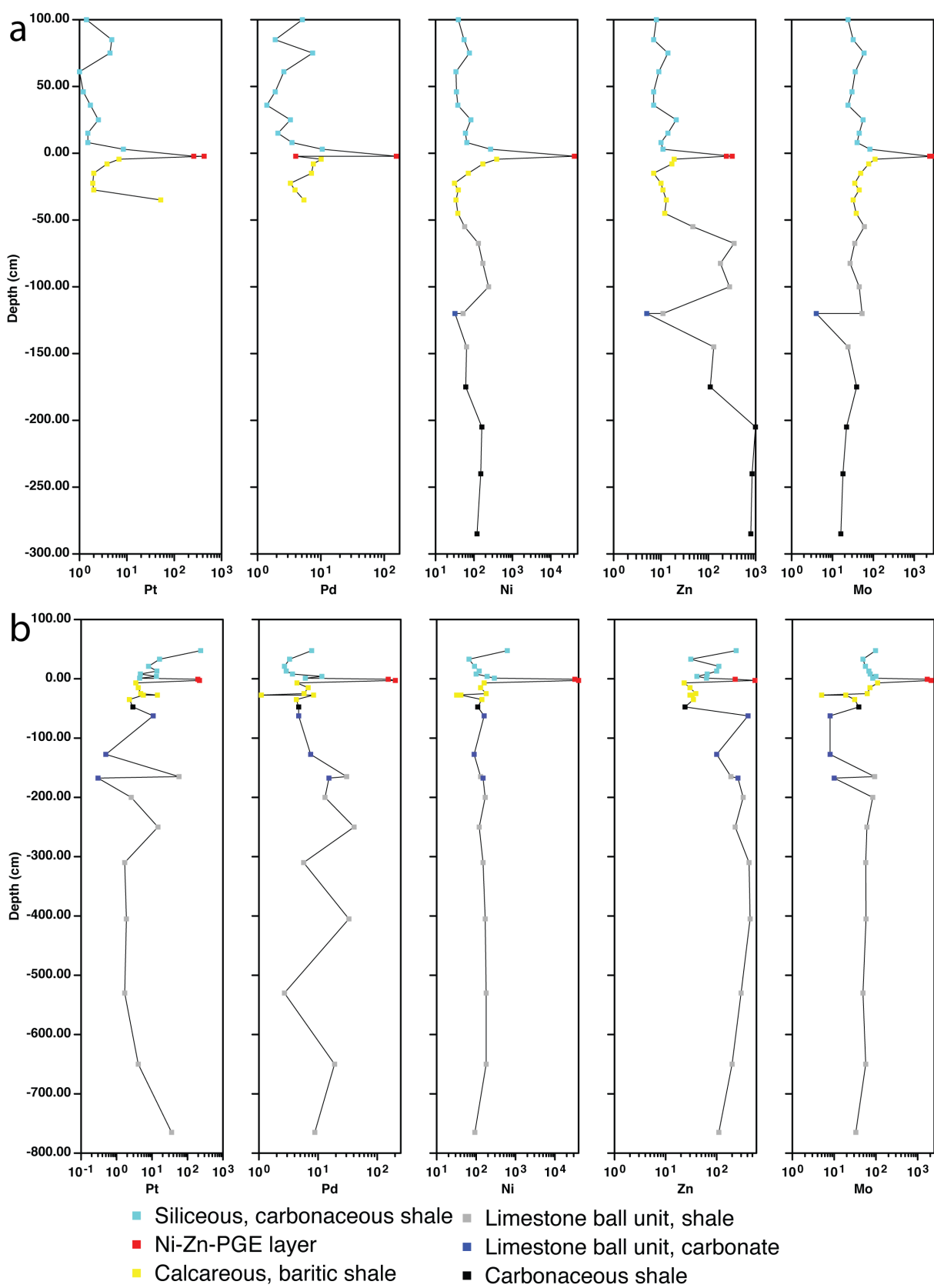
Figure 3. Geochemical profiles of stratigraphic sections at: a) Eagle Plains; and b) Peel River. Note that Pt and Pd are ppb and Ni, Zn and Mo are ppm.

Table 1. Compositional data for HEBS mineralization in northern Yukon

Locality	Fe (wt.%)	S (wt.%)	Os (ppb)	Ir (ppb)	Ru (ppb)	Rh (ppb)	Pt (ppb)	Pd (ppb)	Au (ppb)	Re (ppb)	Ni (ppm)	V (ppm)	Cr (ppm)
Peel River, north bank[1]	14.06	22.20	<2	1.10	<5	4.10	254.0	120.00	68.50	22700	70000	5	210
Peel River, north bank[1]	12.17	19.20	<2	0.90	7.00	6.10	185.0	88.00	37.60	10200	45000	5	60
Peel River, south bank[1]	18.26	23.60	<2	1.20	2.50	3.70	196.0	153.00	46.80	20800	32000	5	42
Peel River, south bank[1,2]	15.04	21.90	<2	1.10	2.50	9.00	218.0	202.00	2.80	25800	40000	450	42
Eagle Plains[1,2]	15.95	23.70	<2	0.92	1.80	9.30	259.0	155.00	66.50	21200	41000	5	56
Eagle Plains[1]	20.98	28.90	<2	0.90	1.60	7.10	429.0	4.00	21.90	13500	41000	5	53
Monster River[1]	16.44	21.70	<2	2.40	6.00	3.20	322.0	107.00	65.40	10300	33000	5	98
Nick deposit (avg. n=8)[2,3]	19.68	27.91	38.5	1.85	NA	3.38	410.0	214.00	86.00	25875	55375	601	160

	Co (ppm)	Cu (ppm)	Zn (ppm)	As (ppm)	Se (ppm)	Mo (ppm)	Ag (ppm)	Cd (ppm)	Sb (ppm)	Hg (ppb)	Tl (ppm)	Pb (ppm)
Peel River, north bank[1]	330	480	23000	10680	4513	2500	3.70	23.00	348.3	5345	310.0	12
Peel River, north bank[1]	130	380	6900	3893	1260	1800	8.00	54.00	124.6	430	170.0	58
Peel River, south bank[1]	80	160	230	2910	1600	1700	1.80	3.20	67.2	65	110.0	12
Peel River, south bank[1,2]	78	89	560	2882	2100	2100	1.80	5.20	62.3	45	200.0	12
Eagle Plains[1,2]	89	120	320	2863	2340	2400	2.10	4.30	116.0	1020	180.0	35
Eagle Plains[1]	97	140	240	4161	1421	3000	2.00	4.70	125.0	1210	240.0	35
Monster River[1]	240	300	5100	3370	1871	600	6.90	50.00	230.2	210	190.0	41
Nick deposit (avg. n=8)[2,3]	264	319	7325	3102	1333	2208	4.00	61.00	66.0	NA	NA	82

[1]Goodfellow et al. (2010); [2]Data plotted in Fig. 8; [3]Hulbert et al. (1992); NA: Not analyzed

Table 2. LA-ICP-MS analytical settings

LA

Model	Teledyne Photon Machines Analyte G2 Excimer
Wavelength	193 nm
Pulse duration	4 ns
Repetition rate	10 Hz
Fluence	5.45 J/cm^2
Scan mode	Line
Spot size	25 - 50 μm
Mapping area	2 mm x 5 mm
Pre-ablation scan speed	50 - 83 μm/s
Flushing after pre-ablation	40 s
Mapping scan speed	8 - 17 μm/s
Pause between scans	50 s
Gas blank data acquisition time	20 s per line
He carrier gas flow rate (into HelEx sample cell base)	0.6 L/min
He carrier gas flow rate (into HelEx cup)	0.4 L/min

Calibration Standards

	GSE-1G - doped synthetic basalt glass[1]
	Po726 - doped synthetic pyrrhotite (S, PGE + Au)[2]
	Calcite - NMC calcite mineral (C)

ICP-MS

Model	Agilent 7700x with additional interface rotary pump
Forward power	1550 kW
Shield torch	Used
Sampling depth	6.5 mm
Make up Ar gas flow rate	1.05 L/min
He collision gas flow rate	2.0 mL/min
ThO$^+$/Th$^+$	<0.2%
Data acquisition protocol	Time Resolved Analysis
Scanning mode	Peak hopping, 1 point per peak
Isotopes determined	^{12}C, ^{23}Na, ^{25}Mg, ^{27}Al, ^{29}Si, ^{31}P, ^{34}S, ^{39}K, ^{42}Ca, ^{51}V, ^{53}Cr, ^{55}Mn, ^{57}Fe, ^{59}Co, ^{60}Ni, ^{65}Cu, ^{66}Zn, ^{75}As, ^{77}Se, ^{89}Y, ^{95}Mo, ^{99}Ru, ^{101}Ru, ^{103}Rh, ^{105}Pd, ^{108}Pd, ^{109}Ag, ^{111}Cd, ^{115}In, ^{118}Sn, ^{121}Sb, ^{125}Te, ^{137}Ba, ^{139}La, ^{140}Ce, ^{141}Pr, ^{173}Yb, ^{177}Hf, ^{181}Ta, ^{185}Re, ^{189}Os, ^{193}Ir, ^{195}Pt, ^{197}Au, ^{205}Tl, ^{206}Pb, ^{207}Pb, ^{208}Pb, ^{232}Th, ^{238}U
Dwell time per isotope	2-3 ms (majors), 4-5 ms (most traces), 15 ms (PGE)
Time per reading (mass sweep)	0.375 s

[1]Guilong et al. (2005); [2]Sylvester et al. (2005)

Peel River, Monster River and Eagle Plains HEBS occurrences possesses several morphologies. Most commonly, millerite is subhedral to euhedral and interstitial to pyrite grains and/or euhedral quartz (Fig. 4c, d). Millerite also encrusts pyrite nodules (Fig. 4e) and forms thin, discrete laminae and disseminat-ed clots within bedding (Fig. 4f, g). Electron probe microanalysis data indicate that the major element composition (n = 29) of millerite is 60.5 to 64 weight % Ni, 29.8 to 36.4 weight % S and 0.24 to 9.5 weight % Se; millerite also contains <0.1 to 0.14 weight % As, <0.1 to 2.8 weight % Fe and <0.1 to 0.18 weight % Tl. Gersdorffite is a relatively rare mineral in Yukon HEBS deposits and is most common at the Peel River locality. There, 10 to 20 mm thick veneers of euhedral gersdorffite mantle 50 to 100 mm diameter grains of millerite and/or sphalerite (Fig. 4f). These sulphide minerals are enclosed within minute, enigmatic Ba-K feldspar ellipsoidal structures that may be of biogenic origin. The major element composition of gersdorffite (n = 11) is 34.8 ± 0.5 weight % Ni and 19.4 ± 0.5 weight % S, 43.6 ± 0.6 weight % Ni and 2.1 ± 0.3 weight % Se.

Pyrite in the HEBS layers has varied and complex textures. The textures are similar at all of the occurrences, and include framboids (<0.003 to approximately 0.1 mm in diameter; Fig. 4a-d), minute crystals (0.01 to 0.1 mm; Fig. 4b, d), replacements of organic remains (Fig. 4a) and anhedral masses (Fig. 4b, e, f). Individual grains and masses commonly possess two to three textural varieties, suggesting that pyrite formed during several stages. For the sake of brevity, pyrite EPMA data are presented as framboidal and non-framboidal. The major element composition (n = 23) of framboidal pyrite is homogeneous across the HEBS occurrences, with 45.6 ± 0.4 weight % Fe and 52.8 ± 0.6 weight % S; framboids also contain <0.1 to 0.77 weight % Ni and <0.1 to 0.18 weight % As. The major element composition (n = 24) of non-framboidal pyrite is 44.7 ± 1.12 weight % Fe and 52.7 ± 0.48 weight % S; non-framboidal pyrite also contains <0.1 to 4.5 weight % Ni, <0.1 to 1.41 weight % As and <0.1 to 1.96 weight % Se.

Analyses by LA-ICP-MS reveal that PGE are associated predominantly with nickel sulphide minerals and to a lesser extent with pyrite. The most abundant PGE are Pd and Pt (and Os, to a lesser extent), whereas Ru, Rh and Ir are rare to absent. A salient difference between the Nick deposit and the Peel River, Monster River and Eagle Plains HEBS showings is the deportment of precious metals within the HEBS horizons. At the Nick deposit, LA-ICP-MS data indicate that vaesite is the principal PGE host-mineral, containing up to 10 ppm Pd and 10 ppm Pt (Fig. 5a). The distribution of these metals within vaesite is complex and inhomogeneous. At the Peel River locality, the principal PGE host is very fine-grained sulphidic, carbonaceous matrix material (Fig. 5b). The sulphide minerals within the matrix consist of micron-scale pyrite and millerite

Table 3. Mineral abundances in HEBS mineralization

	Vaesite	Millerite	Gersdorffite	Pyrite	Sphalerite	Barite	Pyrobitumen
Nick deposit	+++	-	+	+++	++	+	++
Peel River	+	+++	++	+++	++	++	++
Eagle Plains	-	+++	+	+++	++	+	+
Monster River	-	+++	+	+++	++	+	+

Major	Minor	Trace	Absent
+++	++	+	-
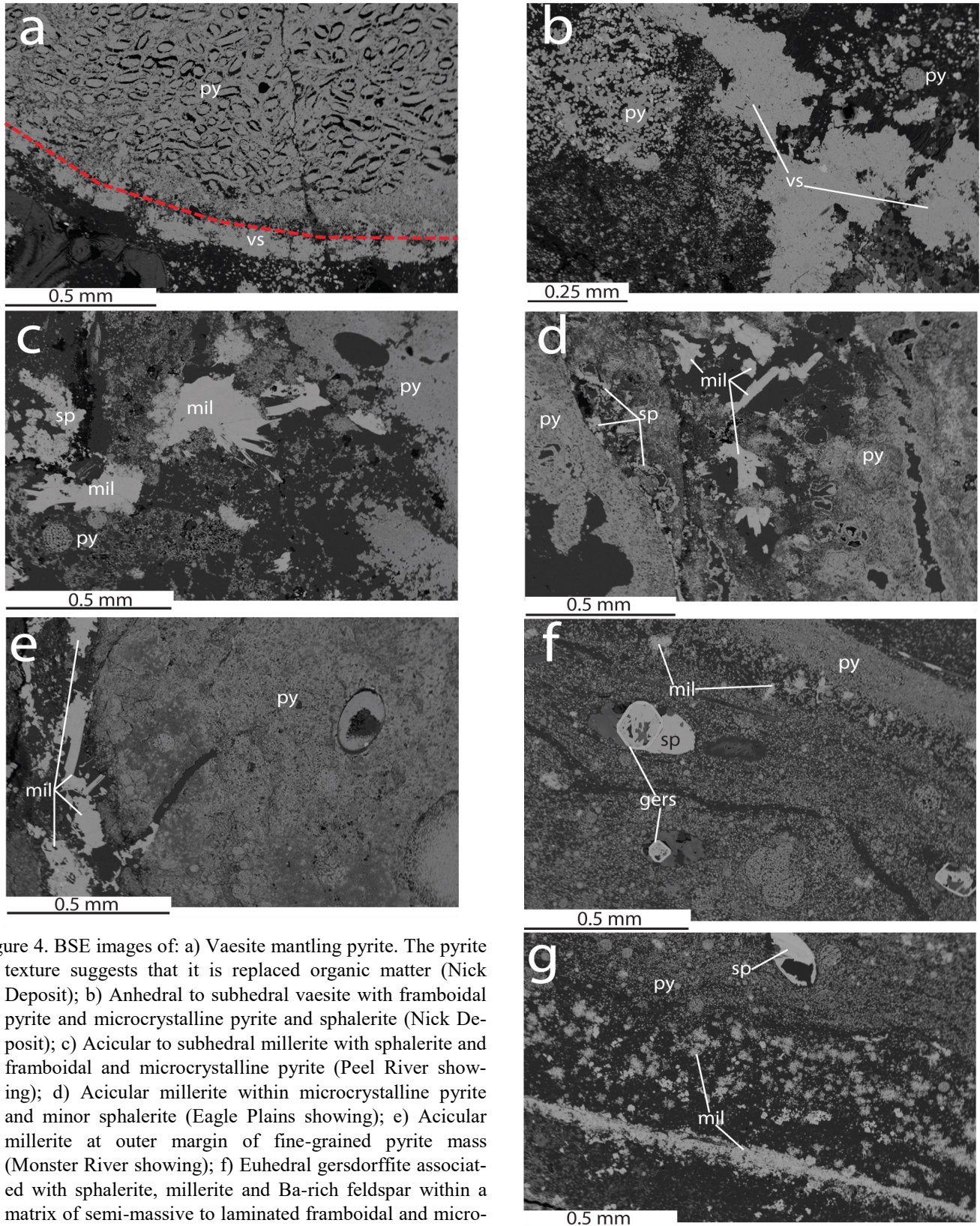
Figure 4. BSE images of: a) Vaesite mantling pyrite. The pyrite texture suggests that it is replaced organic matter (Nick Deposit); b) Anhedral to subhedral vaesite with framboidal pyrite and microcrystalline pyrite and sphalerite (Nick Deposit); c) Acicular to subhedral millerite with sphalerite and framboidal and microcrystalline pyrite (Peel River showing); d) Acicular millerite within microcrystalline pyrite and minor sphalerite (Eagle Plains showing); e) Acicular millerite at outer margin of fine-grained pyrite mass (Monster River showing); f) Euhedral gersdorffite associated with sphalerite, millerite and Ba-rich feldspar within a matrix of semi-massive to laminated framboidal and microcrystalline pyrite (Peel River showing); g) Laminated semi-massive sulphides with discrete, thin millerite lamination below laminated, disseminated millerite and laminated framboidal pyrite (Peel River showing). vs = vaesite; py = pyrite; sp = sphalerite; mil = millerite; gers = gersdorffite.

199
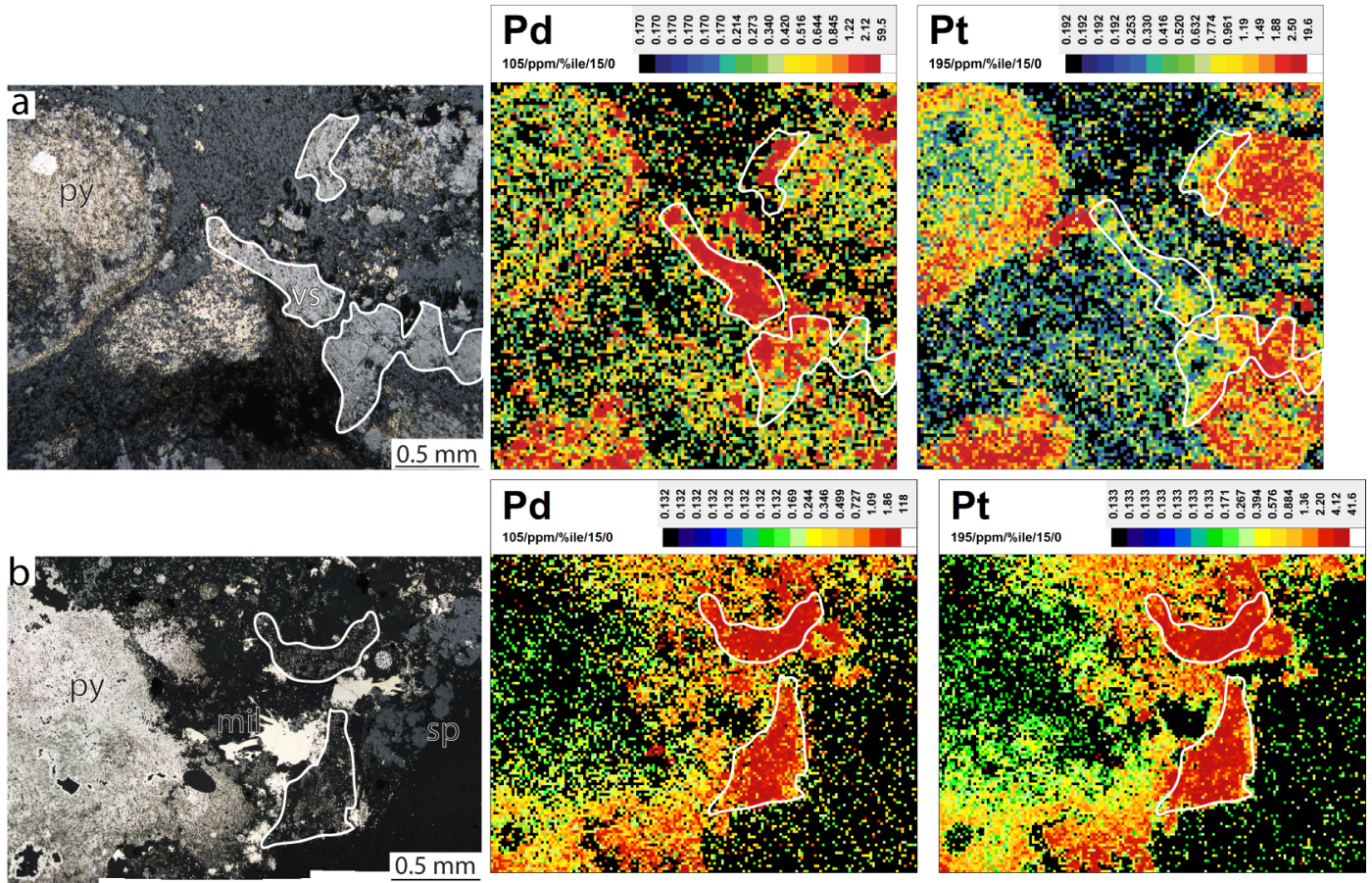
Figure 5. a) Photomicrograph of vaesite-pyrite mineralization from the Nick deposit accompanied by LA-ICP-MS raster maps of Pt and Pd. Note white outlines of relatively coarse vaesite. b) Photomicrograph of millerite-sphalerite-pyrite mineralization from the Peel River HEBS locality accompanied by LA-ICP-MS raster maps of Pt and Pd. Note white outlines of fine-grained sulphidic matrix material, within which Pt and Pd are concentrated. Vs = vaesite; py = pyrite; mil = millerite; sp = sphalerite.

that contain up to 3 ppm Pd and 10 ppm Pt, but it is not clear whether pyrite or millerite hosts the PGE in this sample. Notably, the relatively coarse-grained, inclusion-free millerite is essentially devoid of PGE. PGE are also absent from coarse-grained millerite at the Eagle Plains and Monster River localities. Although it is clear that pyrite at the different HEBS localities contains a minor proportion of Pd and Pt, the absolute abundances of the PGE are very difficult to determine because of the fine-grained, inclusion-rich nature of pyrite and the overall low abundance of PGE within the rocks.

Discussion

Age of mineralization

Determination of the age of the HEBS deposits is a critical first step to elucidating the processes responsible for their formation. Horan et al. (1994) conducted Re-Os isotope analyses of HEBS and host black shales at the Nick deposit. They found that Re-Os-PGE enrichment took place during or shortly after

deposition, and that mineralization occurred between 380 and 367 Ma. Goodfellow et al. (2010) recovered conodont elements from the limestone-ball unit a few meters below HEBS mineralization at Peel River that gave Emsian to Middle Eifelian (Middle Devonian) ages. No conodont elements were recovered from the HEBS deposits themselves. Radiolaria recovered from shale 40 cm above the HEBS layer yield Middle Frasnian to Early Famennian (early Late Devonian) ages (Goodfellow et al., 2010). There is no chronostratigraphic or biostratigraphic information for the other HEBS localities, but they are surmised to be contemporaneous because of their nearly identical stratigraphy and bulk geochemical compositions.

We have identified conodont elements within the uppermost HEBS layer at the north bank of Peel River. Despite multiple attempts by us to extract these conodonts using electrodynamic pulse disaggregation and weak digestion methods, conodonts could not be liberated from the indurated shale matrix. However, microcomputed tomographic analyses of small (<5

mm) rock fragments known to contain conodont elements (partly exposed on a surface), allowed us to generate a voxel model of a conodont element (Fig. 6) from within this HEBS layer. Tentatively, this microfossil is identified as *Polygnathus affinus P. pseudofoliatus* (S. Gouwy, pers. comm. 2017), which would give a Givetian age (387.7–382.7 Ma). This is the first biostratigraphic age reported for any of the HEBS mineralization in Yukon. This age corresponds well with the established stratigraphic framework of the Richardson trough, which indicates a Givetian age for the contact between the Road River Group and Canol Formation sedimentary rocks (Morrow, 1999; Lane, 2007).

Petrified wood in the HEBS mineralization at the Peel River localities was discovered by us during fieldwork there in summer 2017 (Fig. 7a–c). Where present, the petrified wood consists of pyrite and millerite permineralizations (Fig. 7), in which the primary carbonaceous plant material is partially to completely replaced by sulphide minerals. Given the Middle Devonian age of these rocks, it is possible that the tree remains belong to the extinct class Cladoxylopsid. C.M. Berry (pers. comm., 2017) indicates that Figure 7a–c is an isodichotomously branching stem, however additional work is required for a positive identification.

Peter et al. (this vol.) document pyritized plant material in HEBS nickel-zinc mineralization underlying the Cardiac Creek sedimentary exhalative lead-zinc-silver deposit. Similarly, Orberger et al. (2003) identify biogenic remains at the Nick deposit that they describe as hydrothermal vent fauna. However, given that these features are nearly identical to sulphidized plant debris preserved at the Peel River HEBS, it seems likely that such features are in fact petrified wood (Fig. 4a). The discovery, abundance and ubiquity of terrestrially derived petrified wood

macrofossils raises several questions. A major question relates to the relative abundance of these fossils, which are especially common at or near the top of the uppermost HEBS layer at Peel River.

Fraser and Hutchison (2017) present sedimentological, lithogeochemical and isotopic data for the Trail River section. This stratigraphic section, which is about 50 km north of the Peel River sections, comprises the same package of rocks as the Peel River and Eagle Plains (and Nick?) sections, but lacks the associated HEBS mineralization. Despite the absence of HEBS mineralization, the sedimentological (i.e. thin-bedded, very fine-grained, calcareous cement, organic carbon-rich) and lithogeochemical (i.e. relatively high abundances of redox sensitive oxyanions) suggest this is a condensed section (Fraser and Hutchison, 2017). Globally, condensed sections form in response to shoreline transgressions and maximum sea level rise, and are generally considered to represent maximum flooding surfaces (Loutit et al., 1988). Such sections are clastic sediment-starved, resulting in relatively thin successions that represent extended periods of time. Condensed sections accumulate authigenic minerals (e.g. carbonate concretions or phosphorites) and benthic and pelagic fossils because of the lack of clastic sedimentation (Loutit et al., 1988; Haq and Schutter, 2008).

The Givetian was dominated by cyclic, high-frequency sea-level changes that produced abundant condensed sections on a global-scale (Haq and Schutter, 2008). Middle to Late Devonian paleogeographic reconstructions indicate that the Richardson trough (Fig. 1) was bounded to the west by a drowned carbonate shelf (i.e. the Yukon Stable Block) and to the east by the Laurentian continental land mass (Morrow, 1999). Landward excursions of seawater may have flooded deltaic environments that hosted terrestrial flora, and these may have been
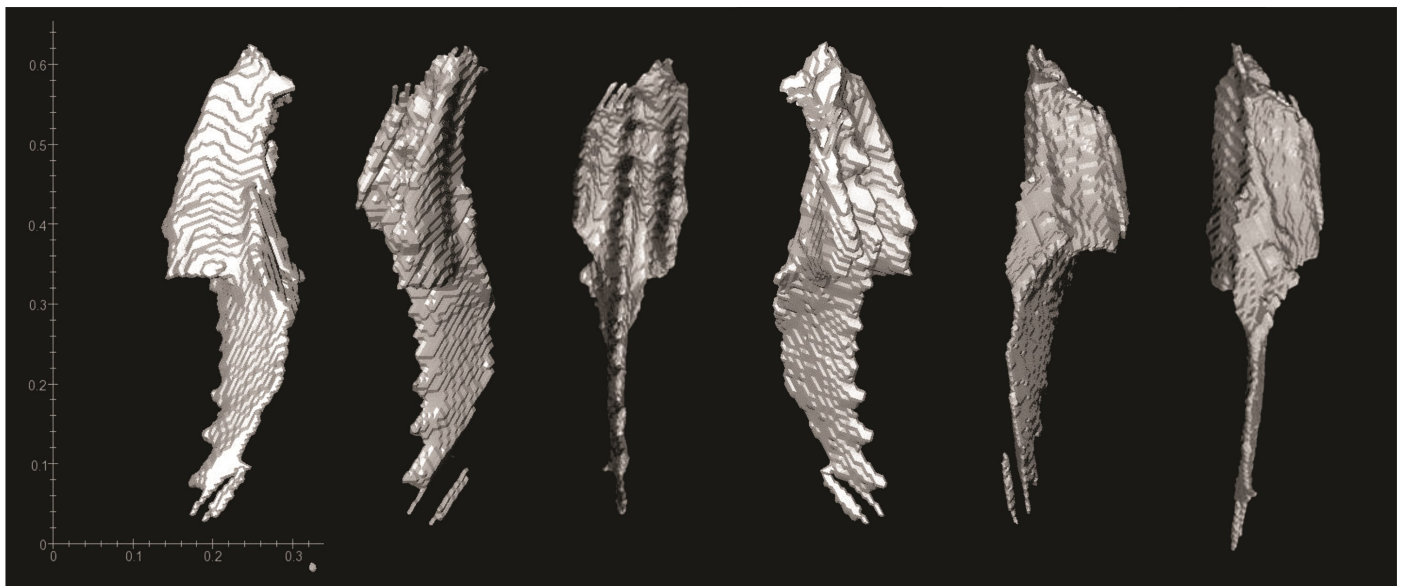

Figure 6. X-ray micro-tomography-generated 3D models of conodont elements within semi-massive sulphides of the HEBS layer at Peel River.
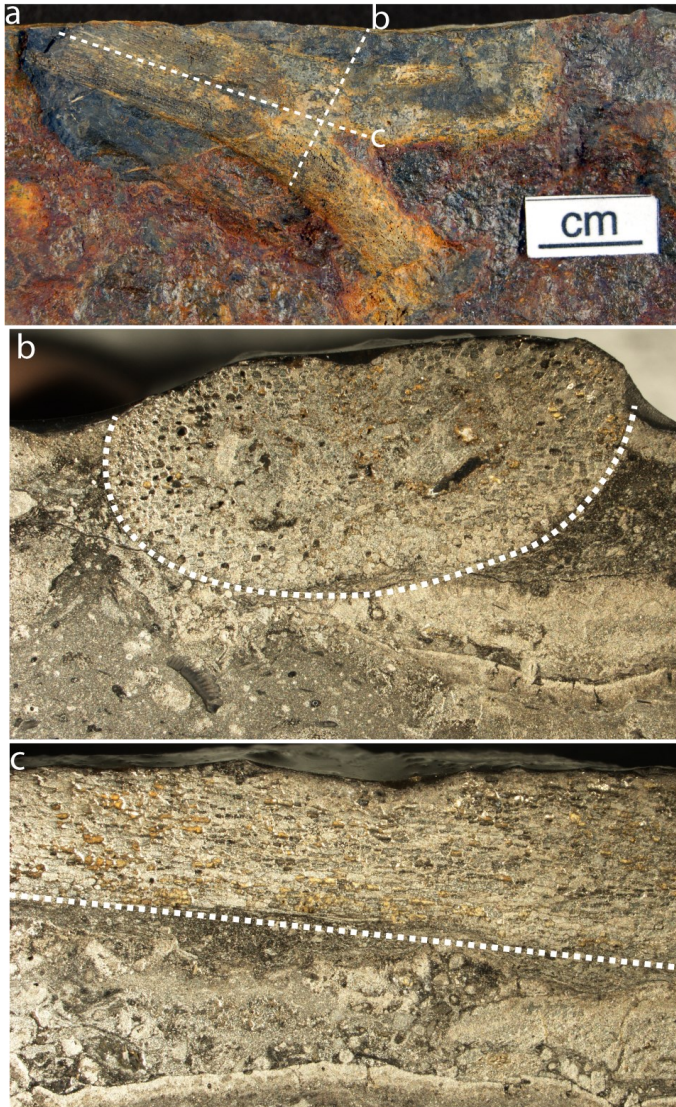
Figure 7. a) Plan view of the top of a bedding plane within which an isodichotomous branch of petrified wood is preserved. b) Radial section and c) longitudinal sections of branch. Note that the original carbonaceous material has been almost completely replaced by pyrite and/or millerite.

washed into, and deposited in, the basin. That the Road River Group-Canol Formation transition is a condensed section (Fraser and Hutchison, 2017), replete with pelagic conodont microfossils and terrestrial floral detritus, supports this interpretation.

Sulphide mineralogy and mineral chemistry

The sulphide mineralogy is relatively simple, but there are myriad textures that are likely the result of long-lived processes that began during sedimentation or shortly thereafter through to shallow(?) burial. Although the mineralogy at the Nick deposit is somewhat different than at the other HEBS localities, the sulphide mineral parageneses are essentially the same. Framboidal pyrite is the earliest paragenetically, and the wide range of framboid diameters (0.003–0.1 mm; Fig. 4b, c, f, g) suggests that it precipitated at and/or below the sediment-water interface (Wilkin et al., 1997; Wignall and Newton, 1998; Bond and Wignall, 2010). Pyrite occurs also as aggregated microcrystals within minute nodules (1–2 mm diameter) and thin layers (1–2 mm thick). The fluids responsible for precipitating sulphides persisted into diagenesis, as evidenced by replacement of original carbonaceous material with pyrite (and nickel sulphides?). Epitaxial vaesite crusts on pyrite indicate that nickel sulphide mineralization at the Nick deposit post-dates pyrite precipitation (Fig. 4a), whereas relatively coarse, subhedral vaesite crystals within the mudstone matrix were unlithified during precipitation (Fig. 4b). The presence of anhedral clots of millerite interstitial to pyrite (Fig. 4c, f, g) imply that millerite precipitated after pyrite. The textural interpretation is somewhat complicated at Peel River, Eagle Plains and Monster River by late remobilization (i.e. euhedral millerite in late, euhedral quartz; Fig. 4c–e).

A notable and perhaps significant difference between the Nick deposit and the other HEBS localities is the residence of PGE. At the Nick deposit, PGE are hosted within vaesite crystals, and, although Pt and Pd are distributed irregularly within single crystals (Fig. 5a), the distribution is relatively homogeneous in vaesite that is either Pt- or Pd-enriched. This suggests that the PGE are lattice-bound within vaesite, rather than within discrete mineral inclusions, and indicates that vaesite and PGE share a common metalliferous fluid source (see further below). Pyrite has substantially lower PGE contents, and it is not clear if these metals reside within the pyrite lattice or within nanometre-scale mineral inclusions. The latter option seems more likely due to the inhomogeneous distribution of Pd and Pt within pyrite (Fig. 5a).

The relationship between millerite and PGE is less clear for the Peel River HEBS. There, PGE are all but absent within the relatively coarse-grained millerite, but are concentrated within the very fine-grained pyritic matrix (Fig. 5b). It is difficult to ascertain exactly which mineral hosts PGE within the fine matrix because the minimum LA-ICP-MS beam resolution (15 μm) is substantially larger than individual sulphide grains. The absence of PGE in relatively coarse millerite in Yukon HEBS deposits suggests that this mineral does not host significant quantities of these elements. However, the coarse-grained nature of this millerite indicates it is remobilized or recrystallized. Smith et al. (2014) investigated PGE contents of a variety of base metal sulphide minerals, including millerite and pyrite, at the Bushveld Complex. Although this magmatic, mafic-ultramafic rock-hosted Ni-Cu-PGE mineralization is not analogous to HEBS deposits, their research suggests that secondary millerite (and pyrite) can accommodate PGE in solid-solution (i.e. within the mineral lattice). Thus, fine-grained millerite from the Peel River, Eagle Plains and Monster River localities,

which is less conspicuous and more difficult to analyze, warrants further analytical work.

Source(s) of metals and genetic models

Hulbert et al. (1992) suggest that the mineralization was formed from a seafloor-hydrothermal system, whereby carbonaceous shales underlying the HEBS layer supplied metalliferous brines. In their model, basinal brines were discharged into carbonaceous oozes within a euxinic, stratified water mass. Steiner et al. (2001) suggest a similar origin for Cambrian Chinese HEBS deposits, however other researchers favour formation by quantitative scavenging of metals from seawater by organic matter under biologically productive, sediment-starved basinal conditions (Lehmann et al., 2007; Lingang et al., 2011). Goodfellow et al. (2010) proposed that Yukon HEBS deposits are of extraterrestrial origin. They suggest that the underlying limestone-ball member is a tsunami deposit that was generated by a large bolide impact. These authors also suggest that the laterally widespread mineralized horizon and the pronounced Ir anomaly are best accounted for by an impacting iron meteorite, and that the impacting event perhaps coincided with the Frasnian – Famenian extinction interval.

Our conodont age and 2017 field observations provide evidence against the bolide model. The biostratigraphic age of the HEBS mineralization is Givetian, an age that is consistent with the uppermost Road River Group across the Richardson trough. Moreover, the existence of several discrete mineralized layers precludes a single, catastrophic event. The so-called limestone ball unit, purported to be a tsunami deposit related to a bolide impact, preserves shale bedding within carbonate concretions and stratiform massive carbonates. The textures strongly support an authigenic origin for the carbonate-rich horizon immediately preceding the HEBS Ni-Zn-PGE mineralization. Indeed, Hulbert et al. (1992) report uniformly negative $\delta^{13}C$ isotope compositions for these carbonates at the Nick deposit, which they interpret to form as a result of bacterial sulphate reduction and organic carbon oxidation. Highly negative $\delta^{34}S$ of bulk sulphides from the Nick mineralization supports this (Hulbert et al., 1992).

The hydrothermal exhalative model for Yukon HEBS deposits is also problematic. A point source for debouching hydrothermal and/or petroleum-bearing metalliferous fluids has only been proposed for the Nick deposit (i.e. discordant pyrobitumen-rich veins; Hulbert et al., 1992). However, this fails to explain the widespread geographical distribution of the HEBS deposits because no other vent-like complexes have been identified. Additionally, Lehmann et al. (2016) demonstrate that organic-rich fluids contain substantially less Re and Os than their shale source rocks, indicating that extracted oil fluids are unlikely sources of metals for HEBS mineralization on the Yangtze platform. Analysis of pyrobitumen grains from the HEBS layer at the Peel River locality (Gadd et al., 2017) provide additional support for petroleum fluids as poor carriers of metals, revealing that only a minor proportion of metals and metalloids are contained within the altered organic matter.

Rather than hydrothermal or extra-terrestrial sources, Lehmann et al. (2007) and Lingang et al. (2011) suggest that ambient seawater is the primary metal source for Cambrian HEBS in China. Because metal concentrations in seawater are so low, several critical factors must work in tandem to generate favourable conditions. Lehmann et al. (2016) suggest that on the Early Cambrian Yangtze platform combinations of extremely low rates of clastic sedimentation and extremely efficient organic carbon remineralization are two of the driving forces for hyper enrichment of metals. At least during the Early Cambrian, increased atmospheric oxygen also is thought to have played a critical role in increasing the abundance of critical trace element nutrients to marine environments by increasing oxidative weathering on land masses (Johnson et al., 2017). The late Middle Devonian HEBS layer in north Yukon lags the drastic increase in atmospheric oxygen of the late Early Devonian (Figure 4 in Johnson et al., 2017), suggesting that additional factors (e.g. condensed sedimentation) must have been operating. Assuming very low clastic sedimentation rates combined with highly efficient organic matter remineralization and steady diffusional exchange between the upper sediment pile and the overlying water column, seawater is a viable source of metals in Yukon HEBS deposits. Continental crust-normalized PGE patterns for Yukon HEBS compared with modern seawater show very similar topologies (Fig. 8), and the patterns are also very similar to Cambrian HEBS deposits (Lehmann et
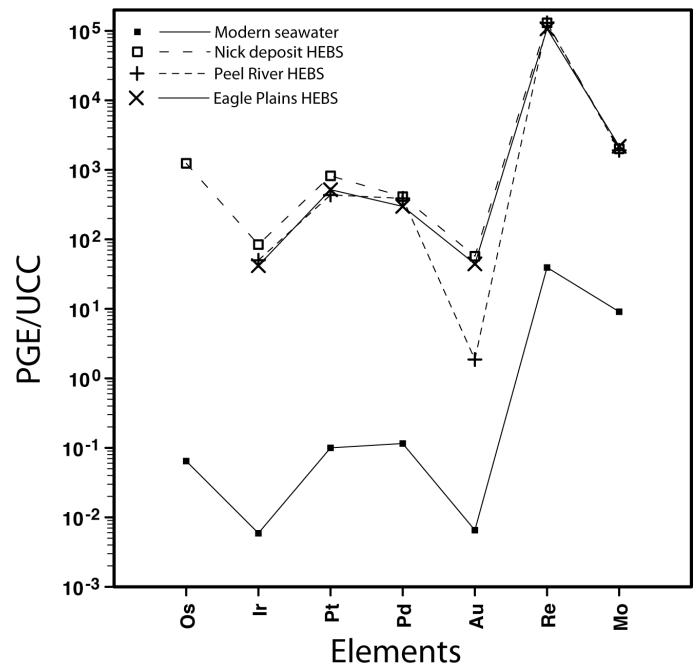

Figure 8. Upper continental crust-normalized (UCC) PGE, Au, Re and Mo contents (Rudnick and Gao, 2014) of the HEBS layers for Peel River (Goodfellow et al., 2010), Eagle Plains (Goodfellow et al., 2010), Nick deposit (Hulbert et al., 1992) and modern seawater (Nozaki, 1997).

al., 2016). This suggests a seawater control on their formation, assuming modern seawater is a reasonable analogue for the Middle Devonian (cf. Lehmann et al., 2016).

Conclusions

Preliminary LA-ICP-MS data reveal that PGE are hosted within sulphide minerals, although the deportment of PGE is apparently controlled by local mineralogical variability. The implications for this are manifold, but the salient points relate to the relative timing of mineralization and how these minerals might be processed if the deposits are mined. With respect to the former, there are additional implications about the timing of mineralization and, hence, genetic and exploration models. With respect to the latter, a full inventory of where PGE reside will assist in decisions for how to process the rocks for maximum PGE extraction.

Developing and refining internally consistent genetic and exploration models for Yukon HEBS deposits remains the primary long-term goal. Our recent work contradicts the model of a single, catastrophic bolide impact being the driving force behind the HEBS mineralization. We can additionally discount major contributions of metals from exhalative hydrothermal activity on the paleo-seafloor of the Richardson trough. Instead, several lines of evidence – geographically widespread distribution, abundant diagenetic mineral textures, pelagic microfossils, terrestrially derived plant fossils, similarities between modern seawater PGE and ancient HEBS – suggest that hyper enrichment of metals in Yukon HEBS deposits was a consequence of extremely efficient adsorptive scavenging from ambient paleo-seawater. Ongoing research into the age and distribution of metals within the stratigraphically different HEBS layers aims to refine our working hypothesis for hyper enrichment.

Future work

Samples from the 2017 field season have been submitted for polished thin section preparation, with petrographic and LA-ICP-MS work to commence once the samples are returned. Additionally, samples will be submitted for µCT analysis after prospective samples (i.e. conodont-bearing) are identified during petrographic analyses. Future work must constrain the ages of the different HEBS horizons within individual stratigraphic sections. It must also determine whether the HEBS mineralization was coeval basin-wide or diachronous by constraining ages at the different geographic localities.

Samples have also been selected for lithogeochemical analyses. These analyses will include major, minor and trace element analyses. The next steps will aim at fully characterizing the sulphide mineral suite, particularly at Peel River, where the trace element compositions of fine-grained millerite and gersdorffite are not well constrained. The lower HEBS horizon(s) at the Peel River localities have not been studied in detail, but a goal of our ongoing research is to identify the type(s) of bio-

genic debris contained within them. A subset of samples will be submitted for full suite of PGE analysis. Fieldwork is planned for 2018 to examine other HEBS localities (Nick deposit, Monster River, Akie) in northern Yukon and British Columbia.

Acknowledgments

References

Blakey, R., 2013. Middle Devonian (395–385 Ma) paleogeographic reconstruction of North America; *in* North American Key Time Slices, (ed.) R. Blakey; Colorado Plateau Geosystems Inc.

Bond, D.P.G. and Wignall, P.B., 2010. Pyrite framboid study of marine Permian-Triassic boundary sections: A complex anoxic event and its relationship to contemporaneous mass extinction; Geological Society of America Bulletin, v. 122, p. 1265–1279.

Cabri, L.J. and Jackson, S.E., 2011. New developments in characterization of sulfide refractory Au ores; Proceedings of World Gold 2011, 50th Conference of Metallurgists, Montreal, Quebec, p. 51–62.

Carne, R., 1989. Nick Property; Yukon Territory assessment report, 8 p.

Dumala, M., 2007. Assessment report describing prospecting, mapping, geochemical sampling, geophysical surveys and diamond drilling at the Rich property, prepared for Southampton Ventures Inc. and Strategic Metals Ltd.; Whitehorse, Yukon, 455 p.

Fraser, T.A. and Hutchison, M.P., 2017. Lithogeochemical characterization of the Middle–Upper Devonian Road River

Group and Canol and Imperial formations on Trail River, east Richardson Mountains, Yukon: Age constraints and a depositional model for fine-grained strata in the Lower Paleozoic Richardson trough; Canadian Journal of Earth Sciences, v. 54, p. 731–765.

Gadd, M.G., Peter, J.M., Goodfellow, W., Jackson, S.E., and Yang, Z., 2017. Geology, geochemistry and mineralogy of hyper-enriched black shale deposits, Yukon; Proceedings of Exploration 17: Sixth Decennial International Conference on Mineral Exploration, Toronto, Ontario, p. 841–845.

Garrett, R.G., Goodfellow, W., and Lund, N.G., 1977. Uranium reconnaissance program national stream sediment + water geochemical reconnaissance data northern Yukon Territory; Geological Survey of Canada, Open File 418, p. 1–15.

Goodfellow, W., Geldsetzer, H.H.J., Pride, K., Uyeno, T., and Gregoire, C., 2010. Geochemistry and origin of geographically extensive Ni-(Mo, Zn, U)-PGE sulphide deposits hosted in Devonian black shales, Yukon; TGI-3 Workshop: Public Geoscience in Support of Base Metal Exploration, Simon Fraser University, Vancouver, British Columbia, p. 15–18.

Guillong, M., Hametner, K., Reusser, E., Wilson, S.A., and Günther, D., 2005. Preliminary characterisation of new glass reference materials (GSA-1G, GSC-1G, GSD-1G and GSE-1G) by laser ablation-inductively coupled plasma-mass spectrometry using 193 nm, 213 nm and 266 nm wavelengths; Geostandards and Geoanalytical Research, v. 29, p. 315–331.

Haq, B. and Schutter, S., 2008. A chronology of Paleozoic sea-level changes; Science, v. 322, p. 64–68.

Horan, M.F., Morgan, J.W., Grauch, R.I., Coveney, J.R.M., Murowchick, J.B., and Hulbert, L.J., 1994. Rhenium and osmium isotopes in black shales and Ni-Mo-PGE-rich sulfide layers, Yukon Territory, Canada, and Hunan and Guizhou provinces, China; Geochimica et Cosmochimica Acta, v. 58, p. 257–265.

Hulbert, L.J., Gregoire, D., Paktunc, D., and Carne, R., 1992. Sedimentary nickel, zinc, and platinum-group-element mineralization in Devonian black shales at the Nick Property, Yukon, Canada: A new deposit type; Exploration and Mining Geology, v. 1, p. 39–62.

Hutchison, M.P. and Fraser, T.A., 2015. Paleoenvironment, paleohydrography and chemostratigraphic zonation of the Canol Formation, Richardson Mountains, north Yukon; *in* Yukon Exploration and Geology 2014, (ed.) K.E. MacFarlane, M.G. Nordling and P.J. Sack; Yukon Geological Survey, p. 73–98.

Johnson, S.C., Large, R.R., Coveney, R.M., Kelley, K.D., Slack, J.F., Steadman, J.A., Gregory, D.D., Sack, P.J., and Meffre, S., 2017. Secular distribution of highly metalliferous black shales corresponds with peaks in past atmosphere oxygenation; Mineralium Deposita, v. 52, p. 791–798.

Jowitt, S.M. and Keays, R.R., 2011. Shale-hosted Ni-(Cu-PGE)

mineralisation: A global overview; Transactions of the Institution of Mining and Metallurgy Section B – Applied Earth Science, v. 120, p. 187–197.

Lane, L., 2007. Devonian–Carboniferous paleogeography and orogenesis, northern Yukon and adjacent Arctic Alaska; Canadian Journal of Earth Sciences, v. 44, p. 679–694.

Lehmann, B., Frei, R., Xu, L., and Mao, J., 2016. Early Cambrian black shale-hosted Mo-Ni and V mineralization on the rifted margin of the Yangtze Platform, China: Reconnaissance chromium isotope data and a refined metallogenic model; Economic Geology, v. 111, p. 89–103.

Lehmann, B., Nägler, T.F., Holland, H.D., Wille, M., Mao, J., Pan, J., Ma, D., and Dulski, P., 2007. Highly metalliferous carbonaceous shale and Early Cambrian seawater; Geology, v. 35, p. 403.

Lingang, X., Lehmann, B., Jingwen, M., Wenjun, Q., and Andao, D., 2011. Re-Os age of polymetallic Ni-Mo-PGE-Au mineralization in Early Cambrian black shales of south China – A reassessment; Economic Geology, v. 106, p. 511–522.

Loutit, T., Hardenbol, J., Vail, P., and Baum, G., 1988. Condensed sections: The key to age-dating and correlation of continental margin sequences; *in* Sea Level Changes – An Integrated Approach, (ed.) C. Wilgus, B. Hastings, C.G.S.C. Kendall, H. Posamentier, C. Ross and J. Van Wagoner; 42 SEPM Special Publication, p. 183–213.

Morrow, D., 1999. Lower Paleozoic stratigraphy of northern Yukon Territory and northwestern District of Mackenzie; Geological Survey of Canada Bulletin 538, 202 p.

Nozaki, Y., 1997. A fresh look at element distribution in the north Pacific Ocean; EOS Transactions of the American Geophysical Union, v. 78, p. 221–223.

Orberger, B., Pasava, J., Gallien, J.P., Daudin, L., and Pinti, D.L., 2003. Biogenic and abiogenic hydrothermal sulfides: Controls of rare metal distribution in black shales (Yukon Territories, Canada); Journal of Geochemical Exploration, v. 78, p. 559–563.

Peter, J.M., Bocking, N., Gadd, M.G., Layton-Matthews, D., and Johnson, N., 2018. Textural and mineralogical characterization of a Ni-Zn-rich black shale occurrence at the Akie property, Kechika Trough, northern British Columbia, and comparison with examples from Yukon; *in* Targeted Geoscience Initiative: 2017 report of activities, volume 1, (ed.) N. Rogers; Geological Survey of Canada, Open File 8358, p. 207–216.

Pugh, D.C., 1983. Pre-Mesozoic geology in the subsurface of Peel River map area, Yukon Territory and District of Mackenzie; Geological Survey of Canada Memoir 401, 61 p.

Rudnick, R.L. and Gao, S., 2014. Composition of the Continental Crust; *in* Treatise on Geochemistry 2nd Edition, v. 4: The Crust, (ed.) R.L. Rudnick; Elsevier, p. 1–51.

Smith, J.W., Holwell, D.A., and McDonald, I., 2014. Precious and base metal geochemistry and mineralogy of the Gras-

vally Norite–Pyroxenite–Anorthosite (GNPA) member, northern Bushveld Complex, South Africa: Implications for a multistage emplacement; Mineralium Deposita, v. 49, p. 667–692.

Steiner, M., Wallis, E., Erdtmann, B.-D., Zhao, Y., and Yang, R., 2001. Submarine-hydrothermal exhalative ore layers in black shales from South China and associated fossils – Insights into a Lower Cambrian facies and bio-evolution; Palaeogeography, Palaeoclimatology, Palaeoecology, v. 169, p. 165–191.

Sylvester, P., Cabri, L.J., Tubrett, M., McMahon, G., Laflamme, J., and Peregoedova, A., 2005. Synthesis and evaluation of a fused pyrrhotite standard reference material for platinum group elements and gold analysis by laser ablation-ICPMS; Conference Proceedings, 10th International Platinum Symposium, Oulu, Finland, p. 16–20.

Wignall, P.B. and Newton, R., 1998. Pyrite framboid diameter as a measure of oxygen deficiency in ancient mudrocks; American Journal of Science, v. 298, p. 537–552.

Wilkin, R., Arthur, M., and Dean, W., 1997. History of water-column anoxia in the Black Sea indicated by pyrite framboid size distributions; Earth and Planetary Science Letters, v. 148, p. 517–525.

Textural and mineralogical characterization of a Ni-Zn-rich black shale occurrence at the Akie property, Kechika Trough, northern British Columbia, and comparison with examples from Yukon

J.M. Peter[1], N. Bocking[2*], M.G. Gadd[1], D. Layton-Matthews[2] and N. Johnson[3]

[1]*Geological Survey of Canada, 601 Booth Street, Ottawa, Ontario, K1A 0E8*

[2]*Department of Geological Sciences and Geological Engineering, Queen's University, 36 Union Street, Kingston, Ontario, K7L 3N6*

[3]*Canada Zinc Metals Corp., #2050, 1055 West Georgia Street, Vancouver, British Columbia, V6E 3P3*

*present address: Aurora Geoscience, 3506 McDonald Drive, Yellowknife, Northwest Territories, X1A 2H1

Abstract

Hyper-enriched black shales (HEBS) that are enriched in Ni, Zn, Mo, and other elements occur within the Devonian strata of Yukon over 100s to 1000s km^2. The mineralization is typically up to several tens of centimetres thick. Recently, during exploration for SEDEX deposits, mineralization that is potentially analogous (and time-stratigraphically equivalent) to HEBS mineralization in Yukon was discovered in the Kechika Trough of northeastern British Columbia. Here, about 3 to 20 m stratigraphically below the SEDEX mineralization of the Cardiac Creek deposit, an approximately 2 to 20 cm thick stratiform horizon hosts sphalerite, chalcopyrite, millerite, gersdorffite, clausthalite, pentlandite and pyrite within Devonian black, carbonaceous shale. This mineralization is strikingly similar in broad stratigraphic age, metal enrichments, textures and mineralogy to HEBS localities in Yukon. Based on these similarities, this mineralization likely was formed at a discrete time interval, over a wide area (likely 1000s km^2) within the Selwyn Basin and the adjacent carbonate platform. This has implications for any genetic and exploration model(s) for this style of mineralization.

Introduction

Hyper-enriched black shales (HEBS) or polymetallic shales are a significant global resource for Zn, Ni, Cu, Mo, Se, U, V, ± Cr, Co, Ag, Au, PGE and REE (e.g. Jowitt and Keays, 2011). HEBS Ni-Zn-Mo deposits and showings are known in Yukon (e.g. Hulbert et al., 1992; Goodfellow et al., 2010; Fig. 1), where they occur within Devonian sedimentary strata as a massive-sulphide layer primarily composed of pyrite (FeS_2), vaesite (NiS_2), millerite (NiS), marcasite (FeS_2), gersdorffite (NiAsS), sphalerite and wurtzite ([Zn,Fe]S) and molybdenite (MoS_2).

This style of mineralization is colloquially referred to as 'Nick-type"' mineralization after the Nick deposit, Yukon, which was discovered by Archer, Cathro & Associates (1981) Ltd. Further exploration work by Archer, Cathro & Associates (1981) Ltd. and work by Goodfellow (2002) and Goodfellow et al. (2010) identified additional occurrences of the Nick horizon in the Eagle Plains, Peel River and Monster River areas. It had been speculated that similar deposits may occur in the Kechika Trough of northern British Columbia, as it is a continuation of the HEBS-bearing stratigraphy of the Selwyn Basin (Lefebure, 1995). The recent discovery by Canada Zinc Metals Corporation of Ni-Zn sulphide mineralized black shale in drillholes on the Akie property (Sim, 2016) appears to confirm the extension of HEBS units into the Kechika Trough, northeast British Columbia, hundreds of kilometres south-southeast of the previously known Yukon examples (Fig. 1).

The salient questions being addressed by the study of Akie Ni-Zr-rich mineralization are: 1) is this occurrence the time-stratigraphic equivalent to Yukon HEBS mineralization?; 2) is the mineralogical suite of elements of potential economic interest (e.g. Ni, Mo, Zn, PGE) the same as in Yukon?; and 3) what are the genetic and exploration implications of the close juxtaposition in space and time of the Akie HEBS mineralization and the SEDEX mineralization of the Cardiac Creek deposit? Herein, we report on mineralogical and textural characterization of the Ni-Zn mineralization, and make comparisons with similar mineralization in Yukon.

Geology

The Akie property is located in northern British Columbia within the Kechika Trough, a >500 km long, finger-like southeast extension of the Palaeozoic Selwyn Basin that predominately comprises sedimentary and metasedimentary rocks ranging in age from the Proterozoic to the Triassic, as well as minor volcanic and intrusive rocks of similar age (MacIntyre, 1998a).
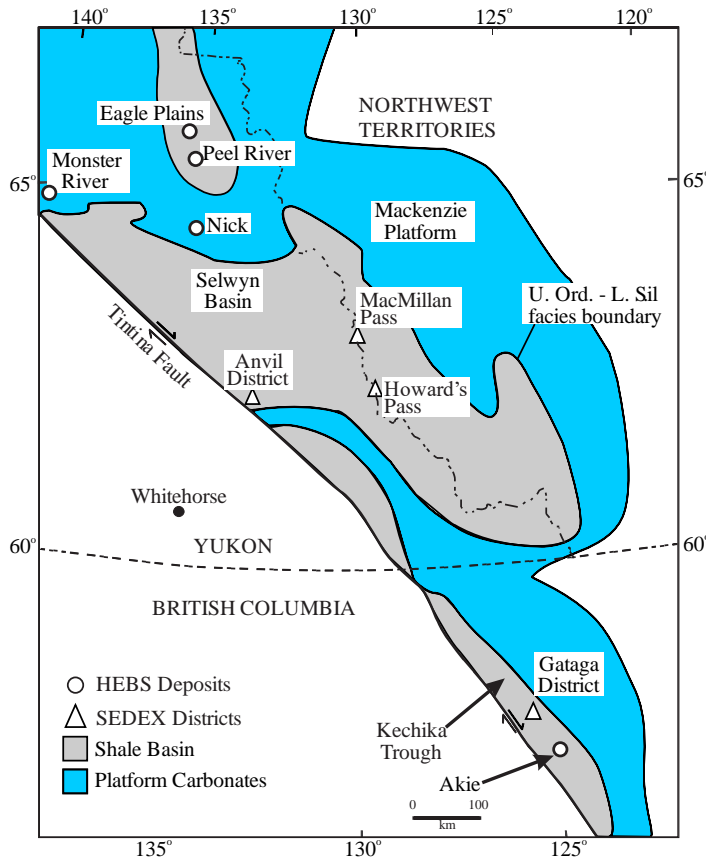
Figure 1. Location map of the present distribution of continental margin facies of Ancestral North America. The major SEDEX districts of the Selwyn Basin and the known HEBS occurrences are shown. Modified from Goodfellow (2007).

At the Akie property, all rocks are Paleozoic in age, and mostly siliciclastic and carbonate sedimentary rocks with minor mafic volcanic flows and one isolated diorite plug (Fig. 2). All the rock units were deformed as part of the Rocky Mountain Fold and Thrust belt during the Late Jurassic and early Paleogene (MacIntyre, 1998a). Major thrust faults and fold-axes strike northwest, however on the western side of the property the major faults dip to the west, whereas on the eastern side the major fault systems dip to the east. Faults on both sides of the property have an unknown amount of displacement. Between these thrust faults are mapable units that are tightly folded and in part overturned (MacIntyre, 2005). Generally, the structure of the property can be characterized as a large thrust-bounded anticline with smaller scale folding and thrusting within the larger structure.

The Kechika Trough hosts a variety of mineral deposits, including SEDEX, stratiform barite, and vein-hosted copper (e.g. Ferri et al., 1999). The SEDEX deposits (e.g. Cardiac Creek (Akie), Cirque, South Cirque and Driftpile) occur along a northwest oriented trend and range from Middle Ordovician to late Middle Devonian. The Cardiac Creek Zn-Pb-Ag SEDEX deposit is situated at the transition between reefoidal limestone and basinal strata, within siliceous shales along the base of the Gunsteel Formation, Earn Group, near the contact with siliceous shales of the underlying Paul River Formation (Fig. 3). The Cardiac Creek deposit, which is characterized by laminated to mottled sulphide mineralization, contains indicated resources of 19.6 million tonnes (Mt) grading 8.17 weight % Zn, 1.58 weight % Pb, and 13.6 g/t Ag at a 5 weight % Zn cutoff grade, and inferred resources of 8.1 Mt grading 6.81 weight % Zn, 1.16 weight % Pb, and 11.2 g/t Ag at a 5 weight % Zn cutoff grade (Sim, 2016).

Ni-Zn mineralized sulphide horizon

The lower parts of nine drillholes, collared to intersect SEDEX mineralization of the Cardiac Creek deposit, intersected a sulphidic horizon within shale typically about 3 to 20 m below the base of the SEDEX mineralization over a strike length of 5.5 km extending southeast and northwest of the deposit (Fig. 2). The drill core intersections of the sulphidic shale are up to 1.17 m thick, but the thickest intersection displays significant folding (see below) and the true stratigraphic thickness is likely much lower, in the region of approximately 10 to 20 cm. Nick-type mineralization is stratigraphically controlled, occurring at the contact between the Road River Group and the overlying Devonian Kwadacha limestone, and within Paul River Formation reef marginal debris flow and deep water cherty shale (red solid and dashed line with white margins in Figure 3). This mineralized layer grades 0.39 to 2.69 weight % Zn, 0.6 to 0.89 weight % Ni and up to 4.36 g/t Ag (Sim, 2016).

Methods

Polished cut slabs and polished thin sections (PTS) were prepared from Ni-Zn mineralized intersections and immediately adjacent host rocks from two diamond-drill holes (A-10-72 and A-13-103). The PTS were examined using transmitted and reflected light optical microscopy. Automated mineralogical determinations were conducted on the slabs from hole A-13-103 using mineral liberation analysis (MLA). Originally developed to characterize ore and mill feeds for the metallurgical processing industry (e.g. Gottlieb et al., 2000; Gu, 2003), it is now a proven method to quantitatively characterize rocks, ores and other sample types (e.g. Fandrich et al., 2007).

The MLA analyses were conducted using a FEI-MLA Quanta 650 field emission gun-environmental scanning electron microscope (FEG-ESEM) at the Queen's Facility for Isotope Research, Queen's University, Kingston. Samples were carbon coated and analyzed under high vacuum at 25 kV and a spot size to achieve a beam current of 10 nA. Brightness and contrast were optimized to an AgPd alloy to achieve differentiation of mineralogy needed for this study. The MLA automated mineralogy software uses back-scatter electron imagery and energy dispersive X-ray analysis to analyze each particle's shape, size, and mineralogical information. Energy dispersive X-ray data are compared to a user-generated mineral reference library consisting of known phases and corresponding EDS
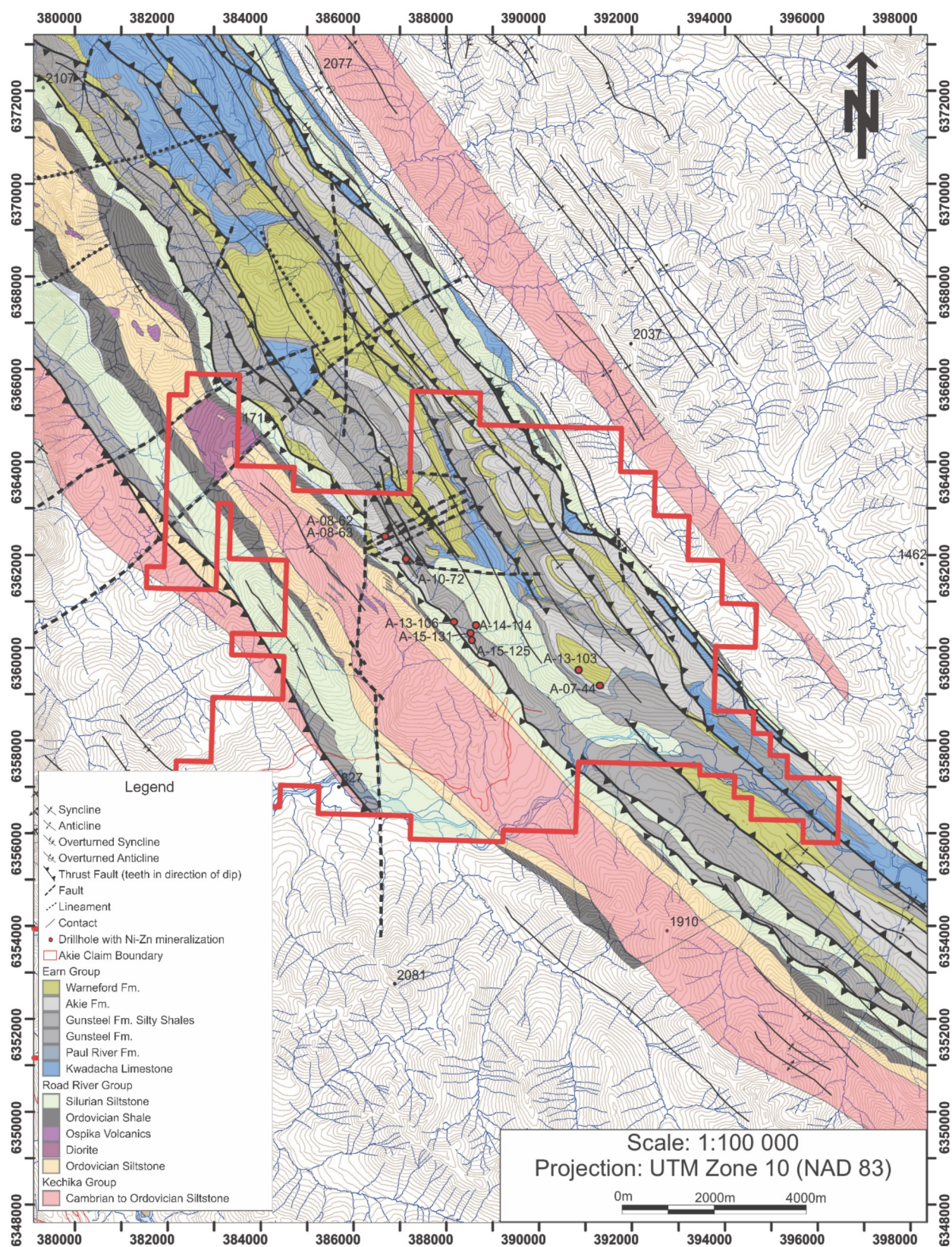
208

Figure 2. Geology map of the Akie property showing the collars of diamond-drill holes that intersected Ni-Zn mineralized shale. Lithologies and faults are from Canada Zinc Metals Corp. (unpub., 2017). Fold traces are from regional mapping by Mac-Intyre (1998b).
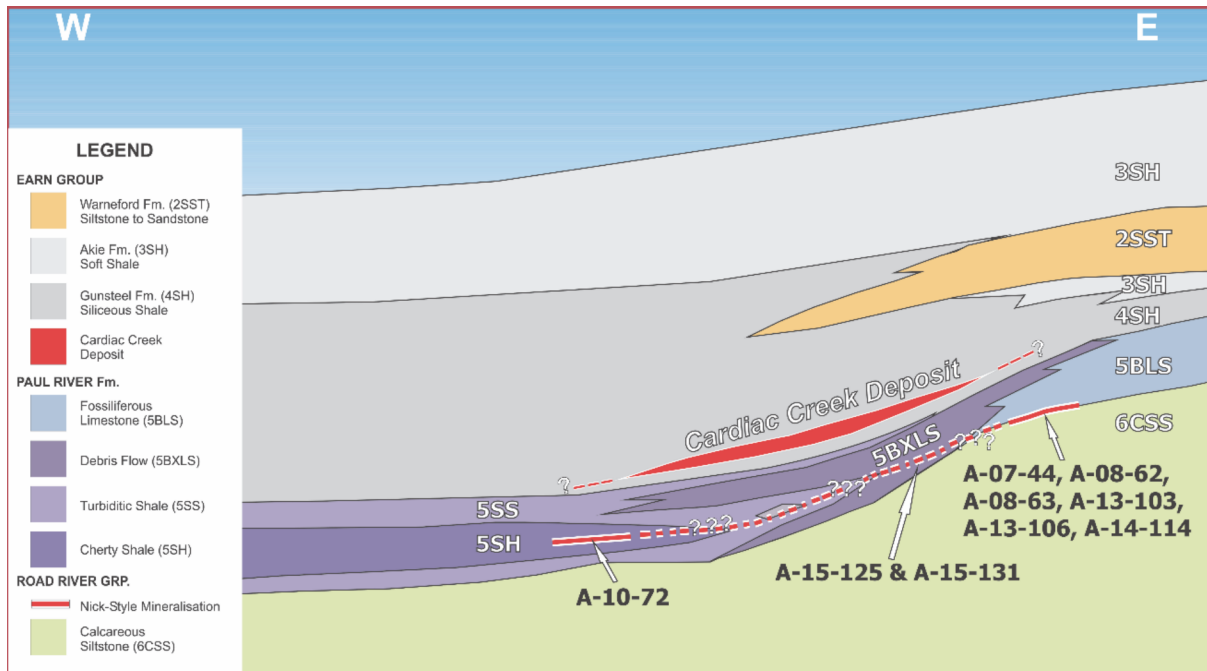
Figure 3. Schematic cross section through Cardiac Creek SEDEX deposit and stratigraphically underlying Ni-Zn mineralized shale, with drillholes that intersected it shown. Modified from Sim (2016).

spectra to classify each particle. Three MLA analysis modes were completed, including complete characterization (BSE STD), specific range atomic mass characterization (SPL) and grid-based modal mineralogy (XMOD) (Gu, 2003; Fandrich et al., 2007).

Mineralogy

Optical microscopy

Drillhole A-10-72

Drillhole A-10-72 contains the thickest (1.17 m) intersected Ni-Zn mineralized horizon, though the estimated true stratigraphic thickness is 10 to 30 cm, as it is folded and deformed (Fig. 4a). Polished thin section TS-01 (see Figure 4a for location) is composed of foliated, dark grey, extremely fine grained, possibly carbonaceous mudstone cut by microveinlets of medium grained (0.5 to 1 mm) quartz-calcite-muscovite displaying epitaxial textures (Fig. 5a). The dark grey mudstone matrix hosts clusters of framboids (Fig. 5b) and disseminated pyrite and low- to moderate-Fe (based on colour in transmitted light) sphalerite that occur as fine grained euhedral crystals, and coarser recrystallized grains (Fig. 5c). Recrystallized sulphides are dominantly disseminated fine grained pyrite and sphalerite. Some of the sphalerite shows chalcopyrite disease (Barton and Bethke, 1987; Fig. 5c). No significant millerite or other nickel-bearing phases were identified in TS-01, in contrast to what is observed in hole A-13-103 (see below).

Strain localization is demonstrated by distinct zones that contain undeformed primary (?) textures and zones that show well-developed shear fabrics. The undeformed zones have the appearance of boudins, and contain pyrite as framboids and disseminated euhedra. Within the veinlets, some of the quartz grains exhibit undulatory extinction and display epitaxial textures (Fig. 5a). These discrete zones of deformation can also be identified by the truncation of primary textures and structures by shears containing the remnants of the primary structures (e.g. Fig. 5d).

Drillhole A-13-103

A PTS of drillhole A-13-103 from the 5 cm-thick carbonaceous shale interval immediately adjacent/below (downhole from) the mineralized zone was examined. The PTS is dominated by calcite veins which also contain some finer grained quartz (Fig. 4b). Within the laminated vein complex are foliae of black, microcrystalline, organic material thought to be graphite, based on its properties in reflected light (Fig. 5e, f). This PTS also contains predominantly fine grained (approximately 5 µm diameter), euhedral, disseminated pyrite and chalcopyrite, with minor, elongated recrystallized sulphide blebs up to about 0.5 mm in size (Fig. 5g). The presence and mode of occurrence of the laminated veins and the well-developed cleavage are evidence of structural deformation.

The mineralized interval is characterized by layers and stringers of fine-grained, semi-massive sulphides with black apatite, calcite and dolomite clasts cross-cut by the sulphide veinlets (Fig. 5h). These sulphide stringers comprise pyrite and sphalerite and/or millerite (Fig. 5h). Based on colour variations in transmitted light, the sphalerite in this interval has variable iron contents (Fig. 5i), and this is evidenced in the MLA anal-
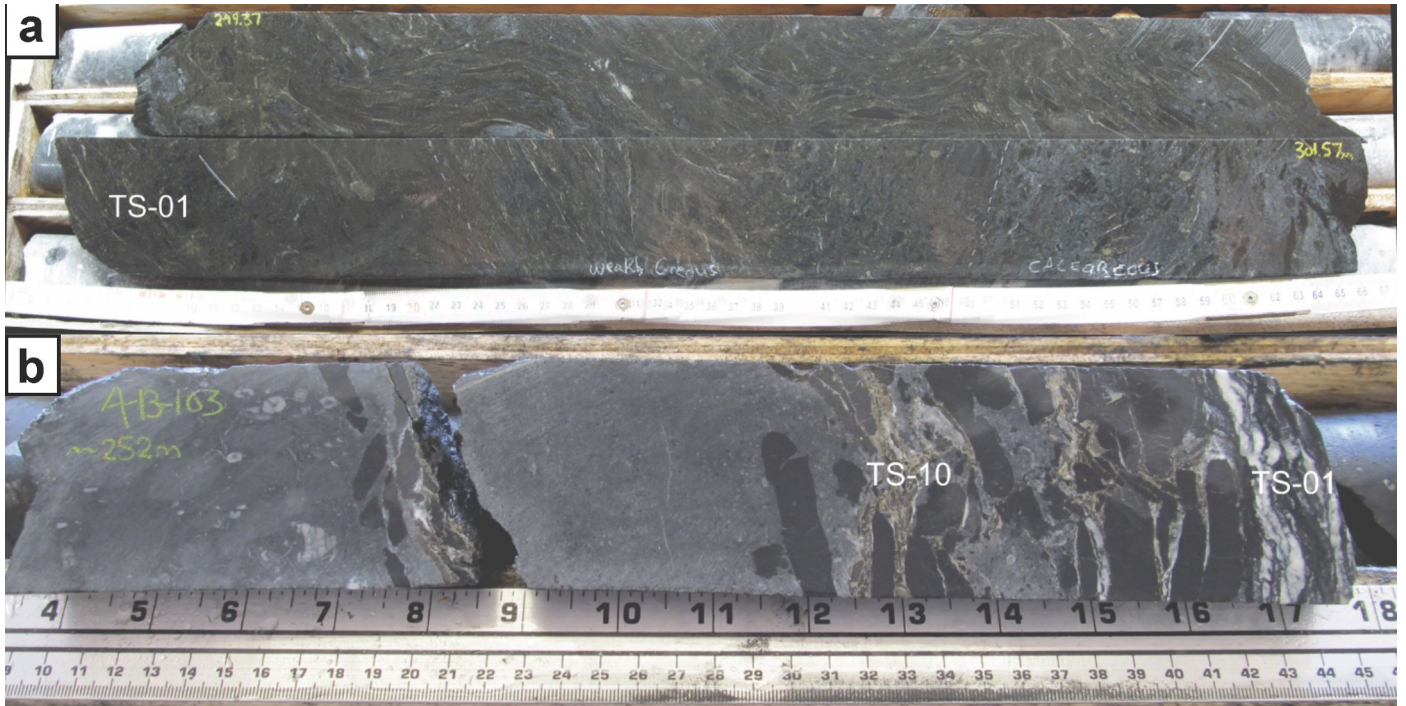
Figure 4. Photographs of Ni-Zn sulphide mineralized shale intervals intersected in drill core. a) Fine-grained disseminated Ni-Zn sulphide mineralization in hole A-10-72, 299.3 m to 301.57 m; the top cut (in half) drill core piece is the upper part of the intersection, and the lower cut piece the lower part. Note the weakly and moderately calcareous areas (white chalk writing). This intersection is significantly deformed (folded). TS-01 indicates position of polished thin section. b) Hole A-13-103, approximately 252.0 m to 252.36 m. Note crinoid fragments in overlying limestone and dismembered shale beds (clasts) associated with sulphide mineralization. Below the mineralized horizon are quartz-carbonate veins and poorly crystalline graphite.

yses (see below). Other minor metallic phases are also present, including gersdorfitte, chalcopyrite, and clausthalite (PbSe), together with other minor phases identified using MLA. Disseminated, fine-grained sulphides (dominantly pyrite and sphalerite) also occur within the clasts (Fig. 5j).

Based on the textural habits of the sulphides in the stringers and layers, and the cross-cutting relationships between the sulphide stringers and the clasts (Fig. 5h–k), the sulphides within the layers and clasts appear primary, whereas the recrystallized sulphides in the veins and the stringers are either remobilized primary sulphides or are secondary replacements. Clusters of pyrite framboids occur within the sulphide stringers (Fig. 5b) and in the clasts. Interstitices between framboids arranged in clusters in sulphide stringers are infilled with other sulphides (sphalerite and millerite; Fig 5k), indicating that the framboids predate the sulphide stringers.

The recrystallized nature of the sulphides in the stringers hinders determination of a paragenetic sequence, however general temporal information indicates that the disseminated sulphides within the clasts formed first, followed by the framboidal pyrite clusters and lastly the sulphide stringers.

Mineral Liberation Analysis

Figure 6a, c presents the backscatter electron images for the section of polished core (A-13-103; 252.3 m) in the same area as TS-10. In these images the brighter grey areas are sulphides, whereas the darker grey to black areas are gangue minerals. Figure 6b, d show the results of the MLA analysis for the same areas as the backscatter images; note the zonation of the sulphides within the veinlets. The edges of the veinlets are dominantly composed of pyrite, whereas the cores of the veinlets are composed of sphalerite and millerite. Other minor metallic mineral phases identified within the stringers are gersdorffite, chalcopyrite, pentlandite and clausthalite (Fig. 6d). These phases are difficult to recognize and differentiate from the other sulphide minerals in transmitted light due to the fine-grained nature and similar colour and reflectance. However, these were readily identified and characterized by MLA. Associated with the sulphides are grains and nodules of apatite, calcite and dolomite that contain disseminated sulphides (see Fig. 6b).

Due to the lengthy processing time of the MLA software required to analyze fine-grained, texturally complex samples, XMOD point counting modal mineralogy analysis was used to determine modal mineralogy. The XMOD analysis indicates that calcite, apatite, pyrite, quartz, and dolomite are the main
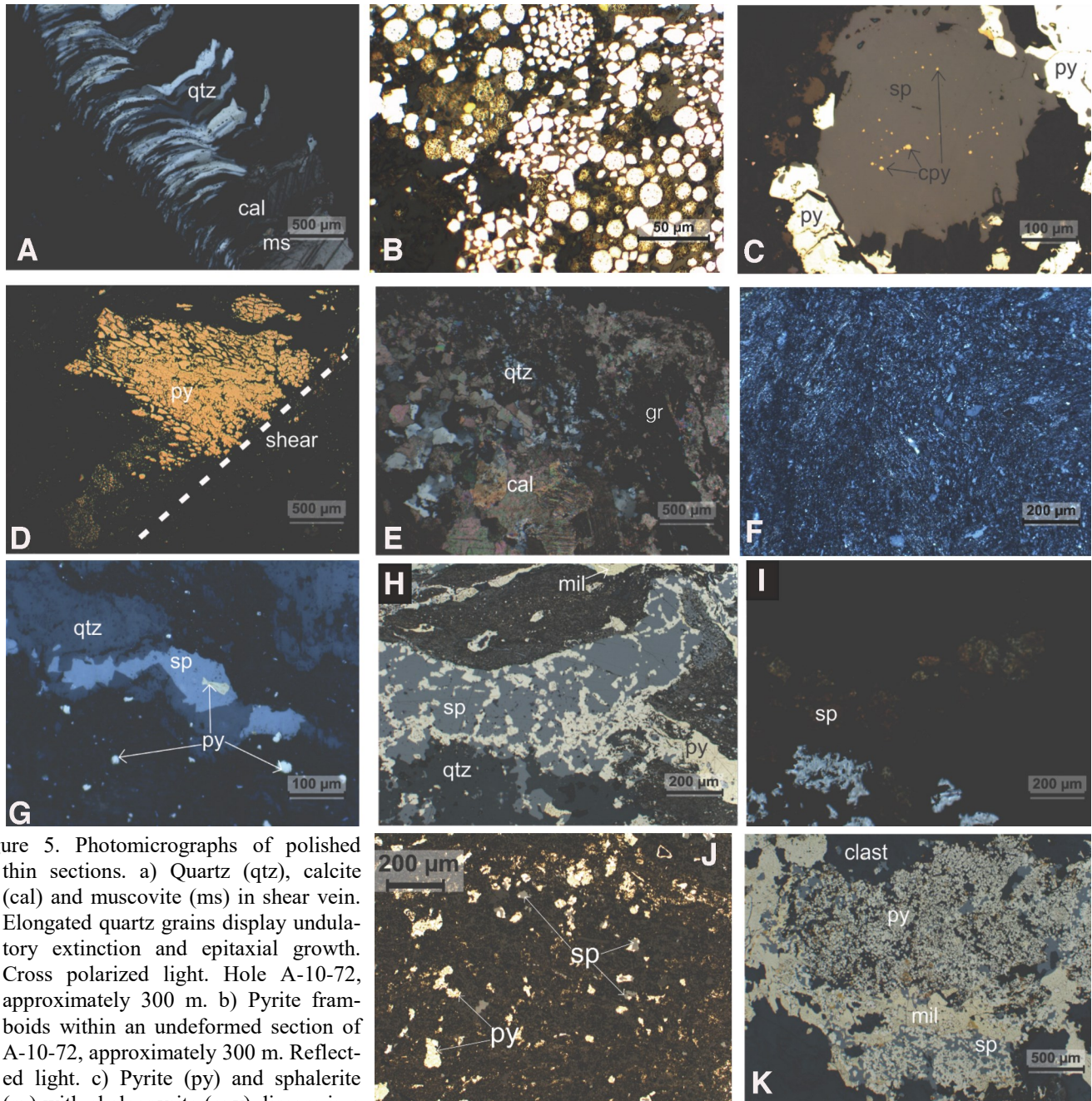
Figure 5. Photomicrographs of polished thin sections. a) Quartz (qtz), calcite (cal) and muscovite (ms) in shear vein. Elongated quartz grains display undulatory extinction and epitaxial growth. Cross polarized light. Hole A-10-72, approximately 300 m. b) Pyrite framboids within an undeformed section of A-10-72, approximately 300 m. Reflected light. c) Pyrite (py) and sphalerite (sp) with chalcopyrite (cpy) disease in a deformed portion of the HEBS horizon in A-10-72, approximately 300 m. Reflected light. d) Pyrite replacing and pseudomorphing plant(?) cellular material adjacent to a shear; hole A-10-72, approximately 300 m. Reflected light. e) Calcite (cal) and quartz (qtz) veins immediately below the mineralized horizon. The black material is likely microcrystalline graphite (gr). Cross polarized transmitted light. Hole A-13-103, 252.33 m. f) Microcrystalline graphite in shale clast. Note the violet grey colour of graphite in cross polarized reflected light. Hole A-13-103, 252.33 m. g) Sphalerite (sp) with minor pyrite (py) contained within graphitic shale clasts immediately downhole of the sulphide mineralized layer. Plane reflected light. Hole A-13-103, 253.2 m. h) Sphalerite (sp) and pyrite (py) stringer between clasts in the mineralized horizon of A-13-103. 252.33 m. Millerite (mil) crosscuts the shale clast. Coarser grained quartz (qtz) associated with the sulphide vein Reflected light. i) Same as (h), but plane transmitted light. Note variation in colour of sphalerite (sp) indicating varying iron contents. j) Disseminated sulphides (predominantly pyrite (py) and minor sphalerite (sp)) within one of the shale clasts. Reflected light. Hole A-13-103, 252.33 m. k) Intergrowth of partly recrystallized framboidal pyrite (py), with interstitial millerite (mil), sphalerite (sp) and pyrite (py) adjacent to a shale clasts (clast). Reflected light. Hole A-13-103, 252.33 m.
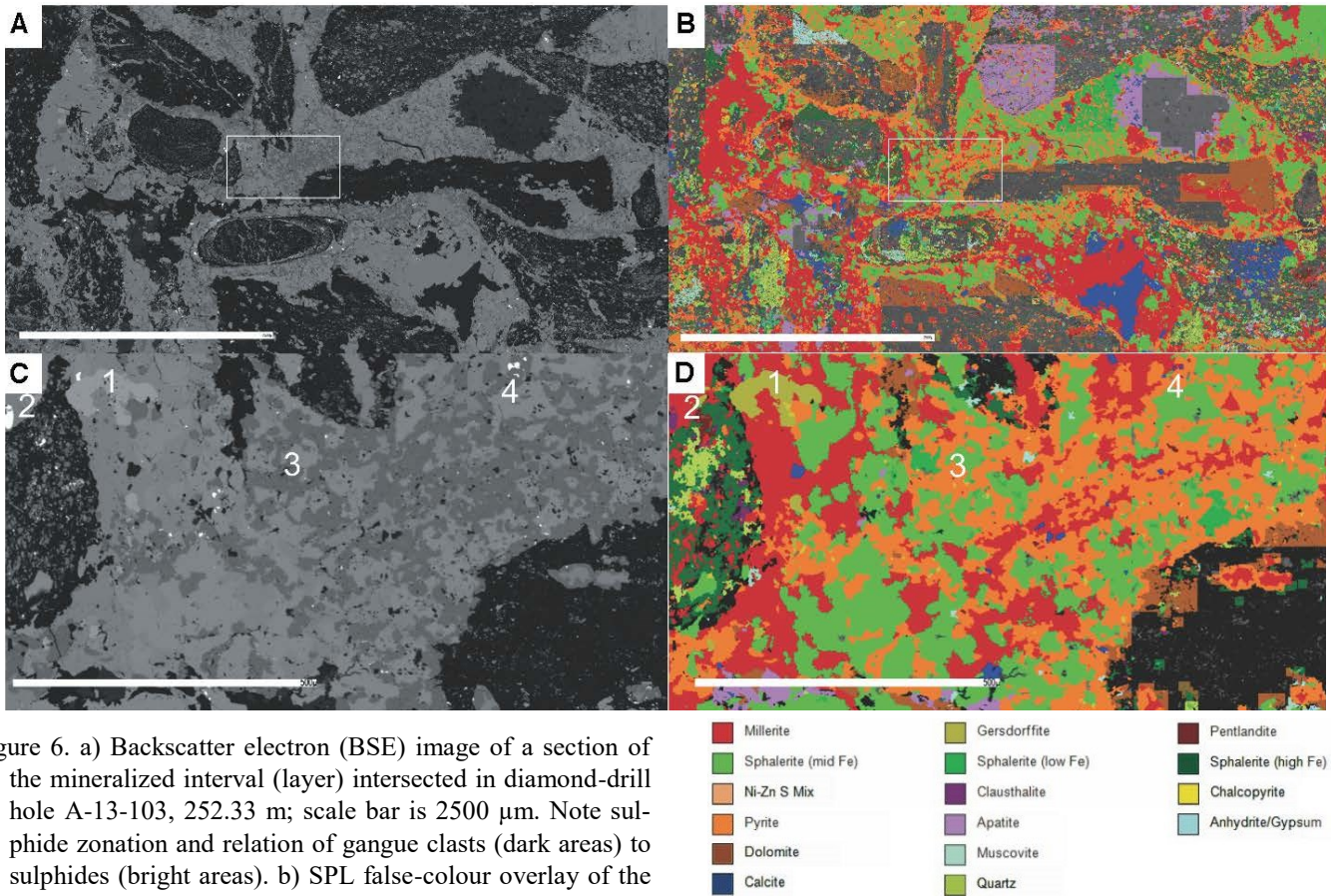
Figure 6. a) Backscatter electron (BSE) image of a section of the mineralized interval (layer) intersected in diamond-drill hole A-13-103, 252.33 m; scale bar is 2500 µm. Note sulphide zonation and relation of gangue clasts (dark areas) to sulphides (bright areas). b) SPL false-colour overlay of the same area shown in A); scale bar is 500 µm. c) Detailed backscatter electron (BSE) image of the area outlined by the white rectangle in (a) and (b); scale bar is 2500 µm. d) SPL false-colour overlay of the same area shown in (c) (white outlined rectangle in (a) and (b); scale bar is 500 µm. Legend pertains to (b) and (d). Note the zonation of pyrite, millerite and sphalerite, and the presence of minor metal bearing phases gersdorffite (1), pentlandite (2), chalcopyrite (3), and clausthalite (4) (in (b) and (d)).

gangue minerals. The dominant ore minerals are sphalerite and millerite, with very minor pentlandite, gersdorffite, clausthalite and chalcopyrite. A limitation of XMOD is the collection of mixed spectra that occurs when the measurement is taken on the edge of a grain or overlaps multiple minerals. Additionally, it cannot identify fine-grained (<1 µm) phases as the MLA is limited by the excitation area of the field emission gun.

Comparison of Akie and Yukon HEBS

Age and stratigraphy

High resolution, absolute age determinations for Yukon HEBS deposits have proven elusive. Horan et al. (1994) obtained Middle to Late Devonian model Re-Os dates for the Nick deposit. Goodfellow et al. (2010) recovered conodont elements from the limestone ball unit (see below) a few meters below HEBS mineralization at Peel River that yield Emsian to Middle Eifelian (Middle Devonian) ages. Conodont elements directly within the HEBS mineralization at the Peel River lo-

cality that were imaged in three dimensions by x-ray microtomography span from Early to Middle Devonian, indicating a maximum age of late Middle Devonian (Gadd et al., 2017).

Conodonts within clasts in debris flow breccias below the Cardiac Creek SEDEX deposit give early Frasnian and early Fammenian (Late Devonian) ages, with the latter likely indicating the age of deposition (Paradis et al., 1998). The Akie HEBS horizon is (partly) hosted within this breccia unit (Sim, 2016), and this Late Devonian age is likely the deposition age for the Akie HEBS. Collectively, the broadly similar ages for the Akie and Yukon HEBS occurrences indicate that they represent an event horizon, or horizons (see below), deposited within a relatively short period of time over a wide areal range, perhaps on a basinal scale.

At each of the HEBS deposits in Yukon, there was previously thought to be only a single stratiform and stratabound mineralized layer (bed) of variable thickness, averaging 5 to 15 cm (Goodfellow, 2002). The HEBS mineralization at Akie is also recognized to be a single horizon (Sim, 2016) of compara-

ble thickness (estimated at 10–20 cm). However, recent investigations indicate that the HEBS mineralization in at least one general area (Peel River localities) occurs in three distinct, discrete horizons separated by meters of shale (Gadd and Peter, 2018).

Yukon HEBS occurrences display strong similarities in their stratigraphic profiles. A distinctive unit termed the 'limestone ball' member comprised of 1 to 1.5 m diameter calcareous concretions within a matrix of shale occurs in the footwall, and extend upward to within <1 m to approximately 2 m of the HEBS mineralization. This unit varies between 2 to 20 m in thickness. A <1 m to approximately 2 m unit of carbonaceous to siliceous shale with centimetre scale barite and calcite nodules overlies the limestone ball member, and separates it from the mineralization. The immediate hanging wall to mineralization is a carbonaceous, siliceous shale to black-cherty shale that is in sharp contact with mineralization (e.g. Goodfellow et al., 2010). A salient distinction of the Akie HEBS from Yukon HEBS is the conspicuous absence of the limestone ball member in the stratigraphic section at Akie. Indeed, at Akie, fossiliferous (crinoids, bivalves, corals, bryozoans, stromatoporoids) limestone forms the immediate hanging wall to the HEBS. According to interpretations of the drill logs and sections for the nine drill core intersections of HEBS there, the HEBS mineralization occurs at a bathymetric high (shelf-slope transition?), and extends away from it to a more distal facies setting. This provides (still circumstantial) evidence that the mineralization is spatially (and perhaps temporally also) associated with transgressive and/or regressive events (see Gadd and Peter, 2018, for discussion). The lack of a distinctive calcareous concretion unit (a.k.a. limestone ball member) at Akie is likely caused by differences in water depth.

The uppermost HEBS layer in Yukon occurs at the top of the Road River Group, which is where it is interpreted at the Akie property. There are regional differences in nomenclature between lithologies in the Kechika Trough versus those in the Selwyn Basin to the north, however there is consensus that the Road River Group is equivalent throughout (at least from a lithologic standpoint). If the HEBS layer at the Akie property is Fammenian (Late Devonian), and Givetian in Yukon exposures of the Nick-type mineralization, then it is possible that the contact between Road River Group and overlying sediments is diachronous across the basin.

Bulk geochemical composition

Yukon HEBS mineralization contains up to 7.0 weight % Ni, 2.3 weight % Zn, 0.33 weight % Mo, Pt (511 ppb), Pd (202 ppb), Ir (10.9 ppb), Ru (12 ppm), Re (25.8 ppm), Se (0.57 weight %) and As (1.1 weight %) (Gadd et al., 2017). The Akie HEBS mineralization displays element enrichments in Zn, Ni, U, V, P, Cr and Se, among others (Sim, 2016). The mineralized interval in hole A-10-72 grades 7.4 weight % Fe, 2.69 weight % Zn, 0.75 weight % P, and 0.6 weight % Ni, 710 ppm As, 450 ppm Cu, 195 ppm Se, 170 ppm V, 128 ppm Mo, 111 ppm Co,

57 ppm U, 4.36 g/t Ag, 0.11 g/t Au, 28 ppb Pt, and 126 ppb Pd (Canada Zinc Metals Corp., unpublished). The mineralized interval in hole A-13-103 grades 0.85 weight % Fe, 0.39 weight % Zn, 3.80 weight % P, and 0.89 weight % Ni, 220 ppm As, 94 ppm Cu, 431 ppm Se, 111 ppm V, 58 ppm Mo, 38 ppm U, 18 ppm Co, 1.1 g/t Ag, 1.9 ppb Au, 36 ppb Pt, and <10 ppb Pd (Canada Zinc Metals Corp., unpub. data, 2010). The atypical metal enrichment suite of Ni and Zn in both Yukon and Akie HEBS occurrences supports a common genetic origin. These and the other enriched elements are all present in seawater and their abundances in seawater and sediments are redox controlled (Lehmann et al., 2007).

Mineralogy

The mineralogy of Yukon HEBS in generally quite similar, with the following metallic minerals: pyrite, millerite (NiS), vaesite (NiS_2), gersdorffite (NiAsS), sphalerite. Non-sulphide minerals are predominantly quartz, barite, apatite, pyrobitumen and trace to minor hyalophane (Ba-K feldspar) and K feldspar. Metallic minerals comprise approximately 60 volume %, with non-sulphide gangue minerals comprising the remainder (Hulbert et al., 1992).

At Akie, the HEBS mineralization comprises the following metallic minerals: pyrite, sphalerite, chalcopyrite, millerite, gersdorffite, clausthalite (PbSe) and pentlandite; vaesite has not been identified. In contrast to Akie, clausthalite has not been documented in Yukon HEBS. The reason for this is not understood, but may it be because vaesite is the principal/sole residence site for Se in Yukon HEBS. Similarly, pentlandite $((Fe,Ni)_9S_8)$ which is present at Akie, is not identified in Yukon HEBS, perhaps because other Ni-bearing sulphides (e.g. vaesite) are the principal residence(s) for the Ni. Non-sulphide minerals at Akie are apatite, calcite, dolomite, quartz, and muscovite.

The colour variability and zoning in sphalerite (in textural equilibrium with an iron sulphide phase), and the MLA distinction between low- and high-Fe varieties, in the Akie HEBS indicates variable Fe contents, which may reflect fluctuating sulphur activity (Scott and Barnes, 1971) during primary precipitation, or subsequent modification (e.g. during deformation and metamorphism).

The presence of chalcopyrite disease in the Akie HEBS sphalerite presents a conundrum. Viable proposed mechanisms for its formation are exsolution or replacement by copper-bearing fluids (Barton and Bethke, 1987; Eldridge et al., 1988). Current genetic models for HEBS are myriad and interpreted sources of metals include seafloor hydrothermal, ambient seawater / phosphogenesis / high organic productivity, and extra-terrestrial (e.g. Hulbert et al., 1992; Lehmann et al., 2007; Goodfellow et al., 2010). If the chalcopyrite disease is a primary feature, this would support a seafloor hydrothermal origin. However, if it is a secondary feature, it may be related to migration of copper-bearing fluids and replacement of pre-existing Fe-bearing sphalerite.

Mineral textures

Yukon HEBS contain ubiquitous framboidal pyrite (e.g. see figure 3D of Goodfellow et al., 2010), as does the Akie HEBS (see Fig. 5b). The most commonly accepted mechanisms for pyrite framboid formation is crystallization in a water column (synsedimentary) or within fine grained unconsolidated sediments in the shallow subsurface (early diagenetic) (e.g. Wilkin and Barnes, 1997). Apatite patches and nodules are evident in the Akie HEBS (see light purple colour in Fig. 6b), and also present in Yukon HEBS.

Replaced 'cellular' materials are a characteristic texture observed in the Akie HEBS. Similar features have been documented in Yukon HEBS, but previous authors (Orberger et al., 2003; Goodfellow et al., 2010) have not specified what type of cells they might be (animal or plant). However, during recent geological sampling by us at the Peel River, Yukon HEBS locality, we have documented abundant woody plant fossils directly within the mineralization (see Gadd and Peter, 2018, for details). We therefore surmise that the cellular textures present in the Akie mineralization (e.g. Fig. 5d), and in the other Yukon HEBS mineralization (e.g. figures 4A of Gadd et al., 2017, and 1B of Orberger et al., 2003, which misidentifies the cellular structures as tubeworm tubes) are plant material that has been selectively replaced by sulphides. The ubiquity of fossilized, sulphide mineralized plant debris in several Yukon localities and at Akie strongly suggests that this feature should be accounted for in any genetic model developed for these deposits.

Conclusions

Mineralogical work done to date on the Akie HEBS has shown strong similarities (and some differences) with Yukon HEBS occurrences. Complex folding and structural thickening have modified primary textures, element siting and grade of mineralization. We have shown that MLA analysis is a useful tool ideally suited for investigating the mineralogy of these occurrences, and is ideally suited for characterizing minor metal bearing phases not readily identifiable with a petrographic microscope. This technique is also particularly useful in identifying the composition of the carbonaceous shale clasts, as they are mostly opaque in transmitted light.

Future work

Fieldwork originally planned for the 2017 field season at the Akie property was not completed due to a washout of the access road to the property. However, this work is planned for the 2018 field season. Laboratory work will also focus on identification of the platinum group element-bearing (PGE) phases, and the salient controls on mineralization.

Acknowledgments

References

Barton, P.B., Jr. and Bethke, P., 1987. Chalcopyrite disease in sphalerite: Pathology and epidemiology; American Mineralogist, v. 72, p. 451–467.

Eldridge, C.S., Bourcier, W.L., Ohmoto, H., and Barnes, H.L., 1988. Hydrothermal inoculation and incubation of the chalcopyrite disease in sphalerite; Economic Geology, v. 83, p. 978–989.

Fandrich, R., Gu, Y., Burrows, D., and Moeller, K., 2007. Modern SEM-based mineral liberation analysis; International Journal of Mineral Processing, v. 84, p. 310–320.

Ferri, F., Rees, C., Nelson, J., and Legun, A., 1999. Geology and mineral deposits of the northern Kechika Trough between Gataga River and the 60th Parallel; B.C. Ministry of Energy and Mines Bulletin, v. 107, 122 p.

Gadd, M.G. and Peter, J.M., 2018. Field observations, mineralogy and geochemistry of Middle Devonian Ni-Zn-Mo-PGE hyper-enriched black shale deposits, Yukon; *in* Targeted Targeted Geoscience Initiative: 2017 report of activities, volume 1, (ed.) N. Rogers; Geological Survey of Canada, Open File 8358, p. 193–206.

Gadd, M.G., Peter, J.M., Goodfellow, W.D., Jackson, S., and Yang, Z., 2017. Geology, geochemistry and mineralogy of hyper-enriched black shale deposits, Yukon; *in* Proceedings of Exploration 17: Sixth Decennial International Conference on Mineral Exploration, (ed.) V. Tschirhart and M.D. Thomas; Decennial Mineral Exploration Conferences, Toronto, Ontario, p. 841–845.

Goodfellow, W.D., 2002. A meteoritic impact origin for Late Devonian Ni-PGE sulphide and associated tsunami deposits, northern Yukon, Canada; *in* 11th Quadrennial IAGOD Symposium and Geocongress, Windhoek, Namibia, Extended Abstracts Volume, (ed.) L.J. Robb and R. Montjoie; International Association on the Genesis of Ore Deposits, 1 CD-ROM, 4 p.

Goodfellow, W.D., 2007. Base metal metallogeny of the Selwyn Basin, Canada; *in* Mineral Deposits of Canada: A Synthesis of Major Deposit-Types, District Metallogeny,

the Evolution of Geological Provinces, and Exploration Methods, (ed.) W.D. Goodfellow; Geological Association of Canada, Mineral Deposits Division, Special Publication no. 5, p. 553–579.

Goodfellow, W.D., Geldsetzer, H., Gregoire, C., Orchard, M., and Cordey, F., 2010. Geochemistry and origin of geographically extensive Ni-(Mo, Zn, U)-PGE sulphide deposits hosted in Devonian black shales, Yukon; TGI-3 Workshop: Public Geoscience in Support of Base Metal Exploration: Programme and Abstracts, Vancouver, British Columbia, p. 15–18.

Gottlieb, P., Wilkie, G., Sutherland, D., Ho-Tun, E., Suthers, S., Perera, K., Jenkins, B., Spencer, S., Butcher, A., and Rayner, J., 2000. Using quantitative electron microscopy for process mineralogy applications; Journal of The Minerals, Metals & Materials Society, v. 52, p. 24–25.

Gu, Y., 2003. Automated scanning electron microscope based mineral liberation analysis; Journal of Minerals and Materials Characterization and Engineering, v. 2, p. 33–41.

Horan, M.F., Morgan, J.W., Grauch, R.I., Coveney, R.M., Jr., Murowchick, J.B., and Hulbert, L.J., 1994. Rhenium and osmium isotopes in black shales and Ni-Mo-PGE-rich sulfide layers, Yukon Territory, Canada, and Hunan and Guizhou provinces, China; Geochimica et Cosmochimica Acta, v. 58, p. 257–265.

Hulbert, L.J., Grégoire, D.C., Paktunc, D., and Carne, R.C., 1992. Sedimentary nickel, zinc, and platinum-group-element mineralization in Devonian black shales at the Nick Property, Yukon, Canada: a new deposit type; Exploration and Mining Geology, v.1, p. 39–62.

Jowitt, S.M. and Keays, R.R., 2011. Shale-hosted Ni-(Cu-PGE) mineralisation: A global review; Transactions of the Institution of Mining and Metallurgy (Applied Earth Science), v. 120, p. 187–197.

Lefebure, D.V., 1995. Two intriguing mineral deposit profiles for British Columbia; *in* Geological Field Work 1994; British Columbia Geological Survey Branch, Paper 1995-1, p. 491–499.

Lehmann, B., Nägler, T.F., Holland, H.D., Wille, M., Mao, J., Pan, J., Ma, D., and Dulski, P., 2007. Highly metalliferous carbonaceous shale and Early Cambrian seawater; Geology, v. 35, p. 403–406.

MacIntyre, D.G., 1998a. Geology, geochemistry and mineral deposits of the Akie River Area, northeast British Columbia; British Columbia Ministry of Energy and Mines Bulletin 103, 93 p.

MacIntyre, D.G., 1998b. Geology of the Akie River Area, northeast British Columbia, British Columbia; British Columbia Ministry of Energy and Mines Bulletin 103, scale 1:100 000.

MacIntyre, D.G., 2005. Geological report on the Akie Property, Omineca Mining Division, Northeast British Columbia; Mantle Resources Inc., NI 43-101 Technical Report, 54 p.

Paradis, S., Nelson, J.L., and Irwin, S.E.B., 1998. Age constraints on the Devonian shale-hosted Zn-Pb-Ba deposits, Gataga district, northeastern British Columbia, Canada; Economic Geology, v. 93, p. 184–200.

Scott, S. D. and Barnes, H.L., 1971. Sphalerite geothermometry and geobarometry; Economic Geology, v. 66, p. 653–669.

Sim, R.C., 2016. Mineral resource estimate for the Akie Zinc-Lead-Silver Project, British Columbia, Canada; Canada Zinc Metals Corp., NI 43-101 Technical Report, 159 p.

Wilkin, R.T. and Barnes, H.L., 1997. Formation processes of framboidal pyrite; Geochimica et Cosmochimica Acta, v. 61, p. 323–339.

Are there genetic links between carbonate-hosted barite-zinc-lead sulphide deposits and magnesite mineralization in southeast British Columbia?

S. Paradis[1] and G.J. Simandl[2,3]

[1] *Geological Survey of Canada, 9860 West Saanich Road, Sidney, British Columbia, V8L 4B2*

[2] *British Columbia Geological Survey, Ministry of Energy and Mines, Victoria, British Columbia, V8W 9N3*

[3] *University of Victoria, School of Earth and Ocean Sciences, Victoria, British Columbia, V8W 2Y2*

Abstract

Paleozoic carbonate-hosted barite-sulphide deposits in southeast British Columbia are hosted by Middle to Upper Cambrian massive to bedded dolostone of the Jubilee Formation (Grotto, Jubilee, Silver Giant, Lead Mountain, and Lancaster), and Middle Ordovician to Silurian massive and brittle dolostone of the Beaverfoot-Brisco Formation (Pedley). These deposits share characteristic of i) veins; ii) open-space filling of cavities, fractures, and breccias; and iii) stratabound replacement of host dolostone. The Middle Cambrian Cathedral Formation hosts numerous stratabound sparry magnesite occurrences including the Mount Brussilof magnesite deposit and Mississippi Valley-type deposits (e.g. Kicking Horse, Monarch, Munroe). These occurrences and deposits are located near (below) a major unconformity, hosted by altered dolostone, and associated with hydrothermal sparry dolomite and local quartz. Most of them appear at least partly controlled by structures. The timing and nature of hydrothermal or low temperature metamorphic fluids responsible for the formation of the above deposits, sparry dolomite, and creation or recrystallization of sparry magnesite is the subject of ongoing and future studies.

Introduction

This report summarizes the 2017 field activity that focused on selected carbonate-hosted barite-sulphide deposits (Pedley, Grotto-Maverick, Silver Giant, Lead Mountain and Lancaster) and a magnesite deposit (Mount Brussilof) located in the 'carbonate corridor' of the Canadian Cordillera in southeast British Columbia (Fig. 1). It compliments a 2016 study on Mississippi Valley-type (MVT) mineralization (Paradis and Simandl, 2017).

The main objectives of this study are to: i) document carbonate-hosted barite-sulphide deposits from a wide stratigraphic range (Mesoproterozoic to upper Devonian); and ii) sample the host rocks and mineralization for geochemical and geochronological studies to provide constraints on the timing and processes of ore formation.

This activity is part of a broader project investigating the geological and genetic links between various types of mineralization (e.g. Mississippi Valley-type, carbonatite-related REE, magnesite) in terms of large-scale fluid flow and tectonic processes operating in sedimentary basins. The spatial coexistence of these types of deposits in southeastern British Columbia with intrusive breccia diatremes (Helmstaedt et al., 1988; Pell, 1994) suggests deep-seated structural control and several successive periods of mineralization.

Physical and geochemical parameters, depositional conditions, age of formation, and the origins of metals and sulphur will be examined to define the geochemistry of the ore-forming solutions/fluids with the goals to constrain the ore-forming processes of the deposit-types.

Key Activity Highlights and summary

Three types of barite-sulphide mineralization from the 'carbonate corridor' of the southern Canadian Cordillera were investigated. However, most of the examined deposits share characteristics with more than one of the following categories: i) vein; ii) open-space filling of cavities, fractures, and breccias; and iii) stratabound replacement of host dolostone by sphalerite, galena, pyrite, and barite.

For instance, the majority of barite-sulphide deposits are stratabound vein systems located at or close to geological contacts and/or unconformities. Additionally, they are accompanied by breccias and replacement of the host dolostone by barite and sulphides (e.g. Silver Giant, Jubilee, Lancaster, and Lead Mountain deposits). Mineralized zones are hosted by dolostone and associated with hydrothermal sparry dolomite and locally quartz. Sparry dolomite occurs in a variety of settings including intergranular porosity within the dolostone, cavity and fracture fill, and zebra textures. Mount Brussilof magnesite deposit is a stratabound deposit of unconfirmed origin in Middle Cambrian carbonates of the Cathedral Formation.

These deposits occur in carbonate platformal rocks, but they are not restricted to a single stratigraphic level. Minerali-
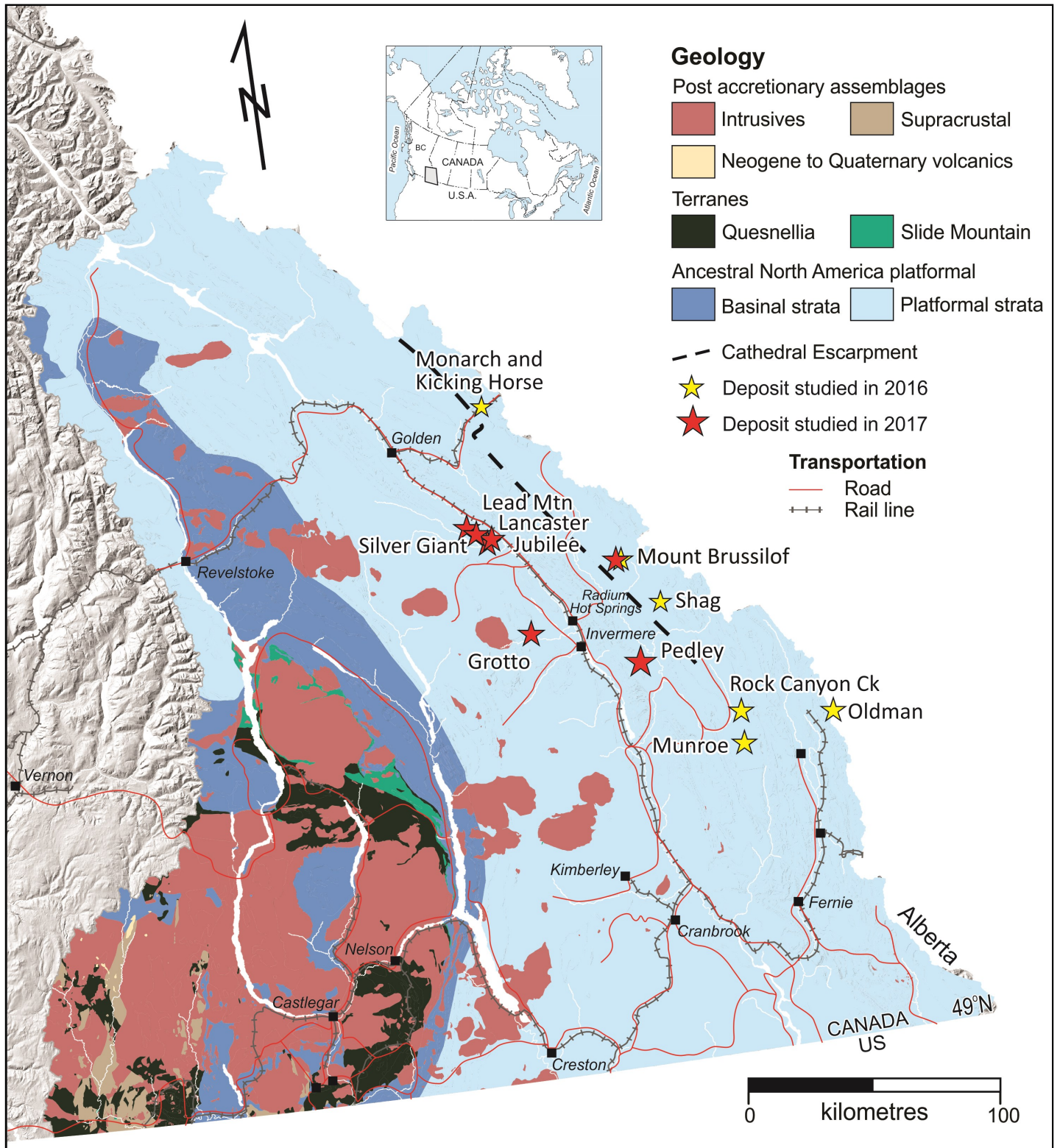
Figure 1. Regional geological map of south-eastern British Columbia showing the location of the Zn-Pb sulphide deposits, Rock Canyon Creek REE-fluorite deposit and the Mount Brussilof magnesite deposit. Modified from Katay (2017). Terranes are from BC digital geology map (Cui et al., 2015).

zation is encountered in the Middle Cambrian, Upper Cambrian, Middle Ordovician-Silurian, and Upper Devonian. Based on the number of mineral occurrences and deposit tonnage, the Cambrian carbonates seem to be the most favourable host rocks.

The Middle to Upper Cambrian Jubilee Formation hosts the Silver Giant, Jubilee, Lancaster, Lead Mountain, and Grotto deposits in altered dolostone at or near to its contact with the shales of the Upper Cambrian-Ordovician McKay Group. At least locally, a regional unconformity is recognized at this contact (Pope, 1980). In the Jubilee Mountain and Lead Mountain areas, numerous occurrences of barite and/or sulphide-barite mineralization occur at this contact on the southern and northern limbs and axes of synclines and anticlines. This apparent correlation suggests that lithologies and structures influenced deposit location.

The Middle Ordovician to Silurian, massive and brittle dolostone of Beaverfoot-Brisco Formation hosts the Pedley barite (±sulphides) deposit. No Upper Devonian carbonate-hosted deposits were encountered during the 2017 field season, however several deposits studied in 2016 (Paradis and Simandl, 2017) are hosted by the Upper Devonian dolostone of the Palliser Formation (e.g. Oldman, Munroe).

Field observations

Silver Giant

Silver Giant is located on the western slopes of Jubilee Mountain, 68 km north of Invermere (Fig. 1). It was one of the larger barite-lead-zinc-antimony and cadmium producing mines of southeast British Columbia. It was discovered in 1883, but most production for lead, zinc, antimony and cadmium took place between 1947 and 1957. Barite was recovered from 1959 to 1983.

Barite-sulphide mineralization occurs in pale grey, fine-grained dolostone of the Middle to Upper Cambrian Jubilee Formation close to its contact with the shales of the McKay Group (Fig. 2a, b). The overlying McKay Group consists of recessively weathering shales, thin sandstones and dolomitic biowackestones (Reesor, 1973). Although generally conformable, locally an unconformity has been identified at this stratigraphic level (Pope, 1990).

Silver Giant orebodies occur along the nose of an overturned anticline that has been subsequently folded and faulted, and along the west limb of this anticline where it follows the contact of the Jubilee Formation/McKay Group (Hedley, 1949; British Columbia Geological Survey, 2001) The orebodies strike nearly east and dip to the southwest. The plunge of the nose is westerly, and underground development has shown it to vary from 45° near the surface to flat-lying on the No. 8 level. A large regional thrust fault has been mapped 400 m to the west and in the underground workings.

The mineralized zones consists of barite with varying amounts of sulphides, sparry dolomite, and silica replacing the dolostone and forming veins (Fig. 2c). The sulphides are mostly fine-grained galena with lesser amounts of sphalerite, pyrite, chalcopyrite, malachite, chalcocite, and bornite (Fig. 2d–f). Stibnite (Sb_2S_3; the main Sb-bearing mineral) and an unidentified grey copper mineral (possibly tennantite) were also observed.

Barite is white and it varies from fine-grained to coarse bladed crystals. Quartz and carbonates can be interstitial to the barite crystals. Galena is mostly fine-grained, forming stringers and aggregates (pods) in the coarse-grained barite (±carbonate, ±quartz) matrix of the veins. It also forms rims around the walls of cavities that are filled by coarse-grained barite. Galena is typically associated with sphalerite, pyrite, and copper minerals (mainly malachite [$Cu_2CO_3(OH)$] and azurite [$Cu_3(CO_3)_2$ $(OH)_2$]). These copper carbonate hydroxides visible on surface are interpreted as alteration products of chalcopyrite and the unidentified grey copper mineral. They form disseminated grains and patches within barite and sparry dolomite that fills cavities (Fig. 2e, f). Sphalerite has a pale yellowish to reddish colour in hand specimens and is associated with the other sulphides.

Jubilee

The Jubilee barite (±sulphides) deposit is located on the eastern slopes of Jubilee Mountain, approximately 68 km north of Invermere (Fig. 1). It consists of barite veins containing subordinate hematite, minor pyrite, and traces of sphalerite and galena. Breccia zones with angular clasts of dolostone and limestone in a granular carbonate matrix containing disseminated sulphides, and barite-sulphide filled vugs have been reported (Henkle and Willis, 2015), but were not observed during this investigation.

The main barite vein, called 'West Heli Vein' by Voyageur Industrial Ltd., is approximately 0.5 to 1 m wide, subvertical, striking 25° to 40° and hosted by altered dolostone of the Middle to Upper Cambrian Jubilee Formation adjacent to, and coplanar with, the contact between the Jubilee dolostone and the shales of the McKay Group (Fig. 3a, b). Several other barite (±sulphides) deposits on Jubilee Mountain are also located at this contact, on both the southern and northern limbs of the Jubilee Mountain Syncline. The host dolostone has a reddish to tan colour on weathered surfaces (Fig. 3c) and is pale grey on fresh surfaces. It is silicified adjacent to the veins and locally contains traces of malachite in hairline fractures and patches (Fig. 3d). Abundant veinlets and seams of hematite crosscut the barite crystals and stain its cleavages giving them a reddish appearance. Barite crystals are up to 2 cm in length. Other minerals such as pyrite, galena, sphalerite and a black unidentified mineral are interstitial to the barite crystals and occur along fractures in the dolostone.
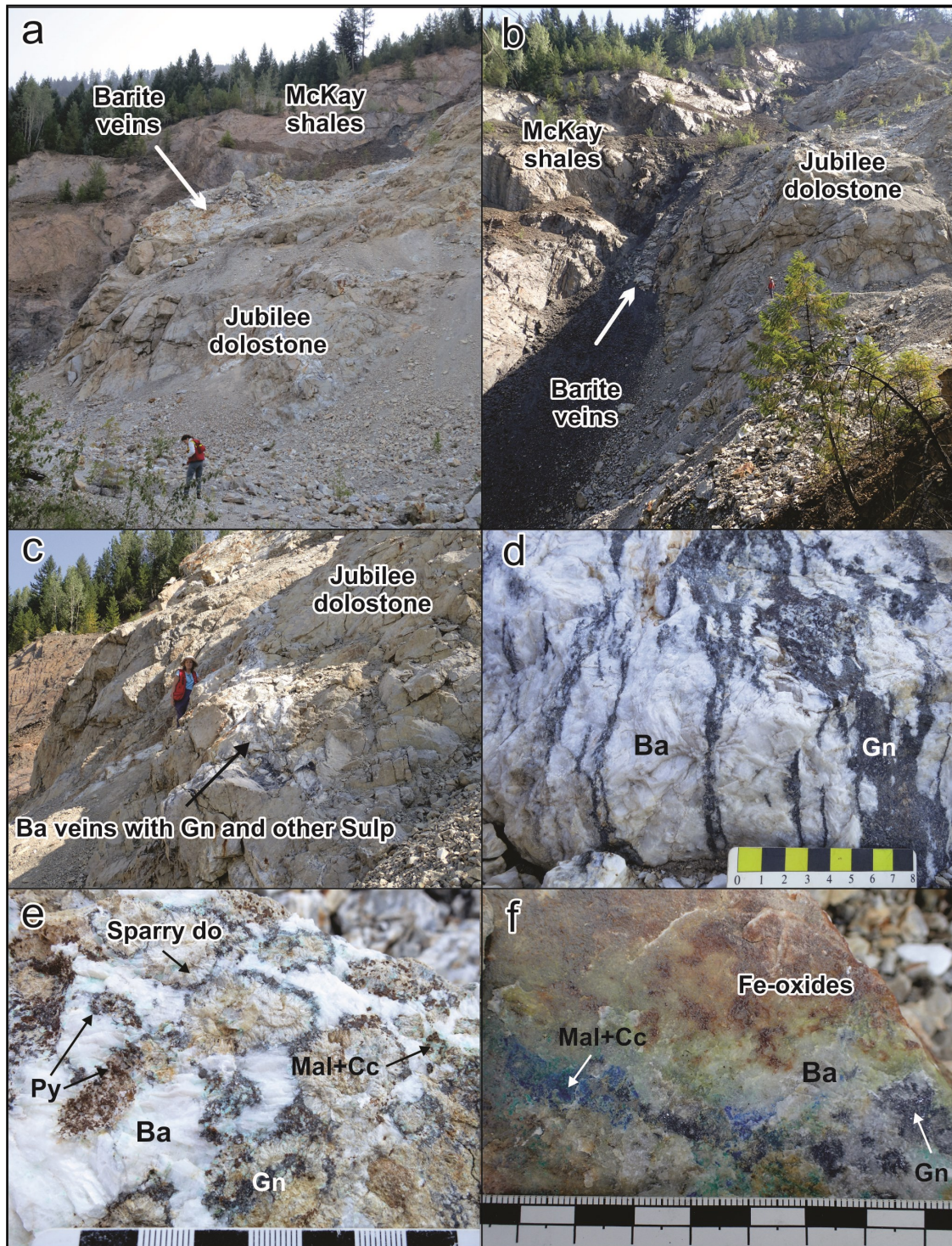
Figure 2. Silver Giant deposit. a) View of the dolostone of the Jubilee Formation in contact with the shales of the McKay Group; photo taken in the abandoned open pit of the mine. b) Looking NE along the main barite-sulphide vein in contact with the dolostone of the Jubilee Formation and the shales of the McKay Group. c) One of several subsidiary barite (Ba)-sulphide veins branching from the main vein, hosted by dolostone of the Jubilee Formation. d) Close-up photo of the barite-sulphide vein shown in C consisting mainly of barite (Ba) cut by galena (Gn) stringers. e) Open-space feature filled by sparry dolomite (Do) variably replaced by pyrite (Py) and sphalerite (not visible), and rimmed by galena (Gn), and filled by coarse-grained barite (Ba). f) Close–up photo of malachite (Mal), chalcocite (Cc) and Fe-oxide minerals associated barite (Ba).
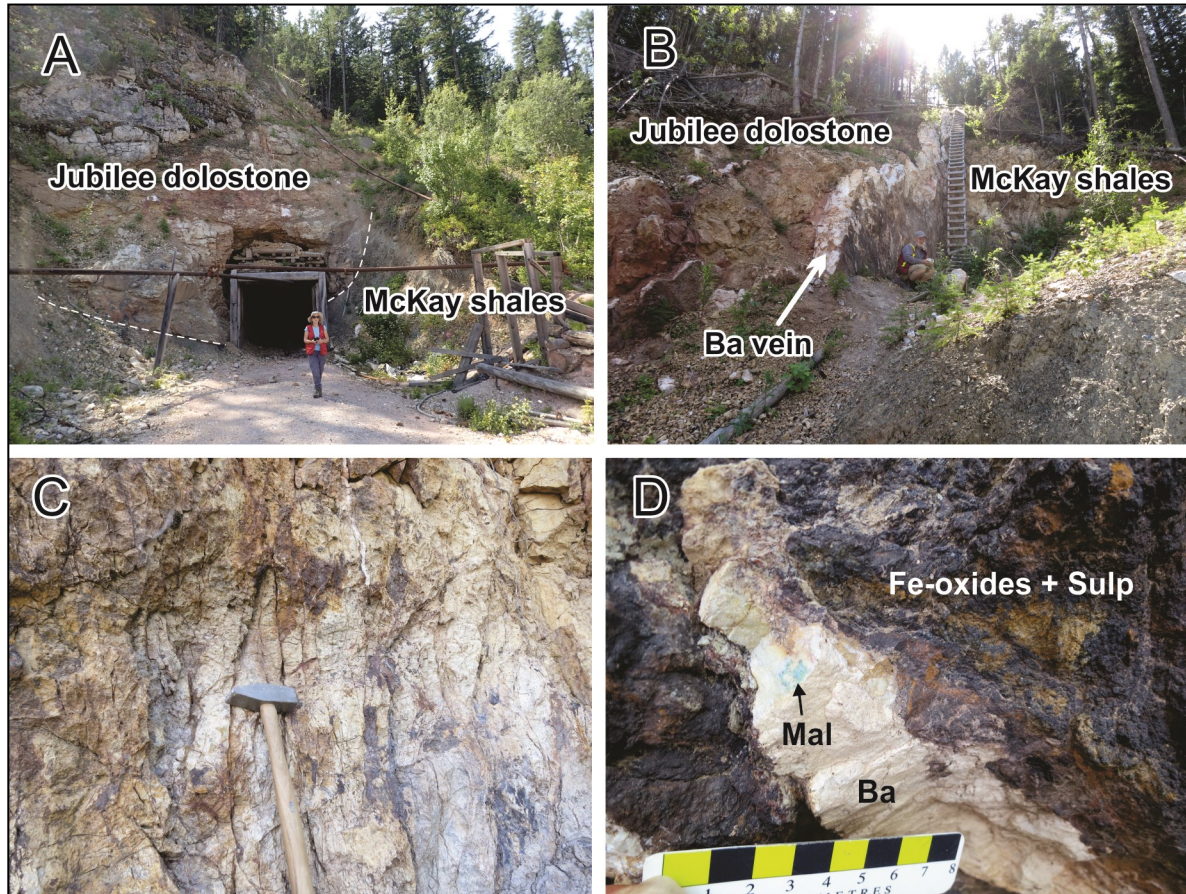
Figure 3. Jubilee deposit. a) View of the adit at the West Heli vein. The adit's entrance is at the contact between the dolostone of the Jubilee Formation and the shales of the McKay Group. b) West Heli barite vein (Ba) above the adit; the vein strikes 025° to 040° and dips vertically. c) Altered (bleached) dolostone of the Jubilee Formation that is crosscut by numerous veinlets and seams of hematite. d) Close-up photo of one of the barite veins with traces of malachite (Mal). Note the presence of abundant iron-oxides (Fe-oxides) and altered sulphides (Sulp) in the adjacent dolostone.

Lancaster

The Lancaster barite (±sulphides) occurrence is also located on the eastern slopes of Jubilee Mountain, approximately 70 km north of Invermere (Fig. 1). It is hosted by dolomitic limestone of the Upper Jubilee Formation close to its contact with shales of the McKay Group. Mineralization occurs as numerous, small, massive barite veins and vein breccias containing disseminated galena, sphalerite, chalcopyrite, malachite, and chalcocite (Fig. 4a, b). The thickest is approximately 20 cm in width.

Grotto

The Grotto sulphide occurrence (also known as the Larrabee's prospect; Fig. 5a, b) is located 26 km west-southwest of Radium Hot Springs (Fig. 1). Some disseminated pyrite, galena, sphalerite, smithsonite, and hydrozincite occur in stylolites, fractures, and breccias within the altered dolostone of the Jubilee Formation; however, most sulphides are oxidized (Fig. 5c,

d). High-grade mineralization, as recently described by Minfocus Exploration Corp. (2017), was not observed.

Lead Mountain

The Lead Mountain barite (±sulphides) occurrence is located at the top of Lead Mountain, approximately 75 km north of Invermere (Fig. 1). Mineralized outcrops show massive barite veins and breccias with traces of malachite, galena, pyrite, and possibly weathered sphalerite. These veins cut weathered, pale brown and pale grey coloured dolostone of the Jubilee Formation. The dolostone is fine to medium crystalline and contains 1 to 10% dolospar forming patches, veinlets, and cavity fills. Rhodes (1985) describes the mineralized breccias and tension fractures as located at the axis of a syncline that strikes east.

Barite is white and fine to medium-grained. It locally contains disseminated specs of malachite and azurite (Fig. 6a). It is commonly associated with oxidized pyrite (and possibly other
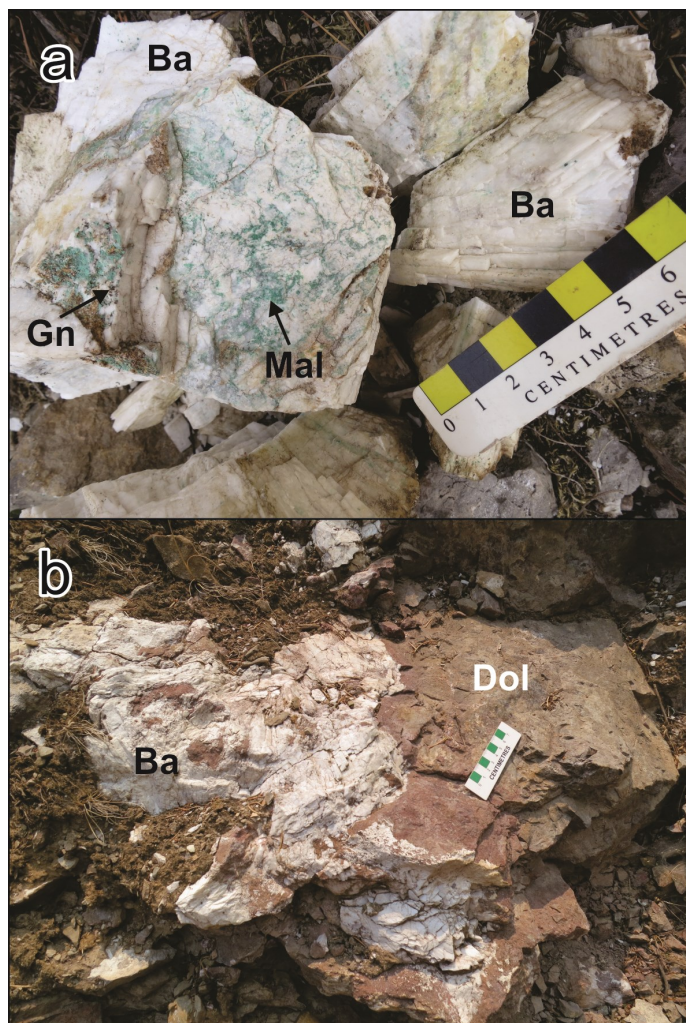
Figure 4. Lancaster deposit. a) Specimens of coarse-grained crystalline barite (Ba) with galena (Gn) and malachite (Mal). b) Irregular, coarse-grained crystalline barite (Ba) vein cutting dolostone (Dol) of the Jubilee Formation.

sulphides), which forms irregular patches and stringers in the barite and dolostone host rock (Fig. 6b). At least two adits intercept the mineralization at depth. Galena (and possibly sphalerite) observed in blocks of dolostone found adjacent to the entrance of the lower adit is fine-grained. It lines cavities within white sparry dolomite patches and it forms fine stringers in the dolostone.

Pedley deposit

The Pedley prospect consists of barite- (and minor sulphides) cemented veins and breccias hosted by bedded to massive and blocky, light grey dolostone and dark grey limestone of the Upper Ordovician to Middle Silurian Beaverfoot-Brisco Formation. It is located on a steep, north-facing slope, 2.5 km northeast of Mount Pedley and 82 km southeast of Invermere (Fig. 1). The Beaverfoot-Brisco Formation is tectonically over-

lain by the quartzite of the older Ordovician Mount Wilson Formation. The contact between the two formations is sharp and concordant. Bedding is overturned, striking 300° at 25° dip. The quartzite is a white to pale grey, medium-grained, thin - to thick-bedded and partly cross-stratified quartz sandstone that is well-cemented by clear quartz grains.

The deposit consists of white, massive, coarse-grained barite veins and barite cemented breccias with traces of galena and sphalerite (Fig. 7a). The main vein that extends over several hundred of metres is subvertical and strikes 250° (Fig. 7b). The width of the main vein varies from 1 to 5.5 m but numerous smaller veinlets branch from it (Henkle, 2016). Mason (1981) interpreted the main barite vein to occupy a tension fracture of left lateral strike-slip fault with displacement of up to 10 km. The white, coarse-grained barite-cemented dolomite breccia zone with many branches and offshoots strikes approximately northeast and dips steeply towards the north-northwest. Coarse-grained barite, cementing the breccia, contains minor concentrations of galena, sphalerite, and pyrite (Fig. 7c, d).

Mount Brussilof

The Mount Brussilof sparry magnesite deposit is located approximately 82 km northeast of Invermere on the western margin of a north-northwest trending tectonic feature commonly referred to as 'Kicking Horse Rim' (Simandl et al., 1991). This margin corresponds to the projection of the Cathedral Escarpment, a submarine paleocliff, along which there are a number of talc, magnesite, and Mississippi Valley-type Zn-Pb deposits (Simandl and Hancock, 1991; Simandl et al., 1992; McMechan, 2010; Paradis and Simandl, 2017; Johnston et al., 2017).

Mount Brussilof deposit is currently the only magnesite mine operating in Canada (Fig. 8a). It is hosted by shallow marine carbonates of the Cathedral Formation where it forms layers, lenses, pods, and irregular masses (Simandl and Hancock, 1991; Simandl et al., 1992; Fritz and Simandl, 1993). Sparry (coarse-grained) magnesite is white or pale grey in colour and buff when weathered, and nearly monomineralic (Fig. 8b). Spectacular pinolitic textures and bipolar crystal growths identical to those observed at Mount Brussilof were historically interpreted of hydrothermal origin, however similar textures also occur in evaporitic environments. The main gangue minerals (i.e. dolomite, quartz, calcite, pyrite and clay) are disseminated within the magnesite ore, fill fractures and veins, and occur as open space fillings (Fig. 8c, d; Simandl and Hancock, 1999). Pyrite is common as disseminations, irregular veinlets, and pods (Fig. 8e, f). Chalcocite, fersmite, phlogopite, talc and coarse, white, acicular palygorskite were also observed in the open pit. Boulangerite, huntite and brucite were reported by White (1972).

Two main theories addressing the origin of sparry magnesite deposits are: i) replacement of dolomitized, permeable carbonates by magnesite due to interaction with a metasomatic fluid (essentially an extreme case of dolomitization); and ii)
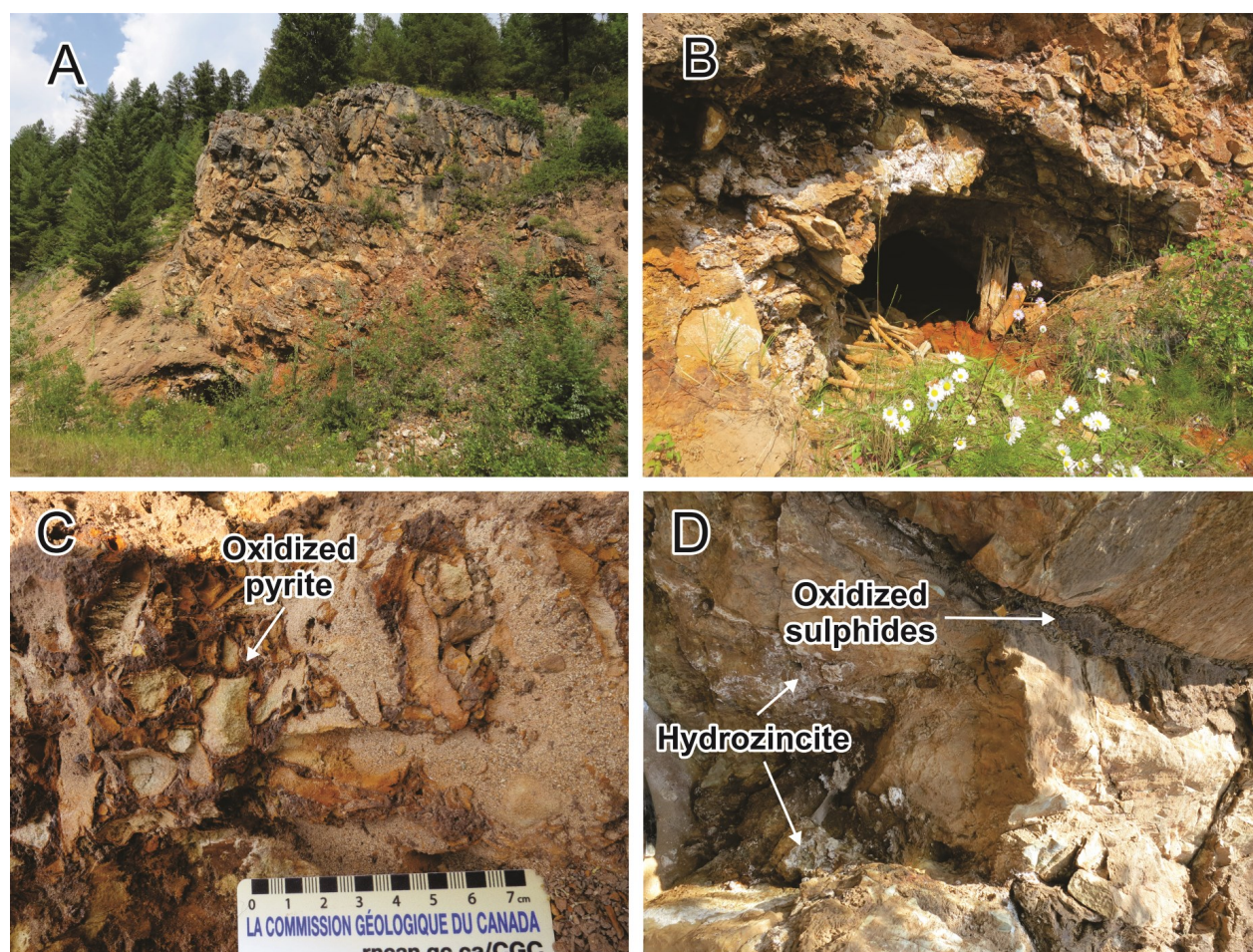
222

Figure 5. Grotto deposit. a) Main outcrops along a small forestry road on the north side of the Horsethief River. b) Adit within outcrops shown in photo A. Note the strong oxidation of the dolostone and presence of hydrozincite (white material) partially covering the outcrops. c) Oxidized pyrite veinlets in altered dolostone of Jubilee Formation. d) Vein filled by oxidized sulphides and disseminated sulphides altered to hydrozincite within the dolostone.

low temperature recrystallization of a magnesia-rich protolith (e.g. fine-grained magnesite, hydromagnesite, huntite) deposited as chemical sediments in marine or lacustrine settings and later recrystallized during diagenesis or exposure to hot fluids. The main difference between these hypotheses is the source of magnesia; external for classic metasomatic replacement and in situ in the case of diagenetic/metamorphic recrystallization (Simandl and Hancock, 1999).

In addition to magnesium, Mount Brussilof magnesite ore also contains isolated and uncommon vuggy pockets of exotic REE, Be and Nb minerals (e.g. fersmite, Nb-bearing rutile, goyazite and euclase). Niobium, Be and REE mineralization postdates magnesite formation and most likely sparry dolomite formation. Attempts are currently under way to radiometrically date the fersmite and to interpret the Ar-Ar dates on uncommon pink and pale green micas present in vugs. These age dates may provide indirect upper age bracket for MVT-related sparry dolomite and MVT mineralization itself.

Next Steps

Samples collected from the sites described above are being prepared for the following analytical studies:

- Detailed petrography, whole rock geochemistry, mineral chemistry using the electron microprobe, and where appropriate, in-situ trace element analysis using laser ablation ICP-MS. This is essential analytical work for all occurrences selected for detailed studies. The trace element composition of carbonate minerals may be particularly revealing.

- Specialty metal content (e.g. Ge, Ga, In) of sulphides in deposits will be investigated. Germanium, Ga and In content of carbonate-hosted Zn-Pb deposits in SE British Columbia is relatively low and poorly documented relative to other worldwide carbonate-hosted Zn-Pb deposits.

- Documentation of Nb-, REE-, and (possibly) Be-bearing minerals from fractures and vugs within the magnesite ore
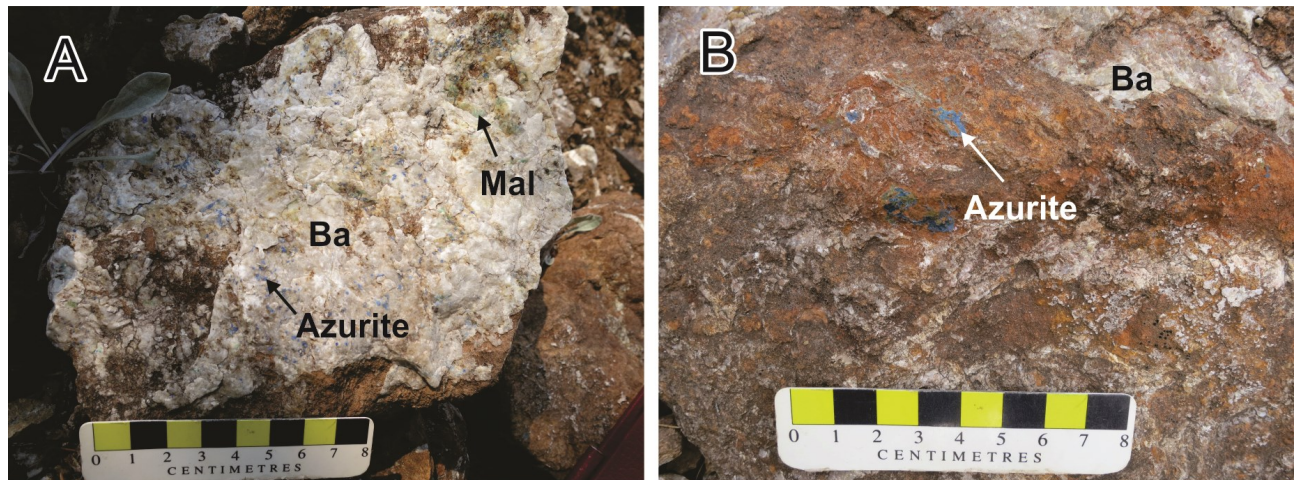
Figure 6. Lead Mountain deposit. a) White coarse-grained barite (Ba) with disseminated malachite (Mal) and azurite. b) Patch and disseminated grains of azurite in altered dolostone that is crosscut by barite (Ba) veins.
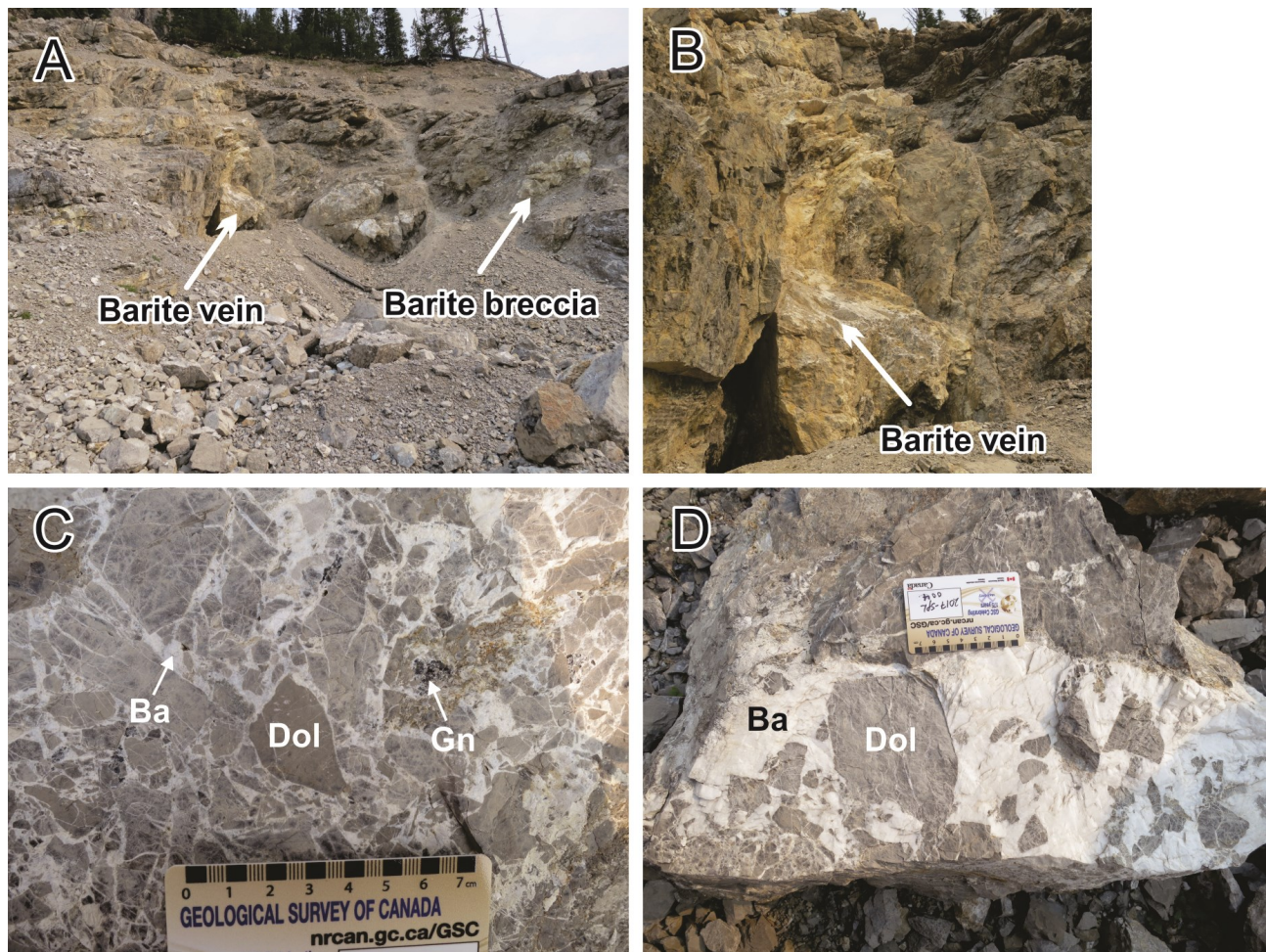
Figure 7. Pedley deposit. a) Site of old workings showing exposure of main barite vein and white barite cemented breccias. b) Main barite vein striking 250° and dipping vertically. c) Close-up of barite (Ba) cemented dolostone (Dol) breccias; note the minor amounts of galena (Gn) in barite (Ba) cement. Pyrite and sphalerite may be present in trace amounts. d) Barite (Ba) cemented dolostone (Dol) breccias.
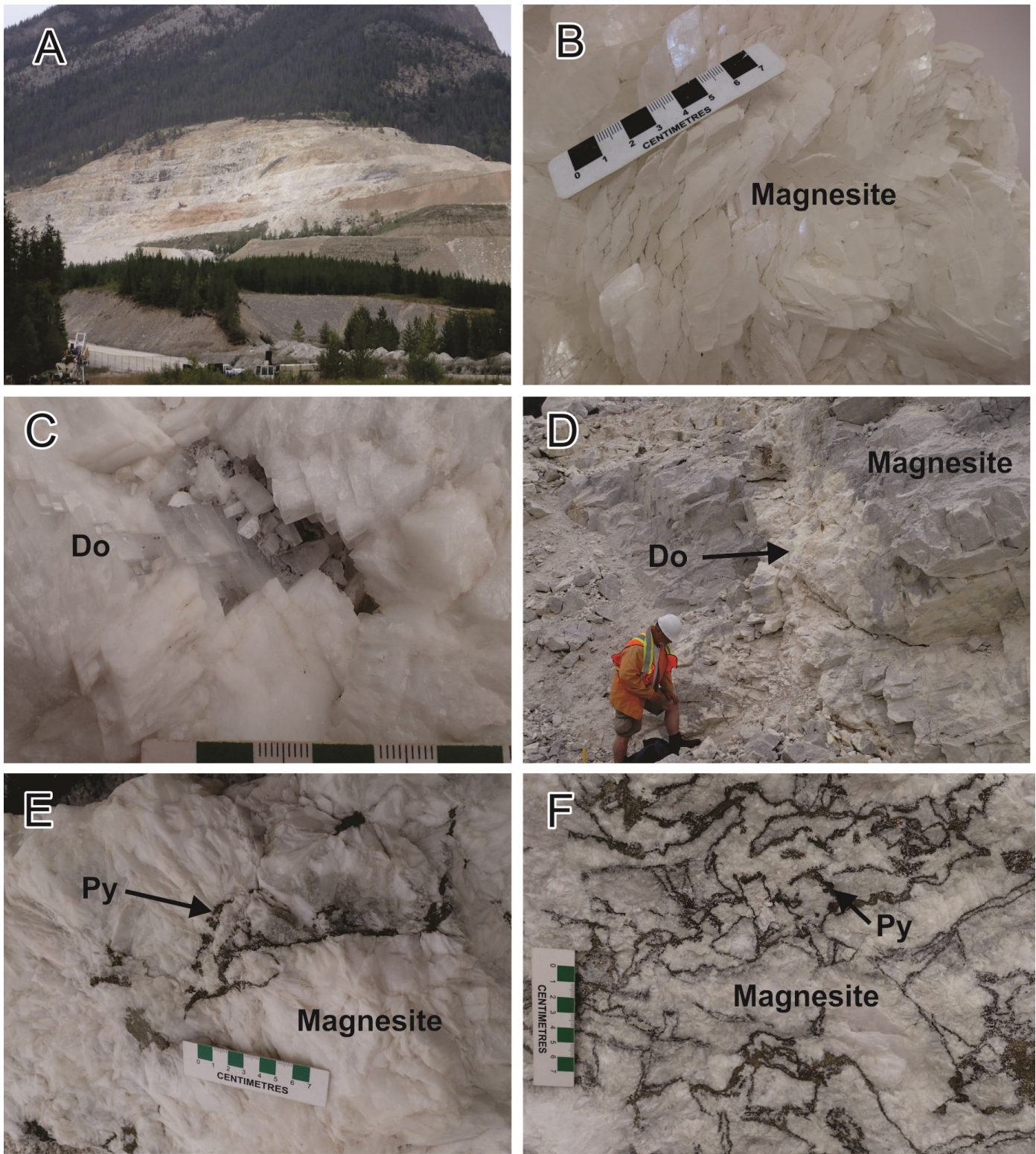
Figure 8. Mount Brussilof magnesite deposit. a) View of the Baymag Mine. b) Coarse-grained magnesite crystals. c) Sparry dolomite (Do) filling cavity in magnesite. d) White sparry dolomite (Do) vein crosscutting magnesite ore. e) Coarse-grained magnesite with fine-grained fracture-filling pyrite (Py). f) Complex network consisting of pyrite (Py) in coarse-grained magnesite.

at Mount Brussilof. This is possibly a new style of mineral occurrence in the Canadian Cordillera, resembling the style of mineralization commonly referred to as 'Alpine clefts' or 'Alpine fissures'.

- Isotopic analyses (e.g. O, C, Sr, S, Pb) of sulphides, barite, and carbonates. Isotope geochemistry is a powerful tool for determining the sources of ore-forming fluids and metals in hydrothermal mineral deposits.

- Age dating of pyrite mineralization in the carbonate-hosted deposits using the Re-Os isotope system (assuming that the Re-Os concentration is suitable) will constrain the age of the sulphide mineralization in cases where pyrite is contemporaneous with the sulphide mineralization. Age dating of dolomite-hosted fersmite that post-dates sparry magnesite at the Mount Brussilof mine by electron microprobe using a Cameca SX50 $^{238}U/^{206}Pb$ system and dating of micas hosted locally by sparry carbonates by Ar/Ar method will also be attempted. If interpretable data is obtained, the dates will help to constrain the ages of MVT mineralization, sparry dolomitization, recrystallization of sparry magnesite, and REE-fluorite mineralization at Rock Canyon Creek (Paradis and Simandl, 2017; Green et al., 2017; Hoshino et al., 2017). Based on field observations, fersmite postdates sparry dolomitization and sparry magnesite formation. Assuming a single period of sparry carbonate formation in SE BC, the fersmite date will provide a maximum age on all of the events mentioned above. It will also provide a constraint on REE and Nb remobilization from carbonatite or peralkaline intrusion-related deposits.

Acknowledgments

References

British Columbia Geological Survey, 2001. BC Minfile: Silver Giant, Silver Giant Mine, Giant Mascot, Spillimacheen. British Columbia Geological Survey, <https://minfile.gov.bc.ca/Summary.aspx?minfilno=082KNE018> [accessed on September 20, 2017].

Cui, Y., Miller, D., Nixon, G., and Nelson, J., 2015. British Columbia digital geology; British Columbia Ministry of Energy and Mines, British Columbia Geological Survey, Open File 2015-2.

Fritz, W.H. and Simandl, G.J., 1993. New Middle Cambrian fossil and geological data from the Brussilof Magnesite Mine area, southeastern British Columbia; *in* Current Research, Part A, Cordillera and Pacific Margin; Geological Survey of Canada; Paper no. 93-1A, p. 183–190.

Green, C., Simandl, G.J., Paradis, S., Katay, F., Hoshino, M., Kon, Y., Kodama, S., and Graf, C., 2017. Geological setting of the Rock Canyon Creek REE-fluorite deposit, British Columbia, Canada; *in* Geological Fieldwork 2016, British Columbia Ministry of Energy and Mines, British Columbia Geological Survey Paper 2017-1, p. 195–203.

Hedley, M.S., 1949. Spillimacheen, Silver-Lead-Zinc, Silver Giant Mines, Limited. British Columbia Ministry of Energy and Mines, British Columbia Geological Survey, Assessment Report 1949-A200-A204.

Helmstaedt, H.H., Mot, J.A., Hall, D.C., Schulze, D.J., and Dixon, J.M., 1988. Stratigraphic and structural setting of intrusive breccia diatremes in the White River - Bull River area, southeastern British Columbia; *in* Geological Fieldwork 1987, British Columbia Ministry of Energy, Mines Resources, Paper 1988-1, p. 363–368.

Henkle, W.R. and Willis, B., 2015. Technical report of the Voyageur Industrial Minerals Ltd. exploration stage barite projects, province of British Columbia, Canada; Voyageur Industrial Minerals Ltd., British Columbia Ministry of Energy and Mines, British Columbia Geological Survey, Assessment Report 35086, 151 p.

Henkle, W.R., 2016. Updated technical report of the Voyageur Industrial Minerals Ltd., barite exploration projects, province of British Columbia, Canada; Voyageur Industrial Minerals Ltd., Internal report, 113 p.

Hoshino, M., Kon, Y., Kodama, S., Simandl, G.J., Paradis, S., Green, C., Namatame, C., Matsunaga, I., and Takagi, T., 2017. Mineralogy of the Rock Canyon Creek REE-Fluorite deposit, British Columbia, Canada; *in* Geological Fieldwork 2016, British Columbia Ministry of Energy and Mines, British Columbia Geological Survey Paper 2017-1, p. 205–213.

Johnston, P.A., Collom, C.J., and Desjardins, P., 2017, Lower toe Middle Cambrian of the southern Canadian Rockies; *in* Geologic Field Trips of the Canadian Rockies: 2017 Meeting of the GSA Rocky Mountain Section, (ed.) J.C.C. Hsieh; Geological Society of America Field Guide 48, p. 71

–121.

Katay, F., 2017. Exploration and mining in the Southeast Region, British Columbia; *in* Exploration and Mining in British Columbia, 2016. British Columbia Ministry of Energy and Mines, British Columbia Geological Survey, Information Circular 2017-1, p. 73–107.

Mason, G., 1981. Pedley Property Examination Report; Bar Well Resources, Ltd., Internal Report.

McMechan, M.E., 2010. Basement controlled mineralization, intrusions and facies, southeastern British Columbia. "Two for One Exploration Targets"; Geological Survey of Canada, Open File 5874, 44 p.

Minfocus Exploration Corp, 2017. Minfocus Exploration announces encouraging results from initial field program at Peregrine Zinc property in SE British Columbia; Minfocus Exploration Corp, < http://minfocus.com/wp-content/ uploads/2017/09/MFX-News-Release-Peregrine-sampling-results-September_2017-12-FINAL.pdf> [accessed December 10, 2017].

Paradis, S. and Simandl, G.J., 2017. Is there a genetic link between the SEDEX and MVT deposits of the Canadian Cordillera?; *in* Targeted Geoscience Initiative, 2016 Report of Activities, (ed.) N. Rogers; Geological Survey of Canada, Open File 8199, p. 107–113.

Pell, J., 1994. Carbonatites, nepheline syenites, kimberlites and related rocks in British Columbia; British Columbia Ministry of Energy, Mines and Petroleum Resources, Geological Survey Branch, Bulletin, No. 88, 136 p.

Pope, A.J., 1990. Geology and mineral deposits of the Toby-Horsethief Creek area, northern Purcell Mountains, southeast BC; British Columbia Ministry of Energy, Mines and Petroleum Resources, Open File 1990-26, 53 p.

Reesor, J.E., 1973. Geology of the Lardeau Map Area - East Half, British Columbia; Geological Survey of Canada, Ottawa, Memoir 369, 145 p.

Rhodes, D., 1985. Assessment report, geochemistry, geology, trenching, channel sampling, Mitten and Luck properties, Golden Mining Division; British Columbia Assessment Report 13290, 37 p.

Simandl, G.J. and Hancock, K.D., 1991. Geology of the Mount Brussilof magnesite deposit, southeastern British Columbia; Geological Fieldwork 1990, British Columbia Ministry of Energy and Mines, Paper 99-1, p. 269–278.

Simandl, G.J. and Hankock, K.D., 1999. Sparry Magnesite; *in* Selected British Columbia Mineral Deposit Profiles, Volume 3 - Industrial Minerals and Gemstones, (ed.) G.J. Simandl, Z.D. Hora and D.V. Lefebure; British Columbia Ministry of Energy, Mines and Petroleum Resources, Open File 1999-10, p. 24E-1–24E-3.

Simandl, G.J., Hancock, K.D., Hora, Z.D., MacLean, M.E., and Paradis, S., 1991. Regional geology of the Mount Brussilof Magnesite deposit, south-eastern British Columbia, Canada; *in* Proceedings of the 27th Forum on the Geology of Indus-

trial Minerals, (ed.) Z.D. Hora, W.N. Hamilton, B. Grant and P.D. Kelly; Alberta Geological Survey – Alberta Research Council, Information Series 115, p. 57–65.

Simandl, G.J., Hancock, K.D., Fournier, M., Koyanagi, V.M., Vilkos, V., Lett, R., and Colbourne, C., 1992. Geology and major element geochemistry of the Mount Brussilof magnesite area, southeastern British Columbia (NTS 82J/12, 13); British Columbia Ministry of Energy and Mines, Open File 1992-14, 19 p.

White, G.P.E., 1972. Mineralogy of the Baymag Mines Ltd. Magnesite Prospect, South Kootenay area, BC; Acrers Western Ltd., Internal Report, 17 p.

Elucidating mineralizing fluid pathways from the geophysical responses to hydrothermal alteration: Integrated 3D modelling of lithogeochemical, petrophysical, seismic and magnetotelluric data, Lalor volcanogenic massive sulphide deposit, Manitoba

E.M. Schetselaar[1], G. Bellefleur[1], J.A. Craven[1], S.M. Ansari[1] and R.J. Enkin[2]

[1]*Geological Survey of Canada, 601 Booth Street, Ottawa, Ontario, K1A 0E8*
[2]*Geological Survey of Canada, 9860 West Saanich Road, Box 6000, Sidney, British Columbia, V8L 4B2*

Abstract

This research activity aims a developing a better understanding of the geophysical response of hydrothermally-altered rocks associated with volcanogenic massive sulphide (VMS) deposits. Integrated modelling of physical rock property, whole rock geochemistry and 3D seismic data from the Lalor VMS deposit, Snow Lake, Manitoba enhanced insight into the seismic responses of hydrothermally-altered rocks in the footwall of the massive sulphide ore zone. Multivariate regression of P-wave velocity and density on lithogeochemical proxies for protolith composition, mineralization and hydrothermal alteration suggests that hydrothermal alteration in the footwall of the Lalor deposit enhanced acoustic impedance contrast between mafic to felsic volcanic units. Compositional variations between mafic, intermediate and felsic volcanic rocks, as modelled by the $log(Zr/TiO_2)$ immobile element ratio, remains the predominant factor that controls seismic response, independent from the intensity of hydrothermal alteration. The results obtained from the multivariate regression model are further corroborated by seismic forward modelling experiments, yielding enhanced seismic reflectivity in the intensely-altered footwall when alteration proxies are included in the 3D seismic rock property models. In parallel, geophysical response modelling of magnetotelluric (MT) data will be developed based on forward and inverse modelling routines on tetrahedral meshes, which yield results that are compatible with the general geological structure of the deposit. Initial unconstrained 3D MT inversions show a conductive zone between 600 to 800 m depth corresponding to the Lalor deposit, as well as, a highly conductive zone between depths of 500 to 1500 m, about 0.5 to 1.2 km to the southwest of the deposit.

Introduction

Volcanogenic massive sulphide (VMS) deposits have contrasting physical properties with their host rocks, which allows for their subsurface detection using a number of geophysical methods. Although this direct detection of sulphide ore has resulted in significant discoveries in the past, the extent to which geophysical signatures of the more distal VMS ore system elements, such as those from altered host rocks of hydrothermal conduits, can be detected and imaged, is poorly known. Imaging these host rock signatures, however, is important, as it could provide insight into the architecture of mineralizing fluid pathways drill core and potentially inform regional-scale targeting strategies of VMS ore systems.

This research activity aims at tracing the effects of hydrothermal alteration on host rock geophysical signatures by integrated analysis of lithogeochemical, petrophysical, seismic and magnetotelluric data from the Lalor VMS deposit, Snow Lake, Manitoba. Considering that both conformable and disconformable alteration zones (even though they are commonly transposed by tectono-metamorphic events) are typically orders of magnitude larger in size than the sulphide ore zones themselves, identifying their signatures should provide a more robust exploration target and give key insights on the overall structure of VMS ore systems. The research questions identified at the start of this activity were:

1. Is there a measurable effect of hydrothermal alteration on physical rock properties (e.g. density, conductivity, P-wave and shear-wave velocities)?

2. What are the lithogeochemical and mineralogical variations that are responsible for these variations in physical rock properties?

3. Can proxies be defined from major oxides and trace element analyses to separately model the effects of hydrothermal alteration from those originating from variations in protolith composition?

4. If so, can this model be subsequently expanded from lithogeochemical - petrophysical multivariate sample space to 3D coordinate space to support interpretation of the hydro-

thermal vent stockwork using forward and inverse models of seismic and magnetotelluric surveys?

Geological Setting

The Lalor volcanogenic massive sulphide deposit is located near Snow Lake, Manitoba, about 700 km north of Winnipeg, and is hosted in volcanic and volcaniclastic rocks of the Snow Lake arc assemblage in the eastern Paleoproterozoic Flin Flon greenstone belt. The 1.89 Ga Snow Lake arc assemblage is a ≥6 km thick section comprised of three volcanic sequences displaying a geodynamic evolution from primitive arc (Anderson sequence) to mature arc (Chisel sequence), followed by arc-rifting (Snow Creek sequence; Bailes and Galley, 1999). The Snow Lake arc assemblage is affected by at least four episodes of deformation (Galley et al., 1993). The deformation events are related to fold-and-thrust–style stacking and interleaving of volcanic assemblages and younger sedimentary rocks during the Trans-Hudson orogeny (Kraus and Williams, 1999). The D1 and D2 events produced tight to isoclinal, south-verging folds, shallowly dipping thrusts and the main foliation (Kraus and Williams, 1999; Bailes et al., 2013). These structures are refolded by north-northeast-trending F3 folds and an associated S3 crenulation cleavage (Kraus and Williams, 1999). The F4 folds with east-trending axes locally overprint F3 folds (Kraus and Williams, 1999). The Snow Lake assemblage was metamorphosed at lower to middle almandine-amphibolite facies 75 Ma after the formation of the volcanic arc assemblage, peaking during D2 deformation (Bailes and Galley, 1999; Bailes et al., 2016).

The Chisel sequence has been subdivided into the Lower and Upper sequences (Bailes and Galley, 2007) forming respectively the footwall and hanging wall of the main mineralized horizon. This contact, informally known as the Chisel-Lalor structural contact (CHLSC) is generally located at 10 to 200 m above the uppermost lenses of the Zn-rich VMS deposits (Fig. 1, 2). In the mine sequence, the Chisel-Lalor structural contact has been interpreted as a thrust fault due to: i) contrasting lithogeochemical trace element signatures with calc-alkaline affinities in the Lower Chisel subsequence and transitional to tholeiitic magmatic affinities in the Upper Chisel subsequence (Bailes et al., 2013; Caté et al., 2014a); and 2) an abrupt change in dip with opposing facing directions across the contact (Bailes et al., 2013).

Elsewhere, however, it is observed to be a sequential stratigraphic contact (Engelbert et al., 2014). The Chisel sequence was intruded by voluminous synvolcanic to late successor-arc (<1.83 Ga) felsic and mafic rocks (Fig. 1).

Geology of the Lalor deposit

The Lalor VMS deposit is hosted in the Lower Chisel subsequence and consists of 12 mineralized zones starting at a vertical depth of 570 m below surface and extending down to approximately 1160 m. As of January 2014, the Lalor deposit had a proven and probable reserve estimate of 15 Mt grading 6.7% Zn, 0.63% Cu, 2.01 g/t Au and 23 g/t Ag, and an inferred resource estimate of 10 Mt with 2.5% Zn, 1.03% Cu, 4.23 g/t Au and 28 g/t Ag. The mineralization zones trend to the northwest and have dips between 10 and 30° to the north-northeast. The ore lenses are relatively thin (average thickness is less than 12 m) and vary in size and grade. The deposit comprises seven zinc-rich and five gold-rich zones (Duff et al., 2015). The upper zinc-rich zones account for approximately 60% of the resource and comprise near-massive to massive sulphide mineralization. Sulphides in the zinc-rich zones dominantly consist of sphalerite interstitial to pyrite crystals. The gold-rich zones are generally found below the zinc zones in the footwall rocks. However, some of the gold zones overlap and cut through the zinc zones (Caté et al., 2015; Duff et al., 2015). The gold zones (including 8.8 Mt at 4.6 g/t Au: Caté et al., 2015; Duff et al., 2015) tend to be disseminated with some stringers of sulphide mineralization. These zones contain a low amount of iron sulphide, typically less than 4 to 5%. One of the gold zones (zone 27) is also associated with higher copper grades (average grade 4.64% Cu) and is referred to as the gold-copper zone. The continuation of the strongly transposed gold-copper mineralization found in the deeper part of the deposit remains an active and open exploration target at greater depths.

A large subconcordant hydrothermal alteration system developed in the footwall of the Zn-rich VMS deposits of the Chisel sequence. This alteration is closely associated in space and time to the magmatic evolution of the Richards subvolcanic intrusion, which is considered as a probably heat source for the ore forming hydrothermal system at Chisel (Bailes et al., 2016). Discordant alteration zones that can be traced up section to the Chisel, Chisel North and Lalor deposits are rooted within the intrusion (Bailes et al., 2013). The footwall hydrothermal alteration below the Lalor VMS deposit evolved in two stages. The first alteration stage produced a semi-conformable zone of albitization, silicification and epidotization 1 to 2 km below the deposits. This large scale alteration is spatially associated with synvolcanic dykes and intrusions (Bailes et al., 2013). The second stage produced sub-concordant to discordant zones of intense hydrothermal alteration in the immediate footwall of the massive sulphide deposits (Bailes et al., 2013, Fig. 2). These hydrothermal alteration zones were overprinted by metamorphism to amphibolite facies, causing major recrystallization and transformed volcanic and volcaniclastic rocks of mafic to felsic composition into granoblastic assemblages often described as 'schists' and 'gneisses' in the mine nomenclature. These rocks are rich in large aluminosilicate porphyroblasts, including garnet, staurolite, cordierite, kyanite and anthophyllite-cummingtonite (Caté et al., 2013, 2015). Alteration in close proximity to the sulphide ore zones at Lalor also includes pervasive zones of finely disseminated sulphides (pyrite, pyrrhotite, sphalerite, chalcopyrite and galena) associated with carbonate, tremolite, anthophyllite, talc and chlorite-rich rocks (Bailes et al., 2013; Caté et al., 2013, 2015). Five chemical associations, each corresponding to distinct metamorphic min-

INTRUSIVE ROCKS (1.88 to 1.83 Ga)

- ![pink] Granodiorite to tonalite
- ![purple] Ultramafic rocks
- ![violet] Mafic intrusive rocks (gabbro, diorite, quartz diorite)

JUVENILE ARC ASSEMBLAGE (1.92 to 1.87 Ga)

- ![orange] Hypabyssal intrusions
- ![yellow-pale] Felsic to intermediate volcaniclastic rocks (fragmentals, tuff, lapilli tuff)
- ![brown] Mafic volcaniclastic rocks (fragmentals, tuff, lapilli tuff)
- ![yellow] Rhyolite to dacite (flows, flow breccia)
- ![green] Basalt, basaltic andesite (pillowed and massive flows)

SEDIMENTARY ROCKS (1.85 to 1.84 Ga)

- ![tan] Graphitic greywacke, derived gneiss and migmatite
- ![red] Surface-projected ore
- ![pink] Tonalite to granodiorite, granite
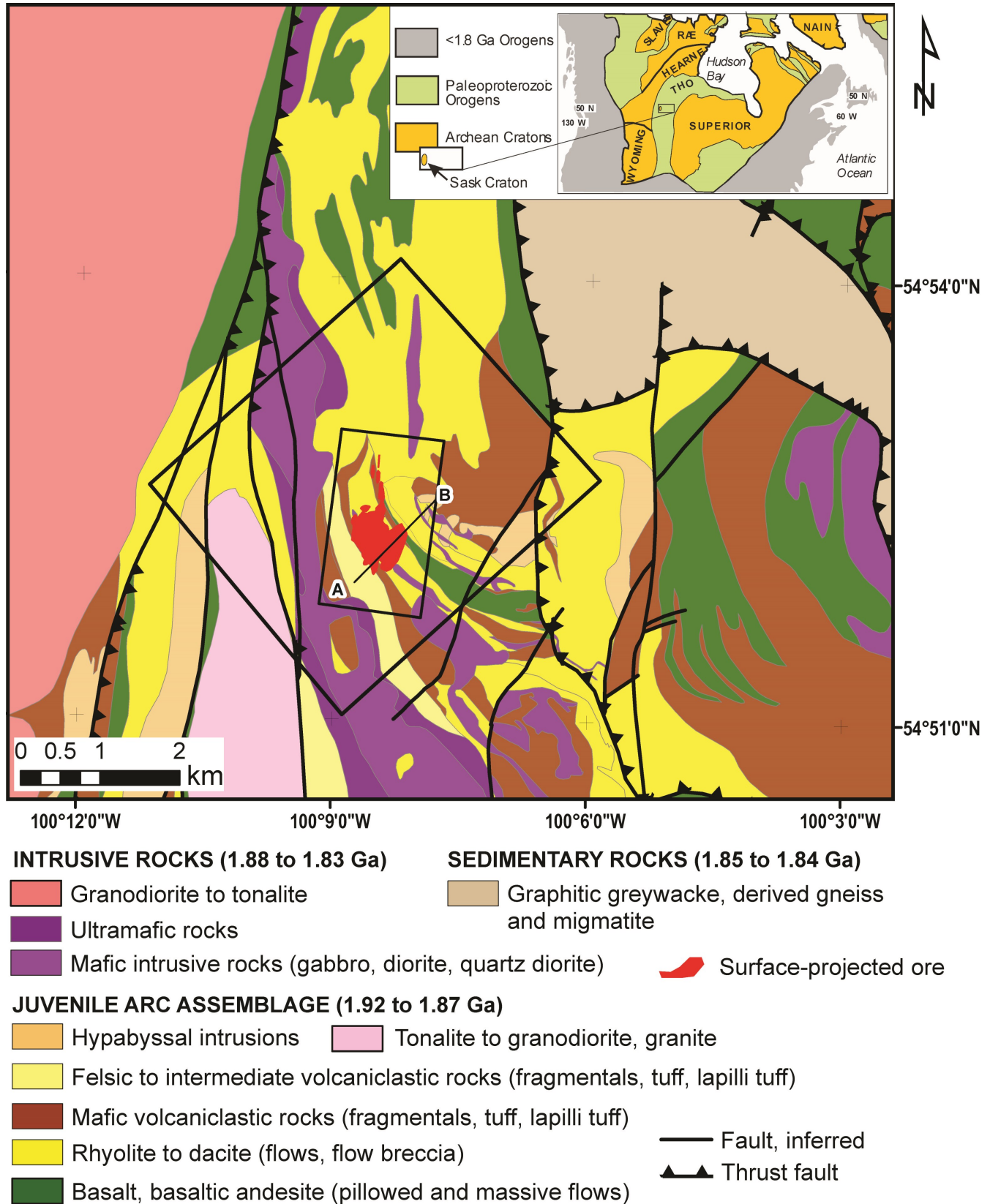- —— Fault, inferred
- ▲▲▲ Thrust fault

Figure 1. Geological map of the Chisel basin (after Bailes and Galley, 2007) showing the location of the Lalor VMS deposit, the outline of the 3D seismic survey (large box) and the outline of the 3D modelling area.
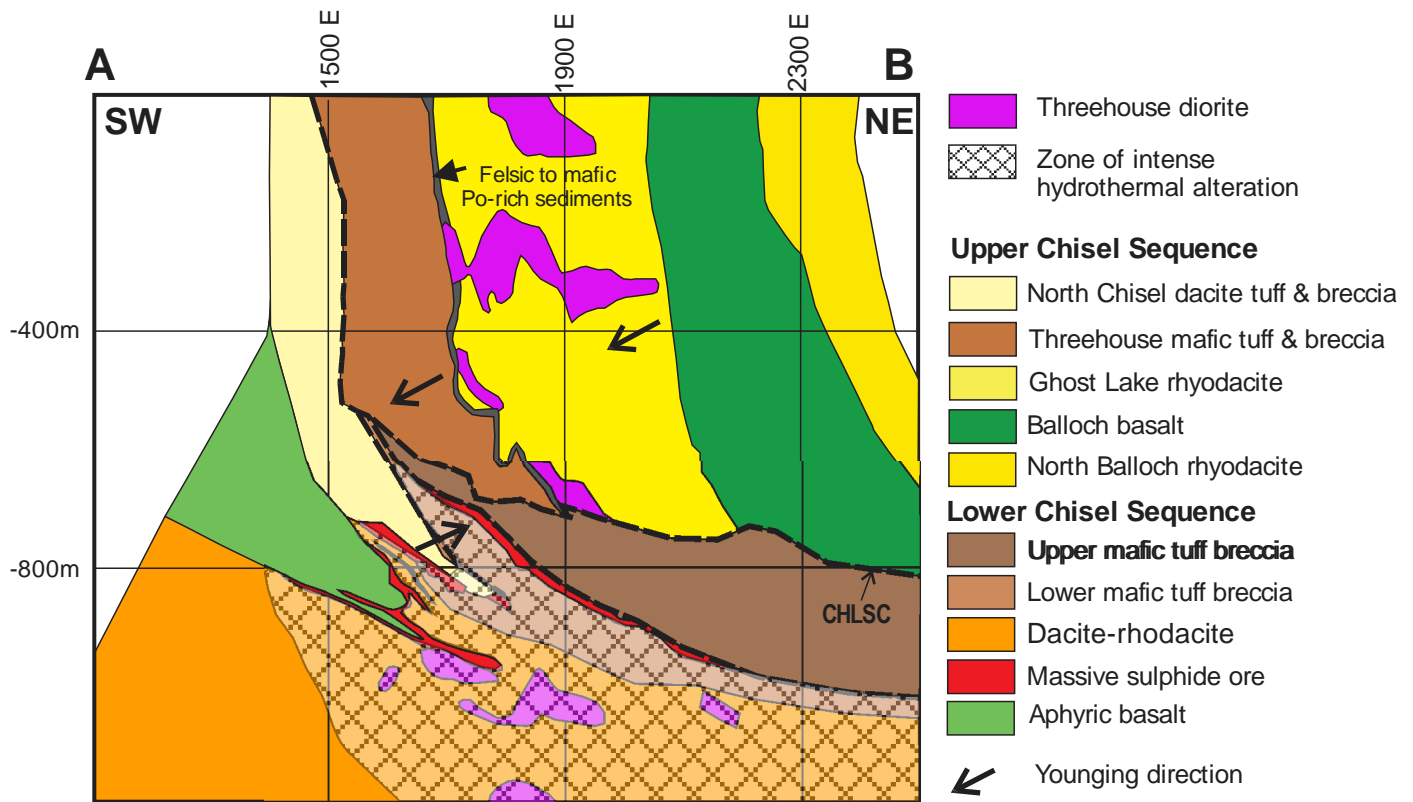
Figure 2. Generalized SW-NE-oriented cross section (see Fig.1 for location) of the Lalor volcanogenic massive sulphide deposit and host rock Chisel sequence (after Bailes, 2013). CHLSC = Chisel Lake structural contact.

eral assemblages can be distinguished in the proximal hydrothermal alteration system associated with the Lalor deposit ore lenses, reflecting both primary (protolith) and secondary (hydrothermal) alteration metamorphic metasomatism and lithogeochemical variations.

The Lalor deposit and its host rocks were affected by D1 to D3 regional polyphase ductile deformation. The main foliation at Lalor is a S2 penetrative mineral shape to gneissic fabric with local evidence of transposition of F1 isoclinal folds and S1 (Bailes et al., 2013; Caté et al., 2014b; Engelbert et al., 2014). F2 folds are also isoclinal, verge towards the south and involve the upper massive sulphide ore lenses. The F2 folds were refolded by open north-northeast upright F3 folds locally resulting in Type 1 (Ramsay, 1967) fold interference patterns (Caté et al., 2014b). The limbs of these fold structures are locally attenuated by shear zones often displaying boudinage of competent rock units and quartz-carbonate veins with both normal and thrust sense of displacement. The upper massive sulphide ore, and sub-concordant zone of intensely hydrothermally-altered rocks, were brought up in a southwestward direction against a succession of relatively weakly altered volcanic and volcaniclastic rocks (Bailes et al., 2013; Caté et al., 2013). This moderately to steeply northeast-dipping structure is sub-parallel to S2 and interpreted as a high-strain transposition zone (Caté et al., 2014b) that accommodated ductile shear and possibly attenuated earlier F2 south-verging isoclinal fold structures.

Modelling Vp and ρ as a function of lithogeochemical proxies for hydrothermal alteration

Vp-density plots from wireline log data were combined with alteration indices calculated from major oxide analyses and a lithofacies classification based on drill log descriptions and the Zr/TiO_2 ratio (Fig. 3). These integrated representations of multi-parameter drill logs suggest that P-wave velocity increases with the intensity of hydrothermal alteration, particularly in volcanic rocks of mafic composition (Schetselaar et al., 2016a). In addition to these interpretations, integrated 3D visualization of the seismic cube with interpolated alteration indices, show that prominent seismic reflections dominantly occur in the zone with the highest intensity of hydrothermal alteration in the footwall of the Lalor VMS deposit (Fig. 4). To further corroborate and quantify the associations between seismic reflectivity and hydrothermal alteration, a data set of physical rock property measurements was used for modelling seismic rock properties as a linear function of lithogeochemical proxies for protolith composition, alteration and mineralization.
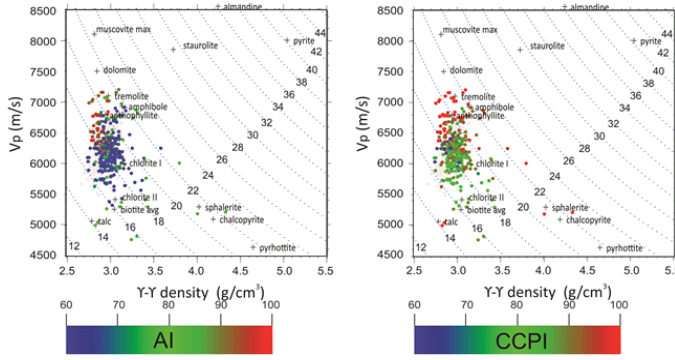
Figure. 3. Vp-density plots of collocated lithogeochemical analysis and physical rock property wireline log samples. The continuous hue range annotation of the samples is proportional to the intensity of alteration computed from: Hashimoto (= AI) index (left) and Carbonate-Chorite-Pyrite (= CCPI) index (right). Labelled Vp-density values of silicate, carbonate and sulphide minerals are from Carmichael (1989).
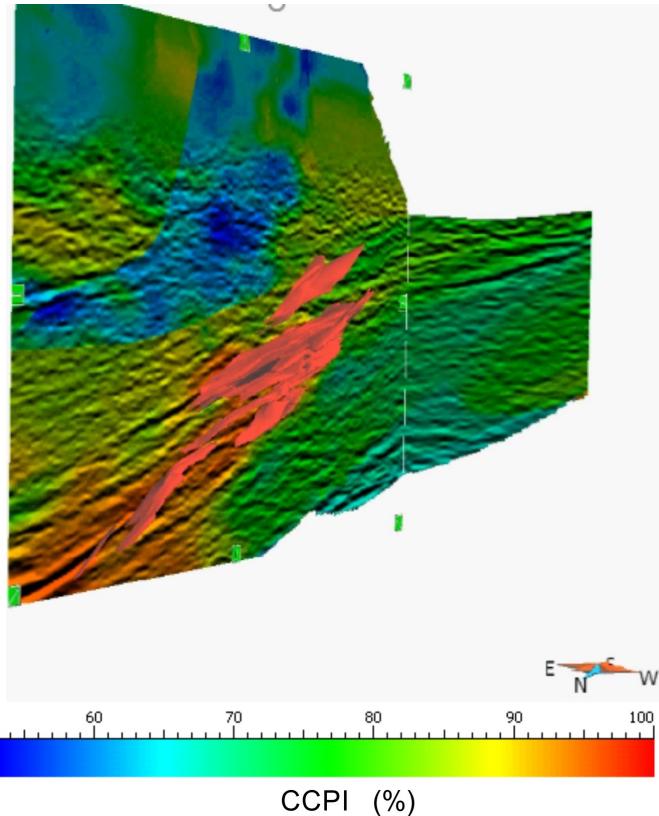

Figure 4. Integrated visualization of 3D seismic data with CCPI alteration index interpolated from drill core lithogeochemical data. Note spatial association between strong seismic reflectivity and high CCPI values (orange to red). Sulphide ore lenses (in red) are shown for reference.

The dataset subjected to regression modelling consisted of 130 NQ-diameter drill core samples of host rocks of the Chisel sequence, as well as massive and stringer sulphide mineralization, split in two halves. Minicores were cut from one half for petrophysical measurements, Density was measured using the immersion method (Enkin et al., 2012). P-wave velocity measurements were made on a subset of 29 dry samples at hydrostatic confining pressures ranging from 20 to 600 MPa using the pulse transmission technique of Birch (1960) and Christensen (1985) at the Dalhousie University/GSC High Pressure Laboratory in Halifax, NS.

The measurements were conducted on minicores which were jacketed in copper foil and neoprene tubing to prevent the pressure fluid from invading the samples at elevated pressures. Vp measurements were made with 1 MHz lead zirconate and lead zirconate titanate transducers and are considered accurate to 0.5%. The other half of the drill core sample was pulverized for whole-rock major oxide and trace element geochemical analyses using ICP (see Mercier-Langevin et al., 2014, for details).

P-wave velocity, Vp, density, ρ and acoustic impedance, Ω (computed from the product $\rho.Vp$) were modelled as a linear function of proxies derived from geochemical analyses, including $\log(Zr/TiO_2)$, FeO, the Ishikawa (AI) and carbonate-chlorite-pyrite CCPI alteration indices (Large et al., 2001) following a step-wise linear multivariate regression approach:

$$\rho = c_0^{\rho} + c_1^{\rho} \log(\frac{[Zr]}{[TiO_2]}) + c_2^{\rho}[FeO] + c_3^{\rho}AI + c_4^{\rho}CCPI \quad [1]$$

$$Vp = c_0^{Vp} + c_1^{Vp} \log(\frac{[Zr]}{[TiO_2]}) + c_2^{Vp}[FeO] + c_3^{Vp}AI + c_4^{Vp}CCPI \quad [2]$$

$$\Omega = c_0^{\Omega} + c_1^{\Omega} \log(\frac{[Zr]}{[TiO_2]}) + c_2^{\Omega}[FeO] + c_3^{\Omega}AI + c_4^{\Omega}CCPI \quad [3]$$

where :

$$AI = \frac{100\{[K_2O] + [MgO]\}}{\{[K_2O] + [MgO] + [Na_2O] + [CaO]\}},$$

$$CCPI = \frac{100\{[MgO] + [FeO]\}}{\{[MgO] + [FeO] + [Na_2O] + [K_2O]\}}$$

The first two (dependent) variables in this multivariate regression model served as proxies for protolith composition and mineralization respectively, while the latter two served as proxies for hydrothermal alteration. A summary of the results of the regression analysis is provided in Table 1.

The proxy variables were analyzed for their relative contribution to the total variance in the regressed seismic rock prop-

Table 1. Results of regression modelling for density (ρ), P-wave velocity (Vp) and acoustic impedance (Ω) as a function of protolith composition, mineralization and alteration lithogeochemical proxies, R = multivariate correlation coefficient, RMSE – root mean square error. The regression model is significant at the 95% confidence limit.

	n	**C_0**	**C_1**	**C_2**	**C_3**	**C_4**	**R**	**RMSE**
ρ	88	2.613	0.219	0.136	-	0.102	0.80	0.067 g/cm^3
Vp	29	5600	1003	97	696	137	0.77	286 m/s
Ω	29	15.37	2.61	1.39	0.26	1.61	0.87	0.82

erties using the approach outlined in Budescu (1993). The alteration proxy (AI + CCPI) yielded a 22 percent contribution to modelled density variance, a 40 percent contribution to modelled P-wave velocity variance and a 28 percent contribution to modelled acoustic impedance variance. The latter, which directly controls seismic reflectance, is about 16 percent lower than the 44 percent contribution of the proxy used for protolith composition. This result suggest that although alteration significantly effects seismic response, it is dominantly governed by variations in the composition of the precursor host rocks (i.e. the protoliths) This finding seems to be consistent with our qualitative interpretations of the seismic data, which show that: i) the strongest seismic reflections are associated to the contacts between mafic and felsic volcanic units; and (ii) the observation that the seismic reflectivity of these contacts remain intact or increase in zones with the highest intensity of hydrothermal alteration. We also learned that the AI index was dominantly relevant for modelling the Vp response, which is consistent with dominant variations in AI values in the Vp direction on Vp-density plots. Because the CCPI index also significantly contributes to the variance in Vp, the combined use of AI and CCPI in modelling the seismic response to the intensity of hydrothermal alteration is superior than using each of these alteration indices individually.

3D seismic rock property modelling

In order to investigate the effect of hydrothermal alteration on the seismic response, a 3D grid attributed with modelled Vp, ρ and Ω responses was created as an input for seismic forward modelling. This seismic rock property grid was compiled in three steps:

1. Interpolation of the log(Zr/TiO$_2$), FeO, AI and CCPI proxies from Hudbay's larger (n = 7235) lithogeochemical drill core dataset on a curvilinear grid conformable to the structure of the Lalor VMS deposit (Schetselaar et al., 2016b; Fig. 5).
2. Vp, ρ and Ω responses for the lithogeochemical proxies were computed at each grid cell using the coefficients of the regression model (Table 1). Adding the responses for the different proxies to each other yielded: i) protolith; ii) protolith + mineralization; and iii) protolith + mineralization + alteration Vp, ρ and Ω response models (Fig. 6). Dif-

ferential models, exclusively modelling the Vp and ρ response due to hydrothermal alteration (shown for acoustic impedance in Figure 6) were obtained by subtracting the second model from the third model.

3. The seismic rock property values resampled on a grid with 5 m voxels to run the seismic forward modelling routine.

3D seismic forward modelling

The finite difference modelling method, implemented in the open source SOFI3D parallel modelling code (Bohlen, 2002) was used to simulate the propagation and subsequent reflection of P-waves through the investigated volume. This allowed comparing the forward-modelled seismic responses of seismic rock property models that incorporated the seismic response from proxies for hydrothermal alteration with models that were solely based on proxies for protolith composition and mineralization (Fig. 5).

The finite difference models generated from these two inputs used a shot point – receiver subset corresponding to the bounds of the seismic rock property models. A Ricker wavelet (Hosken, 1988) with a frequency of 75 Hz, corresponding to the dominant frequency content in the Lalor seismic survey, was used to synthesize the seismic waves in the finite difference modelling routine. The forward modelling was restricted to acoustic conditions in order to focus the analysis on P-wave reflections, while avoiding interference from shear and surface waves simulated in elastic media. Shot gathers were sorted and processed using a simplified sequence that included spherical divergence compensation, bandpass filtering, and first arrival muting. Final synthetic seismic volumes were generated with pre-stack time migration using a velocity function obtained from the field seismic data. This 3D velocity function was obtained from the analysis of Kirchhoff prestack-time migrated gathers and sections following a standard procedure (Robein, 2005). Following Robein (2005) a series of migrated gathers and sections were computed for a range of percentages of an initial velocity function and subsequently analyzed to select optimal migration velocities. Velocities were chosen based on objective and interpretative criteria with the goal of improving the lateral continuity of reflections and structural details in the 3D volume. Residual move outs on gathers were estimated and corrected following an approach described in Górszczyk et al.,
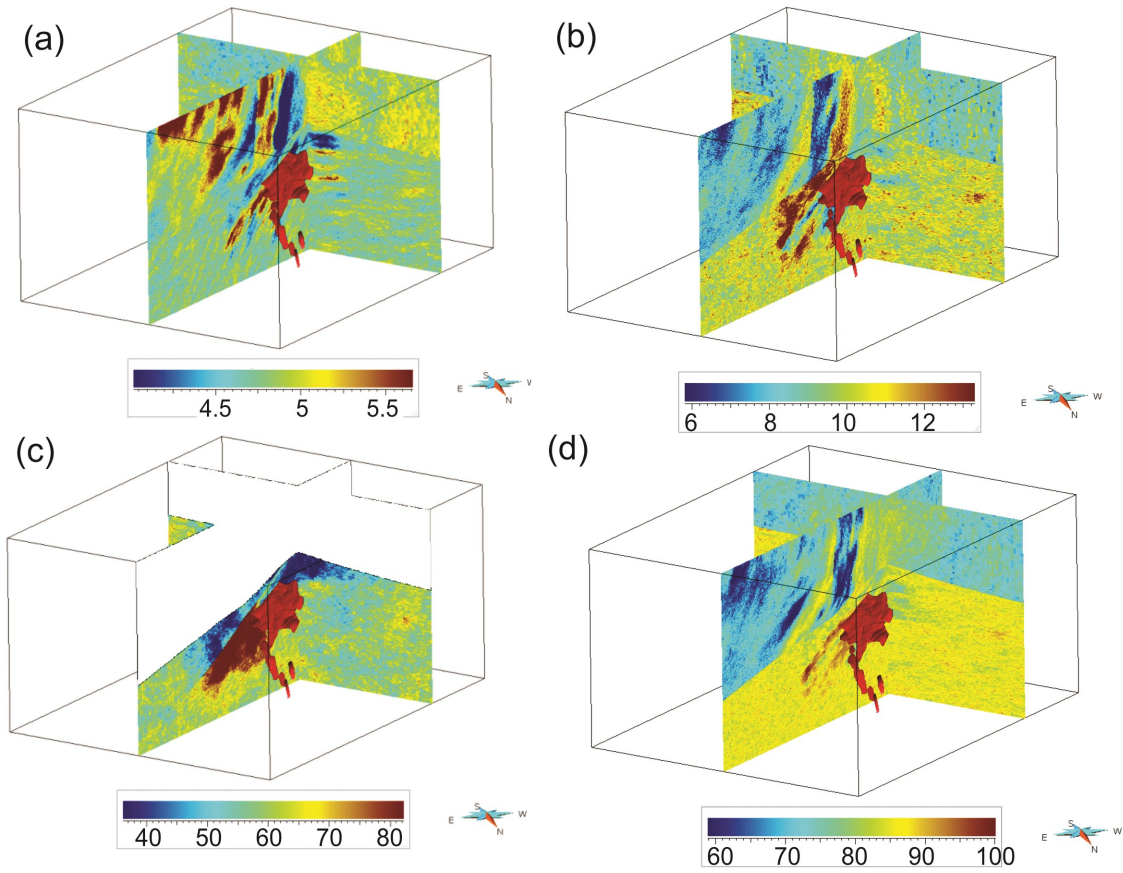
Figure 5. 3D grid models obtained by averaging 25 sequential Gaussian simulations of a) log(Zr/TiO$_2$), b) FeO, c) AI alteration (only for footwall) and d) CCPI alteration proxies for modelling the response of Vp, ρ and Ω density as a function of protolith composition, mineralization and hydrothermal alteration.

(2016). The final velocity model is relatively smooth to allow proper stacking in the image domain of reflections measured at source-receiver pairs with various offsets and azimuths.

3D seismic rock property and forward seismic response modelling

The seismic rock property models show the cumulative effects of adding the modelled response of mineralization and alteration to the response in seismic rock properties related to protolith composition (Fig. 6). dding the mineralization proxy leads to an increase in density in felsic units in the hanging wall reducing their overall density contrast with mafic units. A possible explanation for this reduction is the additive effect of Fe-oxides and sulphides in veins and disseminated mineralization. Adding the alteration density response seems to reverse this effect. This enhancement of density contrast is most likely due to preferential enrichment of Mg-Fe rich silicates with high P-wave velocities in altered mafic units. The largest effect of mineralization and hydrothermal alteration, is however on the modelled Vp response. Adding the mineralization response increases contrast in Vp, particularly in the footwall of the

Lalor deposit, which is further enhanced by adding the alteration response. The additive effects of the seismic rock property response models in Ω largely follows the increases in contrast seen in the Vp models, although the effects are not as pronounced. The residual ΔΩ response model of hydrothermal alteration obtained from subtracting the protolith + mineralization model from the protolith + mineralization + alteration model, shows a strong enhancement of Ω contrast in the footwall, particularly in the vicinity of the massive sulphide ore zones. This residual model also shows a strong decrease in impedance contrast in the hanging wall, which is consistent with the weak intensity of alteration in its constituting rock units (Fig. 6). The seismic forward models obtained from the Vp and density models are shown in Figure 7. Adding the alteration proxy to the protolith and mineralization proxies (Fig. 7b) clearly enhances seismic reflectivity in the footwall of the sulphide ore lenses in comparison to the seismic forward model that is solely based on the protolith composition and mineralization proxies (Fig. 7a). Overall, these forward modelling results confirm the qualitatively inferred spatial associations between the footwall hydrothermal alteration zone of the Lalor deposit and strong seismic reflectivity (Fig. 3, 4).
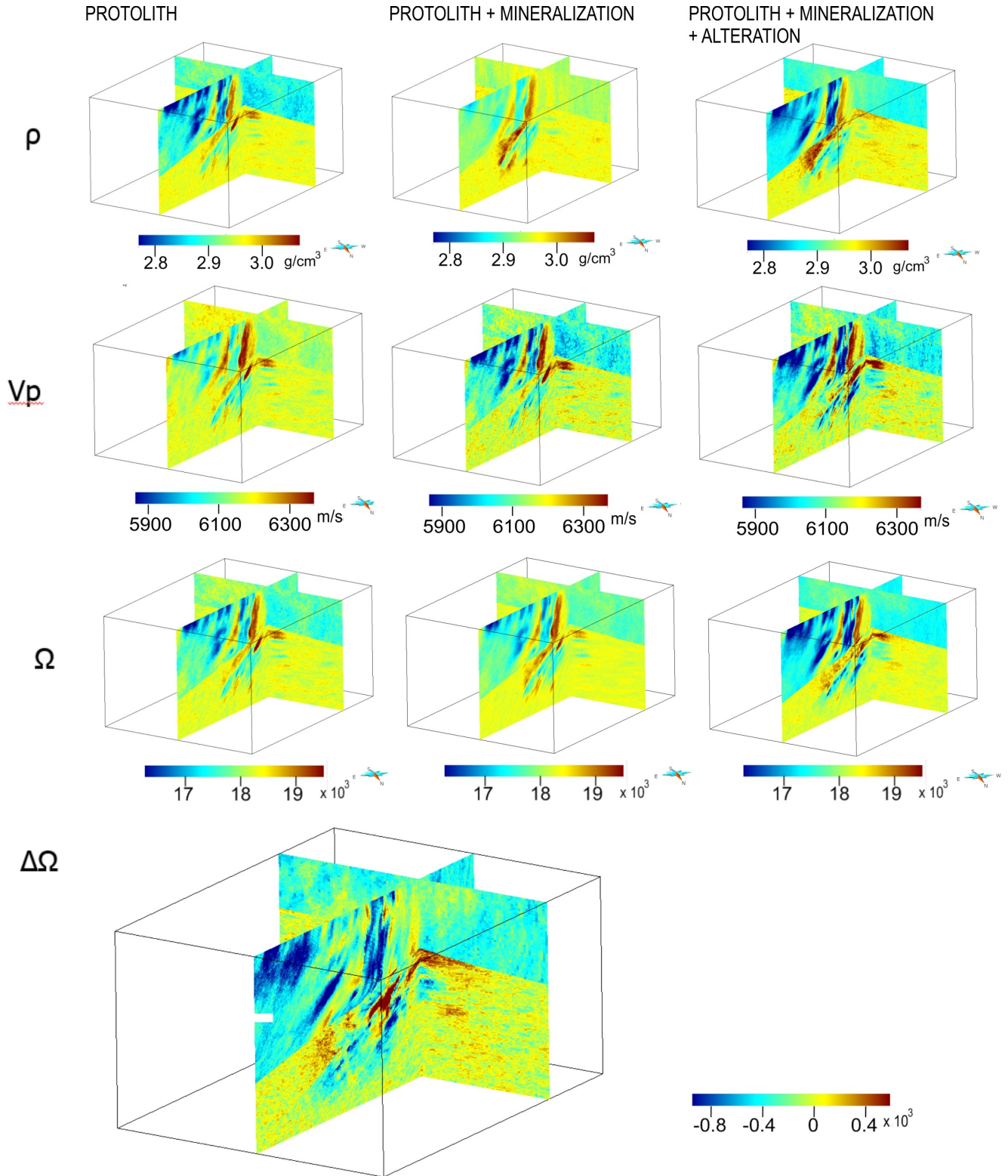
Figure 6. 3D grid models of seismic rock properties (Vp, ρ and Ω) by applying the results of the multivariate regression model (Table 1) on interpolated lithogeochemical proxies for protolith composition, mineralization and alteration (Fig. 5). The delta acoustic impedance model: ΔΩ, computed by subtraction of the protolith + mineralization model from the protolith + mineralization + alteration model, shows the effects of hydrothermal alteration in isolation. Note the prominent contrast in acoustic impedance in the footwall in comparison to the diminished contrast in the hanging wall.

236
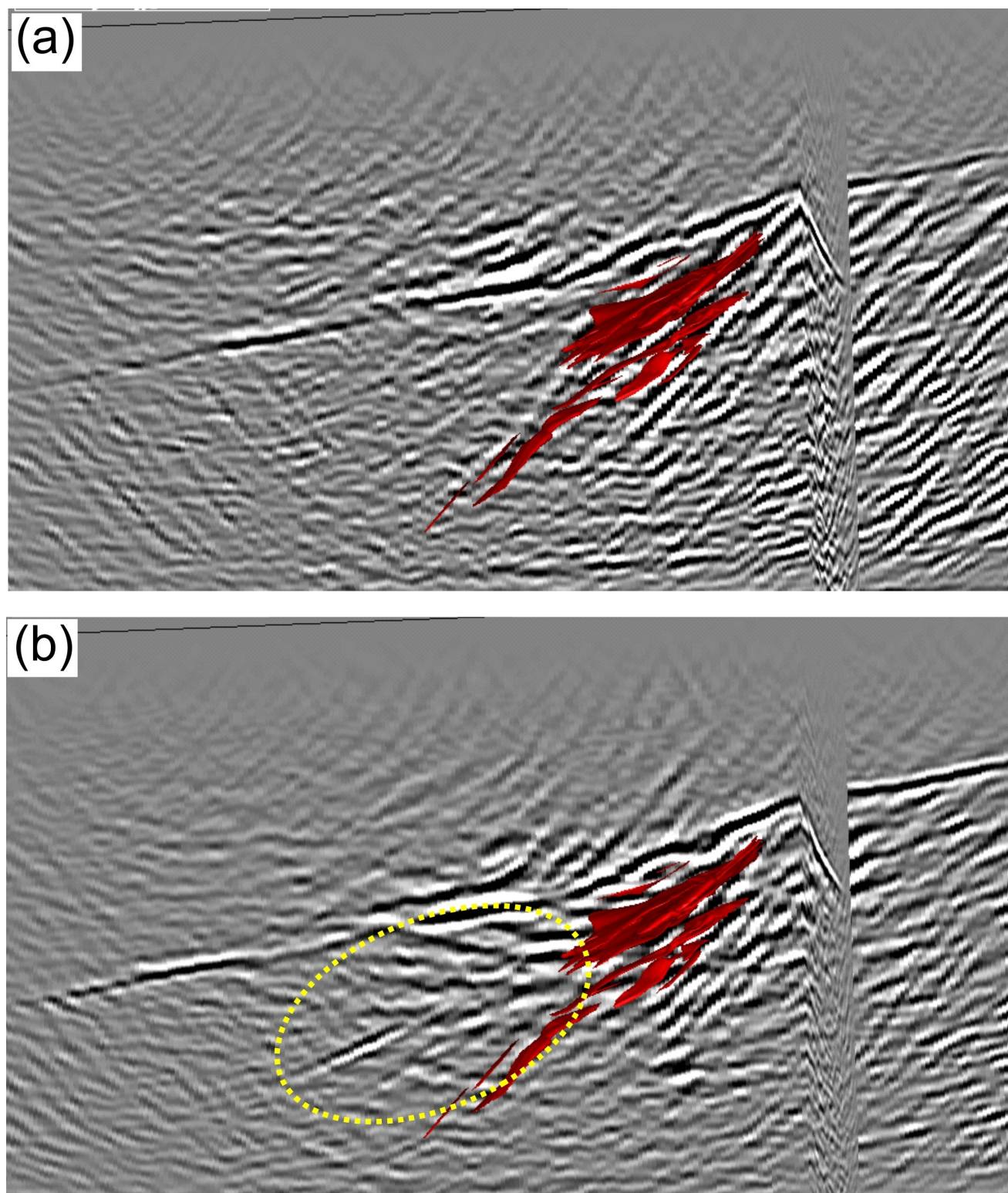
Figure 7. Finite difference forward models (inline 57, crossline 191) from seismic rock property models based on (a) protolith composition + mineralization proxies, (b) protolith composition + mineralization + alteration proxies. Models of sulphide ore lenses are shown for reference purpose. Note subtle enhancement of seismic reflector (outlined by yellow ellipse) in vicinity of upper ore lenses in (b) and enhanced seismic reflectivity in footwall (outlined by yellow ellipse) down dip from the Lalor massive sulphide ore zones.

Forward and inverse modelling of magnetotelluric data

The lithogeochemical - petrophysical multivariate space discussed so far is a basis for an interpretation of the hydrothermal vent stockwork beyond the sample space through models and images arising from seismic and regional electromagnetic surveys (i.e. MT). Hudbay Minerals Inc. has provided the GSC with access to its magnetotelluric (Titan-24) and ZTEM datasets. MT and ZTEM data respond to the electrical conductivity (σ) structure of the subsurface and are economical methods of investigation of regionally significant ore system components.

Although a detailed evaluation of the petrophysical relationships among lithogeochemistry, alteration and σ at Lalor is currently being developed, it is expected that the key relationship will be the effect of alteration and mineralization to increase the ambient conductivity of the ore system. In tandem with the development of these relationships, preliminary inverse modelling of the Titan data and development of unstructured mesh forward algorithms have been completed.

The preliminary inversions conducted so far have been unconstrained. The methodology is similar to that reported by Roots and Craven (2017), and images along three profiles in Figure 8 have been obtained. The image along line 176 is shown in Figure 9 as a representative image of the subsurface portrayed by the unconstrained 3D inversion technique. Increasing conductivity is shown with hotter colours. The known
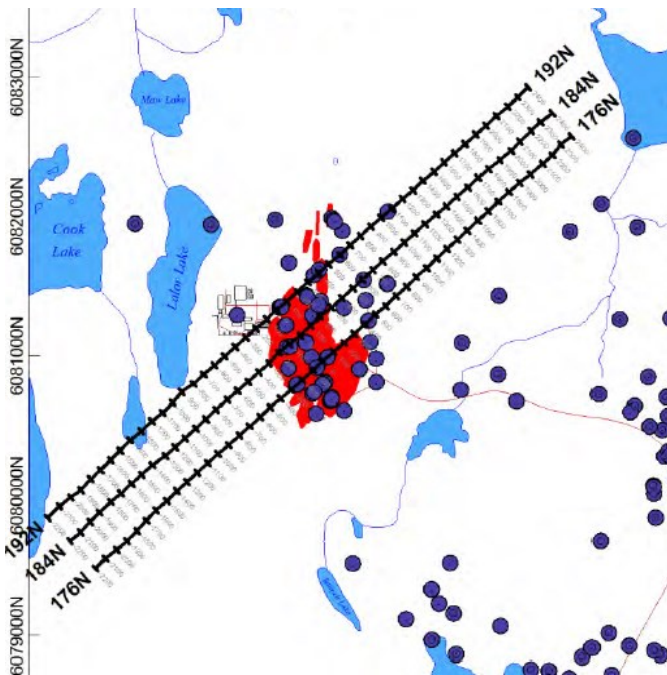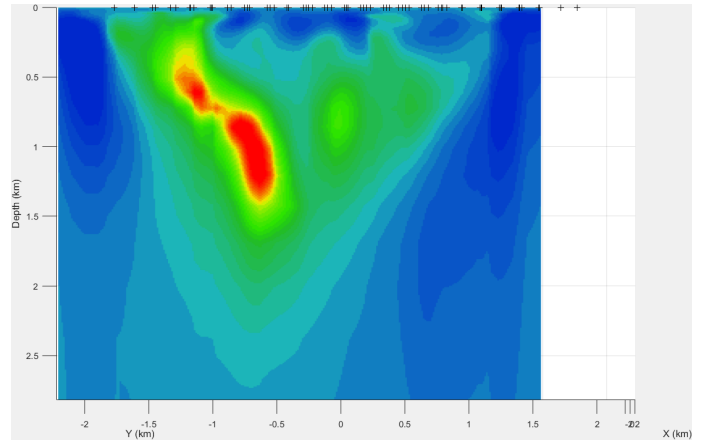

Figure 9. Shallow portion of the preliminary unconstrained inversion of the Titan MT data. The model is a full 3D model and the section shown here corresponds to profile 176 in Figure 7.

ore shells correspond to the feature at 600 to 800 m depth at the horizontal location of approximately 0 km on the figure. This region is less conductive than other slices though the ore shells presumably due to the increased content of less conductive sphalerite at this location.

The bright highly conductive area visible in the model from depths of 500 m to 1.5 km at a horizontal distance of -1.25 to -0.5 km is of uncertain origin. Enigmatic features such as these in the full 3D space explored by MT and ZTEM data can only be rigorously explained through utilization of petrophysical and geometrical models that take into account the effects of alteration and post-emplacement tectonic deformation.

To understand the complex petrophysical and geometrical effects associated with alteration and post-emplacement tectonism we need better algorithms to generate synthetic responses. We have begun to develop forward and inverse MT and ZTEM modelling codes that are compatible with structural and rock property parameterizations that take into account these complex effects. The new algorithms are based on the unstructured mesh code developed by Ansari and Farquharson (2014) and facilitate the utilization of planar source fields associated with MT and ZTEM responses. Figure 10 is an example mesh or the sulphide ore lenses that was created to reproduce the complex geometrical effects. Figure 11 is a representative result of simulated electromagnetic fields at specific frequencies of electromagnetic field oscillations for a ground MT survey. In the future we expect to be able to incorporate a site specific petrophysical conductivity parameterization that accounts for alteration within the full 3D space. We are also actively developing an inversion algorithm to constrain the geophysical model space to this parameterization. These two developments will enable us to provide a new innovative tool to investigate ore system processes that reduces the effects of post emplacement tectonism and alteration.

Figure 8. Map of the Titan MT lines with the location of the ore shells shown in plan view. Figure provided by HudBay.
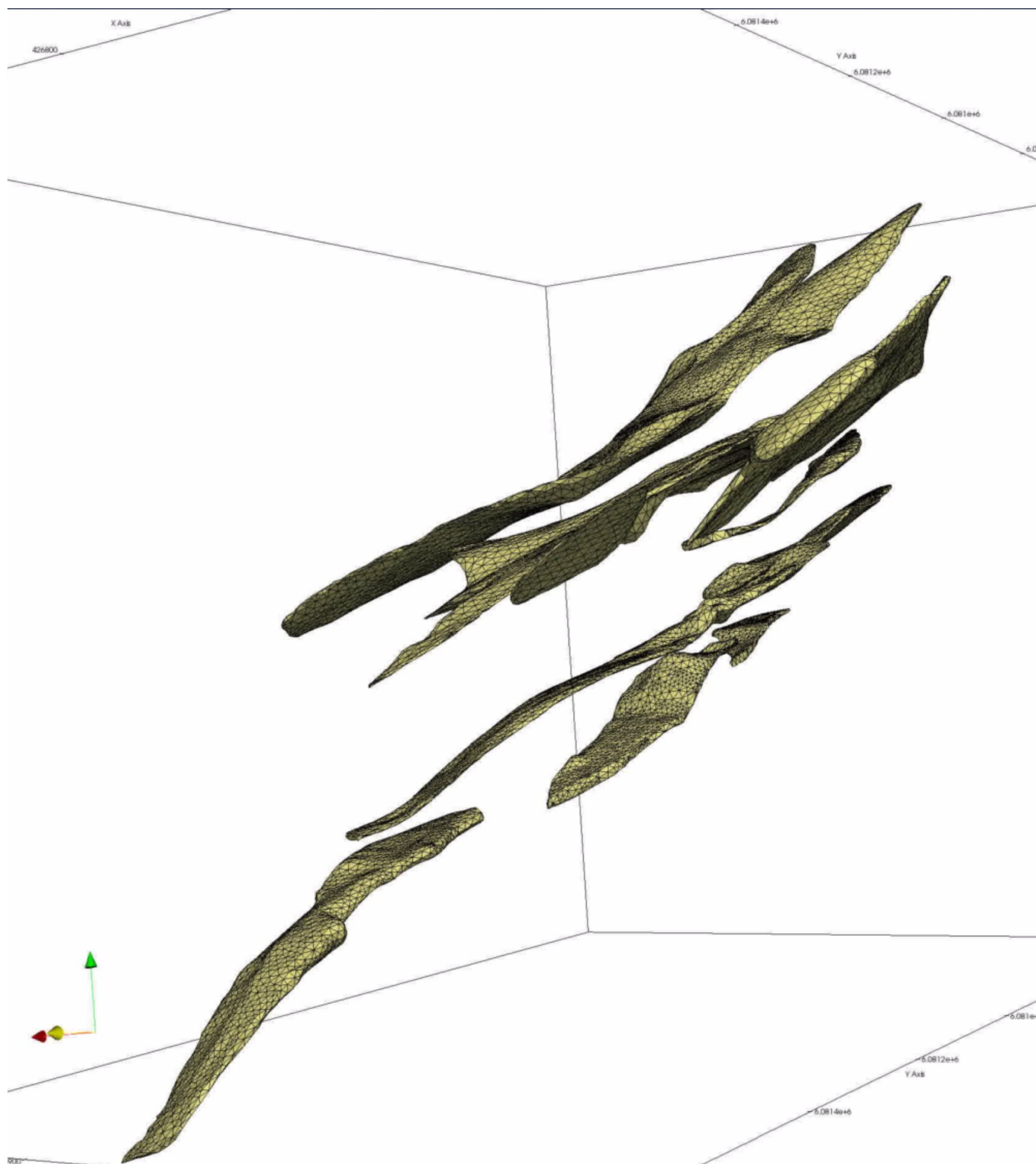
Figure 10 Example unstructured mesh used to calculate the electromagnetic fields associated with the Lalor ore shells. The current model has uniform ore and background conductivities. Future work will involve the use of petrophysical models to populate the full 3D parameter space.
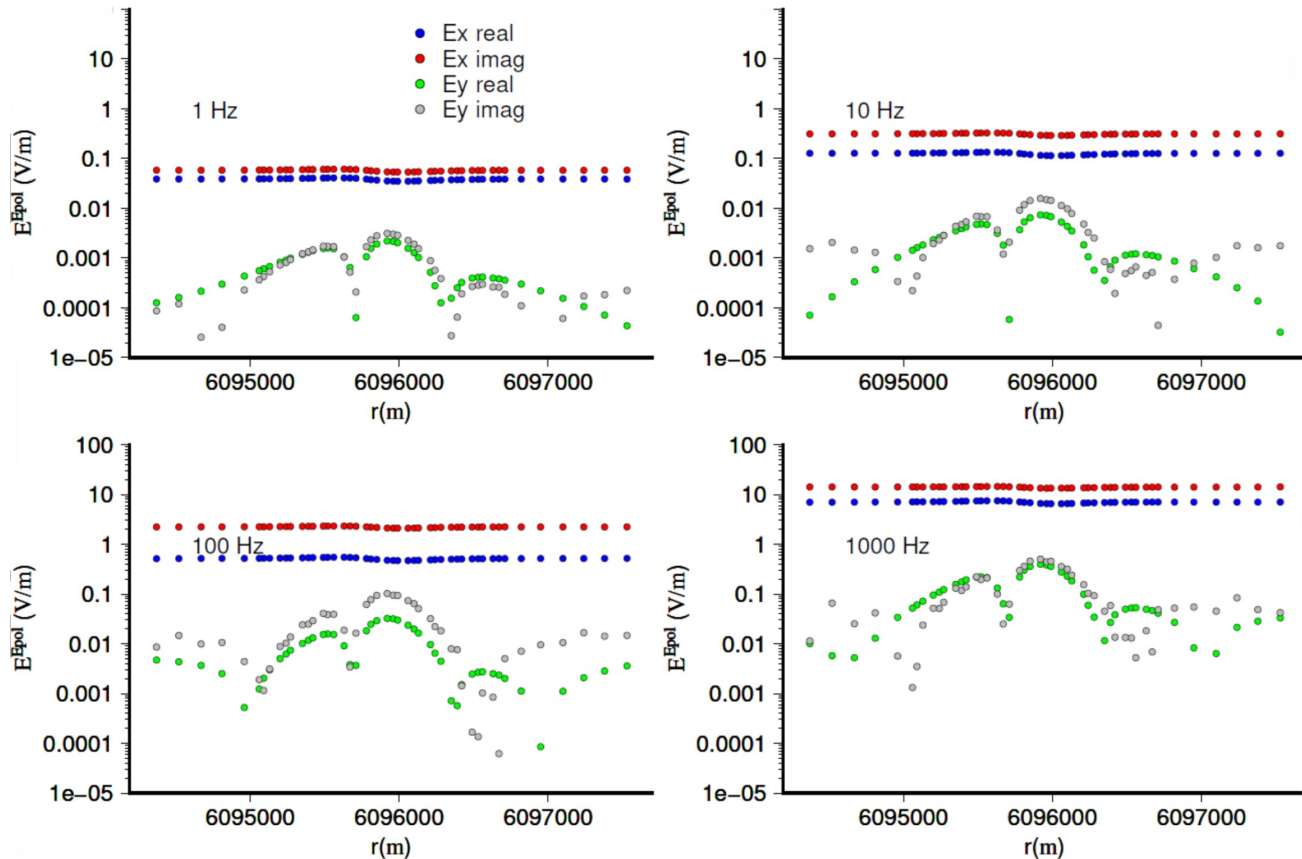
Figure 11. Example of a forward calculation of electromagnetic fields that would be obtained in a MT survey across the Lalor ore shells at frequencies of 1, 10, 100 and 1000 Hz.

Future Work

The next phase of this research activity aims to generate shear wave velocity (Vs) and conductivity (σ) models to expand the seismic forward modelling approach to elastic media. This should also enable consideration of geological factors (in addition to ore) governing conductivity of the Lalor deposit and its host rock envelope in forward and inverse modelling of the MT and ZTEM data. This 3D petrophysical modelling work will be conducted in parallel with continued development of the MT/ZTEM tetrahedral mesh inversion algorithm. We will also use SEM analysis of selected thin sections to corroborate inferences on the Fe-Mg mineral species responsible for the increase in drill core Vp measurements.

Acknowledgments

References

Ansari, S.M. and Farquharson, C.G., 2014. 3D finite element forward modeling of electromagnetic data using vector and scalar potentials and unstructured grids; Geophysics, v. 79, p. E149–E165

Bailes, A.H. and Galley, A.G., 1999. Evolution of the Paleoproterozoic Snow Lake arc assemblage and geodynamic setting for associated volcanic-hosted massive sulphide deposits, Flin Flon Belt, Manitoba, Canada; Canadian Journal of Earth Sciences, v. 36, p. 1789-1805.

Bailes, A.H. and Galley, A.G., 2007. Geology of the Chisel-Anderson lakes area, Snow Lake, Manitoba (NTS areas 63K16SW and west half of 63J13SE); Manitoba Science, Technology, Energy and Mines, Manitoba Geological Survey, MAP Geoscientific map 2007-1, 1 colour map with accompanying notes, scale 1:20 000.

Bailes, A.H., Rubingh, K., Gagné, S., Taylor, G., Galley, A.G., Bernauer, S., and Simms, D., 2013. Volcanological and structural setting of Paleoproterozoic VMS and gold deposit at Snow Lake, Manitoba; Geological Association of Canada – Mineralogical Association of Canada Joint Annual Meeting, Field Trip Guidebook FT-A2, Manitoba Innovation, Energy and Mines, Manitoba Geological Survey, Open File OF2013-3, 63 p.

Bailes, A.H., Galley, A.G., Paradis, S., and Taylor, B., 2016. Variations in large synvolcanic alteration zones at Snow Lake, Manitoba, Canada, with proximity to associated volcanogenic massive sulfide deposits; Economic Geology, v. 11, p. 933–962.

Birch, F., 1960. The velocity of compressional waves in rocks to 10 kilobars, 1. Journal of Geophysical Research, v. 65, p. 1083–1102.

Bohlen, T., 2002. Parallel 3-D viscoelastic finite difference seismic modelling; Computer & Geosciences, v. 28, p. 887–899.

Budescu, D.V., 1993. Dominance analysis: a new approach to the problem of relative importance of predictors in multiple regression. Psychological Bulletin, v. 114, p. 542–551.

Carmichael, R. (ed.) 1989 Physical properties of rocks and minerals, CRC Press, 741 p.

Caté, A., Mercier-Langevin, P., Ross, P.-S., Duff, S., Hannington, M.D., Dubé, B., and Gagné, S., 2013. The Paleoproterozoic Lalor VMS deposit, Snow Lake, Manitoba: Observations on the nature and architecture of the gold and base metal-rich ore zones and associated alteration. Geological Survey of Canada, Open File Report 7483, 19 p.

Caté, A., Mercier-Langevin, P., Ross, P.-S., Duff, S., Hannington, M.D., Gagné, S., and Dubé, B., 2014a. Insight on the chemostratigraphy of the volcanic and intrusive rocks of the Lalor auriferous volcanogenic massive-sulphide deposit host succession, Snow Lake, Manitoba; Geological Survey of Canada, Current Research 2014-6, 19 p.

Caté, A., Mercier-Langevin, P., Ross, P.-S., and Simms, D., 2014b. Structural controls on geometry and ore distribution in the Lalor auriferous VMS deposit. Snow Lake, west-central Manitoba (part of NTS 63K16): Preliminary results from underground mapping; *in* Report of Activities, Manitoba Science, Technology, Energy and Mines, Manitoba, Geological Survey, p. 104–115.

Caté, A., Mercier-Langevin, P., Ross, P.-S., Duff, S., Hannington, M.D., Gagné, S., and Dubé, B., 2015. Geology and Au enrichment processes at the Paleoproterozoic Lalor auriferous volcanogenic massive sulphide deposit, Snow Lake, Manitoba; *in* Targeted Geoscience initiative 4: Contributions to the understanding of volcanogenic massive sulphide deposit genesis and exploration methods development, (ed.) J.M. Peter and P. Mercier-Langevin; Geological Survey of Canada, Open File 7853, p. 131–145.

Christensen, N.I., 1985. Measurement of dynamic properties of rocks at elevated temperatures and pressures; American Society for Testing and materials, Special Technical Publication, v. 869, p. 93–107.

Duff, S., Hannington, M.D., Caté, A., Mercier-Langevin, P., and Kjarsgaard, I.M., 2015. Major ore types of the Paleoproterozoic Lalor auriferous volcanogenic massive sulphide deposit, Snow Lake,Manitoba; *in* Targeted Geoscience initiative 4: Contributions to the understanding of volcanogenic massive sulphide deposit genesis and exploration methods development, (ed.) J.M. Peter and P. Mercier-Langevin; Geological Survey of Canada, Open File 7853, p. 147–170.

Engelbert, M.S., Friesen, V., Gibson, H., and Lafrance, B., 2014. Volcanic reconstruction of the productive VMS ore interval in the Paleoproterozoic Chisel sequence. Snow Lake, Manitoba; Program with Abstracts, Geological Association of Canada – Mineralogical Association of Canada, joint annual meeting, Fredericton, New Brunswick., p. 83–84.

Enkin, R.J., Cowan, D., Tigner, J., Severide, A., Gilmour, D., Tkachyk, A., Kilduff, M., Vidal, B., and Baker, J., 2012. Physical property measurement at the GSC Paleomagnetism and Petrophysics Laboratory, including electric impedance spectrum methodology and analysis; Geological Survey of Canada, Open File 7227, 42 p.

Galley, A.G., Bailes, A.H., and Kitzler, G., 1993. Geological setting and hydrothermal evolution of the Chisel Lake and North Chisel Zn-Pb-Cu-Ag-Au massive sulfide deposits, Snow Lake, Manitoba; Exploration and Mining Geology, v. 2, p. 271–295.

Górszczyk, A., Malinowski, M., and Bellefleur, G., 2016. Applications of curvelet transform in hardrock seismic exploration; EAGE/DGG Workshop on Deep Mineral Exploration, Munster, Germany, Extended abstract. <http://earthdoc.eage.org/publication/publicationdetails/?publication=84008> [accessed December 20, 2017]

Hosken, J.W., 1988. Ricker wavelets in their various guises; First break, v. 61, p. 24–33.

Kraus, J. and Williams, P.F., 1999. Structural development of the Snow Lake allochthon and its role in the evolution of the southeastern Trans-Hudson Orogen in Manitoba, central Canada; Canadian Journal of Earth Sciences, v. 36, p. 1881-1899.

Large, R.R., Gemmell, J.B., and Paulick, H., 2001. The alteration box plot: A simple approach to understand the relationship between alteration mineralogy and lithogeochemistry associated with volcanic-hosted massive sulphide deposits; Economic Geology, v. 96, p. 957–971.

Mercier-Langevin, P., Caté, A., and Ross, P.-S., 2014. Whole-rock oxygen-isotope mapping of the footwall alteration zones at the Lalor auriferous VMS deposit, Snow Lake, west-central Manitoba (NTS 63K16); *in* Report of Activities 2014; Manitoba Mineral Resources, Manitoba Geological Survey, p. 94–103.

Ramsay, J.G., 1967. Folding and fracturing of rocks; McGraw-Hill, 568 p.

Robein, E., 2005. Velocities, time-imaging and depth-imaging: Principles and methods; EAGE Publications, Houten, Netherlands, 464 p.

Roots, E. and Craven, J.A., 2017. 3-D modelling of magnetotelluric data from the Abitibi and Pontiac subprovinces of the Superior Province, Ontario and Québec; Geological Survey of Canada, Open File 8233, 24 p.

Schetselaar, E.M., Bellefleur, G., and Craven, J.A., 2016a. Elucidating VMS mineralizing fluid pathways from the geophysical responses to hydrothermal alteration; *in* Targeted Geoscience Initiative, 2016 report of activities, (ed.) N. Rogers; Geological Survey of Canada, Open File 8199, p. 123–127.

Schetselaar, E.M., Bellefleur, G., Craven, J.A., Roots, E., Cheraghi, S., Shamsipour, P., Caté, A., Mercier-Langevin, P., El Goumi, N., Enkin, R.J., and Salisbury, M., 2016b. Geologically-driven 3D modelling of physical rock properties in support of interpreting the seismic response of the Lalor volcanogenic massive sulphide deposit, Snow Lake, Manitoba, Canada; *in* Characterization of Ore-Forming Systems from Geological, Geochemical and Geophysical Studies, (ed.) K. Gessner, T.G. Blenkinsop and P. Sorjonen-Ward; Geological society, London, Special Publication 453.

Laser ablation-inductively coupled plasma-mass spectrometric analysis of fluid inclusions from the Windy Craggy Cu-Co-Au volcanogenic massive sulphide deposit: Method development and preliminary results

M.A. Schmidt[1], J.M. Peter[2], S.E. Jackson[2], Z. Yang[2], M.I. Leybourne[1] and D. Layton-Mathews[1]

[1] *Department of Geological Sciences and Geological Engineering, Queen's University, 36 Union Street, Kingston, Ontario, K7L 3N6*

[2] *Geological Survey of Canada, 601 Booth Street, Ottawa, Ontario, K1A 0E8*

Abstract

There is increasing recognition that there is a variable magmatic component to mineralizing fluids in volcanogenic massive sulphide (VMS) deposit formation. A previous fluid inclusion study conducted on the Windy Craggy Cu-Co-Au deposit in northwestern British Columbia documented primary inclusion fluids salinities that are higher than typical VMS fluids. The previous study concluded that the high salinity indicates a magmatic contribution to the ore-forming system. This makes Windy Craggy an ideal study location to test if there is in fact a magmatic influence on the fluids and to quantify that contribution. Preliminary results of this study show fluids consistent in salinity and temperature with those observed in the previous study. Fluids with salinities between 6.2 and 12.2 weight % NaCl equivalent are documented. Laser ablation ICP-MS analysis of these inclusions detects Na, K, Ca, Cu, Sr, Sn, Sb, Ba and Pb as well as trace elements of potential magmatic origin, including Au, W, Sn, In and Bi. Due to the multiple possible sources of Sn, we will be focusing on other potential magmatic elements such as Au, Bi and In as the study progresses. The small number of samples analyzed to date precludes us from making definitive conclusions. However, the detection of some potential magmatic elements in 17 inclusions is promising.

Introduction

Early methods for determining fluid inclusion chemical compositions employed several bulk extraction techniques, such as: 1) grinding/crushing the sample under vacuum (Roedder, 1972); 2) decrepitation by stepwise heating (Piperov and Penchev, 1973); and 3) decrepitation under vacuum (Welhan, 1987). Analysis of decrepitate mounds is performed using electron microprobe, but the inhomogeneity of the mounds can result in non-representative analytical data. Additionally, fractionation of the contents of the inclusions can occur upon decrepitation and incomplete dissolution of daughter minerals can cause inaccuracies in bulk compositional determinations (Roedder, 1984). Also, application of such methods typically results in the fluids of several generations of inclusions being liberated together, making detailed interpretation difficult, if not impossible.

Recently, development of laser ablation-inductively coupled plasma-mass spectrometry (LA-ICP-MS) has provided an effective tool for microanalysis of major and trace elements in minerals (Gagnon et al., 2003). With the application of LA-ICP-MS to fluid inclusions, in situ, multi element analysis of microscopic inclusions has become possible (Audetat et al., 1998). These techniques provide cost-effective analysis with limited sample preparation, high spatial resolution, high sensi-

tivity and rapid results (Audetat et al., 1998). Previous fluid inclusion studies of ore deposits using LA-ICP-MS have generally focused on high salinity fluids, as they have a higher concentration of total dissolved solids (e.g. magmatic-hydrothermal deposits) resulting in a higher signal to noise ratio and more precise fluid analysis, especially for smaller inclusions (Audetat et al., 1998).

In the genetic model for volcanogenic massive sulphide (VMS) deposits, the mineralizing fluids are modified seawater (Shanks and Koski, 2012). Salinities of fluid inclusions in VMS deposits are typically close to that of seawater (3.2 weight % NaCl; Bischoff and Rosenbauer, 1985), generally falling within the range of 2 to 6 weight % NaCl equivalent (Bodnar et al., 2014). Salinities greater than seawater being attributed to a variety of processes, including phase separation and boiling (Coumou et al., 2009; Vanko et al., 2004), hydration of rocks in the subsurface (Seyfried et al., 1986), the presence of ephemeral Cl-bearing phases in the subsurface (Vanko et al., 2004), dissolution of evaporites (Ramboz et al., 1988), and the direct contribution of a saline magmatic fluid (Stanton, 1990).

The Windy Craggy Cu-Co-Au deposit in northwestern British Columbia is the world's largest Besshi-type VMS (Peter and Scott, 1999), and a previous fluid inclusion study

there documented primary inclusion fluids that are more saline than most VMS fluids. The authors surmised that the high salinity indicates a magmatic fluid contribution, which might in turn explain the atypically large size of the deposit (Peter and Scott, 1993). Since this work was completed, several researchers have addressed the role of magmatic fluids and volatiles in VMS deposits (i.e. de Ronde, 1995; Huston et al., 2011), although compositional data for major, minor, and trace elements, especially those in fluid inclusions, were not the basis of these studies. Certain trace elements are considered indicators of a magmatic source (e.g. Hg, As, Sb, Bi, Te, Sn, Au; Stanton, 1990, 1994; Hedenquist and Lowenstern, 1994). The presence of these elements in fluid inclusions would thus suggest a magmatic source (e.g. Peter et al., 2017). In order to address the larger question of the importance of magmatic fluids and volatiles in the formation of VMS deposits, we have used LA-ICP-MS to study the fluid chemistry of inclusions from the Windy Craggy deposit, as there is a suite of legacy samples and fluid inclusion chips, for which there are good thermometric and petrographic data. Windy Craggy is of particular interest due to its impressive metal endowment and relatively high salinity fluids compared to other VMS deposits.

Geologic Setting

The Windy Craggy deposit contains >300 million tonnes grading 2.12% Cu, 0.083% Co, 0.16 g/t Au, and 3.30 g/t Ag (Downing et al., 1991). The deposit consists of several lenses of Cu-Co-Au mineralization with separate feeder and stockwork zones (Peter and Scott, 1999). Windy Craggy is located within the Alexander terrane of the Insular tectonic belt and extends for over 1000 km from coastal British Columbia to the Saint Elias Mountains in Yukon and eastern Alaska (Peter and Scott, 1999). The Alexander terrane consists of a wide belt of weakly metamorphosed, complexly deformed, Precambrian to Permian basinal, carbonate, and clastic rocks with a minor volcanic component (Campbell and Dodds, 1979, 1983; MacIntyre, 1984). The Precambrian to Permian units are unconformably overlain by calcareous turbidites and upper Triassic bimodal volcanic rocks. The Alexander terrane is host to several VMS deposits other than Windy Craggy, including Greens Creek and Mount Henry Clay (Taylor et al., 2008). The late Triassic units in close proximity to Windy Craggy consist of mafic submarine volcanic rocks (Peter et al., 2014) with interbedded calcareous argillaceous sedimentary rocks, informally named the 'Tats volcanic complex'. The volcanic rocks in the area of Windy Craggy have been dated by conodonts obtained from the interbedded and underlying sedimentary units and are early Norian (ca. 225 Ma; Orchard, 1986). Felsic volcanic rocks are not present in the immediate area of the Windy Craggy deposit. However, other parts of the Alexander Terrain do contain felsic volcanic rocks or their metamorphosed equivalents, and these indicate volcanism was bimodal at the regional scale (Taylor et al., 2008).

Methods

Fluid Inclusions

The fluid inclusions used in this study are from a previously prepared suite of doubly polished thin section chips (Peter, 1992; Peter and Scott, 1993). Only fluid inclusions hosted in quartz were studied. Photomicrographs were taken of the sample chips and the observed inclusions were carefully mapped. Fluid inclusions were classified using the criteria of Roedder (1984). Fluid inclusions for which there are existing microthermometric data (Peter, 1992; Peter and Scott, 1993) were analyzed by LA-ICP-MS. Microthermometric measurements were also made on additional inclusions, as these were needed so that they also could be analyzed by LA-ICP-MS (see below regarding internal standard). These microthermometric measurements were made using a Linkham THMSG600 heating-freezing stage coupled to an automated controller unit and a Nikon OPTIPHOT microscope, at the Harquail School of Earth Sciences, Laurentian University. The system was calibrated using synthetic fluid inclusion standards for CO_2 (-56.6°C), the freezing point of H_2O (0°C) and critical point of H_2O (374.1°C). Microthermometric observations include first melting temperature (T_f), last melting temperature (T_m) and temperature of homogenization (T_h). The percentage of vapour and liquid, and size of the inclusion were also recorded. The salinity of each fluid inclusion was calculated using the H_2O-NaCl system based on Bodnar (1994).

LA-ICP-MS

The LA-ICP-MS analyses of fluid inclusions were performed at the Geological Survey of Canada in Ottawa, Ontario using a Teledyne Photon Machines Analyte G2 excimer laser ablation system (λ = 193 nm) with a HelEx ablation cell couple to an Agilent 7700x ICP-MS equipped with a second rotary vacuum pump that improves instrument sensitivity across the mass range by 2 to 3 times (Cabri and Jackson, 2011). The instrument was set up using the parameters listed in Table 1.

Table 1. Instrumental and analytical parameters for LA-ICP-MS analyses.

Laser system type	Teledyne Photon Machines Analyte G2 Excimer
Wavelength	193 nm
Energy density for quartz ablation	4.54 J/cm2
Repetition rate	8 hz
Crater size for FI analysis	Varied from 10μm to 20μm
ICP-MS	Agilent 7700x
Carrier gas flow	1.00 L/min He
Rf power	1550 W
Dwell time per isotope	5 ms seconds with the exception of Na, K, Si, at 2.5 ms & Au at 10 ms

The fluid inclusion chips were positioned on a thin slice of a pipette resting on a glass slide that was placed in the sample chamber. The samples remained stationary throughout the analysis. The fluid inclusions were located using chip photomicrographs. The sample was observed using the 100% magnification of the LA-ICP-MS optical system and the smallest laser spot diameter selected that contained the entire inclusion, typically 10 to 15 µm. The laser was then set to 50% magnification and focused on the surface of the chip. Each analysis was programmed to collect a 40 second gas blank (no ablation), ablate the sample for 20 seconds, and then continue to collect until 100 seconds was reached. Some samples were ablated for shorter periods to prevent further sample damage and decrepitation of adjacent inclusions.

Two standard reference materials (SRM) were used (synthetic glass SRM NIST 610 (Norman et. al., 1996), and pyrrhotite SRM Po689 (Mungall et. al., 2005)), together with an in-house aqueous solution. Standard Po689 was used solely to obtain S/Fe signal intensity ratios for calibration of S. Due to the low Cl and Br concentrations in the NIST glass, a multi-element, in-house solution standard was used to obtain Cl and Br concentrations. The solution was contained within wells made of cut pipette tips, sealed on the bottom and top using Parafilm to limit the evaporation of the solution within the ablation chamber. Prior to analysis, the wells were opened by ablation of hole through the Parafilm using a 40 µm spot size. The solution was ablated directly using a 30 µm spot size. SILLS (see below) only allows for the use of one standard in its analysis. NIST 610 was used for all data discussed in this paper.

The initial LA-ICP-MS test analyses were performed without a signal smoothing device and using a dwell time per element of 4 ms. However, this setup produced a signal that was too transient to measure all of the elements of interest (^{109}Ag, ^{75}As, ^{197}Au, ^{11}B, ^{137}Ba, ^{209}Bi, ^{79}Br, ^{42}Ca, ^{111}Cd, ^{140}Ce, ^{35}Cl, ^{59}Co, ^{133}Cs, ^{65}Cu, ^{57}Fe, ^{202}Hg, ^{115}In, ^{39}K, ^{7}Li, ^{25}Mg, ^{55}Mn, ^{95}Mo, ^{23}Na, ^{208}Pb, ^{85}Rb, ^{34}S, ^{121}Sb, ^{77}Se, ^{29}Si, ^{118}Sn, ^{88}Sr, ^{125}Te, ^{205}Ti, ^{182}W and ^{66}Zn). This was remedied by adding to the line a small mixing chamber constructed from a plastic test tube.

Dwell times were lengthened to 5 ms, except for Na, K, Si (2.5 ms) and Au (10 ms), to improve duty cycle and provide greater accuracy and precision in the measurements.

Data Reduction

Initial data reduction was performed using elemental ratios. The data were plotted using iogas (Reflex) to allow for visualization of the fluid inclusion signal. The time span of the inclusion ablation signal was recorded. The length of the host mineral signal was recorded previously during the analysis process. The host mineral, quartz, represents the matrix signal, which is removed from the fluid inclusion signal. Background is removed by calculating the average counts per second (CPS) for each element in the matrix and then subtracting this value from the CPS of each element in the fluid inclusion signal.

The data were also processed using SILLS (Guillong et al., 2008), a Matlab program for reduction of LA-ICP-MS data obtained from solids and fluid inclusions. Data reduction of fluid inclusion data is difficult due to the transient nature of the signal. SILLS allows for the isolation of the signal from that of the host mineral through manual selection of the various peaks by the user, and also for the definition of an internal standard. Sodium was used as the internal standard and was determined prior to ablation by fluid inclusion microthermometry at below ambient temperatures. The salinity (internal standard) varies by inclusion, as does the length of the inclusion and matrix signals. Back calculations were performed to ensure the veracity of the SILLS corrections. This was done by converting the concentrations of the cations (Na, K, Ca, Mg) to weight % NaCl equivalent and then calculating the required Cl assuming all of the cations are present as a salt. The sum of these values equates to the calculated salinity. The calculated weight % equivalent salinities were compared to the salinities determined by microthermometric measurements. The difference between these values ranges from 0 to 35%. Any differences >30% were omitted from the results. Closer inspection of the trace elements reveals inconsistencies between the measured CPS and corrected parts per million values from SILLS. Data reduction using SILLS returned values for trace elements in samples
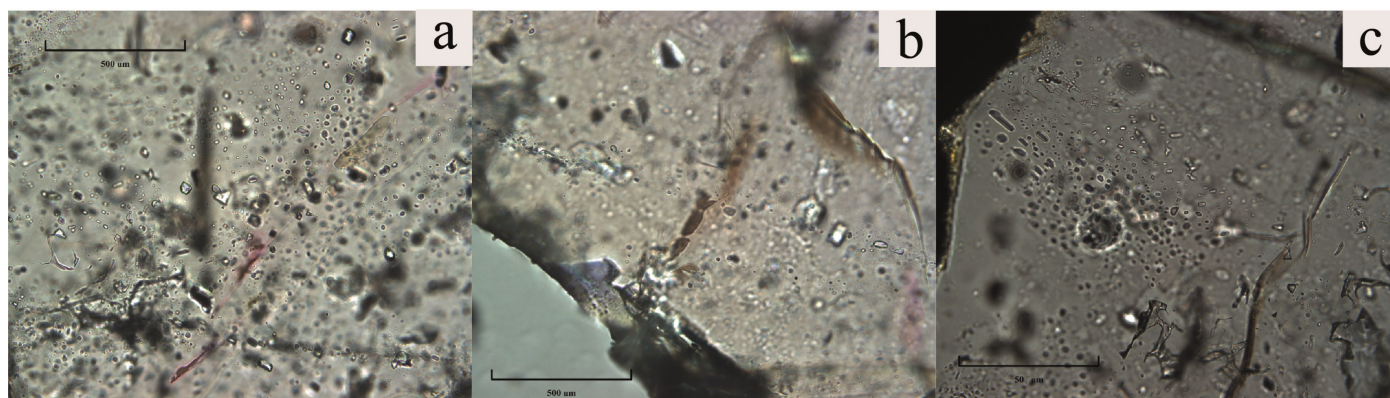

Figure 1. Photomicrographs of representative fluid inclusions in the samples: a) Intersecting planes of secondary inclusions; b) Suspected primary inclusion; c) Plane of monophase secondary inclusions.

where no CPS were recorded and also failed to return values for trace elements where CPS are well above background. This is likely caused by the absence of a matrix signal, as there is no evidence of quartz being ablated after the initial rupture of the inclusion.

Results

Petrography

The majority of the inclusions observed in the samples are secondary (Fig. 1a), however there are some primary inclusions (Fig. 1b). Primary inclusions are identified by their negative crystal morphology or occurrences along growth planes of the quartz. They range in size from 5 to 24 μm and are circular, oval, or hexagonal in cross section. The primary inclusions display consistent phase (liquid/vapour, or L/V) ratios indicat-
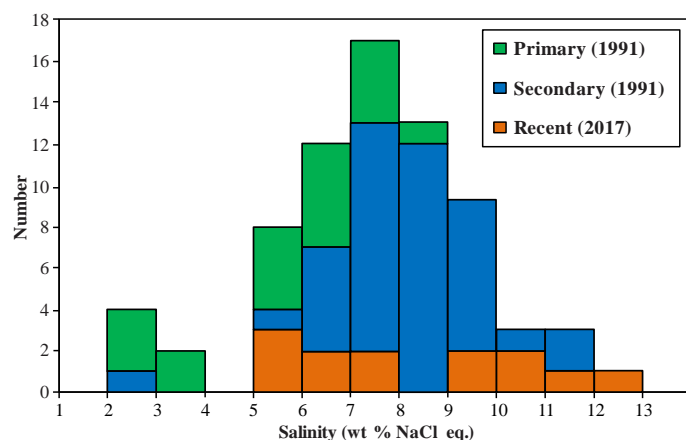
Figure 2. Histogram of microthermometric data showing the distribution of measured salinities (weight % NaCl equivalent). Includes both previous work (Peter and Scott, 1993) and this study.
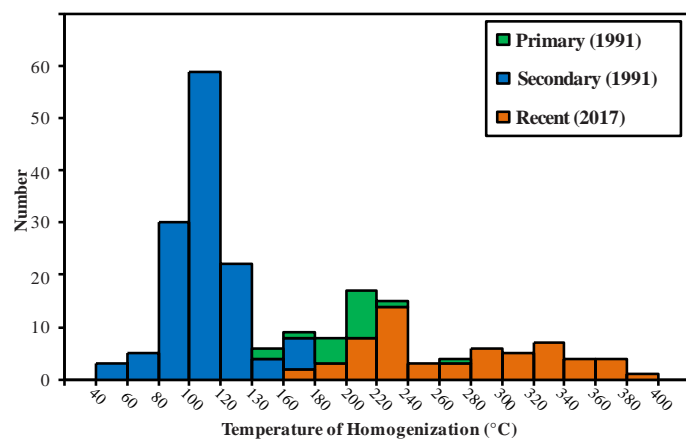
Figure 3. Histogram of microthermometric data showing the distribution of measured temperatures of homogenization. Includes both previous work (Peter and Scott, 1993) and this study.
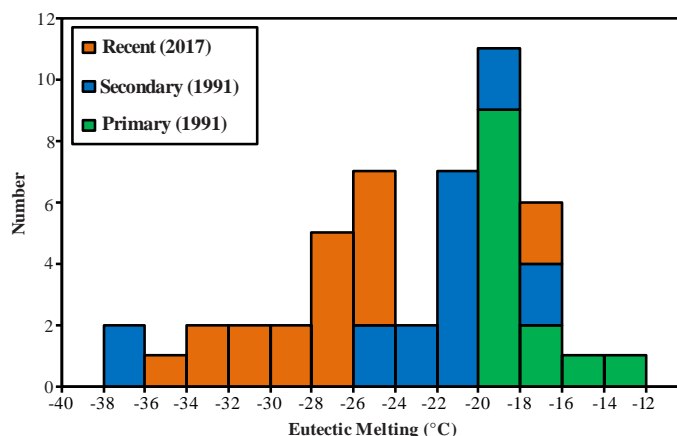
Figure 4. Histogram of microthermometric data showing the distribution of measured first melts (eutectic melting). Includes both previous work (Peter and Scott, 1993) and this study.

ing that the fluids did not boil at the time of entrapment. This is consistent with the observations of Peter and Scott (1993). The secondary inclusions are defined primarily by their occurrence along fractures and planes crossing growth features in the quartz. They range in size from 1 to 16 μm, are oval and circular in cross section. The secondary inclusions have varying L/V ratios from 5 to 100% (monophase liquid). There is a large abundance of monophase inclusions (Fig. 1c) present in the samples. The monophase inclusions are not useful for salinity measurements. However, a few two-phase (liquid-vapour) inclusions may occur within a particular cluster of monophase inclusions. No daughter minerals were observed within any of the inclusions.

Microthermometry

Additional microthermometric measurements beyond those of Peter and Scott (1993) were made on 22 inclusions. The salinities of these range from 6.2 to 12.2 weight % NaCl equivalent (Fig. 2), and the homogenization temperatures range from 115 to 234°C (Fig. 3). First melting temperatures (eutectic melting) range from -20 to -39.6°C (Fig. 4). The microthermometric observations of the L-V inclusions agree closely with the ice melting in the monophase inclusions. Therefore, salinity data for these monophase liquid inclusions are deemed to be representative of this population of inclusions as a whole.

Laser Ablation

Laser ablation-ICP-MS was performed on 19 inclusions for which there are salinity data. Due to the discrepancies between the calculated salinities and measured salinities only 17 inclusions remain in the data set (see above for discussion). Table 2 provides a summary of the results. Sodium, K, Ca, Cu, Sr, Sn, Sb, Ba, and Pb consistently give well-defined peaks that permit quantification. Lithium, B, Si, S, As, Se, Br, Mo, Cd, Te, Cs, Mg and Ti did not return usable values.

Discussion

Our additional microthermometric measurements fall within the same first melting temperature, homogenization temperature and salinity ranges as those of Peter and Scott (1993) (Figs. 2–4). The similarities in the data (Fig. 3) indicate that both primary and secondary inclusion populations are represented in our new data. The new (additional) homogenization temperatures demonstrate relatively low fluid temperatures for a typical VMS deposit. Conversely, the recorded salinities in this study and that of Peter and Scott (1993) are relatively elevated compared to a typical VMS deposit (Bodnar et al., 2014).

The salinities recorded in this study plot mostly within the lower salinity fluids observed by Peter and Scott (1993) (Fig. 2). The observed first melting temperatures (Fig. 4) are not consistent with a NaCl – H_2O system. The NaCl-H_2O system has a eutectic of -21.2°C (Bodnar, 2003). The addition of KCl to the NaCl-H_2O system depresses the eutectic to -22.9°C (Bodnar, 2003). The addition of $CaCl_2$ to the NaCl – H_2O system depresses the eutectic to -52°C (Bodnar, 2003). The first melting temperatures measured in this study suggest the influence of other salts including KCl and $CaCl_2$, consistent with the geochemistry of the ablated inclusions (see below). Comparison of the concentrations of the major cations (LA-ICP-MS) to the
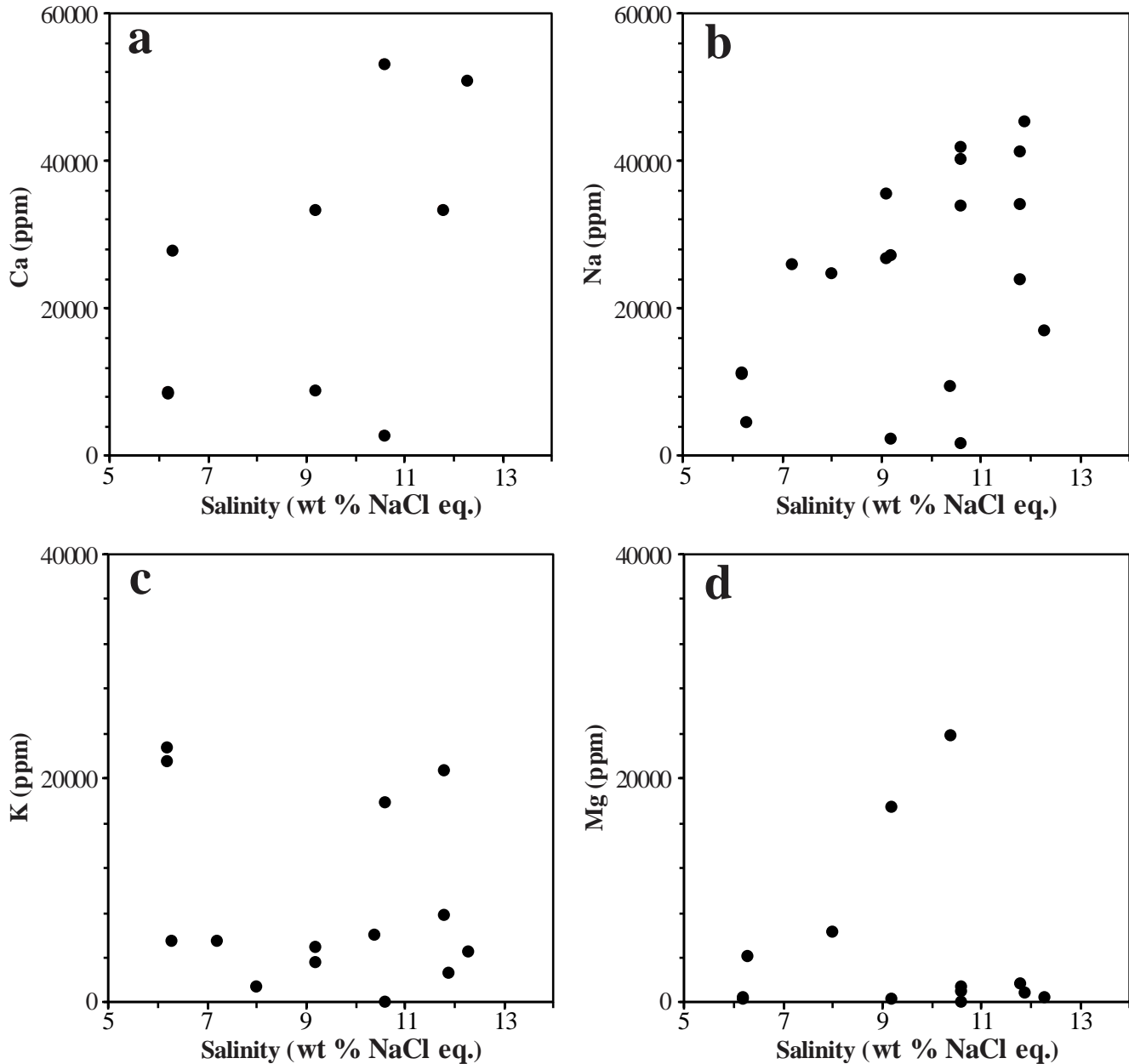

Figure 5. Bivariate plots of salinity (weight % NaCl equivalent) determined by microthermometry versus the major cations determined by LA-ICP-MS: a) Ca; b) Na; c) K; d) Mg.
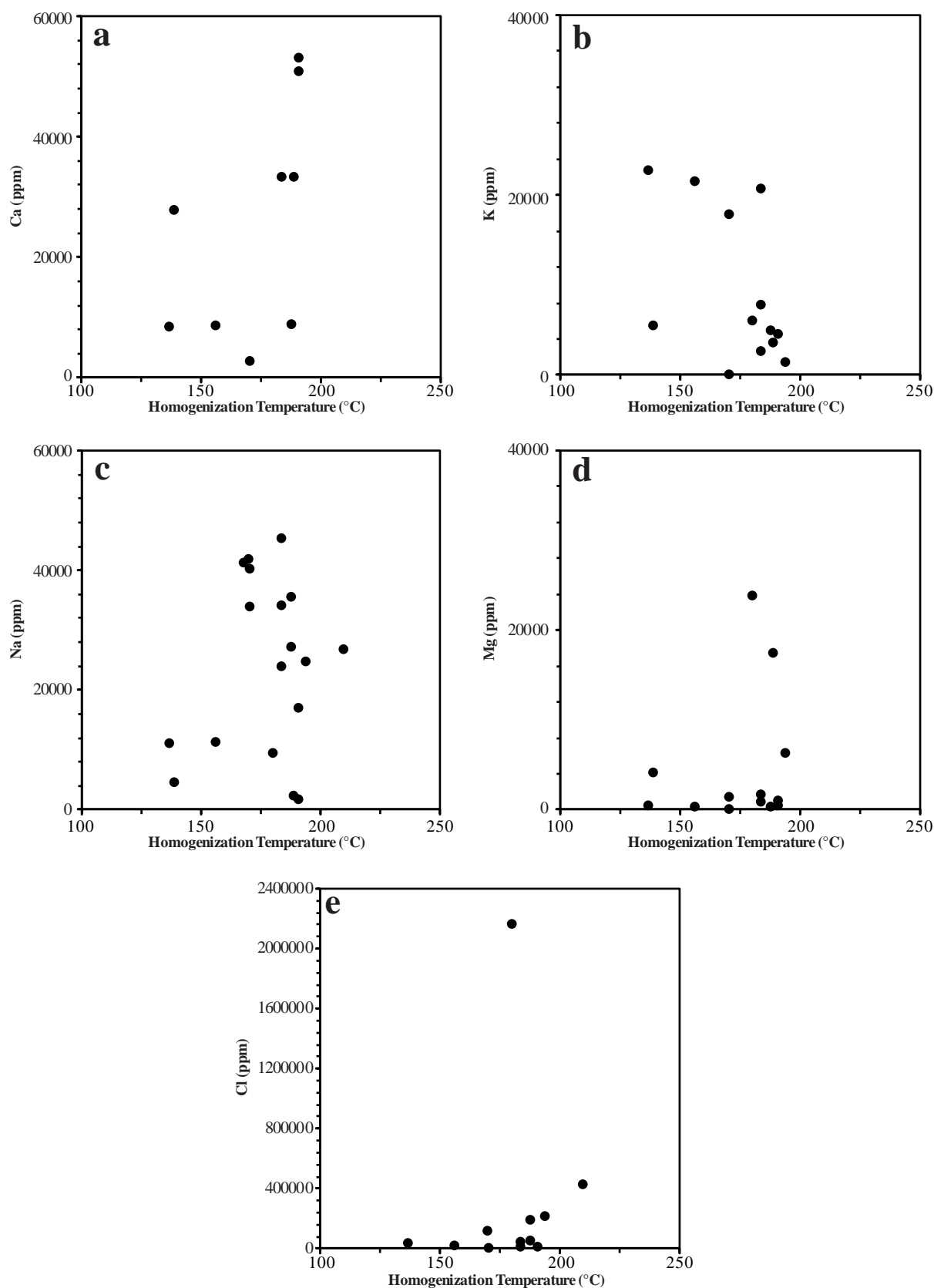
Figure 6. Bivariate plots of fluid inclusion homogenization temperature versus the major cations and Cl, as determined by LA-ICP-MS: a) Ca; b) K; c) Na; d) Mg; e) Cl.

Table 2. Microthermometric and LA-ICP-MS data for the 19 fluid inclusions in the present study. ND indicates that the element was not detected. Li, B, Si, S, As, Se, Br, Mo, Cd, Te, Cs, Mg and Ti were not detected in any of the inclusions analyzed.

Sample #	1st Melt (°C)	Salinity (wt.% eq. NaCl)	Homogenization Temperature	Na^{23} (ppm)	Mg^{25} (ppm)	Cl^{35} (ppm)	K^{39} (ppm)	Ca^{42} (ppm)	Mn^{55} (ppm)	Fe^{57} (ppm)	Co^{59} (ppm)	Cu^{65} (ppm)	Zn^{66} (ppm)	Rb^{85} (ppm)	Sr^{88} (ppm)	Ag^{109} (ppm)	In^{115} (ppm)	Sn^{118} (ppm)	Sb^{121} (ppm)	Ba^{137} (ppm)	Ce^{140} (ppm)	W^{182} (ppm)	Au^{197} (ppm)	Pb^{208} (ppm)	Bi^{209} (ppm)
MR20A07	-29	6.2	128	11238	312	17769	21509	ND	ND	417	ND	314	225	15	15	ND	ND	6.7	ND	4.3	0.9	ND	ND	271	ND
MR20A08	-31	6.2	115	10939	439	29219	22730	ND	122	ND	ND	303	329	11	23	39	ND	ND	ND	ND	ND	ND	ND	491	ND
MR20A09	-31	6.3	117	4515	4121	ND	5489	27604	83	ND	ND	8490	ND	14	18	4.2	ND	31	59	17	ND	ND	8.9	2.4	5801	ND
MR20B07	-20	10.4	150	9421	23786	2162430	5977	ND	ND	3488	ND	127	4734	ND	28	ND	ND	1029	ND	ND	ND	ND	ND	ND	2866	ND
MR20B08	-21	8	169	24634	6259	214799	1361	ND	ND	3370	ND	63	ND	ND	19	18	ND	ND	11	37	ND	ND	ND	ND	375	ND
MR20B09	-33	10.6	165	1615	892	ND	ND	53056	ND	ND	2.2	ND	ND	ND	3.7	ND	1.6	ND	ND	4.5	ND	ND	ND	ND	201	0.62
MR21C07	-39.6	11.8	137	41110	ND	ND	ND	ND	ND	11895	ND	ND	ND	ND	ND	ND	ND	ND	ND	ND		ND	ND	ND	ND	ND
MR21C08	-34	11.8	155	34123	1654	ND	20652	ND	328	ND	ND	682	699	ND	42	66	ND	ND	ND	ND	138	ND	ND	ND	2969	ND
MR21C09	-34	11.8	155	23849	ND	ND	7745	33266	ND	3469	ND	199	624	14	163	ND	ND	49	ND	62	ND	ND	ND	520	ND	ND
MR21C10	-33	11.9	155	45302	ND	7654	2520	ND	ND	ND	ND	21	ND	ND	43	ND	ND	43	ND	199	ND	ND	ND	51	ND	ND
MR21C11	-37.5	12.3	163.9	16854	371	4799	4511	50827	26	4197	0.73	147	30	4.8	45	ND	4.4	11	15	111	18	1.9	33	606	ND
MR22C07	-31	9.2	160	27111	ND	185735	4878	8823	58	4990	18	163	7272	ND	16	ND	1.1	195	10	41	1.4	ND	ND	698	ND
MR22C08	-31	9.2	161	ND	17429	ND	3499	33299	ND	2397	ND	824	ND	ND	13	ND	ND	74	17	ND	ND	ND	ND	8967	ND
MR22C09	-31	9.1	160	35348	ND	ND	ND	ND	ND	345	ND	ND	ND	ND	ND	ND	ND	67	ND	ND	ND	ND	ND	2124	ND
MR23A07	-28	10.6	140.6	40219	13	2826	44	2671	ND	ND	ND	26	5.1	0.14	0.19	ND	ND	ND	0.16	1.1	ND	1.1	ND	31	ND
MR23A08	-28	10.6	140	41700	ND	ND	ND	ND	ND	ND	ND	ND	2742	ND	ND	ND	ND	ND	ND	ND	ND	ND	ND	ND	ND
MR23A09	-28	10.6	140.6	33749	1280	ND	17808	ND	2859	ND	ND	308	ND	ND	ND	ND	ND	62	18	ND	ND	ND	ND	14361	ND
MR23B07	-36	7.2	234	25840	ND	39226	5428	ND	ND	ND	ND	172	ND	ND	ND	ND	ND	ND	ND	ND	ND	ND	ND	219	ND
MR23B08	-29.7	9.1	185	ND	ND	ND	ND	ND	ND	20368	ND	ND	1172	ND	ND	ND	ND	ND	ND	ND	ND	ND	ND	ND	ND

salinities (NaCl weight % equivalent determined by microthermometry) reveals an agreement between Ca (Fig. 5a), Na (Fig. 5b) and salinity giving r_s (spearman rank correlation) of 0.53 (n = 9) and 0.46 (n = 17), respectively. This indicates that the dominant cations are Ca and Na. Potassium and Mg are also present in the inclusion fluids, but they show weak to no correlation with salinity (Fig. 5c, d). Due to the difficulty of analyzing for Cl and the high detection limits (approximately 7500 ppm), correlation of Cl with salinity is not possible. Comparison of the concentrations of the major cations (Na, K, Ca, Mg; LA-ICP-MS) to the temperature of homogenization reveals a correlation between Ca, K and T_h (Fig. 6a, b) giving $r_s = 0.67$ (n = 9) and $r_s = 0.60$ (n = 14) respectively. High Ca values are associated with higher Th values and higher K values are associated with lower T_h values. Sodium, Mg, and Cl all show poor correlations with T_h (Fig. 6c–e). Comparison of the temperature of homogenization and salinity values for our new data and previous (Peter and Scott, 1993) microthermometric data

Figure 7. Bivariate plot of fluid inclusion homogenization temperature versus salinity (weight % NaCl equivalent).

reveal two, and possibly three, unique groupings within the data (Fig. 7).

A ternary of the relative concentrations in ppm of K-Na-Ca (Fig. 8) shows that the low temperature, low salinity fluids are primarily Na-K fluids, whereas the higher salinity fluids are primarily Na-Ca in composition. Based on the observations made by Peter and Scott (1993), secondary fluids have a temperature range of 60 to 180°C whereas primary fluids have a temperature range of 160 to 380°C. Inclusions with elevated K are confined to fluids < 170°C, which indicates that K occurs primarily in secondary inclusion fluids.

Trace elements of potential magmatic origin (Au, W, Sn, In, Bi) are present in the inclusion fluids (Table 2). Tin is present in 9 of the 17 inclusions analyzed, and although Sn is considered to be a magmatic element when associated with felsic melts, there is no evidence of felsic or intermediate rocks in the deposit stratigraphy. The abundance of Sn is around 2.5 ppm in the Earth's continental crust and 6 ppm in shales (Taylor and McLennan, 1986). In oceanic rocks, such as N-MORB, Sn concentration ranges between 0.8 and 1.36 ppm (Taylor and McLennan, 1986; Anderson, 1989; Sun and McDonough, 1989). However, Sn is also noted in seafloor sulphides in ultramafic rocks (Evrard et al., 2015), and magmatic Sn in a mafic environment is possible. Tin is also commonly present in modern seafloor sulphide deposits in sedimentary settings (e.g. Escanaba Trough) and in sediment hosted deposits such as SEDEX (e.g. Sullivan; Pentland, 1943; Campbell et al., 1980). In sedimentary settings, Sn enrichment in the sulphides is typically attributed to leaching from sediments by circulating hydrothermal fluids (see Hamilton, 1984). Due to the multiple possible sources of Sn, we are focusing on other potential magmatic elements (Au, Bi, In) that are less likely to be leached from sediments underlying the Windy Craggy deposit.

At present, our data are too few to make concrete conclusions. We require additional microthermometric data and LA-ICP-MS data for those same inclusions. Considering the small sample size of 19 inclusions, detection of most of the elements
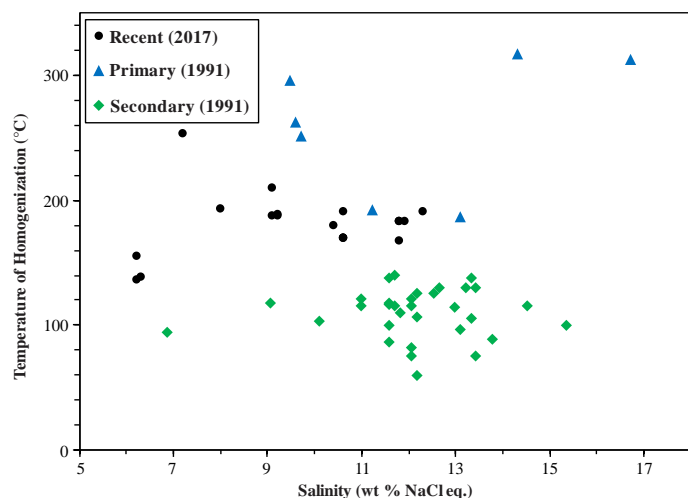
of interest in the inclusions is promising, although further analyses are needed to confirm these observations.

Future Work

Additional microthermometric work will be performed at Queen's University in preparation for additional LA-ICP-MS work at the Geological Survey of Canada LA-ICP-MS laboratory in Ottawa. Due to the discrepancies in the trace element data, further work needs to be done to establish a larger data set of analyzed fluid inclusions with detailed microthermometric data. Changes to the ablation parameters may be required, together with restriction of the number of elements determined.

A more encompassing understanding of the hallmarks of a magmatic signal in seafloor hydrothermal systems (in all magmatic affinities) needs to be developed. Key distinguishing features need to be isolated to distinguish between a magmatic source and hydrothermal fluid that originated from seawater and subsequently modified by water-rock interaction.

Laser ablation-ICP-MS analysis of the sulphide phases present in the fluid inclusion and mineralization samples will be done. The intention is to document residence sites of magmatic metals and metalloids including Sn, In and Au. This will give a better definition of the composition of the mineralizing fluids and assist in classifying the various fluids present in the inclusions.

In the coming months, further work will be done on method development. Various operating parameters of the laser (i.e. fluence, repetition rate) will be altered and tested with the goal of ablating the host mineral (quartz) to obtain a matrix signal. This will allow for a proper matrix correction to be performed in SILLS with the intention of obtaining accurately reduced trace element data.

Acknowledgments

References

Anderson, D.L., 1989. Where on Earth is the crust?; Physics Today, v. 42, p. 38-46.

Audetat, A., Gunther, D., Heinrich, C.A., 1998. Formation of a magmatic-hydrothermal ore deposit: insights with LA-ICP-MS analysis of fluid inclusions. Science, v. 279, p. 2091–2094.

Bischoff, J.L., Rosenbauer, R.J., 1985. An empirical equation of state for hydrothermal seawater (3.2 percent NaCl); American Journal of Science, v. 285, p. 725–763.

Bodnar, R., 1994. Synthetic fluid inclusions: XII. The system H_2O-NaCl. Experimental determination of the halite liquidus and isochores for a 40 wt% NaCl solution; Geochimica et Cosmochimica Acta, v. 58, p. 1053-1063.

Bodnar, R.J., 2003. Introduction to aqueous-electrolyte fluid inclusions; *in* Fluid Inclusions Analysis and Interpretation, (ed.) I. Samson, A. Anderson and D. Marshall; Mineralogical Association of Canada, Short Course Series, v. 32, p. 81–100.

Bodnar, R.J., Lecumberri-Sanchez, P., Mocada, D., and Steele-MacInnis, M., 2014. Fluid inclusions in hydrothermal ore deposits; *in* Geochemistry of Mineral Deposits. Treatise of Geochemistry, 2nd Edition, (ed.) S.D. Scott; Elsevier, p. 119–142.

Cabri, L. and Jackson, S., 2011. New developments in characterization of sulfide refractory Au ores: Proceeding of MetSoc; *in* World Gold 2011, 50th Conference of Metallurgists. Montreal, Quebec, p. 51–62.

Campbell, R.B. and Dodds, C.J., 1979. Operation Saint Elias, British Columbia; Geological Survey of Canada Paper 79-1A, p. 17–20.

Campbell, R.B. and Dodds, C.J., 1983. Geology of Tatshenshini River Map Area (114P), British Columbia; Geological Survey of Canada Open File 926, scale, 1:125 000.

Campbell, F.A., Ethier, V.G. and Krouse, H.R., 1980. The massive sulfide zone: Sullivan orebody; Economic Geology v. 75, p. 916–926.

Coumou, D., Driesner, T., Weis, P., and Heinrich, C.A., 2009. Phase separation, brine formation, and salinity variation at Black Smoker hydrothermal systems; Journal of Geophysical Research, v. 114, B03212.

de Ronde, C.E.J., 1995. Fluid chemistry and isotopic characteristics of seafloor hydrothermal systems and associated VMS deposits: potential for magmatic contributions; *in* Mineralogical Association of Canada Short Course Series 23, (ed.) J.F.H. Thompson; Ottawa, Ontario, p. 479–510.

Downing, B.W., Webster, M.P., and Beckett, R.J., 1991. The Windy Craggy Massive - Sulphide Deposit northwestern British Columbia, Canada; *in* Mineral Deposits of the northern Canadian Cordillera, Yukon, (ed.) J.G. Abbott and R.J.W. Turner; Geological Survey of Canada, Open File 2169, p. 31–36.

Evrard, C., Fouquet, Y., Moëlo, Y., Rinnert, E., Etoubleau, J., and Langlade, J.A., 2015. Tin concentration in hydrothermal sulphides related to ultramafic rocks along the Mid-

Atlantic Ridge: A mineralogical study; European Journal of Mineralogy, v. 27, p. 627–638.

Gagnon, J., Samson, I., and Fryer, B., 2003. Laser ablation ICP-MS analysis of fluid inclusions; *in* Fluid Inclusions: Analysis and Interpretation, Mineralogical Association of Canada Short Course Series 32, (ed.) I. Samson, A. Anderson and D. Marshall; Mineralogical Association of Canada, Québec, Quebec, p. 291-322.

Guillong, M., Meier, D.L., Allan, M.M., Heinrich, C.A., and Yardley, B.W.D., 2008. SILLS: A Matlab-based program for the reduction of laser ablation ICP–MS data of homogeneous materials and inclusions; Mineralogical Association of Canada Short Course Series, v. 40, p. 328–333.

Hamilton, J.M., 1984. The Sullivan deposit, Kimberley, British Columbia - A magmatic component to genesis?; The Belt, Montana Bureau of Mines and Geology, Special Publication 90, p. 58–60.

Hedenquist, J.W. and Lowenstern, J.B., 1994. The role of magmas in the formation of hydrothermal ore deposits; Nature, v. 370, p. 519–527.

Huston, D., Relvas, J., Gemmell, J., and Drieberg, S., 2011. The role of granites in volcanic-hosted massive sulphide ore-forming systems: an assessment of magmatic-hydrothermal contributions; Mineralium Deposita, v. 46, p. 473–507.

MacIntyre, D.G., 1984. Geology of the Alsek-Tatshenshini Rivers Area (114P); Geological Fieldwork 1983, B.C. Ministry of Energy, Mines and Petroleum Resources Paper 1984, p. 173–184.

Mungall, J.E., Andrews, D.R.A., Cabri, L.J., Sylvester, P.J., and Tubrett, M., 2005. Partitioning of Cu, Ni, Au, and platinum-group elements between monosulfide solid solution and sulfide melt under controlled oxygen and sulfur fugacities; Geochimica et Cosmochimica Acta v. 69. p. 4349–4360.

Norman, M.D., Pearson, N.J., Sharma, A., Griffin, W.L., 1996. Quantitative analysis of trace elements in geological materials by laser ablation ICPMS: Instrumental operating conditions and calibration values of NIST glasses; Journal of Geostandards and Geoanalysis v. 20, p. 247–261.

Orchard, M.J., 1986. Conodonts from western Canadian Chert: Their nature, distribution and stratigraphic application; *in* Conodonts: Investigative techniques and applications, (ed.) R.L. Austin; Ellis Horwood Ltd. for British Micropaleontological Society, Chichester, UK, p. 94–119.

Pentland, A., 1943. Occurrence of tin in the Sullivan Mine; Transactions of the Canadian Institute of Mining and Metallurgy, v. 46, p. 17–22.

Peter, J.M., 1992. Comparative geochemical studies of the Upper Triassic Windy Craggy and modern Guaymas Basin deposits: A contribution to the understanding of massive sulfide formation in volcano-sedimentary environments; Ph.D. thesis, University of Toronto, Toronto, Ontario, 562 p.

Peter, J.M. and Scott, S.D., 1993. Fluid inclusion and light stable isotope geochemistry of the Windy Craggy Besshi-type massive sulfide deposit, northwestern British Columbia; Resource Geology Special Issue, v. 17, p. 229–248.

Peter, J.M. and Scott, S.D., 1999. Windy Craggy, northwestern British Columbia: The world's largest Besshi-type deposit; *in* Volcanic-Associated Massive Sulfide Deposits: Processes and Examples in Modern and Ancient Settings, (ed.) C.T. Barrie and M.D. Hannington; Reviews in Economic Geology, v. 8, p. 261–295.

Peter, J.M., Leybourne, M.I., Scott, S.D., and Gorton, M.P., 2014. Geochemical constraints on the tectonic setting of basaltic host rocks to the Windy Craggy Cu-Co-Au massive sulfide deposit, northwestern British Columbia; International Geology Review, v. 56, p. 1484-1503.

Peter, J.M., Jackson, S.E., Leybourne, M.I., Kontak, D.J., McClenaghan, M.B., Layton-Matthews, D., and Taylor, B.E., 2017. Fingerprinting fluid source regions and pathways of volcanogenic massive sulphide deposits; in Targeted Geoscience Initiative – 2016 Report of Activities, (ed.) N. Rogers; Geological Survey of Canada, Open File 8199, p. 129–131.

Piperov, N.B. and Penchev, N.P., 1973. A study on gas inclusions in minerals. Analysis of the gases from micro-inclusions in allanite; Geochimica et Cosmochimica Acta, v. 37, p. 2075–2097.

Ramboz, C., Oudin, E., and Thisse, Y., 1988. Geyser-type discharge in Atlantis II Deep, Red Sea: Evidence of boiling from fluid inclusions in epigenetic anhydrite; Canadian Mineralogist, v. 26, p. 765–786.

Roedder, E., 1972. Composition of Fluid Inclusions; U.S. Geological Survey Professional Paper, v. 440JJ, p. 1689–1699.

Roedder, E., 1984. Fluid Inclusions: Reviews in Mineralogy, v. 12; Mineralogical Society of America, Washington D.C., 644 p.

Shanks, W.C.P. and Koski, R.A., 2012. Introduction: Volcanogenic massive sulfide occurrence model, *in* U.S. Geological Survey Scientific Investigations Report 2010-5070-C, p. 167–180.

Seyfried, W.E., Jr., Berndt, M.E., and Janecky, D.R., 1986. Chloride depletions and enrichments in seafloor hydrothermal fluids: Constraints from experimental basalt alteration studies; Geochimica et Cosmochimica Acta, v. 50, p. 469–475.

Stanton, R.L., 1990. Magmatic evolution and the ore type-lava type affiliations of volcanic exhalative ores; *in* Geology and Mineral Deposits of Australian and Papua New Guinea, Australasian Institute of Mining and Metallurgy Monograph 14, p. 101–108.

Stanton, R.L., 1994. Ore Elements in Arc Lavas; Oxford University Press, New York, New York, 391 p.

Sun, S.-S. and McDonough, W.F., 1989. Chemical and isotopic systematics of oceanic basalts: implications for mantle

composition and processes; in Magmatism in the Ocean Basins, (ed.) A.D. Saunders and M.J. Norry; Geological Society of London Special Publication 42, London, UK, p. 313–345.

Taylor, S.R. and McLennan, S.M., 1985. The Continental Crust: Its composition and evolution; Blackwell Scientific Publications, Oxford, UK, 312 p.

Taylor, C.D., Premo, W.R., Meier, A.L., and Taggart, J.E., 2008. The metallogeny of Late Triassic rifting of the Alexander terrane in southeastern Alaska and northwestern British Columbia; Economic Geology, v. 103, p. 89–115.

Vanko, D.A., Bach, W., Roberts, S., Yeats, C.J., and Scott, S.D., 2004. Fluid inclusion evidence for subsurface phase separation and variable fluid mixing regimes beneath the deep-sea PACMANUS hydrothermal field, Manus Basin back arc rift, Papua New Guinea; Journal of Geophysical Research Solid Earth, v. 109, 14 p.

Welhan, A.J., 1987. Methane and hydrogen in mid-ocean-ridge basalt glasses: Analysis by vacuum crushing; Canadian Journal of Earth Sciences, v. 25, p. 155–167.